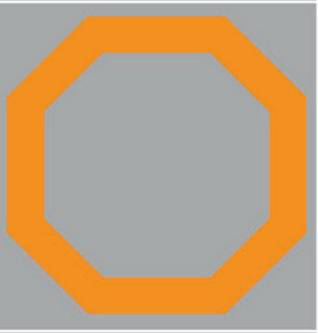

J.-C.G. Bünzli and V.K. Pecharsky
Editors

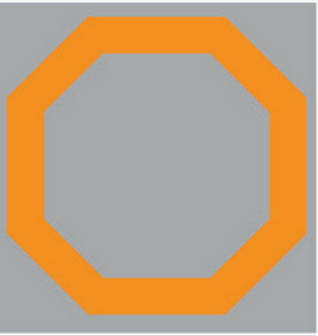

HANDBOOK ON THE
PHYSICS AND CHEMISTRY OF

RARE EARTHS

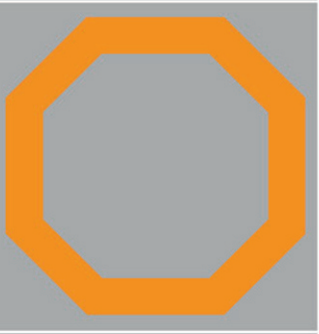

Volume 43

North-Holland

Including Actinides

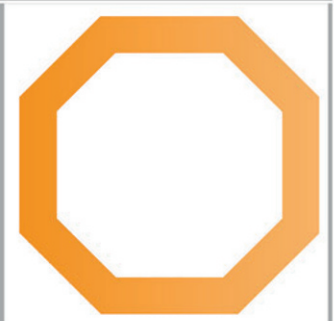

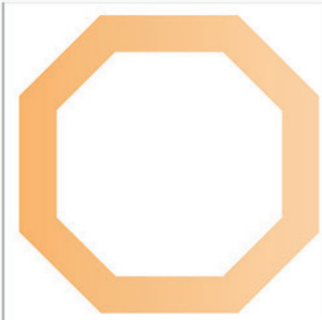

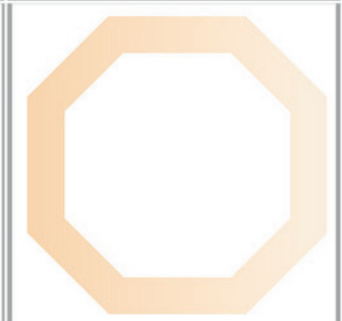

Handbook on the Physics and Chemistry of Rare Earths

Including Actinides

Volume 43

HANDBOOK ON THE PHYSICS AND CHEMISTRY OF RARE EARTHS

Including Actinides

Handbook on the Physics and Chemistry of Rare Earths

Including Actinides

Volume 43

Editors

Jean-Claude G. BÜNZLI
Swiss Federal Institute of Technology, Lausanne (EPFL)
Institute of Chemical Sciences and Engineering
BCH 1402
CH-1015 Lausanne
Switzerland

Vitalij K. PECHARSKY
The Ames Laboratory, U.S. Department of Energy, and
Department of Materials Science and Engineering
Iowa State University
Ames, Iowa 50011-3020
USA

ELSEVIER

Amsterdam • Boston • Heidelberg • London • New York • Oxford
Paris • San Diego • San Francisco • Singapore • Sydney • Tokyo
North-Holland is an imprint of Elsevier

North-Holland is an imprint of Elsevier
Radarweg 29, PO Box 211, 1000 AE Amsterdam, The Netherlands
The Boulevard, Langford Lane, Kidlington, Oxford OX5 1GB, UK

British Library Cataloguing in Publication Data
A catalogue record for this book is available from the British Library

Library of Congress Cataloging-in-Publication Data
A catalog record for this book is available from the Library of Congress

ISBN: 978-0-444-59536-2
ISSN: 0168-1273

Printed and Bound in Great Britain

13 14 15 12 11 10 9 8 7 6 5 4 3 2 1

Preface

Jean-Claude G. Bünzli and Vitalij K. Pecharsky

These elements perplex us in our reaches [sic], baffle us in our speculations, and haunt us in our very dreams. They stretch like an unknown sea before us—mocking, mystifying, and murmuring strange revelations and possibilities.

Sir William Crookes (February 16, 1887)

Volume 43 of the *Handbook on the Physics and Chemistry of Rare Earths* adds five chapters to the series, which span a broad range of subjects, from liquid-crystalline materials to extraction and separation from actinides, recycling technologies, and structural and thermodynamic properties of the elements. The volume is therefore in tune with some of the present concerns about worldwide rare earth supplies. Chapter 254 is devoted to lanthanidomesogens, which are lanthanide complexes with liquid-crystalline properties and/or lanthanide-doped liquid crystals. Lanthanidomesogens combine the exceptional luminescent or magnetic properties of lanthanide ions with the peculiar features of liquid crystals, anisotropy and response to electric and magnetic fields, for instance. The various liquid-crystalline phases are described for each category of compounds, as well as the experimental methods for characterizing them. The less-documented field of actinidomesogens is also covered. Chapter 255 deals with recycling of the rare earths, presently a hot topic in view of the limited availability of some of the critical elements and, also, of the rising environmental cost of extracting and separating rare earths. Reprocessing of permanent magnets, lamp and screen phosphors, nickel metal hydride batteries, and polishing powders is described. Classical technologies such as physical separation, hydrometallurgy, and pyrometallurgy are detailed, along with emerging techniques such as high-gradient magnetic separation. Difficulties inherent to each class of recyclable materials are pointed out and solutions outlined. In a way, Chapter 256 complements the preceding one in critically assessing the potential of ionic liquids as new extractant agents for the separation of lanthanides and of lanthanides from actinides in the context of nuclear waste management. Ionic liquids present advantages over classical solvents in that they are more resistant to radioactive damage, have very low vapor pressure, and are highly tunable with regard to their physical and chemical properties. The review carefully assesses the potential of ionic liquids in liquid–liquid extraction compared to conventional solvents,

either as replacement solvents or additives and ends with a mechanistic description of extraction in ionic liquids. Chapter 257 focuses on structural changes induced in lanthanide elements by high hydrostatic pressure (up to about 200 GPa). Physical and chemical properties of the metals are governed by the nature of the 4f electrons, which, in turn, is sensitive to pressure: at high compression, the 4f shell delocalizes and participates in bonding, hence influencing crystal structures. The chapter details element by element the structural studies carried out over the last decade. The volume concludes with a comprehensive and critical compilation of the thermodynamic properties of all rare earth elements. Selected best values for heat capacity, enthalpy and entropy of formation, melting temperature, boiling point, enthalpy and entropy of melting, as well as sublimation enthalpy are listed element by element (Chapter 258). The availability of high-purity metals renders these values quite trustable; however, some areas for which further measurements are required are identified and experiments suggested.

CHAPTER 254. LANTHANIDOMESOGENS

By KOEN BINEMANNS
Katholieke Universiteit Leuven, Belgium

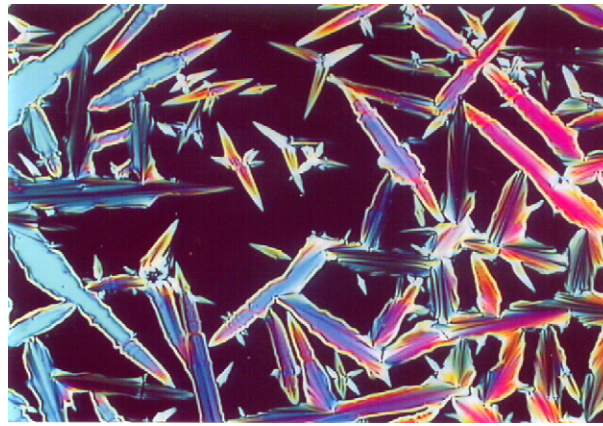

Liquid crystals (LCs) are a state of matter between liquid and solid and the corresponding compounds present at least two melting points, the first corresponding to the transition to the LC cloudy phase and the second being a clarification to pure liquid. Some LCs are seen in living systems; for instance, certain proteins and cell membranes are LCs. Technically, the properties of LCs are exploited in electronic displays (LCDs). Lanthanidomesogens can be defined as liquid-crystalline lanthanide complexes or lanthanide-containing LCs. These compounds combine the unique properties

of lanthanide ions, luminescence and paramagnetism, with those of LCs: fluidity, anisotropy, and response to electric and magnetic fields. Lanthanidomesogens allow obtaining materials that emit linearly polarized light or that can be aligned by an external magnetic field. The reader is first introduced to the different types of mesophases and to the experimental methods used for identifying them. A detailed presentation of the different classes of lanthanidomesogens is then given, with the focus on their structural, luminescent, magnetic, and electric properties. The classes of compounds reviewed include Schiff's base complexes, β-enaminoketonates, β-diketonates, bis(benzimidazolyl)pyridine complexes, phthalocyanine complexes, porphyrin complexes, lanthanide alkanoates, polyoxometalate-surfactant complexes, ionic liquid-crystalline lanthanide complexes, and lyotropic lanthanidomesogens. The chapter concludes with an overview of the less-documented actinide-containing LCs (actinidomesogens).

CHAPTER 255. RECYCLING OF RARE EARTHS FROM SCRAP

By MIKIYA TANAKA, TATSUYA OKI, KAZUYA KOYAMA, HIROKAZU NARITA AND TETSUO OISHI

National Institute of Advanced Industrial Science and Technology (AIST) Tsukuba, Ibaraki, Japan

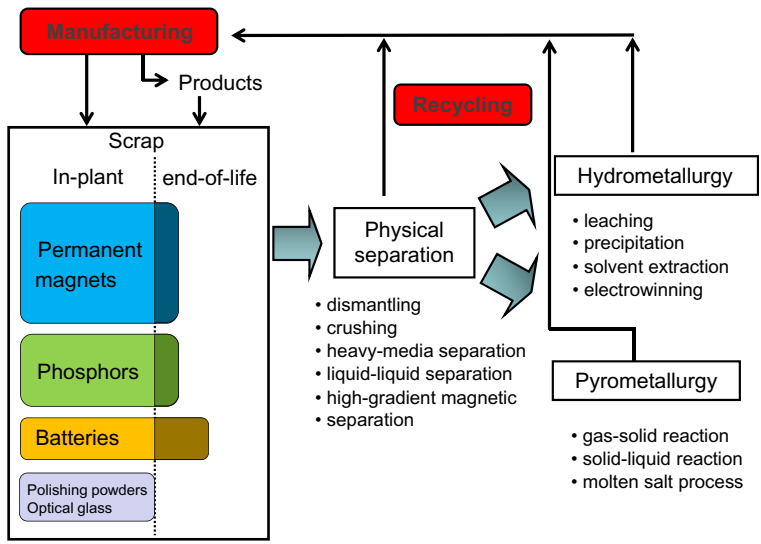

More and more attention is being paid to the recycling of rare earth elements from industrial scrap in order to help secure the supply of these elements, mostly because of their limited occurrence in minable primary resources and also because of the environmental concerns associated with mining and separation operations. The chapter presents a comprehensive review of the

technologies developed for the recycling of rare earth elements from industrial scrap such as permanent magnets, phosphors, metal hydride batteries, and polishing materials. The review will be useful as reference material for researchers and engineers active in rare earth and other metal recycling communities.

The current situation of rare earth supply, the industrial practice of rare earth recycling, and rare earth material flows are first summarized. Studies covering fundamental and practical aspects for each material are then systematically described with respect to (i) pretreatment processes such as crushing and magnetic separation, (ii) hydrometallurgical methods including leaching, precipitation, solvent extraction (classical and advanced), adsorption, and molten salt electrolysis, (iii) pyrometallurgical methods including chemical vapor transport and selective reduction–distillation, and (iv) uses of the recovered products.

Since neodymium magnets are the most important targets of rare earth recycling at present, the corresponding procedures are described in detail along with the problem of removing the large amount of iron (ca. 70%) present in these magnets.

CHAPTER 256. IONIC LIQUIDS: NEW HOPES FOR EFFICIENT LANTHANIDE/ACTINIDE EXTRACTION AND SEPARATION?

By ISABELLE BILLARD
CNRS/IN2P3 and Université de Strasbourg, France

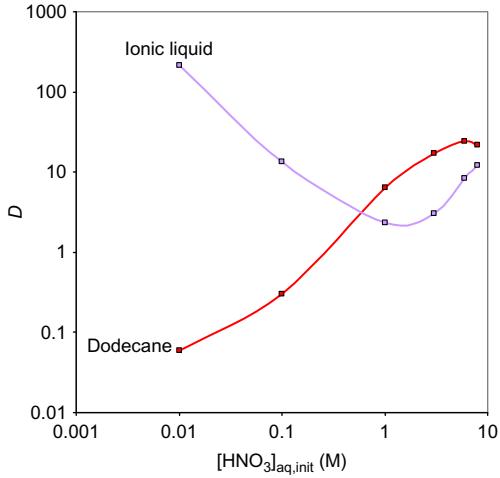

The cost induced by the off-shoring of rare earth mining and separation to China is generating a renewed interest in liquid–liquid extraction methods for these strategic elements. Moreover, recovery of actinides, in particular

uranium and plutonium, by liquid–liquid extraction processes from nuclear wastes is at the heart of the development of the nuclear industry. In this context, new methods and new extractants are being intensely sought, and ionic liquids could be an alternative to classical solvents. Ionic liquids are defined as salts with melting temperatures below 100 °C. They are at present of great interest in all fields of chemistry and materials science. Apart from their "green" properties, their resistance to radioactivity and amazing chemical versatility offer a new playground to f-element researchers and engineers.

Following a brief summary of rare earth extraction and liquid–liquid extraction of actinides using molecular solvents, the author reviews and discusses the main properties of ionic liquids that are of importance to liquid–liquid extraction. The various ways in which ionic liquids are used for the extraction/separation of rare earths and actinides either as replacement solvents or as simple additives are then critically reviewed. The focus of the chapter is on the mechanisms of extraction in ionic liquids, and the differences between ionic liquids and molecular solvents are highlighted.

CHAPTER 257. STRUCTURE AND PROPERTIES OF LANTHANIDES AT ULTRA-HIGH PRESSURE

By GOPI K. SAMUDRALA AND YOGESH K. VOHRA
University of Alabama at Birmingham, USA

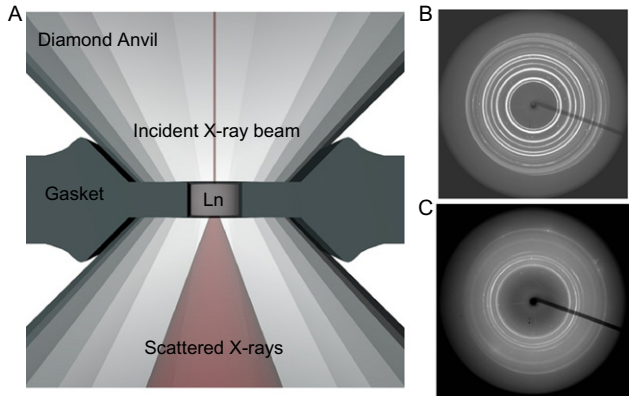

The nature of 4f electrons in lanthanides and their compounds, either "localized" or "itinerant," is responsible for most of their physical and chemical properties. Localized states corresponding to tightly bound electron shells or to narrow bands of correlated electrons near the Fermi level are observed for all lanthanides. Pressure has a striking effect on the electronic structure, which, in turn, induces structural changes. For instance, crystal structure transitions from hexagonal closed packed (*hcp*) → samarium type → double

hexagonal closed packed (*dhcp*) → face-centered cubic (*fcc*) → distorted-*fcc* phases (*dfcc*) are well established and documented at low and medium pressure. High pressure studies in diamond anvil cell devices have now been extended up to 200 GPa, a pressure at which a reduction of 70% in unit cell volume is documented. The chapter reviews structural studies conducted under high pressure for each lanthanide element over the past decade. They reveal that (i) the stability of the *fcc* phase is limited for some of the heavy lanthanides, (ii) the nature of the distorted-*fcc* phase is finally established—the best fits to the available data indicate that it is rhombohedral with 24 atoms/unit cell, and (iii) the latter phase usually transforms at ultra-high pressure into a low-symmetry monoclinic *C*2/*m* phase, signaling participation of 4f electrons in bonding, as inferred from the increasing transition pressure with increasing number of 4f electrons.

CHAPTER 258. SELECTED VALUES OF THE THERMODYNAMIC PROPERTIES OF SCANDIUM, YTTRIUM, AND THE LANTHANIDE ELEMENTS

By JOHN W. ARBLASTER
Poolhouse Farm, West Midlands, United Kingdom

Thermodynamic parameters of elements are basic information much needed for both theoretical and practical studies. Gathering such parameters for the rare earth metals has long been cumbersome in view of the difficulty in getting highly pure materials. Present-day separation and purification techniques, however, yield rare earth metals with less than 10 ppm impurities from other R elements while nonmetallic impurities are reduced to less than 300 ppm. This leads to highly trustable experimental data, especially in the low temperature range. At the beginning of this contribution, a short section summarizes the melting points, upper transition temperatures, analytical expressions, and partition functions adopted, as well as the method for calculating the nuclear heat capacities. The core of the chapter lists the selected best values for heat capacity, enthalpy and entropy of formation, melting temperature, boiling point, enthalpy and entropy of melting, as well as vapor pressure and sublimation enthalpy, element by element. Interpolated data for radioactive promethium are included. The chapter is unique in that (i) the low temperature thermodynamic data (below 298.15 K) are given in complete detail, (ii) in the high temperature region, thermodynamic functions for the condensed phases are not only tabulated but also fully described by analytical equations, including estimated values for promethium, (iii) free energy equations are given separately for consideration of phase stability, (iv) vapor pressure data have been thoroughly reviewed in order to arrive at recommended values for the enthalpies of sublimation, (v) for each element, vapor pressure curves are described by equations for both the solid and liquid phases allowing vapor

pressure values to be easily calculated at any temperature within the limits of the equations. Whenever possible, thermodynamic values are corrected to the 2009 atomic weights. Areas for which further measurements are required are identified and further experiments suggested.

Intentionally left as blank

Contents

Intentionally left as blank

Contents of Volumes 1–42

VOLUME 7

1984; ISBN 0-444-86851-8

VOLUME 8

1986; ISBN 0-444-86971-9

VOLUME 9

1987; ISBN 0-444-87045-8

VOLUME 10: High energy spectroscopy

1987; ISBN 0-444-87063-6

VOLUME 11: Two-hundred-year impact of rare earths on science
1988; ISBN 0-444-87080-6

VOLUME 12
1989; ISBN 0-444-87105-5

VOLUME 13
1990; ISBN 0-444-88547-1

VOLUME 18: Lanthanides/Actinides: Chemistry
1994; ISBN 0-444-81724-7

VOLUME 19: Lanthanides/Actinides: Physics – II
1994; ISBN 0-444-82015-9

VOLUME 35

2005; ISBN 0-444-52028-7

VOLUME 36

2006; ISBN 0-444-52142-9

VOLUME 37: Optical Spectroscopy

2007; ISBN 978-0-444-52144-6

VOLUME 38

2008; ISBN 978-0-444-52143-9

Index of Contents of Volumes 1–43

D

E

F

G

H

I

K

L

M

N

O

P

Q

R

S

T

U

V

X

Intentionally left as blank

Chapter 254

Lanthanidomesogens

Koen Binnemans
Department of Chemistry, KU Leuven – University of Leuven, P.O. Box 2404, Heverlee, Belgium

Chapter Outline

1. INTRODUCTION

Lanthanidomesogens can be defined as liquid-crystalline lanthanide complexes or lanthanide-containing liquid crystals (Piguet et al., 2006). *Liquid crystals* (LCs) are substances that are observed to flow like a liquid, but they also show the direction-dependent (anisotropic) physical properties of crystalline solids. LCs can be considered to be crystals in which the molecules have lost some or all of their positional order, while maintaining most of their

Handbook on the Physics and Chemistry of Rare Earths, Vol. 43.
http://dx.doi.org/10.1016/B978-0-444-59536-2.00001-5

orientational order. The main application of LCs is their use as the active substances in liquid crystal displays (LCDs). Research efforts to combine the properties of LCs and metal complexes have led to the development of liquid-crystalline metal complexes (*metallomesogens*, Bruce, 1993). The development of the field of metallomesogens has been described in several reviews (Binnemans, 2005c; Binnemans and Görller-Walrand, 2002; Bruce, 1996, 2000; Collinson and Bruce, 1999; Davidson and Gabriel, 2005; Donnio, 2002; Donnio and Bruce, 1999; Donnio et al., 2003; Espinet et al., 1992; Gabriel and Davidson, 2000, 2003; Giroud-Godquin, 1998; Giroud-Godquin and Maitlis, 1991; Hoshino, 1998; Hudson and Maitlis, 1993; Neve, 1996; Oriol and Serrano, 1995; Oriol et al., 1997; Polishchuk and Timofeeva, 1993; Serrano, 1996; Serrano and Sierra, 2003; Sonin, 1998). Lanthanidomesogens are a subclass of the metallomesogens. Whereas the first examples of metallomesogens mimicked the rodlike- or disklike-shape of conventional organic LCs, it gradually became clear that mesomorphism can also be observed for coordination geometries other than linear or square-planar ones. However, obtaining high coordination number LCs remains a challenge (Bruce, 1994). The next logical step toward metallomesogens with a coordination number higher than six, was the design of LCs containing lanthanide ions (or rare-earth ions in general). The coordination number of the trivalent lanthanide ions is typically eight or nine. The search for metallomesogens with a high coordination number is not the only reason why scientists are looking for new lanthanide-containing LCs. The driving forces for the development of this type of advanced materials are the unique physical properties of lanthanide ions. Several of the lanthanide ions show a very intense luminescence. By incorporating lanthanide ions into LCs, one can obtain luminescent LCs, which might be useful for the design of emissive LCDs or other devices. Most of the trivalent lanthanide ions are paramagnetic, due to unpaired electrons in their 4f subshell. They have a high magnetic moment, and more importantly, often a large magnetic anisotropy. A large magnetic anisotropy and a low viscosity are factors which reduce the threshold magnetic field strength for the alignment of molecules in an external magnetic field. Switching of molecules by a magnetic field can have some advantages over switching by an electric field. First of all, whereas due to the presence of the electrode on the walls of the LC cell, molecules in an external electric field can only be oriented with their long molecular axis either parallel or perpendicular to the LC cell walls. In principle, a magnetic field can be applied in any given direction with respect to the LC cell walls, and thus magnetic alignment is possible in any desired direction as well. Unwanted charge separation or redox reactions can occur when metallomesogens are placed in strong electric fields. These problems are absent in the case of magnetic switching. Although magnetic switching will never replace electric switching in LCDs, one can think of possibilities in the field of magnetooptical data storage.

Until about 1997, only a very limited number of lanthanidomesogens had been reported in the literature and from then on several research groups worldwide, including the team of the author, have been working on these fascinating materials, resulting in the discovery of several new classes of lanthanidomesogens with different molecular shapes and with different types of mesophases. This body of work has also resulted in a better understanding of the structure-property relationships of these materials and it allows at present to design lanthanide complexes that exhibit liquid-crystalline behavior at room temperature or even at lower temperatures. The aim of this chapter is to introduce the reader to the different aspects of lanthanidomesogens: their synthesis, thermal behavior, mesophase structure, luminescence, electrical properties and switching by external magnetic fields. The first part of the review consists of an introduction to LCs and to methods used to identify mesophases. Besides the pure lanthanidomesogens, also host-guest systems consisting of lanthanide complexes dissolved in a LC host matrix will be discussed. The reader will be familiarized with methodologies of designing new lanthanide-containing LCs and will be informed about how ligands of a given lanthanide complex can be modified in order to introduce LC behavior. Also an overview of actinide-containing LCs (*actinidomesogens*) is given. This chapter is the first comprehensive review on lanthanidomesogens since the publication of the Chemical Reviews review written by the author in 2002 (Binnemans and Görller-Walrand, 2002). Since that time, several shorter reviews have appeared, but none of them covers the whole field of lanthanidomesogens (Binnemans, 2005b, 2009, 2010; Eliseeva and Bünzli, 2010; Piguet et al., 2006; Terazzi et al., 2006a). Present review covers the literature to the end of 2011.

2. OVERVIEW OF LCs AND MESOPHASES

2.1. Different Types of LCs

A main difference between crystals and liquids is that the molecules in a crystal are well ordered in a three-dimensional (3D) lattice, whereas the molecules in a liquid are totally disordered. A molecular crystal consists of a more or less rigid arrangement of molecules, which possess both orientational and positional order. The molecules are constrained to occupy specific positions in the crystal lattice. At low temperatures, the attractive intermolecular forces in a crystal are strong enough to hold the molecules firmly in place, even though they all exhibit a random motion due to thermal vibrations. When a crystalline compound is heated, the thermal motions of the molecules increase and eventually become so strong that the intermolecular forces cannot keep the molecules in their position and the solid melts (Fig. 1). The long-range orientational and positional order is lost to yield a disordered isotropic liquid.

However, this melting process, which transforms a compound in one step from a highly ordered to a totally disordered phase, is a very destructive one

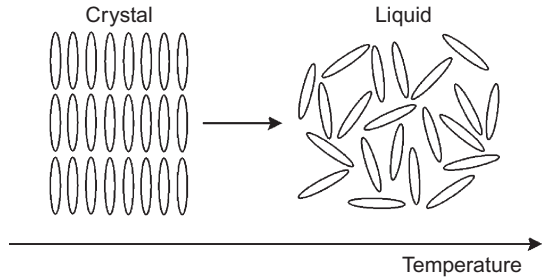

FIGURE 1 Schematic representation of the melting process of a nonmesomorphic molecular compound.

and is not universal for all types of compounds. There exist phases that are called "orientationally ordered liquids" or "positionally disordered crystals." In other words, these phases have more order than present in liquids, but less order than in typical molecular crystals. Compounds that exhibit such phases are called *liquid crystals*, since they share properties generally associated with both liquids and crystals. A more proper name for a LC molecule is *mesogen* and the phase it forms is known as *mesophase* (from the Greek "mesos" = middle, between, intermediate). The terms "mesogenic" and "mesomorphic" are often used as synonyms, but strictly spoken, they are not. A *mesogenic compound* has all the structural characteristics that are required to form a mesophase, but when a mesogenic compound is heated, it does not necessarily form a mesophase. The term "mesogenic" tells something about the shape of the molecule, but nothing about the thermal behavior. *Mesomorphic compounds* have the shape required for the formation of a mesophase and effectively exhibit a mesophase. The expression "mesomorphic" tells something about both the shape and the thermal behavior of a compound.

The motion of the molecules in liquid-crystalline phases is comparable with that of the molecules in an ordinary liquid, but the molecules maintain some degree of orientational order and sometimes some positional order as well (Fig. 2). A vector, called the *director* ($\tilde{\boldsymbol{n}}$) of the LC, represents the preferred orientation of the molecules.

In the case of *thermotropic liquid crystals*, a liquid-crystalline phase is obtained by heating a solid mesomorphic compound. At the *melting point* (T_m), the thermal motion of the molecules has increased to such an extent that the material passes from the crystalline phase to the liquid-crystalline phase. A mesomorphic compound that exists in the glass state will enter the liquid-crystalline phase at the glass-transition temperature (T_g). On further heating, the orientational order of the molecules is lost as well. The LC transforms into an isotropic, clear liquid at the *clearing point* (or *isotropization point*; T_c). Many materials are liquid-crystalline at room temperature. Several types of liquid-crystalline phases can occur between the solid state and the isotropic liquid state. Sometimes decomposition of the material occurs before the

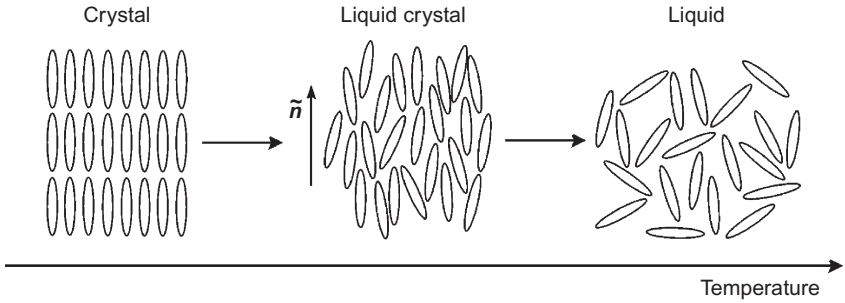

FIGURE 2 Schematic representation of the melting behavior of a liquid crystal.

clearing point is reached. The LC-to-LC transitions and the LC-to-liquid transitions are essentially reversible and usually occur with only little hysteresis in temperature, in contrast to the recrystallization process, which can be subject to supercooling (due to the induction period of nucleation and crystallization). When the mesophase is formed on both heating and cooling the material, the mesophase is thermodynamically stable and is termed *enantiotropic*. When the mesophase only appears on cooling a material below its melting point, and is therefore metastable (in fact, thermodynamically less stable than the crystalline phase), the mesophase is termed *monotropic*. One and the same compound can exhibit both enantiotropic and monotropic mesophases. For example, it is possible to have an enantiotropic nematic phase with an accompanying, monotropic smectic A phase. The liquid-crystalline order can sometimes be frozen into a glassy solid state, by cooling the liquid-crystalline phase very rapidly, thus preventing the formation of nucleation sites to initiate crystallization. Phase transitions of a thermotropic LC are usually presented in the following way: Cr 50 Cr′ 60 M_1 90 M_2 120 I (°C), for a material that exhibits a crystalline phase Cr between room temperature and 50 °C, another (distinct) crystalline phase Cr′ between 50 and 60 °C, one type of liquid-crystalline mesophase M_1 between 60 and 90 °C and another type of liquid-crystalline mesophase M_2 between 90 and 120 °C, and that clears out into an isotropic liquid at 120 °C. Transitions to monotropic phases appear between round parentheses, for example, Cr (N 90) 120 I. Upon heating, the compound melts at 120 °C into the isotropic phase, without going through a mesophase. Below 90 °C, the isotropic melts is transformed in a monotropic mesophase. The notation Cr 60 M 120 dec. designates a compound that melts at 60 °C to a mesophase M, and that decomposes at 120 °C before the clearing is reached. M is a general symbol for a mesophase. The use of the symbol M implicates that nothing can be said about the structure of the mesophase, otherwise more specific symbols have to be used (*vide infra*). In Table 1, an overview of the different mesophases formed by thermotropic LCs is given.

Another way to induce mesomorphism is by adding a solvent to the solid phase, which has a disruptive effect on the crystal lattice (*lyotropic liquid crystals*). The types of lyotropic mesophases formed depend on the type of

TABLE 1 Overview of Mesophases Formed By Thermotropic Liquid Crystals

Symbol	Name	Molecular shape
N	Nematic phase	Rod
N*	Chiral nematic phase (cholesteric phase)	Rod
SmA	Smectic A phase	Rod
SmA*	Chiral smectic A phase	Rod
SmC	Smectic C phase	Rod
SmC*	Chiral smectic C phase	Rod
SmB	Smectic B phase	Rod
SmI	Smectic I phase	Rod
SmF	Smectic F phase	Rod
B	Crystal B phase	Rod
J	Crystal J phase	Rod
G	Crystal G phase	Rod
E	Crystal E phase	Rod
K	Crystal K phase	Rod
H	Crystal H phase	Rod
cub	Cubic phase	Rod
N_D	Discotic nematic phase	Disk
N_C	Nematic columnar phase	Disk
Col_h	Hexagonal columnar phase	Disk
Col_r	Rectangular columnar phase	Disk
Col_o	Oblique columnar phase	Disk

A detailed description of the molecular order in the mesophases can be found in the text.

solvent, on the concentration of the compound in the solution and on the temperature. Usually lyotropic LCs are *amphiphiles*. In the compounds, different parts of the molecules have different solubility properties: the molecules consist of a very polar (hydrophilic) part (ionic or nonionic) and a nonpolar (hydrophobic or lipophilic) part (often hydrocarbon chains). One of the driving forces for lyotropic mesophase formation is the entropy-driven *hydrophobic effect*. Compounds that exhibit both thermotropic and lyotropic mesomorphism are termed *amphotropic liquid crystals*.

2.2. Thermotropic Mesophases

Many factors determine the type of mesophase formed by thermotropic LCs, but the molecular shape is by far the most important one. The most common classification scheme of liquid-crystalline phases is therefore based on the specific *anisometric* shape of the constituent mesogenic molecules (Demus et al., 1998; Kelker and Hatz, 1980). This shape is usually rod-like (*calamitic* mesogens), disk-like (*discotic* mesogens), or V-shaped (*bent-core* or *banana-shaped* mesogens). *Polycatenar* LCs have a structure intermediate between that of purely rod-like and disk-like molecules and are also considered as a separate class of thermotropic LCs (Nguyen et al., 1997). Some kind of analogy can be drawn between the mesophases exhibited by calamitic mesogens and the phases exhibited by discotic mesogens (Fig. 3). In both cases, the molecules can be described as cylinders with a high degree of structural

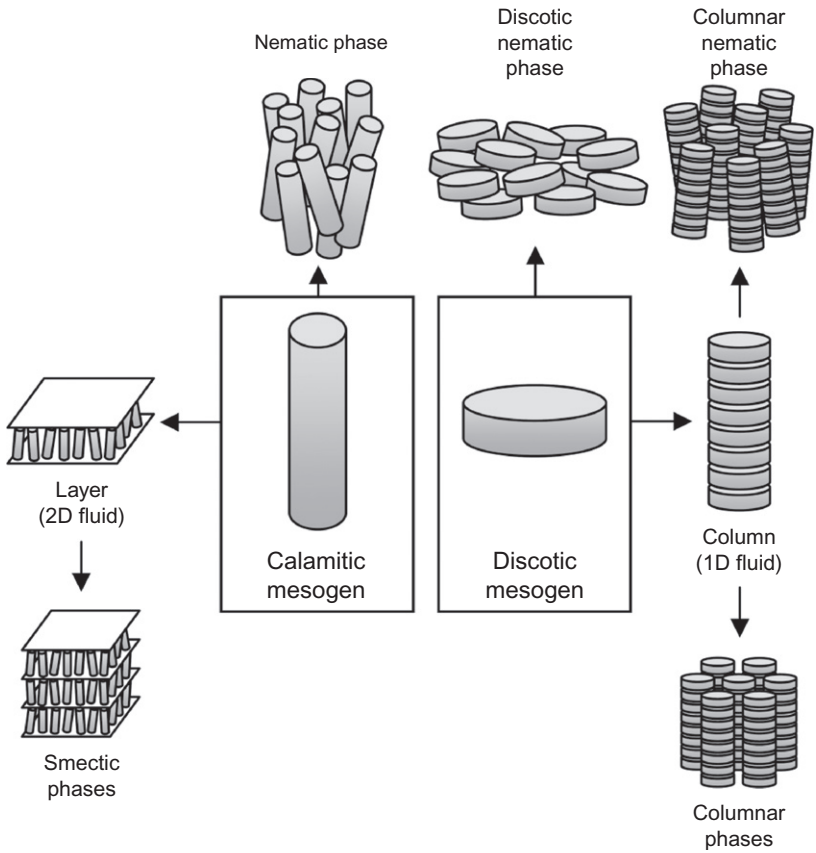

FIGURE 3 Mesophases exhibited by calamitic mesogens (rod-like shape) versus mesophases exhibited by discotic mesogens (disk-like shape).

anisotropy. Even though the representation of the detailed molecular structure by a simple cylinder seems to be a rather crude simplification, this approach turned out to be quite successful since mesogens in fluid phases are free to rotate (at different rates) about their molecular axis. The cylinder thus represents the average (or effective) shape of the molecule in the liquid-crystalline structure. Both calamitic and discotic mesogens are able to form nematic phases, which show only orientational order (*vide infra*). On the other hand, it is possible that these compounds show a stacking of the molecules, which leads to the formation of layers or columns. In this way, smectic or lamellar phases and columnar phases are formed, respectively (*vide infra*). Besides long-range orientational order, fluid smectic phases and columnar phases also show long-range translational order. It should be noted that discotic mesogens can also form a columnar nematic phase (N_C), in which the column motif can be found. Liquid-crystalline mesophases originate from the self-organization of mesogenic molecules. The concept is called supramolecular self-assembly: an internal system spontaneously opens a new route to increased complexity via molecular recognition processes. In the case of liquid-crystalline mesophases, the self-assembly process is driven by the (anisotropy of the) *intermolecular interactions* (dispersion forces, dipole-dipole interactions, π–π stacking between aromatic moieties, steric interactions, Coulomb forces or ionic interactions between charged moieties, hydrogen bonding or halogen bonding, charge-transfer interactions between electron donor and electron acceptor components, ...) between the constituent molecules. By increasing the temperature, the molecular mobility increases, and as a consequence the weak interactions break up and the stronger interactions remain. The latter interactions dominate liquid state superstructures such as liquid-crystalline phases (but also micellar structures, etc.). Another, related driving force is so-called *microsegregation*, caused by chemical or structural contrasts within the mesomorphic molecules (Tschierske, 1998). Examples are the incompatibility between hydrophilic and hydrophobic moieties, polar and nonpolar regions, hydrocarbon and fluorocarbon parts, hydrocarbon and oligosiloxane parts, rigid and flexible moieties, etc. Compatible regions will interact with one another, while incompatible molecular segments segregate into distinct subspaces, thus causing *microphase segregation*. This driving force does not apply to nematic phases, but it is of prime importance in the case of amphiphilic mesogens, which are not necessarily anisometric. Owing to the chemical bonding between the incompatible regions, segregation does not lead to macroscopic phase separation, but it results in the formation of different regions which are separated by *interfaces* at a molecular scale. *Macrophase separation* gives rise to thermodynamically different phases, while microphase separation occurs in a single phase. The relative size and volume fraction of the incompatible segments determine the interface curvature and strongly influence the mesophase morphology. Another factor which determines the type of mesophase is *space filling*. The whole space must be

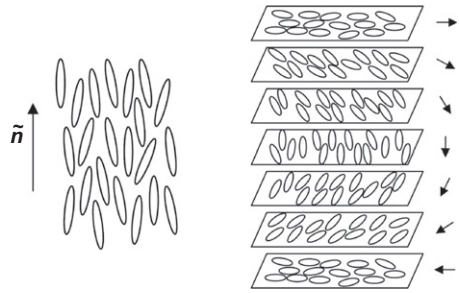

FIGURE 4 Schematic representation of the molecular order in the nematic phase (left), and schematic representation of the molecular order in the chiral nematic phase (right).

"reachable" and filled up by the mesogenic molecules. The desire of rigid anisometric units to minimize the excluded volume (which is in fact a general organization principle of matter) adds extra limitations to the structures that can be displayed by thermotropic LCs.

The optically uniaxial *nematic phase* (N) is the least ordered mesophase exhibited by calamitic mesogens. Its name is derived from ancient Greek *nematos* (=thread-like), because of the characteristic thread-like texture observed by polarizing optical microscopy. It can be formed when rod-like mesogens align their long molecular axes to a certain degree along a common direction defined by a vector, the *director* $\tilde{\boldsymbol{n}}$ (Fig. 4). This results in long-range orientational order with full rotational symmetry around $\tilde{\boldsymbol{n}}$. However, the molecular centers of mass are, as in an ordinary fluid, arranged randomly in all directions without long-range correlation, so there is no long-range positional or translational ordering. The nematic phase can be considered as a one-dimensionally ordered elastic fluid, wherein the molecules can move freely. While the molecules are free to rotate about their long molecular axis, rotation about their short molecular axis can occur to a certain degree as well. In the bulk nematic phase, there are as many molecules pointing in one direction relative to the director as there are pointing in the opposite direction (i.e., the molecules have a disordered head-to-tail arrangement in the phase). The director's orientation varies with temperature, pressure, applied electric and magnetic fields, and—for mixtures—composition. It is also influenced by the thickness of the cell containing the LC sample, and by possible treatments of the cell surfaces. Many practical applications of LCs rely on the control of the molecular orientation by external stimuli. As the nematic phase is the least viscous mesophase displayed by calamitic mesogens, fast *switching* of the molecules (i.e., changing the director's orientation, usually by application of an external electric field) is possible. This is the reason why the nematic phase is of interest for display applications. In the *chiral nematic phase* (N*), the director precesses through the material, describing a helix (Fig. 4). The pitch of a chiral nematic phase is the distance along the helix over which the director

rotates by 360°. The chiral nematic phase is also called *cholesteric phase*, because it was first observed for cholesterol derivatives. Chirality can directly be introduced within the mesomorphic molecules by incorporation of chiral elements, mostly chiral centers (asymmetric carbon atoms).

Smectic phases are characterized by a one-dimensional (1D) periodic stacking of "layers" formed by orientationally ordered LC molecules. The name is derived from ancient Greek *smegma* (=soap), because it was already known in the beginning of the twentieth century that soaps formed smectic mesophases. Smectic phases are also called *lamellar phases*. In the most typical cases, each layer can be seen as a two-dimensional (2D) anisotropic fluid. Smectic phases thus have a fluid-like structure in two dimensions combined with a long-range positional/translational order in the third dimension, normal to the smectic layers. The thickness of the layers is the so-called layer periodicity *d*. The smectic layers are not necessarily well defined, but can be rather flexible and often show a curved arrangement. The formation of smectic layers is mainly driven by microsegregation.

The *smectic A phase* (SmA) is the least ordered smectic modification, and therefore it shows the lowest viscosity of all smectic mesophases. The molecules in the smectic layers have, on average, their long molecular axes parallel to the normal to the layer planes (Fig. 5). The lateral distribution of the molecules within each layer is random, and the molecules have a considerable freedom for rotation about their long molecular axis and even for translation in the smectic layer. The molecules can also be tilted to some degree within the individual layers. However, since the tilt direction is random, the situation is averaged out to give a mean orthogonal, uniaxial arrangement of the long molecular axes. In general, the layer thickness is not constant, but fluctuates as a function of the local average tilt angle and as a function of the temperature. The smectic layers are free to slide over one another and relatively diffuse. In the *smectic C phase* (SmC), in contrast to the SmA phase, the molecules are tilted within the layers, along a preferred direction (Fig. 5). Consequently, the director $\tilde{\boldsymbol{n}}$ is not parallel anymore to the normal to the layer planes. The *tilt angle* θ_t is the angle between the director and the normal to the layer planes. Just like the SmA phase, the SmC phase is a fluid smectic phase: the molecules are arranged randomly within each layer and can move within the layer, and the layers are free to slide over one another. This inherent

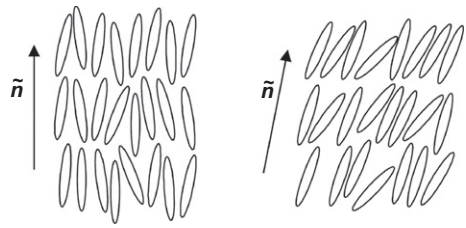

FIGURE 5 Schematic representation of the SmA phase (left) and the SmC phase (right).

molecular mobility results in a rather low viscosity for the SmC phase. The molecules can also rotate freely about their long axes. The tilt angle has been shown to vary with temperature. It often increases with decreasing temperature in a uniform way. The value of the tilt angle can be experimentally determined. Typical values are between 10° and 35°. There are also chiral versions of all the tilted smectic phases, for example, SmC^*. In this phase the director maintains a constant tilt angle with respect to the layer normal and rotates around this normal in going from one layer to the next.

SmA and SmC phases are the least ordered smectic phases and are also the most commonly observed ones. Due to the molecular mobility inherent in these phases and their relative low viscosities, they are called *true smectic phases*. Over the years, many smectic phases with ordering within the layers have been discovered. For example, in the *smectic B* (hexatic B, SmB) phase the molecules are arranged with their long molecular axis normal to the layer planes, but they are in the planes additionally ordered according to a 2D hexagonal lattice. SmF and SmI phases are tilted analogues of the SmB phase. While all of the previously described phases are genuine liquid-crystalline phases, there exist other phases in which there is a long-range positional order. They differ from true crystalline phases in one important aspect: the molecules in them have the freedom of (at least) rotation around their long axis and their thermal motion is not completely frozen out. These phases are labeled *crystal phases* (denoted by the letters B, E, G, H, J, K; Goodby, 1998).

Cubic phases (Cub) are mesophases of cubic symmetry (Diele, 2002). Because of their high symmetry, their physical properties are no longer anisotropic. No defect texture is observed by polarizing optical microscopy (POM; *vide infra*) and the image between crossed polarizers remains black. The cubic mesophases are very viscous and often their formation kinetics is very slow. Although cubic mesophases are very common for lyotropic LCs, where a cubic phase is possible between any pair of phases, there are only relatively few examples of cubic mesophases in thermotropic LCs. Whereas a cubic mesophase can be relatively easily detected when it is present between two anisotropic mesophases, it is difficult to observe the formation of the cubic phase when it is formed by cooling an isotropic liquid. In this case, a deformation of air bubbles in the melt is observed, as well as a sharp increase in the viscosity of the liquid.

The mesophases of calamitic molecules mentioned above have a well-defined thermodynamic order: when a hypothetical calamitic mesomorphic compound exhibiting almost all types of mesophases (enantiotropic with respect to the melting point and disregarding the various chiral phases) is heated, the mesophases will occur in a certain defined sequence:

$$\mathrm{Cr} - \mathrm{H} - \mathrm{K} - \mathrm{E} - \mathrm{G} - \mathrm{J} - \mathrm{B} - \mathrm{SmF} - \mathrm{SmI} - \mathrm{SmB} - \mathrm{SmC} - \mathrm{SmA} - \mathrm{N} - \text{isotropic liquid} \rightarrow \text{decreasing order, increasing temperature} \rightarrow$$

Three general types of LC state can be distinguished in this sequence: an anisotropic plastic crystal range (crystal phases), a smectic LC region and an

orientationally ordered nematic state. Cubic phases may appear at different locations in the sequence.

Molecules of a disk-like shape form either nematic or columnar phases (Laschat et al., 2007). Structurally the simplest mesophase is the *discotic nematic phase* (N_D). Just as in the case of the nematic phase formed by calamitic molecules, the molecules possess orientational order, but no positional order (Fig. 6). The *nematic columnar phase* (N_C) consists of short columns of a few molecules that act like the rod-like molecules in the nematic calamitic phase (Fig. 6). There is no organization of the columns in a 2D lattice. Most of the mesogenic molecules with a disk-like shape tend to be stacked one on top of the other into columns, and these columns are arranged side-by-side according to a 2D lattice. There are several types of columnar mesophases, depending on the symmetry of the 2D lattice (hexagonal, tetragonal, or rectangular) and depending on the order or disorder of the molecular stacking within the columns (ordered and disordered columnar mesophases). Figure 7 shows the molecular arrangement in the *hexagonal columnar phase* (Col_h). Other types of columnar phases are the *rectangular columnar phase* (Col_r) and the *oblique columnar phase* (Col_o). A schematic representation of the 2D lattices of the Col_r and the Col_o phases is shown in Fig. 8. In some types of columnar phases, the order of the molecules within the columns is a-periodical (disordered columnar phase), while in other cases there is an ordered, regular stacking inside the columns (ordered columnar phase). If

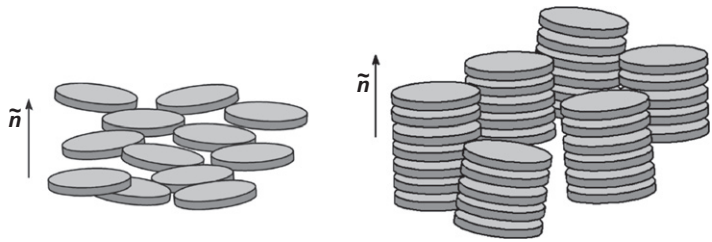

FIGURE 6 Schematic representation of the discotic nematic phase, N_D (left) and of the columnar nematic phase, N_{col} (right).

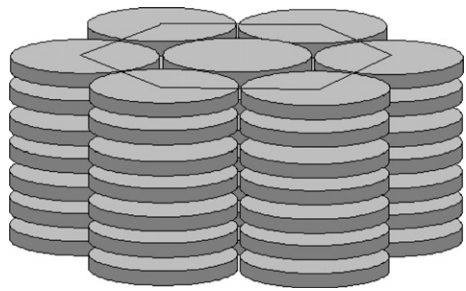

FIGURE 7 Schematic representation of the hexagonal columnar phase, Col_h.

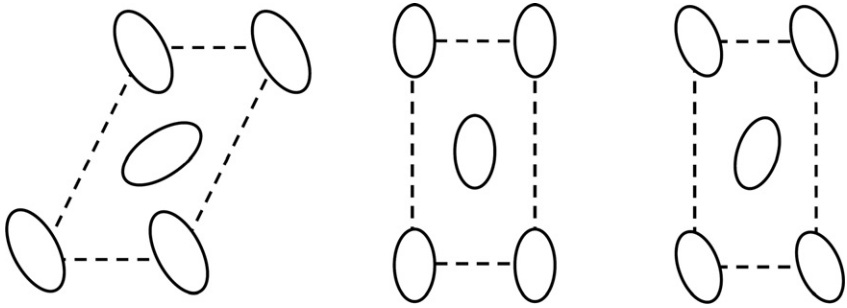

FIGURE 8 Schematic representation of the 2D lattices of the oblique columnar phase (left, plane group p1) and the rectangular columnar phase (middle, plane group c2mm; right, plane group p2gg).

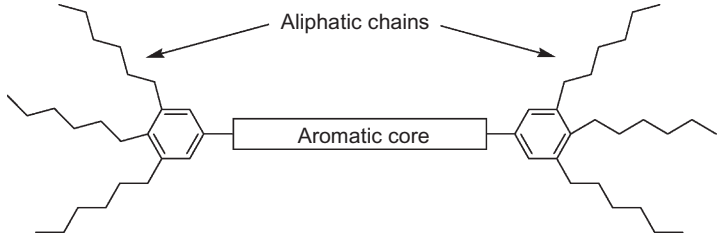

FIGURE 9 General structure of polycatenar liquid crystals. In this figure a hexacatenar liquid crystal is shown.

the molecules in the columns are ordered, the symbol is further specified as Col_{ho}, if the molecules are disordered, as Col_{hd} or, if the molecules are tilted, as Col_{ht}. The Col_{ho} phase is best defined as a disordered crystal phase, because of the long-range positional order of the molecules in three dimensions (thus also within the column). However, the Col_{hd} phase can be defined as being a true liquid-crystal phase, because of the disordered arrangement of the molecules within the columns.

Polycatenar (literally *many-tailed*) LCs consist of an extended, linear, normally aromatic core that is decorated with several long alkoxy chains at both ends (Fig. 9; Fazio et al., 2001; Nguyen et al., 1997). The nomenclature of polycatenar systems is related to the number of terminal chains, so that those containing four chains are named *tetracatenar*, those with six chains *hexacatenar* and so on. The chains can be placed in different positions leading to several isomeric possibilities. In general, the core of a polycatenar mesogen consists of at least four rings, usually aromatic. Additionally, there must be a balance between the number of chains attached to the core and the length of the core to obtain mesomorphic properties. In general, the core must have as many rings as terminal chains. Polycatenar mesogens have aroused interest due to their rich mesomorphism, and tetracatenar mesogens with the terminal

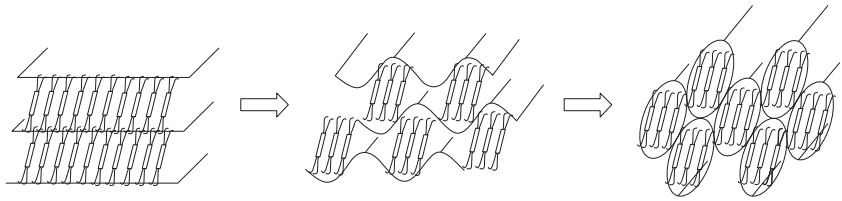

FIGURE 10 Schematic representation of the transition from the SmC phase to a columnar mesophase in tetracatenar compounds. *Adapted from Donnio and Bruce (1997).*

chains in the 3- and 4-positions are the most interesting polycatenar mesogens. They can show nematic, lamellar, cubic, and columnar mesophases in the same series at differing chain lengths, making them quite unique liquid-crystalline materials. When the chain length is short, the materials have a rod-like shape and so nematic or smectic phases are expected. With these systems, it is always the tilted SmC phase which is observed: at the interface between the rigid core and the chains, the cross-sectional area of the chains is greater than that of the core and so to fill space efficiently, the cores must tilt. However, at longer chain lengths and/or at higher temperatures, the chains occupy a greater volume and, in order to compensate this additional volume, the cores tilt even further. Eventually, the smectic layers can no longer hold together and they break up, leading to the formation of a columnar phase (Fig. 10). The transition from the SmC phase to the columnar phase normally takes place gradually (one or two compounds showing both phases) and is classically achieved via a cubic phase.

2.3. Lyotropic Mesophases

The types of molecular structure that generate lyotropic mesophases are amphiphilic (Fairhurst et al., 1998; Hyde, 2001). *Amphiphilic molecules* have two parts, a polar head group that is therefore hydrophilic, and a nonpolar tail that is therefore hydrophobic. In the description of the lyotropic phases, a new parameter, besides the temperature, must be considered, namely the solvent. Most often, the solvent is water. As a result, not only the temperature, but also the number of components in the solution and their concentrations are decisive factors for the appearance of these mesophases. In dilute solutions, the surfactant forms *micelles* that are "dissolved" in the solvent. Such micelles behave as an isotropic fluid. Micelles are aggregates of molecules in a way that the nonpolar chains aggregate together and are effectively removed from the water by the surrounding polar head groups. *Reverse micelles* can also form where the nonpolar chains radiate away from centrally aggregated head groups that surround the water. Such reverse micelle formation usually occurs in oil-water mixtures where the amount of water is small and fills the gap surrounded by the polar head groups (Fig. 11). Micelles dissolved in water can thus be regarded as an isotropic liquid. If the concentration of the surfactant is increased, more ordered phases (lyotropic mesophases) can be generated.

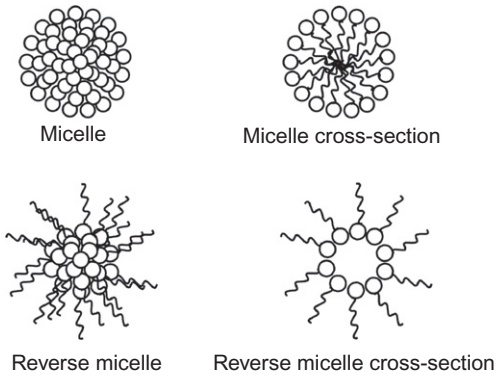

FIGURE 11 Structures of micelles formed by amphiphilic molecules. *Adapted from Collings and Hird (1997).*

Surfactants dissolved in water have a *Krafft point*, defined as the temperature below which micelles are insoluble. Above the Krafft point lyotropic liquid-crystalline phases can be generated. As the temperature increases, lyotropic liquid-crystalline phases exist until the melting point of the surfactant is reached. It should be noted that many amphiphiles do not form lyotropic mesophases, but rather aggregate into micelles and vesicles without any further organization.

The three main classes of lyotropic mesophase structures are lamellar, hexagonal, and cubic phases. In the *lamellar* phase, water is sandwiched between the polar heads of adjacent layers, while the hydrophobic tail, which are disordered, are in a nonpolar environment (Fig. 12). As the name implies, the *hexagonal* lyotropic mesophases have a molecular aggregate ordering, which corresponds to a hexagonal arrangement. The molecules form cylinders of indefinite length rather like the columnar phase of discotic molecules (Fig. 13). The reversed hexagonal phase also exists and is basically the same as the normal hexagonal phase except that the micellar cylinders are reversed with the nonpolar chains radiating outward from the cylinders. In *cubic* lyotropic mesophases the surfactant forms micelles that are arranged in a cubic lattice. Again, the normal manner as well as the reversed manner is a possible phase (Fig. 14). The lamellar mesophases are less viscous than hexagonal mesophases despite the fact that they contain less water. This is because the parallel layers can slide over each other. The hexagonal phase, on its turn, is less viscous than the cubic one because the columns are not restrained to each other.

3. CHARACTERIZATION OF MESOPHASES

Three techniques are commonly used to characterize mesophases: polarizing optical microscopy (POM), differential scanning calorimetry (DSC), and X-ray diffraction (XRD).

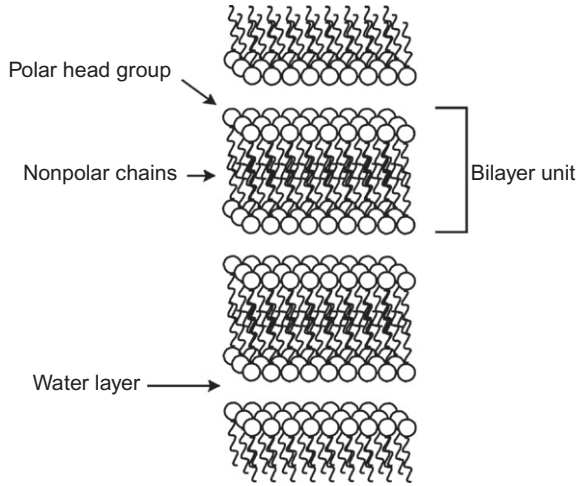

FIGURE 12 Structure of the lamellar lyotropic liquid-crystalline phase. *Adapted from Collings and Hird (1997).*

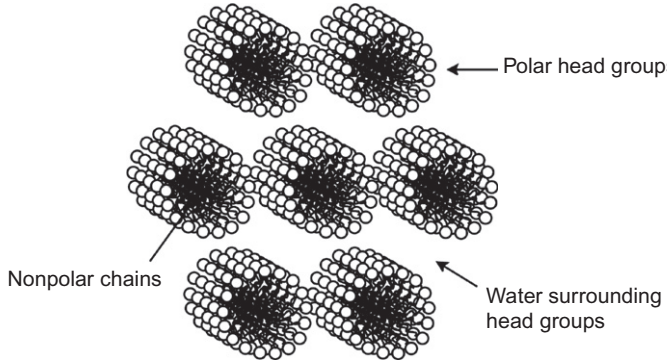

FIGURE 13 Structure of the hexagonal lyotropic liquid-crystalline phase. *Adapted from Collings and Hird (1997).*

3.1. Polarizing Optical Microscopy (POM)

Mesophases can be identified by studying the characteristic pattern (*textures*, also called *defect textures*) that are observed when a thin film of a LC is placed between the crossed polarizers of a POM. This method is based on the optical anisotropy and birefringence of LCs. Most LCs are optically uniaxial materials, with the optical axis being defined by the director. An optically anisotropic material is able to change the polarization state of light. Unpolarized light contains both *x*-polarized and *y*-polarized electric field components (Fig. 15). When an unpolarized light beam passes a first polarizer, only one electric field component remains and linearly polarized light is

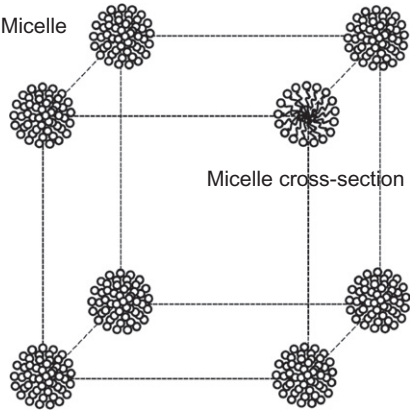

FIGURE 14 Structure of the cubic lyotropic liquid-crystalline phase. *Adapted from Collings and Hird (1997).*

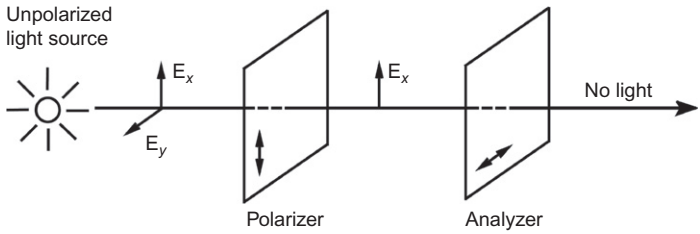

FIGURE 15 Principle of crossed polarizers.

obtained. When an isotropic material (or no material at all) is present between the two crossed polarizers, the polarization direction of the light beam will not be changed and the *x*-polarized light beam cannot pass the second polarizer (which is called the "analyzer").

The situation is totally different when a LC is placed between the crossed polarizers. The first polarizer is oriented so that the direction of the linearly polarized light beam makes an angle other than 0° or 90° with the director of the LC. One can consider this light beam as being composed of light polarized along the director and light polarized perpendicular to the director with zero phase difference. In passing through the LC, the two linearly polarized light beams get out of phase and in general emerge as elliptically polarized light. Since the electric field of elliptically polarized light is constantly rotating completely around during each cycle, it is parallel to the polarization axis of the second polarizer twice during each cycle. Therefore, some light will pass through the second polarizer. In general, the introduction of a LC between crossed polarizers causes the field of view to appear bright, whereas the field is dark with no LC between the polarizers. However, there are two

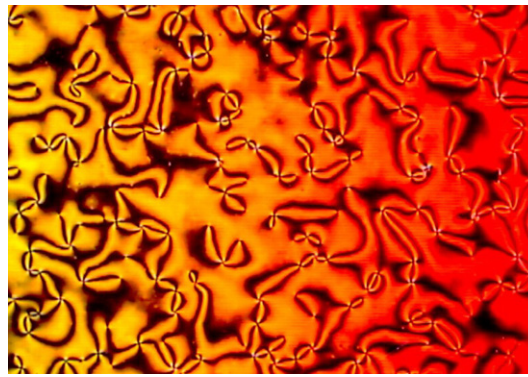

FIGURE 16 Schlieren texture of the nematic phase of 4-nonyloxybenzoic acid.

conditions under which LCs continue to appear black: if the incident linearly polarized light beam has its polarization direction either parallel or perpendicular to the director of the LC. There are also several positions in the texture where the brightness at once changes from very bright to black. These points or lines are called *disclinations* and represent places where the director is undefined, since it points to many directions within an extremely small region. Due to these defects and the symmetry of the phase, each liquid-crystalline phase has a different texture. In Fig. 16, the typical *Schlieren* texture of a nematic phase is shown. Often the textures show many colors because of interference effects. The textures are often diagnostic for a particular mesophase, although it can sometimes be difficult to determine the mesophase type from the texture alone. Especially the identification of columnar phases can be difficult on the sole basis of optical textures. Isotropic materials only possess one refractive index and cannot change the polarization direction of the incident light beam. Therefore, they appear black between crossed polarizers.

A POM for liquid-crystal studies is equipped with two crossed polarizers and a heating stage (hot stage). One polarizer is placed between the light source and the heating stage (polarizer) and the other is localized between the heating stage and the observer (analyzer). For observing liquid-crystalline phases the polarizers are typically crossed. The heating block of the heating stage is made of silver, because of the high thermal conductivity of this metal. The temperature of the heating stage can accurately be controlled by an electronic temperature controller, and most heating stages can also be cooled in a controlled way. To observe the texture, a small amount of the LC (typically less than 1 mg) is placed between two microscope cover slips, and the compound is transformed into the mesophase by heating it on the heating stage. The best textures are observed when the mesophase is formed by cooling of the isotropic liquid. When the compound is thermally unstable at the clearing

point or even decomposes before the clearing point is reached, the defect texture can only be observed by heating the compound. In that case, it is recommended to keep the mesophase some time at a constant temperature so have a good texture developed. The heating or cooling rates of the heating stage can be varied between 0.5 and 10 °C min^{-1}. The fast heating/cooling rates are useful to get an overall impression of the thermal behavior of the compound, whereas the slower rates are used to obtain good textures or to determine the transition temperatures. One can learn to interpret the textures by studying the textures of compounds with known mesophases or to study textbook examples of textures (Demus and Richter, 1978; Dierking, 2003). Besides the determination of phase types, observations by POM can also be used for other purposes in LC research: (1) to determine the phase transition temperatures of a given material, although not as accurately as by DSC; (2) to observe thermal decomposition of samples; (3) to check the viscosity of a liquid-crystalline sample (which often supports the identification of a particular type of mesophase); (4) to judge the purity of a compound in a quick way: for a single thermotropic liquid-crystalline material, only one type of phase should be observed at a given temperature and pressure, because the *Gibbs phase rule* ($F = C - P + 2$, where F is the variance, C is the number of components, and P is the number of phases at equilibrium) has to be obeyed; (5) to make estimates of the sample alignment; and (6) to follow voltage-controlled switching processes. Finally, a POM can be used to perform *miscibility studies*. This phase identification method was very common before the appearance of structural studies using XRD, and is based on the comiscibility of identical types of mesophases shown by different compounds. Pioneering work in this field was performed by Horst Sackmann from the LC group in Halle, Germany (Demus and Richter, 1978; Gray and Goodby, 1984).

3.2. Differential Scanning Calorimetry (DSC)

Phase transitions are accompanied by a change in enthalpy, ΔH, and thus by a change in entropy, ΔS ($\Delta S = \Delta H / T_{\text{transition}}$ under equilibrium conditions, $\Delta G = 0$). The magnitude of the entropy change is related to the amount of order that is lost or gained during the transition. In a DSC experiment, the enthalpy changes corresponding to the different phase transitions of a sample are measured by determining the power supplied to (or absorbed by) the sample. The phase transition temperatures can be accurately determined by this method. Phase transitions can be of first or second order. A *first-order phase transition* is characterized by a discontinuous jump in the first derivative of the Gibbs free energy (G) in function of the temperature (T), $\partial G(T)/\partial T$. The enthalpy H, entropy S, and volume V can all be defined by appropriate first derivatives of the Gibbs free energy (e.g., $\Delta S = -\Delta(\partial G/\partial T)$) and consequently all these variables change discontinuously at a first-order transition. In a so-called *thermogram*, in which the heat flow is plotted as a function of time (t) or temperature (T), first-order phase transitions can be visually

distinguished by sharp peaks and large enthalpy changes (i.e., large peak areas). Typical first-order phase transitions are the melting and clearing process of a LC, but also some mesophase-to-mesophase transitions can be of first order. A *second-order phase transition* is characterized by a continuous first derivative of the Gibbs free energy, but a discontinuous second derivative. In this case, the heat capacity C_p will exhibit a discontinuous jump, and results in a step in the baseline of the thermogram. The SmA–SmC transition (with a continuous change of the tilt angle) is a typical example of a second-order transition.

DSC is a widely used technique in the investigation of phase transitions of LCs. There are two types of DSC modules on the market: the *heat-flux DSC* and the *power-compensation DSC*. The principle of *heat-flux DSC* is illustrated in Fig. 17. Heat-flux DSC makes use of one furnace to heat both the sample crucible and an empty reference crucible, which corrects for the heat capacity of the crucible material. Symmetrical heating is achieved by constructing the furnace from a metal with a high thermal conductivity, such as silver. The temperature is measured at the heat-flux plate, which generates a very controlled heat flow from the furnace surface wall to the sample and reference, and between the two crucibles. When a sample *S* and a reference *R* are uniformly heated in a furnace and when an exothermic effect takes place in the sample, the temperature of the sample T_S will be higher than that of the reference, T_R. In the case of an endothermic effect the temperature of the sample will be lower than that of the reference. The temperature difference $\Delta T = T_S - T_R$ is recorded against the temperature T_R. Because the sample and reference are placed on the heat-flux plate, ΔT is proportional to the heat-flux difference between the sample and reference. When the sample mass is known and the temperature lag is measured very accurately, the energy of the transition (the enthalpy change) can be calculated. In addition, precise transition temperatures are obtained. However, calibration with a standard compound (e.g., indium, $T_m = 156.6\ ^\circ C$) remains necessary. In a *power-compensating DSC*, the sample and reference are placed in two different

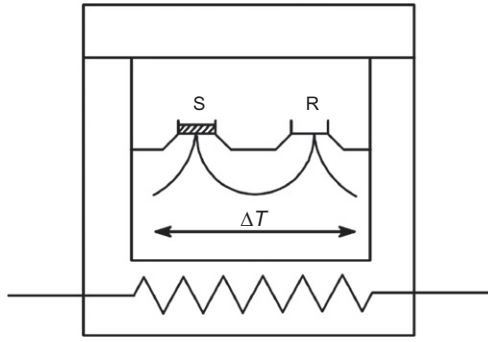

FIGURE 17 Heat-flux DSC cell. S = sample, R = reference.

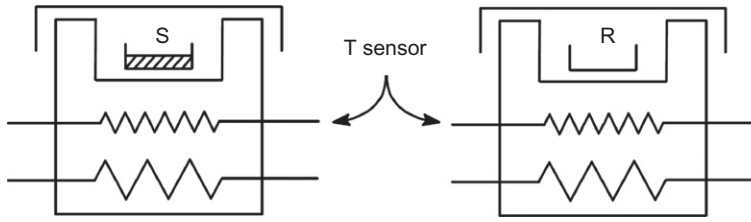

FIGURE 18 Power-compensation DSC cell. S = sample, R = reference.

furnaces. The temperature difference between the sample and the reference is kept at zero ($\Delta T = T_S - T_R = 0$) by independent heaters in the sample and reference furnaces (Fig. 18). The small crucibles or sample pans for DSC measurements are usually made of aluminum ($T_m = 660\,^{\circ}C$), and sealed with a lid. A hole can be pierced into the lid to allow possible decomposition products to escape from the crucible, instead of building up an internal pressure, and/or to create a specific atmosphere around the sample (e.g., a helium atmosphere). A few milligrams of sample are needed (e.g., 2 mg if a good resolution of phase transition peaks is required, 5 mg if a good sensitivity is required). Typical heating rates for the investigation of liquid-crystalline samples are 2–10 $^{\circ}C\,min^{-1}$. Heating normally occurs under an inert atmosphere, preferentially helium (because of the good thermal conductivity of this gas).

In a thermogram, the heat flow ($\partial Q/\partial t$, in mW) is plotted as a function of time (t) or temperature (T). The enthalpy change ΔH associated with a certain transition corresponds to the integral of the DSC curve with respect to time (peak area). According to the commonly used definition in LC research, the heat flow It has a positive value for *endothermic transitions* (in which heat is absorbed by the sample), and a negative value for *exothermic transitions* (in which heat is released by the sample). Enthalpy changes between successive liquid-crystalline phases or between a liquid-crystalline phase and the isotropic liquid are typically quite small, around 0.5–10 $kJ\,mol^{-1}$. Mesophase-to-mesophase transitions are sometimes not even detectable by DSC. The enthalpy change between a crystalline phase and a liquid-crystalline phase is usually quite large, in the range 10–80 $kJ\,mol^{-1}$. However, the ΔH values strongly depend on the types of solid and liquid-crystalline phases. Large enthalpy changes correspond to large changes of molecular organization in the sample. The change in entropy can be determined by dividing the enthalpy change ΔH by the transition temperature, $T_{transition}$ (expressed in Kelvin): $\Delta S = \Delta H/T_{transition}$. DSC is strictly complementary to optical microscopy. Sometimes a phase transition is accompanied by only a very small textural change, which might be overlooked by the observer. On the other hand, not all textural changes result from phase changes. Enthalpy and entropy values can give an indication of the type of mesophase. An example of DSC trace is given in Section 4 (Figure 30).

3.3. X-ray Diffraction (XRD)

XRD is the most powerful experimental technique to determine the structure of liquid-crystalline phases (Seddon, 1998; Templer, 1998). X-rays interact with the electron cloud of the material. The various scattered wavelets from the different atomic sites combine and undergo constructive or destructive interference, depending on the relative phases of the different wavelets, thus on their path difference. This can be expressed by Bragg's law:

$$n\lambda = 2d\sin\theta. \tag{1}$$

As shown in Fig. 19, this expression states that X-rays reflected by successive atomic planes separated by a distance d interfere constructively when the path difference between them is an integer multiple (n) of the wavelength λ. Note that the diffraction angle is often expressed in degrees 2θ. The XRD is typically recorded between $1^\circ < 2\theta < 40^\circ$, so that that the region of interest is positioned between the true small-angle region that is of interest for polymer scientists (SAXS; small-angle X-ray scattering) and the wide-angle region in which powder diffractograms are recorded for phase identification. The positions of the diffraction peaks are reciprocally related to the separations between molecules (or groups of molecules), in other words, the smaller the d spacing, the larger is the diffraction angle 2θ.

The XRD pattern of a mesophase gives several types of information, depending on the angular region investigated. In general, two regions are

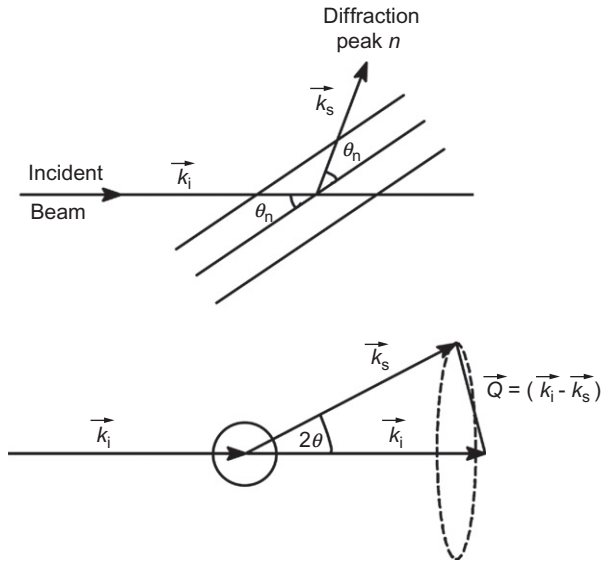

FIGURE 19 Diffraction from parallel planes (top), and definition of the scattering vector $\vec{Q}$ (bottom).

examined in the pattern, the small-angle region and the wide-angle region. The small-angle diffraction maxima are due to intermolecular interferences along the director in case of rod-like molecules (calamitic mesogens) or along a direction perpendicular to the director in case of disk-like molecules (discotic mesogens), and correspond to long distances (tens of Å). Periodic distances d in the structure, such as the interlayer spacing, are calculated from these maxima by applying Bragg's law. In general, this d value corresponds roughly to the molecular length in rod-like compounds and to the molecular diameter in disk-like compounds. The sharpness of the peaks is related to the extent to which the atomic layers extend periodically over large distances. The ratio of the Bragg peak positions reveals the long-range organization of the phase. The wide-angle maxima are due to intermolecular interferences in the direction perpendicular to the director in the case of calamitics or along the director in the case of discotics, and correspond to short distances (3–6 Å). These distances correspond roughly to the molecular width in the case of calamitic compounds and to the molecular thickness in the case of discotic compounds. The more order is present in the short-range organization of the molecules, the sharper are the peaks in the wide-angle region. Each type of mesophase gives a characteristic diffraction pattern.

Diffuse peaks are observed in both the small-angle and the wide-angle region of the X-ray pattern of the *nematic phase*. The broad signal in the wide-angle region corresponds to the average lateral separations of the close-packed molecules and to the short-range order of the molten alkyl chains. The signal in the small-angle region, with distances of the order of the molecular length, corresponds to *cybotactic groups* (i.e., local smectic ordering), a consequence of the molecular anisotropy and amphipathic character of the molecule. In many cases, the diffraction pattern of the isotropic phase is very similar to that of the nematic phase. However, a nematic phase can be aligned by an external magnetic field. This is not the case for the isotropic phase. The alignment of the nematic phase in a magnetic field can be observed by XRD if a 2D detector is used. *Lamellar structures* are characterized by the layer periodicity d. In the small-angle region, the XRD pattern consists of sharp reflections with reciprocal spacings in the ratio 1, 2, 3, ... are observed, corresponding to the indexation $(00l) = (001), (002), (003), \ldots$ The higher order reflections have much lower intensities than the first order reflection (001). In the wide-angle region of the X-ray pattern, a broad signal is observed at ca. 4.5 Å, corresponding to the liquid-like order of the molten aliphatic chains. To get a better understanding of the molecular packing in smectic phases, it is necessary to consider the molecular area, A_M, and to compare it with the cross-sectional area of the rigid core of the molecules A_{core} and the cross-sectional area of the aliphatic chains of the molecules A_{chains}. In general, if at the interface between the rigid core and the aliphatic chains, the cross-sectional area of the chains is similar to that of the core, a nontilted SmA phase is obtained. However, if the cross-sectional area of the chains is greater

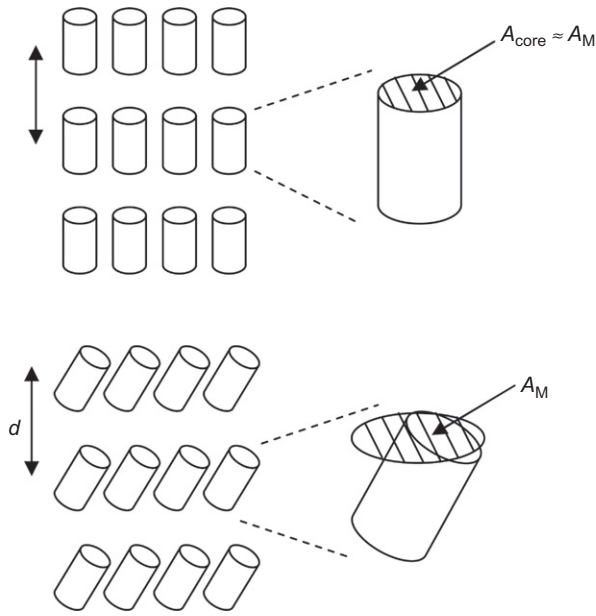

FIGURE 20 Schematic representation of the molecular area in the SmA phase (top) and the SmC phase (bottom). A_M is the molecular area, A_{core} is the cross-sectional area of the rigid core of the molecules, and d is the layer thickness.

than that of the core, the cores must tilt in order to fill space efficiently and a SmC phase is obtained. Thus, as a rule of thumb, there must be a balance between the molecular area and the cross-sectional area of the aliphatic chains: $A_M \approx A_{chains}$. Figure 20 shows a schematic representation of the cross-sectional area of the rigid cores in the SmA ($A_{core} \approx A_{chains} \approx A_M$) and SmC ($A_{core} < A_{chains} \approx A_M$) phase. The molecular area A_M can directly be deduced from the molecular volume V_{mol} and the layer thickness d by the formula:

$$A_M = \frac{V_{mol}}{d}. \tag{2}$$

The rigid part, build up by the rigid cores of two molecules, can be considered as a cylindrical unit with molecular area A_M. In this case,

$$A_M = \frac{2V_{mol}}{d}. \tag{3}$$

In general, for a cylindrical unit build up by the rigid cores of N molecules, the molecular area A_M is related to the layer thickness d and the molecular volume V_{mol} as follows:

$$A_M = \frac{NV_{mol}}{d}. \tag{4}$$

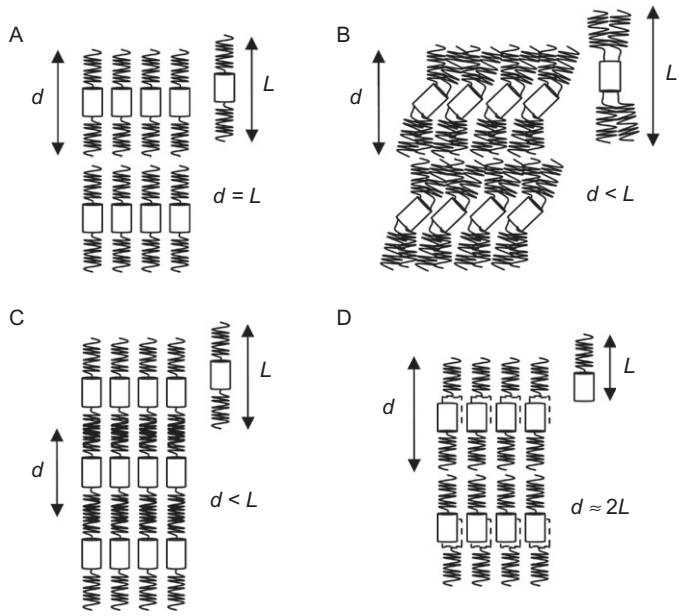

FIGURE 21 Schematic representation of different lamellar arrangements; d is the layer thickness, N is the number of molecules per cylindrical unit, and L is the molecular length. The description of the different structures can be found in the text.

A comparison of the molecular length L with the layer thickness d also provides useful information about the molecular packing. L can be determined via molecular modeling (computer calculations) or can be obtained from XRD on a single crystal (although this provides information about the molecular structure in the crystalline state). Figure 21 shows a schematic representation of different lamellar arrangements. In case (A) of Fig. 21, there is one rigid core per cylindrical unit and the molecules are nontilted. In case (B) of Fig. 21, there is one rigid core per cylindrical unit and the molecules are tilted within the layers to compensate the cross-sectional area of the aliphatic chains. In case (C) of Fig. 21, there is one rigid core per cylindrical unit and the molecules are nontilted. In addition, the aliphatic chains are interdigitated. Finally in case (D) of Fig. 21, there are two rigid cores per cylindrical unit and the molecules are nontilted.

From a geometrical point of view, the *columnar structures* are characterized mainly by two parameters: the columnar cross section S and the stacking periodicity along the columnar axis h (Fig. 22). Knowledge of these two structural parameters permits the interpretation of the molecular packing inside the columns and a better understanding of the influence of this packing on the 2D arrangement of the columns, and, therefore on the mesophase symmetry. The periodicity h, the columnar cross section S, and the molecular volume V_{mol} are linked analytically through the relation:

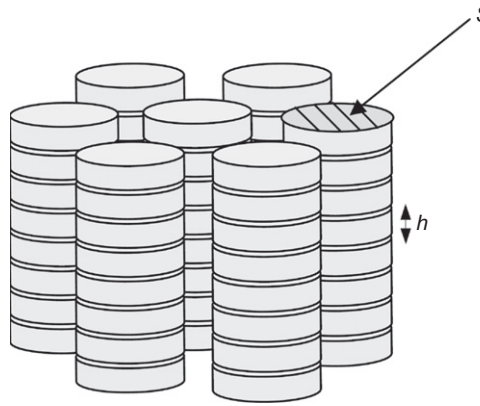

FIGURE 22 Schematic representation of a hexagonal arrangement of columns. *S* is the columnar cross section and *h* is the stacking periodicity along the columnar axis.

$$hS = NV_{\text{mol}}, \tag{5}$$

where N is the number of molecules within a volume fraction of a column. The cross-sectional area of the columns S can be calculated from the lattice parameters obtained from XRD and h can usually be obtained directly from the X-ray pattern (or can be determined experimentally by dilatometry). Although the molecular volume V_{mol} can be determined experimentally by dilatometry, this quantity can also be estimated by the formula:

$$V_{\text{mol}} = \frac{M}{0.6022\rho}, \tag{6}$$

where M is the molecular mass (g mol^{-1}) and ρ (g cm^{-3}) the molecular density (Felder-Flesch et al., 2006). A good approximate value of the molecular density can be calculated via the following equation:

$$\rho = \frac{27.0673}{V_{\text{CH}_2}}, \tag{7}$$

where V_{CH_2} is the volume of one methylene unit, which can be calculated via the relation:

$$V_{\text{CH}_2} = 26.5616 + 0.02023T, \tag{8}$$

where T is the absolute temperature (Marcos et al., 2001). The number of molecules within a repeat unit of a column depends on the shape and the size of the molecules. For large discotic molecules, there is usually one molecule per repeat unit and for hemidisk-like molecules, there are usually two molecules per repeat unit. Polycatenar molecules also form columnar phases at long chain lengths and usually three or four molecules arrange into a repeat unit. Figure 23 gives a schematic overview of these arrangements.

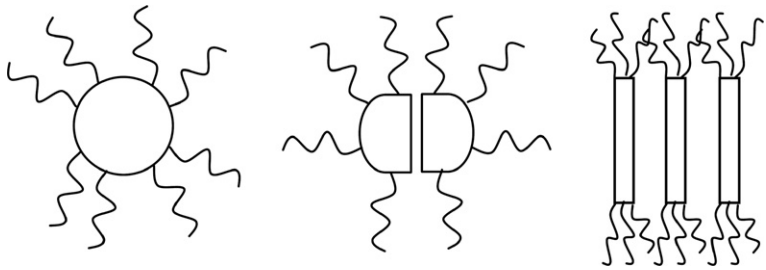

FIGURE 23 Schematic overview of the arrangement of large discotic molecules (left), hemidisk-like molecules (center), and polycatenar molecules (right) into a repeat unit.

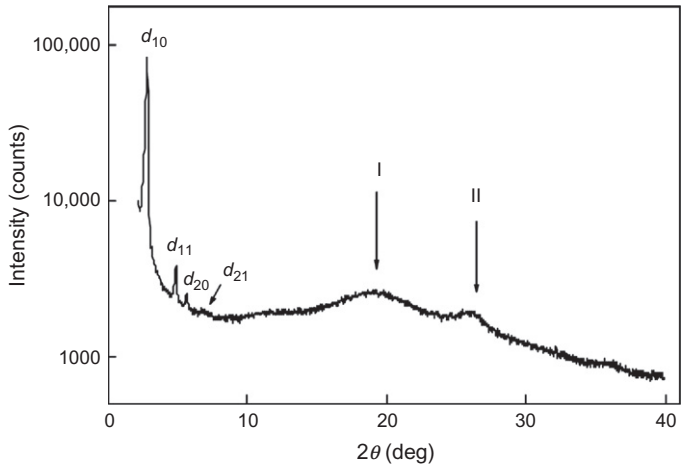

FIGURE 24 X-ray diffractogram of the hexagonal columnar mesophase of octa-tetradecyloxy phthalocyanine at 125 °C (Cu K_α radiation). In the small-angle region, sharp reflections with reciprocal spacings in the ratio $1, \sqrt{3}, 2, \sqrt{7}, \ldots$ corresponding to the indexation $(hk) = (10)$, (11), (20), (21), … are observed. The broad band I at $2\theta = 19°$ corresponds to the molten aliphatic chains, with an average spacing of 4.6 Å. The broad band II corresponds to the stacking distance of the phthalocyanine cores within the columns (spacing of 3.4 Å).

The hexagonal symmetry results from the hexagonal close-packing of cylindrical columns. Their projection onto the lattice plane perpendicular to the columnar axis leads to circular columnar cross sections, separated from one other by the molten aliphatic medium (aliphatic continuum). A representation of the arrangement of the columns in the *hexagonal columnar mesophase* (Col_h) is shown in Fig. 22. In Fig. 24, an example of an X-ray diffractogram of a hexagonal mesophase is shown. For the hexagonal lattice, the d spacings are correlated as follows:

$$d_{hk} = \frac{a}{\sqrt{\frac{4}{3}(h^2 + k^2 + hk)}}, \tag{9}$$

where h and k are the Miller indices defining a set of planes in the hexagonal lattice and a is the lattice parameter. Thus, in the small-angle region of the X-ray pattern, sharp reflections with reciprocal spacings in the ratio $1, \sqrt{3}, 2, \sqrt{7}, 3, \ldots$ are observed, corresponding to the indexation $(hk) = (10)$, (11), (20), (21), (30), … In general, the higher order reflections have much lower intensities than the fundamental reflection (10). In the wide-angle region of the X-ray pattern, a broad signal is observed at ca. 4.5 Å, corresponding to the liquid-like order of the molten aliphatic chains. As the unit cell of the hexagonal lattice contains only one column, the cross section S of the columns corresponds exactly to the lattice area S_h (Fig. 22), and can be directly calculated from the measurement of d_{10}:

$$S = \frac{2}{\sqrt{3}} d_{10}^2. \tag{10}$$

Note that the lattice parameter a corresponds to the diameter of a circular columnar cross-section and can also be directly calculated from the measurement of d_{10}:

$$a = \frac{2}{\sqrt{3}} d_{10}. \tag{11}$$

If the diameter of the circular cross section is smaller than the molecular length, the molecules are tilted within the columns. The rectangular symmetry results from the packing noncylindrical columnar cores, and their projection onto the lattice plane perpendicular to the columnar axis leads to elliptical, columnar cross sections, separated from one other by the molten aliphatic medium. Such elliptical cross sections are generated either by the molecular shape itself, hindered molecular rotation of nondisklike-molecules around the columnar axis, or by the tilt of the molecular discs perpendicular to the columnar axis. Two types of 2D rectangular arrangements of columns are possible for the *rectangular columnar mesophase* (Col_r), characterized by two different plane groups, namely *c2mm* and *p2gg* depending on the mutual orientation of these ellipses in the rectangular lattice.

4. SCHIFF'S BASE COMPLEXES

Because Schiff's base (or imine) complexes have often been used for the design of metallomesogens, and because the trivalent lanthanides are known to form complexes with these ligands, it was expected that Schiff's bases could be used to prepare lanthanidomesogens. Whereas the major part of the Schiff's base metallomesogens described in the literature are complexes of *N*-aryl substituted salicylaldimines, lanthanide complexes of this type of ligands are more difficult to synthesize in comparison with the *N*-alkyl substituted salicylaldimines (Fig. 25). For this reason, most Schiff's base lanthanidomesogens described in the literature have *N*-alkyl substituted ligands. The

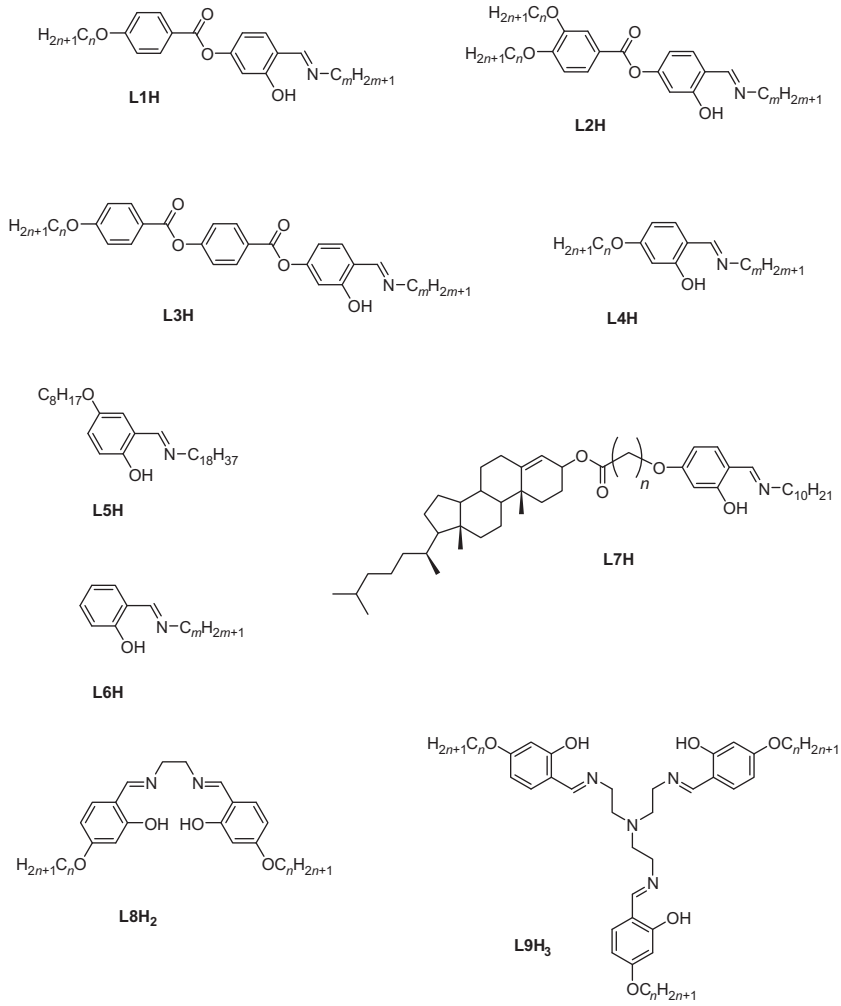

FIGURE 25 Overview of N-alkyl salicylaldimine Schiff's base ligands.

Schiff's base complexes reported in 1991 by Galyametdinov and coworkers were the first examples of calamitic (rod-like) lanthanidomesogens (Galyametdinov et al., 1991). In a very short, yet seminal paper, the authors describe the synthesis and thermal behavior of lanthanide complexes of an *N*-alkyl salicylaldimine ligand **L1H** ($C_nH_{2n+1} = C_7H_{15}$, $C_mH_{2m+1} = C_{12}H_{25}$). The stoichiometry of the complexes was believed to be $[RL_3X_2]$, but this formula does not lead to an electrically neutral complex. No base was used to deprotonate the ligand for complex formation. The ligand exhibits a nematic phase. The lanthanide complexes form a highly viscous smectic mesophase, which was later identified as a smectic A phase (Table 2). Much lower transition

TABLE 2 Thermal Behavior of Lanthanide Compounds With Two-Ring Schiff's Base Ligands L1H

Compound	C_nH_{2n+1}	C_mH_{2m+1}	Temperatures (°C)	Reference
$[La(LH)_3(NO_3)_3]$	C_6H_{13}	$C_{12}H_{25}$	Cr 70 SmA 184 dec.	Binnemans et al. (2001b)
$[La(LH)_3(NO_3)_3]$	C_6H_{13}	$C_{18}H_{37}$	Cr 71 SmA 191 I (dec.)	Binnemans et al. (2001b)
$[La(LH)_3(NO_3)_3]$	C_8H_{17}	$C_{18}H_{37}$	Cr 66 SmA 199 I (dec.)	Binnemans et al. (2001b)
$[La(LH)_2L(NO_3)_2]$	$C_{10}H_{21}$	$C_{12}H_{25}$	Cr 87 SmA 178 dec.	Binnemans et al. (2001b)
$[La(LH)_2L(NO_3)_2]$	$C_{10}H_{21}$	$C_{18}H_{37}$	Cr 70 SmA 177 dec.	Binnemans et al. (2001b)
$[La(LH)_2L(NO_3)_2]$	$C_{12}H_{25}$	$C_{12}H_{25}$	Cr 87 SmA 187 dec.	Binnemans et al. (2001b)
$[La(LH)_2L(NO_3)_2]$	$C_{12}H_{25}$	$C_{18}H_{37}$	Cr 88 SmA 169 dec.	Binnemans et al. (2001b)
$[La(LH)_2L(DOS)_2]$	$C_{12}H_{25}$	$C_{18}H_{37}$	Cr 113 SmA 132 I	Galyametdinov et al. (1999)
$[Pr(LH)_2L(NO_3)_2]$	C_7H_{15}	$C_{12}H_{25}$	Cr 96 SmA 181 I	Galyametdinov et al. (1991)
$[Nd(LH)_2L(NO_3)_2]$	$C_{10}H_{21}$	$C_{18}H_{37}$	Cr 74 SmA 173 dec.	Binnemans et al. (2001b)
$[Nd(LH)_3(NO_3)_3]$	$C_{12}H_{25}$	$C_{12}H_{25}$	Cr 96 SmA 164 dec.	Binnemans et al. (2001b)
$[Nd(LH)_2L(NO_3)_2]$	$C_{12}H_{25}$	$C_{18}H_{37}$	Cr 85 SmA 170 dec.	Binnemans et al. (2001b)
$[Eu(LH)_2LCl_2]$	C_7H_{15}	$C_{12}H_{25}$	Cr 146 SmA 236 I	Galyametdinov et al. (1991)
$[Gd(LH)_2L(NO_3)_2]$	C_7H_{15}	$C_{12}H_{25}$	Cr 98 SmA 192 I	Galyametdinov et al. (1991)
$[Gd(LH)_2L(DOS)_2]$	$C_{12}H_{25}$	$C_{18}H_{37}$	Cr 106 SmA 113 I	Galyametdinov et al. (1999)
$[Tb(LH)_3(NO_3)_3]$	C_6H_{13}	$C_{12}H_{25}$	Cr 75 SmA 172 dec.	Binnemans et al. (2001b)
$[Tb(LH)_2L(DOS)_2]$	$C_{12}H_{25}$	$C_{18}H_{37}$	Cr 106 SmA 126 I	Galyametdinov et al. (1999)

TABLE 2 Thermal Behavior of Lanthanide Compounds With Two-Ring Schiff's Base Ligands L1H—Cont'd

Compound	C_nH_{2n+1}	C_mH_{2m+1}	Temperatures (°C)	Reference
$[Dy(LH)_2L(NO_3)_2]$	C_7H_{15}	$C_{12}H_{25}$	Cr 92 SmA 186 I	Galyametdinov et al. (1991)
$[Dy(LH)_2L(DOS)_2]$	$C_{12}H_{25}$	$C_{18}H_{37}$	Cr 102 SmA 124 I	Galyametdinov et al. (1999)

Cr, crystalline phase; SmA, smectic A phase; I, isotropic liquid; dec., decomposition.

temperatures were observed for complexes with nitrate anions than for complexes with chloride counter ions. Exploration of the physical properties of these lanthanidomesogens was hampered by the very high viscosity of the mesophase and by their low thermal stability (in general, they decompose at the clearing point). Binnemans et al. (2001b) prepared homologues of ligand **L1H**. Depending on the chain length, the ligands exhibit a nematic or a smectic C phase. Depending on the ligand or the lanthanide ion, two types of stoichiometries were found: $[R(LH)_3(NO_3)_3]$ and $[R(LH)_2L(NO_3)_2]$. The complexes formed a viscous mesophase, which was identified by XRD as a smectic A phase. The melting point of the complexes was rather low, for one complex even as low as 70 °C, and the smectic A phase was stable over about 100 °C (Table 2). However, all the complexes thermally decomposed before the clearing point was reached. Complexes with dodecylsulfate anions had transition temperatures that were 80–100 °C lower than those of the complexes with chloride or nitrate anions, and in this case the complexes cleared without decomposition (Galyametdinov et al., 1999). By placing a second alkoxy chain on the benzoyloxy group, Bruce and coworkers were able to obtain lanthanide complexes with a hexagonal columnar mesophase (ligand **L2H**; Martin et al., 2000). The authors showed that substantially lower transition temperatures could be achieved by selecting triflate anions. The transition temperatures of these complexes were rather low, with the melting point just above 50 °C and the clearing point just below 90 °C. The melting and clearing points showed hardly any variation with the lanthanide ion (Table 3). Lodewyckx et al. (2001) prepared lanthanide complexes of a Schiff's base ligand with three aromatic rings (**L3H**, $C_nH_{2n+1}=C_6H_{13}$, $C_mH_{2m+1}=C_{18}H_{37}$). The influence of the lanthanide ion on the transition temperatures is marginal, although it was found that the nematic phase of the ligand was suppressed, in favor of the smectic C phase. The complexes thermally decomposed before the clearing point was reached. This work shows that the thermal properties of the complexes are largely defined by the Schiff's base ligands, rather than

TABLE 3 Thermal Behavior of the Lanthanide Complexes of the *N*-alkyl-4-(3,4-dialkoxylbenzoyloxy)salicylaldimine Schiff's Base Ligands L2H

Compound	C_nH_{2n+1}	C_mH_{2m+1}	Temperatures (°C)	Reference
$[Nd(LH)_2L(NO_3)_2]$	$C_{12}H_{25}$	$C_{12}H_{25}$	Cr 84 Col_h 112 I	Martin et al. (2000)
$[Nd(LH)_2L(CF_3SO_3)_2]$	$C_{12}H_{25}$	$C_{12}H_{25}$	Cr 57 Col_h 88 I	Martin et al. (2000)
$[Gd(LH)_2L(CF_3SO_3)_2]$	$C_{12}H_{25}$	$C_{12}H_{25}$	Cr 51 Col_h 89 I	Martin et al. (2000)
$[Tb(LH)_2L(CF_3SO_3)_2]$	$C_{12}H_{25}$	$C_{12}H_{25}$	Cr 48 Col_h 88 I	Martin et al. (2000)
$[Dy(LH)_2L(CF_3SO_3)_2]$	$C_{12}H_{25}$	$C_{12}H_{25}$	Cr 51 Col_h 88 I	Martin et al. (2000)
$[Dy(LH)_2L(NO_3)_2]$	$C_{12}H_{25}$	$C_{12}H_{25}$	Cr 85 Col_h 146 I	Martin et al. (2000)
$[Er(LH)_2L(NO_3)_2]$	$C_{12}H_{25}$	$C_{12}H_{25}$	Cr 77 Col_h 128 I	Martin et al. (2000)
$[Er(LH)_2L(CF_3SO_3)_2]$	$C_{12}H_{25}$	$C_{12}H_{25}$	Cr 51 Col_h 88 I	Martin et al. (2000)

Cr, crystalline phase; Col_h, hexagonal columnar phase; I, isotropic liquid.

by the lanthanide ions. This is different from what is observed for the Schiff's base ligands with one aromatic ring (*vide infra*).

The lanthanidomesogens derived of the two-ring or three-ring Schiff's base ligands are not very suitable for exploration of their spectroscopic, electric or magnetic properties, due to their high transition temperatures, highly viscous mesophases and low thermal stability. It was realized that metallomesogens with more favorable physicochemical properties were required, otherwise nobody would be interested in this class of LCs. A breakthrough was the discovery of lanthanide Schiff's base complexes with an enhanced thermal stability and exhibiting a smectic A phase with a relatively low viscosity (Galyametdinov et al., 1994a). The ligands in these complexes are remarkable because they contain only one aromatic ring and because they are not liquid-crystalline themselves (ligand **L4H**). Mesomorphism is induced by the lanthanide ion. Such a behavior is quite unique. In general, the mesophase of organic ligands disappears upon complexation, or at least the mesophase is strongly destabilized. Determination of the stoichiometry and the structure of these lanthanidomesogens turned out to be a challenge, since no single crystals suitable for XRD could be obtained at that time. The analytical data for the first reported compounds were in agreement with the stoichiometry $[R(LH)_2LX_2]$, where LH is the salicylaldimine Schiff's base, L is its deprotonated form and X is the counter ion (Galyametdinov et al., 1994a, 1996a). Thermal analysis data showed the absence of water or ethanol in the complexes. The complexes were prepared by reaction of the Schiff's base ligand with an excess of the lanthanide salt in absolute ethanol. Because the

complexes are insoluble in ethanol—in contrast to the ligand and lanthanide salts—the complexes precipitate upon formation. The complexes can be purified by extensive washing with ethanol, rather than by recrystallization. It was observed that trials to purify the complexes by recrystallization resulted in complexes of lower purity. They are soluble in halogenated organic solvents, such as chloroform, dichloromethane, or carbon tetrachloride. The complexes with chloride counter ions have a much lower solubility than the nitrate complexes.

Further work done by the research groups of Galyametdinov, Bruce, and Binnemans gave more insight in the structure of these Schiff's base complexes (Binnemans et al., 1999d, 2000a). By performing the complex formation at temperatures around room temperature, compounds could be obtained with a stoichiometry consistent with $[R(LH)_3(NO_3)_3]$. ^{1}H NMR studies on diamagnetic lanthanum(III) complexes showed that in the complexes the Schiff's base ligand is present in a *zwitterionic form*, that is, the phenolic oxygen has been transferred to the imine nitrogen (Fig. 26; Binnemans et al., 1999d). It was found that the ^{1}H signal corresponding to the imine hydrogen (CH═N) was broadened in the lanthanum(III) complex in comparison with the same signal in the Schiff's base ligand. In some cases, even a splitting of the imine signal was observed. The value of the coupling constant was of the same order of magnitude as the expected value for a trans-coupling in H—C═N$^+$—H. The signal at $\delta = 12.29$ ppm could be assigned to a NH resonance and not to an OH resonance by a homonuclear decoupling experiment. Irradiation of the NH signal led to a collapse of the CH═N doublet. Further evidence for the existence of a zwitterionic form in the metal complexes was given by infrared spectra, and more particularly by the band frequencies of the C═N stretching vibration. The shift to higher wavenumbers in the complexes compared to the corresponding values in the ligands indicated that the nitrogen atom is not involved in the complex formation and that a C═N$^+$ group is present. The best piece of evidence for the type of bonding in the complexes are the single crystal X-ray structures of homologous nonmesogenic complexes formed by ligands with short alkyl chains (Fig. 27; Binnemans et al., 2000a; Van Meervelt et al., 2003a,b). The crystal structures show that three Schiff's base ligands and three nitrate groups are present for each metal ion. The Schiff's base ligands are in the zwitterionic form, as assumed from the NMR data. The ligands coordinate to the metal ion only via the negatively

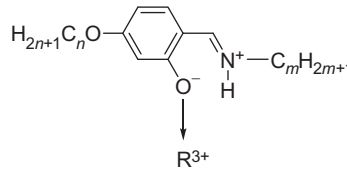

FIGURE 26 Zwitterionic form of a Schiff's base ligand coordinating to a rare-earth ion R^{3+}.

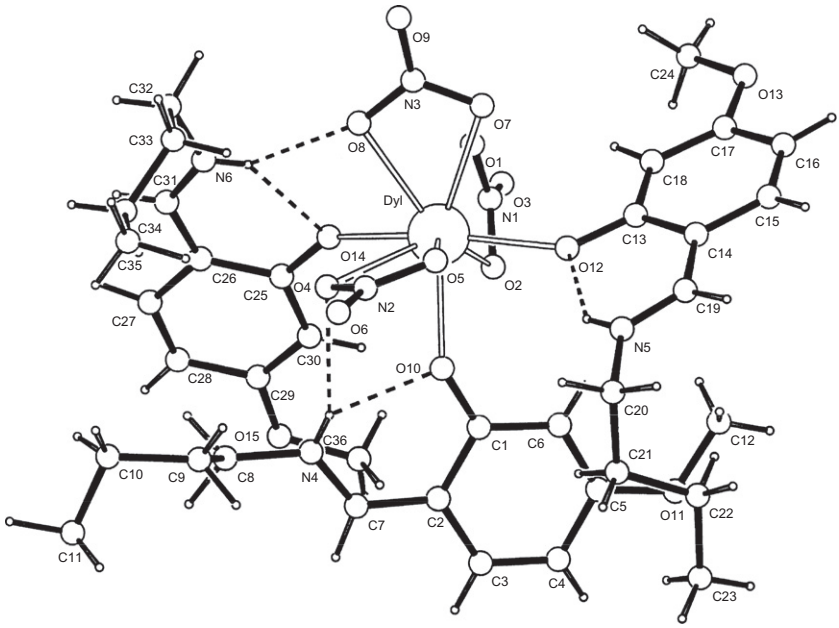

FIGURE 27 Crystal structure of complex $[Dy(LH)_3(NO_3)_3]$. LH is the Schiff's base ligand **L4H** with $C_nH_{2n+1} = CH_3$, $C_mH_{2m+1} = C_4H_9$. Reprinted with permission from Binnemans et al. (2000a). Copyright 2000 American Chemical Society.

charged phenolic oxygen. No binding occurs between the lanthanide ion and the imine nitrogen, and the three nitrate groups coordinate in a bidentate fashion. The coordination number of the lanthanide ion is nine, and the coordination polyhedron can be described as a distorted monocapped square antiprism. The phenolic proton is transferred to the imine nitrogen, but two of the three transferred protons in the complex form a double hydrogen bond (with the phenolic oxygen and with an oxygen atom of a nitrate group), whereas the third proton only forms a single hydrogen bond (with a phenolic oxygen). The formation of a zwitterionic form can be rationalized by the tendency of the lanthanide ions to coordinate to negatively charged ligands (with a preference for O-donor ligands). By transfer of the phenolic proton to the imine nitrogen, the phenolic oxygen becomes negatively charged and can coordinate to the lanthanide ion. The *N*-alkyl substituted imine nitrogen has a sufficiently basic character to bind the proton. However, under the same reaction conditions, no lanthanide complexes could be obtained with *N*-aryl Schiff's bases. In this type of ligands, the imine nitrogen is probably not basic enough for the uptake of the proton (and thus no zwitterion can be formed). It should been noticed that it is not feasible to deprotonate the Schiff's base ligand, because in the complexes formed no small inorganic counter ions will be present and probably they will have an oligomeric or polymeric structure.

It turned out that the stoichiometry of these complexes with deprotonated Schiff's base ligands is variable. Although the complexes prepared at room temperature have the $[R(LH)_3X_3]$ stoichiometry, the complexes prepared at higher temperatures, often have the stoichiometry $[R(LH)_2LX_2]$. This can be explained by the stronger dissociation of the phenolic proton of the Schiff's base ligand at higher temperatures. The temperature is thus a critical factor in the synthesis of these lanthanidomesogens. One should not heat the ethanolic solution above 40 °C, if formation of $[R(LH)_3X_3]$ complexes is wanted. It should be noted that the proton transfer from the phenolic oxygen atom to the imine nitrogen atom in nonmesogenic Schiff's bases has been studied in detail by both experimental and computational techniques (Filarowski et al., 2004; Koll et al., 2007).

All the lanthanide complexes of the one-ring salicylaldimine Schiff's base ligands exhibit a smectic A phase. Neither the alkoxy chain length (Binnemans et al., 2000a), nor the *N*-alkyl chain length has a substantial influence on the transition temperatures (Van Deun and Binnemans, 2000). However, the position of the alkoxy chain is of importance: a shift of the chain from the 4-position (ligand **L4H**. $C_nH_{2n+1} = C_8H_{17}$, $C_mH_{2m+1} = C_{18}H_{37}$) to the 5-position (ligand **L5H**) led to the disappearance of the liquid-crystalline behavior in the corresponding lanthanide complexes (Van Deun and Binnemans, 2003). Also a chain on the phenyl ring is a requirement for liquid-crystallinity of the lanthanide complexes. Complexes of ligands without an alkoxy chain are not liquid-crystalline (Van Deun and Binnemans, 2003; ligand **L6H**). Even a methoxy chain is sufficient to get LCs, provided that the *N*-alkyl chain has a sufficient length (ligand **L4H**. $C_nH_{2n+1} = CH_3$, $C_mH_{2m+1} = C_{18}H_{37}$). For the nitrate series, the lanthanide ion has a strong influence on the mesophase behavior (Fig. 28; Binnemans et al., 1999c). Whereas the melting point increases over the lanthanide series, the clearing point decreases simultaneously, so that the overall effect is a decrease of the mesophase stability range over the lanthanide series. The fact that there exists a correlation between the ionic radius of the lanthanide ion and the liquid-crystalline properties is convincingly demonstrated by comparison of the thermal properties of the holmium(III) complex (Cr 134 SmA 144 I) with those of the corresponding yttrium(III) complex (Cr 132 SmA 142 I; Binnemans et al., 1999c; Collinson et al., 2001). It is known that the ionic radii of Ho^{3+} and Y^{3+} are very similar. The increase in melting points in the La-Lu series (see Fig. 28) can be attributed to a stronger electrostatic interaction between the smaller lanthanide ions and the ligands. As the size of the lanthanide ion becomes smaller over the lanthanide series (*lanthanide contraction*), whilst the charge remains constant, the charge density of the lanthanide ion increases and therefore the electrostatic interactions with the ligands become stronger. The decrease of the clearing point over the lanthanide series is more difficult to explain, but it presumably reflects the stronger steric interactions between the ligands in the complexes with the smaller lanthanide ions. It is

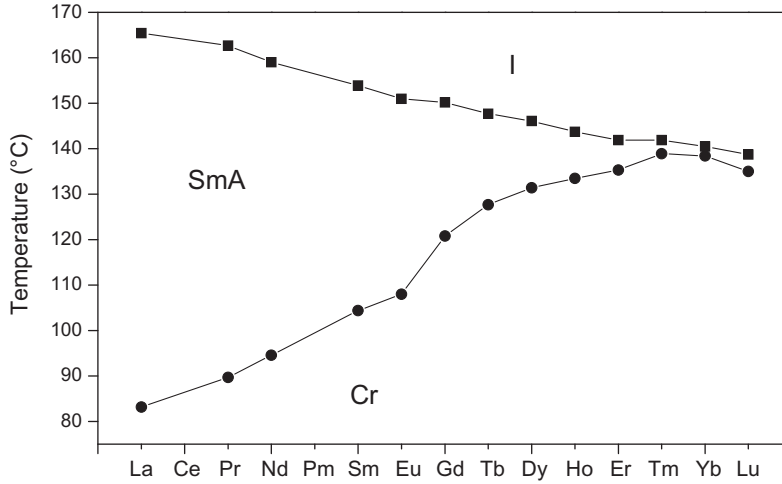

FIGURE 28 Influence of the lanthanide ion on the transition temperatures of the complexes [R(LH)$_3$(NO$_3$)$_3$]. LH is the Schiff's base ligand **L4H** with $C_nH_{2n+1} = C_8H_{17}$ and $C_mH_{2m+1} = C_{18}H_{37}$. Cr, crystalline phase; SmA, smectic A phase; I, isotropic liquid. (Drawn using the data in Table 1 of Binnemans et al., 1999c).

also not evident why this strong dependence of the melting and clearing temperatures on the lanthanide ion is observed for complexes with nitrate counter ions, but not for the corresponding chloride complexes (Binnemans et al., 2002a; Van Deun and Binnemans, 2001a). For the dodecylsulfate complexes, the trend over the lanthanide series is even opposite to that observed for the nitrate complexes: decrease in melting point over the lanthanide series, and as a consequence an increase in mesophase stability over the lanthanide series (Van Deun and Binnemans, 2001b). It is evident that further work is required to give an adequate explanation for the observed relationship between the thermal and structural properties of these Schiff's base metallomesogens. Counter ions other than the nitrate group have been investigated, but much less is known about their structural features, except that probably always zwitterionic Schiff's base ligands are present. It has already been mentioned that the chloride complexes have higher transition temperatures than the corresponding nitrate complexes. Because chloride ions can only be monodentate ligands and because the lanthanide ions prefer high coordination numbers (typically 8 or 9), complexes of the type [R(LH)$_3$Cl$_3$] are most likely dimeric or even oligomeric. In contrast to the nitrate complexes, the lanthanide ion has a much less pronounced influence on the transition temperatures of the chloride complexes: both melting and clearing points remain virtually constant over the lanthanide series. In Tables 4 and 5, the transition temperatures of the Schiff's base complexes with nitrate and chloride anions, respectively, are summarized

TABLE 4 Thermal Behavior of the Lanthanide Complexes of the One-Ring Schiff's Base Ligands L4H with Nitrate Counter Ions

Compound	C_nH_{2n+1}	C_mH_{2m+1}	Temperatures (°C)	Reference
$[Nd(LH)_3(NO_3)_3]$	CH_3	$C_{18}H_{37}$	Cr 119 SmA 127 A	Binnemans et al. (2000a)
$[Nd(LH)_3(NO_3)_3]$	C_2H_5	$C_{18}H_{37}$	Cr 132 SmA 147 A	Binnemans et al. (2000a)
$[Nd(LH)_3(NO_3)_3]$	C_3H_7	$C_{18}H_{37}$	Cr 112 SmA 149 A	Binnemans et al. (2000a)
$[Nd(LH)_3(NO_3)_3]$	C_4H_9	$C_{18}H_{37}$	Cr 119 SmA 158 A	Binnemans et al. (2000a)
$[Nd(LH)_3(NO_3)_3]$	C_5H_{11}	$C_{18}H_{37}$	Cr 115 SmA 155 A	Binnemans et al. (2000a)
$[Nd(LH)_3(NO_3)_3]$	C_6H_{13}	$C_{18}H_{37}$	Cr 110 SmA 156 A	Binnemans et al. (2000a)
$[Nd(LH)_3(NO_3)_3]$	C_7H_{15}	$C_{18}H_{37}$	Cr 104 SmA 155 A	Binnemans et al. (2000a)
$[Tb(LH)_2L(NO_3)_2]$	C_7H_{15}	$C_{14}H_{29}$	Cr 141 (SmA 139) I	Galyametdinov et al. (1996a)
$[Dy(LH)_2L(NO_3)_2]$	C_7H_{15}	$C_{14}H_{29}$	Cr 143 (SmA 142) I[a]	Galyametdinov et al. (1996a)
$[La(LH)_2L(NO_3)_2]$	C_7H_{15}	$C_{16}H_{33}$	Cr 92 SmX 128 I	Ovchinnikov et al. (1995)
$[Gd(LH)_2L(NO_3)_2]$	C_7H_{15}	$C_{16}H_{33}$	Cr 128 SmA 146 I	Ovchinnikov et al. (1995)
$[Dy(LH)_2L(NO_3)_2]$	C_7H_{15}	$C_{16}H_{33}$	Cr 140 SmA 142 I	Ovchinnikov et al. (1995)
$[La(LH)_2L(NO_3)_2]$	C_7H_{15}	$C_{18}H_{37}$	Cr 146 (SmA 145) I[a]	Galyametdinov et al. (1994a)
			Cr 127 SmA 165 I	Galyametdinov et al. (1996b)
$[Nd(LH)_2L(NO_3)_2]$	C_7H_{15}	$C_{18}H_{37}$	Cr 135 SmA 146 I	Galyametdinov et al. (1996b)
$[Eu(LH)_2L(NO_3)_2]$	C_7H_{15}	$C_{18}H_{37}$	Cr 140 SmA 153 I	Galyametdinov et al. (1996b)
$[Gd(LH)_2L(NO_3)_2]$	C_7H_{15}	$C_{18}H_{37}$	Cr 135 SmA 146 I	Galyametdinov et al. (1994a)
			Cr 148 SmA 155 I	Galyametdinov et al. (1996b)

Continued

TABLE 4 Thermal Behavior of the Lanthanide Complexes of the One-Ring Schiff's Base Ligands L4H with Nitrate Counter Ions—Cont'd

Compound	C_nH_{2n+1}	C_mH_{2m+1}	Temperatures (°C)	Reference
$[Tb(LH)_2L(NO_3)_2]$	C_7H_{15}	$C_{18}H_{37}$	Cr 148 SmA 151 I	Galyametdinov et al. (1996b)
$[Dy(LH)_2L(NO_3)_2]$	C_7H_{15}	$C_{18}H_{37}$	Cr 138 SmA 141 I	Galyametdinov et al. (1994a)
			Cr 151 (SmA 150) I[a]	Galyametdinov et al. (1996b)
$[Y(LH)_3(NO_3)_3]$	C_8H_{17}	$C_{18}H_{37}$	Cr 132 SmA 141 I	Binnemans et al. (1999c)
$[La(LH)_3(NO_3)_3]$	C_8H_{17}	$C_{18}H_{37}$	Cr 83 SmA 165 I	Binnemans et al. (1999c)
$[Pr(LH)_3(NO_3)_3]$	C_8H_{17}	$C_{18}H_{37}$	Cr 90 Sm 163 I	Binnemans et al. (1999c)
$[Nd(LH)_3(NO_3)_3]$	C_8H_{17}	$C_{18}H_{37}$	Cr 95 SmA 159 I	Binnemans et al. (1999c, 2000a)
$[Sm(LH)_3(NO_3)_3]$	C_8H_{17}	$C_{18}H_{37}$	Cr 105 SmA 154 I	Binnemans et al. (1999c)
$[Eu(LH)_3(NO_3)_3]$	C_8H_{17}	$C_{18}H_{37}$	Cr 108 SmA 151 I	Binnemans et al. (1999c)
$[Gd(LH)_3(NO_3)_3]$	C_8H_{17}	$C_{18}H_{37}$	Cr 121 SmA 150 I	Binnemans et al. (1999c)
$[Tb(LH)_3(NO_3)_3]$	C_8H_{17}	$C_{18}H_{37}$	Cr 128 SmA 148 I	Binnemans et al. (1999c)
$[Dy(LH)_3(NO_3)_3]$	C_8H_{17}	$C_{18}H_{37}$	Cr 131 SmA 146 I	Binnemans et al. (1999c)
$[Ho(LH)_3(NO_3)_3]$	C_8H_{17}	$C_{18}H_{37}$	Cr 134 SmA 144 I	Binnemans et al. (1999c)
$[Er(LH)_3(NO_3)_3]$	C_8H_{17}	$C_{18}H_{37}$	Cr 135 SmA 142 I	Binnemans et al. (1999c)
$[Tm(LH)_3(NO_3)_3]$	C_8H_{17}	$C_{18}H_{37}$	Cr 139 SmA 142 I	Binnemans et al. (1999c)
$[Yb(LH)_3(NO_3)_3]$	C_8H_{17}	$C_{18}H_{37}$	Cr 138 SmA 141 I	Binnemans et al. (1999c)
$[Lu(LH)_3(NO_3)_3]$	C_8H_{17}	$C_{18}H_{37}$	Cr 135 SmA 139 I	Binnemans et al. (1999c)
$[Nd(LH)_3(NO_3)_3]$	C_9H_{21}	$C_{18}H_{37}$	Cr 100 SmA 158 I	Binnemans et al. (2000a)

TABLE 4 Thermal Behavior of the Lanthanide Complexes of the One-Ring Schiff's Base Ligands L4H with Nitrate Counter Ions—Cont'd

Compound	C_nH_{2n+1}	C_mH_{2m+1}	Temperatures (°C)	Reference
$[Nd(LH)_3(NO_3)_3]$	$C_{10}H_{21}$	$C_{18}H_{37}$	Cr 101 SmA 158 I	Binnemans et al. (2000a)
$[Nd(LH)_3(NO_3)_3]$	$C_{11}H_{23}$	$C_{18}H_{37}$	Cr 103 SmA 157 I	Binnemans et al. (2000a)
$[Pr(LH)_3(NO_3)_3]$	$C_{12}H_{25}$	$C_{16}H_{33}$	Cr 105 SmA 148 I	Binnemans et al. (2000a)
$[Nd(LH)_3(NO_3)_3]$	$C_{12}H_{25}$	$C_{16}H_{33}$	Cr 105 SmA 147 I	Binnemans et al. (2000a)
$[Gd(LH)_3(NO_3)_3]$	$C_{12}H_{25}$	$C_{16}H_{33}$	Cr 107 SmA 145 I	Binnemans et al. (2000a)
$[Tb(LH)_3(NO_3)_3]$	$C_{12}H_{25}$	$C_{16}H_{33}$	Cr 107 SmA 147 I	Binnemans et al. (2000a)
$[Er(LH)_3(NO_3)_3]$	$C_{12}H_{25}$	$C_{16}H_{33}$	Cr 107 SmA 147 I	Binnemans et al. (2000a)
$[La(LH)_2L(NO_3)_2]$	$C_{12}H_{25}$	$C_{18}H_{37}$	Cr 81 SmA 138 I	Galyametdinov et al. (1996a)
$[La(LH)_3(NO_3)_3]$	$C_{12}H_{25}$	$C_{18}H_{37}$	Cr 81 SmA 138 I	Binnemans et al. (2000a)
$[Nd(LH)_2L(NO_3)_2]$	$C_{12}H_{25}$	$C_{18}H_{37}$	Cr 100 SmA 151 I	Galyametdinov et al. (1996a)
$[Nd(LH)_3(NO_3)_3]$	$C_{12}H_{25}$	$C_{18}H_{37}$	Cr 100 SmA 158 I	Binnemans et al. (2000a)
$[Eu(LH)_2L(NO_3)_2]$	$C_{12}H_{25}$	$C_{18}H_{37}$	Cr 113 SmA 147 I	Galyametdinov et al. (1996a)
$[Gd(LH)_2L(NO_3)_2]$	$C_{12}H_{25}$	$C_{18}H_{37}$	Cr 115 SmA 147 I	Galyametdinov et al. (1995)
	$C_{12}H_{25}$	$C_{18}H_{37}$	Cr 112 SmA 144 I	Galyametdinov et al. (1996a)
$[Tb(LH)_2L(NO_3)_2]$	$C_{12}H_{25}$	$C_{18}H_{37}$	Cr 114 SmA 148 I	Galyametdinov et al. (1996a)
			Cr 114 SmA 147 I	Galyametdinov et al. (1995)
			Cr 96 SmA 148 I	Galyametdinov et al. (1999)
$[Dy(LH)_2L(NO_3)_2]$	$C_{12}H_{25}$	$C_{18}H_{37}$	Cr 130 SmA 144 I	Galyametdinov et al. (1996a)

Continued

TABLE 4 Thermal Behavior of the Lanthanide Complexes of the One-Ring Schiff's Base Ligands L4H with Nitrate Counter Ions—Cont'd

Compound	C_nH_{2n+1}	C_mH_{2m+1}	Temperatures (°C)	Reference
$[Ho(LH)_2L(NO_3)_2]$	$C_{12}H_{25}$	$C_{18}H_{37}$	Cr 129 SmA 143 I	Galyametdinov et al. (1996a)
$[Er(LH)_2L(NO_3)_2]$	$C_{12}H_{25}$	$C_{18}H_{37}$	Cr 127 SmA 146 I	Galyametdinov et al. (1996a)
$[Nd(LH)_3(NO_3)_3]$	$C_{13}H_{27}$	$C_{18}H_{37}$	Cr 100 SmA 158 I	Binnemans et al. (2000a)
$[Nd(LH)_3(NO_3)_3]$	$C_{14}H_{29}$	C_8H_{17}	Cr 116 SmA 158 I	Van Deun and Binnemans (2000)
$[Gd(LH)_3(NO_3)_3]$	$C_{14}H_{29}$	C_8H_{17}	Cr 125 SmA 143 I	Van Deun and Binnemans (2000)
$[Ho(LH)_3(NO_3)_3]$	$C_{14}H_{29}$	C_8H_{17}	Cr [143 SmA] 133 I[a]	Van Deun and Binnemans (2000)
$[Nd(LH)_3(NO_3)_3]$	$C_{14}H_{29}$	$C_{12}H_{25}$	Cr 106 SmA 160 I	Van Deun and Binnemans (2000)
$[Gd(LH)_3(NO_3)_3]$	$C_{14}H_{29}$	$C_{12}H_{25}$	Cr 130 SmA 150 I	Van Deun and Binnemans (2000)
$[Ho(LH)_3(NO_3)_3]$	$C_{14}H_{29}$	$C_{12}H_{25}$	Cr 138 SmA 144 I	Van Deun and Binnemans (2000)
$[La(LH)_3(NO_3)_3]$	$C_{14}H_{29}$	$C_{18}H_{37}$	Cr 92 SmA 138 I	Van Deun and Binnemans (2000)
$[Nd(LH)_3(NO_3)_3]$	$C_{14}H_{29}$	$C_{18}H_{37}$	Cr 102 SmA 155 I	Binnemans et al. (2000a) and Van Deun and Binnemans (2000)
$[Gd(LH)_3(NO_3)_3]$	$C_{14}H_{29}$	$C_{18}H_{37}$	Cr 115 SmA 145 I	Van Deun and Binnemans (2000)
$[Ho(LH)_3(NO_3)_3]$	$C_{14}H_{29}$	$C_{18}H_{37}$	Cr 132 SmA 141 I	Van Deun and Binnemans (2000)
$[Nd(LH)_3(NO_3)_3]$	$C_{15}H_{31}$	$C_{18}H_{37}$	Cr 103 SmA 154 I	Binnemans et al. (2000a)
$[Nd(LH)_3(NO_3)_3]$	$C_{16}H_{33}$	$C_{18}H_{37}$	Cr 103 SmA 152 I	Binnemans et al. (2000a)
$[Nd(LH)_3(NO_3)_3]$	$C_{17}H_{35}$	$C_{18}H_{37}$	Cr 104 SmA 150 I	Binnemans et al. (2000a)
$[Nd(LH)_3(NO_3)_3]$	$C_{18}H_{37}$	$C_{18}H_{37}$	Cr 101 SmA 150 I	Binnemans et al. (2000a)

TABLE 4 Thermal Behavior of the Lanthanide Complexes of the One-Ring Schiff's Base Ligands L4H with Nitrate Counter Ions—Cont'd

Compound	C_nH_{2n+1}	C_mH_{2m+1}	Temperatures (°C)	Reference
$[Nd(LH)_3(NO_3)_3]$	$C_{19}H_{39}$	$C_{18}H_{37}$	Cr 101 SmA 146 I	Binnemans et al. (2000a)
$[Nd(LH)_3(NO_3)_3]$	$C_{20}H_{41}$	$C_{18}H_{37}$	Cr 100 SmA 144 I	Binnemans et al. (2000a)

Cr, crystalline phase; SmA, smectic A phase; SmX, unidentified smectic phase; I, isotropic liquid.
[a]*Monotropic mesophase.*

TABLE 5 Thermal Behavior of the Lanthanide Complexes of the One-Ring Schiff's Base Ligands L4H with Chloride Counter Ions

Compound	C_nH_{2n+1}	C_mH_{2m+1}	Temperatures (°C)	Reference
$[Tb(LH)_2LCl_2]$	C_7H_{15}	$C_{18}H_{37}$	Cr 182 SmA 203 I	Galyametdinov et al. (1996b)
$[Y(LH)_3Cl_3]$	C_8H_{17}	$C_{18}H_{37}$	Cr 175 SmA 192 I	Van Deun and Binnemans (2001b)
$[Pr(LH)_3Cl_3]$	C_8H_{17}	$C_{18}H_{37}$	Cr 158 SmA 187 I	Van Deun and Binnemans (2001b)
$[Sm(LH)_3Cl_3]$	C_8H_{17}	$C_{18}H_{37}$	Cr 168 SmA 161 I	Van Deun and Binnemans (2001b)
$[Eu(LH)_3Cl_3]$	C_8H_{17}	$C_{18}H_{37}$	Cr 170 SmA 193 I	Van Deun and Binnemans (2001b)
$[Gd(LH)_3Cl_3]$	C_8H_{17}	$C_{18}H_{37}$	Cr 171 SmA 194 I	Van Deun and Binnemans (2001b)
$[Tb(LH)_3Cl_3]$	C_8H_{17}	$C_{18}H_{37}$	Cr 169 SmA 191 I	Van Deun and Binnemans (2001b)
$[Dy(LH)_3Cl_3]$	C_8H_{17}	$C_{18}H_{37}$	Cr 174 SmA 192 I	Van Deun and Binnemans (2001b)
$[Ho(LH)_3Cl_3]$	C_8H_{17}	$C_{18}H_{37}$	Cr 174 SmA 191 I	Van Deun and Binnemans (2001b)
$[Er(LH)_3Cl_3]$	C_8H_{17}	$C_{18}H_{37}$	Cr 174 SmA 188 I	Van Deun and Binnemans (2001b)
$[Tm(LH)_3Cl_3]$	C_8H_{17}	$C_{18}H_{37}$	Cr 174 SmA 190 I	Van Deun and Binnemans (2001b)

Continued

TABLE 5 Thermal Behavior of the Lanthanide Complexes of the One-Ring Schiff's Base Ligands L4H with Chloride Counter Ions—Cont'd

Compound	C_nH_{2n+1}	C_mH_{2m+1}	Temperatures (°C)	Reference
$[Yb(LH)_3Cl_3]$	C_8H_{17}	$C_{18}H_{37}$	Cr 176 SmA 193 I	Van Deun and Binnemans (2001b)
$[Lu(LH)_3Cl_3]$	C_8H_{17}	$C_{18}H_{37}$	Cr 175 SmA 190 I	Van Deun and Binnemans (2001b)
$[Nd(LH)_2LCl_2]$	$C_{12}H_{25}$	$C_{18}H_{37}$	Cr 162 SmA 187 I	Binnemans et al. (1998)
$[Gd(LH)_2LCl_2]$	$C_{12}H_{25}$	$C_{18}H_{37}$	Cr 164 SmA 185 I	Galyametdinov et al. (1996a)
			Cr 164 SmA 188 I	Binnemans et al. (1998)
$[Tb(LH)_2LCl_2]$	$C_{12}H_{25}$	$C_{18}H_{37}$	Cr 137 SmA 186 I	Galyametdinov et al. (1999)
$[Dy(LH)_2LCl_2]$	$C_{12}H_{25}$	$C_{18}H_{37}$	Cr 166 SmA 186 I	Binnemans et al. (1998)
$[Ho(LH)_2LCl_2]$	$C_{12}H_{25}$	$C_{18}H_{37}$	Cr 168 SmA 185 I	Binnemans et al. (1998)
$[Yb(LH)_2LCl_2]$	$C_{12}H_{25}$	$C_{18}H_{37}$	Cr 169 SmA 185 I	Binnemans et al. (1998)

Cr, crystalline phase; SmA, smectic A phase; I, isotropic liquid; g, glassy phase.

The Schiff's base complexes with dodecylsulfate counter ions (or with alkylsulfate counter ions in general) are an interesting class of compounds, because their transition temperatures are much lower than those of the nitrate or chloride complexes (Table 6). Complexes with dodecylsulfate counter ions were first prepared by Binnemans et al. (1998) via a metathesis reaction between the corresponding chloride complex and AgDOS ($DOS = dodecylsulfate, C_{12}H_{25}OSO_3^-$) However, Galyametdinov et al. (1999) developed a more elegant synthetic route, being the reaction of R $(DOS)_3 \cdot xH_2O$ salts with the Schiff's base ligand. These Schiff's base complexes have an opposite temperature dependence on the lanthanide ion in comparison with the nitrate complexes, in the sense that the mesophase stability range increases over the lanthanide series (Fig. 29; Van Deun and Binnemans, 2001a). The DSC traces of the dodecylsulfate complexes are textbook examples, with narrow melting and clearing transitions (Fig. 30). It is evident that the enthalpy changes associated with the melting/crystallization processes are much larger than the enthalpy change of the isotropization process

TABLE 6 Thermal Behavior of the Lanthanide Complexes of the One-Ring Schiff's Base Ligands L4H with Alkylsulfate Counter Ions

Compound	C_nH_{2n+1}	C_mH_{2m+1}	Temperatures (°C)	Reference
$[Tb(LH)_3(C_2H_5OSO_3)_3]$	$C_{12}H_{25}$	$C_{16}H_{33}$	Cr 85 SmA 123 I	Malykhina et al. (2001)
$[Tb(LH)_3(C_3H_7OSO_3)_3]$	$C_{12}H_{25}$	$C_{16}H_{33}$	Cr 102 SmA 138 I	Malykhina et al. (2001)
$[Tb(LH)_3(C_4H_9OSO_3)_3]$	$C_{12}H_{25}$	$C_{16}H_{33}$	Cr 107 SmA 142 I	Malykhina et al. (2001)
$[Tb(LH)_3(C_5H_{11}OSO_3)_3]$	$C_{12}H_{25}$	$C_{16}H_{33}$	Cr 103 SmA 138 I	Malykhina et al. (2001)
$[Tb(LH)_3(C_6H_{13}OSO_3)_3]$	$C_{12}H_{25}$	$C_{16}H_{33}$	Cr 100 SmA 131 I	Malykhina et al. (2001)
$[Tb(LH)_3(C_7H_{15}OSO_3)_3]$	$C_{12}H_{25}$	$C_{16}H_{33}$	Cr 106 SmA 140 I	Malykhina et al. (2001)
$[Tb(LH)_3(C_8H_{17}OSO_3)_3]$	$C_{12}H_{25}$	$C_{16}H_{33}$	Cr 69 SmA 115 I	Malykhina et al. (2001)
$[Tb(LH)_3(C_9H_{19}OSO_3)_3]$	$C_{12}H_{25}$	$C_{16}H_{33}$	Cr 56 SmA 72 I	Malykhina et al. (2001)
$[Tb(LH)_3(C_{10}H_{21}OSO_3)_3]$	$C_{12}H_{25}$	$C_{16}H_{33}$	Cr 61 SmA 80 I	Malykhina et al. (2001)
$[Tb(LH)_3(C_{12}H_{25}OSO_3)_3]$	$C_{12}H_{25}$	$C_{16}H_{33}$	Cr 71 SmA 86 I	Malykhina et al. (2001)
$[Tb(LH)_3(C_{13}H_{27}OSO_3)_3]$	$C_{12}H_{25}$	$C_{16}H_{33}$	Cr 72 SmA 90 I	Malykhina et al. (2001)
$[Tb(LH)_3(C_{15}H_{31}OSO_3)_3]$	$C_{12}H_{25}$	$C_{16}H_{33}$	Cr 74 SmA 104 I	Malykhina et al. (2001)
$[Tb(LH)_3(C_{18}H_{37}OSO_3)_3]$	$C_{12}H_{25}$	$C_{16}H_{33}$	Cr 75 SmA 84 I	Malykhina et al. (2001)
$[Tb(LH)_3(C_{19}H_{39}OSO_3)_3]$	$C_{12}H_{25}$	$C_{16}H_{33}$	Cr 72 SmA 89 I	Malykhina et al. (2001)
$[Er(LH)_3(C_2H_5OSO_3)_3]$	$C_{12}H_{25}$	$C_{16}H_{33}$	Cr 90 SmA 129 I	Malykhina et al. (2001)

Continued

TABLE 6 Thermal Behavior of the Lanthanide Complexes of the One-Ring Schiff's Base Ligands L4H with Alkylsulfate Counter Ions—Cont'd

Compound	C_nH_{2n+1}	C_mH_{2m+1}	Temperatures (°C)	Reference
$[Er(LH)_3(C_8H_{17}OSO_3)_3]$	$C_{12}H_{25}$	$C_{16}H_{33}$	Cr 100 SmA 113 I	Malykhina et al. (2001)
$[Er(LH)_3(C_{18}H_{37}OSO_3)_3]$	$C_{12}H_{25}$	$C_{16}H_{33}$	Cr 70 SmA 90 I	Malykhina et al. (2001)
$[La(LH)_3\{CF_3(CF)_5CH_2OSO_3\}_3]$	$C_{12}H_{25}$	$C_{16}H_{33}$	Cr 110 SmA 121 I	Galyametdinov et al. (2001b)
$[Pr(LH)_3\{CF_3(CF)_5CH_2OSO_3\}_3]$	$C_{12}H_{25}$	$C_{16}H_{33}$	Cr 113 SmA 120 I	Galyametdinov et al. (2001b)
$[Nd(LH)_3\{CF_3(CF)_5CH_2OSO_3\}_3]$	$C_{12}H_{25}$	$C_{16}H_{33}$	Cr 114 SmA 122 I	Galyametdinov et al. (2001b)
$[Eu(LH)_3\{CF_3(CF)_5CH_2OSO_3\}_3]$	$C_{12}H_{25}$	$C_{16}H_{33}$	Cr 110 SmA 125 I	Galyametdinov et al. (2001b)
$[Gd(LH)_3\{CF_3(CF)_5CH_2OSO_3\}_3]$	$C_{12}H_{25}$	$C_{16}H_{33}$	Cr 106 SmA 119 I	Galyametdinov et al. (2001b)
$[Tb(LH)_3\{CF_3(CF)_5CH_2OSO_3\}_3]$	$C_{12}H_{25}$	$C_{16}H_{33}$	Cr 103 SmA 119 I	Galyametdinov et al. (2001b)
$[Ho(LH)_3\{CF_3(CF)_5CH_2OSO_3\}_3]$	$C_{12}H_{25}$	$C_{16}H_{33}$	Cr 96 SmA 120 I	Galyametdinov et al. (2001b)
$[Er(LH)_3\{CF_3(CF)_5CH_2OSO_3\}_3]$	$C_{12}H_{25}$	$C_{16}H_{33}$	Cr 98 SmA 125 I	Galyametdinov et al. (2001b)
$[La(LH)_3\{CHF_2(CF)_5CH_2OSO_3\}_3]$	$C_{12}H_{25}$	$C_{16}H_{33}$	Cr 111 SmA 131 I	Galyametdinov et al. (2001b)
$[Ce(LH)_3\{CHF_2(CF)_5CH_2OSO_3\}_3]$	$C_{12}H_{25}$	$C_{16}H_{33}$	Cr 114 SmA 131 I	Galyametdinov et al. (2001b)
$[Pr(LH)_3\{CHF_2(CF)_5CH_2OSO_3\}_3]$	$C_{12}H_{25}$	$C_{16}H_{33}$	Cr 115 SmA 135 I	Galyametdinov et al. (2001b)
$[Nd(LH)_3\{CHF_2(CF)_5CH_2OSO_3\}_3]$	$C_{12}H_{25}$	$C_{16}H_{33}$	Cr 109 SmA 133 I	Galyametdinov et al. (2001b)

$[Sm(LH)_3\{CHF_2(CF)_5CH_2OSO_3\}_3]$	$C_{12}H_{25}$	$C_{16}H_{33}$	Cr 106 SmA 131 I	Galyametdinov et al. (2001b)
$[Eu(LH)_3\{CHF_2(CF)_5CH_2OSO_3\}_3]$	$C_{12}H_{25}$	$C_{16}H_{33}$	Cr 106 SmA 132 I	Galyametdinov et al. (2001b)
$[Gd(LH)_3\{CHF_2(CF)_5CH_2OSO_3\}_3]$	$C_{12}H_{25}$	$C_{16}H_{33}$	Cr 108 SmA 126 I	Galyametdinov et al. (2001b)
$[Tb(LH)_3\{CHF_2(CF)_5CH_2OSO_3\}_3]$	$C_{12}H_{25}$	$C_{16}H_{33}$	Cr 99 SmA 128 I	Galyametdinov et al. (2001b)
$[Dy(LH)_3\{CHF_2(CF)_5CH_2OSO_3\}_3]$	$C_{12}H_{25}$	$C_{16}H_{33}$	Cr 102 SmA 125 I	Galyametdinov et al. (2001b)
$[Ho(LH)_3\{CHF_2(CF)_5CH_2OSO_3\}_3]$	$C_{12}H_{25}$	$C_{16}H_{33}$	Cr 98 SmA 125 I	Galyametdinov et al. (2001b)
$[Er(LH)_3\{CHF_2(CF)_5CH_2OSO_3\}_3]$	$C_{12}H_{25}$	$C_{16}H_{33}$	Cr 98 SmA 140 I	Galyametdinov et al. (2001b)
$[Yb(LH)_3\{CHF_2(CF)_5CH_2OSO_3\}_3]$	$C_{12}H_{25}$	$C_{16}H_{33}$	Cr 103 SmA 138 I	Galyametdinov et al. (2001b)
$[La(LH)_2L(DOS)_2]$	$C_{12}H_{25}$	$C_{18}H_{37}$	Cr 78 SmA 92 I	Galyametdinov et al. (1999)
$[Nd(LH)_2L(DOS)_2]$	$C_{12}H_{25}$	$C_{18}H_{37}$	Cr 61 SmA 98 I	Binnemans et al. (1998)
$[Gd(LH)_2(DOS)_2]$	$C_{12}H_{25}$	$C_{18}H_{37}$	Cr 59 SmA 112 I	Binnemans et al. (1998)
			Cr 61 SmA 110 I	Galyametdinov et al. (1999)
$[Tb(LH)_2L(DOS)_2]$	$C_{12}H_{25}$	$C_{18}H_{37}$	Cr 71 SmA 86 I	Galyametdinov et al. (1999)
$[Tb(LH)_2L(Pr^iOSO_3)_2]$	$C_{12}H_{25}$	$C_{18}H_{37}$	Cr 102 SmA 138 I	Galyametdinov et al. (1999)
$[Dy(LH)_2L(DOS)_2]$	$C_{12}H_{25}$	$C_{18}H_{37}$	Cr 61 SmA 89 I	Binnemans et al. (1998)
			Cr 61 SmA 90 I	Galyametdinov et al. (1999)
$[Ho(LH)_2L(DOS)_2]$	$C_{12}H_{25}$	$C_{18}H_{37}$	Cr 59 SmA 81 I	Binnemans et al. (1998)
$[Yb(LH)_2L(DOS)_2]$	$C_{12}H_{25}$	$C_{18}H_{37}$	Cr 59 SmA 111 I	Binnemans et al. (1998)
$[Eu(LH)_3\{CF_3(CF)_5CH_2OSO_3\}_3]$	$C_{14}H_{29}$	$C_{18}H_{37}$	Cr 74 SmX 97 SmA 125 I	Gainullina et al. (2003)

Continued

TABLE 6 Thermal Behavior of the Lanthanide Complexes of the One-Ring Schiff's Base Ligands L4H with Alkylsulfate Counter Ions—Cont'd

Compound	C_nH_{2n+1}	C_mH_{2m+1}	Temperatures (°C)	Reference
$[Eu(LH)_3\{CHF_2(CF)_5CH_2OSO_3\}_3]$	$C_{14}H_{29}$	$C_{18}H_{37}$	Cr 60 SmX 106 SmA 132 I	Gainullina et al. (2003)
$[Tb(LH)_3\{CF_3(CF)_5CH_2OSO_3\}_3]$	$C_{14}H_{29}$	$C_{18}H_{37}$	Cr 64 SmX 100 SmA 126 I	Gainullina et al. (2003)
$[Tb(LH)_3\{CHF_2(CF)_5CH_2OSO_3\}_3]$	$C_{14}H_{29}$	$C_{18}H_{37}$	Cr 60 SmX 99 SmA 128 I	Gainullina et al. (2003)
$[Dy(LH)_3\{CF_3(CF)_5CH_2OSO_3\}_3]$	$C_{14}H_{29}$	$C_{18}H_{37}$	Cr 65 SmX 74 SmA 125 I	Gainullina et al. (2003)
$[Dy(LH)_3\{CHF_2(CF)_5CH_2OSO_3\}_3]$	$C_{14}H_{29}$	$C_{18}H_{37}$	Cr 63 SmX 102 SmA 125 I	Gainullina et al. (2003)
$[Ho(LH)_3\{CF_3(CF)_5CH_2OSO_3\}_3]$	$C_{14}H_{29}$	$C_{18}H_{37}$	Cr 67 SmX 110 SmA 140 I	Gainullina et al. (2003)
$[Ho(LH)_3\{CHF_2(CF)_5CH_2OSO_3\}_3]$	$C_{14}H_{29}$	$C_{18}H_{37}$	Cr 62 SmX 98 SmA 125 I	Gainullina et al. (2003)
$[Er(LH)_3\{CF_3(CF)_5CH_2OSO_3\}_3]$	$C_{14}H_{29}$	$C_{18}H_{37}$	Cr 64 SmX 101 SmA 141 I	Gainullina et al. (2003)
$[Er(LH)_3\{CHF_2(CF)_5CH_2OSO_3\}_3]$	$C_{14}H_{29}$	$C_{18}H_{37}$	Cr 60 SmX 90 SmA 140 I	Gainullina et al. (2003)
$[Tm(LH)_3\{CF_3(CF)_5CH_2OSO_3\}_3]$	$C_{14}H_{29}$	$C_{18}H_{37}$	Cr 74 SmX 96 SmA 135 I	Gainullina et al. (2003)
$[Tm(LH)_3\{CHF_2(CF)_5CH_2OSO_3\}_3]$	$C_{14}H_{29}$	$C_{18}H_{37}$	Cr 60 SmX 100 SmA 138 I	Gainullina et al. (2003)
$[La(LH)_3(DOS)_3]$	$C_{14}H_{29}$	$C_{18}H_{37}$	Cr 67 SmA 80 I	Van Deun and Binnemans (2001a)
$[Ce(LH)_3(DOS)_3]$	$C_{14}H_{29}$	$C_{18}H_{37}$	Cr 66 SmA 80 I	Van Deun and Binnemans (2001a)
$[Pr(LH)_3(DOS)_3]$	$C_{14}H_{29}$	$C_{18}H_{37}$	Cr 66 SmA 80 I	Van Deun and Binnemans (2001a)

$[Nd(LH)_3(DOS)_3]$	$C_{14}H_{29}$	$C_{18}H_{37}$	Cr 65 SmA 79 I	Van Deun and Binnemans (2001a)
$[Sm(LH)_3(DOS)_3]$	$C_{14}H_{29}$	$C_{18}H_{37}$	Cr 62 SmA 78 I	Van Deun and Binnemans (2001a)
$[Eu(LH)_3(DOS)_3]$	$C_{14}H_{29}$	$C_{18}H_{37}$	Cr 62 SmA 78 I	Van Deun and Binnemans (2001a)
$[Gd(LH)_3(DOS)_3]$	$C_{14}H_{29}$	$C_{18}H_{37}$	Cr 61 SmA 77 I	Van Deun and Binnemans (2001a)
$[Tb(LH)_3(DOS)_3]$	$C_{14}H_{29}$	$C_{18}H_{37}$	Cr 61 SmA 80 I	Van Deun and Binnemans (2001a)
$[Dy(LH)_3(DOS)_3]$	$C_{14}H_{29}$	$C_{18}H_{37}$	Cr 61 SmA 82 I	Van Deun and Binnemans (2001a)
$[Ho(LH)_3(DOS)_3]$	$C_{14}H_{29}$	$C_{18}H_{37}$	Cr 62 SmA 84 I	Van Deun and Binnemans (2001a)
$[Er(LH)_3(DOS)_3]$	$C_{14}H_{29}$	$C_{18}H_{37}$	Cr 61 SmA 85 I	Van Deun and Binnemans (2001a)
$[Tm(LH)_3(DOS)_3]$	$C_{14}H_{29}$	$C_{18}H_{37}$	Cr 61 SmA 86 I	Van Deun and Binnemans (2001a)
$[Yb(LH)_3(DOS)_3]$	$C_{14}H_{29}$	$C_{18}H_{37}$	Cr 60 SmA 87 I	Van Deun and Binnemans (2001a)
$[Lu(LH)_3(DOS)_3]$	$C_{14}H_{29}$	$C_{18}H_{37}$	Cr 59 SmA 86 I	Van Deun and Binnemans (2001a)

DOS, dodecylsulfate; Cr, crystalline phase; SmA, smectic A phase; SmX, unidentified smectic phase; I, isotropic liquid.

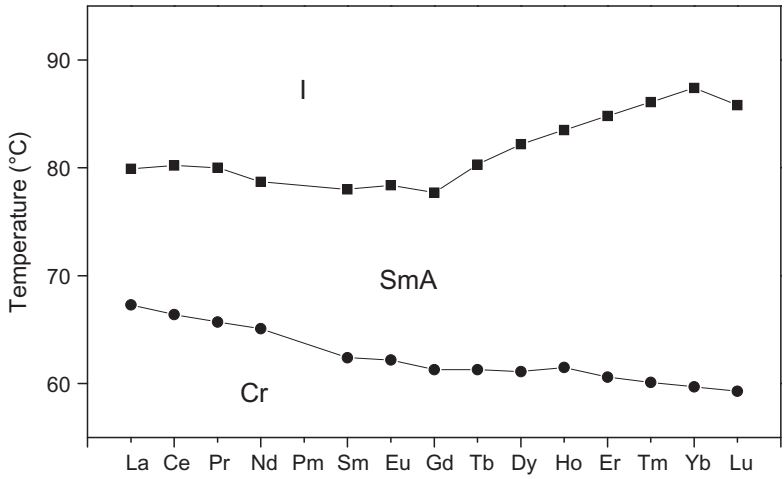

FIGURE 29 Influence of the lanthanide ion on the transition temperatures of the dodecylsulfate complexes $[R(LH)_3(DOS_3)_3]$. LH is the Schiff's base ligand **L4H** with $C_nH_{2n+1} = C_8H_{17}$, $C_mH_{2m+1} = C_{18}H_{37}$, and $DOS = C_{12}H_{25}OSO_3^-$. Cr, crystalline phase; SmA, smectic A phase; I, isotropic liquid. (Drawn using the data in Table 2 of Van Deun and Binnemans, 2001a).

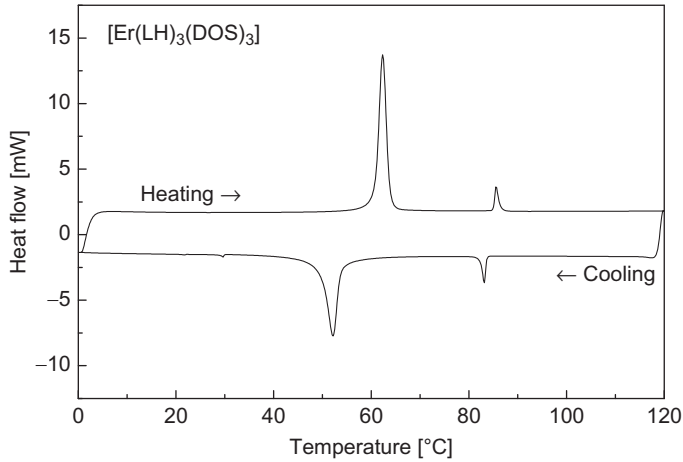

FIGURE 30 DSC trace (second heating and cooling run) of the complex $[Er(LH)_3(DOS)_3]$. Endothermic peaks are pointing upward. LH is the Schiff's base ligand **L4H** with $C_nH_{2n+1} = C_8H_{17}$, $C_mH_{2m+1} = C_{18}H_{37}$, and $DOS = C_{12}H_{25}OSO_3^-$. Reprinted with permission from Van Deun and Binnemans (2001a). Copyright 2001 Taylor and Francis.

(clearing process). The influence of the alkyl chain length on the transition temperatures of terbium(III) and erbium(III) complexes was investigated by Galyametdinov and coworkers (Fig. 31; Malykhina et al., 2001). The transition temperatures increase when the chain length is increased from ethylsulfate to butylsulfate, and then decrease sharply to nonylsulfate (the heptylsulfate being

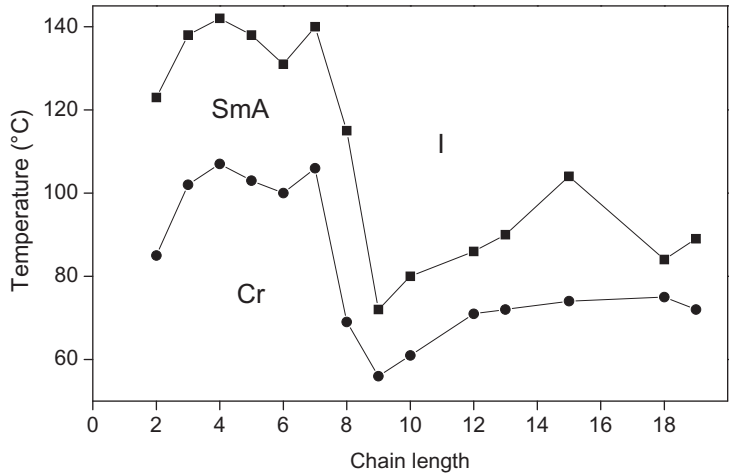

FIGURE 31 Influence of the alkylsulfate chain length on the transition temperatures of [Tb(LH)$_3$($C_pH_{2p+1}OSO_3$)$_3$] complexes. LH is the Schiff's base ligand **L4H** with $C_nH_{2n+1}=C_{12}H_{25}$ and $C_mH_{2m+1}=C_{16}H_{33}$. Cr, crystalline phase; SmA, smectic A phase; I, isotropic liquid. (Drawn using the data in Table 1 of Malykhina et al., 2001).

an exception). Again from nonylsulfate to nonadecylsulfate the transition temperatures gradually decrease. Because both the melting point and the clearing point are influenced by the same extent, the mesophase stability range does not depend largely on the alkyl chain length. Although the perfluoroalkylsulfate complexes have slightly higher transition temperatures than the alkylsulfate complexes, they have the advantage that their mesophase is much less viscous (Galyametdinov et al., 2001b). The low viscosity is most probably due to the immiscibility of the alkyl chains of the Schiff's base ligand and the perfluoroalkyl chains of the counter ion. These low viscous mesophases can easier be aligned in an external magnetic field. The lanthanide Schiff's base complexes with perfluooralkylsulfate anions all show a smectic A phase. Below this SmA phase, most complexes exhibit an unidentified highly ordered SmX phase and a crystal phase. For a thulium(III) complex with the dodecafluoroheptylsulfate anion, this underlying highly ordered mesophase was identified as a crystal F phase by XRD (Galyametdinov et al., 2002a). Although replacement of $CF_3(CF_2)_5CH_2OSO_3^-$ anions by $CHF_2(CH_2)_5CH_2OSO_3^-$anions seems to be only a minor structural modification, significant changes of the transition temperatures were observed (Galyametdinov et al., 2001b). In general, the clearing points of the compounds of the $CHF_2(CF_2)_5CH_2OSO_3^-$ series are about 10 °C higher than those of the $CF_3(CF_2)_5CH_2OSO_3^-$ series, with marginally different melting point, so that $CHF_2(CF_2)_5CH_2OSO_3^-$ leads to more stable mesophases. Complexes with $CF_3(CF_2)_8CH_2OSO_3^-$anions were found to have a similar mesophase behavior as the complexes with shorter perfluoroalkylsulfate anions

(Gainullina et al., 2003). Schiff's base complexes with triflate and $CF_3(CF_2)_5CH_2OSO_3^-$ anions have in CCl_4 solution a hydrodynamic radius which is only about half that of the corresponding complexes with nitrate counter ions (Lavrenkov et al., 2005). This smaller size was attributed to a stronger folding of the alkyl chains of the ligands in the case of perfluorinated anions, although the underlying reason of the stronger folding is still unknown.

Optically active lanthanidomesogens have been obtained by binding a cholesteryl group via a long flexible oxyalkanoyloxy spacer to a salicylaldimine (Yelamaggad et al., 2009). Whereas the ligands **L7H** ($n = 3$, 4, 5, 7, see Fig. 25) exhibited a very rich mesomorphism, with chiral nematic, chiral smectic A and smectic C phases, and even a twist grain boundary (TGB) phase, the lanthanum(III), gadolinium(III), and ytterbium(III) complexes only exhibited a chiral smectic A phase (SmA*). The clearing temperatures of the lanthanide complexes showed a pronounced odd–even effect, in the sense that the compounds with an even number of carbon atoms in the flexible spacer have relatively higher transition temperatures than the compounds with an odd number of carbon atoms. Condensation of a 4-alkoxy-substituted salicylaldehyde with 2-amino-1-ethanol, resulted in the formation a Schiff's base with only one alkyl chain (Bhattacharjee et al., 2011). The proposed structure of the complexes, $[R(LH)_3(NO_3)_3]$ is similar to that of the Schiff's bases with two long alkyl chains (*vide supra*). The Schiff's base ligand is coordinated through the phenolic oxygen only, and not via the imine nitrogen atom or via the alcohol function. The Schiff's base is considered to be in a zwitterionic form.

A disadvantage of metallomesogens is their low thermal stability in comparison with classic organic LCs. Many metallomesogens decompose at the clearing point or they decompose in the mesophase before the clearing point is even reached. In this context, the high thermal stability of the Schiff's base complexes is remarkable. Thermal decomposition starts more than 100 °C above the clearing point. This makes these compounds well-suitable for physical studies, because good alignment can in most cases be achieved only by heating the compounds to the isotropic liquid and cooling them into the mesophase. In general, no supercooling is observed for the clearing point of LCs, so that clearing is observed both on cooling and heating at the same temperature. However, for the Schiff's base complexes and especially those with alkylsulfate counter ions, supercooling can be as large as 5–25 °C (Malykhina et al., 2001). The Schiff's base complexes have a low tendency to crystallize when their mesophase is being cooled. Most probably this is due to the high viscosity of the smectic A phase. The mesophase can be supercooled into a glass state (Galyametdinov et al., 1996a). In this way, anisotropic glasses can be obtained. Glass formation is especially evident in thin samples used for optical microscopy studies, where the defect texture can be frozen in room temperature. The vitrified mesophase is stable for several days, but they tend to crystallize over a longer time period.

Although crystal structures of the nonmesomorphic Schiff's base complexes have been determined (Binnemans et al., 2000a; Van Meervelt et al., 2003a,b), much less is known about the actual structure of the mesomorphic lanthanide complexes themselves. The presence of a smectic A phase indicates that the Schiff's base ligands are arranged around the central metal ion in such a way that the formation of a layered structure is possible. Spectroscopic data indicate that the first coordination sphere around the lanthanide ion is not changed by elongation of the alkyl chains. Therefore, it was assumed that the bonding in the nonmesogenic complexes is the same as in the mesogenic complexes. Of course, changes in the packing of the molecules can occur. A molecular structure has been proposed by Galyametdinov et al. (1996a), which can be described as a trigonal prism where the nitrate groups occupy equatorial or axial positions (Fig. 32). Because the smectic layer thickness d (determined by XRD) was found to be shorter than the calculated length of the Schiff's base ligand, it was assumed that the molecules of each layer penetrate the adjacent layer to a limited depth.

Soon after the discovery of this type of lanthanidomesogens, it became evident that they have very interesting magnetic properties, such as a huge magnetic anisotropy (Galyametdinov et al., 1995). Due to their high magnetic anisotropy, the mesophase formed by these compounds can be much easier aligned in an external magnetic field than organic LCs. The magnetic behavior of the Schiff's base complexes is discussed in detail in Section 14.2. The spectroscopic properties have been investigated much less intensively. Because of the presence of the N^+—H group in the zwitterionic ligand, which can effectively deactivate the excited states of the lanthanide ions, most of the Schiff's base lanthanidomesogens show a weak photoluminescence only or do not luminesce at all. Interestingly, the europium(III) complexes with the perfluorinated alkylsulfate counter ions do show a strong photoluminescence (Galyametdinov et al., 2001b). It was found that the europium(III) complexes experience in these complexes a very strong crystal field effect. In fact the B_0^2crystal-field parameter for these compounds are among the largest ever reported for europium complexes. In the absorption spectra of the Schiff's base complexes dissolved in chloroform, the so-called *hypersensitive transitions* have a very high intensity (Binnemans et al., 2000b). Temperature-dependent absorption and linear dichroism spectra of neodymium(III), terbium(III) and erbium(III) complexes have been recorded from the crystalline to the isotropic state, through the mesophase (Vaisnoras et al., 1998).

In all the Schiff's base complexes described above, no base was used to deprotonate the Schiff's base ligand. Therefore, the Schiff's base binds in a neutral, albeit an zwitterionic form to the central metal ion, resulting in complexes with stoichiometry $[R(LH)_3X_3]$. It was also mentioned that in some complexes, only one of the ligands looses spontaneously a proton, giving complexes of stoichiometry $[R(LH)_2LX_2]$. With dimeric *salen*-type ligands (*salen* = 2,2′-*N*,*N*′-bis(salicylidene)ethylenediamine) is was possible to form

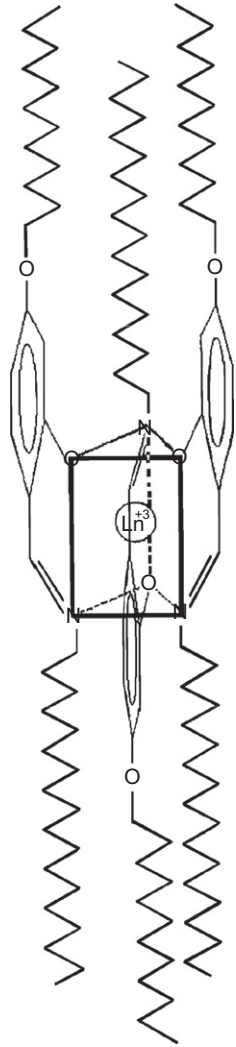

FIGURE 32 Molecular structure of the $[R(LH)_3(NO_3)_3]$ Schiff's base complex of ligand **L4H** ($C_nH_{2n+1} = C_{12}H_{25}$, $C_mH_{2m+1} = C_{18}H_{37}$), as suggested by Galyametdinov et al. (1996a). The nitrate groups have been omitted for clarity. Reprinted with permission. Copyright 1996 American Chemical Society.

by use of piperidine as the base neutral complexes in which the lanthanide ion was bound to one monoanionic ligand and one dianionic ligands (ligand **L8H$_2$**; Binnemans et al., 1999d; Collinson et al., 2001). The ligands themselves are mesomorphic (SmC or SmA phase) and the bis(*salen*) complexes exhibit a highly viscous smectic mesophase. In the absence of a base, the salen-type ligands form complexes with three counter ions, but with two

TABLE 7 Thermal Behavior of the Lanthanide Complexes of the Salen-Type Schiff's Base Ligands $L8H_2$

Compound	C_nH_{2n+1}	Temperatures (°C)	Reference
$[La(LH_2)_2Cl_3]\cdot 4H_2O$	$C_{12}H_{25}$	Cr 220 SmX 288 dec.	Collinson et al. (2001)
$[La(LH_2)_2(CF_3SO_3)_3]\cdot 4H_2O$	$C_{12}H_{25}$	Cr 170 SmX 240 I	Collinson et al. (2001)
$[La(LH)(LH_2)]\cdot 4H_2O$	$C_{12}H_{25}$	Cr 176 SmX 190 I	Collinson et al. (2001)
$[Nd(LH)(LH_2)]$	$C_{12}H_{25}$	Cr 182 SmX 209 I	Collinson et al. (2001)
$[Eu(LH)(LH_2)]\cdot 2H_2O$	$C_{12}H_{25}$	Cr 150 SmX 190 I	Binnemans et al. (1999d)
$[Er(LH)(LH_2)]\cdot 3H_2O$	$C_{12}H_{25}$	Cr 165 SmX 230 I	Binnemans et al. (1999d)
$[La(LH)_3(NO_3)](NO_3)_2$	$C_{16}H_{33}$	Cr 93 SmX 200 I (dec.)	Kumari et al. (2009a)
$[Pr(LH)_3(NO_3)](NO_3)_2$	$C_{16}H_{33}$	Cr 113 SmF 173 SmC 240 I (dec.)	Kumari et al. (2009a)
$[Nd(LH)(LH_2)]$	$C_{12}H_{25}OC_6H_4CO$	Cr 140 SmX 200 dec.	Binnemans et al. (1999d)

Cr, crystalline phase; SmC, smectic C phase; SmF, smectic F phase; SmX, unidentified smectic phase; I, isotropic liquid; dec., decomposition.

ligands for each lanthanide ion. An overview of the transition temperatures is given in Table 7. Kumari et al. (2009a) reported on lanthanide complexes of ligand $\mathbf{L8H_2}$ with $C_nH_{2n+1} = C_{16}H_{33}$. The stoichiometry of the complexes was $[R(LH_2)_3(NO_3)](NO_3)_2$ for R = La, Pr, Nd, Sm, Eu, and $[R_2(LH_2)_3(NO_3)_4](NO_3)_2$ for R = Gd, Tb, Dy, Ho. Liquid-crystalline behavior was only observed for the lightest lanthanides. The lanthanum(III) complex formed an unidentified smectic X phase, while the praseodymium(III) complexes exhibited a smectic C and smectic F phase. A modified ligand was prepared by replacing ethylenediamine by 1′,8′-diamino-3′,6′-dioxaoctane (Kumari et al., 2009b). The authors report that the complexes of lanthanum(III) and praseodymium(III) form a nematic phase, whereas the complexes of the heavier lanthanides form a smectic A phase. However, a nematic phase for this type of complexes with long alkyl chains is unexpected and further work is needed to confirm these results. The ligand design was taken a step further and it was tried to encapsulate the lanthanide ion in a tripodal Schiff's base ligand $\mathbf{L9H_3}$, derived of tris(2-aminoethyl)

amine, TREN (Binnemans et al., 1999d). Lanthanide complexes were obtained as neutral species, for which on the basis of the crystal structure of an analogous compound with short alkyl chains a dimeric complex was proposed. The type of mesophase formed by these complexes could not yet be unequivocally identified, but it is most probably a smectic phase. The transition temperatures are quite high: the majority of the complexes melt only above 200 °C, with clearing points up to 280 °C (Table 8). Serrano and coworkers formed *in situ* lanthanide complexes of a tripodal Schiff's base ligand by reaction of $R(TREN)_2(CF_3SO_3)$ with 4-(4′-octadecyloxybenzoyloxy)salicylaldehyde in methanol (Marcos et al., 2004). The resulting complexes were monometallic with stoichiometry RL, with R = Sm, Gd, Lu, and L is the tripodal Schiff's base ligand **L10H$_3$** (Fig. 33). The complexes exhibit an unidentified smectic mesophase. The transition temperatures are: for SmL: C 104.3 SmX 240 I, for GdL: Cr 99.8 SmX 230 I, and for LuL: Cr 96.5 SmX 246 I (dec.). Besides the reflections that are characteristic for a smectic (lamellar) system, several relatively sharp diffraction peaks could be observed in the XRD patterns of the mesophases, at middle and large diffraction angles. These additional reflections were not consistent with conventional smectic mesophases and were attributed to in-plane correlations between the polar groups. The average *d* spacing of the lanthanide complexes is 44 Å, which is considerably larger than the layer spacing measured for the ligand (58 Å). On the basis of the experimental data, it was for the authors not possible to conclude whether the structure consists of a bilayer array with pairs of antiparallel stacked tripodal monomeric molecules or whether the structure is a monolayer of dimers.

Binnemans and Lodewyckx (2001) showed that it is possible to obtain mesomorphic lanthanide complexes by forming Lewis-base adducts of simple

TABLE 8 Thermal Behavior of the Lanthanide Complexes of the Tripodal Schiff's Base Ligands L9H$_3$

Compound	C_nH_{2n+1}	Temperatures (°C)	Reference
$[LaL_3]\cdot H_2O$	$C_{12}H_{25}$	Cr 209 SmX 221 I	Binnemans et al. (1999d)
$[GdL_3]\cdot H_2O$	$C_{12}H_{25}$	Cr 205 SmX 278 I	Binnemans et al. (1999d)
$[ErL_3]\cdot 2H_2O$	$C_{12}H_{25}$	Cr 230 SmX 270 I	Binnemans et al. (1999d)
$[LaL_3]\cdot 4H_2O$	$C_{12}H_{25}OC_6H_4CO$	Cr 216 SmX 230 I	Binnemans et al. (1999d)
$[LaL_3]\cdot H_2O$	3,4-$(C_{12}H_{25}O)C_6H_3CO$	Cr 122 SmX 180 I	Binnemans et al. (1999d)

Cr, crystalline phase; SmX, unidentified smectic phase; I, isotropic liquid.

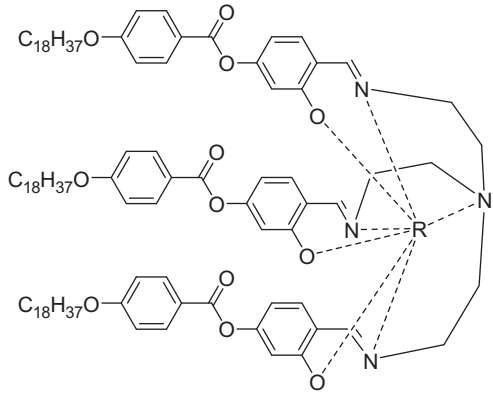

FIGURE 33 Lanthanide complexes of the tripodal Schiff's base ligand **L10H$_3$** (Marcos et al., 2004).

tris(β-diketonato)lanthanide(III) complexes with mesogenic ligands. More particularly, they studied *bis* adducts of [R(dbm)$_3$] complexes (Hdbm = 1,3-diphenyl-1,3-propanedione or dibenzoylmethane, R = La, Nd, Eu) with the one-ring Schiff's base ligands (Fig. 34). The compounds were prepared by dissolving accurately weighed amounts of [R(dbm)$_3$] and LH in a 1:2 molar ratio in dichloromethane and subsequently evaporating the solvent. In these compounds, neither the Schiff's base nor the tris(β-diketonato)lanthanide(III) complex show a mesophase, but the resulting bis adducts are liquid-crystalline. The adducts [R(dbm)$_3$(LH)$_2$] exhibited a smectic A phase, albeit only upon cooling of the isotropic liquid (monotropic mesophase). This result was unexpected, because work by Giroud-Godquin and Rassat (1982) had shown that six alkyl chains are insufficient for octahedral tris(β-diketonato) iron(III) complexes to form a liquid-crystalline. Swager and Zheng found that tris(β-diketonato) complexes of iron(III), manganese (III), and chromium(III) should have 12 or more alkyl chains (attached to the β-diketone ligand) in order to exhibit mesomorphism (Swager and Zheng, 1995; Zheng and Swager, 1994). In the [R(dbm)$_3$(LH)$_2$] complexes, only four long alkyl chains are present. The work on the Schiff's base adducts of the [R(dbm)$_3$] complexes was later extended to all other lanthanide(III) ions, except cerium(III) and promethium(III) (Binnemans et al., 2003a). The number of Schiff's bases bound to a metal complex was found to depend on the size of the lanthanide ion: two for most of the lanthanide ions and one for the ions at the end of the lanthanide series (R = Tm, Yb, Lu). Both the X-ray crystal structure of a complex with short-chain Schiff's base ligands and NMR spectra showed that the Schiff's base in the adducts is present in a zwitterionic form. This is similar to what was observed for the Schiff's base complexes with simple inorganic counter ions. The complexes [R(dbm)$_3$(LH)$_2$] of the

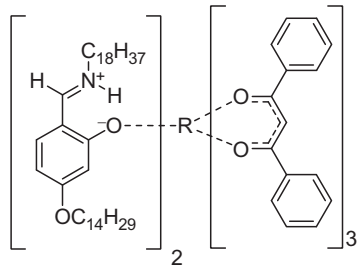

$[R(dbm)_3(LH)_2]$

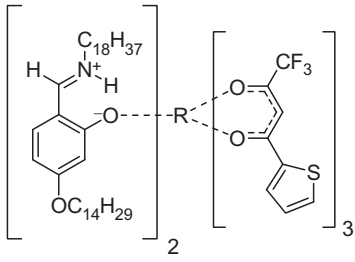

$[R(tta)_3(LH)_2]$

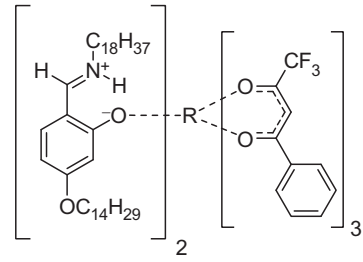

$[R(bta)_3(LH)_2]$

FIGURE 34 Liquid-crystalline Lewis base adducts formed between a tris β-diketonate complex and a salicylaldimine Schiff's base.

series R = La–Eu exhibited a monotropic smectic A phase. The temperature difference between the melting point and the clearing point of the monotropic mesophase increased over the lanthanide series. The complexes of the heavier lanthanides were not liquid-crystalline. By replacing the dibenzoylmethanate ligands by 2-thenoyltrifluoroacetonate (tta) or benzoyltrifluoroacetonate (bta), the transition temperatures of the lanthanide complexes could be reduced and the mesophases could be stabilized (Yang et al., 2006). The resulting complexes exhibited a smectic A phase at room temperature or at slightly higher temperatures. The transition temperatures of the benzoyltrifluoroacetonate complexes $[R(bta)_3(LH)_2]$ were lower than those of the 2-thenoyltrifluoroacetonate complexes $[R(tta)_3(LH)_2]$. For the two series of compounds, the mesophase stability range decreased over the lanthanide series from the lanthanum(III) complex to the erbium(III) complex. The thulium(III), ytterbium(III), and lutetium(III) complexes were not mesomorphic and melted directly to the isotropic state. The transition temperatures of the yttrium(III) complexes are very comparable to those of the dysprosium(III) and holmium(III) complexes. This indicates that the size of the lanthanide ion has a strong influence on the transition temperatures of the mesogenic lanthanide complexes, a phenomenon that was also

observed for other liquid-crystalline Schiff's base complexes of the lanthanides (*vide supra*). In Table 9, an overview of the transition temperatures of the Schiff's base adducts to the lanthanide(III) tris β-diketonate complexes is given. Because the lanthanide(III) β-diketonate complexes often show a very intense photoluminescence, it is not a surprise that also the liquid-crystalline complexes are luminescent (see Section 14.1). Yang et al. (2008c) performed

TABLE 9 Thermal Behavior of Adducts of the One-Ring Schiff's Base Ligands L4H to Lanthanide β-Diketonate Complexes

Compound	C_nH_{2n+1}	C_mH_{2m+1}	Temperatures (°C)	Reference
$[La(LH)_2(dbm)_3]$	$C_{12}H_{25}$	$C_{16}H_{33}$	Cr 100 (SmA 81) I[a]	Binnemans and Lodewyckx (2001)
$[Y(LH)_2(tta)_3]$	$C_{14}H_{29}$	$C_{18}H_{37}$	g 23 SmA 49 I	Yang et al. (2006)
$[Y(LH)_2(bta)_3]$	$C_{14}H_{29}$	$C_{18}H_{37}$	g 18 SmA 31 I	Yang et al. (2006)
$[La(LH)_2(dbm)_3]$	$C_{14}H_{29}$	$C_{18}H_{37}$	Cr 95 (SmA 81) I[a]	Binnemans and Lodewyckx (2001) and Binnemans et al. (2003a)
$[La(LH)_2(tta)_3]$	$C_{14}H_{29}$	$C_{18}H_{37}$	g 23 SmA 68 I	Yang et al. (2006)
$[La(LH)_2(bta)_3]$	$C_{14}H_{29}$	$C_{18}H_{37}$	g 19 SmA 50 I	Yang et al. (2006)
$[Pr(LH)_2(dbm)_3]$	$C_{14}H_{29}$	$C_{18}H_{37}$	Cr 94 (SmA 75) I[a]	Binnemans and Lodewyckx (2001)
$[Pr(LH)_2(tta)_3]$	$C_{14}H_{29}$	$C_{18}H_{37}$	g 20 SmA 67 I	Yang et al. (2006)
$[Pr(LH)_2(bta)_3]$	$C_{14}H_{29}$	$C_{18}H_{37}$	g 18 SmA 44 I	Yang et al. (2006)
$[Nd(LH)_2(dbm)_3]$	$C_{14}H_{29}$	$C_{18}H_{37}$	Cr 93 (SmA 71) I[a]	Binnemans et al. (2003a)
$[Nd(LH)_2(tta)_3]$	$C_{14}H_{29}$	$C_{18}H_{37}$	g 22 SmA 65 I	Yang et al. (2006)
$[Nd(LH)_2(bta)_3]$	$C_{14}H_{29}$	$C_{18}H_{37}$	g 19 SmA 43 I	Yang et al. (2006)
$[Sm(LH)_2(dbm)_3]$	$C_{14}H_{29}$	$C_{18}H_{37}$	Cr 93 (SmA 64) I[a]	Binnemans et al. (2003a)
$[Sm(LH)_2(tta)_3]$	$C_{14}H_{29}$	$C_{18}H_{37}$	g 22 SmA 64 I	Yang et al. (2006)
$[Sm(LH)_2(bta)_3]$	$C_{14}H_{29}$	$C_{18}H_{37}$	g 18 SmA 41 I	Yang et al. (2006)
$[Eu(LH)_2(dbm)_3]$	$C_{14}H_{29}$	$C_{18}H_{37}$	Cr 90 (SmA 60) I[a]	Binnemans and Lodewyckx (2001) and Binnemans et al. (2003a)

Continued

TABLE 9 Thermal Behavior of Adducts of the One-Ring Schiff's Base Ligands L4H to Lanthanide β-Diketonate Complexes—Cont'd

Compound	C_nH_{2n+1}	C_mH_{2m+1}	Temperatures (°C)	Reference
$[Eu(LH)_2(tta)_3]$	$C_{14}H_{29}$	$C_{18}H_{37}$	g 22 SmA 62 I	Yang et al. (2006)
$[Eu(LH)_2(bta)_3]$	$C_{14}H_{29}$	$C_{18}H_{37}$	g 18 SmA 40 I	Yang et al. (2006)
$[Gd(LH)_2(dbm)_3]$	$C_{14}H_{29}$	$C_{18}H_{37}$	Cr 86 I	Binnemans et al. (2003a)
$[Gd(LH)_2(tta)_3]$	$C_{14}H_{29}$	$C_{18}H_{37}$	g 23 SmA 49 I	Yang et al. (2006)
$[Gd(LH)_2(bta)_3]$	$C_{14}H_{29}$	$C_{18}H_{37}$	g 19 SmA 39 I	Yang et al. (2006)
$[Tb(LH)_2(dbm)_3]$	$C_{14}H_{29}$	$C_{18}H_{37}$	Cr 80 I	Binnemans et al. (2003a)
$[Tb(LH)_2(tta)_3]$	$C_{14}H_{29}$	$C_{18}H_{37}$	g 23 SmA 57 I	Yang et al. (2006)
$[Tb(LH)_2(bta)_3]$	$C_{14}H_{29}$	$C_{18}H_{37}$	g 18 SmA 37 I	Yang et al. (2006)
$[Dy(LH)_2(dbm)_3]$	$C_{14}H_{29}$	$C_{18}H_{37}$	Cr 74 I	Binnemans et al. (2003a)
$[Dy(LH)_2(tta)_3]$	$C_{14}H_{29}$	$C_{18}H_{37}$	g 23 SmA 54 I	Yang et al. (2006)
$[Dy(LH)_2(bta)_3]$	$C_{14}H_{29}$	$C_{18}H_{37}$	g 18 SmA 35 I	Yang et al. (2006)
$[Ho(LH)_2(dbm)_3]$	$C_{14}H_{29}$	$C_{18}H_{37}$	Cr 72 I	Binnemans et al. (2003a)
$[Ho(LH)_2(tta)_3]$	$C_{14}H_{29}$	$C_{18}H_{37}$	g 22 SmA 52 I	Yang et al. (2006)
$[Ho(LH)_2(bta)_3]$	$C_{14}H_{29}$	$C_{18}H_{37}$	g 18 SmA 33 I	Yang et al. (2006)
$[Er(LH)_2(dbm)_3]$	$C_{14}H_{29}$	$C_{18}H_{37}$	Cr 67 I	Binnemans et al. (2003a)
$[Er(LH)_2(tta)_3]$	$C_{14}H_{29}$	$C_{18}H_{37}$	g 24 SmA 48 I	Yang et al. (2006)
$[Er(LH)_2(bta)_3]$	$C_{14}H_{29}$	$C_{18}H_{37}$	g 18 SmA 29 I	Yang et al. (2006)
$[Tm(LH)(dbm)_3]$	$C_{14}H_{29}$	$C_{18}H_{37}$	Cr 73 I	Binnemans et al. (2003a)
$[Tm(LH)_2(tta)_3]$	$C_{14}H_{29}$	$C_{18}H_{37}$	Cr 66 I	Yang et al. (2006)
$[Tm(LH)_2(bta)_3]$	$C_{14}H_{29}$	$C_{18}H_{37}$	Cr 64 I	Yang et al. (2006)
$[Yb(LH)(dbm)_3]$	$C_{14}H_{29}$	$C_{18}H_{37}$	Cr 72 I	Binnemans et al. (2003a)
$[Yb(LH)_2(tta)_3]$	$C_{14}H_{29}$	$C_{18}H_{37}$	Cr 64 I	Yang et al. (2006)
$[Yb(LH)_2(bta)_3]$	$C_{14}H_{29}$	$C_{18}H_{37}$	Cr 60 I	Yang et al. (2006)
$[Lu(LH)(dbm)_3]$	$C_{14}H_{29}$	$C_{18}H_{37}$	Cr 69 I	Binnemans et al. (2003a)

TABLE 9 Thermal Behavior of Adducts of the One-Ring Schiff's Base Ligands L4H to Lanthanide β-Diketonate Complexes—Cont'd

Compound	C_nH_{2n+1}	C_mH_{2m+1}	Temperatures (°C)	Reference
$[Lu(LH)_2(tta)_3]$	$C_{14}H_{29}$	$C_{18}H_{37}$	Cr 59 I	Yang et al. (2006)
$[Lu(LH)_2(bta)_3]$	$C_{14}H_{29}$	$C_{18}H_{37}$	Cr 58 I	Yang et al. (2006)
$[La(LH)_2(dbm)_3]$	$C_{16}H_{33}$	$C_{18}H_{37}$	Cr 93 (SmA 77) I[a]	Binnemans and Lodewyckx (2001)
$[Nd(LH)_2(dbm)_3]$	$C_{16}H_{33}$	$C_{18}H_{37}$	Cr 89 (SmA 63) I[a]	Binnemans and Lodewyckx (2001)

bta, benzoyltrifluoroacetonate; dbm, dibenzoylmethanate; tta, 2-thenoyltrifluoroacetonate; Cr, crystalline phase; SmA, smectic A phase; I, isotropic liquid; g, glassy phase
[a]*monotropic mesophase.*

a high-pressure study of the complex $[Eu(bta)_3(LH)_2]$, which is liquid-crystalline a room temperature (SmA phase). The pressure was varied between atmospheric pressure and 8.0 GPa. The complex underwent a transition from the SmA phase to a solid lamellar structure around 0.22 GPa and another transition from the solid lamellar phase to an amorphous state from 1.6 to 3.5 GPa. At low pressures, the smectic layer spacing increased, and the intermolecular distance decreased. Above pressures above 3.5 GPa, both the interlamellar and the intermolecular spacings hardly changed, but the intensity of X-ray reflections exhibited a remarkable decrease and eventually vanished upon going to higher pressures. It was found that less interdigitation of the alkyl chains situated in adjacent layers and/or a full extension of the alkyl chains occurred at low pressures and that the second phase transition was accompanied by a transfer of the hydrogen atom from the nitrogen atom of the imine group to the oxygen atom of the Schiff's base ligand. The effect of applying pressure equals that of the lanthanide contraction on the phase behavior, where the most stable mesophases are found at the beginning of the lanthanide series and where mesomorphism is often lost at the end of the lanthanide series.

All the Schiff's base complexes discussed so far are low-molecular weight complexes. An erbium(III)-containing methacrylate metallopolymer was prepared by free-radical polymerization of a Schiff's base monomer **L11H**, followed by complex formation with hydrated erbium nitrate (Haase et al., 1996). By XRD, the presence of a smectic mesophase was shown. A special feature of the polymer is that the complexing group is an *N*-aryl substituted Schiff's base, rather than an *N*-alkyl substituted one. No further structural data were reported. A detailed study of the mesophase behavior of lanthanide complexes of *N*-aryl substituted Schiff's base ligands **L12H** was reported by Rao et al. (2002, 2010). The complexes were synthesized by reaction between the

ligand and a lanthanide nitrate in boiling ethanol. After reaction, cooling of the mixture resulted in partial precipitation of the complexes. Further precipitation of the compounds was induced by slow addition of acetonitrile. Notice the differences in the synthetic procedures. In the case of the *N*-alkyl substituted Schiff's base complexes, the ethanolic solution must not be heated above 40 °C, because otherwise no pure compound can be obtained (*vide supra*). Under these conditions, no complexes of the *N*-aryl substituted Schiff's bases with lanthanide ions are formed. Heating of the reaction mixture to higher temperatures is required in the latter case. The stoichiometry of all the complexes was $[R(LH)_2L(NO_3)_2]$ (R = Gd, Tb, Dy). The complexes showed a rich mesomorphism. Depending on the chain length on the *N*-aryl group and the lanthanide ion, different mesophases were observed: smectic A, smectic E or a hexagonal columnar phase. An interesting observation is that some complexes first melt to form a hexagonal columnar phase, and that upon further heating a smectic A phase is formed. Upon cooling of the smectic A phase, the hexagonal columnar phase is observed again. The authors present a structural model for the crossover phenomenon from the discotic columnar behavior (Col_h) to the calamitic lamellar behavior (SmA). In Fig. 35, an overview of the *N*-aryl Schiff's base ligands is given. The transition temperatures of the complexes are given in Table 10.

Binnemans et al. (2002b) described liquid-crystalline f–d complexes, which were called *mixed f–d metallomesogens*. Their approach consisted of modifying the structures of previously described nonmesomorphic *f–d* complexes of *salen*-type Schiff's base ligands in such a way that a sufficient structural anisotropy was obtained to favor the formation of a mesophase. Such a modification could be achieved by extending the aromatic parts of the central rigid core on the one hand and to attach long alkyl chains to the extremities of the core complex on the other hand. Kahn et al. (2000) described adducts of lanthanide(III) nitrates with the Cu(*salen*) complex. Binnemans et al. (2002b) obtained a heterotrinuclear $[La(NO_3)_3\{Cu(C_{14}salen)\}_2]$ complex

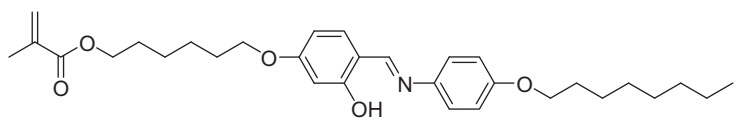

L11H

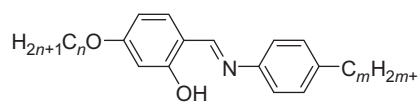

L12H

FIGURE 35 *N*-aryl Schiff's bases.

TABLE 10 Thermal Behavior of the Lanthanide Complexes of *N*-Aryl Schiff's Base Ligands L12H

Compound	C_nH_{2n+1}	C_mH_{2m+1}	Temperatures (°C)	Reference
$[Tb(LH)_2L(NO_3)_2]$	C_7H_{15}	$C_{14}H_{29}$	Cr 60 SmA 142 I	Rao et al. (2002)
$[Tb(LH)_2L(NO_3)_2]$	C_7H_{15}	$C_{14}H_{29}$	Cr 65 SmA 148 I	Rao et al. (2002)
$[Gd(LH)_2L(NO_3)_2]$	$C_{10}H_{21}$	C_4H_9	Cr 173 I	Rao et al. (2010)
$[Gd(LH)_2L(NO_3)_2]$	$C_{10}H_{21}$	$C_{10}H_{21}$	Cr 53 SmE 99 SmA 164 I	Rao et al. (2010)
$[Gd(LH)_2L(NO_3)_2]$	$C_{10}H_{21}$	$C_{14}H_{29}$	Cr 62 SmE 100 SmA 151 I	Rao et al. (2010)
$[Tb(LH)_2L(NO_3)_2]$	$C_{10}H_{21}$	C_4H_9	Cr 181 (Col_h 145 SmA 150) I	Rao et al. (2010)
$[Tb(LH)_2L(NO_3)_2]$	$C_{10}H_{21}$	$C_{10}H_{21}$	Cr 150 Col_h 161 SmA 184 I	Rao et al. (2010)
$[Tb(LH)_2L(NO_3)_2]$	$C_{10}H_{21}$	$C_{14}H_{29}$	Cr 85 SmX 144 Col_h 189 I	Rao et al. (2010)
$[Dy(LH)_2L(NO_3)_2]$	$C_{10}H_{21}$	C_4H_9	Cr 79 (SmA 144) I	Rao et al. (2010)
$[Dy(LH)_2L(NO_3)_2]$	$C_{10}H_{21}$	$C_{10}H_{21}$	Cr 158 SmA 177 I	Rao et al. (2010)
$[Dy(LH)_2L(NO_3)_2]$	$C_{10}H_{21}$	$C_{14}H_{29}$	Cr 92 Col_h 141 SmA 198 I	Rao et al. (2010)

Cr, crystalline phase; SmA, smectic A phase; SmE, smectic E phase; SmX, unidentified smectic phase; Colh, hexagonal columnar phase; I, isotropic liquid.

and a heterobinuclear $[Gd(NO_3)_3\{Cu(C_{14}salen)\}]$ complex, where $C_{14}salen$ represent a *salen*-type ligand with six tetradecyloxy chains (Fig. 36) These complexes formed a hexagonal columnar mesophase. The molecular organization of the molecules in the mesophase is shown in Fig. 37. In order to investigate the influence of the *d*-metal ion, adducts were formed between a mesomorphic Ni(*salen*) complex with six terminal alkoxy chains and a lanthanide nitrate (R = La, Gd; Binnemans and Lodewyckx, 2003). Different alkoxy chain lengths were used: $OC_{12}H_{25}$, $OC_{14}H_{29}$, $OC_{16}H_{33}$, and $OC_{18}H_{37}$. Trinuclear nickel(II)–lanthanum(III) and nickel(II)–gadolinium(III) complexes $[R(NO_3)_3\{Ni(salen)\}_2]$ were obtained. The compounds exhibited a hexagonal columnar mesophase with rather low melting points. By replacing in the

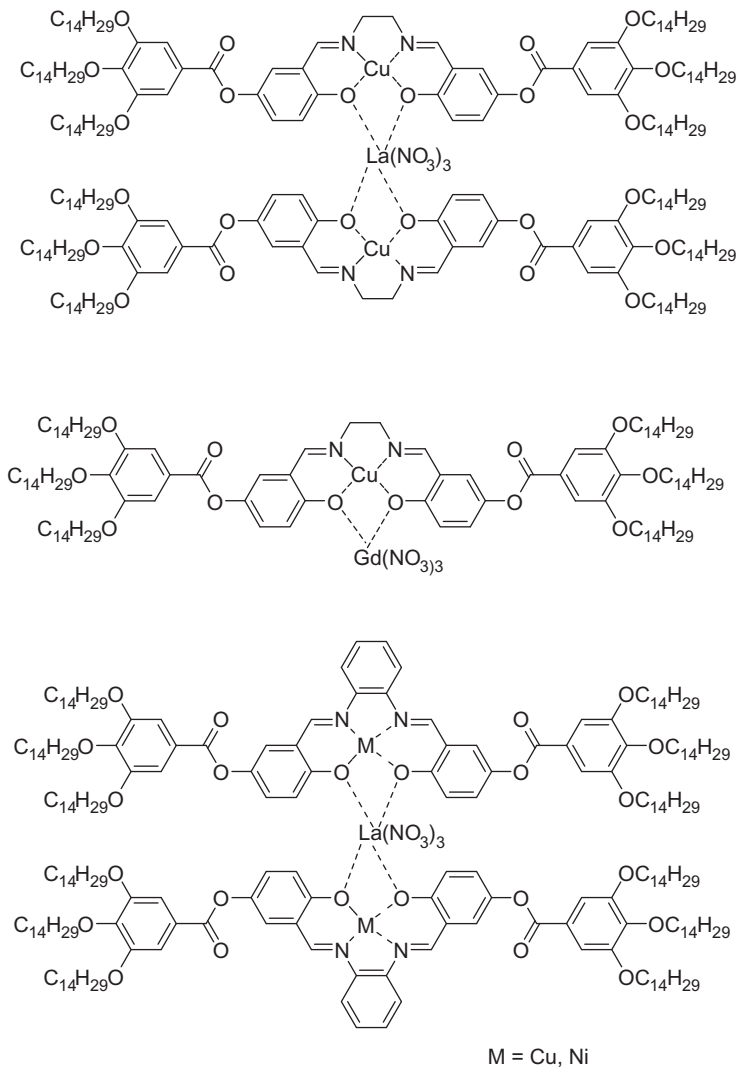

FIGURE 36 Mixed f–d metallomesogens.

synthesis 1,2-ethylenediamine by 1,2-diaminobenzene, a more rigid Schiff ligand could be obtained (Binnemans et al., 2005). This Schiff's base ligand did not show any liquid-crystalline properties. The corresponding copper(II), nickel(II), and dinuclear copper(II)–lanthanum(III) and nickel(II)–lanthanum (III) all exhibited a hexagonal columnar phase (Fig. 36). The geometrical parameters of the mesophase (lattice parameters and column cross-section) are very similar for both the mononuclear and dinuclear complexes. This indicates that the local organization in the mesophase is very similar, despite the structural

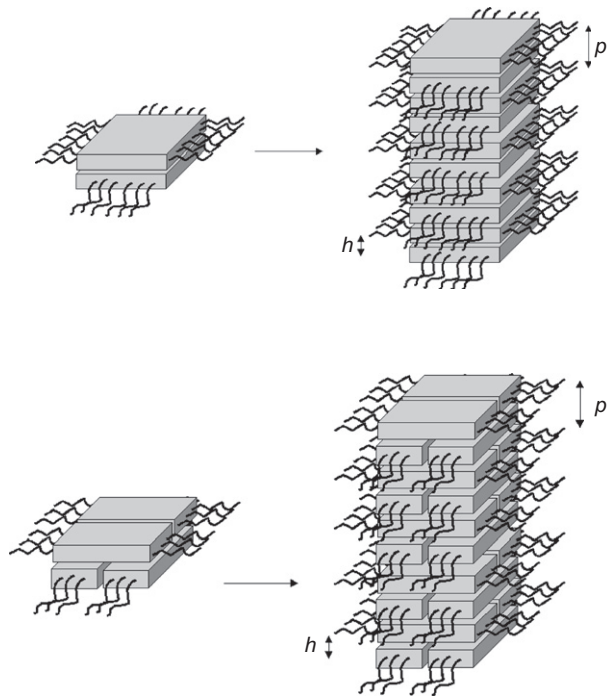

FIGURE 37 Molecular organization of the complexes $[La(NO_3)_3\{Cu(C_{14}salen)\}_2]$ (top) and $[Gd(NO_3)_3\{Cu(C_{14}salen)\}]$ (bottom) within the columnar mesophase. The columnar repeat unit is given by p and h is the average distance between adjacent molten chains. Reproduced with permission from Binnemans et al. (2002b). Copyright 2002 Wiley-VCH.

differences of the complexes. However, the melting points and clearing points of the dinuclear complexes are higher than those of the parent copper(II) and nickel(II) complexes, resulting in about the same temperature range for the mesophase. The thermal stability of the nickel(II)–lanthanum(III) complex was found to be larger than those of the corresponding copper(II)–lanthanum (III) complex. Binnemans et al. (2006) prepared a salen-type Schiff's base ligand with three deprotonable OH group by condensing the substituted salicyaldehyde 3-formyl-4-hydroxyphenyl-3,4,5-tris(tetradecyloxy)benzoate with 1,3-diamino-2-propanol. This ligand allowed to form neutral dinuclear complexes of the type R_2L_2 with trivalent lanthanide ions (R = Nd, Sm, Gd; Fig. 38). The ligand showed a monotropic hexagonal columnar phase: Cr 82 (Col_h 62) I. The complexes exhibited a rectangular columnar phase (Col_r) over a wide temperature range of more than 100 °C. The clearing points of the complexes could not be determined, because of the complexes decomposed above 200 °C. Models were proposed for the molecular structure of the complexes and for the structure of the mesophase. The model of the mesophase contains "bow-tie"-like dimers within the 2D rectangular lattice.

5. β-ENAMINOKETONATE COMPLEXES

Although β-enaminoketones (β-aminovinyl ketones) are structurally closely related to the Schiff's bases (Fig. 39), their lanthanide complexes have much less intensively been investigated. Galyametdinov and coworkers prepared lanthanide complexes of the *N*-alkyl β-enaminoketones **L13H** (Bikchantaev et al., 1996; Galyametdinov et al., 1994b; Kharitonova et al., 1996; Turanova et al., 2005). By reaction with lanthanide nitrates or chlorides in ethanol, the β-enaminoketones form complexes of stoichiometry $[R(LH)_2LX_2]$ ($X = NO_3$, Cl). The complexes were found to be soluble in benzene and chloroform. The ^1H NMR spectrum of a lanthanum(III) compound shows that two ligands (LH) have the ketoamine structure, whereas the third ligand (L) has the enolimine structure (Kharitonova et al., 1996). A coordination number of eight was proposed for the complexes with nitrate ions: three bidentate β-enaminoketone ligands and the two monodentate nitrates. It is doubtful that the latter assumption is true, because nitrate ions are nearly always bidentate in lanthanide complexes (Bünzli et al., 1978; Wickleder, 2002). A coordination number of seven with three monodentate β-enaminoketone ligands and two bidentate nitrates is more realistic hypothesis. Further studies are necessary to elucidate this issue. However, as long as no

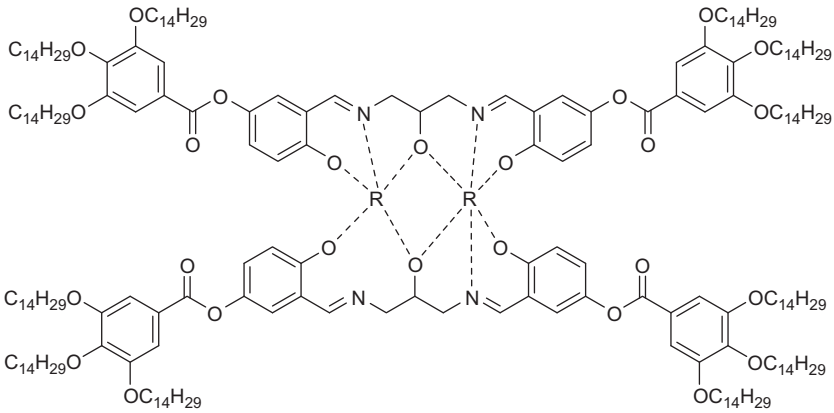

FIGURE 38 Liquid-crystalline dinuclear f–f complex.

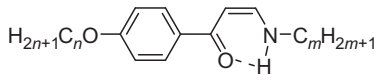

L13H

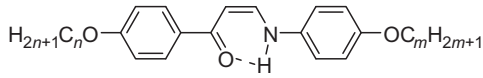

L14H

FIGURE 39 β-Enaminoketones.

single crystal structures of these complexes are available, all statements about the coordination of the lanthanide ions in these mesomorphic β-enaminoketone complexes remain uncertain. The length-to-width ratio of the rotation cylinder of the complexes was calculated to vary between 2.9 and 3.8 depending on the length of the alkyl chain lengths. The ligands are not liquid-crystalline, but the lanthanide complexes exhibit a SmA phase. The transition temperatures of the complexes are given in Table 11. As in the case of the Schiff's base complexes, an increase in transition temperatures was observed when the nitrate ions were substituted by chloride ions. Only a minor influence of the lanthanide ion on the transition temperatures was found (Kharitonova et al., 1996). This is in contrast to the behavior observed for similar complexes nitrate complexes with Schiff's base ligands (Binnemans et al., 2000a). The layer spacings of a lanthanum(III) and a dysprosium(III) complex (alkyl chain = C_7H_{15}, X = NO_3) are respectively 30.7 and 30.0 Å, which is smaller than the length of the ligand with the alkyl chains in the all-*trans* conformation (estimated to be about 40 Å by molecular modeling calculations; Bikchantaev et al., 1996). The magnetic properties of the β-enaminoketone complexes are discussed in Section 14.2.

Turanova and Galyametdinov (2006) succeeded in preparing lanthanide complexes (R = La, Dy) of *N*-aryl-substituted β-aminovinylketones (ligand **L14H**). The authors found that the synthetic procedures used for the synthesis of the complexes of the *N*-alkyl substituted β-aminovinyl ketones could not be used for the synthesis of the *N*-aryl substituted compounds and that more drastic reaction conditions were required (boiling ethanol). Under these conditions the *N*-alkyl substituted compounds decompose. After heating, the solvent had to be immediately removed from the reaction mixture, because otherwise the lanthanide complexes decomposed. No purification by recrystallization or reprecipitation was possible. The lanthanide complexes of the *N*-aryl substituted β-aminovinyl ketones exhibit a smectic A phase at high temperatures. The complexes are thermally quite stable and do not decompose at the clearing points (which are between 208 and 218 °C). The transition temperatures of the complexes are summarized in Table 12.

6. β-DIKETONATE COMPLEXES

Lanthanide(III) ions form three distinct types of complexes with 1,3-diketones (β-diketones): (a) tris complexes with a metal-to-ligand ratio of 1:3, (b) Lewis-base adducts of tris complexes, and (c) tetrakis complexes with a metal-to-ligand ratio of 1:4 (Binnemans, 2005a). It is very difficult to obtain pure monomeric tris complexes, because the coordination number of the lanthanide ion in this type of compounds is six and this is too low for saturation of the first coordination sphere of a trivalent lanthanide ion (except for tris complexes of very bulky 1,3-diketones). Therefore, most of the tris complexes form either dimeric (or even oligomeric or polymeric) complexes, or they form hydrates. The water molecules act as Lewis bases and by addition of

TABLE 11 Thermal Behavior of the Lanthanide Complexes of the *N*-Alkyl β-Enaminoketone L13H

Compound	C_nH_{2n+1}	C_mH_{2m+1}	Temperatures (°C)	Reference
$[La(LH)_2L(NO_3)_2]$	C_7H_{15}	$C_{12}H_{12}$	Cr 142 SmA 153 I	Kharitonova et al. (1996)
$[La(LH)_2L(NO_3)_2]$	C_7H_{15}	$C_{18}H_{37}$	Cr 82 SmA 140 I	Bikchantaev et al. (1996)
$[Dy(LH)L(NO_3)_2]$	C_7H_{15}	$C_{18}H_{37}$	Cr 121 SmA 135 I	Bikchantaev et al. (1996)
$[La(LH)_2L(NO_3)_2]$	$C_{12}H_{25}$	$C_{12}H_{25}$	Cr 121 SmA 149 I	Kharitonova et al. (1996)
$[Gd(LH)_2L(NO_3)_2]$	$C_{12}H_{25}$	$C_{12}H_{25}$	Cr 127 SmA 152 I	Kharitonova et al. (1996)
$[Tb(LH)_2L(NO_3)_2]$	$C_{12}H_{25}$	$C_{12}H_{25}$	Cr 123 SmA 147 I	Kharitonova et al. (1996)
$[Dy(LH)_2L(NO_3)_2]$	$C_{12}H_{25}$	$C_{12}H_{25}$	Cr 125 SmA 147 I	Kharitonova et al. (1996)
$[La(LH)_2L(NO_3)_2]$	$C_{12}H_{25}$	$C_{16}H_{33}$	Cr 153 SmA 164 I	Kharitonova et al. (1996)
$[Tb(LH)_2L(NO_3)_2]$	$C_{12}H_{25}$	$C_{16}H_{33}$	Cr 143 SmA 154 I	Kharitonova et al. (1996)
$[Dy(LH)_2L(NO_3)_2]$	$C_{12}H_{25}$	$C_{16}H_{33}$	Cr 131 SmA 160 I	Kharitonova et al. (1996)
$[Er(LH)_2L(NO_3)_2]$	$C_{12}H_{25}$	$C_{16}H_{33}$	Cr 124 SmA 158 I	Kharitonova et al. (1996)
$[La(LH)_2L(NO_3)_2]$	$C_{12}H_{25}$	$C_{18}H_{37}$	Cr 96 SmX 160 I	Galyametdinov et al. (1994b)
			Cr 101 SmA 143 I	Bikchantaev et al. (1996)
$[La(LH)_3(NO_3)_3]$	$C_{12}H_{25}$	$C_{18}H_{37}$	Cr 101 SmA 143 I	Turanova et al. (2005)
$[Nd(LH)_3(NO_3)_3]$	$C_{12}H_{25}$	$C_{18}H_{37}$	Cr 101 SmA 151 I	Turanova et al. (2005)
$[Eu(LH)_2L(NO_3)_2]$	$C_{12}H_{25}$	$C_{18}H_{27}$	Cr 140 SmA 160 I	Kharitonova et al. (1996)
$[Gd(LH)_2L(NO_3)_2]$	$C_{12}H_{25}$	$C_{18}H_{37}$	Cr 89 SmX 139 I	Galyametdinov et al. (1994b)
			Cr 105 SmA 146 I	Bikchantaev et al. (1996)

TABLE 11 Thermal Behavior of the Lanthanide Complexes of the *N*-Alkyl β-Enaminoketone L13H—Cont'd

Compound	C_nH_{2n+1}	C_mH_{2m+1}	Temperatures (°C)	Reference
$[Gd(LH)_3(NO_3)_3]$	$C_{12}H_{25}$	$C_{18}H_{37}$	Cr 105 SmA 146 I	Turanova et al. (2005)
$[Tb(LH)_2L(NO_3)_2]$	$C_{12}H_{25}$	$C_{18}H_{37}$	Cr 109 SmA 139 I	Bikchantaev et al. (1996)
$[Tb(LH)_3(NO_3)_3]$	$C_{12}H_{25}$	$C_{18}H_{37}$	Cr 101 SmA 139 I	Turanova et al. (2005)
$[Dy(LH)_2L(NO_3)_2]$	$C_{12}H_{25}$	$C_{18}H_{37}$	Cr 84 SmX 134 I	Galyametdinov et al. (1994b)
			Cr 116 SmA 151 I	Bikchantaev et al. (1996)
$[Dy(LH)_3(NO_3)_3]$	$C_{12}H_{25}$	$C_{18}H_{37}$	Cr 103 SmA 151 I	Turanova et al. (2005)
$[Ho(LH)_3(NO_3)_3]$	$C_{12}H_{25}$	$C_{18}H_{37}$	Cr 101 SmA 143 I	Turanova et al. (2005)
$[Er(LH)_2L(NO_3)_2]$	$C_{12}H_{25}$	$C_{18}H_{37}$	Cr 101 SmA 142 I	Bikchantaev et al. (1996)
$[Er(LH)_3(NO_3)_3]$	$C_{12}H_{25}$	$C_{18}H_{37}$	Cr 110 SmA 145 I	Turanova et al. (2005)
$[Gd(LH)_2LCl_2]$	$C_{12}H_{25}$	$C_{18}H_{37}$	Cr 159 SmA 173 I	Bikchantaev et al. (1996)
$[Tb(LH)_2LCl_2]$	$C_{12}H_{25}$	$C_{18}H_{37}$	Cr 161 SmA 165 I	Bikchantaev et al. (1996)

Cr, crystalline phase; SmA, smectic phase; SmX, unidentified smectic phase; I, isotropic liquid.

two water molecules to a tris complex its coordination number can be increased to eight and the coordination sphere will be saturated. The tris complexes can also form adducts with other Lewis bases which have oxygen or nitrogen donor atoms, for example, 2,2′-bipyridine, 1,10-phenanthroline, tri-*n*-octylphosphine. In the tetrakis complexes, the four β-diketonate ligands result in a complex with an eight-coordinate lanthanide ion and with a counter cation to balance the negative charge of the complex. β-Diketones are well known as ligands of metallomesogens (Donnio et al., 2003; Serrano, 1996). Swager and coworkers showed that β-diketones could be used to obtain eight-coordinate metallomesogens containing zirconium(IV) (Swager and Zheng, 1995; Zheng and Swager, 1994). The first attempts to prepare lanthanidomesogens with β-diketonate ligands were not very successful, in the sense

TABLE 12 Thermal Behavior of the Lanthanide Complexes of the *N*-Aryl β-Enaminoketone L14H

Compound	C_nH_{2n+1}	C_mH_{2m+1}	Temperatures (°C)	Reference
$[Dy(LH)_3(NO_3)_3]$	C_9H_{19}	C_4H_9	Cr 178 SmA 217 I	Turanova and Galyametdinov (2006)
$[La(LH)_3(NO_3)_3]$	C_9H_{19}	$C_{10}H_{21}$	Cr 175 SmA 210 I	Turanova and Galyametdinov (2006)
$[Dy(LH)_3(NO_3)_3]$	C_9H_{19}	$C_{10}H_{21}$	Cr 173 SmA 216 I	Turanova and Galyametdinov (2006)
$[La(LH)_3(NO_3)_3]$	C_9H_{19}	$C_{11}H_{23}$	Cr 178 SmA 218 I	Turanova and Galyametdinov (2006)
$[Dy(LH)_3(NO_3)_3]$	C_8H_{17}	$C_{12}H_{25}$	Cr 177 SmA 212 I	Turanova and Galyametdinov (2006)
$[Dy(LH)_3(NO_3)_3]$	$C_{14}H_{29}$	C_8H_{17}	Cr 169 SmA 208 I	Turanova and Galyametdinov (2006)

Cr, crystalline phase; SmA, smectic A phase; I, isotropic liquid.

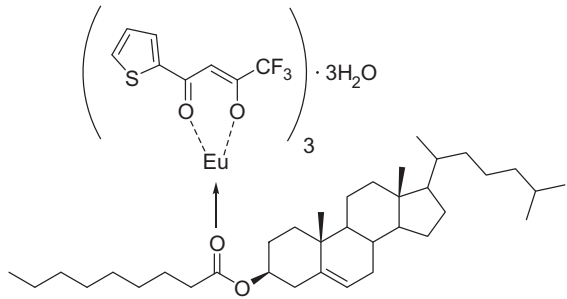

FIGURE 40 Adduct of cholesteryl nonanoate to $[Eu(tta)_3]\cdot 3H_2O$.

that no liquid-crystalline behavior could be observed for the pure compounds. Hapiot and coworkers studied adducts of [R(*tta*)$_3$] (H*tta* = thenoyltrifluoroacetone) and cholesteryl nonanoate and cholesteryl tetradecanoate (Fig. 40; Boyaval et al., 1999; Hapiot and Boyaval, 2001). By means of IR, ^{1}H, ^{13}C and ^{19}F NMR spectroscopy, including 2D NMR and relaxation techniques, the authors were able to show that a 1:1 adduct was formed between [R(tta)$_3$] (R = Nd, Sm, Eu) and the cholesteryl ester, and that bonding of the cholesteryl ester to the metal ion occurs through both oxygen atoms of the ester. The authors argued that the absence of a mesophase in the adducts is not only due to the large size of the [R(tta)$_3$] moiety, but also to a twisted conformation of the ligands, leading to a nonrodlike-structure of the adducts. The optical properties of the corresponding europium(III) complexes in a cholesteric LC

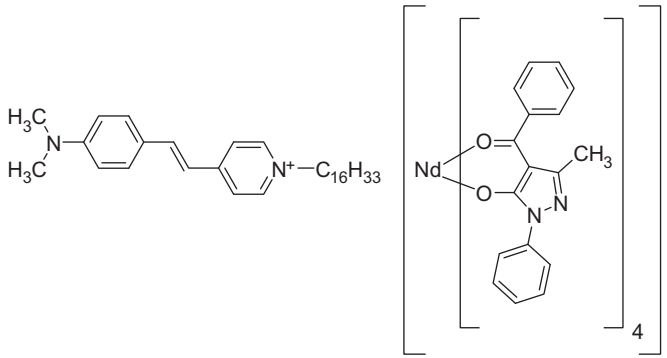

FIGURE 41 Neodymium(III) complex of 1-phenyl-3-methyl-4-benzoyl-5-pyrazolone with a hemicyanine counter ion.

mixture have been investigated, including the refractive index, the wavelength-dependent light scattering, the optical absorption and luminescence spectra (Boyaval et al., 2001). Wang et al. reported the mesomorphic properties of (*E*)-*N*-hexadecyl-4-(*N*′,*N*′-dimethylamino)stilbazolium tetrakis (1-phenyl-3-methyl-4-benzoyl-5-pyrazolonato)lanthanate(III) complexes (R = La, Nd, Dy, Yb; Fig. 41; Wang et al., 1995). The complexes were investigated by DSC, TG-DTA and polarized optical microscopy. (*E*)-*N*-hexadecyl-4-(*N*′,*N*′-dimethylamino)stilbazolium bromide (*hemicyanine bromide*) was found to exhibit an unidentified smectic mesophase with a focal conical texture, melting at 96.3 °C and clearing at 246.3 °C. The lanthanide(III) complexes, except the lanthanum(III) complex, were also reported to be mesomorphic, showing a mosaic texture. Both the melting and clearing points of the lanthanide complexes were lower than those of the corresponding stilbazolium bromide, but the mesophase range was narrower. However, a further study by other authors on similar complexes raised concerns about the liquid-crystalline behavior of this type of lanthanide complexes (Binnemans et al., 1999a). Combination of $[Eu(tta)_4]^-$ with a pyrrolidinium cation with long alkyl chains did not lead to the formation of a LC (Goossens et al., 2009). No mesophase behavior was observed for the $[Eu(tta)_4]^-$ complex in combination with an imidazolium cation with a long alkyl chain or with one or two mesogenic cyanobiphenyl groups linked to them via a long flexible alkyl spacer (Goossens et al., 2008). Also replacement of a cyanobiphenyl group by a cholesteryl group did not lead to liquid-crystal behavior, although it is known that the cholesteryl group has a stronger ability to induce mesophases than the biphenyl group. Finally, it was possible to obtain a LC by combining the $[Eu(tta)_4]^-$ complex with an imidazolium cation with two cholesteryl groups linked to it via a long alkyl spacer (Goossens et al., 2008; Fig. 42). The compound exhibited a monotropic chiral smectic A phase (SmA*). This work shows how difficult it is to obtain lanthanidomesogens on the basis of the very bulky tetrakis β-diketonate complexes. No liquid-crystalline

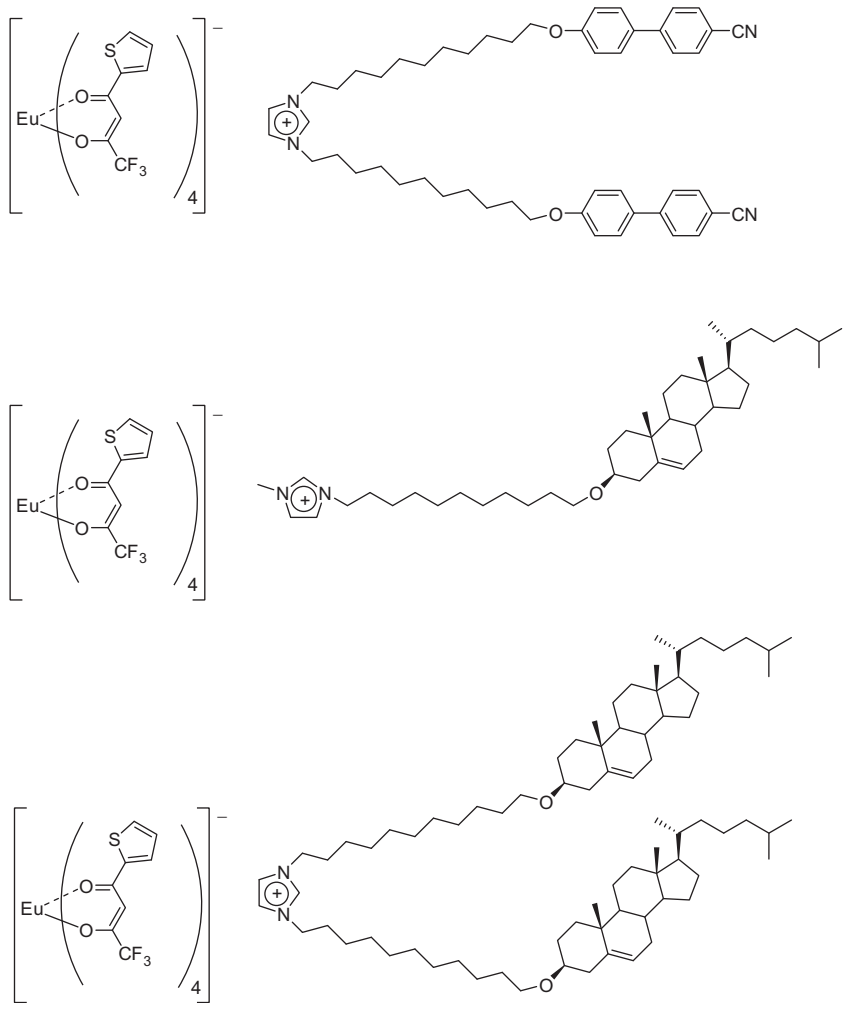

FIGURE 42 Imidazolium salts with terminally attached mesogenic groups and with $[Eu(tta)_4]^-$ counter ions. Only the compound with two cholesteryl groups (structure at the bottom) shows liquid-crystalline properties: Cr 121 (SmA* 101) I (Goossens et al., 2008).

properties were observed for adducts of tris(acetylacetonate)lanthanide complexes with 4,7-disubstituted-1,10-phenanthroline and 4,4′-disubstituted-2.2′-bipyridines, although the induction of a mesophase can be expected upon extending the alkyl chain substituents to sufficient lengths (Bellusci et al., 2005). Other examples of lanthanidomesogens with nonmesogenic β-diketonate ligands are the Schiff's base adducts of tris β-diketonate complexes, which have been described in detail in Section 4 (Binnemans and Lodewyckx, 2001; Binnemans et al., 2003a; Yang et al., 2006). The

β-diketonate ligands in these complexes are simple ligands without long alkyl chains. The long alkyl chains are part of the Schiff's base ligands.

Galyametdinov and Binnemans reported the first examples of lanthanidomesogens in which the mesomorphism is introduced via a β-diketonate ligand (Galyametdinov et al., 2002b). Three different types of Lewis-base adducts of tris(β-diketone)lanthanide complexes were prepared, where the β-diketonate was a substituted 1,3-diphenyl-1,3-propanedione (dibenzoylmethane) with a tetradecyloxy chain in the *para*-position of the two phenyl rings. The Lewis base was either 1,10-phenanthroline, 2,2′-bipyridine, or an alkanoyloxy 4,4′-disubstituted 2,2′-bipyridine. The central metal ions were europium(III) or terbium(III). Depending on the type of Lewis base, the complexes exhibited a monotropic smectic A phase or a monotropic unidentified highly ordered smectic phase. All complexes were strongly luminescent. This work was extended to complexes of the unsymmetrically substituted β-diketone 1-(4-dodecyloxyphenyl)-3-(4-hexadecyloxyphenyl)propane-1,3-dione and 1,10-phenanthroline as co-ligand (Knyazev et al., 2008). The ligand is not liquid-crystalline and melts at 86 °C. No liquid-crystalline phases were observed for the complexes of the light lanthanides (R = La, Nd), whereas the complexes of the heavy lanthanides (R = Eu, Gd, Tb, Dy, Er, Yb) exhibit a monotropic smectic A phase. An X-ray standing wave method has been used to localize the position of the metal ions in corporate in Langmuir–Blodgett films of the europium(III) complex deposited on a silicone substrate (Novikova et al., 2006, 2009). The method also revealed the enrichment of impurities of iron, zinc, copper, and calcium in the Langmuir–Blodgett films, although the concentrations of these metals were below 10^{-7} mol L^{-1} in the aqueous phase. The incorporation of these impurities strongly influenced the molecular organization in the Langmuir–Blodgett films. When 5,5′-di(heptadecyl)-2,2′-bipyridine was used as a co-ligand instead of 1,10-phenanthroline, the corresponding europium(III) complex was found to exhibit a mesophase between 95 and 130 °C (Knyazev et al., 2004). The lanthanide ion has only little effect on the transition temperatures of the liquid-crystalline β-diketonate complexes (Galyametdinov et al., 2002c). Figure 43 shows examples of smectogenic lanthanidomesogens with β-diketonate ligands.

A milestone in the research field of lanthanidomesogens was the discovery of nematogenic lanthanide complexes by Galyametdinov et al. (2008). These complexes (R = La, Nd, Eu, Yb) are ternary complexes consisting of three β-diketonate ligands and the substituted 2,2′-bipyridine ligand 5,5′-bis(heptadecyl)-2,2′-bipyridine (Fig. 44, $C_nH_{2n+1} = C_7H_{15}$). The β-diketonate ligand is rather unconventional because it contains a cyclohexyl group. Neither the β-diketone nor the substituted 2.2′-bipyridine are liquid-crystalline, but the lanthanide complexes are. The complexes form a smectic A phase upon melting, which is transformed into a nematic phase upon further heating. The nematic phase has a low viscosity and is stable over a temperature range of

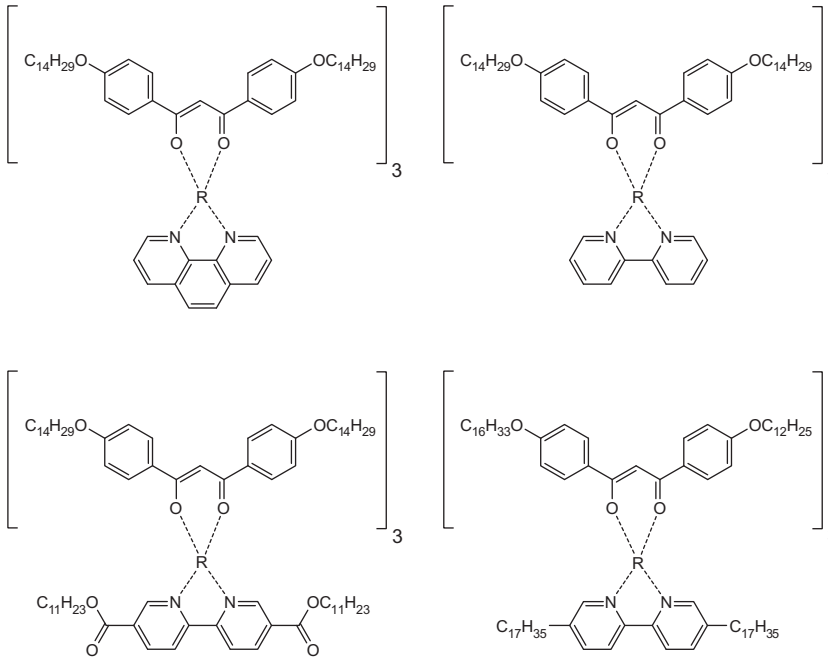

FIGURE 43 Structures of smectogenic lanthanide β-diketonate complexes.

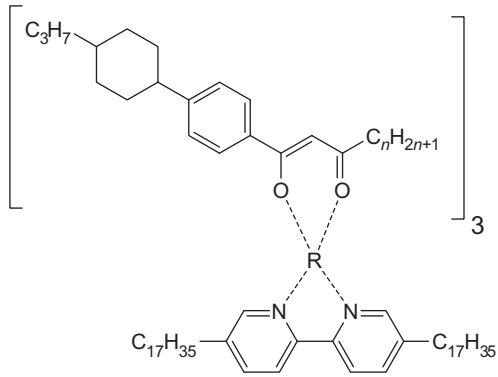

FIGURE 44 Structure of nematogenic lanthanide β-diketonate complexes.

about 30 °C. Supercooled films of an aligned mesophase of the europium(III) complexes emitted linearly polarized luminescence upon irradiation with UV light (see also Section 14.1). A systematic study of the influence of the alkyl substituent length of the β-diketone ligand revealed an even–odd effect for the clearing temperatures of the lanthanide complexes: compound with an even number of carbon atoms in the alkyl chain have a higher melting point than compounds with an odd number of carbon atoms (Dzhabarov et al., 2010).

TABLE 13 Thermal Behavior of the Nematogenic Lanthanide β-Diketonate Complexes Shown in Fig. 44

Lanthanide R	C_nH_{2n+1}	Temperatures (°C)	Reference
La	CH_3	Cr 252 I	Dzhabarov et al. (2010)
La	C_2H_5	Cr 133 SmA 146 N 160 I	Dzhabarov et al. (2010)
La	C_3H_7	Cr 106 N 136 I	Dzhabarov et al. (2010)
La	C_4H_9	Cr 74 SmA 102 N 142 I	Dzhabarov et al. (2010)
La	C_5H_{11}	Cr 76 SmA 94 N 134 I	Dzhabarov et al. (2010)
La	C_6H_{13}	Cr 73 SmA 89 N 138 I	Dzhabarov et al. (2010)
La	C_7H_{15}	Cr 64 SmA 98 N 132 I	Dzhabarov et al. (2010)
		g 64 SmA 98 N 132 I	Galyametdinov et al. (2008)
Nd	C_7H_{15}	g 74 SmA 106 N 140 I	Galyametdinov et al. (2008)
Eu	C_7H_{15}	g 72 SmA 108 142 I	Galyametdinov et al. (2008)
Yb	C_7H_{15}	g 76 SmA 101 134 I	Galyametdinov et al. (2008)
La	C_8H_{17}	Cr 74 SmA 93 N 132 I	Dzhabarov et al. (2010)

Cr, crystalline phase; g, glass; N, nematic phase; SmA, smectic A phase, I, isotropic liquid.

The transition temperatures of these lanthanide complexes are given in Table 13. The preparation of other nematogenic β-diketones with a cyclohexyl group has recently been reported, although they have not been used yet for the synthesis of lanthanidomesogens (Knyazev et al., 2010). The transition temperatures of these nematogenic lanthanidomesogens can be lowered by making binary mixtures with other nematogenic LCs, such as pentyloxycyanobiphenyl and cholesteryl myristate (Knyazev et al., 2011).

7. BIS(BENZIMIDAZOLYL)PYRIDINE COMPLEXES

Piguet and coworkers investigated the thermal behavior of 5,5′- and 6,6′-substituted 2,6-bis(1-ethyl-benzimidazol-2-yl)pyridines and the corresponding lanthanide complexes $[RL(NO_3)_3]$ or $[RL(CF_3SO_3)_3]$ (Escande et al., 2010; Piguet et al., 2006; Terazzi et al., 2006a). The 5,5′-substituted ligands **L16–L19** are shown in Fig. 45 and the 6,6′-substituted ligands **L20–L23** in Fig. 46. The first reported ligands had two terminal alkyl chains, that is, one dodecyloxy chain at both end of the molecules. Conformational changes (*trans–trans* → *cis–cis*) occur upon complexation to lanthanide ions: the I-shaped 5-substituted ligands are transformed into U-shaped lanthanide complexes, whereas the U-shaped 6-substituted ligands give I-shaped lanthanide

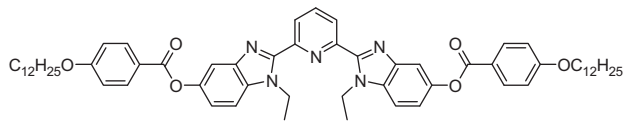

L15 Cr 131 SmC 217 SmA 223 N 226 I

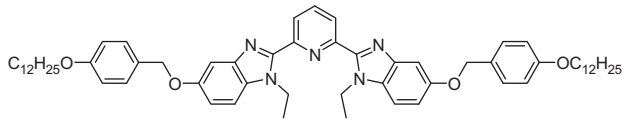

L16 Cr 144 SmA 193 I

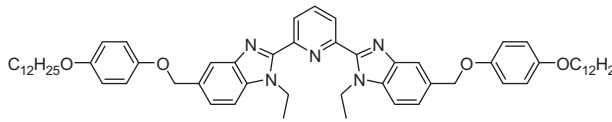

L17 Cr 107 I

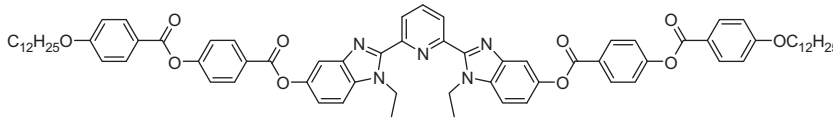

L18 Cr 206 SmX 280 N 322 I

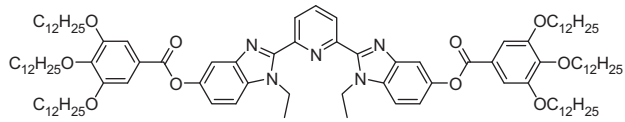

L19 Cr 25 Col_h 61 I

FIGURE 45 5,5′-Substituted 2,6-*bis*(1-ethyl-benzimidazol-2-yl)pyridines and their transition temperatures (in °C). *Abbreviations: Cr = crystalline phase, SmC = smectic C phase, SmA = smectic A phase, N = nematic phase, Col_h = hexagonal columnar phase, I = isotropic liquid.*

complexes (Fig. 47; Nozary et al., 2000). The 5-substituted 2,6-bis(benzimidazol-2-yl)pyridines are calamitic LCs and exhibit a rich mesomorphism (SmC, SmA and/or N). Although it was initially reported that the lanthanide complexes show essentially the same mesomorphism as the ligands (Nozary et al., 1997a), further studies showed that the lanthanide complexes have a low thermal stability and are not mesomorphic (Nozary et al., 1997b, 1998).

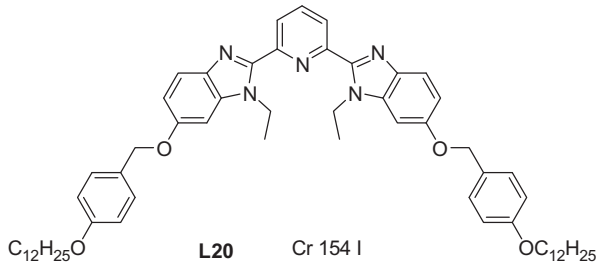

L20 Cr 154 I

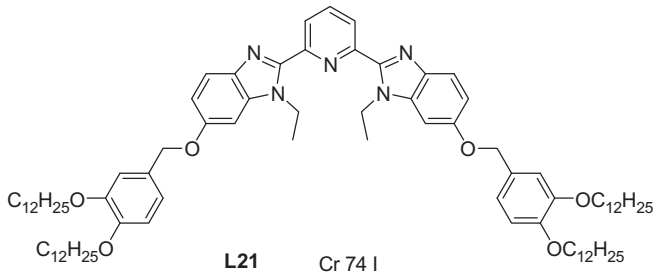

L21 Cr 74 I

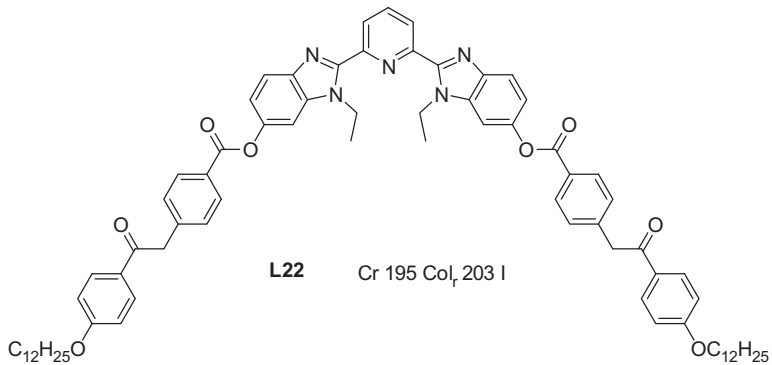

L22 Cr 195 Col_r 203 I

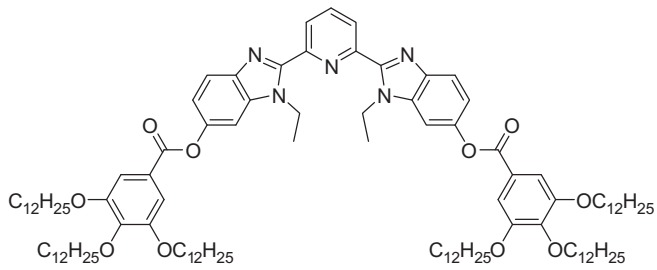

L23 Cr 58 I

FIGURE 46 6,6′-Substituted 2,6-*bis*(1-ethyl-benzimidazol-2-yl)pyridines and their transition temperatures (in °C). *Abbreviations: Cr = crystalline phase, Col_r = rectangular columnar phase, I = isotropic liquid.*

Structurally, the bent 6-substituted ligands have structural similarities to banana LCs. However, no mesomorphism was detected. The corresponding lanthanide complexes have the shape of calamitic LCs, but they decompose at temperatures between 180 and 200 °C, without evidence for mesomorphism. The absence of mesomorphism was attributed to the spatial expansion brought by the bulky $R(NO_3)_3$ groups (Nozary et al., 2002). Two of the three bound bidentate nitrate anions are located on opposite sides of the planar aromatic core, so that they strongly disturb the intermolecular interactions between the rigid cores and reduce the molecular anisotropy. Also a ligand with four terminal chains (**L21**) did not lead to liquid-crystalline lanthanide complexes (Nozary et al., 2000).

Liquid-crystalline lanthanide complexes could be obtained by increasing the number of terminal alkyl chains to six, that is, the complexes of ligands **L19** and **L23** (Fig. 48; Terazzi et al., 2003, 2005). These hexacatenar ligands contain peripheral gallic acid residues with dodecyloxy chains. Interestingly, the type of mesophase depends on the lanthanide ion, and the minor contraction of about 15% on going from La^{3+} to Lu^{3+} is sufficient to cause a change of mesophase behavior from lamellar over cubic to columnar. The hemidisk-shaped complexes [R(**L19**)$(NO_3)_3$] exhibit a sequence of lamella-columnar (L_{col}) and body-centered cubic mesophases for large lanthanide(III) ions (R = La–Nd), a body-centered cubic mesophase (Cub, $Im\bar{3}m$) for the mid-sized lanthanide ions (R = Sm–Ho) and a hexagonal columnar phase for the small lanthanide ions (R = Er–Lu; Terazzi et al., 2005). When ligand **L19** was modified by reversing the esters spacers (benzimidazole-COO-phenyl instead of benzimidazole-OOC-phenyl), the corresponding lanthanide complexes were not liquid-crystalline (Terazzi et al., 2007). This example shows the subtle relationship between molecular structure and the formation of mesophases. Density functional theory (DFT) calculations showed that the inversion of the ester spacers has considerable effects on the electronic structure and polarization of the aromatic groups along the strand of the ligand. The mesophase behavior of the [R(**L23**)$(NO_3)_3$] complexes is very similar to those of [R(**L19**)$(NO_3)_3$] complexes, except that in this case most of the lanthanide complexes (R = La–Ho) form the lamellocolumnar phase at low temperatures. This points to an improved stabilization of the mesophases by ligands that form a rod-like geometrical arrangement upon coordination to the $R(NO_3)_3$ moiety. For the smaller lanthanide(III) ions, the complexes [R(**L19**)$(NO_3)_3$] and [R(**L23**)$(NO_3)_3$] exists as monomeric building blocks in the solid state and probably also in the mesophase. The hemidisk-like monometallic complexes are compact enough to induce pyridine–pyridine interactions between head-to-tail tridentate cores, and these interactions are responsible for the formation of the columns of the hexagonal columnar phase. The weak intercolumnar interactions, responsible for the positional order in the hexagonal columnar mesophase, can be attributed to residual interactions involving pairs of appended gallic acid residues. When

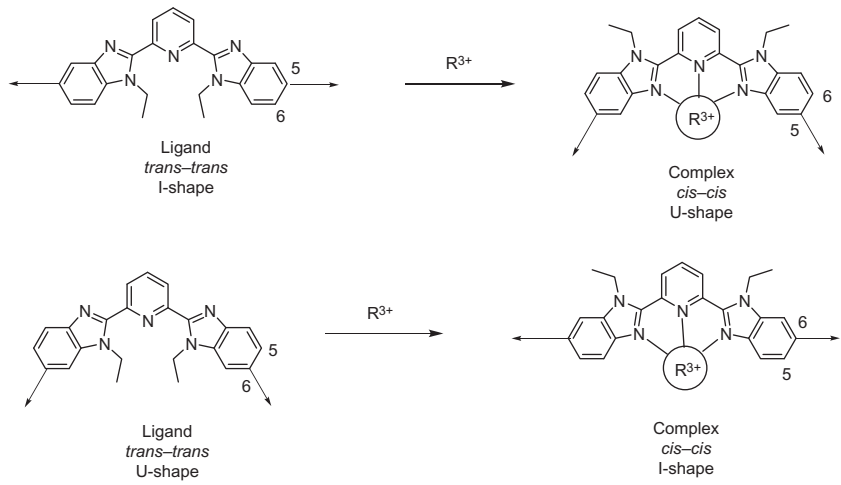

FIGURE 47 Conformational changes (*trans–trans* → *cis–cis*) occurring upon complexation to trivalent lanthanide ions for (A) 5-substituted and (B) 6-substituted 2,6-*bis*(benzimidazol-2-yl)pyridines. Linear substituents have been schematized by rods.

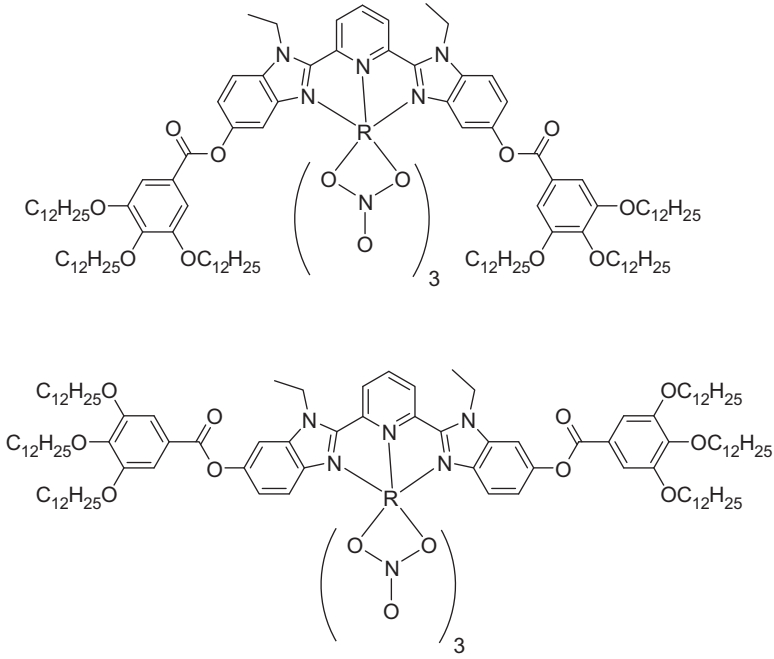

FIGURE 48 Structure of lanthanidomesogens [R(**L19**)$(NO_3)_3$] (top) and [R(**L23**)$(NO_3)_3$] (bottom).

the radius of the lanthanide(III) increases in the monometallic complexes, the intracolumnar interactions becomes weaker. The orthogonal intercolumnar packing occurring between the gallic ester residues with dodecyloxy chains compete with the intracolumnar packing and this leads to an oscillation or puckering of the columns. In the case of oscillations of the columns, dislocations are formed and these dislocation points lead to the isotropic growth of the columns in the three Cartesian directions of space, and to the formation of a bicontinuous structure. In the case of puckering of the columns, the cylindrical rods are pinced off and discrete micelles are formed. The 3D close packing of these soft micelles leads to the formation of a micellar body-centered cubic phase. It is often very difficult to discriminate between cubic bicontinuous and cubic micellar phases, and a detailed study of the XRD patterns of the mesophases in combination with molecular modeling is required. For the larger lanthanide ions the complexes occur as dimers in the solid state and in solution. Therefore, it is assumed that the first mesophase formed upon heating of the complexes of the large lanthanide ions also contain dimers. The existence of the rodlike dimers removes the strong intermolecular π-stacking and a residual lamellar ordering is detected. The complexes [R(**L19**)$(CF_3COO)_3$] form a hexagonal columnar phase at high temperatures, whereas the [R(**L23**)$(CF_3COO)_3$] complexes form a lamellar mesophase (Nozary et al., 2006). The mesophases occur only at high temperatures and they consist of mixtures of complexes, dissociated ligands and metal salts. By attaching 12 peripheral dodecyloxy chains to the central tridentate aromatic binding unit a dodecacatenar ligand **L24** is formed (Fig. 49; Escande et al., 2007). The ligand exhibit a mesophase between -34 and 56 °C, but it was not possible to assign the mesophase with certainty as a SmA or to a Col_h phase. The lanthanide complexes [R(**L24**)$(NO_3)_3$] and the dimeric complex [Eu(**L24**)$(CF_3COO)_3]_2$ are liquid-crystalline at room temperature. The compounds have a remarkably broad mesophase range, sometimes even larger than 250 °C.

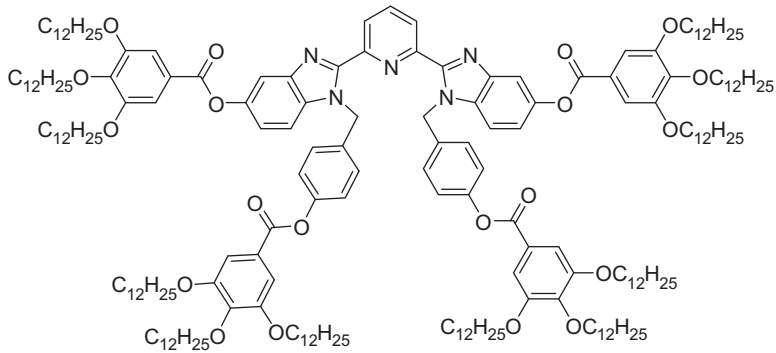

L24

FIGURE 49 Structure of dodecacatenar ligand **L24**.

These complexes are rare examples of room-temperature lanthanidomesogens. A series of dendrimeric 2,6-bis(benzimidazol-2-yl)pyridine ligands **L25–L28** have been synthesized (Fig. 50; Jensen et al., 2008, 2010; Terazzi et al., 2006b). The complexes [R(**L25**)$(NO_3)_3$] and [R(**L26**)$(NO_3)_3$] exhibit for the large lanthanide ions (R = La, Pr) a bilayer smectic mesophase in the temperature range between 90 and 180 °C. Methylation of the terminal cyanobiphenyl groups in [R(**L26**)$(NO_3)_3$] leads to the appearance of an additional interdigitated lamellar phase (R = Gd, Tb, Lu) or a nematic phase (R = Eu, Y, Lu) with the medium-sized or small lanthanide ions. The introduction of the methyl groups destabilizes the layer-like organization in the smectic A phase at higher temperatures, with the formation of a nematic phase as a result. The complexes [R(**L26**)$(NO_3)_3$] of the heavier lanthanide ions are among the rare examples of nematogenic lanthanidomesogens. No mesomorphism was observed for the complexes [R(**L27**)$(NO_3)_3$] and [R(**L28**)

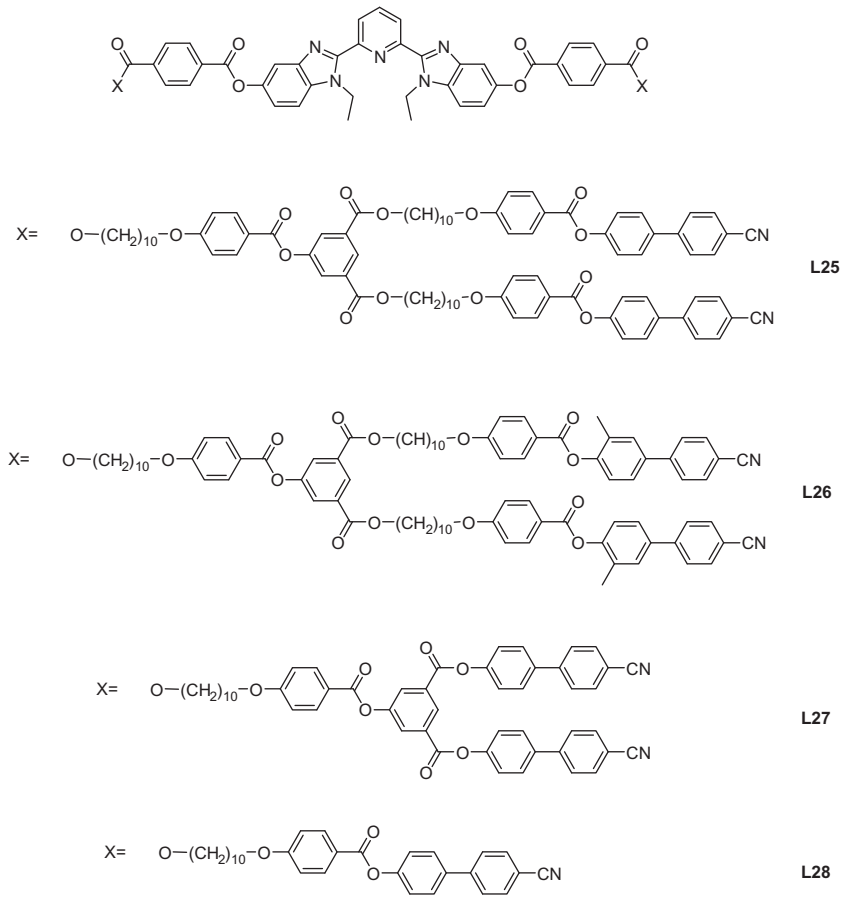

FIGURE 50 Dendrimeric 2,6-*bis*(1-ethyl-benzimidazol-2-yl)pyridine ligands **L25–L28**.

$(NO_3)_3$], neither for the complexes with ligands similar to **L27** and **L28**, but with methyl groups on the terminal cyanobiphenyl groups. An overview of the transition temperatures and mesophase behavior of the 2,6-bis(1-ethyl-benzimidazol-2-yl)pyridine complexes is given in Table 14.

The insight obtained by systematically studying the influence of structural changes in the bis(benzimidazol-2-yl)pyridine ligands on the mesophase behavior of the ligands and the corresponding lanthanide complexes with R $(NO_3)_3$ and R$(CF_3COO)_3$ groups, inspired Piguet to propose a thermodynamic model to rationalize the formation of thermotropic mesophases in metallomesogens with a bulky metal core (Escande et al., 2007, 2010; Piguet et al.,

TABLE 14 Thermal Behavior of the Lanthanide Complexes of 2,6-*Bis* (1-Ethyl-Benzimidazol-2-yl)pyridines Ligands L19, L23, L24, L25, and L26

Complex	Temperatures (°C)	Reference
[Pr(**L19**)$(NO_3)_3$]	g 125 L_{col} 175 Cub 249 I	Terazzi et al. (2005)
[Nd(**L19**)$(NO_3)_3$]	g 70 L_{col} 140 Cub 211 dec.	Terazzi et al. (2005)
[Sm(**L19**)$(NO_3)_3$]	g 130 Cub 180 dec.	Terazzi et al. (2005)
[Eu(**L19**)$(NO_3)_3$]	g 140 Cub > 200 dec.	Terazzi et al. (2005)
[Gd(**L19**)$(NO_3)_3$]	g 145 Cub > 200 dec.	Terazzi et al. (2005)
[Tb(**L19**)$(NO_3)_3$]	g 155 Cub 205 dec.	Terazzi et al. (2005)
[Dy(**L19**)$(NO_3)_3$]	g 155 Cub 212 dec.	Terazzi et al. (2005)
[Ho(**L19**)$(NO_3)_3$]	g 155 Cub 217 dec.	Terazzi et al. (2005)
[Er(**L19**)$(NO_3)_3$]	g 160 Col_h 221 dec.	Terazzi et al. (2005)
[Tm(**L19**)$(NO_3)_3$]	g 160 Col_h 221 dec.	Terazzi et al. (2005)
[Yb(**L19**)$(NO_3)_3$]	g 160 Col_h 223 dec.	Terazzi et al. (2005)
[Lu(**L19**)$(NO_3)_3$]	g 160 Col_h 223 dec.	Terazzi et al. (2005)
[Pr(**L23**)$(NO_3)_3$]	g 100 L_{col} 140 Cub 190 dec.	Terazzi et al. (2005)
[Nd(**L23**)$(NO_3)_3$]	g 120 L_{col} 160 Cub 180 dec.	Terazzi et al. (2005)
[Sm(**L23**)$(NO_3)_3$]	g 160 L_{col} 180 Cub 190 dec.	Terazzi et al. (2005)
[Eu(**L23**)$(NO_3)_3$]	g 120 L_{col} 180 Cub 190 dec.	Terazzi et al. (2005)
[Gd(**L23**)$(NO_3)_3$]	g 100 L_{col} 160 Cub 190 dec.	Terazzi et al. (2005)
[Tb(**L23**)$(NO_3)_3$]	g 160 Cub 171 dec.	Terazzi et al. (2005)
[Dy(**L23**)$(NO_3)_3$]	g 90 L_{col} 180 dec.	Terazzi et al. (2005)

TABLE 14 Thermal Behavior of the Lanthanide Complexes of 2,6-*Bis* (1-Ethyl-Benzimidazol-2-yl)pyridines Ligands L19, L23, L24, L25, and L26—Cont'd

Complex	Temperatures (°C)	Reference
[Ho(**L23**)$(NO_3)_3$]	g 160 Cub 175 dec.	Terazzi et al. (2005)
[Er(**L23**)$(NO_3)_3$]	g 150 Col_h 180 Cub 185 dec.	Terazzi et al. (2005)
[Tm(**L23**)$(NO_3)_3$]	g 160 L_{col} 180 dec.	Terazzi et al. (2005)
[Yb(**L23**)$(NO_3)_3$]	g 175 Col_h 195 dec.	Terazzi et al. (2005)
[Lu(**L23**)$(NO_3)_3$]	g 155 Col_h 190 I	Terazzi et al. (2005)
[La(**L24**)$(NO_3)_3$]	Cr −25 SmA (or Col_h) 110–130 Cub 240 dec.	Escande et al. (2007)
[Pr(**L24**)$(NO_3)_3$]	Cr −43 SmA (or Col_h) 110–130 Cub 207 dec.	Escande et al. (2007)
[Sm(**L24**)$(NO_3)_3$]	Cr −34 Col_h 208 dec.	Escande et al. (2007)
[Eu(**L24**)$(NO_3)_3$]	Cr −31 Col_h 220 dec.	Escande et al. (2007)
[Gd(**L24**)$(NO_3)_3$]	Cr −32 Col_h 220 dec.	Escande et al. (2007)
[Tb(**L24**)$(NO_3)_3$]	Cr −33 Col_h 214 dec.	Escande et al. (2007)
[Yb(**L24**)$(NO_3)_3$]	Cr −32 Col_h 240 dec.	Escande et al. (2007)
[Lu(**L24**)$(NO_3)_3$]	Cr −32 Col_h 21 dec.	Escande et al. (2007)
[Y(**L24**)$(NO_3)_3$]	Cr −35 $Colh_1$ 14 $Colh_2$ 91 SmA 229 dec.	Escande et al. (2007)
[Eu(**L24**)$(CF_3COO)_3]_2$	Cr −37 Col_h 139 I	Escande et al. (2007)
[Pr(**L25**)$(NO_3)_3$]	g 80 SmA2 190 dec.	Jensen et al. (2010)
[Eu(**L25**)$(NO_3)_3$]	g 80 SmA 186 I	Jensen et al. (2008, 2010)
[Gd(**L25**)$(NO_3)_3$]	g 85 SmA2 188 I/dec.	Jensen et al. (2010)
[Tb(**L25**)$(NO_3)_3$]	g 90 SmA2 190 I/dec.	Jensen et al. (2010)
[Lu(**L25**)$(NO_3)_3$]	g 100 SmA2 150 PCr 170 SmA2 200 I/dec.	Jensen et al. (2010)
[La(**L26**)$(NO_3)_3$]	g 90–110 SmA2 159 I	Jensen et al. (2010)
[Pr(**L26**)$(NO_3)_3$]	g 90–110 SmA2 147 I	Jensen et al. (2010)
[Eu(**L26**)$(NO_3)_3$]	g 100 SmA 138 N 144 I	Jensen et al. (2008)
	g 90–110 SmA2 138 N 144 I	Jensen et al. (2010)
[Gd(**L26**)$(NO_3)_3$]	g 90–110 SmA2 139 SmAd 144 I/dec.	Jensen et al. (2010)

Continued

TABLE 14 Thermal Behavior of the Lanthanide Complexes of 2,6-*Bis*(1-Ethyl-Benzimidazol-2-yl)pyridines Ligands L19, L23, L24, L25, and L26—Cont'd

Complex	Temperatures (°C)	Reference
[Tb(**L26**)$(NO_3)_3$]	g 90–100 SmA2 137 SmAd 144 I/dec.	Jensen et al. (2010)
[Y(**L26**)$(NO_3)_3$]	g 90–110 SmA2 134 N 144 I/dec.	Jensen et al. (2010)
[Lu(**L26**)$(NO_3)_3$]	g 90–100 L 130 N 144 I/dec.	Jensen et al. (2010)

Cr, crystalline phase; g, glass; SmA, smectic A phase; SmA2, bilayer smectic A phase; SmAd, partially interdigitated smectic A phase; N, nematic phase; Cub, cubic phase; L, lamellar phase; L_{col}, lamellar-columnar phase; Col_h, hexagonal columnar phase; I, isotropic liquid; dec., decomposition. PCr, re-entrant partially crystallized phase.

2006; Terazzi et al., 2006a, 2007). In this qualitative thermodynamic model, it is assumed that a thermotropic liquid-crystalline phase results from the melting of a microsegregated solid, in which the packed polarizable aromatic cores of the molecules are grafted with long, flexible and poorly polarizable alkyl chains. The microsegregation organization corresponds to a minimum in energy in the crystalline solids, because the intermolecular multipolar electrostatic interactions between the polarizable aromatic cores are maximized, while the fully extended alkyl chains (in all-*trans* conformation) fill the voids between the aromatic cores. The melting process corresponds to the melting of the packed alkyl chains (hydrocarbon chains). The breaking of the moderate intermolecular interactions resulting from the packing of the alkyl chains in the all-*trans* conformation is largely compensated by the large entropic increase, resulting from the relaxation of the vibrational and rotational degrees of freedom. A thermotropic mesophase can thus be considered as a state of matter made up of clusters of packed semiorganized rigid cores, dispersed in a liquid continuum of molten alkyl chains. The melting temperature T_m is given by the following equation:

$$T_m \approx T_m^{chains} = \frac{\Delta H_m^{chains}}{\Delta S_m^{chains}}, \quad (12)$$

where ΔH_m^{chains} is the enthalpy change upon melting, and ΔS_m^{chains} is the corresponding entropy change. The melting point of LCs is low because the interactions between the poorly polarizable alkyl chains are weak (ΔH_m^{chains} is small) and the release of configurational entropy upon melting is considerable for the flexible alkyl chains (ΔS_m^{chains} is large). In first approximation, the melting temperature is rather insensitive to the length of the alkyl chain, because ΔH_m^{chains} and ΔS_m^{chains} both increase to the same extent upon increasing

the alkyl chain length and the melting temperature is the ratio between these two quantities (Eq. 12). This is the *enthalpy/entropy compensation* effect. However, increasing the number of alkyl chains on the rigid polarizable aromatic core leads to significant deviations from the enthalpy/entropy compensation. Lower melting temperatures are produced due to an increase in entropy incompletely balanced by some parallel increase in enthalpy. Further heating of the mesophase produces a second phase transition that is characterized by the clearing temperature T_c:

$$T_c \approx T_m^{cores} = \frac{\Delta H_m^{cores}}{\Delta S_m^{cores}} \tag{13}$$

where ΔH_m^{cores} is the enthalpy change at the clearing point, and ΔS_m^{cores} is the corresponding entropy change. At the clearing temperature, the rigid polarizable cores become completely decorrelated and an isotropic liquid is formed. The phenomena of chain and core melting are not independent in real liquid-crystalline systems. Some loss of cohesion between the rigid cores will already occur at the melting temperature T_m and this partial loss can explain the fluidity of mesophases. This simple model predicts that the introduction of a bulky molecular groups close to the rigid core, such as the $R(NO_3)_3$ and $R(CF_3COO)_3$ groups upon complex formation of the mesogenic ligands with lanthanide(III) nitrate or trifluoroacetate salts, is harmful for the liquid-crystalline properties, because ΔH_m^{cores} decreases to such an extent that the clearing and melting processes coincide, so that no mesophase is formed. Piguet recognizes four strategies to design lanthanidomesogens (Terazzi et al., 2007):

1. Embedding of the R^{3+} ions or RX_3 fragments in a cocoon of wrapped aromatic rings, to ensure a significant entropic contribution ΔH_m^{cores} to the clearing process. This strategy is found in the phthalocyanine complexes (see Section 8).
2. Attaching a large number of diverging flexible chains to the central aromatic binding units in order to give polycatenar ligands with large entropic contributions ΔS_m^{chains}, which produce a melting point low enough to promote the formation of a mesophase. This is the most popular approach to obtain lanthanidomesogens with low melting points.
3. Spatially decoupling the rigid aromatic cores responsible for the residual intermolecular cohesion in the mesophase from the bulky lanthanide unit, preserving ΔH_m^{cores} large enough to give high clearing temperatures.This approach was followed for the complexes of ligands **L25–L28** and **L49–L51**.
4. Tuning enthalpic contributions to the melting and clearing processes (ΔH_m^{chains} and ΔH_m^{cores}) by the judicious design of aromatic rings with opposite polarization along the ligand strand. Experiments show that ΔH_m^{cores} is more influences by minor changes in the intramolecular stacking interactions occuring in the condensed phases (Terazzi et al., 2007).

8. PHTHALOCYANINE COMPLEXES

The first lanthanide-containing metallomesogens described in the literature were the substituted bis(phthalocyaninato)lutetium(III) complexes, which were reported by the research group of Simon in 1985 (Piechocki, 1985; Piechocki et al., 1985). In these compounds, the lanthanide(III) ion is sandwiched between two phthalocyanine rings. The structure of these double-decker compounds is somewhat similar to that of ferrocene. The phthalocyanines were prepared as part of a search for 1D molecular semiconductors. The conductivity behavior of the unsubstituted bis(phthalocyaninato)lutetium(III) sandwich complexes was already known, but it was not realized previously that aligned columnar mesophases formed by such metallophthalocyanines can be considered as electrical wires at a molecular level, with the molten alkyl chains acting as insulating layers. There is a similarity between the molecular arrangement of the phthalocyanine complexes in the columnar mesophase and that of 1D conducting organic crystal. The phthalocyanine ring is one of the most stable macrocycles. Different substitution patterns are possible on the macrocycle ring, but the octakis-substituted phthalocyanines, with eight substituents on the peripheral positions of the phthalocyanine ring, are the easiest to synthesize. Substitution patterns which have been reported for bis(phthalocyaninato)lanthanide(III) complexes are: alkoxy substitution (**L29**), alkoxymethyl substitution (**L30**), alkylthio substitution (**L31**), alkyl substitution (**L32**), and poly(oxyethylene) substitution (**L33**) (Fig. 51). A structure of an octakis-alkoxysubstituted bis(phthalocyaninato)lanthanide(III) sandwich complex is shown in Fig. 52.

The synthetic routes to the bis(phthalocyaninato)lanthanide(III) complexes can be divided into two general classes: (a) reaction between a metal free phthalocyanine and a lanthanide(III) salt and (b) reaction between phthalocyanine precursors and a lanthanide(III) salt (*template reaction*). Piechocki obtained alkoxymethyl-substituted complexes $[(C_nH_{2n+1}OCH_2)_8Pc]_2Lu$ ($n = 8$, 12, 18) by reaction between the corresponding metal-free phthalocyanines $(C_nH_{2n+1}OCH_2)_8PcH_2$ and lutetium(III) acetate, in 1-pentanol at 140 °C (Piechocki, 1985; Piechocki et al., 1985). In order to form the phthalocyanine dianion Pc^{2-}, a very large excess of potassium pentanolate was necessary (50 times the stoichiometric amount). Before reaction, the lutetium(III) salt was dissolved in refluxing 1,2-propanediol. During the reaction, first the intermediate product $[(C_nH_{2n+1}OCH_2)_8Pc]Lu(OAc)$ is supposed to be formed, and subsequently a mixture of the anionic complex $[(C_nH_{2n+1}OCH_2)_8Pc]_2Lu^-K^+$ (blue–green) was formed and the neutral compound $[(C_nH_{2n+1}OCH_2)_8Pc]_2Lu$ (green) is formed. The crude reaction mixture contained mainly the anionic $[(C_nH_{2n+1}OCH_2)_8Pc]_2Lu^-K^+$. By treatment of the organic phase with a diluted aqueous solution of hydrochloric acid, the green $[(C_nH_{2n+1}OCH_2)_8Pc]_2Lu$ complex was generated from $[(C_nH_{2n+1}OCH_2)_8Pc]_2Lu^-K^+$ and isolated. The compounds were purified

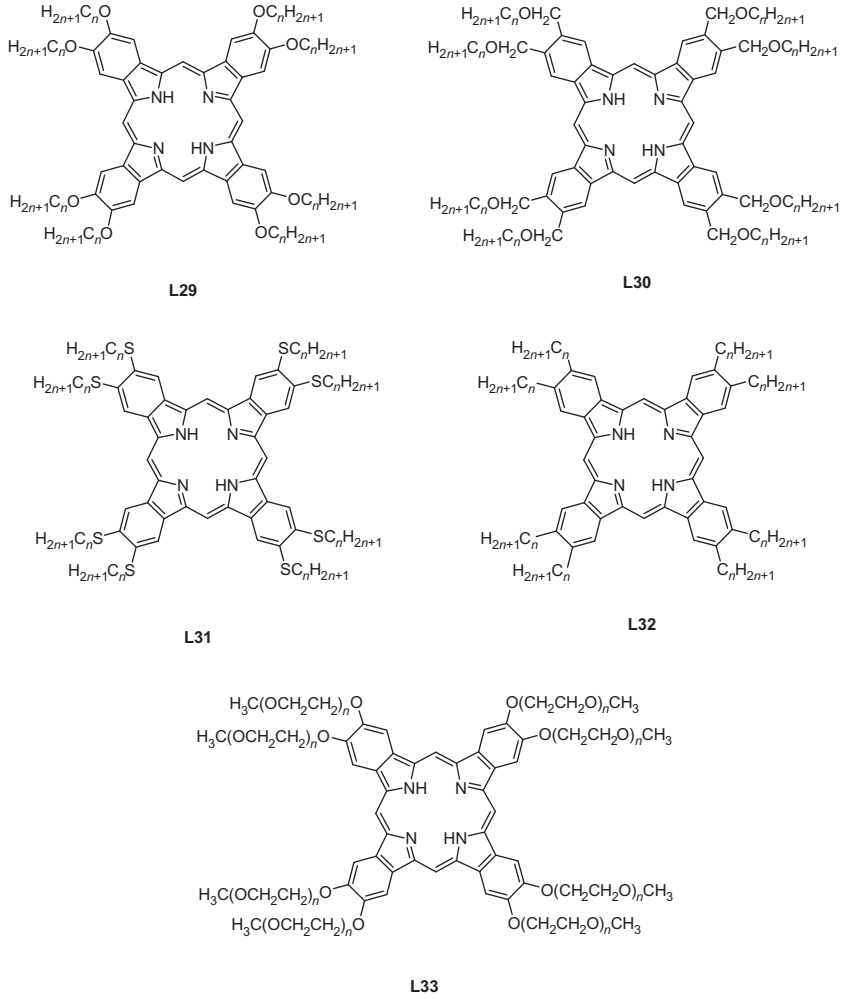

FIGURE 51 Overview of different phthalocyanine ligands.

by flash chromatography on a silica column. The yield of the reaction decreased from 50% to 30% for the octyloxymethyl to the octadecyloctomethyl chain. The red oxidized form $[(C_nH_{2n+1}OCH_2)_8Pc]_2Lu^+[SbCl_6]^-$ was obtained by reaction in dichloromethane of $[(C_nH_{2n+1}OCH_2)_8Pc]_2Lu$ with a stoichiometric amount of the mild oxidizing reagent phenoxathiin hexachloroantimonate. This reagent is a radical cation and can be obtained by reaction between $SbCl_5$ and phenoxathiin in dichloromethane (Gans et al., 1981). An alternative synthetic route to these sandwich complexes is a *template reaction*. By treatment of 4,5-di(octyloxy)phthalonitrile with $R(acac)_3 \cdot nH_2O$ (acac = acetylacetonate) in the ratio 6:1 using the sterically hindered organic

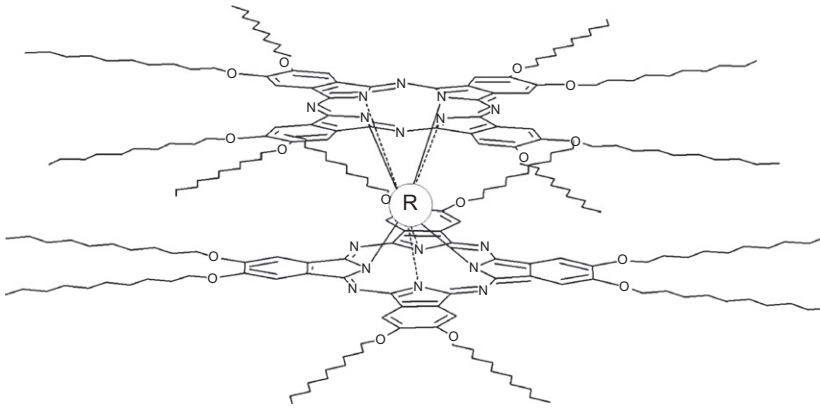

FIGURE 52 Structure of an octakis-substituted *bis*(phthalocyaninato)lanthanide(III) sandwich complex.

base 1,8-diazabicyclo[5.4.0]undec-7-ene (DBU) as the catalyst in refluxing 1-pentanol, the protonated forms $[(C_8H_{17}O)_8Pc]_2RH$ (R = La, Pr, Nd, Sm, Eu, Gd, Tb, Dy, Ho, Er, Tm, Y) were obtained as the initial products (Liu et al., 2000). Except for R = Ce, the protonated forms underwent oxidation upon exposure of the chloroform solutions to air, resulting in the formation of $[(C_8H_{17}O)_8Pc]_2Ce$ complexes. The oxidation process could be monitored by UV–VIS spectra. The conversion was found to be accelerated by the acidity of the silica gel used for chromatographic purification. Depending on the lanthanide ion, different reaction products were found. Whereas for lanthanum(III), the bis(phthalocyaninato)lanthanum(III) complex was formed only in small quantities (the metal-free phthalocyanine being the major product), the amount of metal-free phthalocyanines gradually decreased in favor of the amount of bis(phthalocyaninato)lanthanide(III) complex when going in the lanthanide series from lanthanum(III) to neodymium(III). From samarium(III) to thulium(III), no metal-free phthalocyanine PcH_2 could be isolated. However, a large amount of monomeric $[(C_8H_{17}O)_8Pc](acac)Tm$ was found in the case of thulium(III). In general, it is difficult to obtain good CHN microanalysis data for the phthalocyanine complexes and these compounds are most often characterized by electronic absorption spectra and by MALDI-TOF mass spectrometry. Jiang et al. (1999) prepared substituted bis(phthalocyaninato)cerium(IV) complexes $[(C_7H_{15})_8Pc]_2Ce$ and $[(C_5H_{11}O)_8Pc]_2Ce$ by heating a mixture of $Ce(acac)_3 \cdot H_2O$, DBU and the corresponding dicyanobenzene in 1-pentanol. The authors report that these compounds could not be obtained by reaction of $Ce(acac)_3 \cdot H_2O$ with $[(C_7H_{15})_8Pc]Li$ or $[(C_5H_{11}O)_8Pc]Li$, and only metal-free phthalocyanines could be isolated in that case. The $[(C_nH_{2n+1})_8Pc]_2Lu$ compounds are soluble in *n*-hexane, benzene, toluene, chloroform, dichloromethane, diethyl ether and tetrahydrofuran (Komatsu et al., 1994a), but they are insoluble in DMF, acetonitrile, acetone,

methanol, and ethanol. The best solvent for recrystallization is often ethyl acetate. On the other hand, the poly(oxyethylene)-substituted lutetium phthalocyanines are soluble in chloroform, dichloromethane, methanol, ethanol (and higher alcohols), acetone, ethyl acetate, diethyl ether, DMF, and even in water (up to 10^{-4} M), but insoluble in alkanes (Toupance et al., 1996).

Electron paramagnetic resonance measurements have been carried out on the $[(C_nH_{2n+1}OCH_2)_8Pc]_2Lu$ compounds ($n = 8$, 12, and 18) as a function of the temperature (Piechocki, 1985; Piechocki et al., 1985). In chloroform solution, the EPR signal is inhomogeneous (10 G) with a g factor corresponding to a free electron ($g = 2.0021$). In the solid state, the EPR signal is much narrower (2 G) and the band shape can be described by a Lorentzian function instead of a Gaussian function. The compounds follow the Curie–Weiss law down to 4.2 K, which indicates that the interactions between the spins are weak. The intensity of the signal, both for the sample in solution and in the solid state, corresponds to about one spin per molecule. The spin density of the Lu^{3+} ion is negligible. The free ion is delocalized on the macrocycles and not on the metal ion. The EPR signal line width of a π-radical system depends on the strength of the spin exchange interaction (J_s) and on the degree of order. The EPR line width of $[(C_{18}H_{37}OCH_2)_8Pc]_2Lu$ is very similar in the mesophase and in the isotropic liquid (5 G), but much smaller in the crystalline state (2 G, as mentioned above). For $[(C_{12}H_{25}O)_8$-$Pc]_2Lu$, no change in EPR line width was observed at the crystal-to-mesophase transition, but an important line broadening from 3.2 to 4.7 G occurred at the mesophase-to-isotropic transition (Belarbi et al., 1989). It was concluded that the solid state and mesophase structure are closely related in this compound. The change in line width between the mesophase and the isotropic liquid was attributed to the difference in dipolar interaction associated with the structural change. The difference in EPR line width behavior between the alkoxymethyl- and the alkoxy-substituted compounds are an indication for strong differences in ordering within the columns for these two types of compounds. In contrast to the neutral complexes, no EPR signal was observed for the oxidized forms $\{[(C_nH_{2n+1}OCH_2)_8Pc]_2Lu\}^+[SbCl_6]^-$ and $\{[(C_{12}H_{25}O)_8Pc]_2Lu\}^+[BF_4]^-$ (Belarbi et al., 1989; Piechocki et al., 1985) It was impossible to conclude whether these compounds can be described as a strongly coupled biradical $Pc^{\bullet -}Lu^{III}Pc^{\bullet -}$ or as a diamagnetic system (Piechocki et al., 1985). The free electron in both the unsubstituted and substituted bis(phthalocyaninato)lutetium(III) is associated with the extensive π-system of the phthalocyanine macrocycles. The individual Pc_2Lu units can nominally be considered as $Lu^{3+}Pc_2^{\bullet 3-}$ There remains some discussion whether the unpaired electron is localized on a single Pc macrocycle at a given time, thus with formula $Pc^{2-}Lu^{3+}Pc^{\bullet -}$, (Tran-Thi et al., 1987), or, whether it can be considered to be completely delocalized between the two macrocycles (Orti et al., 1990). It has been suggested that one Pc macrocycle is slightly more distorted than the other ring, because one of the ligands is dianionic and the other is a radical (De Cian et al., 1985). By heating,

the free electron can more easily be delocalized over the both phthalocyanine rings, so that the two rings will become structurally equivalent (Naito et al., 2001). In any case, the lutetium ion is in the trivalent state (Lu^{3+}), and not in the (impossible) tetravalent state. The latter wrong conclusion could be drawn on the basis of the formula Pc_2Lu. However, in cerium double-deckers Pc_2Ce, the cerium ion is in the tetravalent state and both phthalocyanine ligands are dicationic (Nekelson et al., 2006, 2007a,b). The molecular structure of the complexes $[(C_6H_{13}S)_8Pc]_2R$ (R = Sm, Gd, Dy) have been determined by single-crystal XRD (Gürek et al., 2006). These structures very clearly show that the sandwiched lanthanide ion is eight-coordinate by the isoindole nitrogen atoms of the two phthalocyanine macrocycles and that the two phthalocyanine rings adopt a staggered conformation (one ring is rotated over an angle of about 45° with respect to the other ring). The coordination sphere of the lanthanide ion can be described as a slightly distorted square antiprism. The phthalocyanine rings are distorted from planarity and have a saucer shape. In the crystal structure of $[(C_8H_{17}S)_8Pc]_2Ce$, the two phthalocyanine rings are equally distorted Nekelson et al. (2007a,b). The electric and electrochromic properties of the liquid-crystalline phthalocyanine double-deckers are described in Section 14.3.

The thermal behavior of the substituted bis(phthalocyaninato)lanthanide (III) complexes has been summarized in Table 15. The compound $[(C_{18}H_{37}OCH_2)_8Pc]_2Lu$ melts at 51 °C to a mesophase and the clearing temperature is 56 °C (Piechocki et al., 1985). The mesophase behavior was

TABLE 15 Thermal Behavior of Substituted *Bis*(phthalocyaninato) lanthanide(III) Compounds

Compound	Temperatures (°C)	Reference
$[(C_8H_{17}S)_8Pc]_2Ce$	Cr 95 Col_{hd} 257 dec.	Nekelson et al. (2007a)
$[(C_{10}H_{21}S)_8Pc]_2Ce$	Cr 4 Col_{ho} 54 Col_{hd} 217 I	Nekelson et al. (2007a)
$[(C_{12}H_{25}S)_8Pc]_2Ce$	Cr 4 Col_{ho} 54 Col_{hd} 217 I	Nekelson et al. (2007a)
$[(C_{14}H_{29}S)_8Pc]_2Ce$	Cr −3 Col_{ho} 37 Col_{hd} 180 I	Nekelson et al. (2007a)
$[(C_{16}H_{33}S)_8Pc]_2Ce$	Cr 49 Col_{hd} 139 I	Nekelson et al. (2007a)
$[(C_{18}H_{37}S)_8Pc]_2Ce$	Cr 53 Col_{hd} 119 I	Nekelson et al. (2006, 2007a)
$[(C_{12}H_{25}O)_8Pc]_2Pr$	Cr 74 Col_h 208 I	Binnemans et al. (2003b)
$[(C_{12}H_{25}O)_8Pc]_2Nd$	Cr 66 Col_h 206 I	Binnemans et al. (2003b)

TABLE 15 Thermal Behavior of Substituted *Bis*(phthalocyaninato) lanthanide(III) Compounds—Cont'd

Compound	Temperatures (°C)	Reference
$[(C_6H_{13}S)_8Pc]_2Sm$	Cr 52 Col_h 258 I	Gürek et al. (2006)
$[(C_{12}H_{25}O)_8Pc]_2Eu$	Cr 65 Col_h 203 I	Binnemans et al. (2003b)
$[(C_8H_{17}S)_8Pc]_2Eu$	Cr 98 Col_h 252 I	Ban et al. (2001)
$[(C_{10}H_{21}S)_8Pc]_2Eu$	X −1 M 68 Col_h 209 I	Ban et al. (2001)
$[(C_{12}H_{25}S)_8Pc]_2Eu$	X 22 M 64 Col_h 181 I	Ban et al. (2001)
$[(C_{14}H_{29}S)_8Pc]_2Eu$	Cr 13 Col_h 152 I	Ban et al. (2001)
$[(C_{16}H_{33}S)_8Pc]_2Eu$	Cr 50 Col_h 134 I	Ban et al. (2001)
$[(C_6H_{13}S)_8Pc]_2Gd$	Cr 55 Col_h 250 I	Gürek et al. (2006)
$[(C_{12}H_{25}O)_8Pc]_2Gd$	Cr 68 Col_h 218 I	Binnemans et al. (2003b)
$[(C_{12}H_{25}O)_8Pc]_2Tb$	Cr 72 Col_h 205 I	Binnemans et al. (2003b)
$[(C_8H_{17}S)_8Pc]_2Tb$	Cr 102 Col_h 242 I	Ban et al. (2001)
$[(C_{10}H_{21}S)_8Pc]_2Tb$	X 3 M 56 Col_h 205 I	Ban et al. (2001)
$[(C_{12}H_{25}S)_8Pc]_2Tb$	X 20 M 53 Col_h 172 I	Ban et al. (2001)
$[(C_{14}H_{29}S)_8Pc]_2Tb$	X 22 M 47 Col_h 144 I	Ban et al. (2001)
$[(C_{16}H_{33}S)_8Pc]_2Tb$	Cr 46 Col_h 132 I	Ban et al. (2001)
$[(C_{18}H_{37}S)_8Pc]_2Tb$	Cr 33 Col_h 116 I	Ban et al. (2001)
$[(C_{12}H_{25}OCH(CH_3)CH_2O)_8Pc]_2Tb$	Col_h 31 I	Gonidec et al. (2010)
$[((p\text{-}C_{12}H_{25}O)(m\text{-}C_2H_5O)Ph)_8Pc]_2Tb$	Col_L 65 Col_{rd} 116 I	Mukai et al. (2010)
$[((p\text{-}C_{12}H_{25}O)(m\text{-}C_4H_9O)Ph)_8Pc]_2Tb$	Col_L 121 Col_{rd1} 148 Col_{rd2} 171 I	Mukai et al. (2010)
$[((p\text{-}C_{12}H_{25}O)(m\text{-}C_6H_{13}O)Ph)_8Pc]_2Tb$	Col_L 127 Col_{rd1} 137 Col_{rd2} 210 I	Mukai et al. (2010)
$[((p\text{-}C_{12}H_{25}O)(m\text{-}C_8H_{17}O)Ph)_8Pc]_2Tb$	Col_{rd1} 142 Col_{rd2} 148 Col_{rd3} 214 I	Mukai et al. (2010)
$[((p\text{-}C_{12}H_{25}O)(m\text{-}C_{10}H_{21}O)Ph)_8Pc]_2Tb$	Col_{rd1} 146 Col_{rd1} 162 Cub 185 I	Mukai et al. (2010)
$[((p\text{-}C_{12}H_{25}O)(m\text{-}C_{12}H_{25}O)Ph)_8Pc]_2Tb$	See text	Mukai et al. (2010)
$[(C_6H_{13}S)_8Pc]_2Dy$	Cr 60 Col_h 240 I	Gürek et al. (2006)
$[(C_{12}H_{25}O)_8Pc]_2Dy$	Cr 83 Col_h 205 I	Binnemans et al. (2003b)

Continued

TABLE 15 Thermal Behavior of Substituted *Bis*(phthalocyaninato) lanthanide(III) Compounds—Cont'd

Compound	Temperatures (°C)	Reference
$[(C_{12}H_{25}O)_8Pc]_2Ho$	Cr 85 Col_h 190 I	Binnemans et al. (2003b)
$[(C_4H_9O)_8Pc]_2Er$	Cr 202 Col_h >280 dec.	Binnemans et al. (2003b)
$[(C_5H_{11}O)_8Pc]_2Er$	Cr 174 Col_h >280 dec.	Binnemans et al. (2003b)
$[(C_6H_{13}O)_8Pc]_2Er$	Cr 147 Col_h >280 dec.	Binnemans et al. (2003b)
$[(C_8H_{17}O)_8Pc]_2Er$	Cr 137 Col_h 263 I	Binnemans et al. (2003b)
$[(C_9H_{19}O)_8Pc]_2Er$	Cr 93 Col_h 239 I	Binnemans et al. (2003b)
$[(C_{10}H_{21}O)_8Pc]_2Er$	Cr 63 Col_h 180 I	Sleven et al. (2001)
	Cr 71 Col_h 180 I	Binnemans et al. (2003b)
$[(C_{12}H_{25}O)_8Pc]_2Er$	Cr 54 Col_h 174 I	Sleven et al. (2001)
	Cr 68 Col_h 174 I	Binnemans et al. (2003b)
$[(C_{14}H_{29}O)_8Pc]_2Er$	Cr 58 Col_h 180 I	Binnemans et al. (2003b)
$[(C_{15}H_{31}O)_8Pc]_2Er$	Cr 44 Col_h 170 I	Binnemans et al. (2003b)
$[(C_{16}H_{33}O)_8Pc]_2Er$	Cr 43 Col_h 163 I	Binnemans et al. (2003b)
$[(C_{18}H_{37}O)_8Pc]_2Er$	Cr 61 Col_h 154 I	Sleven et al. (2001) and Binnemans et al. (2003b)
$[(C_{12}H_{25}O)_8Pc]_2Tm$	Cr 68 Col_h 182 I	Binnemans et al. (2003b)
$[(C_{12}H_{25}O)_8Pc]_2Yb$	Cr 84 Col_h 192 I	Binnemans et al. (2003b)
$[(C_{10}H_{21}O)_8Pc]_2Lu$	Cr 43 Col_{ro} 96 Col_h 215 I	Maeda et al. (2003)
$[(C_{12}H_{25}O)_8Pc]_2Lu$	Cr_I 41 Cr_{II} 85 Col_h 189 I	Belarbi et al. (1989)
	Cr 45 Col_x 90 Col_h 196 I	van de Craats et al. (1997)
	Cr 61 Col_x 90 Col_h 196 I	Naito et al. (2001)
	Cr 85 Col_h 185 I	Sleven et al. (2001)
	Cr 61 Col_{ro} 90 Col_{ho} 196 I	Maeda et al. (2003)
	Cr 92 Col_h 188 I	Binnemans et al. (2003b)

TABLE 15 Thermal Behavior of Substituted *Bis*(phthalocyaninato) lanthanide(III) Compounds—Cont'd

Compound	Temperatures (°C)	Reference
$[(C_{12}H_{25}O)_8Pc]_2Lu^+BF_4^-$	Cr −7 Col_h 253 I	Belarbi et al. (1989)
$[(C_{14}H_{29}O)_8Pc]_2Lu$	Cr 51 Col_{ro} 72 Col_{ho} 171 I	Maeda et al. (2003)
$[(C_{16}H_{33}O)_8Pc]_2Lu$	Cr 51 Col_{ro} 61 Col_{ho} 149 I	Maeda et al. (2003)
$[(C_{18}H_{37}O)_8Pc]_2Lu$	Cr 54 Col_{ro} 64 Col_{ho} 131 I	Maeda et al. (2003)
$[(C_6H_{13}S)_8Pc]_2Lu$	Cr_I 102 Cr_{II} 120 Col_h 242 I	Basova et al. (2004)
$[(C_8H_{17}S)_8Pc]_2Lu$	Cr_I 45 Cr_{II} 84 Col_h 219 I	Ban et al. (2001)
$[(C_{10}H_{21}S)_8Pc]_2Lu$	X 6 M 40 Col_h 192 I	Ban et al. (2001)
$[(C_{12}H_{25}S)_8Pc]_2Lu$	X 27 M 38 Col_h 167 I	Ban et al. (2001)
$[(C_{14}H_{29}S)_8Pc]_2Lu$	Cr 38 Col_h 146 I	Ban et al. (2001)
$[(C_{16}H_{33}S)_8Pc]_2Lu$	Cr 46 Col_h 126 I	Ban et al. (2001)
$[(C_{18}H_{37}S)_8Pc]_2Lu$	Cr_I 32 Cr_{II} 53 Col_h 110 I	Ban et al. (2001)
$[(C_8H_{17})_8Pc]_2Lu$	Cr 79 Col_h 82 I	Komatsu et al. (1994a)
$[(C_{12}H_{25})_8Pc]_2Lu$	See text	Komatsu et al. (1994a)
$[(C_{18}H_{37})_8Pc]_2Lu$	See text	Komatsu et al. (1994a)
$[(C_8H_{17}OCH_2)_8Pc]_2Lu$	Cr 25 I	Piechocki et al. (1985)
$[(C_8H_{17}OCH_2)_8Pc]_2Lu^+[SbCl_6]^-$	Cr −10 Col_h 130 I	Piechocki et al. (1985)
$[(C_{12}H_{25}OCH_2)_8Pc]_2Lu$	Cr 24 Col_h 30 I	Piechocki et al. (1985)
$[(C_{12}H_{25}OCH_2)_8Pc]_2Lu^+[SbCl_6]^-$	Cr 13 Col_h 118 I	Piechocki et al. (1985)
$[(C_{18}H_{37}OCH_2)_8Pc]_2Lu$	Cr 51 Col_h 56 I	Piechocki et al. (1985)
$[(C_{18}H_{37}OCH_2)_8Pc]_2Lu^+[SbCl_6]^-$	Cr 56 Col_h 132 I	Piechocki et al. (1985)
$[(C_{18}H_{37}OPh)_8Pc]_2Lu$	Col_t 46.9 Col_h 242 I	Komatsu et al. (1994b)
$[(CH_3(OCH_2CH_2)_3O)_8Pc]_2Lu$	Cr 53 Col_t 57.6 I	Toupance et al. (1996)
$[(C_6H_{13}S)_4Pc]_2Lu$	Cr 34 Col_h 250 dec.	Atilla et al. (2009)
$[(C_8H_{17}S)_4Pc]_2Lu$	Cr 54 I 103 Col_h 230 I	Atilla et al. (2009)
$[(C_{10}H_{21}S)_4Pc]_2Lu$	Cr 40 I 75 Col_h 245 I	Atilla et al. (2009)

Continued

TABLE 15 Thermal Behavior of Substituted *Bis*(phthalocyaninato) lanthanide(III) Compounds—Cont'd

Compound	Temperatures (°C)	Reference
$[(C_{12}H_{25}S)_4Pc]_2Lu$	Cr 45 I 96 Col_h 240 I	Atilla et al. (2009)
$[(C_{16}H_{33}S)_4Pc]_2Lu$	Cr 53 I 83 Col_h 210 I	Atilla et al. (2009)

Cr, crystalline phase; I, isotropic phase; dec., decomposition; X, unidentified phase; M, new mesophase; Col_h, hexagonal columnar phase; Col_{ho}, hexagonal ordered columnar mesophase; Col_{hd}, hexagonal ordered columnar mesophase Col_{rd}, rectangular disordered mesophase; Col_{ro}, rectangular ordered mesophase; Col_t, tetragonal columnar phase; Col_x, unidentified columnar phase; Col_L, lamellocolumnar phase; Cub, cubic phase. The Col_h and Col_{hd} mesophases are identical.

investigated by temperature-dependent XRD measurements. In the small-angle region, a series of five sharp Bragg reflections was observed, with the reciprocal spacings in the ratio $1:\sqrt{3}:\sqrt{4}:\sqrt{7}:\sqrt{9}$. This is characteristic for a hexagonal columnar mesophase (Col_h). The intercolumnar distance is 37 Å, and the lutetium to lutetium spacing (intracolumnar distance) is about 7.3 Å. The XRD patterns remain unchanged over the temperature range from room temperature to the isotropic liquid, so that the structures of the solid phase and the mesophase are similar. In the solid state, the aliphatic chains are at least partially crystallized, whereas they are molten in the mesophase. $[(C_8H_{17}OCH_2)_8Pc]_2Lu$ was a room-temperature liquid, whereas $[(C_{12}H_{25}OCH_2)_8Pc]_2Lu$ exhibited a mesophase over the narrow temperature range from 24 to 30 °C, and only after a full cycle of heating to the isotropic liquid and cooling to the crystal state had been performed. The small mesophase stability range of the neutral forms can be due to the concave form of the phthalocyanine macrocycles. For the complexes $\{[(C_nH_{2n+1}OCH_2)_8Pc]_2Lu\} + [SbCl_6]^-$, the melting point was found to increase strongly with the length of the alkoxymethyl chain, whereas the mesophase stability range varies much less as a function of the chain length. Although the oxidized forms exhibit a mesophase over a much larger temperature range than the neutral forms, the former are relatively unstable: after several times of heating to the isotropic state and cooling to the crystalline state, the compounds change color from red to green (Piechocki, 1985). The green color is that of the neutral species. However, not the pure neutral form was reobtained, but rather a mixture. Even when only 10% of the neutral form was present, the mixture already had a greenish appearance. No XRD data are available for the oxidized forms. In comparison with the metal-free phthalocyanines, the enthalpy changes of the $[(C_nH_{2n+1}OCH_2)_8Pc]_2Lu$ complexes are large (Piechocki, 1985). In the case of $[(C_{12}H_{25}OCH_2)_8Pc]_2Lu$, $\Delta H = 167.2\ kJ\ mol^{-1}$ for the melting process and $\Delta H = 58.5\ kJ\ mol^{-1}$ for the clearing process. The values for $(C_{12}H_{25}OCH_2)_8PcH_2$ are respectively, 112.9 and 4.6 $kJ\ mol^{-1}$. This is an

indication that the degree of molecular organization is much higher for the lutetium complex than for the corresponding metal-free phthalocyanine, and that intermolecular interactions are more important in the mesophase than in the isotropic state.

The alkoxy-substituted compound $[(C_{12}H_{25}O)_8Pc]_2Lu$ forms a mesophase over a more extended temperature range (from 85 to 189 °C) than the corresponding alkoxymethyl substituted analogues (Belarbi et al., 1989). The mesophase of the oxidized species $\{[(C_{12}H_{25}O)_8Pc]_2Lu\}^+[BF_4]^-$ is even more stable than that of the neutral compound, with a hexagonal columnar mesophase being formed between −3 and 253 °C. The stabilization of the mesophase in the ionic derivative was attributed to electrostatic contributions or to partial orbital overlap within the columns. The solid phase of $[(C_{12}H_{25}O)_8Pc]_2Lu$ has an orthorhombic unit cell ($a = 29$ Å, $b = 24.6$ Å), whereas $\{[(C_{12}H_{25}O)_8Pc]_2Lu\}^+[BF_4]^-$ is a liquid at room temperature. For $[(C_{12}H_{25}O)_8Pc]_2Lu$, a crystal-to-crystal transition was observed at 42 °C. In the mesophase both compounds exhibit an ordered hexagonal columnar mesophase (Col_{ho}), with an intercolumnar distance of 34.6 Å. The oxygen linkage leads to significantly larger intercolumnar distances than the oxymethyl linkage. The conjugation of the oxygen atom with the aromatic macrocycle stiffens the anchoring point of the paraffinic chain. The ordered character of the mesophase is evident from a rather narrow peak found at large angles in the XRD patterns. The stacking period along the columns is 3.3 Å for both compounds, whereas the correlation length of the disordered side chains is in the range 4.5–4.6 Å. The stacking period along the columns is in this case less than half of the value observed for $[(C_{18}H_{37}OCH_2)_8Pc]_2Lu$, and seems to be related to a regular intermacrocyclic spacing uncorrelated to the position of the Lu^{3+} ion. This was attributed to the presence of impurities in the percent range in the monocyclic $(C_{18}H_{37}OCH_2)_8PcH_2$, which introduce a dephasing in the position of the lutetium ions. If the concentration of the impurity leads to unperturbed column lengths smaller than the spatial coherent domain of the incident X-ray beam (200–300 Å), XRD will only detect the intermacrocyclic distance, which is not changed by the presence of impurities. The mesophase behavior of $[(C_{12}H_{25}O)_8Pc]_2Lu$ was reinvestigated by van de Craats et al. (1997). They found nearly the same transition temperatures as Belarbi et al. (1989), but the crystal-to-crystal transition at 61 °C was considered as a crystal-to-mesophase transition ($\Delta H = 202$ kJ mol^{-1}), which involves only partial melting of the alkyl chains (Col_x phase). Melting is complete at the transition of this Col_x mesophase to the hexagonal columnar mesophase Col_h ($\Delta H = 70$ kJ mol^{-1}). The clearing point is at 196 °C ($\Delta H = 5.9$ kJ mol^{-1}). Upon cooling, no supercooling was observed for the isotropic-to-Col_h transition, but a supercooling of 10 °C for the Col_h-to-Col_x transition. The Col_x mesophase crystallizes at 35 °C to another crystalline solid than the virgin sample. In the second heating run, the crystal-to-Col_x transition was found at 45 °C (instead of 61 °C in the first heating run). In the Col_h phase, the

phthalocyanine macrocycles adopt a planar geometry. They are equidistant within the columnar stacks and uninfluenced by the presence or absence of a Lu^{3+} ion between alternate pairs. Indeed, the lack in correlation of the spacing of the phthalocyanine macrocycles with the position of the lutetium ion, is evident from the absence of a reflection corresponding to a distance of 6.6 Å, which is expected for an orthogonal stacking of Pc_2R molecular units. All Pc macrocycles are equivalent. There is a gradual change from a well-ordered columnar structure at a temperature close to 90 °C to an increasingly disordered columnar structure as the temperature is raised. This is evident from the gradual decrease of the intensity of the 3.3 Å reflection, which is the characteristic cofacial contact distance between aromatic moieties. The Col_x phase was reinvestigated by Naito et al. (2001) and was established as a new type of Col_{ro} phase ($P2_1/a$ symmetry) with two different stacking distances. Sleven et al. (2001) found an increase of both the melting and clearing point over the lanthanide series for $[(C_{12}H_{25}O)_8Pc]_2R$ complexes (R = Nd, Eu, Er, Lu). An increase of the chain length in the series $[(C_nH_{2n+1}O)_8Pc]_2Er$ ($n = 10$, 12, 18) appeared to influence the clearing temperatures only slightly. The incorporation of the lanthanide ion resulted in a smaller mesomorphic range with respect to the metal-free ligand. An XRD study of a series of $[(C_nH_{2n+1}O)_8Pc]_2Lu$ complexes ($n = 10$, 12, 14, 16, 18) revealed that these compounds form a rectangular ordered columnar mesophase Col_{ro} with two different stacking distances h_1 and h_2, which were attributed to a trampoline movement and rotation of the phthalocyanine macrocycles (Maeda et al., 2003). A hexagonal ordered columnar mesophase Col_{ho} was found at higher temperatures. Binnemans et al. (2003b) investigated the influence of the lanthanide ion and the chain length on the thermal properties of $[(C_nH_{2n+1}O)_8Pc]_2R$ complexes. Two series of complexes were considered: a first series in which the alkoxy chain was kept constant with different lanthanide ions (R = Pr, Nd, Eu, Gd, Tb, Dy, Ho, Er, Tm, Yb, Lu), namely $[(C_{12}H_{25}O)_8Pc]_2R$, and a second series of bis(phthalocyaninato) erbium(III) double-deckers, $[(C_nH_{2n+1}O)_8Pc]_2Er$, with different alkoxy chain-lengths ($n = 4$–18). All the complexes exhibited a hexagonal columnar mesophase (Col_h) over wide temperature ranges, independent of the chain length or the lanthanide ion. The compounds with the shorter chain lengths thermally decomposed before the clearing point was reached. However, the transition temperatures were found to be chain-length dependent rather than lanthanide-dependent unlike other mesomorphic lanthanide complexes, decreasing with extension of the chain, but being overall constant for different lanthanide ions. In order to get insight in the 2D ordering of such sandwich complexes in contact with a substrate, the orientational behavior of the erbium sandwich ($[(C_{12}H_{25}O)_8Pc]_2Er$) was investigated at room temperature at the liquid (1-phenyloctane)/solid (graphite) interface by means of scanning tunneling microscopy (STM) and compared with that of a metal-free alkyl-substituted phthalocyanine $(C_{12}H_{25}O)_8PcH_2$. The data show that the disks

are in a side-on position with the phthalocyanine units parallel to the graphite substrate. The Pc_2Tb complex with eight chiral 2-dodecyloxypropyloxy chains, $—CH_2CH(CH_3)O(CH_2)_{11}CH_3$, on each phthalocyanine ring is a room temperature LC (Gonidec et al., 2010). The hexagonal columnar mesophase clears at 31 °C.

In contrast to $[(C_8H_{17}OCH_2)_8Pc]_2Lu$, $[(C_8H_{17})_8Pc]_2Lu$ is a LC and exhibits a disordered hexagonal columnar phase in the 79–82 °C temperature range (lattice parameter $a = 25.0$ Å at 80 °C), the melting enthalpy being 47.2 kJ mol^{-1} and the clearing enthalpy 13.8 kJ mol^{-1} (Komatsu et al., 1994a). A virgin sample of $[(C_{12}H_{25})_8Pc]_2Lu$ showed an oblique disordered columnar phase at room temperature, indicating that the phthalocyanine macrocycles are tilted with respect to the stacking axis of the column. On heating this mesophase, it cleared at 32 °C to an isotropic liquid, but soon relaxed into an disordered hexagonal columnar phase ($a = 31.5$ Å at 42 °C). This mesophase cleared slowly to an isotropic liquid at 44 °C. A sample rapidly cooled from the isotropic liquid gave the disordered oblique columnar phase. When this sample was reheated, it showed the same thermal behavior as the virgin sample. However, a sample slowly cooled from the isotropic liquid gave the disordered hexagonal columnar phase, with horizontal stacking of the macrocycles. This behavior was explained using a Gibbs energy versus temperature diagram. A virgin sample of $[(C_{18}H_{37})_8Pc]_2Lu$ gave at room temperature a discotic lamellar phase (D_L), which cleared at 30 °C to an isotropic liquid, but soon relaxed to a disordered hexagonal columnar phase ($a = 32.9$ Å at 40 °C). The sample cleared slowly to an isotropic liquid at 43 °C. When the sample in the isotropic state was cooled, it gave a mixture of D_L and Col_{hd} phases, independent of the cooling rate.

A Pc_2Lu compound substituted by eight 4-octadecyloxyphenyl groups on the Pc ring showed a tetragonal columnar phase Col_t at room temperature ($a = 40.0$ Å), which transformed at 47 °C into a hexagonal columnar phase ($a = 43.5$ Å at 230 °C) and cleared at 242 °C (Komatsu et al., 1994b). Thermal decomposition of the isotropic liquid was observed at ca. 283 °C. The isotropic liquid sample cooled to room temperature gave a mesophase which was different from that of the virgin sample, but of which the XRD pattern could not be indexed. This unknown mesophase is transformed at 34 °C to a hexagonal columnar phase. In the virgin sample at room temperature in the tetragonal columnar phase, the phthalocyanine core is not able to rotate. When a sample of this mesophase was heated, the thermal mobility of the alkyl side chains increased, causing the packing of the columns to loosen. The phthalocyanine rings start to rotate, resulting in the transformation of the 2D tetragonal lattice in the more stable 2D hexagonal lattice of the hexagonal columnar phase. Ohta and coworkers prepared a series of bis(octaphenoxyphthalocyaninato)terbium(III) complexes, which were substituted by a dodecyloxy chains at the *para*-positions and alkoxy chains of various lengths in the *meta*-position (ligand **L34**, Fig. 53; Mukai et al., 2010). The compounds with shorter chain

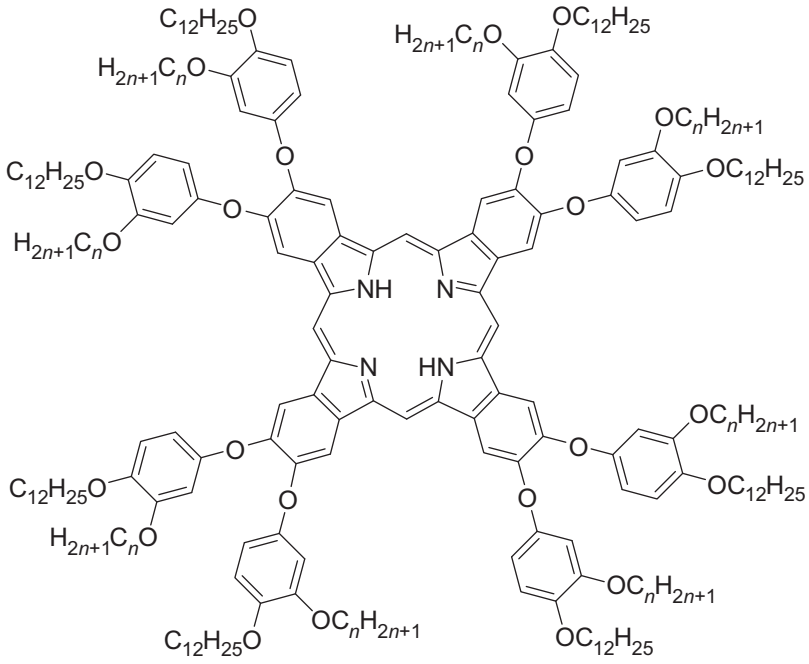

L34

FIGURE 53 Octaphenoxyphthalocyanine ligands.

lengths exhibited a lamellar columnar phase (Col_L) at room temperature. Upon heating, the compounds formed one or two rectangular columnar mesophases (Col_r) with $P2_1/a$ symmetry. The compound with a decyloxy chain in the *meta*-position showed a cubic phase ($Pn\bar{3}m$ symmetry) above the rectangular columnar phase. A complex mesophase behavior was observed for the compound with the decyloxy *meta*-substituent: Col_{hd} 142 $Cub_1(Pn\bar{3}m)$ 165 Cub_2 ($Pm\bar{3}n$) 245 I. On holding the sample at the clearing temperature (245 °C), the isotropic liquid slowly relaxed into a tetragonal columnar phase (Col_t). When the sample was heated again, it cleared at 282 °C. The general tendency is that the complexes change their mesophases in the order $Col_L \rightarrow Col_r \rightarrow Cub \rightarrow Col_t$ upon increasing the chain length.

The poly(oxyethylene)-substituted lutetium phthalocyanine complex $[(CH_3(OCH_2CH_2)_3O)_8Pc]_2Lu$ exhibits a tetragonal columnar phase (Col_t) between 53 and 57.6 °C ($a = 26.7$ Å; Toupance et al., 1996). The high-temperature XRD pattern consists of a series of Bragg reflections which correspond to reciprocal distances in the ratio $1:\sqrt{2}:\sqrt{4}:\sqrt{8}$. Around 4.2 Å, a halo due to the molten poly(oxyethylene) chains is observed both in the mesophase and in the isotropic liquid. The melting enthalpy is 1.6 J g^{-1} and the clearing

enthalpy 6.4 J g^{-1}. The low-temperature phase is crystalline with an orthorhombic unit cell ($a = 25.4$ Å, $b = 19.2$ Å, $c = 13.75$ Å). The analogous compounds with shorter chain length, $[(CH_3OCH_2CH_2O)_8Pc]_2Lu$ and $[(CH_3(OCH_2CH_2)_2O)_8Pc]_2Lu$, or with longer chain length, $[(CH_3(OCH_2CH_2)_4O)_8Pc]_2Lu$, did not show a mesophase. The most pronounced effect was the rapid decrease of the isotropization temperature on increasing the chain length, from 246 °C for $[(CH_3OCH_2CH_2O)_8Pc]_2Lu$ to 138 °C $[(CH_3(OCH_2CH_2)_2O)_8Pc]_2Lu$. $[(CH_3(OCH_2CH_2)_4O)_8Pc]_2Lu$ was a room-temperature liquid. All the members of a series of octakis(alkylthio)-substituted complexes $[(C_nH_{2n+1}S)_8Pc]_2R$ (R = Eu, Tb, Lu; $n = 8$, 10, 12, 14, 16, 18) exhibit a hexagonal columnar phase over a broad temperature range (Ban et al., 2001). A novel pseudo-hexagonal phase with $P2_1/a$ symmetry (labeled as D_{rh}) was found for the complexes with decylthio chains and with dodecylthio chains (and also for the terbium(III) complex with tetradecylthio chains). This mesophase has a 2D rectangular lattice (having a relationship $a = \sqrt{3}b$) for the whole molecules and a 2D hexagonal lattice for the central core disks. On heating, the tilted molecules become stepwise cofacially stacked. In the large angle region of the XRD diffractograms, two peaks due to the stacking distances h_1 (ca. 3.5 Å, corresponding to a single decker) and h_2 (ca. 7 Å, corresponding to a double decker) could be observed. The stacking distance at ca. 3.5 Å was attributed to rapid thermal fluctuations which extinguish the differences between the upper and lower macrocycles in the sandwich compound. Thermal fluctuations may cause trampoline movements of the phthalocyanine rings. The phthalocyanine ring bearing the unpaired electron is not aromatic and not flat, but it bends just like a dome. On increasing the temperature, the trampoline movement may occur faster to give apparent single deckers on the time average. The surface morphology of spin-coated thin films of $[(C_6H_{13}S)_8Pc]_2R$ in the solid state and in the mesophase have been investigated by atomic force microscopy (AFM; Basova et al., 2004). It was observed that the films annealed in the mesophase had a smooth and homogeneous topology. The hexagonal columnar mesophases of the cerium(IV) complexes $[(C_nH_{2n+1}S)_8Pc]_2Ce$ showed a strong tendency for spontaneous homeotropic alignment on nontreated flat substrates and ITO-coated glasses (Nekelson et al., 2007a,b). Large monodomains of homeotropically aligned molecules (i. e., with the phthalocyanine rings parallel to the glass surface) could easily be achieved by slowly cooling of the samples from the isotropic phase. Such a strongly tendency to form monodomains was not observed for the corresponding lutetium double-decker complexes. The homeotropic alignment of columns in the mesophase could be retained at room temperature. The mesophase was frozen into the glass state at room temperature, without any visible tendency for crystallization.

All the phthalocyanine complexes discussed above have eight substituents on the peripheral positions of phthalocyanine ring (2,3,9,10,16,17,23,24 substitution pattern). These eight-substituted compounds have a very symmetrical

structure. The phthalocyanines with four substituents on the peripheral positions are much less symmetric than the eight-substituted compounds. In general, synthetic routes of four-substituted phthalocyanines lead to a statistic mixture of isomers, and it is difficult, if not impossible, to separate these isomer mixtures (McKeown, 1998). Atilla et al. (2009) prepared a series of double-decker lutetium(III) complexes with four alkylthio substituents on each phthalocyanine ring. Interestingly, several of the complexes exhibited a double clearing behavior. The first clearing point corresponding to melting of the compounds from the crystalline state to the isotropic liquid at about 40–55 °C. Upon further heating, the isotropic state was transformed into a hexagonal columnar phase at a temperature between 75 or 103 °C (depending on the chain length). The clearing point of the hexagonal columnar phase was between 210 and 245 °C. By reaction of the double-decker compounds Pc_2R can be transformed into triple-decker compounds Pc_3R_2 by reaction with acetylacetonate complexes $R(acac)_3 \cdot nH_2O$ in boiling 1,2,4-trichlorobenzene (Zhang et al., 2007). The rare-earth triple-decker complexes $[(C_8H_{17}O)_8Pc]_3R_2$ (R = Eu, Gd, Lu, Y) formed rectangular columnar mesophases over a large temperature range (Table 16). Highly-ordered film of the triple-decker complexes $[Pc(15C5)_4]Eu[Pc(15C5)_4]Eu[Pc(OC_8H_{17})_8]$, where 15C5 stands for 15-crown-5 (Chen et al., 2007) and $\{Pc[(OC_2H_4)_2OCH_3]_8\}Eu\{Pc[(OC_2H_4)_2OCH_3]_8\}Eu[Pc(OC_8H_{17})_8]$ (Li et al., 2007) could be obtained by the Langmuir–Blodgett technique, but no thermal properties have been reported for these complexes. Naphthalocyanines (Fig. 54) are macrocycles with a more extended conjugated system than the phthalocyanines (McKeown, 1998). The liquid-crystalline behavior of a series of bis(naphthalocyaninato)lanthanide(III) with eight alkylthio chains $[(C_{12}H_{25}S)_8Nc]_2R$ (R = Nd, Eu, Gd, Tb, Ho, Er, Y; Zhang et al., 2006). The compound melted around 50 °C to a hexagonal columnar phase, and the clearing point was observed between 190 and 243 °C.

TABLE 16 Thermal Behavior of Substituted Triple-Decker Phthalocyanine Lanthanide(III) Compounds

Compound	Temperatures (°C)	Reference
$[(C_8H_{17}O)_8Pc]_2Eu_3$	Cr 90 Col_{r1} 171 Col_{r2} 305 I	Zhang et al. (2007)
$[(C_8H_{17}O)_8Pc]_2Gd_3$	Cr 90 Col_{r1} 167 Col_{r2} 303 I	Zhang et al. (2007)
$[(C_8H_{17}O)_8Pc]_2Y_3$	Cr 92 Col_{r1} 157 Col_{r2} 290 I	Zhang et al. (2007)
$[(C_8H_{17}O)_8Pc]_2Lu_3$	Cr 83 Col_{r1} 140 Col_{r2} 249 I	Zhang et al. (2007)

Cr, crystalline phase; Col_r, rectangular columnar phase; I, isotropic liquid.

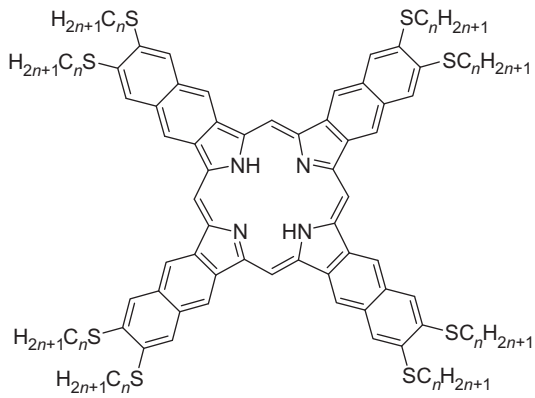

L35

FIGURE 54 Naphthalocyanines.

9. PORPHYRIN COMPLEXES

The synthesis and characterization of bis-(2,3,7,8,12,13,17,18-octylthio)-5,10,15,20-(tetraazaporphyrinato)lutetium(III) has been described (Ricciardi et al., 1993). The compound, abbreviated to $Lu(OOTTAP)_2$, was prepared by reaction of the $H_2OOTTAP$ ligand **L36** (Fig. 55) with hydrated lutetium (III) acetate in a 2:1 molar ratio for 1 week in refluxing 1-hexanol. EPR, NMR, UV–Vis, and NIR data were consistent with a deprotonated and radical structure of the complex. The authors conclude that there is no evidence for a preferential localization of the unpaired electron on the two tetraazaporphyrinato rings. Dark green solutions of the compound in acetone, in alcohols, and in a various series of organic solvents were stable over months. Both the redox properties and UV–VIS absorption spectra are comparable with those of the substituted bis(phthalocyaninato)lutetium(III) complexes, but the NIR vibrational spectra better resemble those of bis(porphyrinato)lutetium(III) complexes. Although this compound and especially the analogous compounds with long alkyl chains have a good potential to exhibit liquid-crystalline behavior, the thermal properties of this class of compounds have not been investigated yet. Triple-decker sandwich complexes consisting of two cerium(III) ions and three 5,15-diarylporphyrins **L37** were prepared by reaction between the parent porphyrins and $Ce(acac)_3 \cdot H_2O$ (acac = acetylacetonate) in 1,2,4-trichlorobenzene at reflux temperature (Miwa et al., 1999). The motivation to carry out this work was to find the border on molecular structure between a discotic mesogen and a calamitic mesogen, when the molecular shape is continuously changed from disklike to rod-like. The parent porphyrins have a strip-like shape, but they can aggregate into columnar structures. The thermal behavior of the triple-decker complexes was investigated in detail. The complexes

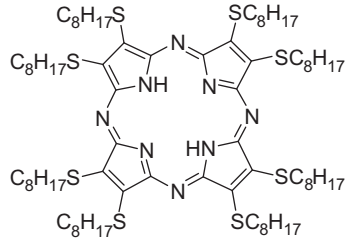

L36

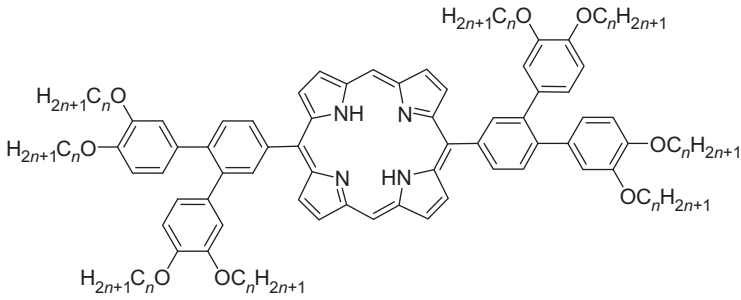

L37

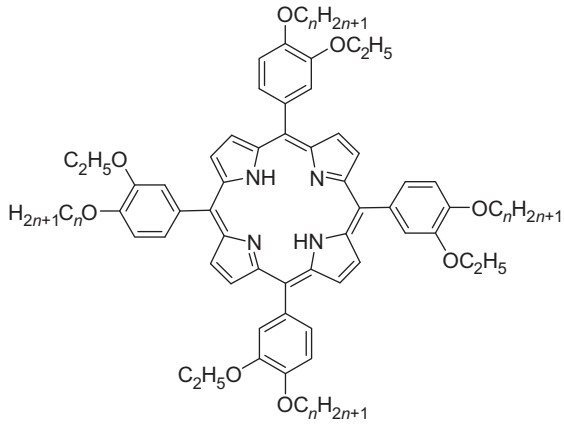

L38

FIGURE 55 Porphyrin ligands.

containing dialkoxyphenyl groups in the 5,15-positions of the parent porphyrin show a mesophase possessing both lamellar and columnar structures at lower temperatures (discotic lamellar columnar mesophase, D_{LC}) and a rectangular columnar mesophase (Col_r) at higher temperatures. The D_{LC} phase could be

observed only in virgin samples. The X-ray pattern of this mesophase gave reciprocal Bragg spacings in the ratio 1:2:3:4 (corresponding to a lamellar structure), and a broad peak around $2\theta = 20°$ (corresponding to the molten alkyl chains). Additionally, a relatively broad peak could be observed at ca. 3.6 Å (h_1), which agrees with a stacking distance of 3.2–3.5 Å between the porphyrin monomers in a columnar structure. Two peaks, one at 7.9 Å (h_2) and one at 10.4 Å (h_3) are close to two and three times 3.6 Å (h_1), respectively. Complexes containing tetraalkoxylated terphenyl groups at the 5,15-position of the parent porphyrin show only a hexagonal columnar phase (Col_h) with a single stacking distance. On the basis of the extinction rules for 2D lattices, the rectangular columnar phase was found to have P2/a symmetry. The differences in mesomorphism were attributed to differences in the steric hindrance of the side chains for rotation along the axis connecting the center of the three porphyrins. In addition to the mesomorphic properties, the electrochemical and spectroscopic properties of the triple-decker complexes have been reported. In a later study, the corresponding cerium(IV) double-decker (sandwich) complexes were investigated (Nakai et al., 2002). The relative ratios of double- and triple-deckers was found to depend very much on the experimental synthesis conditions. Hydroxy [5,10,15,20-tetra[(*p*-decyloxy-*m*-methyloxy)phenyl]porphyrin ytterbium(III) was reported to exhibit a hexagonal columnar phase between −8 and 45 °C (Zhao and Liu, 2002). Also similar complexes with alkyl chain lengths between hexyloxy and hexadecyloxy formed a hexagonal columnar phase (Qi and Liu, 2003). The electrochemical and photophysical properties of these complexes have been investigated. *Meso*-tetraalkyltetrabenzoporphyrins (H_2TATBP) formed with lanthanide acetylacetonates $R(acac)_3 \cdot xH_2O$ (R = Tb, Dy, Ho, Er, Tm, Yb) complexes of the type R(TATBP)(acac) (Qi and Liu, 2004). In contrast to the hydroxo complexes mentioned above, no liquid-crystalline behavior has been reported for these complexes. Hydroxo complexes of [5,10,15,20-tetra[(*p*-alkyloxy-*m*-ethyloxy)phenyl]porphyrins **L38** with lanthanide(III) ions exhibit a hexagonal columnar mesophase (Yu et al., 2005).

10. LANTHANIDE ALKANOATES

Lanthanide(III) alkanoates are salts of alkanoic acids (fatty acids). They are also known as "*lanthanide soaps*" and their general formula is $[R(C_nH_{2n+1}COO)_3]$. The first examples of lanthanide salts of the higher alkanoic acids were described by Mehrotra and coworkers (Mehrotra et al., 1966; Misra et al., 1963a), although shorter homologues have been reported much earlier (Wolff, 1905). The lanthanide(III) alkanoates can be prepared by a metathesis reaction between the corresponding sodium alkanoate and the lanthanide salt (nitrate or chloride) in ethanol/water solution:

$$3C_nH_{2n+1}COONa + RX_3 \rightarrow R(C_nH_{2n+1}COO)_3 + 3NaX. \quad (14)$$

The metal soaps can be purified by recrystallization from 1-pentanol. The pH of the solution used for synthesis is of importance, because the alkanoic

acids precipitate at low pH, and mixed hydroxy compounds of the type $[R(OH)_x(C_nH_{2n+1})_{3-x}]$ are formed at high pH values (Skrylev et al., 1980). The experimental procedures had to be adapted for the short chain homologues, because of too high a solubility of the compounds in the solvents used for the synthesis of the long-chain compounds. Butyrates were obtained by reaction between the corresponding lanthanide(III) hydroxide and butyric acid in a 1:3 molar ratio (Binnemans et al., 2000c) Another synthetic method is the reaction between a lanthanide(III) isopropoxide and butanoic acid in a 1:3 molar ratio in benzene (Hasan et al., 1968). Typically, lanthanide soaps with short chain lengths are obtained as dihydrates, those with an intermediate chain length as mono- or hemihydrates, and the homologues with a long chain length as anhydrous compounds. The water of crystallization is lost upon heating before the melting point is reached or upon melting, so that compounds obtained from cooling of the melt are always anhydrous. Anhydrous soaps can be synthesized by reaction between the alkanoic acid and anhydrous lanthanide(III) chloride in dry toluene (Misra et al., 1963b). By changing the stoichiometric ratio, it is possible to obtain mixed compounds of the type $[RCl_x(C_nH_{2n+1}COO)_{3-x}]$. Misra et al. (1987) prepared lanthanide(III) alkanoates with three different alkyl chains within one and the same compound by stepwise substitution of the isopropoxide groups in lanthanide(III) isopropoxides. The long chain homologues are insoluble in water and have a low solubility in all organic solvents at room temperature. They are soluble at elevated temperatures in the higher *n*-alcohols (1-butanol, 1-pentanol, ...) and in aromatic solvents (benzene, toluene, ...). For crystallization, the *n*-alcohols are preferable over the aromatic solvents, because in the former solvents an easier filterable precipitate is obtained, whereas the use of aromatic solvents leads to gel formation. The best filterable precipitates are obtained in 1-pentanol—ethanol mixtures. The solubility of the short-chain homologues is much higher than that of the compounds with long alkyl chains. Data on scandium(III) alkanoates are scarce (Rai and Parashar, 1979). Perfluorinated alkanoic acids also form metal soaps with trivalent lanthanides (Fan et al., 1988).

In the solid state, the structure of the lanthanide(III) alkanoates can be described as an infinite ionic sheet of lanthanide ions and carboxylate groups, separated by a bilayer of alkyl chains (Binnemans et al., 2000c; Jongen et al., 2001a,b,c; Marques et al., 1998). The alkyl chains are in the all-*trans* conformation and perpendicular to the ionic layer. It is possible to calculate the *d*-spacing using the formula (Marques et al., 1998)

$$d_{calc} = 2d_{C-H} + 2(n-1)d_{C-C}\sin 55^\circ + 2d_{C-O} + 2r_{R^{3+}}, \qquad (15)$$

where n is the total number of carbon atoms in the chain, $d_{C-H} = 1.09$ Å, $d_{C-C} = 1.54$ Å and $d_{C-O} = 1.36$ Å. $r_{R^{3+}}$ is the radius of the trivalent lanthanide ion. The coordination mode of the carboxylate groups in the mesomorphic lanthanide alkanoates is not known in detail yet, although some structural features can be derived from the crystal structures of lanthanum(III) butyrate

hydrate (Jongen et al., 2001e) and neodymium(III) butyrate hydrate (Binnemans et al., 2000c). For these compounds it was observed that different types of lanthanide-carboxylate coordination modes are present. Although it is in principle possible to deduce the type of lanthanide-carboxylate bonding by infrared spectroscopy, these studies do not give an unambiguous answer, probably due to the presence of multiple coordination modes. The lanthanide(III) alkanoates have a polymeric structure. Although only three carboxylate groups are sufficient to balance the tripositive charge of the R^{3+} ion, this only results in six coordinate complexes if three bidentate carboxylate groups bind to one lanthanide ion. The coordination sphere of the lanthanide(III) ion is unsaturated in this situation. The lanthanide(III) ion can saturate its coordination sphere by allowing the carboxylate groups to act as bridges between two lanthanide(III) ions and by sharing of an oxygen atom between two lanthanide ions. Also coordination of water can help to saturate the coordination sphere of the lanthanide(III) ion. Structural changes in the metal-carboxylate network are possible over the lanthanide series because the large ions in the beginning of the lanthanide series typically have higher coordination numbers than the small ions at the end of the series.

Mesomorphism of the lanthanide(III) soaps was first observed by Burrows and coworkers in a series of cerium(III) alkanoates (Marques et al., 1998). These authors found by polarized optical microscopy and by DSC that these compounds exhibit a viscous mesophase which was tentatively assigned as a SmA-like mesophase. Without high-temperature XRD it is difficult to determine the mesophase type unambiguously, because the optical textures of these compounds are not diagnostic. It was observed that the thermal behavior was complex, in the sense that the second heating run of the DSC differed markedly from the first heating run. Especially the ΔH values for two heating runs were markedly different. On the basis of the transition enthalpies, it was concluded that electrostatic interactions in the polar region (due to the essentially ionic character of the metal-carboxylate bond) play an important role in the melting process. In the series of homologous cerium(III) alkanoates, each CH_2 group contributes for 2.5 kJ mol^{-1} to the total melting enthalpy. This value is lower than the 3.8 kJ mol^{-1} associated with complete fusion of aliphatic chains in their fully crystalline state (Seurin et al., 1981). An analysis of the corresponding entropy data showed that the chains melt incompletely, so that molecular aggregates are present in the melt. The mesophase of lanthanum(III) tetradecanoate was identified as a smectic A phase by Binnemans et al. (1999b) via XRD studies. Shortly thereafter, an in-depth study of the thermal behavior of the lanthanide(III) alkanoates was started by Jongen and Binnemans. Both metal ion and the alkyl chain were varied in a systematic way. This work revealed that of the series of the lanthanide(III) dodecanoates, only the lanthanum(III), cerium(III), praseodymium(III) and neodymium(III) compounds form a mesophase, but not samarium(III) dodecanoate and the dodecanoates of the heavier lanthanides (Fig. 56;

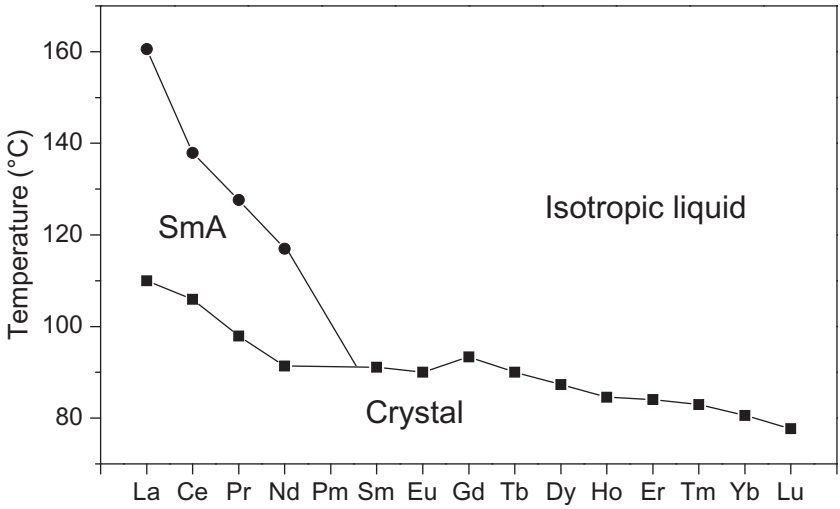

FIGURE 56 Phase diagram of the lanthanide(III) dodecanoates (drawn using the data in Table 2 of Binnemans et al., 2000d).

Binnemans et al., 2000d). It was also observed that the change in *d*-spacing at the crystal-to-mesophase transition increased over the lanthanide series. The alkyl chain length was found to have an influence on the thermal behavior. For the neodymium(III) alkanoates, a mesophase was observed for the homologous series $[Nd(C_4H_9COO)_3]$–$[Nd(C_{14}H_{29}COO)_3]$, but not for neodymium (III) hexadecanoate and the homologues with longer alkyl chains (Binnemans et al., 2000c). The compounds with short alkyl chains exhibit two mesophases: a smectic A phase at high temperature and an unidentified high-ordered smectic phase M at lower temperatures. The mesophase behavior of the alkanoates of lanthanum(III) (Jongen et al., 2001b), cerium(III) (Jongen et al., 2001c), and praseodymium(III) (Jongen et al., 2001a) is very comparable to the mesophase behavior of the neodymium(III) alkanoates, except that these compounds also form a mesophase for the hexadecanoates and the higher homologues. A typical feature for the lanthanide(III) alkanoates is the large supercooling for the clearing temperature. For conventional LCs, the onset temperature of the clearing point in the heating run of a DSC thermogram coincides with the onset temperature of the clearing point in the cooling run. The difference can be more than 10 °C for the lanthanide(III) alkanoates. It is not easy to determine whether some of the lanthanide(III) alkanoates form a mesophase or not. In contrast to many other types of LCs, it is very difficult to obtain well-developed optical textures for the lanthanide soaps. These compounds have a very strong tendency to align homeotropically between two microscope glass slides. As a result, the sample appears black

between crossed polarizers and no optical texture can be observed. Sometimes birefringence can be induced in the samples by pressing with a needle on top of the cover glass slide or by shearing the two glass slides, but often this is only a transient phenomenon. As soon as the pressure or shear force are relieved, the birefringence disappears. It is not evident whether the disappearance of the birefringence is due to the absence of a mesophase in the sample or to the fact that the sample is homeotropically realigned. Therefore, it is not surprising that conflicting results appear in the literature. Whereas Binnemans and Jongen have not obtained evidence for a mesophase in europium(III) dodecanoate, a smectic A phase was reported by other authors for europium(III) alkanoates with longer alkyl chains (Li et al., 2005a). The latter authors state that the higher atomic number of the lanthanide, the longer the alkyl chains of their alkanoates has to be in order to form a mesophase on heating. On the other hand, Binnemans et al. (2000c) observed for the neodymium(III) alkanoates a narrowing of the mesophase stability range with increasing chain lengths and eventually a disappearance of the mesophase. It is evident that further work is needed to solve this issue. In a very interesting paper, Corkery (2008) considers the phase sequence crystalline (Cr)—crystalline smectic rotor phase (CrB)—partially molten-chain smectic (SmA1)—molten-chain smectic (SmA2)—ordered melt for the lanthanum(III), cerium(III), praseodymium(III) and neodymium(III) alkanoates with long alkyl chains ($C_{12}H_{25}$, $C_{14}H_{29}$, $C_{16}H_{33}$, $C_{18}H_{37}$), and the phase sequence crystalline (Cr)—crystalline smectic rotor phase (CrB)—conformationally disordered smectic rotor phase (SmB)—ordered melt for the samarium(III), terbium(III), holmium(III), thulium(III) and ytterbium(III) alkanoates. The SmA1 phase corresponds to the M phase observed by Binnemans et al. (2000c) for the neodymium(III) alkanoates and the SmA2 corresponds to the SmA phase reported by Jongen and Binnemans for the lanthanide(III) alkanoates. The lanthanum(III) soaps show a rotator phase CrB over a narrow temperature range between the crystalline state and the SmA1 phase. This Cr–CrB transition can only be observed in the DSC thermogram as a small skewing of the melting-peak to lower temperatures. The temperature existence region for the CrB phase becomes larger for the alkanoates of the heavier lanthanides. The lanthanum(III), cerium(III) and terbium(III) salts of a C_{17} fatty acid with a methyl group in the mid chain are room-temperature LCs, and they exhibit a hexagonal columnar mesophase (Corkery, 2004). The low melting points of the compounds are attributed to packing frustration of the long alkyl chains due to mid-chain methyl group. The corresponding lutetium(III) compound does not show liquid-crystalline behavior at room temperature, but birefringence can be induced by a shear force. Corkery (2008) gives a detailed interpretation of the thermal phenomena observed for lanthanide soaps. He draws an analogy between lanthanide soaps and metal-organic frameworks (MOFs) and considers the anhydrous and hydrated lanthanide soaps as 2D MOFs at room temperature. During heating, the alkyl chains and the MOF head groups

gradually expand. The rotational and conformational disorder gradually increases, and the compounds are transformed to either a 2D smectic rotor-phase MOF, 2D liquid-crystalline smectic MOFs, or 1D liquid-crystalline smectic MOFs. Hydrated lanthanide soap samples show a significantly higher heat of fusion than samples obtained by crystallization from the melt. This is due to the release of coordinated water. Moreover the hydrated samples also show a higher crystallinity. The thermal and hydration history of the lanthanide(III) alkanoates does not seems to influence the first order transition temperatures, but rather the heat changes and the temperature range of the second order (or weakly first order) transitions that proceed the main first order transition (premelting effects). The escape of water molecules during the heating process softens the polar layer parts, induces disorder in the hydrocarbon chains and causes the transitions to occur over a wider temperature range in the hydrated lanthanide soaps in comparison with the anhydrous salts. Corkery (2008) presents a structural model to explain why a smectic A1 phase can only be formed by large lanthanide ions and not by small ones. The SmA1 phase is considered as a 2D MOF and can be formed by polymerization of 1D MOFs. The interfacial area of the chains defines the distance that the metal-carboxylate bonds must bridge for polymerization of the 1D MOFs into 2D MOFs. The model predicts that the R–O distance must be greater than about 2.64 Å. Because the Nd–O distances in neodymium(III) butyrate monohydrate are between 2.42 and 2.66 Å (Binnemans et al., 2000c), it can be understood why neodymium(III) alkanoates are borderline cases for the occurrence of the SmA1 phase. The SmA2 phase is assumed to consist of 1D MOFs. Transition temperatures of the lanthanide(III) alkanoates are summarized in Tables 17–21. Although samarium(III) dodecanoate and the dodecanoates of the heavier lanthanides do not exhibit a mesophase, it was found that a mesophase could be induced by preparing binary mixtures of these compounds with lanthanum(III) dodecanoate (or with cerium(III), praseodymium(III) or neodymium(III) dodecanoates) (Jongen et al., 2001d). The mole fraction of lanthanum(III) dodecanoate required to induce the mesophase increased over the lanthanide series. Whereas 4 mol.% of lanthanum(III) dodecanoate was sufficient to induce mesomorphism in europium(III) dodecanoate, this amount increased to 48 mol.% for ytterbium(III) dodecanoate. A melt of the higher homologues of the lanthanide(III) alkanoates can be easily supercooled to a transparent glass, although the glass samples tend to crystallize after a period of 1 year or longer. Corkery and Martin (1999) studied the luminescence of vitrified europium(III) dodecanoate. Binnemans et al. (2001a) determined the Judd-Ofelt intensity parameters of glasses of lanthanide(III) octadecanoates. The lanthanum(III) salts of 4-hexyloxybenzoic acid, 4-octyloxybenzoic acid and 4-nonyloxybenzoic acid form a smectic A phase, whereas the corresponding holmium(III) complexes are not liquid-crystalline (Jongen et al., 2003). For the lanthanide(III) salts of 4-hexyloxybenzoic acid, only those of lanthanum(III) and praseodymium(III) show a mesophase (SmA)

TABLE 17 Thermal Behavior of Lanthanum(III) Alkanoates

Compound	Temperatures (°C)	Reference
$[La(C_3H_7COO)_3]$	Cr 188.4 I	Jongen et al. (2001b)
$[La(C_4H_9COO)_3]$	Cr 93.8 M 139.2 SmA 190.2 I	Jongen et al. (2001b)
$[La(C_5H_{11}COO)_3]$	Cr 94.4 M 137.9 SmA 189.9 I	Jongen et al. (2001b)
$[La(C_6H_{13}COO)_3]$	Cr 97.7 M 133.5 SmA 189.3 I	Jongen et al. (2001b)
$[La(C_7H_{15}COO)_3]$	Cr 94.6 M 122.4 SmA 175.9 I	Jongen et al. (2001b)
$[La(C_8H_{17}COO)_3]$	Cr 98.1 M 121.0 SmA 179.8 I	Jongen et al. (2001b)
$[La(C_9H_{19}COO)_3]$	Cr 95.6 M 122.1 SmA 172.3 I	Jongen et al. (2001b)
$[La(C_{10}H_{21}COO)_3]$	Cr 106.9 SmA 165.9 I	Jongen et al. (2001b)
$[La(C_{11}H_{23}COO)_3]$	Cr 110.0 SmA 160.6 I	Jongen et al. (2001b)
$[La(C_{12}H_{25}COO)_3]$	Cr 116.4 SmA 154.6 I	Jongen et al. (2001b)
$[La(C_{13}H_{27}COO)_3]$	Cr 120.3 SmA 157.1 I	Jongen et al. (2001b)
$[La(C_{14}H_{29}COO)_3]$	Cr 121.4 SmA 157.0 I	Jongen et al. (2001b)
$[La(C_{15}H_{31}COO)_3]$	Cr 123.4 SmA 148.2 I	Jongen et al. (2001b)
$[La(C_{16}H_{33}COO)_3]$	Cr 123.9 SmA 149.7 I	Jongen et al. (2001b)
$[La(C_{17}H_{35}COO)_3]$	Cr 125.9 SmA 148.0 I	Jongen et al. (2001b)
$[La(C_{18}H_{37}COO)_3]$	Cr 126.7 SmA 126.7 I	Jongen et al. (2001b)
$[La(C_{19}H_{39}COO)_3]$	Cr 140.1 SmA 140.1 I	Jongen et al. (2001b)
$[La(C_{20}H_{41}COO)_3]$	Cr 128.1 SmA 143.6 I	Jongen et al. (2001b)

Cr, crystalline phase; M, unidentified smectic phase; SmA, smectic A phase; I, isotropic liquid.

(Jongen et al., 2004). The corresponding compounds of the heavier lanthanides (R = Nd, Sm, Eu) are not liquid-crystalline. Singh et al. (2005) investigated the thermal properties of a series of lanthanide(III) complexes of 4-alkoxybenzoates, with different chains lengths (C_nH_{2n+1}, $n = 6$, 8, 10, 12, 16) and lanthanide ions (R = La, Pr, Nd, Eu, Gd, Tb, Dy). Most of the complexes were found to exhibit a smectic A phase. Anhydrous and hydrated samples of lanthanide(III) phytanates show both thermotropic and lyotropic mesomorphism (Conn et al., 2010). Phytanic acid (=3,7,11,15-tetramethyl hexadecanoic acid) has an isoprenoid-type of hydrocarbon chain with four methyl substituents along its saturated backbone. Several of the hydrated salts form a hexagonal columnar phase at room temperature.

TABLE 18 Thermal Behavior of Cerium(III) Alkanoates

Compound	Temperatures (°C)	Reference
$[Ce(C_5H_{11}COO)_3]$	Cr 74 M 110 SmA 159 I	Jongen et al. (2001c)
$[Ce(C_6H_{13}COO)_3]$	Cr 73 M 106 SmA 161 I	Jongen et al. (2001c)
$[Ce(C_7H_{15}COO)_3]$	Cr 75 M 102 SmA 152 I	Jongen et al. (2001c)
$[Ce(C_8H_{17}COO)_3]$	Cr 81 M 96 SmA 148 I	Jongen et al. (2001c)
$[Ce(C_9H_{19}COO)_3]$	Cr 86 M 93 SmA 148 I	Jongen et al. (2001c)
$[Ce(C_{10}H_{21}COO)_3]$	Cr 101 SmA 142 I	Jongen et al. (2001c)
$[Ce(C_{11}H_{23}COO)_3]$	Cr 106 SmA 142 I	Jongen et al. (2001c)
$[Ce(C_{12}H_{25}COO)_3]$	Cr 107 SmA 133 I	Jongen et al. (2001c)
$[Ce(C_{13}H_{27}COO)_3]$	Cr 111 SmA 131 I	Jongen et al. (2001c)
$[Ce(C_{14}H_{29}COO)_3]$	Cr 115 SmA 130 I	Jongen et al. (2001c)
$[Ce(C_{15}H_{31}COO)_3]$	Cr 116 SmA 129 I	Jongen et al. (2001c)
$[Ce(C_{16}H_{33}COO)_3]$	Cr 119 SmA 127 I	Jongen et al. (2001c)
$[Ce(C_{17}H_{35}COO)_3]$	Cr 120 SmA 129 I	Jongen et al. (2001c)

Cr, crystalline phase; M, unidentified smectic phase; SmA, smectic A phase; I, isotropic liquid.

11. POLYOXOMETALATE-SURFACTANT COMPLEXES

Polyoxometalates (POMs) are oxygen cluster anions formed by early transition metals (V, Nb, Ta, Mo, W) in their highest oxidation state. The chemistry of POMs is dominated by molybdenum and tungsten in their +6 oxidation state. An amazingly rich variety of polyoxometalate complexes has been described in the literature. Some polyoxometalate clusters can act as ligands for lanthanide ions (Lis, 2000; Pople, 2008; Yamase, 1998, 2009; Yusov and Shilov, 1999). Of all the known lanthanide-containing polyoxometalates, the lanthanide decatungstates, and especially the europium decatungstate or decatungstoeuropate(9-) anion, show the best luminescence performance. This polyoxoanion was first prepared as a potassium salt by Peacock and Weakley (1971) and originally formulated as $[EuW_{10}O_{35}]^{7-}$, but later studies revealed that its composition is in fact $[EuW_{10}O_{36}]^{9-}$ (Iball et al., 1974). The $[EuW_{10}O_{36}]^{9-}$ anion consists of two $[W_5O_{18}]^{6-}$ fragments (each containing five WO_6 octahedra sharing edges) coordinating to the Eu^{3+} ion. The eight oxygen atoms (four of each W_5O_{18} fragment) around Eu^{3+} define a slightly distorted square antiprism. Typically, lanthanide-containing polyoxometalate complexes have Na^+, $K^{+,}$ or NH^{4+} counter ions and the resulting salts are

TABLE 19 Thermal Behavior of Praseodymium(III) Alkanoates

Compound	Temperatures (°C)	Reference
$[Pr(C_5H_{11}COO)_3]$	Cr 86 M 109 SmA 142 I	Jongen et al. (2001a)
$[Pr(C_6H_{13}COO)_3]$	Cr 90 M 111 SmA 144 I	Jongen et al. (2001a)
$[Pr(C_7H_{15}COO)_3]$	Cr 90 M 112 SmA 144 I	Jongen et al. (2001a)
$[Pr(C_8H_{17}COO)_3]$	Cr 86 M 95 SmA 135 I	Jongen et al. (2001a)
$[Pr(C_9H_{19}COO)_3]$	Cr 90 SmA 136 I	Jongen et al. (2001a)
$[Pr(C_{10}H_{21}COO)_3]$	Cr 99 SmA 133 I	Jongen et al. (2001a)
$[Pr(C_{11}H_{23}COO)_3]$	Cr 102 SmA 129 I	Jongen et al. (2001a)
$[Pr(C_{12}H_{25}COO)_3]$	Cr 105 SmA 124 I	Jongen et al. (2001a)
$[Pr(C_{13}H_{27}COO)_3]$	Cr 106 SmA 122 I	Jongen et al. (2001a)
$[Pr(C_{14}H_{29}COO)_3]$	Cr 110 SmA 120 I	Jongen et al. (2001a)
$[Pr(C_{15}H_{31}COO)_3]$	Cr 112 SmA 120 I	Jongen et al. (2001a)
$[Pr(C_{16}H_{33}COO)_3]$	Cr 113 SmA 118 I	Jongen et al. (2001a)
$[Pr(C_{17}H_{35}COO)_3]$	Cr 115 SmA 119 I	Jongen et al. (2001a)
$[Pr(C_{18}H_{37}COO)_3]$	Cr 116 SmA 120 I	Jongen et al. (2001a)
$[Pr(C_{19}H_{39}COO)_3]$	Cr 117 SmA 122 I	Jongen et al. (2001a)

Cr, crystalline phase; M, unidentified smectic phase; SmA, smectic A phase; I, isotropic liquid.

water-soluble. *Surfactant encapsulation* is a technique that is often used for obtaining polyoxometalates, which are soluble in organic solvent (Zhang et al., 2005, 2009a). This technique consists in replacing the inorganic counter cations by cationic surfactant molecules. By creating a hydrophobic shell around the polyoxometalate cluster, water molecules are expelled from the direct environment of the POM. This has a beneficial effect on the luminescence properties of lanthanide-containing POMs. Typical hydrophobic counter ions are dimethyldioctadecylammonium (DODA), dodecyltrimethylammonium (DDTA), or hexadecyltrimethylammonium (CTA).

Some of these surfactant-encapsulated polyoxometalate complexes exhibited liquid-crystalline behavior. Faul and coworkers obtained room temperature LCs by complexation of the sandwiched europium-containing polyoxometalate $[Eu(SiW_9Mo_2O_{39})_2]^{13-}$ with a series of cationic surfactants (Zhang et al., 2005). For the quaternary ammonium cations with one long chain a hexagonal (columnar?) phase and possibly a cubic phase were observed, whereas for the quaternary ammonium cation with two long chains

TABLE 20 Thermal behavior of neodymium(III) alkanoates

Compound	Temperatures (°C)	Reference
$[Nd(C_3H_7COO)_3]$	Cr 166 I	Binnemans et al. (2000c)
$[Nd(C_4H_9COO)_3]$	Cr 77 M 95 SmA 113 I	Binnemans et al. (2000c)
$[Nd(C_5H_{11}COO)_3]$	Cr 81 M 94 SmA 128 I	Binnemans et al. (2000c)
$[Nd(C_6H_{13}COO)_3]$	Cr 86 M 101 SmA 133 I	Binnemans et al. (2000c)
$[Nd(C_7H_{15}COO)_3]$	Cr 83 M 92 SmA 126 I	Binnemans et al. (2000c)
$[Nd(C_8H_{17}COO)_3]$	Cr 82 M 90 SmA 127 I	Binnemans et al. (2000c)
$[Nd(C_9H_{19}COO)_3]$	Cr 85 M 94 SmA 125 I	Binnemans et al. (2000c)
$[Nd(C_{10}H_{21}COO)_3]$	Cr 90 M 97 SmA 120 I	Binnemans et al. (2000c)
$[Nd(C_{11}H_{23}COO)_3]$	Cr 91 SmA 117 I	Binnemans et al. (2000c)
$[Nd(C_{12}H_{25}COO)_3]$	Cr 101 SmA 116 I	Binnemans et al. (2000c)
$[Nd(C_{13}H_{27}COO)_3]$	Cr 98 SmA 111 I	Binnemans et al. (2000c)
$[Nd(C_{14}H_{29}COO)_3]$	Cr 108 SmA 114 I	Binnemans et al. (2000c)
$[Nd(C_{15}H_{31}COO)_3]$	Cr 107 I	Binnemans et al. (2000c)
$[Nd(C_{16}H_{33}COO)_3]$	Cr 111 I	Binnemans et al. (2000c)
$[Nd(C_{17}H_{35}COO)_3]$	Cr 112 I	Binnemans et al. (2000c)
$[Nd(C_{18}H_{37}COO)_3]$	Cr 116 I	Binnemans et al. (2000c)
$[Nd(C_{19}H_{39}COO)_3]$	Cr 115 I	Binnemans et al. (2000c)

Cr, crystalline phase; M, unidentified smectic phase; SmA, smectic A phase; I, isotropic liquid.

TABLE 21 Thermal behavior of lanthanide(III) dodecanoates

Compound	Temperatures (°C)	Reference
$[La(C_{11}H_{23}COO)_3]$	Cr 110.0 SmA 160.6 I	Jongen et al. (2001b)
$[Ce(C_{11}H_{23}COO)_3]$	Cr 106 SmA 142 I	Jongen et al. (2001c)
$[Pr(C_{11}H_{23}COO)_3]$	Cr 102 SmA 129 I	Jongen et al. (2001a)
$[Nd(C_{11}H_{23}COO)_3]$	Cr 91 SmA 117 I	Binnemans et al. (2000c)
$[Sm(C_{11}H_{23}COO)_3]$	Cr 91 I	Binnemans et al. (2000d)
$[Eu(C_{11}H_{23}COO)_3]$	Cr 90 I	Binnemans et al. (2000d)

TABLE 21 Thermal behavior of lanthanide(III) dodecanoates—Cont'd

Compound	Temperatures (°C)	Reference
$[Gd(C_{11}H_{23}COO)_3]$	Cr 93 I	Binnemans et al. (2000d)
$[Tb(C_{11}H_{23}COO)_3]$	Cr 90 I	Binnemans et al. (2000d)
$[Dy(C_{11}H_{23}COO)_3]$	Cr 87 I	Binnemans et al. (2000d)
$[Ho(C_{11}H_{23}COO)_3]$	Cr 85 I	Binnemans et al. (2000d)
$[Er(C_{11}H_{23}COO)_3]$	Cr 84 I	Binnemans et al. (2000d)
$[Tm(C_{11}H_{23}COO)_3]$	Cr 83 I	Binnemans et al. (2000d)
$[Yb(C_{11}H_{23}COO)_3]$	Cr 81 I	Binnemans et al. (2000d)
$[Lu(C_{11}H_{23}COO)_3]$	Cr 78 I	Binnemans et al. (2000d)
$[Y(C_{11}H_{23}COO)_3]$	Cr 85 I	Binnemans et al. (2000d)

Cr, crystalline phase; SmA, smectic A phase; I, isotropic liquid.

the corresponding europium(III) complexes shows a lamellar phase. Zhang et al. (2003) prepared highly ordered luminescent films by interaction between the polyoxometalate anion $[Eu(W_{10}O_{36})]^{9-}$ and the hexadecyltrimethylammonium cation. Although the thermal properties of the europium(III) compound was not investigated in detail, the presence of an endothermic transition around 40 °C in the DSC trace could point to a mesophase transition. Stable smectic mesophases were observed for materials based on the surfactant *N*-[12-(4-carboxylphenoxy) dodecyl]-*N*-dodecyl-*N*, *N*-dimethylammonium, which is a benzoic-acid terminated surfactant (Yin et al., 2009). The mesophases (SmA or SmC) are stabilized by intermolecular hydrogen bond interactions between the benzoic acid moieties. Polyoxometalates incorporated in these materials are $[Eu(W_{10}O_{36})]^{9-}$, $[Eu(PW_{11}O_{39})_2]^{11-}$ and $[Eu(SiW_{11}O_{39})_2]^{13-}$. $[Eu(BW_{11}O_{39})_2]^{15-}$ was combined with cationic surfactants containing biphenyl groups in their chains (Li et al., 2008a). All the complexes formed a smectic C and a smectic A phase. Thermotropic mesophases were observed for combinations of the europium-exchanged derivative of a Pressler-type polyoxometalate, $[EuP_5W_{30}O_{110}]^{12-}$, in combination with hydrophobic cations such as dihexadecyldimethylammonium, dioctadecyldimethylammonium, and trioctadecylmethylammonium (Zhang et al., 2009b). The complex anion has the shape of a donut. The Eu^{3+} is embedded inside the central cavity formed by five P_6WO_{22} units arranged in a crown-like structure and one water molecule is coordinated to this Eu^{3+} ion. The $[EuP_5W_{30}O_{110}]^{12-}$ anion shows a strong luminescence and displays electrochromism (i.e., the color of solutions turns blue upon reduction). The identity and the structure of the mesophase were not determined. A liquid-crystalline terbium-containing

surfactant-encapsulated complex was obtained by combining the $[Tb(SiW_{11}O_{39})_2]^{13-}$ anion with an azobenzene-containing cationic surfactant (Li et al., 2005b). No mesophase was observed for the corresponding complex with dioctadecyldimethylammonium counter cations.

12. MISCELLANEOUS THERMOTROPIC LANTHANIDOMESOGENS

In this section, lanthanidomesogens that do not fit into the classes discussed in the previous sections are discussed. The complex $[C_{12}mim]_3[DyBr_6]$, where $C_{12}mim$ stands for 1-dodecyl-3-methylimidazolium (**L39**), exhibits a smectic phase between −20 and 115 °C (Getsis et al., 2009). The crystal structure of the corresponding acetonitrile solvate $[C_{12}mim]_3[DyBr_6]\cdot 2CH_3CN$ consists of double layers of hydrophobic and hydrophilic parts. The hydrophobic part is formed by the interdigitated dodecyl chains of the 1-dodecyl-3-methylimidazolium cations, whereas the hydrophilic part is formed by the charged head groups of the imidazolium cations and by the $[DyBr_6]^{3-}$ anions. The complex $[C_{12}mim]_3[DyBr_6]$ shows either bright blue-whitish or orange-yellow photoluminescence, depending on the excitation wavelength. It is mentioned that the low viscous mesophase formed by this compounds corresponds to an external magnetic field, but more details are lacking. The complex $[C_{12}mim]_4[EuBr_6]Br$ form a smectic A mesophase between −3 and 98 °C (Getsis et al., 2010). This complex can be considered as a double salt of $[C_{12}mim]_3[EuBr_6]$ and $[C_{12}mim]Br$. The liquid-crystalline samples have a strong tendency for homeotropic alignment between two microscope glass slides. This behavior is typical for ionic LCs. $[C_{12}mim]_4[EuBr_6]Br$ is strongly luminescent at 77 K, showing a red emission with a luminescence decay of no less than 2.6 ms. Besides $[C_{12}mim]_3[TbBr_6]$, also $[C_{12}mpyr]_3[TbBr_6]$, where $C_{12}mpyr$ is *N*-dodecyl-*N*-methylpyrrolidinium (**L40**), shows a smectic mesophase (Getsis and Mudring, 2011). These room-temperature ionic LCs are highly hygroscopic. Very similar mesophases were observed by doping $TbBr_3$ into $[C_{12}mim]Br$ or $[C_{12}mpyr]Br$. The crystal structure of $[C_{12}mim]_3[TbBr_6]\cdot 2CH_3CN$ could be determined. 1,3-Dioctadecylurea $[CO(NHC_{18}H_{37})_2]$ (**L41**) forms with terbium(III) chloride a complex with formula $[CO(NHC_{18}H_{37})_2]_{0.57}[TbCl_3]_{0.43}$ (Kanazawa, 2009). The terbium complex is liquid-crystalline between 109 and 179 °C, with a rectangular columnar phase at low temperature and a hexagonal columnar phase at higher temperatures.

N-(2-hydroxy-4-alkoxybenzaldehydeimino)-2-benzamidoethanamide (habbe, **L42**) forms with lanthanide ions complexes of the type $[R(habbe)_2Cl_2]Cl\cdot 2H_2O$ (R = La, Pr, Nd; Kumar and Pisipati, 2000). The ligands exhibit a smectic A and a smectic B phase. The corresponding lanthanide complexes have been reported to exhibit a smectic C and a nematic phase. However, it turned out that the synthesis of the lanthanide complexes is difficult to reproduce. Following the exact same experimental procedure as described by Kumar and Pisipati (2000), Van Deun et al. (2003b) were not able to obtain any

lanthanide complex of the starting habbe ligands. Instead, rearrangement of these ligands was observed, giving symmetrical azines (**L43**) which showed nematic and/or smectic A phases. A synthetic pathway was proposed, in which the rare-earth ion promotes the decomposition of the habbe ligand into the symmetrical azine. The structures of molecules **L39–L43** is shown in Fig. 57.

Lanthanide complexes of a steroid-substituted benzocrown ether have been synthesized (Binnemans and Gündogan, 2002). All the complexes had a 1:1 metal-to-ligand ratio. The ligand 4′-[(cholesteryloxy)carbonyl]-benzo-15-crown-5**L44** exhibited a monotropic cholesteric phase (Fig. 58). The lanthanide(III) complexes with nitrate counter ions formed a highly viscous mesophase, which decomposed at the clearing point. The transition temperatures changed as a function of the lanthanide ion: the mesophase stability range became narrower when the size of the lanthanide ion decreased. The corresponding lanthanide complexes with dodecylsulfate (DOS) counter-ions did not form a mesophase. Bünzli and coworkers observed a mesophase for europium(III) and terbium(III) complexes of a diaza-18-crown-6 with mesogenic pendant arms (Suarez et al., 2003). Although the mesophase was not

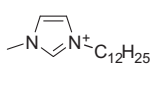

L39

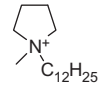

L40

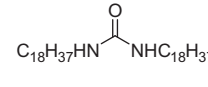

L41

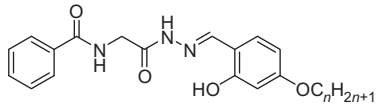

L42

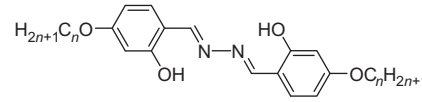

L43

FIGURE 57 Structures of 1-dodecyl-3-methylimidazolium C_{12}mim (**L39**), *N*-dodecyl-*N*-C_{12}mpyr methylpyrrolidinium (**L40**), 1,3-dioctadecylurea (**L41**), *N*-(2-hydroxy-4-alkoxybenzaldehydeimino)-2-benzamidoethanamides (habbe, **L42**), and azines (**L43**).

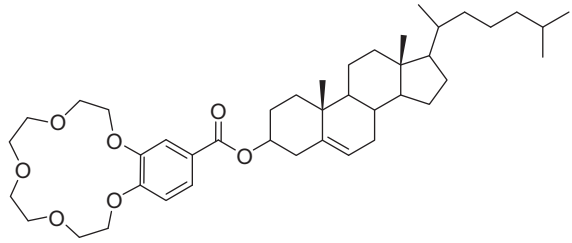

L44

FIGURE 58 4′-[(Cholesteryloxy)carbonyl]-benzo-15-crown-5 (**L44**).

identified unambiguously, it was very likely a hexagonal columnar phase. The authors were able to detect the crystal-to-mesophase transition of the europium(III) complex by temperature-dependent luminescence measurements. In a follow-up study the authors made complexes of different tetracatenar or hexacatenar diaza-18-crown-6 ligands **L45**–**L48** with lanthanide(III) nitrates, chlorides, and triflates (Suarez et al., 2005; Fig. 59). The complexes exhibited hexagonal columnar mesophases. The widest mesophase range was found for the nitrate complexes. It should be noted that the free ligands are not liquid-crystalline. The introduction of the lanthanide ion in the macrocyclic cavity leads to rigidification of the macrocyclic system and favors the formation of a mesophase.

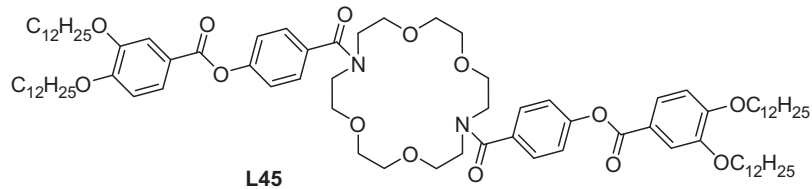

L45

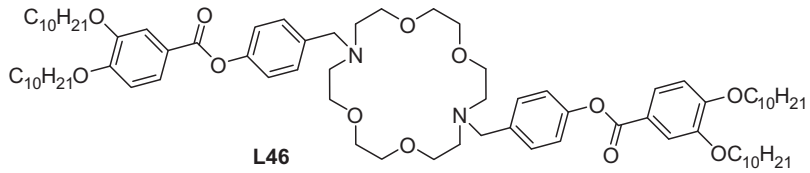

L46

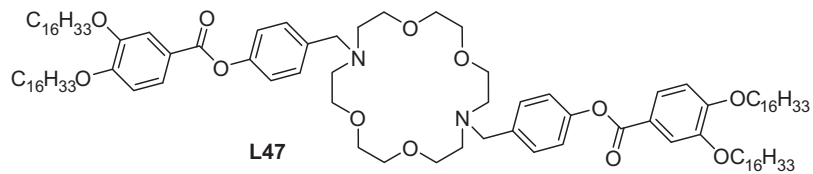

L47

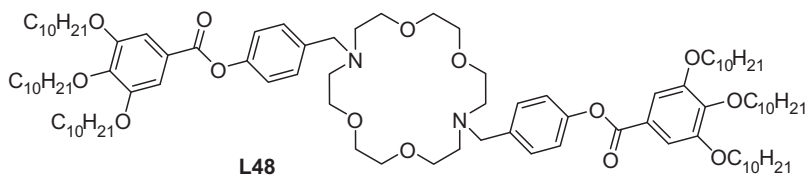

L48

FIGURE 59 Azacrown ligands **L45**–**L48**.

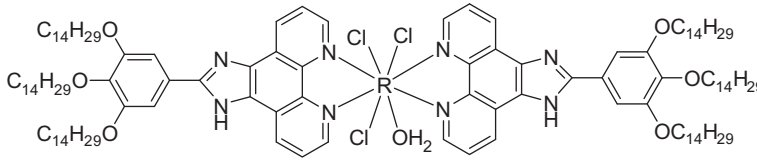

FIGURE 60 Monohydrated complexes of lanthanide(III) chlorides with 2-aryl-substituted imidazo[4,5-f]-1,10-phenanthroline ligands.

2-Aryl-substituted imidazo[4,5-f]-1,10-phenanthrolines with long alkyl chains on the aryl group form monohydrated complexes with lanthanide(III) chlorides (Cardinaels et al., 2008; Fig. 60). The metal-to-ligand ratio in these complexes is 1:2. Although the complexes of ligands with only one or two alkyl chains on the aryl group were not liquid-crystalline, some of the complexes of a ligand with three tetradecyloxy chains were mesomorphic. The complexes of the light lanthanides (R = La, Pr, Nd, Sm, Eu) formed a cubic mesophase, while the complexes of the heavy lanthanides (R = Gd, Tb, Dy, Ho) did not show any thermotropic mesomorphism. On the basis of XRD experiments, it was concluded that the most probable space group for the cubic mesophase is $Pm\bar{3}n$. The structure of this cubic phase is intermediate between micellar and bicontinuous topologies, with an infinite 3D interlocking network of mutually perpendicular, evenly pinched columns, compatible with the symmetry of the space group (three pairs of column sites evenly spaced along the bisectors of the cubic cell faces and two interstitial sites at the centers and corners of the cubic lattice). The 2-aryl-substituted imidazo [4,5-f]-1,10-phenanthroline ligand was modified by attaching one, two, or three cyanobiphenyl groups at the end of the long alkyl chains (Cardinaels et al., 2005a; Fig. 61, ligands **L49–L51**). The basic idea behind this ligand design was to decouple the mesophase-inducing group and the coordination group via a long flexible alkyl chain. This concept is different from other studies on metallomesogens, where the key idea to obtain high coordination number metallomesogens is to increase the number of long alkyl chains attached to the central metal core. Whereas metallomesogens with a large number of long alkyl chains often form columnar mesophases, the compounds with decoupled mesogenic and coordinating groups can form more disordered mesophases. This is illustrated by the fact that the complexes formed by adduct formation of these ligands with lanthanide tris 2-thenoyltrifluoroacetonate complexes $R(tta)_3$ all exhibited a nematic mesophase (Table 22). However, because of the large size of the metal complexes, the nematic phase was rather viscous in comparison of nematic phases formed by small organic molecules and the applicability of these complexes to be aligned by external electric or magnetic fields is limited. The compounds were strongly luminescent in the solid phase and as a solution in the LC host

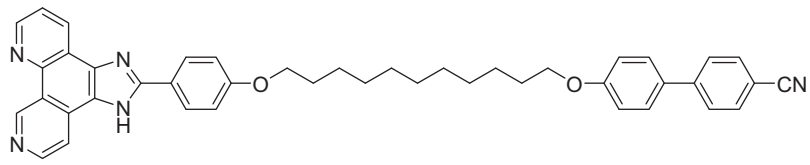

L49

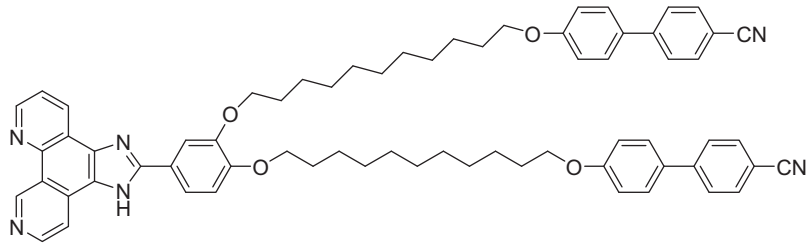

L50

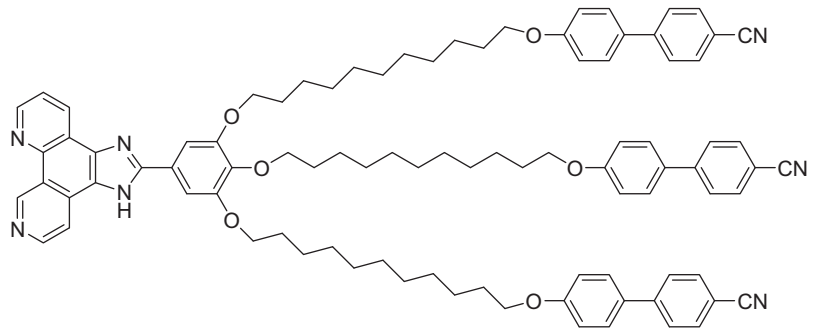

L51

FIGURE 61 2-Aryl-substituted imidazo[4,5-f]-1,10-phenanthroline ligands bearing terminal cyanobiphenyl groups.

matrix 4-pentyl-4′-cyanobiphenyl (5CB). The importance of this work lies in the fact that these complexes represent the first reported examples of nematogenic lanthanidomesogens.

Co-condensates between metallic samarium and 4-pentyl-4′-cyanobiphenyl (5CB) in the solid phase have been obtained via joint atomic/molecular beam deposition on a cooled calcium fluoride surface at liquid nitrogen temperature (Shabatina et al., 2000, 2001, 2005). The film samples have been studied by IR and UV/VIS spectroscopy in the temperature range from 80 to 300 K. Two types of complexes were detected, one complex with a metal to ligand

TABLE 22 Transition Temperatures and Mesophases of the Lanthanide tris 2-Thenoyltrifluoroacetylacetonate Complexes of Substituted Imidazo[4,5-f]-1,10-Phenanthroline Ligands with Appending Cyanobiphenyl Groups

Compound	Transition temperatures (°C)
[Nd(tta)$_3$(**L49**)]	Cr 86 N 138 I
[Eu(tta)$_3$(**L49**)]	Cr 89 N 138 I
[Y(tta)$_3$(**L50**)]	Cr 89 N 127 I
[La(tta)$_3$(**L50**)]	Cr 84 N 124 I
[Nd(tta)$_3$(**L50**)]	Cr 85 N 124 I
[Sm(tta)$_3$(**L50**)]	Cr 86 N 124 I
[Eu(tta)$_3$(**L50**)]	Cr 86 N 125 I
[Er(tta)$_3$(**L50**)]	Cr 90 N 127 I
[Yb(tta)$_3$(**L50**)]	Cr 92 N 127 I
[Eu(tta)$_3$(**L51**)]	Cr 83 N 92 I

Cr, crystalline or semi-crystalline phase; N, nematic phase; I, isotropic liquid.

ratio of 1:1, [Sm$_2$(5CB)$_2$], and another complex with a 1:2 ratio, [Sm(5CB)$_2$]. The solid phase transformation of the 1:2 complex to the 1:1 complex took place when the compound was heated to 183–200 K. The complexes are samarium π complexes, in which a samarium atom interacts with the aromatic ring of 5CB. Similar complexes were formed between metallic europium and 5CB (Vlasov et al., 2005).

13. LYOTROPIC LANTHANIDOMESOGENS

The first examples of lanthanidomesogens forming lyomesophases were the lanthanide(III) alkylsulfates, and especially the lanthanide(III) dodecylsulfates, R(DOS)$_3$ (Galyametdinov et al., 2001a). These compounds were known earlier, because they were being used as starting materials for the synthesis of liquid-crystalline Schiff's base complexes of the lanthanides with DOS counter ions (see Section 4; Binnemans et al., 1998). Lyotropic mesophases were observed for lanthanide tris dodecylsulfates, R($C_{12}H_{25}OSO_3$)$_3$ (R = Y, La, Ce-Lu, except Pm) in the presence of ethylene glycol or water (or mixtures thereof) as the solvent (Galyametdinov et al., 2001a). In ethylene glycol, a normal hexagonal phase and a cubic phase could be detected, whereas in water a normal hexagonal phase and a lamellar phase were found. In water, the mesophases could only be observed after heating the DOS complexes to

85 °C. Upon cooling, the lyotropic mesophases remained present, even at room temperature. The reason why the mesophases could only be observed after heating the system to 85 °C, was attributed to the slow dissolution rate of the $R(DOS)_3$ compounds. That the limiting factor for observing a lyotropic mesophase in water at room temperature is a kinetic one, was also evident from the fact that when contact between $R(DOS)_3$ and water was long enough (> 12 h) at a temperature just above room temperature, lyotropic mesophases could be observed without a preceding heating step. This study was extended to mixtures of ethylene glycol and water (Jongen and Binnemans, 2003). For pure ethylene glycol and mixtures of ethylene glycol and water three different mesophases were observed (i.e., a lamellar, a cubic and a hexagonal phase), whereas when water was used as solvent no cubic phase was formed. The size of the lanthanide ion had no influence on the mesomorphism of lanthanide (III) dodecylsulfates. The smaller the lanthanide ion, the lower the solubility, but the phase behavior did not change through the lanthanide series. The lyomesomorphism of lanthanum(III) dodecylsulfate in ethylene glycol was investigated by POM by Zakharova et al. (2002). A hexagonal mesophase was found. The widest mesophase range was observed for a mixture consisting of 65 wt.% of lanthanum(III) dodecylsulfate and 35 wt.% of ethylene glycol.

A substantial amount of work on lyotropic metallomesogens has been carried out by Selivanova et al. (2005, 2006). They developed several lyotropic systems based on the combination of a nonionic surfactant and a hydrated lanthanide salt, with water or with water-decanol mixtures as solvents. Decaethylene glycol monododecyl ether ($C_{12}EO_{10}$), $C_{12}H_{25}O(CH_2CH_2O)_{10}H$, and $La(NO_3)_3{\cdot}6H_2O$ (1:2 molar ratio) formed a hexagonal lyotropic mesophase in the presence of 10 wt.% of water (Selivanova et al., 2008). These mesophase existed in the temperature range from 4 to 97 °C. The clearing transition was not sharp: it started at 84 °C and was completed at 97 °C. The ternary phase diagram of $C_{12}EO_{10}$:$La(NO_3)_3{\cdot}6H_2O$/water/decanol has been constructed (Selivanova et al., 2010a). The formation of lyomesophases was observed in the concentration ranges from 10 to 70 wt.% of $C_{12}EO_{10}$:$La(NO_3)_3{\cdot}6H_2O$, from 20 to 75 wt.% of water, and from 0 to 60 wt.% of dodecanol. The addition of dodecanol considerably expanded the concentration range over which the mesophases were formed, and caused both hexagonal and lamellar phases to be formed. This is in contrast with the binary system $C_{12}EO_{10}$:$La(NO_3)_3{\cdot}6H_2O$/water in which only the hexagonal phase occurs. However, addition of dodecanol also lowers the highest temperature at which the lyomesophase can occur. The mesophase behavior of the $C_{12}EO_{10}$:$La(NO_3)_3{\cdot}6H_2O$/water can be modified by addition of the polymer poly(ethyleneime) (Zakharova et al., 2007). A stable mesophase was observed within the $La(NO_3)_3{\cdot}6H_2O$ concentration was between 3.2 and 40 wt.%, whereas at higher salt concentrations, the samples crystallized out.

The zwitterionic surfactant *N*,*N*-dimethyldodecylamine oxide ($C_{12}DMAO$) form lyotropic mesophases with $La(NO_3)_3{\cdot}6H_2O$ in water-decanol mixtures (Selivanova et al., 2010b). Different mesophases (hexagonal, lamellar, nematic) are formed depending on the molar ratio between the surfactant

and the lanthanum salt. The surfactant/lanthanum molar ratio was varied between 1 and 7. Whereas the lamellar mesophase was observed for all molar ratios studied, the hexagonal phase occurred for surfactant/lanthanum ratios 1:1 and 4:1, in regions of the phase diagram with a high complex concentration (50–60 wt.%) and high water concentration (35–49 wt.%). The nematic phase occurs for the following composition: 45 wt.% of C_{12}DMAO/lanthanum(III) complex, 50 wt.% of water and 5 wt.% of dodecanol. The nematic phase is formed for the following surfactant/lanthanum ratios: 2:1, 3:1, 4:1, and 7:1. Of interest is the fact that the nematic phase is already observed at temperatures as low as 5 °C. The clearing point was found to increase with increasing surfactant concentration of the system. Before the system became isotropic, a two-phase system with coexistence of the nematic and isotropic phase was observed. This work is of importance because it gives the first examples of nematic lyotropic phases formed by lanthanidomesogens.

Lyotropic mesophases were observed for several lanthanide polyoxometalate surfactant complexes in chloroform at room temperature. Zhang et al. (2005) reported pseudofocal conic fan-shaped textures for the $[Eu(SiW_9Mo_2O_{39})_2]^{13-}$ complex with dihexadecyldimethylammonium counter ions in chloroform. $[EuP_5W_{30}O_{110}]^{12-}$, in combination with hydrophobic cations such as dihexadecyldimethylammonium, dioctadecyldimethylammonium, and trioctadecylmethylammonium, forms unidentified lyotropic mesophases in chloroform (Zhang et al., 2009b). Lanthanide(III) phytanates form a hexagonal columnar phase in the presence of water (Conn et al., 2010). Chelating amphiphiles consisting of ethylene diamine tetraacetic acid (EDTA) with one or two phthanyl chains exhibit lyotropic mesomorphism in water (Moghaddam et al., 2010). However, no evidence for liquid-crystallinity was observed for the corresponding gadolinium(III) complexes dissolved in water. Lanthanide(III) oleates (R = La, Ce, Nd, Sm, Eu, Gd, Tb, and Dy) exhibit lamellar phases in the presence of an excess of water (Liu et al., 2009). The lanthanide(III) oleates can be dispersed in water to form nonswelling lamellar submicrometer particles. Gadolinium(III) oleate was incorporated in the inverse bicontinuous cubic phase formed by Myverol (Liu et al., 2010). Myverol is a lipid system containing 82% of monoacylglycerols and which displays a rich lyomesomorphism, including an inverse hexagonal phase, a lamellar phase and an inverse bicontinuous cubic phase. At gadolinium(III) oleate concentrations below 1 wt.%, phase separation occurred with the formation of a lamellar phase rich in gadolinium(III) oleate and a cubic phase.

14. PHYSICAL PROPERTIES

14.1. Luminescence

Pioneering work in the field of luminescence by lanthanidomesogens in the liquid-crystal state has been done by Bünzli and coworkers. In a seminal paper, they monitored the luminescence intensity and the excited state

lifetime of a solvated $Eu(NO_3)_3$ complex of a 1,7-diaza-18-crown ether with mesogenic pendant arms (ligand **L46**, see Fig. 59) as a function of the temperature, with the aim to detect phase transitions (Suarez et al., 2003). The integrated intensities of the $^5D_0 \rightarrow {}^7F_2$ transition I_{obs} and the Eu($^5D_0$) lifetime τ_{obs} were found to decrease with increasing temperatures due to more efficient nonradiative relaxation of the excited state at higher temperatures. The $\ln(\tau_{obs}/\tau_{295K})$ versus $1/T$ and $\ln(I_{obs}/I_{295K})$ versus $1/T$ curves showed upon heating a sigmoidal shape, with a marked variation at the melting point. Therefore, the luminescence measurements allowed to accurately detect the transition of the crystalline state to the hexagonal columnar phase during the first heating process. The corresponding $\ln(I_{obs}/I_{295K})$ versus $1/T$ curve cooling curve was quite monotonic, whereas the $\ln(\tau_{obs}/\tau_{295K})$ versus $1/T$ cooling curve closely followed the variation observed during heating. By monitoring the integrated intensity of the $^5D_4 \rightarrow {}^7F_5$ transition of Tb^{3+}, it was possible to determine the crystal-to-mesophase transition in a terbium-containing metallomesogen (Suarez et al., 2004; Terazzi et al., 2005). Further luminescence studies on $R(NO_3)_3$ complexes of 2,6-bis(1-ethylbenzimidazol-2-yl)pyridine derivatives synthesized by Piguet and coworkers showed that the transition of a crystalline phase to a cubic mesophase could be detected by measurement of the luminescence properties during the first heating process (Terazzi et al., 2006a). However, the vitrification of the cubic mesophase upon cooling could not be observed. This shows that this luminescence technique cannot be applied to the detection of glass transitions.

Yang et al. (2006) reported on low-melting lanthanidomesogens consisting of Lewis-base adducts of a nonmesomorphic salicylaldimine Schiff's base ligand L and tris(2-2-thenoyltrifluoroacetonato)lanthanide(III) or tris(benzoyltrifluoroacetonate) lanthanide(III) complexes, $[R(tta)_3L_2]$ or $[R(bta)_3L_2]$. These compounds form a smectic A phase at room temperature. The luminescence spectra of the Eu(III), Sm(III), Nd(III) and Er(III) complexes have been measured in the mesophase (Fig. 62). Of interest is the fact that near-infrared emission by Nd(III) and Er(III) could be observed. Plots of the luminescence decay time of the $^5D_0$ level of $[Eu(tta)_3L_2]$ or the $^4G_{5/2}$ level of $[Sm(tta)_3L_2]$ as a function of the temperature show a gradual decrease of the luminescence lifetime with increasing temperatures. A distinct lowering could be observed in these curves at the SmA → I transition (Fig. 63). The intrinsic quantum yield of the complexes $[Eu(tta)_3L_2]$ and $[Eu(bta)_3L_2]$ have been determined by photoacoustic methods (Li et al., 2008b; Yang et al., 2008a,b). Although glass transitions of the vitrified mesophase could not be detected by luminescence measurements, the photoacoustic spectra clearly showed this transition. Yin et al. (2009) observed luminescence in the mesophase for benzoic-acid-terminated surfactant complexes of the europium-containing polyoxometalates $[Eu(W_{10}O_{36})]^{9-}$, $[Eu(PW_{11}O_{39})_2]^{11-}$, and $[Eu(SiW_{11}O_{39})_2]^{13-}$. A review of the luminescence of metallomesogens (including lanthanidomesogens) in the liquid-crystal state was published by Binnemans (2009).

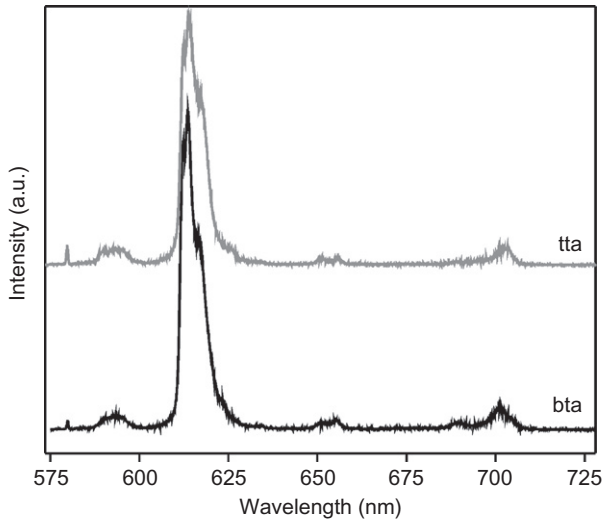

FIGURE 62 Luminescence spectra of $[Eu(tta)_3\mathbf{L}_2]$ (gray curve) and $[Eu(bta)_3\,\mathbf{L}_2\,]$ (black curve) as a thin film in the mesophase at 25 °C. The excitation wavelength was 370 nm. All transitions start from the $^5D_0$ level and end at the different J levels of the ^7F term ($J = 0$–4 in this spectrum). *Adapted from Yang et al. (2006).*

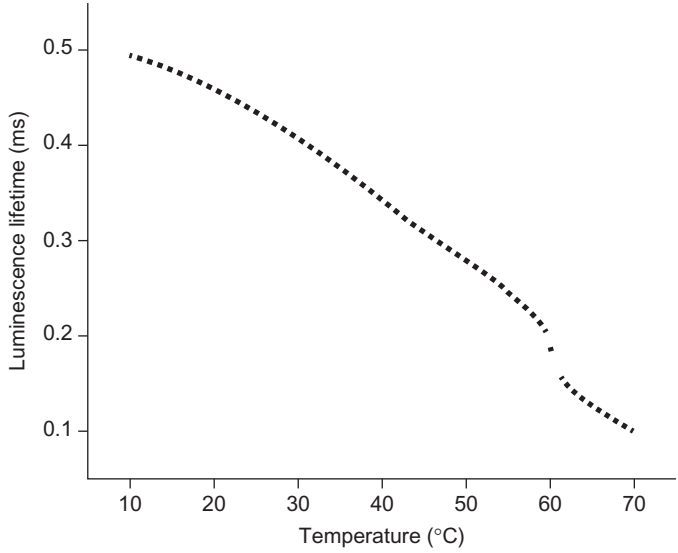

FIGURE 63 Luminescence decay time of the $^5D_0$ level of the $[Eu(tta)_3\mathbf{L}_2]$complex as a function of the temperature. The luminescence was monitored at 613 nm ($^5D_0 \rightarrow {}^7F_2$ line) and the excitation wavelength was 370 nm. The measurements were made during cooling of the sample. The transition SmA↔I (clearing point) can be observed as a jump in the curve at about 60 °C. *Adapted from Yang et al. (2006).*

Galyametdinov and coworkers prepared lanthanidomesogens that exhibit smectic A and nematic phases (Galyametdinov et al., 2008). The ligand was a rather unusual β-diketone with a cyclohexyl ring (Fig. 44, see also Section 6). When a thin film of the corresponding europium(III) complex in the nematic phase was supercooled to a glass phase in a liquid-crystal cell with alignment layers for planar alignment, polarized luminescence could be observed for the aligned samples (Fig. 64). The lanthanide complexes were also well soluble in nematic liquid-crystal mixtures. The polarization effects were observable as differences in the intensities of crystal-field transitions for the two mutually perpendicular polarization directions. The energy transfer in mesogenic europium(III) β-diketonate complexes with 5,5′-diheptadecyl-2,2′-bipyridine as coligand was studied by Lapaev et al. (2008, 2009).

Another approach to obtain luminescent lanthanide-containing LCs is by dissolving a luminescent lanthanide complex in a suitable liquid-crystal host matrix (*guest–host approach*). The advantage of this method is that the luminescence and mesomorphic properties can be optimized independently. This allows easier access to nematic lanthanide-containing LC mixtures. However, one is often facing the poor solubility of the molecular lanthanide complexes in the liquid-crystalline host matrix. The guest–host concept involving luminescent lanthanide complexes was first applied by Yu and Labes (1977) who doped the nematic LC 4-*n*-pentyl-4′-cyanobiphenyl (5CB) with europium(III) 2-thenoyltrifluoroacetonate trihydrate, $Eu(tta)_3 \cdot 3H_2O$. The LC

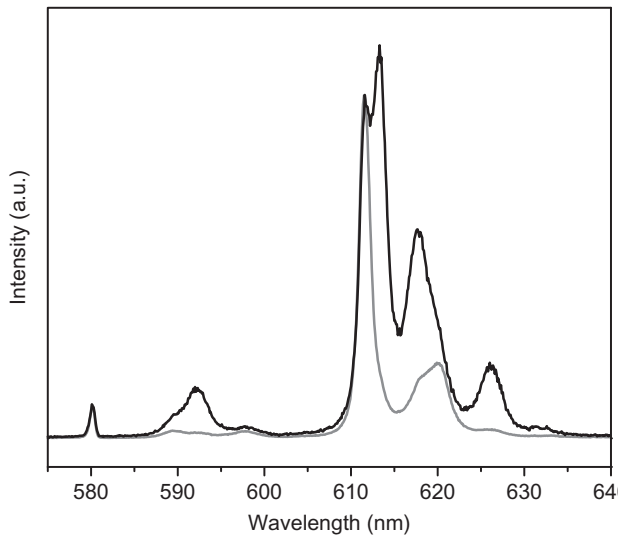

FIGURE 64 Polarization effects in the room-temperature luminescence spectra of an aligned supercooled thin film of the europium(III) complex of the type shown in Fig. 44. The polarizer is either parallel (gray line) or perpendicular (black line) to the alignment layers in the liquid-crystal cell. *Adapted from Galyametdinov et al. (2008).*

mixture gave an intense red photoluminescence with an emission maximum at 612 nm, when excited with UV light. Doping the LC mixture with different chiral additives such as cholesteryl nonanoate or cholesteryl chloride, allowed obtaining luminescent chiral LC mixtures. The chiral LC mixtures in a cell of indium-tin-oxide coated glasses and mylar spacers experienced a cholesteric to nematic phase transition upon application of an electric potential. The homeotropically aligned nematic phase scatters much less light than the cholesteric phase and can absorb the excitation light less efficiently. As a result the luminescence intensity of the europium(III) complex in the cholesteric LC phase is much higher than in the nematic phase. Contrast ratios as high as 9:1 could be observed for the cholesteric phase (off state) in comparison with the nematic phase (on state). The off-on response time was about 100 ms (Labes, 1979). The actual values of the contrast ratios were dependent on the temperature, the cell thickness, the pitch of the cholesteric phase and the concentration of the europium complex. However, the polarization of the luminescence was found to be very small. $Tb(tta)_3 \cdot 3H_2O$ did not show luminescence in the same LC mixture, but the corresponding complex of benzoylmethane did exhibit a weak green luminescence (Labes, 1979). Larrabee (1976) reported luminescence for a europium tetrakis β-diketonate complex dissolved in a commercial nematic LC mixture with a nematic phase range between 26 and 88 °C. Zolin et al. (1980) studied the luminescence of different types of europium(III) complexes dissolved in mixtures of 5CB and cholesteryl nonanoate, in pure cholesteryl nonanoate, as well as in commercial nematic LC mixtures. They authors also investigated the luminescence properties of suspensions of the europium phosphor $Y_2OS_2:Eu^{3+}$ in these LC mixtures. The differences in the luminescence intensities in the different liquid mixtures were attributed to changes in the light scattering: the stronger the light scattering by the LC, the more intense the luminescence. Strong light scattering by the LC can be considered as an increase of the effective optical path length for the excitation radiation. This leads to a stronger light absorption and thus to a brighter luminescence. A 50–100% decrease of the luminescence decay times of the europium chelate complexes was observed for the solid-to-nematic transition and for the nematic-to-isotropic transition. The decrease of the decay times were explained by a more efficient quenching of the excited states in solvents with a lower viscosity. Small changes were observed for the relative intensities of crystal-field transitions for the same complex dissolved in different LC host matrices. These differences were explained by orientational effects of the chelate molecules in the LC solvent. Binnemans and Moors (2002) showed by high-resolution luminescence spectroscopy that well-resolved crystal-field fine structures could be observed for $[Eu(tta)_3(phen)]$ doped in the liquid-crystal hosts *N*-(4-methyloxybenzylidene)-4-butylaniline (MBBA) and 5CB (Fig. 65). The spectra are more reminiscent to what is observed for europium(III) ions doped in crystalline hosts rather than europium(III) complexes dissolved in organic solvents (Fig. 66).

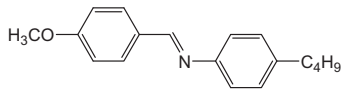

MBBA

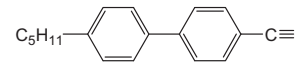

5CB

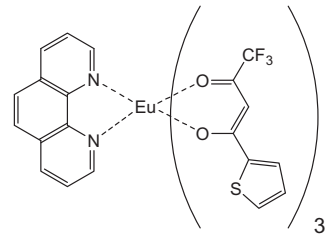

[Eu(tta)$_3$(phen)]

FIGURE 65 Structures of the nematic liquid-crystal host matrices MBBA and 5CB, and structure of the europium(III) complex [Eu(tta)$_3$(phen)].

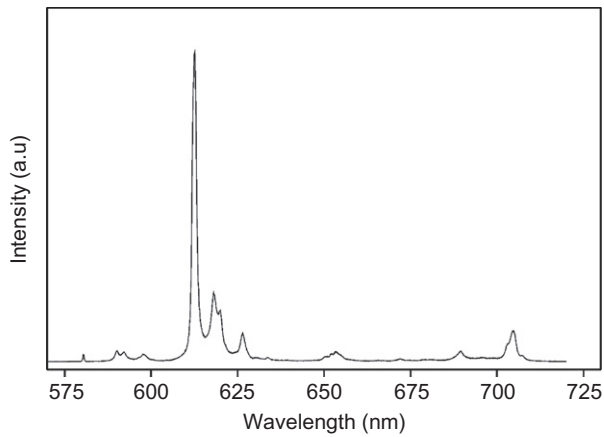

FIGURE 66 Room temperature luminescence spectrum of [Eu(TTA)$_3$(phen)] in the nematic liquid-crystal host MBBA (doping concentration: 4 wt.%. $\lambda_{exc} = 396$ nm). *Adapted from Binnemans and Moors (2002).*

Binnemans and coworkers were the first to observe near-infrared luminescence from lanthanide-doped LC mixtures (Van Deun et al., 2003a). They studied the spectroscopic properties of the lanthanide(III) β-diketonate complexes [R(dbm)$_3$(phen)], where R = Nd, Er, Yb, and dbm is dibenzoylmethane, in the LC MBBA. By incorporation of an erbium(III)-doped nematic LC ($ErCl_3$ dissolved in E7) in the pores of microporous silicon, narrowing of the erbium(III) emission band in the near-infrared was observed

(Weiss et al., 2007). Luminescent optically active LCs were obtained by doping $Eu(tta)_3 \cdot 3H_2O$ into a mixture of cholesteryl nonanoate, cholesteryl tetradecanoate and the ternary LC mixture ZLI 1083 from Merck (Boyaval et al., 1999, 2001). To improve the solubility of lanthanide complexes in chiral LC mixtures, chiral dopants with coordinating groups have been developed (Hapiot, 2006). Up to 6 mol.% of $R(tta)_3$ (R = Nd, Sm, Eu) could be dissolved in the LC matrix. Long alkyl chains on the dopant led to a higher dopant solubility in the LC solvent. Driesen et al. (2007) constructed a switchable near-infrared emitting LC cell. The authors doped the lanthanide complexes [Nd $(tta)_3$(phen)] and [Yb$(tta)_3$(phen)] into the chiral nematic liquid-crystal mixture of E7 and cholesteryl nonanoate. However, the contrast ratios were low. The photoluminescence intensity of europium(III) and terbium(III) complexes dissolved in nematic LC 4-(isothiocyanotophenyl)-1-(*trans*-4-hexyl) cyclohexane (6CHBT) strongly depends on the strength of the applied electric field (Palewska et al., 2007). This effect was tentatively assigned to a complex dipolar orientational mechanism in the LC matrix. Driesen et al. (2009) investigated the luminescence spectra of different europium(III) complexes dissolved in the LC 4′-pentyl-4-cyanobiphenyl (5CB). Upon alignment of the europium(III)-doped nematic liquid-crystal host in a liquid-crystal cell with alignment layers, polarization effects were observed in the emission spectra. These polarization effects were visible as differences in the relative intensities of the crystal-field components of the transitions. Although the europium(III) complexes do not need to be liquid-crystalline themselves, some structural anisotropy (rodlike shape) seems to required for good alignment in the liquid-crystal host and for generation of linearly polarized light. No polarization effects were observed for unaligned bulk samples.

Driesen and Binnemans (2004) prepared glass-dispersed LC films doped with a europium(III) β-diketonate complex [Eu$(dbm)_3$(gly)], where dbm is dibenzoylmethanate and gly is monoglyme (1,2-dimethoxyethane). The films consisted of tiny droplets of the LC 5CB in a silica-titania glass matrix, and were prepared via a sol-gel process. Below the clearing point, the films are strongly scattering light. When the film is heated above the clearing point, the refractive index of the isotropic liquid becomes similar to that of the glass and hardly any light scattering occurs. The luminescence intensity of the film was measured as a function of temperature. A sharp decrease in luminescence intensity was observed for the transition from the nematic phase to the isotropic phase (Fig. 67). This decrease in luminescence intensity at the clearing point was attributed to weaker light scattering and thus less efficient use of the excitation light in the isotropic state. Upon cooling of the sample an increase in light intensity was observed at the clearing point.

The LC host matrix is not restricted to nematic LCs. Bünzli and coworkers dissolved different europium(III) salts in the smectogenic ionic LC 1-dodecyl-3-methylimidazolium chloride [C_{12}mim]Cl, which exhibits a smectic A phase between −2.8 and 104.4 °C (Guillet et al., 2004). It was observed that

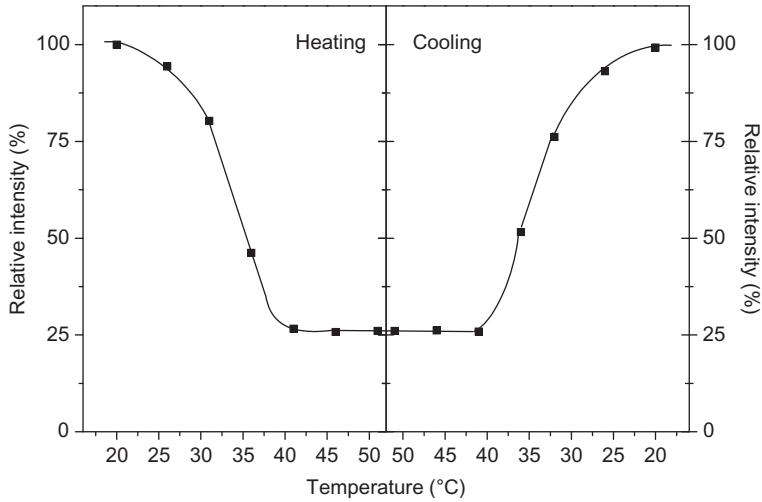

FIGURE 67 Relative intensity change of the $^5D_0 \rightarrow {}^7F_2$ transition upon heating and cooling of a glass-dispersed liquid crystal film doped with the europium(III) complex [Eu(dbm)$_3$(gly)]. *Adapted from Driesen and Binnemans (2004).*

concentrations of europium(III) salts as high as 10 mol.% do not appreciable alter the liquid-crystalline behavior of the host matrix. Interestingly, the emission color of the europium(III)-containing LC mixture could be tuned from blue (emission color of the host matrix) to red (emission color of Eu^{3+}), depending on the excitation wavelength and the counter ion of europium (III). Intense near-infrared emission has been observed by doping the β-diketonate complexes [R(tta)$_3$(phen)] (R = Nd, Er, Yb) in this ionic LC host (Puntus et al., 2005). By doping the lanthanide bromides $EuBr_2$, $SmBr_3$, $TbBr_3$, and $DyBr_3$ in the ionic LC 1-dodecyl-3-methylimidazolium bromide [C_{12}mim]Br, luminescent ionic LCs could be obtained (Getsis and Mudring, 2010). [C_{12}mim]Br forms a smectic A phase between 42 and 100 °C. The doping concentrations of about 1 mol.% did not strongly influence the mesophase behavior of [C_{12}mim]Br. However, it was found that the mesophase of [C_{12}mim]Br is stabilized by addition of larger amounts of the lanthanide bromides to such an extent that the samples stayed liquid-crystalline to temperatures below room temperature. [C_{12}mim]Br itself showed bluish-white emission upon excitation wit UV light, due to the imidazolium cation. The samples doped with $EuBr_2$ showed blue emission due to 4f–5d transitions, $SmBr_3$-doped samples a red emission, $TbBr_3$-doped samples green emission and $DyBr_3$-doped samples an orange emission. Emission by $SmBr_3$, $TbBr_3$, and $DyBr_3$ is due to 4f–4f transitions. An interesting phenomenon is that the emission of the $TbBr_3$-doped samples was tunable from bluish-white to green, depending on the excitation wavelength. The bluish-white emission originates from the imidazolium cation and the green emission is due to $TbBr_3$. In a

similar way, the emission of the $DyBr_3$-doped samples could be tuned from bluish-white to orange-yellow. If the 1-dodecyl-3-methylimidazolium cation was replaced by the *N*-dodecyl-*N*-methylpyrrolidinium cation, the emission became less intense, but the luminescence decay times became somewhat longer (Getsis and Mudring, 2011). The possibility to tune the luminescence color from bluish-white to green by a change of the excitation wavelength is lost by doping $TbBr_3$ in *N*-dodecyl-*N*-methylpyrrolidinium bromide.

14.2. Magnetism

A LC can be macroscopically aligned by applying an external magnetic field. The magnetic alignment arises from the anisotropic magnetic energy of the LCs (Yamaguchi and Tanimoto, 2006). Because of this anisotropy, the magnetic field and the director of the mesophase are coupled. As a consequence, the LC experiences a torque in the magnetic field and orients itself into a direction where its magnetic energy is minimum. Isolated small molecules or ions do not undergo alignment in a magnetic field, because the coupling energy between a molecule (or ion) and the applied magnetic field is small compared to the thermal energy k_BT at room temperature, and thermal agitation will destroy alignment effects. Aggregates or ordered assemblies (e.g., liquid-crystal phases) be magnetically aligned, since their anisotropic magnetic energy exceeds the thermal agitation at room temperature. The molecular orientation in a mesophase by a magnetic field is a cooperative effect involving more than 10^8 molecules in a liquid-crystal microdomain (Alonso, 1996; de Gennes, 1974). The molecules in a mesophase microdomain have orientational order as a consequence of the anisotropic intramolecular interactions between the molecules. Alignment of mesophases by a magnetic field is of importance for the study of mesophases by XRD, because the information content of an X-ray diffractogram of an aligned mesophase is much higher than that of a corresponding diagram of an unaligned mesophase. Also for the measurements of anisotropy of physical properties (e.g., the dielectric permittivity, electrical conductivity or viscosity) aligned mesophases are required. An advantage of magnetic alignment over mechanical alignment by rubbing or by alignment layers is that alignment of the bulk sample rather than of the surface layers can be achieved, because the magnetic field lines can penetrate the material. The direction along which the magnetic field is applied can easily be controlled, so that alignment inclined to a surface is possible. With alignment layers or with alignment by means of an electric field, only parallel or perpendicular alignment can be achieved.

For easy alignment of mesogens in a magnetic field a high magnetic anisotropy is required. The *magnetic anisotropy* $\Delta\chi$ is the difference between the magnetic susceptibility parallel ($\chi_{\parallel}$) and perpendicular ($\chi_{\perp}$) to the director $\tilde{\boldsymbol{n}}$: $\Delta\chi = \chi_{\parallel} - \chi_{\perp}$. The free energy for alignment of LCs in a magnetic field can be expressed as:

$$\Delta G_{\text{align}} = -(1/2)\Delta\chi(H\cdot\tilde{n})^2, \tag{16}$$

where **H** is the applied magnetic field and $\tilde{\boldsymbol{n}}$ is the director. The molar magnetic anisotropy of most organic LCs is less than $100 \times 10^{-6}\,\text{cm}^{-3}\,\text{mol}^{-1}$. This value can be increased by incorporation of paramagnetic metal ions in the LC. Lanthanidomesogens are very attractive for this purpose as they can exhibit a very high magnetic anisotropy, up to one or two orders of magnitude larger than that of organic LCs. The orientation of LCs in a magnetic field depends on the sign and magnitude of the magnetic anisotropy $\Delta\chi$. Depending on the sign of $\Delta\chi$, the director $\tilde{\boldsymbol{n}}$ of the LC is oriented parallel or perpendicular to the external magnetic field. If $\Delta\chi$ is positive, the molecules are oriented with their molecular long axis parallel to the magnetic field. If $\Delta\chi$ is negative, the molecules are aligned with their molecular long axis perpendicular to the magnetic field. A low viscous mesophase is desirable for getting a well aligned sample in a magnetic field. The overall magnetic anisotropy $\Delta\chi$ is the sum of a diamagnetic ($\Delta\chi_{\text{dia}}$) and a paramagnetic contribution ($\Delta\chi_{\text{para}}$). For calamitic molecules, $\Delta\chi_{\text{dia}}$ is nearly always positive, but $\Delta\chi_{\text{para}}$ can be either positive or negative. The diamagnetic contribution to the magnetic anisotropy of most paramagnetic molecules is large in comparison with the paramagnetic contribution. The diamagnetic contribution to the magnetic anisotropy can be calculated by an additive scheme (Pascal's scheme) (Boudreaux and Mulay, 1976) and the paramagnetic contribution can be obtained by subtracting the calculated $\Delta\chi_{\text{dia}}$ value from the experimentally measured $\Delta\chi$ value. In the case where $\Delta\chi_{\text{para}} \approx \Delta\chi_{\text{dia}}$ and with the two contributions having an opposite sign, the resulting $\Delta\chi$ value will be very small, and an aligned monodomain is difficult to obtain by means of a magnetic field.

The situation is quite different in the case of lanthanidomesogens, because the trivalent lanthanide ions (especially Tb^{3+}, Dy^{3+}, Ho^{3+}, Er^{3+}, Tm^{3+}) have a very large magnetic anisotropy in comparison with other paramagnetic ions (e.g., Cu^{2+} or vanadyl). In the case of the paramagnetic lanthanide ions (all rare-earth ions except La^{3+}, Lu^{3+}, Y^{3+}, and Sc^{3+}), the diamagnetic contributions to $\Delta\chi$ can be neglected in comparison to the paramagnetic contribution. An exception is the Gd^{3+} ion, which is magnetically isotropic due to the S ground state $^8S_{7/2}$. The large magnetic anisotropy of lanthanidomesogens was discovered soon after the first calamitic lanthanide complexes had been prepared. Because the sign of the magnetic anisotropy depends on the lanthanide ion, it is possible to obtain with the same ligand and with the proper choice of the lanthanide ion compounds which can either be aligned perpendicular or parallel to the magnetic field (Binnemans et al., 2001c; Galyametdinov et al., 2007). Analysis of the experimental magnetic susceptibility data shows that these compounds can be classified into two distinct groups, depending on the sign of $\Delta\chi$. The first group contains Ce^{3+}, Pr^{3+}, Nd^{3+}, Sm^{3+}, Tb^{3+}, Dy^{3+}, and Ho^{3+} compounds, while the second group contains Eu^{3+}, Er^{3+}, Tm^{3+}, and Yb^{3+} compounds (Galyametdinov et al., 2007;

Mironov et al., 2000). Two compounds not belonging to the same group always have opposite sign of $\Delta\chi$. For instance, if $\Delta\chi$ is negative for the first group of lanthanide compounds, $\Delta\chi$ is positive for the second group, and *vice versa*. All available experimental results are in agreement with a negative $\Delta\chi$ value for the first group and a positive $\Delta\chi$ value for the second group. However, theoretical work has shown that the reverse situation can occur (Mironov et al., 2001, 2002). The highest values of the magnetic anisotropy are observed for the heavy lanthanides Tb^{3+}, Dy^{3+}, Ho^{3+}, $Er^{3+,}$ and Tm^{3+}, because these ions have a high magnetic moment. The effective magnetic moment is related to the magnetic susceptibility:

$$\mu_{\text{eff}} = \sqrt{\frac{3k}{N_A}} \cdot \sqrt{\chi T} = 2.828\sqrt{\chi T}, \tag{17}$$

where μ_{eff} is the effective magnetic moment (in Bohr magneton, μ_B), k is the Boltzmann constant, N_A Avogadro's number, χ the magnetic susceptibility and T the absolute temperature.

However, there exists no one-to-one relationship between a high magnetic moment and a large magnetic anisotropy, but a small magnetic moment cannot result in a large magnetic anisotropy. The magnitude of the magnetic anisotropy for a series of isostructural lanthanidomesogens can be estimated on the basis of the crystal-field splitting of the $^7F_1$ multiplet of a europium(III) compound (Binnemans et al., 2001d). This splitting can be measured by luminescence spectroscopy. Model calculations have been used to relate the magnetic anisotropy to the type of coordination polyhedron around the central lanthanide(III) ion (Mironov et al., 2001, 2002). Another requirement for a high magnetic anisotropy besides a large magnetic moment is a strong crystal-field perturbation. The $^{2S\!I}L_J$ ground state splits under the influence of the crystal-field potential in a number of crystal field levels in up to $2J+1$ for integer J (even number of 4f electrons), and up to $J+½$ sublevels for half-integer J (odd number of 4f electrons). The magnetic anisotropy arises from the fact that a large crystal-field splitting causes differences in the population of the ground state multiplet at a given temperature. The magnetic anisotropy increases upon cooling. At temperatures above room temperature, the magnetic behavior becomes more and more isotropic and approaches the predictions in the free-ion approximation, due to an equal population of the crystal-field levels. However, when the crystal-field perturbation is large it is possible to have a large magnetic anisotropy, even at temperatures at which the mesophase of lanthanidomesogens is stable (Mironov et al., 2000). The main problem to cope with is the high viscosity of the mesophase, which prevents fast switching. In general, cooling rates of less than one degree Celsius per minute are necessary to achieve good alignment in a magnetic field when going from the isotropic liquid to the mesophase. All the Schiff's base complexes reported up to present, display a smectic A phase. The smectic A phase has an intrinsic higher viscosity than the nematic

phase. By a proper choice of the counter ion the viscosity of the mesophase can be reduced considerably. For instance, a smectic A phase with a low viscosity is found for Schiff's base complexes with perfluorinated alkylsulfates as counter ions (Galyametdinov et al., 2001b).

$X_{\parallel}$ and $\chi_{\perp}$ of single crystals can be measured directly by orienting the crystal with the main magnetic axis parallel or perpendicular to the magnetic field (Binnemans et al., 2000a, 2001d; Galyametdinov et al., 2007). The $\chi_{\parallel}$ and $\chi_{\perp}$ values of an aligned mesophase frozen into the glass state can be measured as if one would measure on a single crystal. The situation is quite different for a mesophase in a magnetic field above a certain threshold strength H_0 because in this case the mesophase will be aligned by the magnetic field, and the measurement disturbs the sample. The magnetic anisotropy $\Delta\chi$ of a mesophase cannot be obtained via the relation $\Delta\chi = \chi_{\parallel} - \chi_{\perp}$, because only one of the two components $\chi_{\parallel}$ or $\chi_{\perp}$ can be determined. This problem can be solved by measuring the magnetic susceptibility in the isotropic phase and in the mesophase. In the isotropic phase, χ_{iso} will be measured. It is assumed that χ_{iso} is equal to the average magnetic susceptibility $\bar{\chi}$, which is defined as $\bar{\chi} = \left(\chi_{||} + 2\chi_{\perp}\right)/3$. In the mesophase, the molecules will be oriented in such a way that the axis of maximal magnetic susceptibility will be parallel to the magnetic field. The magnetic susceptibility measured in the oriented state, χ_{or}, is equal to (or less than, if alignment is not complete) the greater of the two components $\chi_{\perp}$ or $\chi_{\parallel}$. χ_{or} corresponds to the maximum of the χ-tensor. The actual value of the experimental magnetic anisotropy $\Delta\chi_{exp}$depends on the relative values of $\chi_{\perp}$or $\chi_{\parallel}$ (i.e., on the sign of $\Delta\chi_{exp}$):

$$\Delta\chi_{exp} = \frac{3}{2}(\chi_{or} - \chi_{iso}) \text{ if } \chi_{||} > \chi (\Delta\chi > 0), \tag{18}$$

$$\Delta\chi_{exp} = -3(\chi_{or} - \chi_{iso}) \text{ if } \chi_{||} < \chi (\Delta\chi < 0). \tag{19}$$

The sign of $\Delta\chi$ cannot be determined by magnetic susceptibility measurements and has to be obtained by an independent measurement, for instance by EPR (angle dependence of the EPR-signal) (Binnemans et al., 2000a) or by XRD in a magnetic field (distribution of the diffraction maxima with respect to the external magnetic field) (Galyametdinov et al., 2001b). It should be realized that the maximal value for the magnetic anisotropy $\Delta\chi$ can only be measured when alignment of the samples is perfect. The alignment is never complete and the measured value of $\Delta\chi$ is smaller than the theoretically predicted one. In Fig. 68, the alignment of a dysprosium(III)-containing LC is shown (Galyametdinov et al., 2007). The sample exhibits a Curie–Weiss behavior for the temperature dependence of their magnetic properties, when heated from the solid state through the smectic A phase until the isotropic phase is reached. When the sample was cooled from the isotropic phase to the mesophase (in a magnetic field), a drastic increase in the magnetic

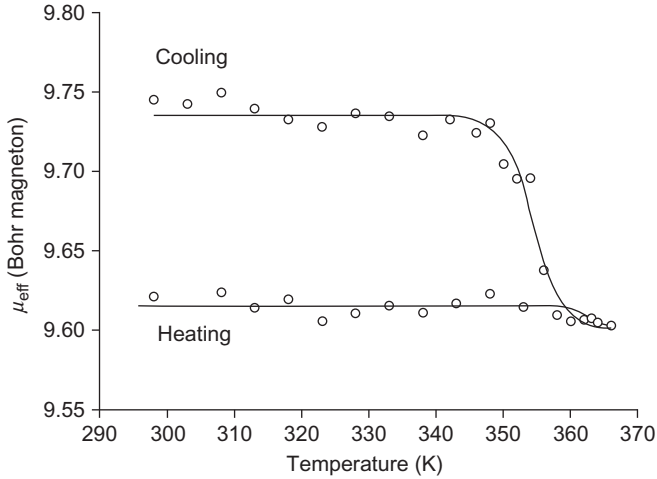

FIGURE 68 Effective magnetic moment μ_{eff} (in Bohr magneton units) of the liquid-crystalline complex $[Tb(LH)_3(DOS)_3]_3$ as a function of the temperature. Redrawn from Galyametdinov et al., 2007.

moment $\mu_{eff}$was observed in comparison to the initial values recorded by heating of the samples. The increase takes place over a narrow temperature range, and upon further cooling, the magnetic properties vary according to the Curie–Weiss law, but with a higher μ_{eff} value than in the heating cycle. This behavior can be explained by a magnetic field-induced orientation in the liquid-crystalline phase of a magnetically anisotropic sample with its axis of maximal magnetic susceptibility parallel to the magnetic field. The experimental values for the magnetic anisotropy in lanthanidomesogens are summarized in Table 23. The $\Delta\chi$ values depend on the counter ion. The highest $\Delta\chi$ have been observed for complexes with perfluorinated counter ions (Galyametdinov et al., 2001b). The magnetic studies have been largely restricted to Schiff's base complexes (e.g., Binnemans et al., 2000a; Galyametdinov et al., 1996a,b, 2001b, 2007; Turanov et al., 1999, 2001). A few data for β-enaminoketone complexes (Turanova et al., 2005) and β-diketonate complexes (Dzhabarov et al., 2011) are available. The values for the magnetic anisotropy reported in Table 23 are often much smaller than the theoretically predicted values, and have to be considered as lower limit values (minimum values). The discrepancies between the calculated and experimental values of the magnetic anisotropy of lanthanidomesogens have been discussed in detail by Mironov et al. (2000). These factors include orientation of the long molecular axis with respect to the principal magnetic axes of the individual molecules, as well as microscopic disorder effects (mainly statistical fluctuations in the alignment of the rod-like molecules with respect to the director) and macroscopic disorder effects (polydomain structure, fluctuations of the

TABLE 23 Magnetic Properties of Mesogenic Schiff's Base Complexes[a]

Compound	C_nH_{2n+1}	C_mH_{2m+1}	χ_{iso}	χ_{or}	$\chi_{or} - \chi_{iso}$	$\Delta\chi_{min}$	Reference
$[La(LH)_3(NO_3)_3]$	$C_{12}H_{25}$	$C_{18}H_{37}$	−1440	−1380	60	90	Turanov et al. (2001)
$[Pr(LH)_3(NO_3)_3]$	$C_{12}H_{25}$	$C_{16}H_{33}$	3850	4160	310	−930	Binnemans et al. (2000a)
$[Nd(LH)_3(NO_3)_3]$	$C_{12}H_{25}$	$C_{16}H_{33}$	3750	4020	270	−810	Binnemans et al. (2000a)
$[Nd(LH)_3(NO_3)_3]$	$C_{12}H_{25}$	$C_{18}H_{37}$	3270	3530	260	−780	Turanov et al. (2001)
$[Eu(LH)_3(NO_3)_3]$	$C_{12}H_{25}$	$C_{18}H_{37}$	3010	3140	130	195	Turanov et al. (2001)
$[Gd(LH)_3(NO_3)_3]$	$C_{12}H_{25}$	$C_{16}H_{33}$	18200	18200	∼0	∼0	Binnemans et al. (2000a)
$[Eu(LH)_3(NO_3)_3]$	$C_{12}H_{25}$	$C_{18}H_{37}$	20280	20330	50	75	Turanov et al. (2001)
$[Tb(LH)_3(NO_3)_3]$	$C_{12}H_{25}$	$C_{16}H_{33}$	27980	29830	1850	−5550	Binnemans et al. (2000a)
$[Tb(LH)_3(NO_3)_3]$	$C_{12}H_{25}$	$C_{18}H_{37}$	32010	33860	1850	−5500	Turanov et al. (2001)
$[Tb(LH)_3(NO_3)_3]$	$C_{14}H_{29}$	$C_{18}H_{37}$	–	–	–	−4665	Galyametdinov et al. (2001b)
$[Dy(LH)_3(NO_3)_3]$	$C_{12}H_{25}$	$C_{16}H_{33}$	–	–	–	−4756	Galyametdinov et al. (2001b)
$[Dy(LH)_3(NO_3)_3]$	$C_{12}H_{25}$	$C_{18}H_{37}$	34670	35790	1120	−3360	Turanov et al. (2001)
$[Ho(LH)_3(NO_3)_3]$	$C_{12}H_{25}$	$C_{18}H_{37}$	35440	36400	960	−2880	Turanov et al. (2001)
$[Ho(LH)_3(NO_3)_3]$	$C_{14}H_{29}$	$C_{18}H_{37}$	–	–	–	−7794	Galyametdinov et al. (2001b)
$[Er(LH)_3(NO_3)_3]$	$C_{12}H_{25}$	$C_{16}H_{33}$	27270	28345	1075	1610	Binnemans et al. (2000a)
$[Er(LH)_3(NO_3)_3]$	$C_{12}H_{25}$	$C_{18}H_{37}$	29540	29930	390	585	Turanov et al. (2001)

$[La(LH)_3(DOS)_3]$	$C_{12}H_{25}$	$C_{18}H_{37}$	−2110	−2030	80	120	Turanov et al. (2001)
$[Nd(LH)_3(DOS)_3]$	$C_{12}H_{25}$	$C_{18}H_{37}$	3200	3420	220	−660	Turanov et al. (2001)
$[Gd(LH)_3(DOS)_3]$	$C_{12}H_{25}$	$C_{18}H_{37}$	24010	24080	70	105	Turanov et al. (2001)
$[Tb(LH)_3(DOS)_3]$	$C_{12}H_{25}$	$C_{18}H_{37}$	37070	39090	2020	−6060	Turanov et al. (2001)
$[Tb(LH)_3(DOS)_3]$	$C_{14}H_{29}$	$C_{18}H_{37}$	38470	39650	1180	−3540	Galyametdinov et al. (2007)
$[Dy(LH)_3(DOS)_3]$	$C_{12}H_{25}$	$C_{18}H_{37}$	44940	46000	1060	−3180	Turanov et al. (2001)
$[Dy(LH)_3(DOS)_3]$	$C_{14}H_{29}$	$C_{18}H_{37}$	48790	44850	3940	−11820	Galyametdinov et al. (2007)
$[Ho(LH)_3(DOS)_3]$	$C_{12}H_{25}$	$C_{18}H_{37}$	44980	46020	1040	−3120	Turanov et al. (2001)
$[Ho(LH)_3(DOS)_3]$	$C_{14}H_{29}$	$C_{18}H_{37}$	41820	43480	1160	−4980	Galyametdinov et al. (2007)
$[Er(LH)_3(DOS)_3]$	$C_{12}H_{25}$	$C_{18}H_{37}$	36860	37350	490	735	Turanov et al. (2001)
$[Er(LH)_3(DOS)_3]$	$C_{14}H_{29}$	$C_{18}H_{37}$	35820	35185	635	952	Galyametdinov et al. (2007)
$[Tm(LH)_3(DOS)_3]$	$C_{14}H_{29}$	$C_{18}H_{37}$	24240	22550	1690	2535	Galyametdinov et al. (2007)
$[Yb(LH)_3(DOS)_3]$	$C_{12}H_{25}$	$C_{18}H_{37}$	6610	6810	200	300	Turanov et al. (2001)
$[Yb(LH)_3(DOS)_3]$	$C_{14}H_{29}$	$C_{18}H_{37}$	7790	8200	410	615	Galyametdinov et al. (2007)
$[Tb(LH)_3(C_2H_5OSO_3)_3]$	$C_{12}H_{25}$	$C_{16}H_{33}$	–	–	760	−2280	Malykhina et al. (2001)
$[Tb(LH)_3(C_8H_{17}OSO_3)_3]$	$C_{12}H_{25}$	$C_{16}H_{33}$	–	–	970	−2910	Malykhina et al. (2001)
$[Tb(LH)_3(C_{10}H_{21}OSO_3)_3]$	$C_{12}H_{25}$	$C_{16}H_{33}$	–	–	1040	−3120	Malykhina et al. (2001)
$[Tb(LH)_3(C_{18}H_{37}OSO_3)_3]$	$C_{12}H_{25}$	$C_{16}H_{33}$	–	–	1125	−3375	Malykhina et al. (2001)

Continued

TABLE 23 Magnetic Properties of Mesogenic Schiff's Base Complexes[a]—Cont'd

Compound	C_nH_{2n+1}	C_mH_{2m+1}	χ_{iso}	χ_{or}	$\chi_{or}-\chi_{iso}$	$\Delta\chi_{min}$	Reference
$[Er(LH)_3(C_2H_5OSO_3)_3]$	$C_{12}H_{25}$	$C_{16}H_{33}$	–	–	2465	3700	Malykhina et al. (2001)
$[Er(LH)_3(C_8H_{17}OSO_3)_3]$	$C_{12}H_{25}$	$C_{16}H_{33}$	–	–	2085	3130	Malykhina et al. (2001)
$[Er(LH)_3(C_{18}H_{37}OSO_3)_3]$	$C_{12}H_{25}$	$C_{16}H_{33}$	–	–	670	1000	Malykhina et al. (2001)
$[Tb(LH)_3\{CF_3(CF_2)_5CH_2OSO_3\}_3]$	$C_{12}H_{25}$	$C_{16}H_{33}$	–	–	2280	−6840	Galyametdinov et al. (2001b)
$[Ho(LH)_3\{CF_3(CF_2)_5CH_2OSO_3\}_3]$	$C_{12}H_{25}$	$C_{16}H_{33}$	–	–	3035	−9100	Galyametdinov et al. (2001b)
$[Nd(LH)_3\{CHF_2(CF_2)_5CH_2OSO_3\}_3]$	$C_{12}H_{25}$	$C_{16}H_{33}$	–	–	195	−580	Galyametdinov et al. (2001b)
$[Eu(LH)_3\{CHF_2(CF_2)_5CH_2OSO_3\}_3]$	$C_{12}H_{25}$	$C_{16}H_{33}$	–	–	470	700	Galyametdinov et al. (2001b)
$[Tb(LH)_3\{CHF_2(CF_2)_5CH_2OSO_3\}_3]$	$C_{12}H_{25}$	$C_{16}H_{33}$	–	–	2740	−8220	Galyametdinov et al. (2001b)
$[Dy(LH)_3\{CHF_2(CF_2)_5CH_2OSO_3\}_3]$	$C_{12}H_{25}$	$C_{16}H_{33}$	–	–	6490	−19470	Galyametdinov et al. (2001b)
$[Ho(LH)_3\{CHF_2(CF_2)_5CH_2OSO_3\}_3]$	$C_{12}H_{25}$	$C_{16}H_{33}$	–	–	4280	−12840	Galyametdinov et al. (2001b)
$[Er(LH)_3\{CHF_2(CF_2)_5CH_2OSO_3\}_3]$	$C_{12}H_{25}$	$C_{16}H_{33}$	–	–	3985	5980	Galyametdinov et al. (2001b)

A structure of the salicylaldimine Schiff's base ligand LH is shown in Fig. 25 (ligand L4H).
[a]*All the magnetic susceptibility values χ are expressed in 10^{-6} cm^3 mol^{-1}. The calculation of the experimental magnetic anisotropy $\Delta\chi_{exp}$ from $(\chi_{or}-\chi_{iso})$ is described in the text.*

director, curvature of smectic layers, wall effects, ...). The magnetic alignment of Schiff's base lanthanidomesogens with dodecylsulfate counter ions was investigated by temperature-dependent magnetic susceptibility measurements and temperature-dependent synchrotron SAXS measurements (Galyametdinov et al., 2007). The experiments gave the signs and values of the magnetic anisotropy of the lanthanide complexes. Although the complexes of the heavy lanthanides exhibit a huge magnetic anisotropy, the alignment of the mesophase samples was far from perfect and the rate of alignment was slow. This was attributed to the high viscosity of the smectic A mesophase and to the fact that the rare-earth center is only a minor component in these large molecules. The best alignment results were obtained for a dysprosium(III) complex.

Paramagnetic lanthanidomesogens can be used to visualize inhomogeneous magnetic fields and domains on the surface of minerals, storage devices, thin magnetic ribbons and other magnetic materials (Tomilin et al., 2005). The basic idea behind this technique is that the director of the LC tends to align parallel with or perpendicular to the direction of the local magnetic field when a liquid-crystal film is coated on the surface of the magnetic material. This preferential alignment results in the formation of distinct patterns for the spatial distribution of the light intensity of polarized transmitted or reflected by the liquid-crystal film. The optical pattern visualized the distribution of the magnetic field on the boundary surface. The large magnetic anisotropy and the easy alignment of lanthanidomesogens are an advantage for their use in visualization of magnetic domains. Moreover, the aligned liquid-crystal films can be supercooled to a glass state, so that the image of the magnetic domains can be stored. The room-temperature LC terbium phthalocyanine double-decker with eight chiral chains, $[(C_{12}H_{25}OCH(CH_3)CH_2O)_8Pc]_2Tb$, is a single molecular magnet at low temperatures (Gonidec et al., 2010). An interesting observation is that when the material is cooled at different rates, the magnetic properties vary, because of different degrees of supramolecular order. Alternating current magnetic susceptibility measurements were performed as a function of temperature and frequency with a SQUID magnetometer.

14.3. Electrical Properties

The only class of lanthanidomesogens for which electrical properties have been investigated in detail, are the bis(phthalocyaninato)lanthanide(III) sandwich complexes. As already described in Section 8, the free electron in these complexes is associated with the extensive π-system of the phthalocyanine macrocycles. The individual Pc_2Lu units can be considered nominally as $Lu^{3+}Pc_2^{\bullet 3-}$ The bis(phthalocyaninato)lutetium(III) complexes are intrinsic molecular semiconductors. The generation of charge carriers can be represented by the reaction $AAA \leftrightarrows A^+A^-A \leftrightarrows$ *free carriers*, where A is the molecular unit. The ionized pair A^+A^- is photochemically or thermally activated.

The self-organization of the discotic phthalocyanine compounds into columnar stacks provides a 1D pathway for charge transport. The *ac* electric properties of $[(C_{18}H_{37}OCH_2)_8Pc]_2Lu$ were studied by Belarbi et al. over a large frequency range (10^{-3}–10^5 Hz), both in the solid state, in the mesophase and in the isotropic liquid (Belarbi et al., 1988). In the solid state and in the mesophase, a $\omega^{0.8}$ frequency dependence was observed, with a very low activation energy of conduction (0.05 eV). The conductivities at 10^4 Hz were $8.2 \times 10^{-10}\ \Omega^{-1}\ cm^{-1}$ in the solid state at room temperature and $1.8 \times 10^{-9}\ \Omega^{-1}\ cm^{-1}$ in the mesophase at 52 °C. A capacitance increase associated with ionic conductivity was detected below 10 Hz. This very low activation energy was attributed to intercolumnar electron hopping of trapped charge carriers. Because of the limited size of the homogenous solid or liquid-crystalline domains, the conductivity at low frequencies was restricted by intercrystallite or intercolumnar hopping processes. In the isotropic liquid, the electric conduction was found to be frequency independent. At 60 °C and below 10^4 Hz, the electrical conductivity was $4 \times 10^{-11}\ \Omega^{-1}\ cm^{-1}$. At higher frequencies, a dipolar relaxation mechanism characterized by a ω^2 frequency dependence was observed. The thermal activation energy of conduction (0.4 eV) corresponds to the energy required for energy hopping between the $[(C_{18}H_{37}OCH_2)_8Pc]_2Lu$ molecular subunits through the molten paraffinic continuum. The electrical conductivity in the solid state, in the mesophase and in the isotropic liquid could be increased by partial oxidation of the compound with phenoxathiin hexachloroantimonate.

Electric studies were later extended by the same authors to $[(C_{12}H_{25}O)_8Pc]_2$-Lu, and the oxidized species $[(C_{12}H_{25}O)_8Pc]_2Lu^+BF_4^-$, obtained by oxidation of the parent compound with nitrosyl tetrafluoroborate (Belarbi et al., 1989). The electrical properties were determined in the frequency range between 10^{-3} and 10^5 Hz. The macroscopic conductivities were very low: $<10^{-10}$–10^{-12} $\Omega^{-1}\ cm^{-1}$. It was shown that the frequency dependence of the electrical conductivity is determined by the intercolumnar order: $\omega^{0.8}$ for the disordered columnar mesophase and $\omega^{0.5}$ for the ordered columnar mesophase. Because the ionization potentials and electron affinities of paraffinic and aromatic moieties are very different, it was concluded that the charge carriers are entirely localized on the aromatic subunits and that therefore the electronic charge processes involve the aromatic cores of the columns. It was estimated that for the same activation energy, the intracolumnar hopping probability is 10^7 times greater than the intercolumnar one. For $[(C_{12}H_{25}O)_8Pc]_2Lu$, the intracolumnar mobility of the charge carriers is in the range 10^{-4}–$10^{-2}\ cm^{-2}\ V^{-1}\ s^{-1}$, with the number of charge carriers being about 10^{11} carriers/cm^3. At 10 GHz, the charge migration occurs over less than 1 Å and involves a hopping between only two localized sites, whereas multiple sites were postulated in the low-frequency range. The electrical conductivity of the liquid-crystalline Pc_2Lu complexes is much lower than that of thin films and single crystals of unsubstituted Pc_2Lu complexes, due to the fact that conduction occurs only inside the columns along the columnar axis and that the

layer of molten alkyl chains is an electric insulator. Berlarbi (1990) has studied the *ac* conductivity of $[(C_{12}H_{25}O)_8Pc]_2Lu$ samples that have partially been aligned in a magnetic field. He found a conduction anisotropy of approximately 10, which means that the conductivity is $10\times$ higher when the columns are parallel to the magnetic field than when they are perpendicular to the field. The conductivity of the unaligned mesophase was in between these two limiting values. Most of the electric studies have been done on lutetium(III) complexes. However, studies on unsubstituted Pc_2R complexes have revealed major differences between the bisphthalocyanine complexes of lutetium (Pc_2Lu) and thulium (Pc_2Tm; Bouvet and Simon, 1990; Guillaud et al., 1990). Whereas Pc_2Lu is an intrinsic molecular semiconductor, Pc_2Tm is an extrinsic molecular semiconductor. The low hole mobility of $[(C_{12}H_{25}S)_8Pc]_2Ce$ in the hexagonal columnar phase (7×10^{-3} cm^2 V^{-1} s^{-1}) in comparison to that of the lutetium analogues was attributed to the absence of free radicals in the cerium complex (Nekelson et al., 2007a). Notice that cerium is in the tetravalent oxidation state in this complex. Basova et al. (2007) reported on the conductivity of $[(C_6H_{13}S)_8Pc]_2Dy$ film in the liquid-crystal state.

Van de Craats et al. (1997) used the *pulse-radiolysis time-resolved microwave conductivity technique* (*PR-TRMC*) to study the charge transport properties of $[(C_{12}H_{25}O)_8Pc]_2Lu$. Their results showed an increase in charge carrier mobility at the crystalline solid to Col_x mesophase transition and a further increase by a factor of three at the transition to the higher temperature mesophase Col_h. In the mesophase above 90 °C, the charge carrier mobility gradually decreased and an abrupt decrease by a factor of about two was observed at the Col_h to isotropic liquid transition. In the solid state, the charge carrier mobility was more than one order of magnitude lower than in the solid state of other alkoxy-substituted phthalocyanines. This is possibly due to the sandwich structure of the individual molecules. The increase at the crystal-to-mesophase transition was attributed to a change from a tilted to an orthogonal stacking. The increase at the Col_x to Col_h transition was linked to the equivalence of the phthalocyanine macrocycles within the columns which leads to delocalization of the radical site between neighboring molecular units and which results in additional intracore binding over and above the electrostatic and π–π interactions normally responsible for columnar self-aggregation. The intracolumnar mobility determined just above the Col_x to Col_h transition at 90 °C was 0.17×10^{-4} m^2 V^{-1} s^{-1} and was at that time the highest value determined using the PR-TRMC technique for a LC forming a columnar mesophase. The increase in charge mobility at the crystal-to-mesophase transition is in contrast to what is observed for other discotic molecules such as porphyrins, perylenes, triphenylenes, and even other alkoxy-substituted phthalocyanines. Because of the fast time-response and ultra-high frequency involved in the PR-TRMC technique, the mobilities obtained were thought to be intrinsic, trap-free values associated with organized domains within the material (Ban et al., 2001). Therefore, these mobilities can be considered

to be close to the maximum value that can be obtained with well-organized monodomain layers.

Replacement of the oxygen atoms of alkoxy-substituted Pc_2Lu phthalocyanine complexes by sulfur atoms (giving alkylthio substituted phthalocyanines) resulted in an increase of more than one order of magnitude in the intramolecular charge mobility to values in the range of 0.15–0.3 $cm^2V^{-1}\,s^{-1}$ (Ban et al., 2001). The pronounced positive effect on the charge transport properties of sulfur compared with oxygen as chain-to-core coupling group was attributed to the larger size of the sulfur atom which hinders rotational and translational displacements of the phthalocyanine macrocycles within the cores of the columns. The resulting decrease in structural disorder within the stacks of the alkylthio-substituted compounds is favorable for fast charge transport. The higher charge mobility can also be explained by differences in electronegativity between the oxygen and sulfur atoms. Whereas the alkoxy group is electron-donating to the phthalocyanine ring, the alkylthio group is in a first approximation neither electron-donating nor electron-withdrawing. As a result, the *HOMO–LUMO* gap is smaller in the alkylthio-substituted compounds, and hence the charge mobility is higher. The 1D intracolumnar charge carrier mobilities exhibit only a weak temperature dependence, except for an abrupt decrease by a factor of about three at the crystal-to-mesophase transition. This decrease can be attributed to the melting of the alkylthio chains, with a resulting increase in the disorder within the columns. The mobility remains high in the isotropic state, which indicates that a high degree of columnar order still exists and allows charge transport to occur via intermolecular charge transfer rather than by molecular ion diffusion. Because of the high charge mobility in the isotropic state, these compounds were considered as the first liquid organic semiconducting materials. The DC electrical properties of tetra-substituted $[(C_nH_{2n+1}S)_4Pc]_2Lu$ in solid state, mesophase, and isotropic liquid were determined by measuring the I-V characteristics and dark current of thin films on interdigital electrodes (Atilla et al., 2009). The phase transitions could be detected by the changes in electrical conductivity. The DC conductivities and the thermal activation energies were found to depend on the alkyl chain lengths. In the solid state, the DC conductivity was in the range of 10^{-8}–10^{-5} S cm^{-1} and decreases with increasing chain length. This decrease in conductivity is related to an increase in hopping distance with increasing length of the alkyl chain. The study also reveals a higher conductivity for the alkylthio-substituted lutetium double-deckers in comparison with the alkyloxy-substituted compounds, both in the crystalline, liquid-crystalline, and isotropic phase. The activation energy varied between 0.12 and 0.38 eV in the solid phase, to 0.36–0.67 eV in the liquid-crystalline phase. The photoconductivity of the $[(C_{16}H_{37}S)_8Pc]_2R$ (R = Eu, Tb, Lu) complexes is very low (Yoshino et al., 2000). Nonradiative relaxation of the photoexcitations is dominating. A significant increase in the photoconductivity was observed after doping with C_{60}. In the case of the lutetium(III) complex,

the photoconductivity parallel to the columns was two orders of magnitude larger than in the case of the undoped sample.

The bis(phthalocyaninato)lanthanide(III) complexes are *electrochromic*: in solution or deposited as thin films they exhibit different colors depending on the applied electric potential (Harnoode et al., 1999; Monk et al., 1995; Nicholson, 1982). For this reason, the potential of these materials for display applications has been evaluated. The electrochromic behavior of the octaalkoxymethyl-substituted Pc_2Lu has been investigated and it has been shown that they have similar properties in solution as the unsubstituted Pc_2Lu complexes (Besbes et al., 1987; Castaneda et al., 1986), but the substituted compounds are far more stable under electrochemical cycling than the unsubstituted ones (Toupance et al., 1999). The green neutral form can be transformed via a one-electron oxidation step into an orange form and via a one-electron reduction step into a blue form:

$$\underset{\text{blue}}{\left[(C_nH_{2n+1}OCH_2)_8Pc\right]_2Lu^-} \overset{-e^-}{\rightleftarrows} \underset{\text{green}}{\left[(C_nH_{2n+1}OCH_2)_8Pc\right]_2Lu} \overset{-e^-}{\rightleftarrows} \underset{\text{orange}}{\left[(C_nH_{2n+1}OCH_2)_8Pc\right]_2Lu^+}$$

These redox processes are reversible. In the blue complex, the *Q*-band is at about 631 nm, in the green complex at about 671 nm and in the orange complex at about 704 nm. The oxidation of $[(C_8H_{17}OCH_2)_8Pc]_2Lu$ or $[(C_{12}H_{25}OCH_2)_8Pc]_2Lu$ films to form an orange cation or reduction to form a blue anion could be achieved when the electrode potential was held for several minutes at $+0.6$ or -0.1 V respectively. It was shown that the potential of the oxidation step depends on the anion of the aqueous electrolyte in contact with the film. The oxidized and reduced compounds were stable in solution. In the presence of an external potential, the orange and blue species remained unchanged over at least 2 days. Without external potential, the colors remained for several hours or days, depending on the impurity concentration. An increase in the chain length makes both the reduction and the oxidation process more difficult (Toupance et al., 1999). For $[(C_{18}H_{37}OCH_2)_8Pc]_2Lu$ films, it was necessary to heat the film at 55 °C and to increase the potential to overcome the ohmic drop (typical potential values were $+1.4$ and -1.0 V). Komatsu et al. (1994a) pointed to the fact that substituents on the phthalocyanine ring have hardly any influence on the colors of the neutral green complex and the reduced blue species. However, the colors of the oxidized species showed remarkable differences in dichloromethane solution: the oxidized form of the unsubstituted Pc_2Lu was yellowish green, $[(C_{12}H_{25}OCH_2)_8Pc]_2Lu^+$ and $[(C_{12}H_{25}O)_8Pc]_2Lu^+$ were orange, whereas $[(C_{12}H_{25})_8Pc]_2Lu^+$ solution was red. With respect to the alkoxy- and alkoxymethyl-substituted Pc_2Lu, the *Q*-band of the alkyl-substituted Pc_2Lu is shifted more than 8 nm to longer wavelengths (and is found at 712 nm). The oxidation potential in the $[(C_nH_{2n+1})_8Pc]_2Lu$ is at -0.17 V and the

reduction potential is at +0.28 or +0.29 V. The electrochromism of these alkyl-substituted Pc_2Lu exhibits the three primary colors (blue, green, red), so that it is possible to construct a full-color display using one single compound. The drawback of this type of display is the long response time: color changes require several hundreds of seconds. On the other hand, once an image is formed by an electrochromic process, no further energy input is required to preserve it.

By attaching electron-donating groups to the phthalocyanine ring, the complexes become more reducing and less oxidizing (Jiang et al., 1997) This behavior was illustrated by binding *n*-pentyloxy or *n*-heptyl groups to the macrocycle ring. However, the difference between the oxidation and reduction potentials, which are a good estimate of the thermal activation energy in the Pc_2R complexes, remained relatively constant at ca. 0.40 V. It should be mentioned that the theoretical explanation of the electrochromic behavior of Pc_2Lu compounds is not without controversies. Some authors claim that the color changes are acid-base in nature and not due to redox processes involving the phthalocyanine rings. Daniels et al. (1993a,b) reported that in acetonitrile solution and in the absence of an applied potential, the color change from blue over green to red could be obtained by the addition of acid and then quantitatively reversed by the addition of base. The blue species is $[Pc_2R]^-$, the green Pc_2RH and the red species Pc_2RH_2. Nananishi et al. (2003) investigated the ion pairing between chemically reduced forms of $[(C_6H_{13}S)_8Pc]_2Lu$ and $[(C_{12}H_{25}S)_8Pc]_2Lu$ with tetra-*n*-octylphosphonium bromide. Reduced double deckers with charges from −1 to −5 could be obtained. The ion-pairing effects are responsible for the shift of the reduction potentials of these compounds.

15. ACTINIDOMESOGENS

Actinidomesogens can be defined an actinide-containing LCs. In comparison to the lanthanidomesogens, examples of actinidomesogens are very scarce. This is not a surprise, given the fact that actinides are radioactive. All actinidomesogens described in the literature are uranium-containing LCs (*uranomesogens*). No thorium-containing LCs (*thoromesogens*) are known yet. In theory, one could imagine the design of LCs containing neptunium, plutonium, or americium, but these metals are much more difficult to handle than uranium or thorium due to their higher radioactivity. From a materials point of view, it does not make much sense to work with these elements, because these radioactive compounds have to be handled in specialized laboratories. For the same reason, it is unlikely that metallomesogens containing actinium, protactinium, or the heavy actinides will ever be prepared. It should be realized that organic complexes of highly reactive compounds suffer from severe radiolysis, so that it is extremely difficult, if not impossible to prepare such compounds in a high purity. Uranium has a rich redox chemistry, but the most

stable oxidation state is the + VI state. In general, hexavalent uranium occurs under the form of the *dioxouranium(VI)* ion, which is better known as the *uranyl* ion (Denning, 1992, 2007). The uranyl ion is an oxocation of hexavalent uranium, with chemical formula $[UO_2]^{2+}$. It has a linear structure with short U-O bonds, which are represented as double bonds, although the molecular orbital description of the chemical bonds in uranyl is quite complicated. Four or more ligands (or two or three bidentate ligands) can bind in the equatorial plane to the uranyl ion. The uranyl ion is chemically a very stable oxocation, and it is very difficult to remove one or both of the oxygen atoms.

The first examples of uranium-containing LCs were the uranyl β-diketonate and tropolonate complexes reported by Sinn and coworkers (Clark et al., 2002; Fig. 69). The ligands are not liquid-crystalline themselves, but the corresponding uranyl complexes exhibit a mesophase. The tropolonate complex forms a highly ordered crystal B (or E) phase over a small temperature range between 207 and 209 °C. The exact nature of the mesophase (B or E) could not be determined with certainty. Extension of the chain lengths leads to a wider mesophase stability range, but otherwise the properties of these complexes are similar (Elliott et al., 2002). The β-diketonate complex forms a smectic C phase at much lower temperatures (between 59 and 75 °C; Clark et al., 2002). However, upon cooling the smectic C phase is reformed from the isotropic liquid at 64 °C and can be supercooled down to room temperature. The uranyl β-diketonate complex is thus an example of a room-temperature metallomesogen. Although the uranyl group (UO_2) has some structural similarity to the vanadyl group (VO^{IV}), but there are striking differences. Whereas the vanadyl ion can form weak intermolecular links

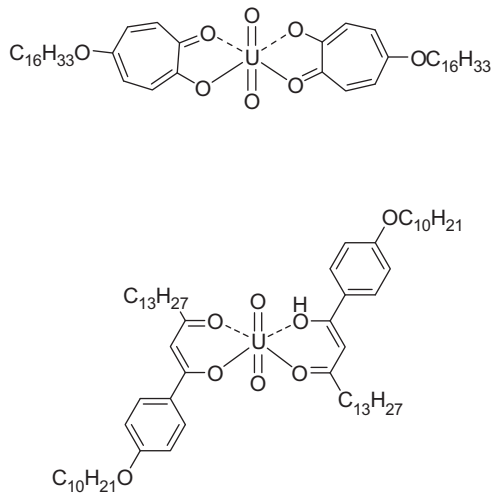

FIGURE 69 Liquid-crystalline uranyl complexes with tropolonate (top) and β-diketonate (bottom) ligands.

V=O···V=O···, the uranyl ion cannot. Ghedini and coworkers prepared uranyl complexes of a series of mesomorphic *N*,*N*′-salicyliden(3,3′-diamine-*N*-methyldipropylamine) ligands **L52H$_2$–L55H$_2$** (Aiello et al., 2005; Fig. 70). In these Schiff's base complexes the uranyl ion is coordinated by 5 atoms in the equatorial plane (N_3O_2 coordination). Some of the complexes showed a smectic C phase at high temperatures. Uranyl complexes of expanded porphyrins are the first examples of discotic uranyl-containing metallomesogens (Sessler et al., 2004, 2006). The ligand is a so-called *alaskaphyrin*, with eight peripheral alkoxy chains (Fig. 71). The uranyl ion acted as a template for the synthesis of the metal complex. The complexes occur as an anisotropic glass at room temperature (vitrified mesophase) and exhibited a hexagonal columnar mesophase over a temperature range of more than 100 °C. Binnemans and coworkers prepared a uranyl mesogen with a propeller shape by coordination of three imidazo[4,5-f]-1,10-phenanthroline to the uranyl ion

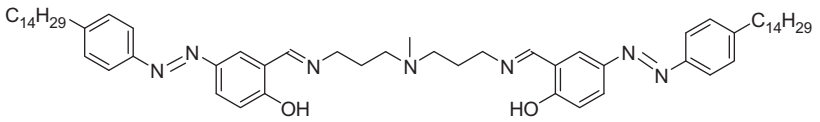

L52H$_2$

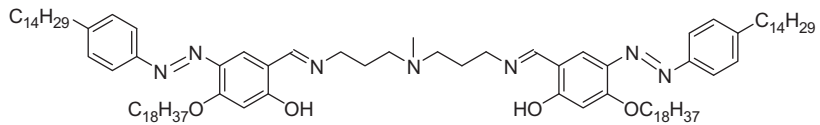

L53H$_2$

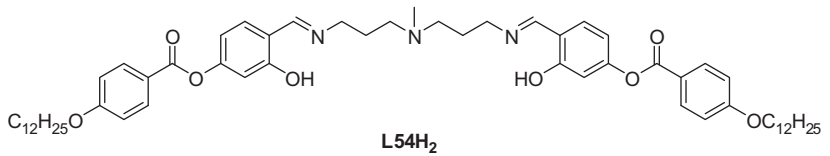

L54H$_2$

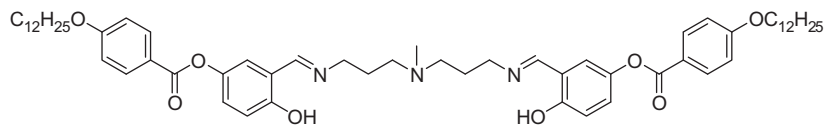

L55H$_2$

FIGURE 70 *N*,*N*′-salicyliden(3,3′-diamine-*N*-methyldipropylamine) ligands.

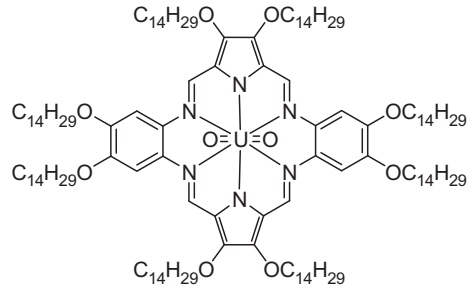

FIGURE 71 Liquid-crystalline uranyl alaskaphyrin complex.

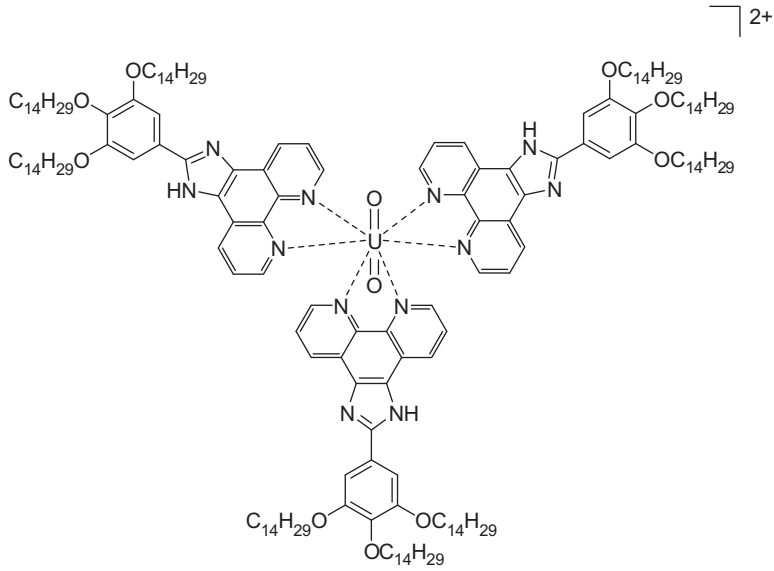

FIGURE 72 Liquid-crystalline uranyl complex with imidazo[4,5-f]-1,10-phenanthroline ligands. The two noncoordinating triflate counter ions have been omitted.

in the equatorial plane (Cardinaels et al., 2005b; Fig. 72). Unlike all other uranyl mesogens reported before, this compound is a cationic complex with triflate counter anions. The complex forms a hexagonal columnar phase between 95 and 181 °C. A rich mesomorphism is displayed by $[UO_2Br_4]^{2-}$ complexes with *N*-alkyl-*N*-methylpyrrolidinium cations (Goossens et al., 2009). Depending on the alkyl chain length, a smectic A, crystal smectic E or a hexagonal columnar phase was observed. The uranyl complexes were not photoluminescent in their pure form due to auto-quenching, but luminescence in the visible spectral region could be observed upon dilution of the complex in an ionic liquid. The *N*-alkyl-*N*-methylpyrrolidinium bromide compounds exhibit a rare smectic phase, a T phase with tetragonal symmetry.

However, replacement of the bromide anions by the $[UO_2Br_4]^{2-}$ anions led to the formation of smectic phases with lower symmetry.

Uranyl fluoride, UO_2F_2, forms a lyotropic nematic phase in mixtures of acetone and (heavy) water (Lychev et al., 1990; Mikhalev and Shcherbakov, 1985a,b, 1986). This behavior is unusual, because the uranyl compound does not contain long alkyl chains and cannot be considered as an amphiphilic. Nevertheless, compounds such as V_2O_5, FeOOH, AlOOH, $Li_2Mo_6Se_6$, and H_2WO_4 are other examples of purely inorganic compounds that can form lyomesophases in water, in organic solvents or in mixtures thereof. These are the so-called *inorganic lyotropic liquid crystals* (Sonin, 1998). It was observed that upon addition of acetone to solution of uranyl fluoride in (heavy) water light scattering occurred. However, the presence of a nematic mesophase was evident from the quadrupole splitting pattern in the ^1H NMR spectrum of acetone. It is assumed that the uranyl fluoride molecules are present in the mesophase as rigid dimers. When the uranyl fluoride concentration was lowered, the clearing temperature decreased. For uranyl fluoride concentrations lower than 0.30 mol $(kg\ D_2O)^{-1}$, the nematic phase was no longer observed. Decrease of the acetone concentration, led to a narrowing of the temperature range of existence of the nematic mesophase. Although there is evidence for the existence of lamellar of hexagonal mesophases in the region of high acetone concentrations (ca. 28–40 mol $(kg\ D_2O)^{-1}$), no detailed studies of these systems have been carried out yet (Sonin, 1998).

16. CONCLUSIONS AND OUTLOOK

More than 10 years ago, I wrote that the study of liquid-crystalline rare-earth complexes was a research field in its infancy (Binnemans, 1999). At that time, only very few classes of lanthanidomesogens had been described in the literature, mainly Schiff's base compounds, β-enaminoketonates, and phthalocyanine complexes, and the number of published papers was very limited. The main research target was to design lanthanidomesogens with low melting points and exhibiting a nematic phase, because such compounds would have a low enough viscosity for easy alignment in external magnetic and electric fields at temperatures close to room temperature. It was realized that lanthanidomesogens could be an interesting class of functional molecular materials due to combination of the magnetic and photophysical properties of lanthanide(III) ions. At present, in 2012, many more classes of metallomesogens have been described in the literature by different research groups, although the Schiff's base and phthalocyanine complexes remain among the most thoroughly investigated classes of lanthanidomesogens. The objective of obtaining nematogenic rare-earth complexes has been achieved, although the number of such compounds is still very limited. Several lanthanidomesogens are liquid-crystalline at room temperature. Magnetic alignment has been

studied in details and polarized luminescence has been observed. However, not all of the original expectations have been fulfilled. For instance, magnetic alignment is too slow to be of practical use. Polarization effects in luminescence spectra are weak. It has been criticized that the liquid-crystalline behavior of the lanthanidomesogens is only marginally influencing their magnetic and photophysical properties (Gimenez et al., 2002). On the other hand, even a small variation of the size of the lanthanide ion can have a dramatic effect on the transition temperatures of lanthanidomesogens or can even destroy the liquid-crystalline behavior. The relationship between the size of the lanthanide ion and the thermal properties of lanthanidomesogens is not well understood yet. Our knowledge of the molecular order of lanthanide complexes in the mesophase is still limited and further work in that direction is needed. For instance, very few structural data are available for the Schiff's base complexes. No examples of scandium-containing LCs have been reported yet. There exist also no promethium-containing LCs, but the development of these compounds is hampered by promethium's radioactivity and restricted availability. Cerium-containing lanthanidomesogens are also underrepresented. These compounds are often difficult to synthesize due to the redox activity of cerium(III) and cerium(IV). In principle, every type of lanthanide complex can be transformed in a LC by suitable modification of the ligands. Typically, a modification consists in attaching a sufficient number of long alkyl chains to the ligand, mostly as alkoxy chains to a phenyl ring. A mistake often made by beginners in the field is to select alkyl chains that are too short or to attach too small a number of alkyl chains to the ligand. This will lead to very high transition temperatures or to the absence of mesophases. Experience learnt that tetradecyloxy chains ($C_{14}H_{29}O$) are often a good starting point, as well as attachment of three alkoxy chains to a phenyl ring. It is not recommended to design lanthanidemesogens by attaching hexyloxy or octyloxy chains to the parent ligand, because these chains are too short. It should be realized that the attachment of a large number of long alkyl chains to a central core often results in the formation of columnar mesophases. Therefore, one has no option other than reducing the number of chains if one wants to design calamitic (rodlike) lanthanidomesogens. A very powerful method to transform lanthanide complexes in to LCs is by attaching mesophase-inducing groups via long flexible alkyl chains to the ligands. Typical examples of such mesophase-promoting groups are the cyanobiphenyl and the cholesteryl groups. A problem with lanthanidomesogens is that they are often obtained as hydrates (or solvates) after synthesis. The presence of coordinated of entrapped water or solvent molecules make the study of the thermal behavior more cumbersome, because these molecules can alter the mesophase behavior. The interpretation of the thermal transitions is made more complicated because the water or solvent molecules can be released during the heating of the compound, so that the heating process changes the actual composition of the complex. Therefore, it is highly recommended to make

extra efforts to prepare lanthanidomesogens in an anhydrous state, without hydration or solvation molecules. I hope that the review will inspire other researchers to further develop the field of lanthanidomesogens and that there will be a significant progress in the next decade.

ABBREVIATIONS AND SYMBOLS

15C5	15-crown-5
5CB	4-*n*-pentyl-4′-cyanobiphenyl
a	lattice parameter a
acac	acetylacetonate
A_{chain}	cross-sectional area of the aliphatic chains
A_{core}	cross-sectional area of the rigid core
A_M	molecular area
b	lattice parameter *b*
bipy	2,2′-bipyridine
C_{12}DMAO	*N*,*N*-dimethyldodecylamine oxide
$C_{12}EO_{10}$	decaethylene glycol monododecyl ether
C_{12}mim	1-dodecyl-3-methylimidazolium
C_{12}mpyr	*N*-dodecyl-*N*-methylpyrrolidinium
Col_h	hexagonal columnar phase
Col_{hd}	disordered hexagonal columnar phase
Col_{ho}	ordered hexagonal columnar phase
Col_{ht}	tilted hexagonal columnar phase
Col_L	lamellar columnar phase
Col_o	oblique columnar phase
Col_r	rectangular columnar phase
Col_t	tetragonal columnar phase
Col_x	unidentified columnar phase
C_p	heat capacity
Cr	crystalline phase
CrB	crystalline smectic rotor phase
CTA	hexadecyltrimethylammonium
Cub	cubic phase
Cub_v	bicontinuous cubic phase
d	layer thickness, interlayer distance
dbm	dibenzoylmethanate
DBU	1,8-diazabicyclo[5.4.0] undec-7-ene
d_{calc}	calculated layer thickness
DDTA	dodecyltrimethylammonium
dec.	decomposition
D_L	discotic lamellar columnar phase
DMF	*N*,*N*-dimethylformamide

DODA	dimethyldioctadecylammonium
DOS	dodecylsulfate
DSC	differential scanning calorimetry
EPR	electron paramagnetic resonance
G	gauss
G	Gibbs free energy
g	glass phase (vitreous phase)
gly	1,2-dimethoxyethane (monoglyme)
GPa	gigapascal (10^9Pa)
h	stacking periodicity along column axis
H	applied magnetic field
Hacac	acetylacetone
Hdbm	1,3-diphenyl-1,3-propanedione (dibenzoylmethane)
Htta	2-thenoyltrifluoroacetone
Hz	hertz
I	isotropic phase
I_{295K}	observed luminescence intensity at 295 K
I_{obs}	observed luminescence intensity
ITO	indium tin oxide
J	total angular momentum (due to spin-orbit coupling)
L	orbital angular momentum
LC	liquid crystal
LCD	liquid crystal display
M	(unidentified) mesophase
M	molecular mass
MBBA	*N*-(4-methyloxybenzylidene)-4-butylaniline
MOF	metal-organic framework
n	order of diffraction
N	nematic phase
N	number of molecules per unit cell
$\tilde{n}$	director of mesophase
N*	chiral nematic phase (= cholesteric phase)
NC	nematic columnar phase
N_D	discotic nematic phase
NMR	nuclear magnetic resonance
Pc	phthalocyanine
phen	1,10-phenanthroline
POM	polarizing optical microscopy
POMs	polyoxometalates
PR-TRMC	pulse-radiolysis time-resolved microwave radiation
$\vec{Q}$	scattering vector
R	general symbol for a rare-earth element
S	spin angular momentum

S	columnar cross section
salen	2,2′-*N*,*N*′-bis(salicylidene)ethylenediamine
SAXS	small-angle X-ray scattering
SmA	smectic A phase
SmA*	chiral smectic A phase
SmA1	partially molten-chain smectic phase
SmA2	molten-chain smectic phase
SmB	smectic B phase or conformationally disordered smectic rotor phase
SmC	smectic C phase
SmF	smectic F phase
SmI	smectic I phase
SmX	unidentified smectic phase
SQUID	Superconducting Quantum Interference Device
S_r	area of rectangular lattice
STM	scanning tunneling microscopy
T	temperature
T_c	clearing temperature
T_g	glass-transition temperature
TGB	twist grain boundary
T_m	melting temperature
TREN	tris(2-aminoethyl)amine
tta	2-thenoyltrifluoroacetonate
$T_{transition}$	transition temperature
V_{cell}	volume of unit cell
V_{mol}	molecular volume
XRD	X-ray diffraction
ΔH	enthalpy change
ΔS	entropy change
$\Delta\chi$	magnetic anisotropy
$\Delta\chi_{dia}$	diamagnetic contribution to the magnetic anisotropy
$\Delta\chi_{para}$	paramagnetic contribution to the magnetic anisotropy
θ	diffraction angle
θ_t	tilt angle
μ_{eff}	effective magnetic moment
ρ	density
τ_{295K}	observed luminescence decay time at 295 K
τ_{obs}	observed luminescence decay time
χ	magnetic susceptibility
$\chi_{\parallel}$	magnetic susceptibility parallel to the director or the main molecular axis
$\chi_{\perp}$	magnetic susceptibility perpendicular to the director or the main molecular axis
Ω	ohm

REFERENCES

Aiello, I., Ghedini, M., Grisolla, A., Pucci, D., Francescangeli, O., 2005. Liq. Cryst. 32, 763.

Alonso, P.J., 1996. Magnetic properties of metallomesogens. In: Serrano, J.L. (Ed.), Metallomesogens, Synthesis, Properties and Applications. VCH, Weinheim, p. 387 (Chapter 10).

Atilla, D., Kilinc, N., Yuksel, F., Gürek, A.G., Öztürk, Z.Z., Ahsen, V., 2009. Synth. Met. 159, 13.

Ban, K., Nishizawa, K., Ohta, K., van de Craats, A.M., Warman, J.M., Yamamoto, I., Shirai, H., 2001. J. Mater. Chem. 11, 321.

Basova, T., Kol'tsov, E., Hassan, A.K., Nabok, A., Ray, A.K., Gürek, A.G., Ahsen, V., 2004. J. Mater. Sci. Mater. Electron. 15, 623.

Basova, T., Gürek, A.G., Ahsen, V., Ray, A.K., 2007. Org. Electron. 8, 784.

Belarbi, Z., Maitrot, M., Ohta, K., Simon, J., André, J.J., Petit, P., 1988. Chem. Phys. Lett. 143, 400.

Belarbi, Z., Sirlin, C., Simon, J., André, J.-J., 1989. J. Phys. Chem. 93, 8105.

Bellusci, A., Barberio, G., Crispini, A., Ghedini, M., La Deda, M., Pucci, D., 2005. Inorg. Chem. 44, 1818.

Berlarbi, Z.J., 1990. Phys. Chem. 94, 7334.

Besbes, S., Plichon, V., Simon, J., Vaxiviere, J., 1987. J. Electroanal. Chem. 237, 61.

Bhattacharjee, C.R., Das, G., Goswani, P., Mondal, P., Prasad, S.K., Rao, D.S.S., 2011. Polyhedron 30, 1040.

Bikchantaev, I., Galyametdinov, Y.G., Kharitonova, O., Ovchinnikov, I.V., Bruce, D.W., Dunmur, D.A., Guillon, D., Heinrich, B., 1996. Liq. Cryst. 20, 489.

Binnemans, K., 1999. Mater. Sci. Forum 315–317, 169.

Binnemans, K., 2005a. Rare-earth beta-diketonates. In: Gschneidner Jr., K.A., Bünzli, J.-C.G., Pecharsky, V.K. (Eds.), Handbook on the Physics and Chemistry of Rare Earths, vol. 35. Elsevier, Amsterdam, pp. 107–272 (Chapter 225).

Binnemans, K., 2005b. Liquid-crystalline lanthanide complexes. In: Meyer, G., Naumann, D., Wesemann, L. (Eds.), Inorganic Chemistry in Focus II. Wiley-VCH, Weinheim, p. 267 (Chapter 15).

Binnemans, K., 2005c. Chem. Rev. 105, 4148.

Binnemans, K., 2009. J. Mater. Chem. 19, 448.

Binnemans, K., 2010. Physical properties of metallomesogens. In: Bruce, D.W., O'Hare, D., Walton, R.I. (Eds.), Molecular Materials. Wiley, Chichester, p. 61.

Binnemans, K., Görller-Walrand, C., 2002. Chem. Rev. 102, 2303.

Binnemans, K., Gündogan, B., 2002. J. Rare Earths 20, 249.

Binnemans, K., Lodewyckx, K., 2001. Angew. Chem. Int. Ed. 40, 242.

Binnemans, K., Lodewyckx, K., 2003. Supramol. Chem. 15, 485.

Binnemans, K., Moors, D., 2002. J. Mater. Chem. 12, 3374.

Binnemans, K., Galyametdinov, Y.G., Collinson, S.R., Bruce, D.W., 1998. J. Mater. Chem. 8, 1551.

Binnemans, K., Bex, C., Bruce, D.W., 1999a. Liq. Cryst. 26, 771.

Binnemans, K., Heinrich, B., Guillon, D., Bruce, D.W., 1999b. Liq. Cryst. 26, 1717.

Binnemans, K., Van Deun, R., Bruce, D.W., Galyametdinov, Yu.G., 1999c. Chem. Phys. Lett. 300, 509.

Binnemans, K., Bruce, D.W., Collinson, S.R., Van Deun, R., Galyametdinov, Y.G., Martin, F., 1999d. Phil. Trans. R. Soc. Lond. A 357, 3063.

Binnemans, K., Galyametdinov, Y.G., Van Deun, R., Bruce, D.W., Collinson, S.R., Polishchuk, A.P., Bikchantaev, I., Haase, W., Prosvirin, A.V., Tinchurina, L., Litvinov, I., Gubajdullin, A., Rakhmatullin, A., Uytterhoeven, K., Van Meervelt, L., 2000a. J. Am. Chem. Soc. 122, 4335.

Binnemans, K., Van Deun, R., Görller-Walrand, C., Collinson, S.R., Martin, F., Bruce, D.W., Wickleder, C., 2000b. Phys. Chem. Chem. Phys. 2, 3753.

Binnemans, K., Jongen, L., Bromant, C., Hinz, D., Meyer, G., 2000c. Inorg. Chem. 39, 5938.

Binnemans, K., Jongen, L., Görller-Walrand, C., D'Olieslager,, W., Hinz, D., Meyer, G., 2000d. Eur. J. Inorg. Chem. 1429.

Binnemans, K., Jongen, L., Görller-Walrand, C., 2001a. Phys. Chem. Chem. Phys. 3, 4796.

Binnemans, K., Lodewyckx, K., Van Deun, R., Galyametdinov, Y.G., Hinz, D., Meyer, G., 2001b. Liq. Cryst. 28, 279.

Binnemans, K., Van Deun, R., Görller-Walrand, C., Haase, W., Bruce, D.W., Malykhina, L., Galyametdinov, Y.G., 2001c. Mater. Sci. Eng. C 18, 247.

Binnemans, K., Malykhina, L., Mironov, V.S., Haase, W., Driesen, K., Van Deun, R., Fluyt, L., Görller-Walrand, C., Galyametdinov, Y.G., 2001d. Chem. Phys. Chem. 2, 680.

Binnemans, K., Moors, D., Parac-Vogt, T.N., Hinz-Hübner, D., Meyer, G., 2002a. Liq. Cryst. 29, 1209.

Binnemans, K., Lodewyckx, K., Donnio, B., Guillon, D., 2002b. Chem. Eur. J. 8, 1101.

Binnemans, K., Lodewyckx, K., Parac-Vogt, T.N., Van Deun, R., Goderis, B., Tinant, B., Van Hecke, K., Van Meervelt, L., 2003a. Eur. J. Inorg. Chem. 3028.

Binnemans, K., Sleven, J., De Feyter, S., De Schryver, F., Donnio, B., Guillon, D., 2003b. Chem. Mater. 15, 3930.

Binnemans, K., Lodewyckx, K., Donnio, B., Guillon, D., 2005. Eur. J. Inorg. Chem. 1506.

Binnemans, K., Lodewyckx, K., Cardinaels, T., Parac-Vogt, T.N., Bourgogne, C., Guillon, D., Donnio, B., 2006. Eur. J. Inorg. Chem. 150.

Boudreaux, E.A., Mulay, L.N. (Eds.), 1976. Theory and Applications of Molecular Paramagnetism. Wiley, New York.

Bouvet, M., Simon, J., 1990. Chem. Phys. Lett. 172, 299.

Boyaval, J., Hapiot, F., Li, C., Isaert, M., Warenghem, M., Carette, P., 1999. Mol. Cryst. Liq. Cryst. A 330, 1387.

Boyaval, J., Li, C., Hapiot, F., Warenghem, M., Isaert, N., Guyot, Y., Boulon, G., Carette, P., 2001. Mol. Cryst. Liq. Cryst. 359, 17.

Bruce, D.W., 1993. J. Chem. Soc. Dalton Trans. 2983.

Bruce, D.W., 1994. Adv. Mater. 6, 699.

Bruce, D.W., 1996. Bruce, D.W., O'Hare, D. (Eds.), Inorganic Materials. 2nd ed. Wiley, Chichester, p. 429 (Chapter 8).

Bruce, D.W., 2000. Acc. Chem. Res. 33, 831.

Bünzli, J.-C.G., Moret, E., Yersin, J.R., 1978. Helv. Chim. Acta 61, 762.

Cardinaels, T., Driesen, K., Parac-Vogt, T.N., Heinrich, B., Bourgogne, C., Guillon, D., Donnio, B., Binnemans, K., 2005a. Chem. Mater. 17, 6589.

Cardinaels, T., Ramaekers, J., Guillon, D., Donnio, B., Binnemans, K., 2005b. J. Am. Chem. Soc. 127, 17602.

Cardinaels, T., Ramaekers, J., Nockemann, P., Driesen, K., Van Hecke, K., Van Meervelt, L., Lei, S.B., De Feyter, S., Guillon, D., Donnio, B., Binnemans, K., 2008. Chem. Mater. 20, 1278.

Castaneda, F., Piechocki, C., Plichon, V., Simon, J., Vaxiviere, J., 1986. Electrochim. Acta 31, 131.

Chen, Y.L., Li, R.J., Wang, R.M., Ma, P., Dong, S., Gao, Y.N., Li, X.Y., Jiang, J.Z., 2007. Langmuir 23, 12549.

Clark, S., Elliott, J.M., Chipperfield, J.R., Styring, P., Sinn, E., 2002. Inorg. Chem. Commun. 5, 249.

Collings, P.J., Hird, M., 1997. Introduction to Liquid Crystals: Chemistry and Physics. Taylor and Francis, London.
Collinson, S.R., Bruce, D.W., 1999. Sauvage, J.P. (Ed.), Transition Metals in Supramolecular Chemistry. Wiley, New York, p. 285 (Chapter 7).
Collinson, S.R., Martin, F., Binnemans, K., Van Deun, R., Bruce, D.W., 2001. Mol. Cryst. Liq. Cryst. 364, 745.
Conn, C.E., Panchagnula, V., Weerawardna, A., Waddington, L.J., Kennedy, D.F., Drummond, C.J., 2010. Langmuir 26, 6240.
Corkery, R.W., 2004. Phys. Chem. Chem. Phys. 6, 1534.
Corkery, R.W., 2008. Curr. Opin. Colloid Interf. Sci. 13, 288.
Corkery, R.W., Martin, J.P.D., 1999. J. Lumin. 82, 1.
Daniels, R.B., Payne, G.L., Peterson, J., 1993a. J. Coord. Chem. 28, 23.
Daniels, R.B., Peterson, J., Porter, W.C., Wilson, Q.D., 1993b. J. Coord. Chem. 30, 357.
Davidson, P., Gabriel, J.C.P., 2005. Curr. Opin. Coll. Surf. Sci. 9, 377.
De Cian, A., Moussavi, M., Fischer, J., Weiss, R., 1985. Inorg. Chem. 24, 3162.
de Gennes, P.G., 1974. The Physics of Liquid Crystals. Oxford, Clarendon.
Demus, D., Richter, L., 1978. Leipzig: Textures of Liquid Crystals. Verlag Chemie, Weinheim.
Demus, D., Goodby, J., Gray, G.W., Spies, H.-W., Vill, V. (Eds.), 1998. In: Handbook of Liquid Crystals, vols. 1, 2A, 2B, 3. Wiley-VCH, Weinheim.
Denning, R.G., 1992. Struct. Bond. 79, 215.
Denning, R.G.J., 2007. Phys. Chem. A 111, 4125.
Diele, S., 2002. Curr. Opin. Colloid Interf. Sci. 7, 333.
Dierking, I., 2003. Textures of Liquid Crystals. Wiley-VCH, Weinheim.
Donnio, B., 2002. Curr. Opin. Colloid Interface Sci. 7, 371.
Donnio, B., Bruce, D.W., 1997. Dalton Trans. 2745.
Donnio, B., Bruce, D.W., 1999. Struct. Bond. 95, 193.
Donnio, B., Guillon, D., Deschenaux, R., Bruce, D.W., 2003. Metallomesogens. In: McCleverty, J.A., Meyer, T.J. (Eds.), Comprehensive Coordination Chemistry II. Elsevier, Oxford, p. 357.
Driesen, K., Binnemans, K., 2004. Liq. Cryst. 31, 601.
Driesen, K., Moors, D., Beeckman, J., Neyts, K., Görller-Walrand, C., Binnemans, K., 2007. J. Lumin. 127, 611.
Driesen, K., Vaes, C., Cardinaels, T., Goossens, K., Görller-Walrand, C., Binnemans, K., 2009. J. Phys. Chem. B 113, 10575.
Dzhabarov, V.I., Knyazev, A.A., Strelkov, M.V., Molostova, E.Y., Schustov, V.A., Haase, W., Galyametdinov, Y.G., 2010. Liq. Cryst. 37, 285.
Dzhabarov, V.I., Knyazev, A.A., Nikolaev, V.F., Galyametdinov, Y.G., 2011. Russ. J. Phys. A Chem. 85, 1450.
Eliseeva, S., Bünzli, J.-C.G., 2010. Chem. Soc. Rev. 39, 189.
Elliott, J.M., Clark, S., Teat, S.J., Sinn, E., 2002. Inorg. Chem. 41, 293.
Escande, A., Guénée, L., Nozary, H., Bernardinelli, G., Gumy, F., Aebischer, A., Bünzli, J.-C.G., Donnio, B., Guillon, D., Piguet, C., 2007. Chem. Eur. J. 13, 8696.
Escande, A., Guénée, L., Terrazzi, E., Jensen, T.B., Nozary, H., Piguet, C., 2010. Eur. J. Inorg. Chem. 2746.
Espinet, P., Esteruelas, M.A., Oro, L.A., Serrano, J.L., Sola, E., 1992. Coord. Chem. Rev. 117, 215.
Fairhurst, C., Fuller, S., Gray, J., Holmes, M.C., Tiddy, G.J.T., 1998. Lyotropic surfactant liquid crystals. In: Demus, D., Goodby, J., Gray, G.W., Spies, H.-W., Vill, V. (Eds.), Handbook of Liquid Crystals, vol. 3. Wiley-VCH, Weinheim, p. 341 (Chapter VII).

Fan, X.J., Colic, M., Kallay, N., Matijevic, E., 1988. Colloid Polym. Sci. 266, 380.
Fazio, D., Mongin, C., Donnio, B., Galerne, Y., Guillon, D., Bruce, D.W., 2001. J. Mater. Chem. 11, 2852.
Felder-Flesch, D., Rupnicki, L., Bourgogne, C., Donnio, B., Guillon, D., 2006. J. Mater. Chem. 16, 304.
Filarowski, A., Koll, A., Karpfen, A., Wolschann, P., 2004. Chem. Phys. 297, 323.
Gabriel, J.C.P., Davidson, P., 2000. Adv. Mater. 12, 9.
Gabriel, J.C.P., Davidson, P., 2003. Top. Curr. Chem. 226, 119.
Gainullina, F.K., Malykhina, L.V., Tinchurina, L.M., Ivanova, G.I., Binnemans, K., Galyametdinov, Y.G., 2003. Russ. J. Coord. Chem. 29, 357.
Galyametdinov, Y.G., Ivanova, G.I., Ovchinnikov, I.V., 1991. Bull. Acad. Sci. USSR Div. Chem. Sci. 40, 1109.
Galyametdinov, Y.G., Ivanova, G.I., Prosvirin, A.V., Kadkin, O., 1994a. Russ. Chem. Bull. 43, 938.
Galyametdinov, Y.G., Kharitonova, O.A., Kadkin, O.N., Ovchinnikov, I.V., 1994b. Russ. Chem. Bull. 43, 1595.
Galyametdinov, Y.G., Atanassopoulo, M., Khaaze, V., Ovchinnikov, I.V., 1995. Russ. J. Coord. Chem. 21, 718.
Galyametdinov, Y., Athanassopoulou, M.A., Griesar, K., Kharitonova, O., Soto Bustamante, E.A., Tinchurina, L., Ovchinnikov, I., Haase, W., 1996a. Chem. Mater. 8, 922.
Galyametdinov, Y.G., Ivanova, G., Ovchinnikov, I., Prosvirin, A., Guillon, D., Heinrich, B., Dunmur, D.A., Bruce, D.W., 1996b. Liq. Cryst. 20, 831.
Galyametdinov, Y.G., Ivanova, G.I., Ovchinnikov, I.V., Binnemans, K., Bruce, D.W., 1999. Russ. Chem. Bull. 48, 385.
Galyametdinov, Y.G., Jervis, H.B., Bruce, D.W., Binnemans, K., 2001a. Liq. Cryst. 28, 1877.
Galyametdinov, Y.G., Haase, W., Malykhina, L., Prosvirin, A., Nikchantaev, I., Rakhmatullin, A., Binnemans, K., 2001b. Chem. Eur. J. 7, 99.
Galyametdinov, Y.G., Wan, W., Malykhina, L., Darius, M., Haase, W., 2002a. Liq. Cryst. 29, 1360.
Galyametdinov, Y.G., Malykhina, L.V., Haase, W., Driesen, K., Binnemans, K., 2002b. Liq. Cryst. 29, 1581.
Galyametdinov, Y.G., Turanova, O.A., Van, V., Knyazev, A.A., Haase, W., 2002c. Dokl. Chem. 384, 206.
Galyametdinov, Y.G., Haase, W., Goderis, B., Moors, D., Driesen, K., Van Deun, R., Binnemans, K., 2007. J. Phys. Chem. B 111, 13881.
Galyametdinov, Y.G., Knyazev, A.A., Dzhabarov, V.I., Cardinaels, T., Driesen, K., Görller-Walrand, C., Binnemans, K., 2008. Adv. Mater. 20, 252.
Gans, P., Marchon, J.C., Reed, A., 1981. Nouv. J. Chim. 5, 203.
Getsis, A., Mudring, A.V., 2010. Z. Anorg. Allgem. Chem. 636, 1726.
Getsis, A., Mudring, A.-V., 2011. Eur. J. Inorg. Chem. 3207.
Getsis, A., Balke, B., Felser, C., Mudring, A.V., 2009. Cryst. Growth Des. 9, 4429.
Getsis, A., Tang, S.F., Mudring, A.V., 2010. Eur. J. Inorg. Chem. 2172.
Gimenez, R., Lydon, D.R., Serrano, J.L., 2002. Curr. Opin. Solid State Mater. Sci. 6, 527.
Giroud-Godquin, A.M., 1998. Coord. Chem. Rev. 178–180, 1485.
Giroud-Godquin, A.M., Maitlis, P.M., 1991. Angew. Chem. Int. Ed Engl. 30, 375.
Giroud-Godquin, A.M., Rassat, A., 1982. C. R. Acad. Sci. Ser. 2 294, 241.
Gonidec, M., Fernando, L., Vilchez, A., Esquena, J., Anabilino, D.B., Veciana, J., 2010. Angew. Chem. Int. Ed. 49, 1623.

Goodby, J., 1998. Guide to the nomenclature and classification of liquid crystals. In: Demus, D., Goodby, J., Gray, G.W., Spies, H.-W., Vill, V. (Eds.), Handbook of Liquid Crystals, vol. 1. Wiley-VCH, Weinheim, p. 17 (Chapter II).
Goossens, K., Nockemann, P., Driesen, K., Goderis, B., Görller-Walrand, C., Van Hecke, K., Van Meervelt, L., Pouzet, E., Binnemans, K., Cardinaels, T., 2008. Chem. Mater. 20, 157.
Goossens, K., Lava, K., Nockemann, P., Van Hecke, K., Van Meervelt, L., Driesen, K., Görller-Walrand, C., Binnemans, T., Cardinaels, K., 2009. Chem. Eur. J. 15, 656.
Gray, G.W., Goodby, J.W., 1984. Smectic Liquid Crystals: Textures and Structures. Leonard Hill, Glasgow, London.
Guillaud, G., Al Sadoun, M., Maitrot, M., Simon, J., Bouvet, M., 1990. Chem. Phys. Lett. 167, 503.
Guillet, E., Imbert, D., Scopelliti, R., Bünzli, J.-C.-G., 2004. Chem. Mater. 16, 4063.
Gürek, A.G., Basova, T., Luneau, D., Lebrun, C., Kol'tsov, E., Hassan, A.K., Ahsen, V., 2006. Inorg. Chem. 45, 1667.
Haase, W., Soto Bustamante, E.A., Groβmann, S., Werner, R., Galyametdinov, Y.G., 1996. Polym. Rep. 37, 64.
Hapiot, F., 2006. Liq. Cryst. 33, 921.
Hapiot, F., Boyaval, J., 2001. Magn. Reson. Chem. 39, 15.
Harnoode, C., Takamura, K., Kubota, H., Sho, K., Fujisawa, K., Kitamura, F., Ohsaka, T., Tokuda, K., 1999. Electrochemistry 67, 832.
Hasan, M., Sankhla, B.S., Misra, S.N., Kapoor, R.N.J., 1968. Prakt. Chem. 38, 313.
Hoshino, N., 1998. Coord. Chem. Rev. 174, 77.
Hudson, S.A., Maitlis, P.M., 1993. Chem. Rev. 93, 861.
Hyde, S.T., 2001. Identification of lyotropic liquid crystalline mesophases. In: Holmberg, K. (Ed.), Handbook of Applied Surface and Colloid Chemistry. Wiley, New York, p. 299 (Chapter 16).
Iball, J., Low, J.N., Weakley, T.J.R., 1974. J. Chem. Soc. Dalton Trans. 2021.
Jensen, J.B., Terrazzi, E., Donnio, B., Guillon, D., Piguet, C., 2008. Chem. Commun. 181.
Jensen, T.B., Terrazzi, E., Buchwalder, K.L., Guénée, L., Nozary, H., Schenk, K., Heinrich, B., Donnio, B., Piguet, C., 2010. Inorg. Chem. 49, 8601.
Jiang, J.Z., Liu, R.C.W., Mak, T.C.W., Chan, T.W.D., Ng, D.K.P., 1997. Polyhedron 16, 515.
Jiang, J.Z., Xie, J.L., Ng, D.K.P., Yan, Y., 1999. Mol. Cryst. Liq. Cryst. A 337, 385.
Jongen, L., Binnemans, K., 2003. J. Rare Earths 21, 101.
Jongen, L., Binnemans, K., Hinz, D., Meyer, G., 2001a. Liq. Cryst. 28, 819.
Jongen, L., Binnemans, K., Hinz, D., Meyer, G., 2001b. Liq. Cryst. 28, 1727.
Jongen, L., Binnemans, K., Hinz, D., Meyer, G., 2001c. Mater. Sci. Eng. C 18, 199.
Jongen, L., Hinz, D., Meyer, G., Binnemans, K., 2001d. Chem. Mater. 13, 2243.
Jongen, L., Meyer, G., Binnemans, K., 2001e. J. Alloys Comp. 323, 142.
Jongen, L., Goderis, B., Dolbnya, I., Binnemans, K., 2003. Chem. Mater. 15, 212.
Jongen, L., Goderis, B., Dolbnya, I.P., Binnemans, K., 2004. J. Rare Earths 22, 193.
Kahn, M.L., Rajendiran, T.M., Jeannin, Y., Mathonière, C., Kahn, O., 2000. C. R.Acad. Sci. II C 3, 131.
Kanazawa, A. 2009, SPIE newsroom, doi: 10.1117/2.1200901.1471.
Kelker, H., Hatz, R., 1980. Handbook of Liquid Crystals. Verlag Chemie, Weinheim.
Kharitonova, O.A., Prosvirin, A.V., Galyametdinov, Y.G., Ovchinnikov, I.V., 1996. Russ. Chem. Bull. 45, 2213.
Knyazev, A.A., Lobkov, V.S., Galyametdinov, Y.G., 2004. Russ. Chem. Bull. 53, 942.
Knyazev, A.A., Galyametdinov, Y.G., Goderis, B., Driesen, K., Goossens, K., Görller-Walrand, C., Binnemans, K., Cardinaels, T., 2008. Eur. J. Inorg. Chem. 756.

Knyazev, A.A., Dzhabarov, V.I., Lapaev, D.V., Lobkov, V.S., Galyametdinov, Y.G., 2010. Russ. J. Gen. Chem. 80, 756.
Knyazev, A.A., Dzhabarov, V.I., Molostova, E.Y., Lapaev, D.V., Lobkov, V.S., Galyametdinov, Y.G., 2011. Russ. J. Phys. Chem. A 85, 1270.
Koll, A., Karpfen, A., Wolschann, P., 2007. J. Mol. Struct. 844, 268.
Komatsu, T., Ohta, K., Fujimoto, T., Yamamoto, I., 1994a. J. Mater. Chem. 4, 533.
Komatsu, T., Ohta, K., Watanabe, T., Ikemoto, H., Fujimoto, T., Yamamoto, I., 1994b. J. Mater. Chem. 4, 537.
Kumar, P.A., Pisipati, V.G.K.M., 2000. Synth. React. Inorg. Met. Org. Chem. 30, 1099.
Kumari, S., Singh, A.K., Kumar, K.R., Sridhar, B., Rao, T.R., 2009a. Inorg. Chim. Acta 362, 4205.
Kumari, S., Singh, A.K., Rao, T.R., 2009b. Mater. Sci. Eng. C 29, 2454.
Labes, M. M. (1979). US Patent 4, 176, 918.
Lapaev, D.V., Nikoforov, V.G., Knyazev, A.A., Dzhabarov, V.I., Lobkov, V.S., Salikhov, K.M., Galyametdinov, Y.G., 2008. Opt. Spectrosc. 104, 851.
Lapaev, D.V., Nikiforov, V.G., Safiullin, G.M., Galyaviev, I.G., Dzabarov, V.I., Knyazev, A.A., Lobkov, V.S., Galyametdinov, Y.G., 2009. J. Struct. Chem. 50, 775.
Larrabee, R. D. (1976). US Patent 3, 960, 753.
Laschat, S., Baro, A., Steinke, N., Giesselmann, F., Hagele, C., Scalia, G., Judele, R., Kapatsina, E., Sauer, S., Schreivogel, A., Tosoni, M., 2007. Angew. Chem. Int. Ed. 46, 4832.
Lavrenkov, P.N., Evlampieva, N.P., Barabanov, V.P., Galyametdinov, Y.G., 2005. Russ. J. Phys. Chem. 79, 408.
Li, H.L., Bu, W.F., Qi, W., Wu, L.X., 2005a. J. Phys. Chem. B 109, 21669.
Li, W., Bu, W.F., Li, H.L., Wu, L.X., Li, M., 2005b. Chem. Commun. 3785.
Li, R.J., Ma, P., Dong, S., Chen, Y.L., Li, X.Y., Jiang, J.Z., 2007. Inorg. Chem. 46, 11397.
Li, W., Yin, S.Y., Wang, J.F., Wu, L.X., 2008a. Chem. Mater. 20, 514.
Li, J.J., Yang, Y.T., Liu, X.J., Zhang, S.Y., Zhang, Z.N., 2008b. J. Rare Earths 26, 320.
Lis, S.J., 2000. Alloys Compd. 300–301, 88.
Liu, W., Jiang, J.Z., Du, D., Arnold, D.P., 2000. Aust. J. Chem. 53, 131.
Liu, G.Z., Conn, C.E., Drummond, C.J., 2009. J. Phys. Chem. B 113, 15949.
Liu, G.Z., Conn, C.E., Waddington, L.J., Mudie, S.T., Drummond, C.J., 2010. Langmuir 26, 2383.
Lodewyckx, K., Van Deun, R., Binnemans, K., 2001. Mater. Sci. Eng. C 18, 217.
Lychev, A.A., Mikhalev, V.A., Suglobov, D.N., 1990. Sov. Radiochem. 32, 158.
Maeda, F., Hatsusaka, K., Ohta, K., Kimura, M., 2003. J. Mater. Chem. 13, 243.
Malykhina, L.V., Prosvirin, A.V., Haase, W., Galyametdinov, Y., 2001. Russ. Chem. Bull. 50, 488.
Marcos, M., Giménez, R., Serrano, J.L., Donnio, B., Heinrich, B., Guillon, D., 2001. Chem. Eur. J. 7, 1006.
Marcos, M., Omenat, A., Barbera, J., Duran, F., Serrano, J.L., 2004. J. Mater. Chem. 14, 3321.
Marques, E.F., Burrows, H.D., Miguel, M.D., 1998. J. Chem. Soc., Faraday Trans. 94, 1729.
Martin, F., Collinson, S.R., Bruce, D.W., 2000. Liq. Cryst. 27, 859.
McKeown, N.B., 1998. Phthalocyanine Materials: Synthesis, Structure and Function. Cambridge University Press, Cambridge.
Mehrotra, R.C., Misra, T.N., Misra, S.N., 1966. J. Indian Chem. Soc. 43, 61.
Mikhalev, V.A., Shcherbakov, V.A., 1985a. Zh. Obsh. Khim. 55, 1223.
Mikhalev, V.A., Shcherbakov, V.A., 1985b. Zh. Obsh. Khim. 55, 1229.
Mikhalev, V.A., Shcherbakov, V.A., 1986. Zh. Obsh. Khim. 56, 541.
Mironov, V.S., Galyametdinov, Y.G., Ceulemans, A., Binnemans, K., 2000. J. Chem. Phys. 113, 10293.

Mironov, V.S., Galyametdinov, Y.G., Ceulemans, A., Görller-Walrand, C., Binnemans, K., 2001. Chem. Phys. Lett. 345, 132.
Mironov, V.S., Galyametdinov, Y.G., Ceulemans, A., Görller-Walrand, C., Binnemans, K., 2002. J. Chem. Phys. 116, 4673.
Misra, S.N., Misra, T.N., Mehrotra, R.C., 1963a. J. Inorg. Nucl. Chem. 25, 195.
Misra, S.N., Misra, T.N., Mehrotra, R.C., 1963b. J. Inorg. Nucl. Chem. 25, 201.
Misra, S.N., Kiran, N., Talale, G., 1987. Indian J. Chem. A 26, 309.
Miwa, H., Kobayashi, N., Ban, K., Ohta, K., 1999. Bull. Chem. Soc. Jpn. 72, 2719.
Moghaddam, M.J., de Campo, L., Waadington, L.J., Drummond, C.J., 2010. Soft Matter 6, 5915.
Monk, P.M.S., Mortimer, R.J., Rosseinsky, D.R., 1995. Electrochromism. VCH, Weinheim.
Mukai, H., Yokokawa, M., Hatsusaka, K., Ohta, K., 2010. Liq. Cryst. 37, 13.
Naito, R., Ohta, K., Shirai, H., 2001. J. Porph. Phthalo. 5, 44.
Nakai, T., Ban, K., Ohta, K., Kimura, M., 2002. J. Mater. Chem. 12, 844.
Nananishi, T., Yilmaz, I., Nakashima, N., Kadish, K.M., 2003. J. Phys. Chem. B 107, 12789.
Nekelson, F., Monobe, H., Shimizu, Y., 2006. Chem. Commun. 3874.
Nekelson, F., Monobe, H., Shiro, M., Shimizu, Y., 2007a. J. Mater. Chem. 17, 2607.
Nekelson, F., Monobe, H., Shimizu, Y., 2007b. Mol. Cryst. Liq. Cryst. 47 (9), 1243.
Neve, F., 1996. Adv. Mater. 8, 277.
Nguyen, H.T., Destrade, C., Malthete, J., 1997. Adv. Mater. 9, 375.
Nicholson, M.M., 1982. Ind. Eng. Chem. Prod. Res. Dev. 21, 261.
Novikova, N.N., Zheludeva, S.I., Stepina, N.D., Tolstikhina, A.L., Gaynutdinov, R.V., Haase, W., Erko, A.I., Knyazev, A.A., Galyametdinov, Y.G., 2009. Appl. Phys. A 94, 461.
Novkova, N.N., Zheludeva, S.I., Stepina, N.D., Tolstikhina, A.L., Gaynutdinov, R.V., Erko, A.I., Haase, W., Galyametdinov, Y.G., 2006. Cryst. Rep. 51, 1041.
Nozary, H., Piguet, C., Tissot, P., Bernardinelli, G., Deschenaux, R., Vilches, M.-T., 1997a. Chem. Commun. 2101.
Nozary, H., Piguet, C., Tissot, P., Bernardinelli, G., Deschenaux, R., Vilches, M.-T., 1997b. Chem. Commun. 2249.
Nozary, H., Piguet, C., Tissot, P., Bernardinelli, G., Bünzli, J.-C.G., Deschenaux, R., Guillon, D., 1998. J. Am. Chem. Soc. 120, 12274.
Nozary, H., Piguet, C., Rivera, J.-P., Tissot, P., Bernardinelli, G., Vulliermet, N., Weber, J., Bünzli, J.-C.G., 2000. Inorg. Chem. 39, 5286.
Nozary, H., Piguet, C., Rivera, J.-P., Tissot, P., Morgantini, P.-Y., Weber, J., Bernadinelli, G., Bünzli, J.-C.G., Deschenaux, R., Donnio, B., Guillon, D., 2002. Xhem. Mater. 14, 1075.
Nozary, H., Torelli, S., Guénée, L., Terazzi, E., Bernardinelli, G., Donnio, B., Guillon, D., Piguet, C., 2006. Inorg. Chem. 45, 2989.
Oriol, L., Serrano, J.L., 1995. Adv. Mater. 7, 348.
Oriol, L., Pinol, M., Serrano, J.L., 1997. Progr. Polymer Sci. 22, 873.
Orti, E., Brédas, J.L., Clarisse, C., 1990. J. Phys. Chem. 92, 1228.
Ovchinnikov, I.V., Galyametdinov, Y.G., Prosvirin, A.V., 1995. Russ. Chem. Bull. 44, 768.
Palewska, K., Miniewicz, A., Bartkiewicz, S., Legendziewicz, J., Strek, W., 2007. J. Lumin. 124, 265.
Peacock, R.D., Weakley, T.J.R.J., 1971. Chem. Soc. A 1836.
Piechocki, C. (1985) Matériaux a base de phthalocyanines substituées crystallines liquids. PhD thesis, Université Pierre et Marie Curie –Paris VI (France).
Piechocki, C., Simon, J., André, J.-J., Guillon, D., Petit, P., Skoulios, A., Weber, P., 1985. Chem. Phys. Lett. 122, 124.
Piguet, C., Bünzli, J.-C.G., Donnio, B., Guillon, D., 2006. Chem. Commun. 3755.

Polishchuk, A.P., Timofeeva, T.V., 1993. Russ. Chem. Rev. 62, 291.
Pople, M.T., 2008. Polyoxometallates. In: Gschneidner Jr., K.A., Bünzli, J.-C., Pescharsky, V. (Eds.), Handbook on the Physics and Chemistry of Rare Earths, vol. 38. Elsevier, Amsterdam (Chapter 240).
Puntus, L.N., Schenk, K.J., Bünzli, J.-C.G., 2005. Eur. J. Inorg. Chem. 4739.
Qi, M.H., Liu, G.F., 2003. J. Phys. Chem. B 107, 7640.
Qi, M.H., Liu, G.F., 2004. J. Porph. Phthalo. 8, 1187.
Rai, A.K., Parashar, G.K., 1979. Synth. React. Inorg. Met. Org. Chem. 9, 301.
Rao, N.V.S., Paul, M.K., Rao, T.R., Prasad, A., 2002. Liq. Cryst. 29, 1243.
Rao, N.V.S., Choudhury, T.D., Deb, R., Paul, M.K., Rao, T.R., Francis, T., Smalyukh, I.I., 2010. Liq. Cryst. 37, 1393.
Ricciardi, G., Lelj, F., Bonosi, F., 1993. Chem. Phys. Lett. 215, 541.
Seddon, J.M., 1998. Structural studies of liquid crystals by X-ray diffraction. In: Demus, D., Goodby, J.W., Gray, G.W., Spiess, H.-W., Vill, V. (Eds.), Handbook of Liquid Crystals. Volume 1: Fundamentals. Wiley-VCH, Weinheim, p. 635.
Selivanova, N.M., Lobkov, V.S., Barabanov, V.P., Salikhov, K.M., Haase, W., Galyametdinov, Y.G., 2005. Dokl. Chem. 401, 353.
Selivanova, N.M., Osipova, V.V., Galyametdinov, Y.G., 2006. Russ. J. Phys. Chem. 80, 649.
Selivanova, N.M., Gnezdilov, O.I., Konov, A.B., Zuev, Y.F., Galyametdinov, Y.G., 2008. Russ. Chem. Bull. 57, 506.
Selivanova, N.M., Galeeva, A.I., Konov, A.B., Gnezdilov, O.I., Salikhov, K.M., Galyametdinov, Y.G., 2010a. Russ. J. Phys. Chem. A 84, 802.
Selivanova, N.M., Galeeva, A.I., Vandyukov, A.E., Galyametdinov, Y.G., 2010b. Russ. Chem. Bull. 59, 469.
Serrano, J.L. (Ed.), 1996. Metallomesogens, Synthesis, Properties and Applications. VCH, Weinheim.
Serrano, J.L., Sierra, T., 2003. Coord. Chem. Rev. 242, 73.
Sessler, J.L., Callaway, W.B., Dudek, S.P., Date, R.W., Bruce, D.W., 2004. Inorg. Chem. 43, 6650.
Sessler, J.L., Melfi, P.J., Tomat, E., Callaway, W., Huggins, M.T., Gordon, P.L., Keogh, D.W., Date, R.W., Bruce, D.W., Donnio, B., 2006. J. Alloys Comp. 418, 171.
Seurin, P., Guillon, D., Skoulios, A., 1981. Mol. Cryst. Liq. Cryst. 65, 85.
Shabatina, T.I., Vlasov, A.V., Vovk, E.V., Stufkens, D.J., Sergeev, G.B., 2000. Spectrochim. Acta A 56, 2539.
Shabatina, T.I., Vlasov, A.V., Sergeev, G.B., 2001. Mol. Cryst. Liq. Cryst. 356, 149.
Shabatina, T.I., Vlasov, A.V., Konyukhov, S.V., Ermilov, A.Y., Nemukhin, A.V., Sergeev, G.B., 2005. Mol. Cryst. Liq. Cryst. 440, 317.
Singh, M.K., Singh, B., Dhar, R., Agrawal, V.K., 2005. Phase Trans. 78, 495.
Skrylev, L.D., Sazonova, V.F., Seifullina, I.I., 1980. Zh. Neorg. Khim. 25, 2948.
Sleven, J., Görller-Walrand, C., Binnemans, K., 2001. Mater. Sci. Eng. C 18, 229.
Sonin, A.A., 1998. J. Mater. Chem. 8, 2557.
Suarez, S., Mamula, O., Imbert, D., Piguet, C., Bünzli, J.-C.G., 2003. Chem. Commun. 1226.
Suarez, S., Imbert, D., Gumy, F., Piguet, C., Bünzli, J.-C.G., 2004. Chem. Mater. 16, 3257.
Suarez, S., Mamula, O., Scopelliti, R., Donnio, B., Guillon, D., Terazzi, E., Piguet, C., Bünzli, J.-C.G., 2005. New. J. Chem. 29, 1323.
Swager, T.M., Zheng, H.X., 1995. Mol. Cryst. Liq. Cryst. 260, 301.
Templer, R.H., 1998. X-ray characterization of liquid crystals: Instrumentation. In: Demus, D., Goodby, J.W., Gray, G.W., Spiess, H.-W., Vill, V. (Eds.), Handbook of Liquid Crystals. Volume 1: Fundamentals. Wiley-VCH, Weinheim, p. 619.

Terazzi, E., Bénech, J.-M., Rivera, J.-P., Bernardinelli, G., Donnio, B., Guillon, D., Piguet, C., 2003. Dalton Trans. 769.

Terazzi, E., Torelli, S., Bernardinelli, G., Rivera, J.-P., Bénech, J.-M., Bourgogne, C., Donnio, B., Guillon, D., Imbert, D., Bünzli, J.-C.G., Pinto, A., Jeannerat, D., Piguet, C., 2005. J. Am. Chem. Soc. 127, 888.

Terazzi, E., Suarez, S., Torelli, S., Nozary, H., Imbert, D., Mamula, O., Rivera, J.-P., Guillet, E., Bénech, J.-M., Bernardinelli, G., Scopelliti, R., Donnio, B., Guillon, D., Bünzli, J.-C.G., Piguet, C., 2006a. Adv. Funct. Mater. 16, 157.

Terazzi, E., Bocquet, B., Campidelli, S., Donnio, B., Guillon, D., Deschenaux, R., Piguet, C., 2006b. Chem. Commun. 13, 2922.

Terazzi, E., Guénée, L., Morgantini, P.Y., Bernardinelli, G., Donnio, B., Guillon, D., Piguet, C., 2007. Chem. Eur. J. 13, 1674.

Tomilin, M.G., Kuznetsov, P.A., Galyametdinov, Y.G., 2005. Mol. Cryst. Liq. Cryst. 438, 91.

Toupance, T., Bassoul, P., Mineau, L., Simon, J., 1996. J. Phys. Chem. 100, 11704.

Toupance, T., Plichon, V., Simon, J., 1999. New. J. Chem. 23, 1001.

Tran-Thi, T.H., Markovitsi, D., Even, R., Simon, J., 1987. Chem. Phys. Lett. 139, 207.

Tschierske, C., 1998. J. Mater. Chem. 8, 1485.

Turanov, A.N., Ovchinnikov, I.V., Galyametdinov, Y.G., Ivanova, G.I., Goncharov, V.A., 1999. Russ. Chem. Bull. 48, 690.

Turanov, A., Ovchinnikov, I., Galyametdinov, Y., Bruce, D., 2001. Liq. Cryst. 28, 845.

Turanova, O.A., Galyametdinov, Yu.G., 2006. Russ. J. Gen. Chem. 76, 1095.

Turanova, O.A., Turanov, A.N., Ovchinnikov, I.V., Galyametdinov, Yu.G., 2005. Russ. J. Coord. Chem. 31, 757.

Vaisnoras, R., Pajediene, S., Pajeda, S., Martunas, D., Ravinskas, J., Galyametdinov, J., Gasparini, F., Rogante, M., Rustichelli, F., Yang, B., 1998. Proc. SPIE 3319, 174.

van de Craats, A.M., Warman, J.M., Hasebe, H., Naito, R., Ohta, K., 1997. J. Phys. Chem. B 101, 9224.

Van Deun, R., Binnemans, K., 2000. J. Alloys Comp. 303–304, 146.

Van Deun, R., Binnemans, K., 2001a. Liq. Cryst. 28, 621.

Van Deun, R., Binnemans, K., 2001b. Mater. Sci. Eng. C 18, 211.

Van Deun, R., Binnemans, K., 2003. Liq. Cryst. 30, 479.

Van Deun, R., Moors, D., De Fré, B., Binnemans, K., 2003a. J. Mater. Chem. 13, 1520.

Van Deun, R., Parac-Vogt, T.N., Van Hecke, K., Van Meervelt, L., Binnemans, K., Guillon, D., Donnio, B., 2003b. J. Mater. Chem. 13, 1639.

Van Meervelt, L., Uytterhoeven, K., Van Deun, R., Moors, D., Binnemansl, 2003a, Z. Krist. New. Cryst. Struct. 218, 118.

Van Meervelt, L., Uytterhoeven, K., Van Deun, R., Binnemans, K., 2003b. Z. Krist., New Cryst. Struct. 218, 488.

Vlasov, A.V., Shabatina, T.I., Ivanov, A.Y., Sheina, G.G., Nemukhin, A.V., Sergeev, G.B., 2005. Mendeleev Commun. 10.

Wang, K.Z., Huang, C.H., Xu, G.X., Zhou, Q.F., 1995. Solid State Commun. 95, 223.

Weiss, S.M., Zhang, J., Fauchet, M.P., Seregin, V.V., Coffer, J.L., 2007. Appl. Phys. Lett. 90, 031112.

Wickleder, M.S., 2002. Chem. Rev. 102, 2011.

Wolff, H.Z., 1905. Anorg. Chem. 45, 7.

Yamaguchi, M., Tanimoto, Y. (Eds.), 2006. Magneto-Science, Magnetic Field Effects on Materials: Fundamentals and Applications. Springer, Berlin.

Yamase, T., 1998. Chem. Rev. 98, 307.

Yamase, T., 2009. Luminescence of polyoxometallolanthanates. In: Gschneidner Jr., K.A., Bünzli, J.-C., Pescharsky, V. (Eds.), Handbook on the Physics and Chemistry of Rare Earths, vol. 39. Elsevier, Amsterdam (Chapter 243).

Yang, Y.T., Driesen, K., Nockemann, P., Van Hecke, K., Van Meervelt, L., Binnemans, K., 2006. Chem. Mater. 18, 3698.

Yang, Y.T., Li, J.J., Liu, X.J., Driesen, K., Nockemann, P., Binnemans, K., 2008a. ChemPhysChem 9, 600.

Yang, Y.T., Li, J.J., Zhang, S.Y., Liu, J., 2008b. Chin. J. Chem. Phys. 21, 99.

Yang, Y.T., Liu, X.J., Nakamura, A., Binnemans, K., Liu, J., 2008c. J. Phys. Chem. B 112, 5291.

Yelamaggad, C.V., Prabhu, R., Shanker, G., Bruce, D.W., 2009. Liq. Cryst. 36, 247.

Yin, S.Y., Sun, H., Yan, Y., Li, W., Wu, L.X., 2009. J. Phys. Chem. B 113, 2355.

Yoshino, K., Lee, S.B., Sonoda, T., Kawagishi, H., Hidayat, R., Nakayama, K., Ozaki, M., Ban, K., Nishizawa, K., Ohta, K., Shirai, H., 2000. J. Appl. Phys. 88, 7137.

Yu, L.J., Labes, M.M., 1977. App. Phys. Lett. 31, 719.

Yu, M., Liu, G.F., Cheng, Y.C., Xu, W.Q., 2005. Liq. Cryst. 32, 771.

Yusov, A.B., Shilov, V.P., 1999. Radiochemistry 41, 1.

Zakharova, L.Y., Valeeva, F.G., Ibragimova, A.R., Kudryavtseva, L.A., Konovalov, A.I., Bruce, D.W., Gainullina, F.K., Galyametdinov, Y.G., 2002. J. Mol. Liq. 100, 229.

Zakharova, L.Y., Ibragimova, A.R., Valeeva, F.G., Kudryavtseva, L.A., Konovalov, A.I., Zakharov, A.V., Selivanova, N.M., Osipova, V.V., Strelkov, M.V., Galyametdinov, Y.G., 2007. J. Phys. Chem. C 111, 13839.

Zhang, T.R., Lu, R., Zhan, H.Y., Xue, P.C., Feng, W., Liu, X.L., Zhao, B., Zhao, Y.Y., Li, T.J., Yao, J.N.J., 2003. Mater. Chem. 13, 580.

Zhang, T.R., Spitz, C., Antonietti, M., Faul, C.F.J., 2005. Chem. Eur. J. 11, 1001.

Zhang, Y., Pan, N., Xue, Q.B., Bai, M., Jiang, J.Z., 2006. J. Porph. Phthalo. 10, 1132.

Zhang, Y., Jiang, W.L., Jiang, J.Z., Xue, Q.B., 2007. J. Porph. Phthalo 11, 100.

Zhang, T.R., Brown, J., Oakley, R., Faul, C.F.J., 2009a. Curr. Opin. Colloid Interfase Sci. 14, 62.

Zhang, T.R., Liu, S.Q., Kurth, D.G., Faul, C.F.J., 2009b. Adv. Funct. Mater. 19, 642.

Zhao, Z.X., Liu, G.F., 2002. Liq. Cryst. 29, 1335.

Zheng, H.X., Swager, T.M.J., 1994. Am. Chem. Soc. 116, 761.

Zolin, V.F., Koreneva, L.G., Samokhina, M.A., 1980. Zh. Prikl. Spektr. 33, 887.

Chapter 255

Recycling of Rare Earths from Scrap

Mikiya Tanaka, Tatsuya Oki, Kazuya Koyama, Hirokazu Narita and Tetsuo Oishi

Research Institute for Environmental Management Technology, National Institute of Advanced Industrial Science and Technology (AIST), 16-1 Onogawa, Tsukuba, Ibaraki, Japan

Chapter Outline

1. INTRODUCTION

Owing to peculiar physical and chemical properties, rare-earth elements are used in various materials and consumer products, and thus, have become indispensable for our modern life. The world-wide rare-earth oxide consumption by the market sector in 2008 (Goonan, 2011) shown in Fig. 1 indicates that rare earths are used in glass industry, catalysts, neodymium magnets, battery alloys and other metallurgical additives, phosphors, ceramics, and other. According to the world mine production of rare earth in 2009 (Cordier, 2011),

Handbook on the Physics and Chemistry of Rare Earths, Vol. 43.
http://dx.doi.org/10.1016/B978-0-444-59536-2.00002-7

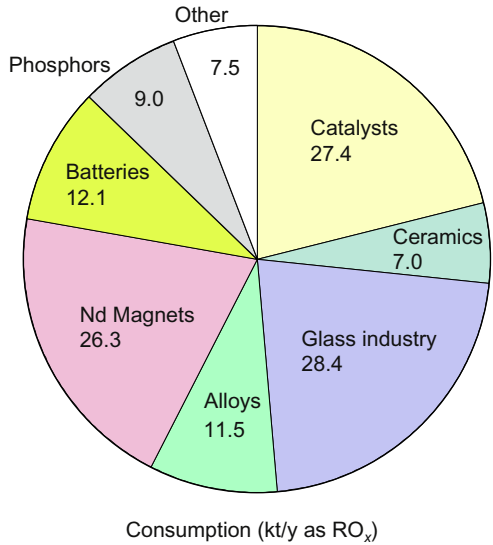

FIGURE 1 Worldwide rare-earth consumption by market sector in 2008. Data taken from Goonan (2011).

129,000 tons of rare earth (as oxide basis) were produced in China, which amounted to over 97% of the world production (130,000 tons) as shown in Fig. 2. Beginning from 2010, China restricts the exports of rare-earth raw materials in order to meet a rapidly growing domestic demand for rare earths and to protect environment caused by mining operations; Environmental regulations in China are becoming more stringent every year, which also increases a supply risk of rare earths (DOE, 2011).

Even though light lanthanides (La through Eu) are generally more abundant in the earth crust, and they find large-scale practical use, all of the rare earth elements are critically important for consumers. For example, addition of a few percent of dysprosium to a neodymium magnet is known to increase its coercivity, and therefore, dysprosium is necessary for electric motors and electric power generators. With increasing demand for the neodymium magnets from now on, dysprosium will become more and more important. Morimoto et al. (2011) estimated the annual demand for dysprosium in Japan through 2020 as shown in Fig. 3. The demand for dysprosium is estimated to increase every year and will exceed 800 tons in 2020, up from 400 tons in 2011. Its supply, however, is uncertain because most of its production is limited to a single source in southern China.

In order to mitigate supply risks, resuscitation of closed mines and exploitation of new mines would be effective in short and long terms, respectively. Studies on replacement materials and materials with decreased rare-earth content are also necessary together with establishing an effective stockpiling

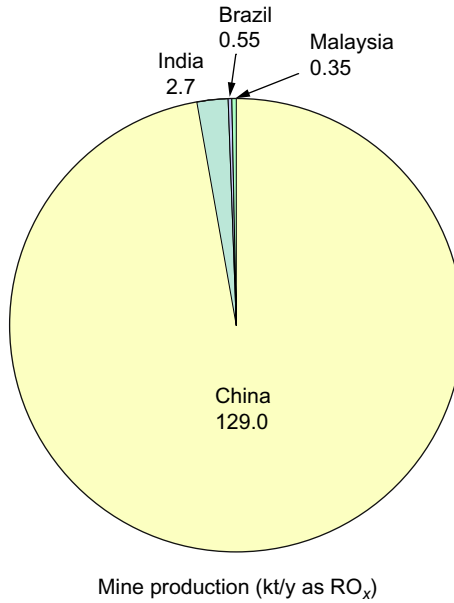

FIGURE 2 Worldwide rare-earth mine production in 2009. Data taken from Cordier (2011).

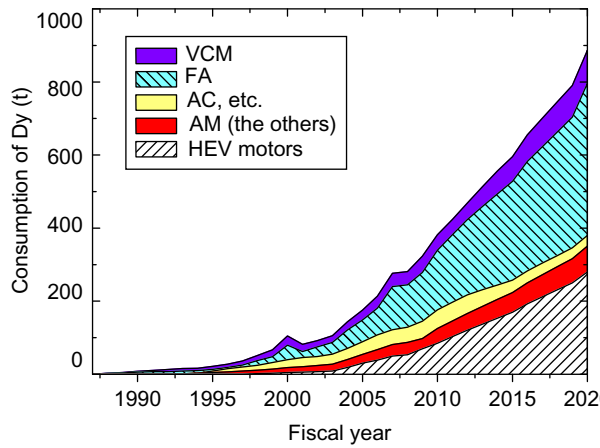

FIGURE 3 Consumption of dysprosium in the past and future in Japan slightly modified from Morimoto et al. (2011). Fiscal year is from April to March. VCM, voice coil motor used in hard disc drives; FA, factory automation; AC, etc.: air-conditioner, electric refrigerators, and electric washing machines; AM, automobiles except for the contribution of HEV motors; HEV motors, motors used for hybrid and electric vehicles.

system. Similarly, promotion of recycling is becoming extremely important. For this purpose, not only the establishment of a social system to recover rare-earth products at the end of their useful life, but also the development of highly efficient recycling technologies is required. One advantage of rare-earth recycling over processing natural ores is that wastes containing rare-earth products have generally much simpler chemical compositions than the natural ores, which eliminates or greatly simplifies the separation process. Another advantage is that the problem of managing radioactive waste, nearly always present in rare earth mining, is no longer present in recovery of rare earth from waste. Natural rare-earth ores often contain a considerable amount of thorium, which should be separated and safely disposed of during the processing. Because industrial products do not contain thorium, recovery of rare earths from waste products does not cause such a problem.

Rare-earth companies are recycling rare earths from the in-plant scrap (scrap generated during the manufacturing processes), while rare earths in the out-of-plant scrap (scrap of the industrial products) are hardly ever recycled (Goonan, 2011; JOGMEC, 2010). Although details of the rare-earth recycling employed by different companies are generally proprietary, a significant number of academic papers and proceedings has been published in order to develop the technologies for recycling both the in-plant and out-of-plant scraps. Recent brief reviews and general articles (Goonan, 2011; Horikawa and Machida, 2011; Itoh and Machida, 2011; Machida, 2003, 2004, 2009; Minowa, 2011; Nakamura, 2011; Shirayama and Okabe, 2009; Takeda, 2000) are dedicated to either general aspects of rare-earth recycling or recycling from a specific scrap material. Considering that the studies on rare-earth recycling have drastically increased recently, it is a good opportunity to thoroughly review the current state-of-the-art in recycling of rare earths.

Generally, metal recycling relies on applications of common mining and metallurgical technologies. Beneficiation (physical separation) processes that are similar to those commonly employed in mining industry play an important role in order to decrease the burden during subsequent metallurgical treatment (s), while pyro- and hydrometallurgical processes have a role in production of metals or metal compounds from scrap.

From these view points, we review recent literature on recycling of rare earths from various rare-earth scrap materials, such as permanent magnets, phosphors, secondary nickel metal hydride batteries, polishing powders, optical glass, and catalysts. The review is concerned initially with each recyclable product and then on each method used in recycling.

2. PERMANENT MAGNETS

Rare-earth permanent magnets are known to show much better magnetic properties compared to conventional Al–Ni–Co and ferrite magnets. Initially, Sm–Co magnets such as $SmCo_5$ (Hubbard et al., 1960) and Sm_2Co_{17} (Tawara

and Strnat, 1976) were developed, followed by the discovery of Nd–Fe–B magnets (Croat et al., 1984; Sagawa et al., 1984). At present, no other permanent magnet material has magnetic properties better than the Nd–Fe–B magnets. Nd–Fe–B magnets not only improve performance of final industrial products, but also minimize their size; this led to many advanced applications, such as miniature high-capacity hard disk drives (HDDs), efficient air conditioners, compact industrial motors, hybrid electric vehicles (HEVs), electric vehicles, and wind-power generation. Nd–Fe–B magnets today continue to find new applications. Typical examples of chemical compositions of rare-earth permanent magnets shown in Table 1 indicate that these magnets are indeed a significant resource of rare earths.

During the manufacturing process of the rare-earth magnets, considerable amounts of scrap and residues are generated because of cutting, grinding, and polishing. Particularly, the residue generated at the final finishing stage is often collectively referred to as "swarf" (Bounds, 1994). Chemical compositions of swarfs from Sm–Co and Nd–Fe–B magnets are shown in Tables 2 and 3, respectively (Bounds, 1994). In the case of the Nd–Fe–B magnets, up to 20–30% of the starting alloy becomes scrap and residue (Ohta, 2003). At present, the scrap and residue generated during the manufacturing process is actively recycled by material manufacturing companies. It is reported that 95% of solid scrap and 90% of powder scrap were recycled in 2003 within the NEOMAX group including plants in Japan and other countries (Ohta, 2003). Detailed recycling process in each company is generally proprietary and undisclosed, but a general flow sheet is shown in Fig. 4 (Machida, 2004; Takeda, 2000). Cutting sludge is a metallic powder coated with oxides and is thus roasted in order to completely oxidize the whole powder. The roasted product is treated by hydrometallurgical method consisting of acid dissolution and solvent extraction followed by precipitation and calcination in order to obtain rare earths as oxides or fluorides. The rare-earth metals

TABLE 1 Typical Examples of the Chemical Composition of Rare-Earth Magnets

	Chemical composition (mass%)					
Magnet	*Sm*	*Co*	*Fe*	*Cu*	*Zr*	Reference
$SmCo_5$	35.3	64.7				Sanuki et al. (1995)
Sm_2Co_{17}	29.7	46.3	14.9	7.5	1.3	
	Nd	*Dy*	*Fe*	*B*	*Others*	
NdFeB	25	4	69	1	1	Minowa (2011)

TABLE 2 Average Composition (Mass%) of Sm_2Co_{17} Magnet Swarf (Bounds, 1994)

Sm	Co	Fe	Zr	Cu	Al
24.1	46.9	15.5	3.0	3.8	0.08
Mg	**Ca**	**C**	**N**	**O**	**Si**
0.03	0.18	0.75	0.15	5.3	0.18

TABLE 3 Average Composition (Mass%) of $Nd_2Fe_{14}B$ Magnet Swarf (Bounds, 1994)

Nd	Dy	B	Fe	Al	Ca
32.4	1.5	1.04	56.2	0.35	0.08
C	**N**	**O**	**Si**		
0.90	0.15	7.12	0.26		

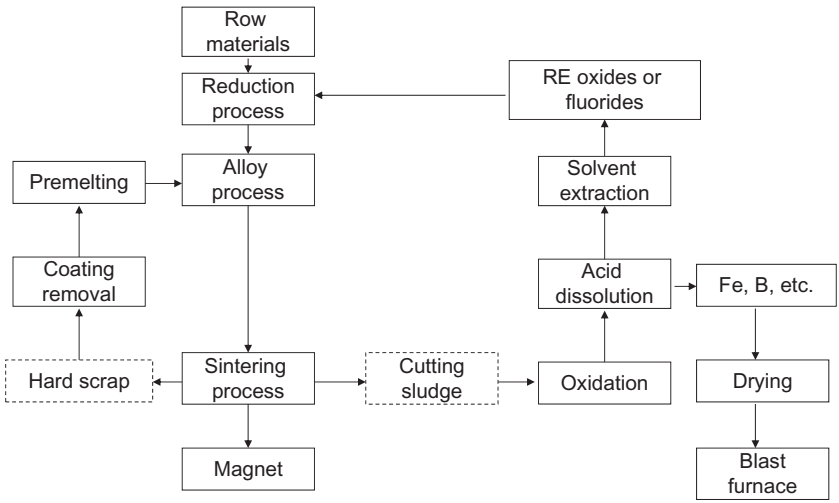

FIGURE 4 General flow sheet for in-plant recycling of neodymium magnet scrap (Machida, 2004; Takeda, 2000).

are recovered from these oxides or fluorides by conventional molten salt electrolysis or thermal reduction process. Solid scrap is generally recovered as alloy via high-frequency vacuum melting. Nickel- or aluminum-chromate plating on the magnet surface will cause problems in magnetic properties of the Nd–Fe–B sintered magnets produced from solid scrap and thus should be removed in advance by a wet process or mechanical processes. However, these removal processes are not economical at present and therefore are seldom applied.

On the other hand, very small quantities of magnets mounted in the products that reached the end of their useful life are recovered because of the following problems: (i) In motors, the magnets are tightly mounted and are very difficult to separate them from other materials. (ii) The quantity of the magnet itself is generally much lower than that of the whole product. (iii) Multiple kinds of magnets would be collected from the waste products. (iv) The magnets are often coated with nickel in order to prevent rusting.

This section reviews the studies related to the rare-earth recycling from the Sm–Co and Nd–Fe–B magnets in terms of the physical separation, and hydro- and pyrometallurgical methods including molten salt electrolysis.

2.1. Physical Separation

The recovery of magnetic materials with physical separation methods is principally considered at this time for the following three products: HDDs, air-conditioner compressors, and direct drive (DD) motors of laundry machines. In addition, efforts are underway in order to recycle relatively large magnets used in automobiles and industrial machines; however, these are excluded from the discussion here because the methods involved do not typically employ mass separation but are rather individual, employing dismantling by hands with only some machine assistance.

2.1.1. Demagnetization

As the initial step of the physical separation process, the target component must be liberated (isolated as a magnet-only component) through dismantling and/or crushing. However, Nd–Fe–B magnets are very strong showing surface flux density of about 0.4 T. Because the magnet in a motor is strongly attached to a steel plate, dismantling of the motor becomes very difficult. When the waste products using the magnets are crushed by conventional methods, the magnets very strongly attach to the inside of the crusher, typically leading to difficulties such as blockage of the screen mesh. In addition, even if the magnetic material leaves the crusher, it would rapidly turn into a magnetic coagulate by attracting the crushed steel plates located nearby. For these reasons, demagnetization is usually applied as an initial stage of the physical separation process.

Both thermal and nonthermal methods, which take advantage, respectively, of the Curie point and the magnetic field, are two examples of industrial demagnetization. Owing to its temperature characteristics, Nd–Fe–B magnets are not suited for use at high temperatures; thus, its magnetic force is easily diminished by heating, even at low temperatures around 350 °C. The thermal method can treat large amounts of the waste products with relatively simple equipment but has the disadvantage that heating of a large volume of nonmagnetic portion is required, which is useless, because the content of the magnets in the product is often quite low. The nonthermal methods can treat the product at ambient temperature in a short time; however, the apparatus is generally expensive and cannot treat a large amount of waste at the same time. Thus, each method has its advantages and disadvantages, and the choice of demagnetization method usually depends on the circumstances. A demagnetizing apparatus employing the magnetic field opposite to the magnetization process has been manufactured and is considered to be applicable to practical use (Miura, 2011).

2.1.2. *Hard Disk Drives*

HDDs generally use Nd–Fe–B magnets in their voice coil motors (VCMs). The Hitachi group has developed a dismantling apparatus for HDDs (Baba et al., 2010; Nemoto et al., 2011). The parts in an HDD are connected by small screws so that manual dismantling takes long time and decreases the productivity (profitability). In addition, the positions of the screws depend on HDD manufacturers and model years, although the basic structures are similar. In light of these difficulties, they developed a method to dismantle HDDs into their constituent parts by initially loosening the screws through impact and vibration for about 30 min and then isolating the magnet as a part of the VCM. The apparatus can treat 100 HDDs in one operation and 200 HDDs per hour.

Oki's group has developed a technique to recover high-purity magnetic powder from HDDs (Oki, 2010, 2011; Oki et al., 2011). Initially, a magnet die puncher (HDD-cutting separator) with a magnetic sensor, which utilizes a nonmagnetic shredder knife, was developed jointly with Kinki Industrial Co., Ltd. The position of the VCM is determined through nondestructive inspection, by detecting the leaked magnetic field of the HDD's surface with four magnetic sensors and two position sensors. After this, the HDD is placed directly under the circular nonmagnetic shredder knife, and only the VCM is removed. Like the Hitachi group's device, 200 HDDs per hour can be treated by this apparatus. The circular shredder knife is used here in order to cut the connecting point of the screw on the VCM. Although the magnet comes out slightly damaged, the body and yoke are easily separated. The use of a square nonmagnetic shredder knife minimizes the damage to the magnet. The magnetic section that is cut into a circular shape is 1/10

of the whole amount, and at this point, it is ten times denser than that before the treatment. Same authors have also developed a technique, whereby the cut out section is processed through impact crushing after thermal or nonthermal demagnetization. By selectively grinding only the magnets into fine particles in this way and collecting them by means of a screen mesh, they succeeded in collecting magnetic powder of 95–97% purity at laboratory scale.

2.1.3. Air-Conditioner Compressors

The recent performance improvement of air conditioners is mainly due to the use of Nd–Fe–B magnets in the rotors of the compressors. In contrast to HDDs, the device configurations are different among manufacturers, production years, and models. The Hitachi group has succeeded in mechanizing the process of collecting the magnets from the compressors (Baba et al., 2010; Nemoto et al., 2011). After cutting off the casing, the rotors are removed and treated by nonthermal demagnetization. The magnets are then collected through a combination of impact and natural drop. On the other hand, Mitsubishi Materials Co., after collecting the rotors from compressors in the same manner, employs thermal demagnetization at a temperature of 400–500 °C, after which the magnets are dismantled and collected using equipment such as drills (Arai, 2010; Arai et al., 2011). By this method, they have succeeded in collecting up to 100 g of Nd–Fe–B magnets from a single compressor. Wang et al. (2011) attempted to disintegrate the rotor by explosion in water. Using 10 g of explosives, both the laminated steel plate and the rotor were disintegrated, and magnetic particles were recovered through collection by a screen mesh after the disintegrated product was thermally demagnetized at 400 °C for 1 min.

2.1.4. Separation from DD Motors in Laundry Machines

Recently, Nd–Fe–B magnets have been incorporated into some DD motors for laundry machines. However, owing to their structural complexity, investigations into their physical separation have not progressed significantly. Here, a magnet is lodged in the rotor, but as the magnet is molded with resin, it is not easy to take out. Attempts to incinerate the resin by heating at a temperature of 400–500 °C, and to simultaneously demagnetize the magnet, were made by Mitsubishi Material Co. (Arai, 2010; Arai et al., 2011). Upon moderate mechanical impact, the demagnetized magnet was released from the rotor.

2.2. Hydrometallurgical Methods

2.2.1. Sm–Co Magnets

Bounds (1994) pointed out that most of the Sm-containing swarf was being processed for recovery and recycling of both the samarium and cobalt and presented a general flow sheet (Fig. 5). He summarized fundamental reactions

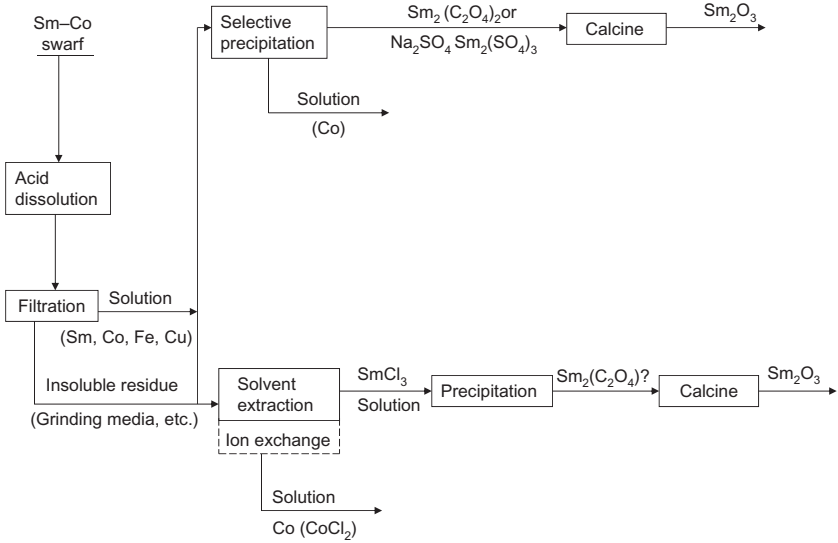

FIGURE 5 Overview of process options for Sm_2 (Co, Fe, Cu, Zr)$_{17}$ swarf (Bounds, 1994).

involved during the recycling processes. The swarf is easily dissolved by common mineral acids such as nitric, sulfuric, and hydrochloric acids. Selective precipitation of samarium from the iron-group metals is possible as oxalate and double salt typically as $Na_2SO_4{\cdot}Sm_2(SO_4)_3{\cdot}2H_2O$. Samarium can also be extracted with TBP or D2EHPA achieving separation from cobalt.

Koshimura studied the recycling processes of the Sm–Co magnet scrap by hydrometallurgical method (Koshimura, 1987, 1988; Koshimura and Yamamoto, 1983, 1984). According to the flow sheet of Koshimura (1987), the scrap is leached by sulfuric acid, and sodium sulfate is added to the obtained liquor in order to precipitate samarium as $Na_2SO_4{\cdot}Sm_2(SO_4)_3{\cdot}2H_2O$ double salt. This double salt is converted to hydroxide by treatment with ammonia solution. The obtained hydroxide is dissolved by hydrochloric acid in order to obtain samarium as samarium chloride solution from which samarium is precipitated as samarium oxalate and then recovered as samarium oxide after calcination at 800 °C. Samarium recovery was more than 95%, and the purity of the samarium oxide was better than 98%. Koshimura also studied the application of solvent extraction using D2EHPA for this purpose. Stripping of samarium from the loaded organic phase is possible with 3 kmol/m^3 hydrochloric acid (Koshimura and Yamamoto, 1983). Number of equilibrium stages required for samarium extraction was assessed by batch simulation method to be, for example, five for 99% extraction from 0.1 kmol/m^3 samarium chloride containing 0.25 kmol/m^3 hydrochloric acid. On the basis of these results, Koshimura (1988) carried out the experiment using a batch counter current extractor consisting of four extraction stages and two stripping

stages, in which the volume of one mixing tank was 2.5 dm^3. The percentage extraction of samarium reached 98–100% from the aqueous solution containing 0.1 $kmol/m^3$ samarium and 0.6 $kmol/m^3$ cobalt in 0.25 $kmol/m^3$ hydrochloric acid. Samarium was concentrated by the factor of seven after stripping. Extraction property of praseodymium during this experiment was also investigated because of the existence of alloy containing praseodymium ($Sm_{1-x}Pr_xCo_5$). It was shown that praseodymium in the organic phase was easily stripped by scrubbing with a solution containing samarium and hydrochloric acid. Using this procedure, highly pure samarium oxide was obtained.

Sato and Nanjo's group studied a process using fractional crystallization from sulfate solutions containing about 30% samarium and 50–60% cobalt (Sato et al., 1997; Wei et al., 1989). They measured the solubilities of $Sm_2(SO_4)_3$ in H_2SO_4–H_2O and $CoSO_4$–H_2O systems in the temperature range of 0–80 °C (Wei et al., 1989) with the following results: (i) with increasing temperature, the solubility of $CoSO_4$ in water increases, while solubility of $Sm_2(SO_4)_3$ decreases sharply; (ii) the solid phase at equilibrium was $Sm_2(SO_4)_3{\cdot}8H_2O$ in this temperature range; (iii) with increasing SO_4^{2-} (H_2SO_4 and $CoSO_4$) concentration, the solubility versus concentration of SO_4^{2-} curve of $Sm_2(SO_4)_3$ shows a peak which shifts to higher SO_4^{2-} concentration with temperature; and (iv) from these facts, it seems to be possible to recover samarium and cobalt from Sm–Co magnet scrap with sulfate fractional crystallization method by controlling temperature and SO_4^{2-} concentration. On the basis of these results, Sato et al. (1997) conducted further study and presented the following results: (i) when sulfuric acid was added into the nitric acid solution containing samarium and cobalt, the solubility of samarium decreased and samarium sulfate hydrate preferentially crystallized; (ii) samarium sulfate hydrate of 96.5% purity with recovery rate of 87.1% was obtained from $SmCo_5$ magnet scrap by fractional crystallization. A similar result was also obtained for Sm_2 (Co, Fe, Cu, Zr)$_{17}$.

Sanuki et al. (1995) investigated the possibility to develop a hydrometallurgical method to recover metals from scrap Sm–Co magnets including $SmCo_5$ and Sm_2Co_{17}. All component metals were easily leached out in 2 $kmol/m^3$ HNO_3 solution, while HCl and H_2SO_4 were less effective, leaving copper in the leach residue. On the basis of this fact, they proposed a new process: From the HNO_3 leach solution, iron (III) and zirconium (IV) are initially extracted in an organic phase with D2EHPA, then samarium (III) is extracted with the same extractant after pH adjustment. Precipitation stripping of samarium (III) with oxalic acid is effective in avoiding coprecipitation of other metals. Copper (II) and cobalt (II) in the raffinate can be extracted with LIX65N and D2EHPA, respectively, and stripped with an aqueous sulfuric acid solution. Iron (III) and Zr (IV)-loaded D2EHPA organic phase is stripped with oxalic acid, followed by the photochemical reduction of Fe (III)-oxalate to the Fe (II) state to selectively precipitate iron, leaving Zr (IV) oxalate in the stripped solution. Expected material balance is shown.

2.2.2. Nd–Fe–B Magnets

2.2.2.1. Fractional Crystallization Method

Sato and Nanjo's group studied fractional crystallization separation between neodymium and iron (Sato et al., 1997; Wei et al., 1989). As fundamental data for the recycling, the solubilities of $Nd_2(SO_4)_3$ in H_2SO_4–H_2O and $FeSO_4$–H_2O systems were measured in the temperature range of 0–80 °C (Wei et al., 1989). With increasing temperature, the solubility of $FeSO_4$ in water increases, while the solubility of $Nd_2(SO_4)_3$ decreases sharply. Neodymium was precipitated as $Nd_2(SO_4)_3{\cdot}8H_2O$ within 0–80 °C and $Nd_2(SO_4)_3{\cdot}5H_2O$ at 80 °C, respectively. With increasing the concentration of SO_4^{2-} (H_2SO_4 and $FeSO_4$ concentrations), the solubility versus concentration of SO_4^{2-} curves of $Nd_2(SO_4)_3$ show a peak which shifts to the higher SO_4^{2-} concentration with temperature. It seems to be possible to recover neodymium from rare-earth magnet scrap with the sulfate fractional crystallization method by controlling temperature and SO_4^{2-} concentration. As a continuation of this study, Sato et al. (1997) reported that the addition of ethanol into the sulfuric acid–nitric acid solution containing neodymium and iron was effective for the decrease in solubility. They obtained neodymium sulfate hydrate of 96.8% purity with the yield of 97.1% from Nd–Fe–B magnet scrap by fractional crystallization of metal sulfates with addition of ethanol as well as H_2SO_4.

2.2.2.2. Whole Leaching Process

Lyman and Palmer (1993a,b) studied the whole leaching process using sulfuric acid followed by precipitating neodymium-(sodium or ammonium) sulfate double salt as an intermediate which could be converted into a variety of useful products. Iron is removed from leach solutions by precipitation as a jarosite, eliminating a major disposal problem. The yields of neodymium recovery are 98% and 70% for sodium and ammonium systems, respectively. The iron-rich effluent after the rare-earth recovery is treated to form sodium and ammonium iron jarosites that can be discarded or converted to hematite. By following this new procedure, many materials handling and economic disadvantages found with fluoride or oxalate direct precipitation processes were said to be avoided. Boron does not precipitate through the precipitation reactions of rare-earth double salt and jarosite. The possibility was mentioned that boron in the spent solution of jarosite formation was removed by adding zinc and raising the pH as zinc borate hydrate; the latter compound is commonly used as flame retardant.

Yoon et al. (2003) studied the oxidative roasting—leaching—double salt precipitation process as a continuation of their preceding paper (Lee et al., 1998) of selective leaching which will be mentioned later. The optimum roasting and leaching conditions were presented: oxidative roasting temperature of 500 °C for sintered scrap and 700 °C for bonded scrap, concentration of sulfuric acid for leaching of 2.0 kmol/m^3, leaching temperature of 50 °C and time of 2 h, and pulp density of 15%. The leaching yields of neodymium

and iron were 99.4% and 95.7%, respectively. The optimum condition for separation of neodymium by double salt precipitation was 2 equiv. of sodium sulfate and 50 °C. The yield of neodymium was above 99.9%.

2.2.2.3. Selective Roasting-Leaching

Lyman and Palmer (1993b) studied the roasting—(magnetic separation or selective leaching process). The roasting here aimed at oxidizing neodymium while leaving iron as metallic form at a controlled H_2–water vapor mixture on the basis of the thermodynamic consideration showing a common stability region of Nd_2O_3 and Fe. Although selective roasting was successful, the subsequent process such as magnetic separation and acid leaching were not because of the extremely fine grain size of the oxidized scrap. Thus, they discontinued the study in this direction and changed the strategy to total dissolution process as has been described previously.

2.2.2.4. Selective Leaching

Lee et al. (1998) studied the roasting in air—sulfuric acid leaching—sulfate precipitation process. The selective leaching was investigated as a function of roasting temperature, H_2SO_4 concentration, and leaching temperature and time. The increase in roasting temperature significantly suppressed the leaching rate because of the formation of $NdFeO_3$. Nevertheless, neodymium was leached more selectively because the leaching of iron was retarded by the concurrent formation of Fe_2O_3 at higher temperatures. The selective leaching of neodymium was favorable at shorter leaching time, lower H_2SO_4 concentration, and lower leaching temperature. Neodymium is selectively precipitated as $Nd_2(SO_4)_3$ on the basis of the solubility difference from $FeSO_4$. When the scrap roasted at 700 °C was leached at the predetermined optimum conditions (H_2SO_4 concentration, 4 kmol/m^3; leaching temperature, 70 °C; leaching time, 180 min; pulp density, 100 kg/m^3), 70% of neodymium was selectively separated as $Nd_2(SO_4)_3$ precipitates. The Nd/Fe ratio in the precipitate was found to be 18.3.

Koyama and Tanaka examined the oxidative roasting—selective leaching—solvent extraction process of the scrap neodymium magnet (Koyama and Tanaka, 2009, 2011a; Koyama et al., 2009; Tanaka et al., 2009). When 1000 kg of scrap magnet ($Nd_2Fe_{14}B$) is dissolved by mineral acid, its required amount is calculated on the basis of the following reactions:

$$Nd + 3H^+ = Nd^{3+} + (3/2)H_2 \quad (1)$$

$$Fe + (3/4)O_2 + 3H^+ = Fe^{3+} + (3/2)H_2O \quad (2)$$

For the dissolution with HCl, the required amounts of HCl are 202 kg for neodymium and 1420 kg for iron. Likewise, for H_2SO_4, the amounts are 272 kg for neodymium and 1900 kg for iron. This means that the required

amount of H_2SO_4 for the total leaching process is almost double of the magnet scrap (Koyama and Tanaka, 2011a). Moreover, even if rare earths can be recovered from the leach solution obtained by the total dissolution, large amount of iron is present in the effluent, which should be removed basically by hydroxide precipitation:

$$Fe^{3+} + 3OH^- = Fe(OH)_3 \tag{3}$$

Calculation from Eq. (3) shows that 1600 kg of NaOH or 1100 kg of CaO per 1000 kg of magnet scrap is necessary for neutralization. Figure 6 is a potential—pH diagram for the Fe–H_2O and Nd–H_2O systems and shows the principle of the selective leaching (Koyama et al., 2009). By using the stability region of Fe_2O_3 and Nd^{3+}, it is possible to dissolve Nd^{3+} leaving iron in the residue as Fe_2O_3. In order to investigate the possibility of selective leaching, commercial neodymium magnets were thermally demagnetized, crushed, roasted in air at 900 °C for 6 h, and then leached by 0.02 kmol/m^3 HCl at 180 °C for 2 h. More than 99% of rare earths were leached, while iron leaching was less than 0.5%. On the contrary, more than 50% of iron was leached without roasting although more than 99% of rare earths were also leached (Koyama and Tanaka, 2009). Selective leaching at lower temperature is also possible. Table 4 shows the results of leaching experiment at 60 °C for 24 h using different concentrations of HCl. Using 0.01 kmol/m^3 of HCl, more than 96% of rare earths were leached, while iron dissolution was at 14% (Koyama and Tanaka, 2011a,b).

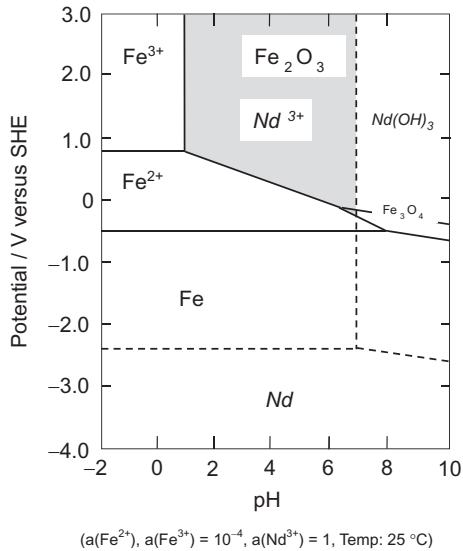

FIGURE 6 Potential–pH diagram of the Fe–H_2O and Nd–H_2O systems calculated from the data in Pourbaix (1966).

TABLE 4 Percentages of Neodymium, Dysprosium, and Iron Leached from Neodymium Magnet After Oxidative Roasting (Koyama and Tanaka, 2011a)

HCl (kmol/m^3)	Nd	Dy	Fe
0.001	15.8	13.1	1.2
0.01	96.4	96.1	14.0
0.1	>99	>99	>99

Leaching was done at 60 °C for 24 h.

2.2.2.5. Hydrothermal Method

Itakura et al. (2006) investigated the hydrothermal treatment of Nd–Fe–B sintered magnet using a mixture of hydrochloric and oxalic acids in order to recover neodymium as oxalate. The obtained optimum condition is temperature 110 °C, time 6 h, the concentration of hydrochloric acid 3 kmol/m^3, the concentration of oxalic acid 0.2 kmol/m^3. As a result, more than 99% of neodymium in the magnet was recovered as solid precipitate of $Nd_2(C_2O_4)_3$ with the purity of 99.8%.

2.2.2.6. Solvent Extraction and Related Techniques

In order to recover rare earths from the leach liquor of neodymium magnet scrap, solvent extraction with acidic organophosphorous reagents such as PC-88A is often used. This is because these reagents exhibit the greatest separation factors for the intragroup separation among various commercially available reagents (Nash, 1994). The extraction stoichiometry of R^{3+} with PC-88A is expressed as

$$R^{3+} + 3H_2L_{2org} = R(HL_2)_{3org} + 3H^+ \quad (4)$$

where H_2L_2 and subscript "org" denote the dimer of PC-88A and organic phase, respectively. This means that when one R^{3+} is extracted three hydrogen ions are released from the organic phase. As the result, on the basis of the mass action law, the extraction efficiency is reduced. This effect is common in cation-exchange system and pronounced when the metal concentration and the initial pH are higher. This problem can be overcome using partially neutralized extractant; that is, part of H_2L_2 is converted to NaL or NH_4L before metal extraction. Lee et al. (2005) performed solvent extraction of neodymium with PC-88A and partially neutralized PC-88A from chloride solution. Compared with the distribution coefficients of neodymium with the H^+-type PC-88A, the use of 40% neutralized PC-88A significantly increased the extraction of neodymium.

Solvent extraction separation of dysprosium from neodymium from the solution obtained by the selective leaching was shown to be possible using acidic organophosphorous reagents (PC-88A) (Tanaka et al., 2009). At the equilibrium pH around 1, 85% of dysprosium was extracted from the solution containing 3 mol/m^3 $DyCl_3$ and 20 mol/m^3 $NdCl_3$ with 5 vol% PC-88A at the unit phase ratio, while only 2% of neodymium was extracted. The separation factor defined by D(Dy)/D(Nd) was 525 at the equilibrium pH of 1.1. Because neodymium concentration is much higher than that of dysprosium in this leach solution, a small portion of neodymium is inevitably extracted in the organic phase. However, the extracted neodymium would be easily scrubbed with $DyCl_3$ solution or dilute HCl.

Naganawa and Shimojo's group presented a novel extractant, *N*,*N*-dioctyldiglycol amic acid (DODGAA) for rare earths (Naganawa et al., 2007; Shimojo et al., 2007). This extractant has a distinct advantage over acidic organophosphorous reagents such as D2EHPA, PC88A, and Cyanex 272, that is, high selectivity of rare earths over iron (III) and zinc (II), and higher mutual separation ability among light lanthanides. The former advantage would be utilized in the recycling process of scrap neodymium magnet. The latter one as shown in Fig. 7 would be also useful for the mutual separation of neodymium and praseodymium, which is the most difficult pair of rare earths to separate.

Kubota and Goto's group studied the selective permeation of dysprosium and neodymium against ferric ion by an ionic liquid-based supported liquid membrane (SLM) using DODGAA as the mobile carrier (Baba et al., 2011) because the DODGAA is soluble in ionic liquids such as l-octyl-3-

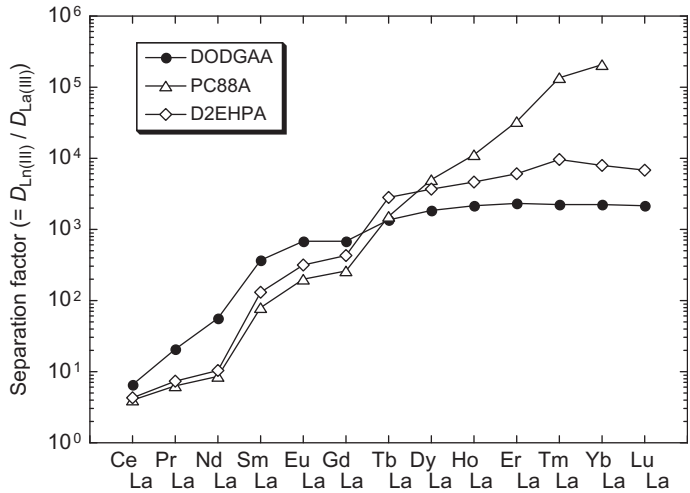

FIGURE 7 Comparison of the separation factors between DODGAA and the acidic organophosphorus extractants (PC-88A and D2EHPA); aqueous phase: nitric acid solution of pH 1.5, organic phase: 30 mol/m^3 extractant in *n*-hexane (Naganawa et al., 2007).

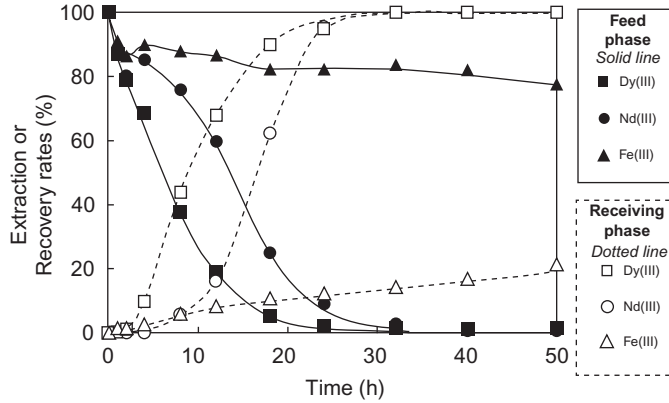

FIGURE 8 Time dependence of the metal ion concentrations in the feed and receiving phases during IL-based SLM operation. Aqueous phase, Nd, Dy, and Fe at 0.1 mol/m^3 each at pH 4 (acetate buffer). SLM was prepared by immersing a hydrophobic porous polyvinylidene fluoride film in [C_8mim][Tf_2N] containing 10 mol/m^3 DODGAA (Baba et al., 2011).

methylimidazolium bis(trifluoromethanesulfonyl)imide ([C_8mim][Tf_2N]) and shows good selectivity to the rare earths and efficient stripping behavior. Although the SLMs using a conventional organic solvent as the liquid membrane phase suffered from instability of the membrane, stable transport of dysprosium and neodymium has been successfully achieved through the SLM impregnated with the [C_8mim][Tf_2N] containing DODGAA as shown in Fig. 8. Dysprosium and neodymium were quantitatively recovered to the receiving phase, while only 10% of ferric ions were transported. These results suggest a potential use of the SLM system for the recovery of the rare earths from the leach solution of magnet scrap which contains a large or small (for selective leaching) amount of iron.

2.2.3. *Mixture of Sm–Co and Nd–Fe–B Magnets*

Recently, the amount of Sm–Co magnets used in consumer products has decreased because of the development of Nd–Fe–B magnet. Nevertheless, a mixture of Nd–Fe–B and Sm–Co magnets as well as ferrite magnets is expected to be collected from various waste streams. This would complicate the process because samarium causes a detrimental effect during the molten salt electrolysis. Processing of mixed $SmCo_5$ and Nd–Fe–B swarf was studied (Lyman and Palmer, 1993b). A flotation-leaching process allows the $SmCo_5$ to concentrate in the froth, while the grinding-medium contaminant sinks and is removed as tailing. The Nd–Fe–B swarf is dissolved by H_2SO_4 during the process. Niinae et al. (1994) studied the recycling process in order to treat the mixed scrap of Nd–Fe–B and Sm–Co magnets. The separation efficiency of neodymium and samarium from hydrochloric acid solutions is better than that from sulfuric acid solutions. The extractant combinations, PC-88A/TOPO

and PC-88A/TOA, are favorable to the extraction and separation of neodymium and samarium, on the basis of the fact that $\Delta pH_{1/2}$ values become larger in these mixed extractant systems than that with PC-88A alone. A hydrometallurgical process of mixed rare-earth magnet scraps based on oxidative roasting, hydrochloric acid leaching, and solvent extraction was proposed.

2.3. Pyrometallurgical Methods

2.3.1. Methods Using Gas–Solid and Solid–Liquid Reactions

For recycling of rare-earth magnets, numerous pyrometallurgical methods have been proposed. Generally, heterogeneous reactions such as gas–solid, solid–liquid, and other are used to achieve the separation. Figure 9 shows the pyrometallurgical recycling processes for rare earths from magnet sludge or magnet waste proposed so far.

On the basis of the difference in vapor pressures of rare-earth chlorides (Boghosian and Papatheodorou., 1996), Murase et al. (1995) developed a process for recovery of rare earths from sludges of Sm_2Co_{17}, $Nd_2Fe_{14}B$, and $LaNi_5$ by chemical vapor transport along a temperature gradient. Chlorine gas and aluminum chloride were used, respectively, as chlorination and transporting reagents, where rare-earth chlorides were transported as vapor complexes such as RAl_nCl_{3+3n}. In the case of Sm_2Co_{17} sludge, samarium chloride was concentrated up to 99.5 mol% in the high-temperature zone (700–1040 °C), and cobalt chloride was concentrated up to 99.1 mol% in the low-temperature zone (350–700 °C). In the case of $Nd_2Fe_{14}B$, rare-earth chloride of 98.4 mol% purity was obtained. The same authors also applied this method for lanthanum recovery from $LaNi_5$. The extraction of iron from the Nd–Fe–B magnet by the carbonylation method was studied (Itoh et al., 2007; Miura et al., 2008). Iron in the magnet reacts with carbon monoxide and forms volatile $Fe(CO)_5$ with sulfur serving as a catalyst. Itoh et al. (2007) found that 92% of iron was recovered by the hydrogenation-disproportionation treatment.

Separation of rare earths from rare-earth magnets by solid–liquid reaction was also studied. Uda (2002) examined chlorination of rare earths in Nd–Fe–B magnet sludge by $FeCl_2$. It was found that 96% of neodymium and 94% of dysprosium were extracted from the magnet sludge, and a mixture of neodymium and dysprosium trichlorides of 99.2% purity was obtained. Based on this and additional experimental results, he proposed a recycling process in which chlorine is recirculated. In this process, $FeCl_2$ is used as chlorination reagent for rare earths, and rare-earth oxides are finally obtained via subsequent hydration and conversion steps from rare-earth chloride hydrate to oxide. Since HCl is obtained in the conversion step and is useful as the chlorination reagent for metallic iron or residue of the magnet sludge after the first chlorination step, chlorine could be recirculated under the ideal condition. Separation of samarium from neodymium or neodymium from praseodymium by

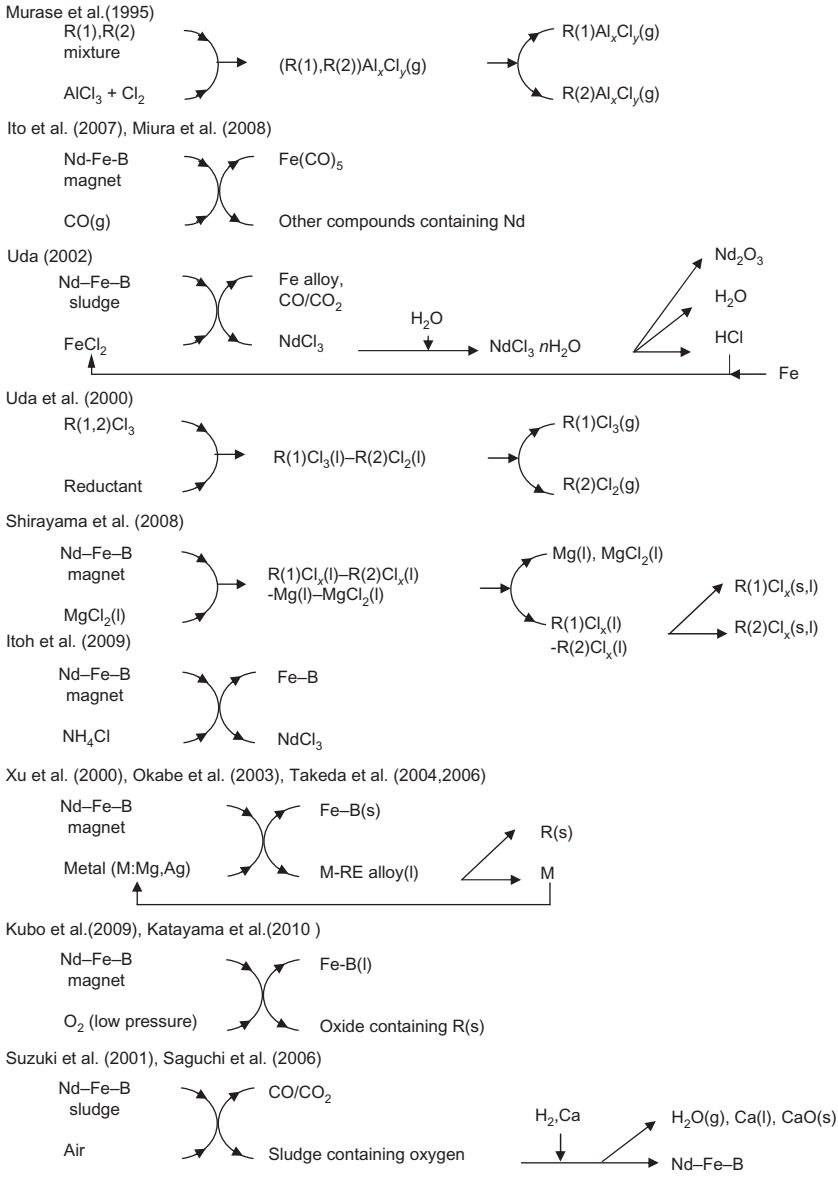

FIGURE 9 Pyrometallurgical processes suitable for recovery of rare-earth elements from sludge or magnet waste.

combining selective reduction and vacuum distillation was also studied (Uda et al., 2000). Shirayama and Okabe (2008) carried out the separation test of neodymium and dysprosium from magnet waste with molten $MgCl_2$ as an extractant. More than 80% of rare earths were shown to be extracted into the molten $MgCl_2$. In their process flow sheet, magnesium chloride was

separated from rare-earth chloride as a gaseous phase and reused as an extractant. They also reported that ZnI_2 is also suitable for the extraction of rare earths from magnet waste (Shirayama and Okabe, 2009). Itoh et al. (2009) studied the application of NH_4Cl as a chlorinating agent. It was shown that about 90% of Nd in $Nd_2Fe_{14}B$ magnet powder was converted to $NdCl_3$, the $Nd_2Fe_{14}B$ primary phase was converted to $NdCl_3$ and α-Fe and Fe–B were also obtained by chlorination at 300–350 °C for 3 h. $NdCl_3$ in the product was selectively dissolved into water, while α-Fe and Fe–B remained in the solid residue. They also studied the application of iron-based residue as by-product and found that it had good electromagnetic wave absorption properties. Xu et al. (2000) reported that neodymium can be dissolved in molten magnesium, leaving iron and boron behind in the temperature range of 675–750 °C. They claimed that thus obtained Nd-rich Mg alloy is useful as master alloy in the Mg casting industry. Okabe et al. (2003) and Takeda et al. (2006) showed that more than 95% of neodymium in the magnet scrap was extracted into liquid magnesium. Neodymium and magnesium were shown to be separately recovered from Mg–Nd alloy. They also examined the extraction of neodymium from magnet scrap using molten silver as an extractant (Takeda et al., 2004).

Control of nonmetallic elements such as carbon and/or oxygen is important in the recycling because these contaminants may deteriorate the magnetic properties of materials manufactured from the recovered rare earths. Suzuki et al. (2001) and Saguchi et al. (2006) studied the removal of carbon and oxygen from the magnet scrap. They removed carbon by oxidation at 800 °C, and then oxygen by the two-stage reduction. The first stage is the reduction of Fe_2O_3 by hydrogen gas at 980 °C, and the second one is to reduce rare-earth oxides by Ca-reduction at 950 °C. Residual Ca, by-product CaO, and soluble $CaCl_2$ were leached with water and removed. Less than 0.001% of the carbon content and a level of 0.1 mass% of oxygen content in the reduced materials were achieved.

2.3.2. *Methods Using Molten Salts*

Most of rare-earth metals are produced commercially via metallothermic reduction or molten salt electrolysis (Gschneidner and Daane, 1988; Itoh et al., 1988). Thus, the employment of molten salt as a reaction medium has certain advantages when one considers the recycling of rare earth from magnet scraps. Actually, in the case of in-plant scrap, Nd or Nd–Pr alloy (Di) are finally recovered by molten salt electrolysis after some hydrometallurgical steps (Machida, 2004). General advantages of molten salts as reaction medium in comparison with water are; high chemical stability, high conductivity, high reaction rates, broad applicable temperature range, low vapor pressure, and so on. Since molten salt electrolysis applied to in-plant scrap is well established (e.g., Machida, 2003; Nakamura, 2011) and is basically the same

as that applied to natural resources, we will focus on the processes under investigation. Such processes seem to be categorized into three groups from the view point of characteristics utilized for the separation of interest. First is electrochemical process which uses the difference in electrochemical behavior of each element in molten salts. Second is called slag or flux process which uses difference in solubility or distribution coefficient of each element in two or more phases. Third utilizes the difference in vapor pressure of rare earth or other compounds after the reaction like chlorination in a molten salt. The third, however, is categorized into usual pyrometallurgical process in the present review (Section 2.3.1) and the remaining two are described here.

2.3.2.1. Electrochemical Process

Availability of literature describing electrochemical recycling process using molten salts is quite limited, although a number of papers exist that describe electrochemical behavior of rare-earth ions, electrodeposition of rare-earth metals, and electrochemical formation of rare-earth alloys in molten salts. According to the literature (e.g., Bard, 1976), the rare-earth metals are less noble (more reactive) than the iron-group metals in common molten salts, and selective anodic dissolution of rare earth from rare-earth magnet scraps is possible from thermodynamic point of view. On the other hand, if impurities, like iron, are dissolved in molten salts, the recovered rare-earth metals or alloys will be contaminated during the cathode step. Therefore, the separation of rare earth from other elements before the recovery step becomes important in any electrochemical process.

Ito (2011) proposed a simple process to recover rare-earth metals from Nd–Fe–B magnet scrap using a bifunctional electrode, which functions as either the cathode or the anode depending on the situation. His proposal consists of two electrolysis steps of (i) anodic dissolution of rare-earth metals (dealloying) from magnet scrap using the bifunctional electrode as the cathode and (ii) rare-earth alloy formation by reduction of rare-earth ions on transition metal cathode using the bifunctional electrode as the anode. Although the details are unclear, this process is simple and has a possibility to achieve a high selectivity because the alloying step has certain selectivity as will be subsequently mentioned.

Oishi et al. (2010) also proposed a process utilizing rare-earth alloy formation and dealloying. This process is characterized by the use of rare earth—iron-group metal alloy as a diaphragm, which functions as a bipolar electrode and enables selective permeation of rare earths. As schematically shown in Fig. 10, rare-earth metals or alloys are recovered via the following steps: (i) a rare earth containing material like Nd–Fe–B magnet scrap is used as the anode and rare-earth metals are selectively dissolved into the melt as ions, (ii) the dissolved rare-earth ions are reduced on the anode side surface of the diaphragm and the rare-earth atoms diffuse through the diaphragm, (iii)

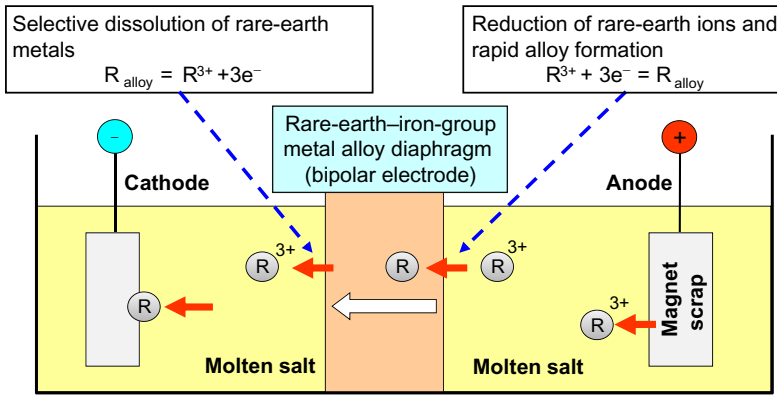

FIGURE 10 Conceptual drawing of rare-earth recycling process using molten salt and alloy diaphragm (Oishi et al., 2010).

the rare-earth atoms are dissolved from the cathode side surface of the diaphragm as ions, and (iv) rare earth is finally recovered as a metal or an alloy on the cathode by reduction of the dissolved rare-earth ions. Although it is still in a fundamental research stage, this process has a potential to enable the recovery of highly pure rare-earth materials and/or selective recovery of rare-earth metals like dysprosium from Nd–Fe–B magnet scraps because of the high selectivity during the alloying step on the anode side surface of the diaphragm, as Konishi et al. (2011) showed using a molten chloride.

Similar alloying and dealloying phenomena were also confirmed in a molten fluoride containing neodymium ions by Kobayashi et al. (2011). This suggests that the above process is also applicable to fluoride melts, which is probably advantageous in commercialization because fluoride melt is widely employed for the electrowinning of rare-earth metals/alloys as the final step of the rare-earth recovery from natural resources. On the other hand, some technical problems to be solved still remain. These include low mechanical strength of rare earth—iron-group metal alloys and difficulties in maintaining of the alloy diaphragm at an appropriate composition. Thus, further investigations are necessary to establish whether this process is applicable to commercial use. Matsuura et al. (2005) proposed another electrochemical process using electromigration. Although this process may also be applicable to recycling of rare-earth magnet scraps, this process will be described in Section 4.3.

2.3.2.2. Flux or Slag Process

The so-called flux or slag process can be categorized into two groups: processes to remove rare-earth oxide in magnet scrap (purification) and the ones to oxidize and extract rare earths as oxides form from magnet scrap into a slag phase.

Takeda et al. (2009) proposed the following process. Rare-earth oxide formed as a result of oxidation of the rare earths during the manufacturing

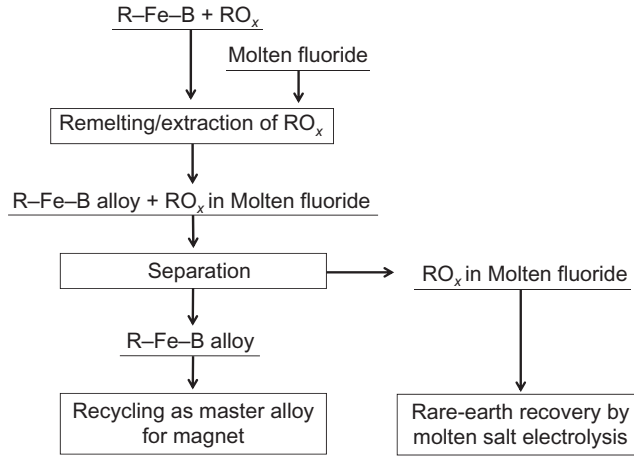

FIGURE 11 Flow sheet of alloy recycling process using molten fluorides (Takeda et al., 2009).

of the magnets is a substance that needs to be removed for reusing the scrap as a master alloy for rare-earth magnet. In this process, molten fluorides like LiF–NdF_3 and LiF–DyF_3 are used as a flux and the rare-earth oxide present in the Nd–Fe–B magnet scraps is extracted, as shown in Fig. 11. According to them, the purified Nd–Fe–B alloy could be reused as the master alloy for magnet production after metal/slag separation. From the rare-earth oxide dissolved in the molten fluorides, the rare-earth metals could be recovered by conventional molten salt electrolysis. In addition, they already succeeded in reducing the oxygen content in Nd–Fe–B magnet scrap from 5000 to 200 ppm by weight in their subsequent study (Takeda et al., 2011), which was sufficiently low as the master alloy for the Nd–Fe–B magnet (Nakamura, 2011). Compared with the conventional or other proposed recycling processes, this process is quite simple, energy-saving, and probably cost-effective as they claimed. One of the disadvantages of this process, however, is that the alloy composition basically does not change during the process which makes it difficult to apply this process to the out-of-plant scrap. In other words, this could be a potential process in the cases that the original composition of magnet scrap is known like off-spec product, or in the case of cascade recycling.

The next process, the so-called glass slag method, was proposed by Saito et al. (2003). Although this process was developed to produce bulk materials with fine grains, they applied it to the Nd–Fe–B magnet scrap for extraction of neodymium using molten B_2O_3 both as the oxidizing agent and the extraction medium. Although the detailed experimental conditions are not clear, the authors heated a small piece of $Nd_2Fe_{14}B$ alloy along with B_2O_3 in a BN crucible under argon atmosphere and obtained Fe–B alloy and Nd-containing glass slag. According to their analysis, almost all neodymium was extracted

from the metal phase. They also applied this process to Sm–Fe–N and Sm–Fe magnets, and similar results were reported (Saito et al., 2005a,b). Similar attempt was reported by Kubo et al. (2011). The differences from the Saito's process are that carbon is added to the metal phase to decrease the melting point and that the slag phase is separated into two liquid phases of B_2O_3 and Nd_2O_3–B_2O_3 at the reaction temperature. Like the Saito's process, almost all of neodymium, dysprosium, and praseodymium were extracted into the slag phase according to their analysis. Although some rare-earth oxide was found to enter the B_2O_3 phase, they claimed that it would not be a rare-earth loss because this phase could be reused in the same process. One of the advantages of these processes using molten boron oxide as slag phase seems to be a good separation of rare-earth and iron-group metals; the iron-group metals remain in the metallic form. In these processes, however, rare-earth oxide coexists with boron oxide and further separation step(s) are necessary before the recovery step of rare-earth metals.

Recently, Yamamoto's group reported that in-plant waste (sludge) was separated into liquid iron and solid rare-earth oxide phases at 1550 °C under argon atmosphere having partial O_2 pressure of 10^{-10} –10^{-25} atm without any flux additions (Kubo et al., 2009). They also showed that almost all of the neodymium and dysprosium existed in the oxide phase and iron content in the oxide phase was less than 0.4 mass% (Katayama et al., 2010).

2.4. Pyrolysis of Epoxy-Resin-Bonded Magnet

Epoxy resin is generally used as a binder for solidifying Nd–Fe–B melt-spun powder into a specific shape because of its high density. Researchers in Matsushita Electric Industrial Co. (Terada et al., 2001; Yamashita et al., 2001) developed a manufacturing and recycling processes of Nd–Fe–B melt-spun powder using liquid-phase pyrolysis of cured epoxy in solvent as shown in Fig. 12. Precrushed bonded magnets with 2.5 wt% epoxy resin binder immersed in the solvent (1,2,3,4-tetrahydronaphtaline) of the same weight is heated at 280 °C for 80 min in a nitrogen gas of 0.49 MPa using an autoclave. The epoxy-resin-bonded magnets are collapsed into powder by the pyrolysis reaction; then the solvent is distilled and transferred to another autoclave. After cooling down, recycled melt-spun powder is obtained by crushing and screening (route B in Fig. 12). Finally, epoxy resin bonded magnets are manufactured using the obtained melt-spun powder (route A in Fig. 12).

3. PHOSPHORS

Rare-earth phosphors are widely used for general illumination (fluorescent lamps) and displays (cathode ray tube, backlights for liquid crystal displays, and plasma display panels). Major rare earths present in the phosphor are cerium, europium, and terbium, which are optically active because of the

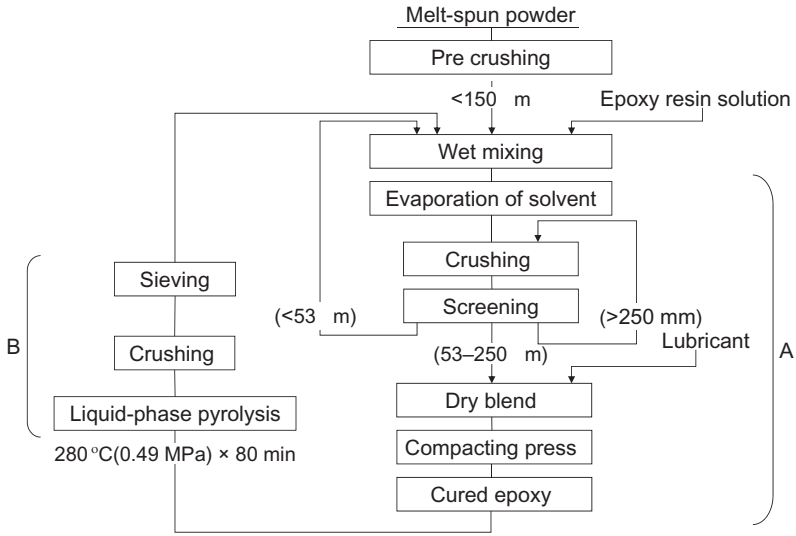

FIGURE 12 Preparation and recycling processes of epoxy resin bonded magnets (Yamashita et al., 2001).

presence of 4f electrons, and yttrium and lanthanum that are optically inactive because of the absence of 4f electrons.

For general illumination, the industrial facilities use fluorescent lamps with calcium halophosphate ($Ca_{10}(PO_4)_6FCl$: Sb, Mn) as a fluorescent material which do not contain rare earths. On the other hand, the demand of three-band phosphor tubes having better color purity and higher luminous efficacy is recently increasing, and more than 90% of the fluorescent tubes in household application use three-band phosphors in Japan (Horikawa and Machida, 2011). Recycling of the rare-earth phosphors is difficult because (i) their emission intensities are sensitive to the concentrations and purities of rare earths, (ii) the kinds of phosphors and their contents depend on the kinds of fluorescent tubes, and (iii) degradation of phosphors depends on the kind of phosphor (Eu^{2+} in blue phosphor tends to be oxidized to Eu^{3+}) (Horikawa and Machida, 2011). Mercury, glass, and metallic parts in the spent fluorescent tubes are recycled, whereas limited amount of the rare-earth phosphors in the spent tubes are reused. The recovered phosphor is not only a mixture of various kinds of phosphors but they are also accompanied by glass and other metallic parts. According to Radeke et al. (1998), ca. 200 tons of fluorescent lamps were being disposed of yearly around 1998 in Germany, of which 80 tons were three-band tubes. These tubes contained 20 tons of yttrium oxide with a market value of > USD 500,000 (for 99.9% purity based on lower prices of Chinese providers at that time). Also, they contained 600 kg of europium with a market value of USD 250,000 assuming 99.99% purity. According to Nagai (2010), 140 tons of Y_2O_3, 8.5 tons of Eu_2O_3,

and 8.5 tons of Tb_4O_7 are estimated to be consumed for the production of illumination tubes in Japan during 2005 fiscal year (April to March), in which their recycling rates seem to be about 20%.

3.1. Physical Separation

Straight-tube fluorescent lamps are commonly used for general lighting, and it is easy to remove their phosphors by air-blowing after cutting off both ends. However, most of such phosphors are of the halophosphate type, and there are only limited amounts of three-band phosphors with a mixture of red, green, and blue, which contain a higher proportion of rare earths. In Japan, significant attempts have been made at first-stage concentration of phosphors by physical separation at laboratory scale, in order to recycle rare earths from phosphors recovered from fluorescent lamp wastes.

3.1.1. Recovery of Mixed Rare-Earth Phosphors

In the recycling of phosphors, the halophosphates, predominant in mixed phosphors, must first be removed so that the three-band phosphors with a mixture of red, green, and blue phosphors can be concentrated.

3.1.1.1. Dry Separation Process

Because the phosphors in straight-tube fluorescent lamps are often recovered by a dry process, it would be natural to first consider the application of a dry separation process. Takahashi et al. (1999, 2001a,b) have employed a centrifugal pneumatic separator (Turbo Classifier TC-25, Nisshin Engineering Inc.) during the studies on the concentration of rare-earth phosphor mixtures. The relationship between the yield and the content of the rare-earth phosphors in the product, with changes in the rotation speed of the rotor (4000–8000 rpm) and air flow (approx. 0.03–0.06 m^3/s at 5000 rpm), has been investigated using phosphor sludge composed of 13.3% rare-earth phosphor, 82.6% halophosphate-type phosphor, and 4.1% glass. The higher rotation speed of the rotor resulted in the lower yield and the higher rare-earth content. Increase in air flow increased the yields; however, the rare-earth content did not change significantly. The optimal separation condition was 5000 rpm of rotation speed and 0.053 m^3/s of air flow, which resulted in a 70% recovery of the rare-earth phosphor and an increase in the rare-earth content from 13.3% to 29.7%.

3.1.1.2. Wet Separation Process

In seeking highly precise component separation, the wet process is generally advantageous because the typical size of rare-earth phosphor particles is around 5 μm. Takahashi et al. (1999, 2001a,b) studied heavy media separation by sink-float separation using diiodomethane (CH_2I_2, specific gravity of 3.3).

TABLE 5 Properties of the Products of Heavy Medium Separation (Takahashi et al., 2001a)

	Rare-earth phosphor (%)	Halophosphate phosphor (%)	Glass (%)	Yield (%)
Sample	13	83	3	
Sink 1	54	45	1	2.5
Sink 2	65	34	1	2.0

Sink 1: pulp concentration is 100 kg/m^3.
Sink 2: pulp concentration is 40 kg/m^3.

The same samples were employed as in the dry process. The specific gravity of halophosphate-type phosphor is 3.07, while the specific gravity of rare-earth phosphor is 4.34–5.23. Therefore, the rare-earth phosphor sank, while the halophosphate-type phosphor was recovered as the floated component, which resulted in a four- to fivefold increase in the concentration of the rare-earth phosphors (Table 5). Hirajima et al. (2005a) studied heavy media separation by centrifugal separation also using diiodomethane. The separation quality improved when the rotation speed was increased, but there was no difference with respect to the separation time, even when it was extended from 10 to 60 min. In addition, the dispersion of phosphors was facilitated by the addition of NaOl (sodium oleate). The optimal procedure was to pretreat with 5×10^{-5} kmol/m^3 NaOl, and then perform centrifugal separation at 400 kg/m^3 of pulp concentration. More than 90% of the halophosphate-type phosphor was recovered as the floated component, and rare-earth phosphor of a grade of 48.6% was recovered as the sediment, in which the recovery and Newton's separation efficiency were 97.3% and 84%, respectively.

Although the experiments involving heavy media separation using heavy liquids are helpful in determining the limit of specific gravity separation, industrial application of such a method is limited by its high cost. Therefore, Hirajima's group (Hirai et al., 2001; Hirajima et al., 2002) tried to concentrate mixtures of rare-earth phosphors by gravity separation using water as the medium, which is easily accessed for industrial use. Using a hydrocyclone (2 in.-cyclone, Mozley), the solution was initially separated by a 14 mm vortex finder and a 9.4 mm diameter spigot, and the halophosphate-type phosphor was removed as the overflow. Then the underflow component was separated by a 14 mm diameter vortex finder and a 6.4 mm diameter spigot. These two steps of separation resulted in a grade of rare-earth phosphor mixture of 27.4% and Newton's separation efficiency of 18%. Hirajima et al. (2002) also carried out gravity separation tests using a multi-gravity separator (MGS, Mozley) and obtained a concentration of rare-earth phosphor mixture of 21.0% and Newton's separation efficiency of 9%.

These procedures offer an effective method for specific gravity separation between rare-earth phosphors and halophosphate-type phosphors; however, because the particle size of the phosphors is small, it is difficult to achieve sufficient separation accuracy with an industrially feasible gravity separation procedure (utilizing a hydrocyclone or MGS). Generally, in the particle size range of rare-earth phosphors, the application of gravity separation using bulk properties is considered to be difficult; however, separation using surface properties is thought to be effective. Therefore, Hirajima et al. (2005b) attempted a separation by flotation, which takes advantage of surface properties. The zeta potential (the electrical potential at the shear plane with respect to the bulk liquid) of halophosphate-type phosphors is negative when the pH is over 4, while the isoelectric points of the rare-earth type are pH 7.7 for red, pH 6.8 for green, and pH 4.8 for blue. This means that the zeta potentials of the rare-earth phosphors are positive in the weakly acidic range, and consequently they coagulate with the halophosphate-type phosphors. Performing a two-step flotation using dodecyl ammonium acetate as a collector at pH 2.5, and sodium dodecyl sulfate as a collector at pH 9.6, they achieved 43% and 27% Newton's separation efficiencies, respectively.

3.1.1.3. Selective Crushing for Bulb-Type Fluorescent Lamps

The studies mentioned in Eqs. (1) and (2) focused on the separation from straight-tube fluorescent lamps collected from the market, which are mixtures of halophosphate-type and three-band phosphors. This is because the 40 W straight-tube lamp is widely used, and because it is easy to process a large amount together since the shapes are the same. In contrast, the bulb-type (compact) fluorescent lamps that have recently come into wide use differ in types and shapes, which makes it difficult to process a large amount at the same time. However, in the case of bulb-type lamps, the removal of halophosphate-type phosphors is not necessary because only three-band phosphors are used. Therefore, using several kinds of bulb-type fluorescent lamps, Oki's group has examined the process of detaching the globe glass, fluorescent lamp glass, and base and also studied the method to recover phosphors from the fluorescent lamp glasses (Nagai, 2010; Oki, 2007; Oki and Kobayashi, 2009). There are three options for selective crushing, according to the amount to be processed and the desired quality of the recovered products. The first is the hammer type, which demolishes the entire glass in order to separate it from the base. The second is the drum type, which demolishes and collects the globe glass and the fluorescent lamp glass individually, separating both from the base. The third is the sorter type, which elevates the glass parts of the bulbs and then demolishes them individually using a continuous-batch process. As an example, using the drum-type option, two-third of the globe glass comprising a high-quality soda glass can be collected in the case of a G-type bulb lamp. Although performed at laboratory scale, this procedure made it possible to recover 100% of the three-band phosphors with a quality of 96%, by using a special elutriator.

TABLE 6 Experimental Results of Liquid–Liquid Separation (Otsuki et al., 2008)

1st product (green)		2nd product (blue)		3rd product (red)	
Grade (%)	*Recovery (%)*	*Grade (%)*	*Recovery (%)*	*Grade (%)*	*Recovery (%)*
90.0	95.2	92.2	91.8	95.3	90.9

3.1.2. Recovery of Individual Rare-Earth Phosphors

As described above, in seeking highly accurate separation of fine particles such as phosphors, the application of gravity separation using bulk properties is considered to be difficult; instead, separation using surface properties is thought to be effective. Otsuki and Fujita's group attempted to separate rare-earth phosphors by color, using liquid–liquid separation based on their surface properties (Fujita et al., 2009; Otsuki and Fujita, 2008; Otsuki et al., 2007, 2008). The mechanism of this method involves the recovery of particles rendered hydrophobic by the application of a surfactant in the two liquid interface: polar (*N*,*N*-dimethyl-formamide, water) and nonpolar liquid (*n*-hexane, *n*-heptane, *n*-octane, *n*-nonane). Then, hydrophilic particles are recovered by settling in a polar liquid phase. Model samples consisting of a mixture of red, blue and green rare-earth phosphors were used. As shown in Table 6, they succeeded in collecting green at the first stage, and separating blue and red at the second stage using *N*,*N*-dimethyl-formamide and *n*-heptane.

Next, we describe a technique developed by Akai (2011a,b) and Akai et al. (2011), who achieved color separation of three-band phosphors using strong magnetic fields, with the principal aim of in-plant recycling during the production of phosphors. Green ($LaPO_4$: Tb, Ce, (LAP)), blue ($BaAl_{10}O_{17}$: Eu, (BAM)), red (Y_2O_3: Eu, (YOX)) phosphors, and calcium halophosphate phosphor were used as samples. A high-gradient magnetic separator (HGMS) with maximum air-core magnetic field of 2 T was employed. The separation was performed using the following procedure: Deionized water, in which phosphor was dispersed, was poured into a separation column under the magnetic field, in order to attach the phosphor to the matrix inside the column. After degaussing the matrix, the phosphor attached inside the separation column was flushed out with water containing a surfactant. The magnetic susceptibilities of the phosphors used in representative fluorescent lamps are shown in Table 7. Given that the magnetic susceptibility of LAP is one or more orders of magnitude higher than those of the other phosphors, it is expected that the recovery of LAP using an HGMS would be the easiest among the phosphors. A mixture containing 1 g of each phosphor was mixed and dispersed in deionized water with 0.1 wt% of poly-carboxylic acid-type polymer dispersant. This slurry was poured into the separation column filled with

TABLE 7 Magnetic Susceptibilities of Typical Phosphors Used in Fluorescent Lamps (Akai et al., 2011)

No.	Phosphor (color)	Magnetic susceptibility
1	$LaPO_4$:Tb,Ce (LAP, green)	1.55×10^{-3}
2	$BaAl_{10}O_{17}$:Eu (BAM, blue)	1.78×10^{-4}
3	Y_2O_3:Eu (YOX, red)	8.56×10^{-5}
4	Calcium halophosphate (cool white)	9.55×10^{-5}
5	Calcium halophosphate (warm white)	1.89×10^{-4}

expanded metal under 2 T of magnetic field. After degaussing the matrix, LAP phosphor was obtained as a magnetic product by flushing the column with deionized water. A final product of LAP of more than 99% purity was obtained by repeating this procedure three times. According to Akai et al. (2011a), BAM and YOX, of which the magnetic susceptibilities are close to each other, can be separated from the phosphor mixture by applying a combination of several surfactants and performing the repeated separation procedure as described here.

3.2. Hydrometallurgical Methods

3.2.1. Direct Leaching

Takahashi's group carried out a series of studies on the hydrometallurgical separation and recovery of rare earths from phosphors in the fluorescent lamp wastes (Takahashi et al., 1994, 1996, 1999, 2001a,b,c, 2003). Sulfuric acid leaching from the rare-earth components was studied under different conditions (Takahashi et al., 2001a). After optimization of the leaching condition, 92% of yttrium and 98% of europium were dissolved at sulfuric acid concentration of 1.5 kmol/m^3, temperature of 70 °C, leaching time of 1 h, and pulp concentration of 30 kg/m^3, in which lanthanum, cerium, and terbium were not dissolved because these elements exist as phosphates while yttrium and europium as oxides.

During leaching, not only the rare-earths but also impurity elements such as calcium, sodium, phosphorus, chlorine, magnesium, antimony, manganese, iron, and aluminum were dissolved. In order to remove these impurities, hydroxide precipitation at pH 10 with ammonia and the subsequent hydrochloric acid leaching of the precipitate were studied. By the hydroxide precipitation, sodium, phosphorus, chlorine, calcium, and magnesium remained in the supernatant and rare earths formed a precipitate. After dissolving the precipitate with hydrochloric acid, rare earths were recovered by the oxalate

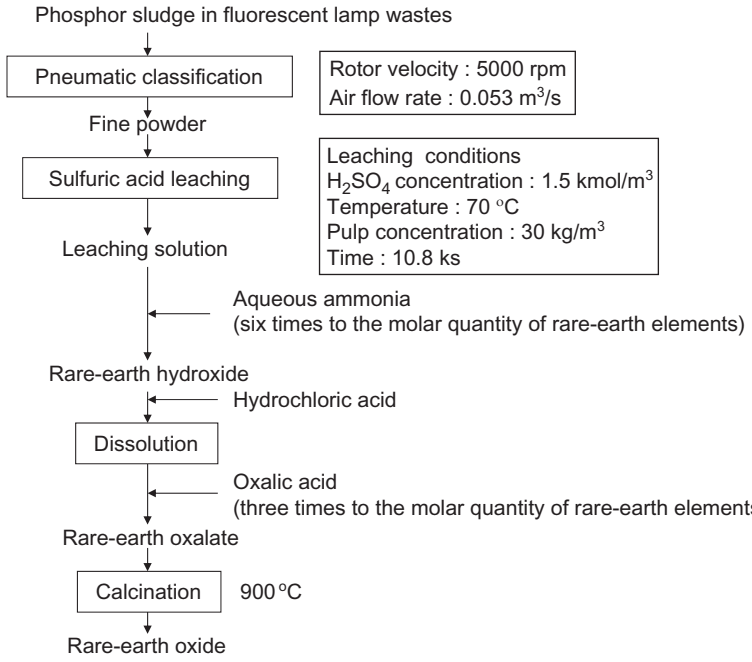

FIGURE 13 Flow sheet for recovery of yttrium and europium oxides from fluorescent lamp wastes. Reproduced with a slight modification from Takahashi et al. (2001a).

precipitation, while antimony, magnesium, and aluminum remained in the supernatant because these elements do not form oxalate precipitates. On the basis of these results, they proposed a process for the yttrium and europium recovery as shown in Fig. 13 and conducted a mini-plant experiment using 10 kg of phosphor sludge. The purity of rare-earth oxide was 98.2% with the yields of 65% for yttrium and 67% for europium (Takahashi et al., 2001a).

They also studied the separation of rare earths in phosphor wastes by chelating resins. The leaching was done in two steps: (i) selective leaching with 1.5 kmol/m^3 sulfuric acid in order to obtain (Y, Eu) fraction and (ii) leaching of its residue with 18 kmol/m^3 sulfuric acid in order to obtain (La, Ce, Tb) fraction. For the mutual separation of the rare earths, the iminodiacetic acid and nitrilotriacetic acid-type resins were used for the (Y, Eu) and (La, Ce, Tb) fractions, respectively. After oxalate precipitation and calcination, each rare-earth oxides were obtained with the yields and purities, respectively, of 50% and 99.8% (Y), 50% and 98.3% (Eu), 30% and 96.0% (La), 30% and 87.3% (Ce), and 90% and 91.8% (Tb) (Takahashi et al., 1996). They applied solvent extraction with PC-88A to achieve mutual separation between yttrium and europium from (Y, Eu) fraction obtained by the selective leaching with 1.5 kmol/m^3 sulfuric acid. Mutual separation was achieved by the

combination of countercurrent 6-stage extraction and 4-stage stripping using small-scale mixer settlers with the mixer compartment volume of ca. 250 cm^3. The purities of yttrium and europium in the obtained oxides were, respectively, 99.3% and 97% with a total rare-earths yield of 65% (Takahashi et al., 1999). They also studied the solvent extraction separation of yttrium and europium from the same leach liquor without precipitation step; that is, yttrium was initially extracted at pH 1.5 and then europium was extracted at pH 2.0. Because the extraction of impurities, such as aluminum, silicon, manganese, strontium, phosphorus, magnesium, and sodium, was less or nonexistent at this pH region, the purification was considered to be achieved. They obtained the purities of 99.7% for Y_2O_3 and 90% for Eu_2O_3. Typical impurities in the rare-earth oxides were 0.20% CaO and 0.05% Sb_2O_3 for Y_2O_3, and 1.95% CaO and 0.40% Sb_2O_3 for Eu_2O_3 (Takahashi et al., 2003).

Takahashi et al. (2001c) synthesized red rare-earth phosphor, Y_2O_3:Eu^{3+} powder, from rare-earth oxalate formed by the process shown in Fig. 13 and showed that the obtained phosphor powder had the equivalent light emission property. Leaching kinetics of yttrium and europium from the rare-earth component with hydrochloric acid was examined by Shimakage et al. (1996) using an autoclave reactor in the temperature range from 40 to 120 °C. Apparent activation energy for the leaching of yttrium and europium were determined to be 20.3 and 18.5 kJ/mol, respectively, and it was suggested that the leaching reaction was limited by the diffusion of H^+ to the rare-earth oxide surface through the Nernst boundary layer.

Recovery of yttrium and europium from spent cathode ray tubes was studied by Toma and Kojima (1995). In the cathode ray tubes, rare earths are present as Y_2O_2S:Eu, and a major component is zinc as ZnS. Thus, they studied two processes: (i) roasting—acid leaching—oxalate precipitation and (ii) direct acid leaching—oxalate precipitation. The leaching after roasting is faster than that of direct leaching, and the oxalate precipitation favors the condition: HCl for leaching, pH 0, and oxalic acid concentration of 80 kg/m^3. The integrated test of roasting, HCl leaching, oxalate precipitation, and calcination gave the products of more than 99% purity of rare-earth oxides; however, a small amount of zinc remained in the product.

Radeke et al. (1998) proposed a process for the separation of mercury, calcium, yttrium, and heavy rare earths in disposed fluorescent tubes containing both halophosphate and three-band phosphors as shown in Fig. 14. After dissolution of Y_2O_3:Eu with hydrochloric acid followed by a multistage extraction separation of rare earths, concentrated yttrium solution is obtained. By precipitation with oxalic acid and calcinations, yttrium oxide with 99.99% purity is produced. Cost–benefit estimations showed that it was reasonable to expect a profitable operation of the process assuming a favorable taxation framework.

Rabah (2008) studied the recovery of europium, yttrium, and some valuable salts from the powder coated on the inner surface of the glass tubes of

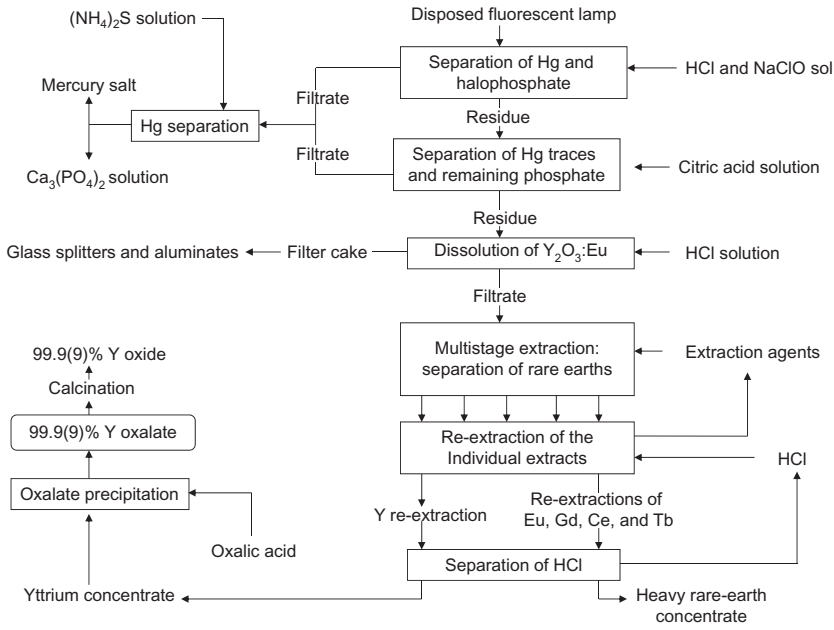

FIGURE 14 Flow sheet for the extraction process from fluorescent lamp wastes proposed by Radeke et al. (1998). The original figure is presented in German.

fluorescent lamps. The tubes were broken under 30% aqueous acetone to avoid emission of mercury vapor to the atmosphere, and the powder was collected by brushing. The isolated powder contained 1.6% europium oxide, 1.7% yttrium oxide, 34.5% calcium sulfate, 61.5% calcium orthophosphate, and 0.7% other impurity metals by weight. Autoclave digestion of the powder in the sulfuric/nitric acid mixture for 4 h at 125 °C and 5 MPa dissolved 96% of the yttrium and 93% of the europium. Sulfate salts of europium and yttrium thus obtained were converted to thiocyanates. Solvent extraction was applied in order to selectively extract europium and yttrium from the thiocyanate solution and to produce nitrate salts of europium and yttrium after stripping. Europium nitrate is separated from yttrium nitrate by dissolving in ethyl alcohol. Economic estimation revealed that the suggested method seemed to be feasible for industrial applications.

3.2.2. *Mechanochemical Treatment*

In order to dissolve rare earths from phosphors under mild condition, a mechanochemical treatment using a planetary mill was applied by Zhang and Saito's group (Zhang and Saito, 1998; Zhang et al., 2000). The mechanochemical treatment was shown to cause disordering of the crystal structures of the phosphor and thus enabled the leaching under mild conditions: yttrium,

europium, terbium, lanthanum, and cerium were dissolved in 1 kmol/m^3 HCl at room temperature after the mechanochemical treatment for 2 h with more than 80% efficiency (Zhang et al., 2000). Recently, the application of mechanochemical treatment was also attempted by Shibata's group (Shiratori et al., 2010a,b). After leaching the rare-earth oxide in a phosphor with 1 kmol/m^3 H_2SO_4, the residue was ground by a planetary mill with10 kmol/m^3 KOH solution in order to convert rare-earth phosphate to hydroxide. The product was leached with 2 kmol/m^3 H_2SO_4. At present, the completeness of leaching of terbium, cerium, and lanthanum is only 10% even after 3-h milling.

3.2.3. Alkaline Fusion

One of the problems during the recovery of rare earths from phosphor wastes is that the green phosphor ($LaPO_3$: Ce, Tb) is much less soluble than the red and blue phosphors. Under several kmol/m^3 of acid concentration, the green phosphor is not leached at all, while other phosphors can be dissolved. As already mentioned, Takahashi et al. (1996) used concentrated sulfuric acid, and Zhang et al. (2000) applied mechanochemical treatment in order to improve leaching of the green phosphor. Effectiveness of concentrated sulfuric acid has been recently confirmed by Koyama and Tanaka (2011b). Another method would be alkaline fusion. JOGMEC is managing a project of recycling phosphor waste from 2009 (JOGMEC, 2011). A basic flow sheet has been proposed as shown in Fig. 15. By applying alkaline fusion followed by HCl leaching, they are planning to dissolve all the rare earths in the waste phosphor. Solvent extraction study using multistage mixer settlers is being carried out in order to separately recover yttrium, terbium, and europium in this sequence.

3.2.4. Separation by Solvent Extraction and Its Related Technique

Nakamura et al. (2007) studied the solvent extraction separation of rare earths and alkali earths using PC-88A using the solution obtained by total leaching of phosphor wastes. Extraction equilibrium constant for each element was initially obtained assuming the stoichiometries for trivalent rare-earth ions (and Al^{3+}) shown in Eq. (4) and for alkali-earth ions (M^{2+}) as

$$M^{2+} + 3H_2L_{2org} = M(HL_2)_2(H_2L_2)_{org} + 2H^+ \quad (5)$$

Then they simulated the extraction and scrubbing behavior from the leaching solution of phosphor waste shown in Table 8 by the equilibrium model for the multicomponent and multistage system. Using simulations, yttrium, europium, and terbium were found to be obtained with the efficiencies and purities shown in Table 9. As such, the simulation based on the equilibrium constant of each element is thought to be useful as a predictive tool and would considerably save the experimental effort to conduct multistage extraction operations.

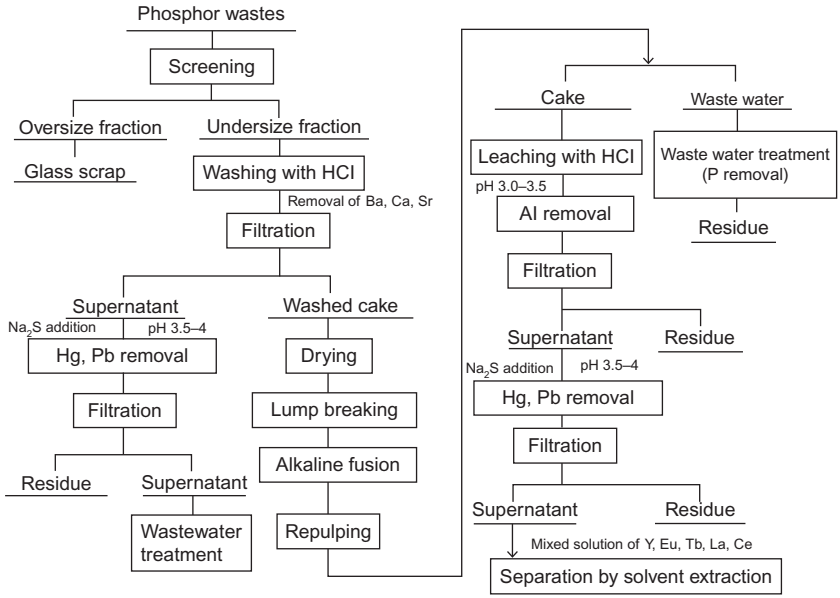

FIGURE 15 Flow sheet for the pretreatment process for phosphor wastes by JOGMEC (2011). The original figure is presented in Japanese.

TABLE 8 Composition of Fluorescence Tube Material Wastes (Nakamura et al., 2007; Tanaka and Maruo, 2007)

Element	Y	La	P	Sr	Ca	Ba	Tb	Eu	Cl	Al
Mass%	31.9	11.8	7.4	6.4	5.5	3.4	2.7	2.2	1.2	0.8

TABLE 9 Recovery Efficiencies and Purities of Rare-Earths Predicted by Simulation of Solvent Extraction (Nakamura et al., 2007)

	Y	Eu	Tb
Recovery (%)	97.8	52.8	58.1
Purity (%)	98.1	100	85.7

Shimojo et al. (2000) applied novel calixarene carboxyl derivative to solvent extraction separation of yttrium, europium, and zinc in the fluorescent powder in cathode ray tubes. Several grams of the fluorescent powder are present in each cathode ray tube. This fluorescent powder typically has a composition (mass%) of 21.1 Y, 1.4 Eu, 43.4 Zn, 0.66 Al, and 0.01 each of Fe,

Co, Ni, Cu, and Pb; thus, the separation of rare earths from a large amount of zinc is important. Conventional carboxylic acid extractant, Versatic 10, extracts yttrium, europium, and zinc at neutral pH and their mutual separation is difficult. On the other hand, calixarene carboxyl derivative was shown to extract rare earths at acidic pH preferentially to zinc, particularly in the presence of sodium ions in the aqueous phase.

As mentioned in Section 2.2.2, DODGAA presented by Naganawa et al. (2007) and Shimojo et al. (2007) has interesting extraction properties for the rare earths. One of these properties is that DODGAA can separate rare earths from zinc, which is effective in the processing of the acid leaching solution of the fluorescent powder from cathode ray tubes. In this context, Kubota et al. (2011) applied DODGAA for the separation of the rare earths from zinc (II) in an acidic solution. They compared the *n*-dodecane and ionic liquid [$C_n$mim] [Tf_2N] ($n = 4, 8, 12$) as diluents. Yttrium (III) and europium (III) can be quantitatively extracted in the presence of zinc (II), because zinc (II) is not extracted at pH less than 3. The extraction efficiency was enhanced for the shorter-alkyl-chain imidazolium ionic liquid. When [C_4mim][Tf_2N] was used, the extraction efficiency was better than in the case of *n*-dodecane. The rare-earth extraction proceeds via proton exchange reaction between DODGAA and the rare-earth ion both in the ionic liquid and *n*-dodecane as

$$R^{3+} + 3HL_{ext} = RL_{3ext} + 3H^{+} \quad (6)$$

where HL and the subscript "ext" denote DODGAA and the extracting phase (ionic liquid or *n*-dodecane). The stripping (recovery) of the rare-earth ions from the extracting phase is easily achieved with an acid solution such as nitric acid. It was also reported that an SLM based on the imidazolium-based ionic liquid is highly stable and that the use of DODGAA as a mobile carrier enables a quantitative transport of yttrium and europium through the membrane and separation from impurity metals (Kubota et al., 2010).

Shimizu et al. (2005) studied the dissolution of rare earths using supercritical carbon dioxide containing TBP complexes with nitric acid and water. By diluting the TBP:HNO_3:H_2O complex with anhydrate TBP, they succeeded in preventing the generation of aqueous droplets accompanied by the dissolution of metal oxides. More than 99% of yttrium and europium were dissolved after static operation for 120 min at 15 MPa and 60 °C.

4. BATTERIES

Rechargeable batteries are extensively used in household and industrial applications. Nickel-cadmium (NiCd) batteries were the only suitable batteries for portable applications for many years. Nickel metal hydride (NiMH) batteries, however, have replaced the NiCd batteries in many applications, after they were developed in 1989 and commercialized primarily in Japan in 1990 (Bernards et al., 2004). Electrochemical properties of the NiMH batteries

are generally better than those of NiCd batteries: they have (i) higher electrochemical capacity (1.5–2 times compared to NiCd), (ii) longer charging–discharging cycle life (more than 1000 cycles), (iii) wide operating temperature range (from −20 to 60 °C), (iv) lower self-discharge rates, and (v) a wide range of materials that store hydrogen effectively. In addition, no hazardous materials are used in the NiMH batteries compared to Cd, toxicity of which is well documented, in the NiCd batteries (Yoshida et al., 1995). In contrast, lithium-ion (Li-ion) rechargeable batteries, which contain no rare earth, show the best specific energy density among the current rechargeable batteries, yet their cost remains relatively high (Heegn and Rutz, 2009). It is expected that the Li-ion batteries will gradually replace the current batteries in the field of HEV during the next 10 years; however, at present, the NiMH batteries are still dominant because of their high reliability, safety, and cost effectiveness (Itoh and Machida, 2011).

Among the many applications of the NiMH batteries, their use in HEV has become important. The NiMH battery market for the HEV use was estimated to be at $600 million in 2006 and is expected to grow to $2.3 billion by 2015 (Rodrigues and Mansur, 2010).

The basic design of NiMH battery is similar to NiCd battery (Yoshida et al., 1995). The positive and negative electrodes are separated by an insulator. The positive electrodes consists of a porous nickel plate and nickel hydroxide as the activate agent. The negative electrodes are made of a porous nickel plate and a hydrogen-absorbing alloy. As the hydrogen-absorbing alloy, the so-called AB_5-type alloys are widely used (Itoh and Machida, 2011). They contain nickel, cobalt, and rare earths (A = La, B = Ni, or Co, in which La is often substituted with a mischmetal consisting of 50–55% of Ce, 18–28% of La, 12–18% of Nd, and 4–6% of Pr, or 50% of La, 30% of Ce, and 14% of Nd (Heegn and Rutz, 2009) or 40% of La, 38% of Nd, 12% of Ce, and 11% of Pr (Rodrigues and Mansur, 2010)). In Japan, the projected amount of spent NiMH batteries in the HEV approaches is 14,000 tons in 2020, which includes 3350 tons of rare earths, 9500 tons of nickel, and 1150 tons of cobalt (Itoh and Machida, 2011). Hence, the recovery of these valuable metals (rare earths, Ni, Co) from spent NiMH batteries is highly needed.

4.1. Physical Separation

Some physical separation methods have been studied which focus on the recovery of the hydrogen-absorbing alloys from the negative electrode of NiMH batteries. Before leaching, cooling, crushing, grinding, and wet classification were performed, and fine particles were collected (Lupi et al., 2000; Toki et al., 2007). Ito et al. (2007, 2009, 2010) have collected the product of cold crushing (to a particle size of less than 75 μm) and applied magnetic separation using a Davis tube and HGMS, which led to significant concentration of the hydrogen-absorbing alloy. Using a three-step magnetic separation

process for a cylindrical type battery, the purity was increased from 86% to 93%, and the separation efficiency was 41%.

4.2. Hydrometallurgical Methods

In the pyrometallurgical process, only Ni-rich metal fraction is recovered leaving rare earths in the slag. Therefore, hydrometallurgical treatment is generally required. The purpose of the hydrometallurgical process is to selectively recover rare earths as well as nickel and cobalt and, at the same time, to remove impurities (iron, aluminum, copper, manganese, cadmium, etc.). Here, the residue obtained after physical separation, which contains the concentrated metals, is first leached by a mineral acid. Among mineral acids, H_2SO_4 and HCl have been widely studied and selected as effective reagents for the leaching; specifically, there have been many papers on leaching using H_2SO_4. One of the typical processes involving leaching using sulfuric acid is shown in Fig. 16 (Yoshida et al., 1995). In the H_2SO_4 system, the rare earths are mainly separated from other metals by precipitation and partly by solvent extraction; on the other hand, the HCl system introduces solvent extraction

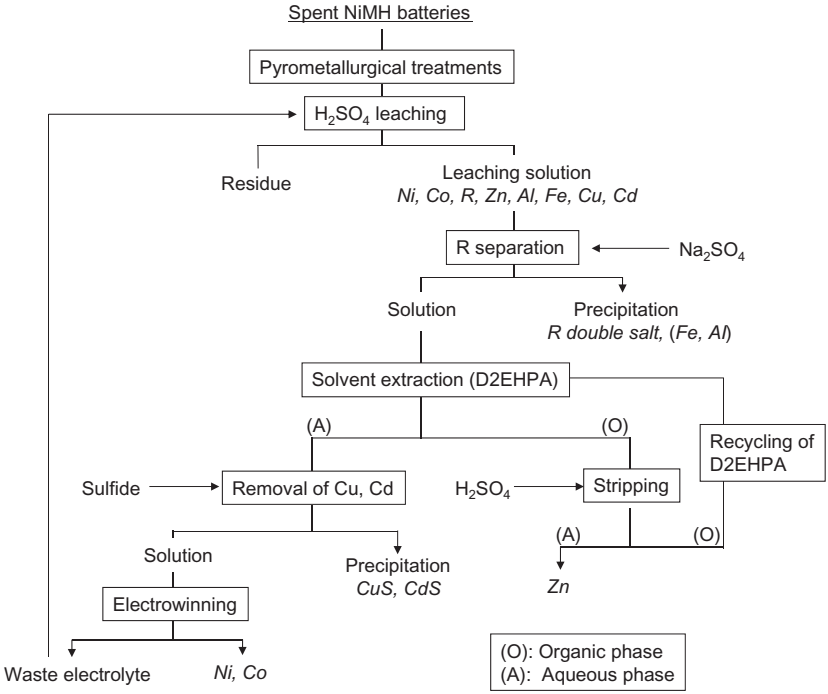

FIGURE 16 A conceptual flow of the hydrometallurgical treatments for the metal recovery from spent NiMH batteries involving sulfuric acid leaching (Yoshida et al., 1995).

into the rare-earth separation. The detailed separation methods in these two systems are described below.

4.2.1. H_2SO_4 System

Most of the leaching tests using some aqueous solutions displayed the advantage of H_2SO_4. According to Yoshida et al. (1995), H_2SO_4 and HCl show much higher leaching efficiencies than $(NH_4)_2CO_3$. By considering the leaching reagent and investment costs, they finally indicated that H_2SO_4 would be the most practical reagent for the actual recycling process. Lupi et al. (2000) investigated the leaching properties of H_2SO_4, HCl, and HNO_3; the rare-earth leaching was complete only with the H_2SO_4 solution, although the HNO_3 solution showed the highest yields for nickel, iron, cobalt, and cadmium. Thus, they selected H_2SO_4 as a leaching reagent, also considering the economic aspect. The leaching condition has been optimized in most of the studies on the hydrometallurgical recovery by investigating the effects of temperature, H_2SO_4 concentration, solid–liquid concentration, reaction time, etc., on the metal extraction yields (Heegn and Rutz, 2009; Li et al., 2009; Lupi et al., 2000; Nan et al., 2006a,b; Provazi et al., 2011; Rodrigues and Mansur, 2010; Yoshida et al., 1995; Zhang et al., 1999). As for the H_2SO_4 concentration, stoichiometric quantity of H_2SO_4 to the metal concentration, 0.5–4 kmol/m^3, was usually selected as a result of leaching tests. In contrast, other parameters (temperature, time, etc.) are highly dependent on the condition of the selected residue.

Another advantage of sulfuric acid is in unique properties of rare-earth sulfates, which are precipitated from the solution by adding KOH, NaOH, Na_2SO_4, etc., in the H_2SO_4 solution. The solubilities of rare-earth sulfates decrease with increasing temperature, while solubilities of $NiSO_4$, $CoSO_4$, $MnSO_4$, $FeSO_4$, and $Fe_2(SO_4)_3$ are high at room temperature, and they generally increase with rising temperature up to 100 °C (Li et al., 2009). This permits selective recovery of rare-earth sulfates. Since the chemical species of the rare-earth sulfates are Na(or K)$R(SO_4)_2$, the separation of rare-earth sulfates by precipitation is called the double sulfates method. The influence of pH on the precipitation of rare earths and other elements were investigated by Nan et al. (2006a). At pH 1.6, over 94% of the rare earths (lanthanum, cerium, praseodymium, and neodymium) were precipitated. The total yields of iron, manganese, and other elements in the precipitate were negligible.

The separation of rare earths by solvent extraction from the H_2SO_4 leaching solution was performed with 25% D2EHPA in kerosene (Zhang et al., 1999). The rare earths and iron were completely extracted at pH 2.5 together with the most of aluminum and zinc, whereas the extraction of cobalt and nickel was negligible. The rare earths and other extracted metals except iron in the organic phase were stripped by 1 kmol/m^3 H_2SO_4. Pure rare-earth products were obtained by selective precipitation with oxalic acid from the strip solution followed by calcination of the precipitate.

The precipitation method from the H_2SO_4 leaching solution was compared with the solvent extraction using a sample composed of a mixture of the main types of spent household batteries: Zn–C alkaline, Zn–C dry cell, NiCd, NiMH, and Li-ion (Provazi et al., 2011). The solvent extraction using Cyanex 272 was more efficient in the separation of metals than the selective precipitation.

Solvent extraction can be also used to recover a small amount of rare earths remaining in the leaching solution after the separation of precipitates of the rare-earth double sulfates (Li et al., 2009). The iron, zinc, and manganese together with the remaining 5.2% rare earths in the solution were almost completely separated from nickel and cobalt by solvent extraction with 20% D2EHPA. The rare earths extracted in the organic phase were recovered by stripping with 2 kmol/m^3 HCl after scrubbing zinc and manganese.

The rare-earth sulfates were often transformed to RCl_3 (Heegn and Rutz, 2009; Li et al., 2009). First, the rare-earth double sulfates were converted to rare-earth hydroxides by treating with NaOH. The obtained product was treated with concentrated HCl, and then the pure rare-earth chlorides were crystallized from the resulting solution.

Various methods are applied to the recovery/removal of other valuable metals (nickel and cobalt) and impurities after the rare earths are separated. Nan et al. (2006b) used two extraction reagents for copper, cobalt, and nickel: 10% Acorga M5640 at pH 1.5–1.7 for Cu; 1 kmol/m^3 Cyanex 272 at pH 5.1–5.3 for Co and at pH 6.3–6.5 for nickel. Zhang et al. (1999) separated cobalt from nickel by solvent extraction using Cyanex 272 at pH 4.8, then recovered nickel in the aqueous phase and then stripped cobalt by precipitation with oxalic acid. Rodrigues and Mansur (2010) carried out selective extraction of cadmium over nickel and cobalt with D2EHPA at pH 3.0, then selectively extracted cobalt over nickel with Cyanex 272 at pH 5.7. Li et al. (2009) indicated that cobalt was easily separated from nickel with Cyanex 272 and pure cobalt and nickel sulfates were recovered by evaporation of the stripping and extraction raffinates, respectively. The difference in the pH dependence of metal sulfate solubilities was used for the selective separation of impurities, nickel and cobalt (Lupi et al., 2000; Nan et al., 2006a). A combination of solvent extraction and electrowinning was investigated by Yoshida et al. (1995): D2EHPA extracted zinc and copper over nickel and cobalt at pH 2–3, then the remaining nickel and cobalt were recovered by electrowinning.

4.2.2. *HCl System*

In the HCl leaching system, 99% of rare earth was leached under the condition of 3 or 4 kmol/m^3 HCl at 95 °C in the 3-h reaction time (Tzanetakis and Scott, 2004a; Zhang et al., 1998). The solvent extraction using D2EHPA was introduced into the separation of rare earth from the HCl leaching solution. Zhang et al. (1998) proposed the metal separation process on the basis

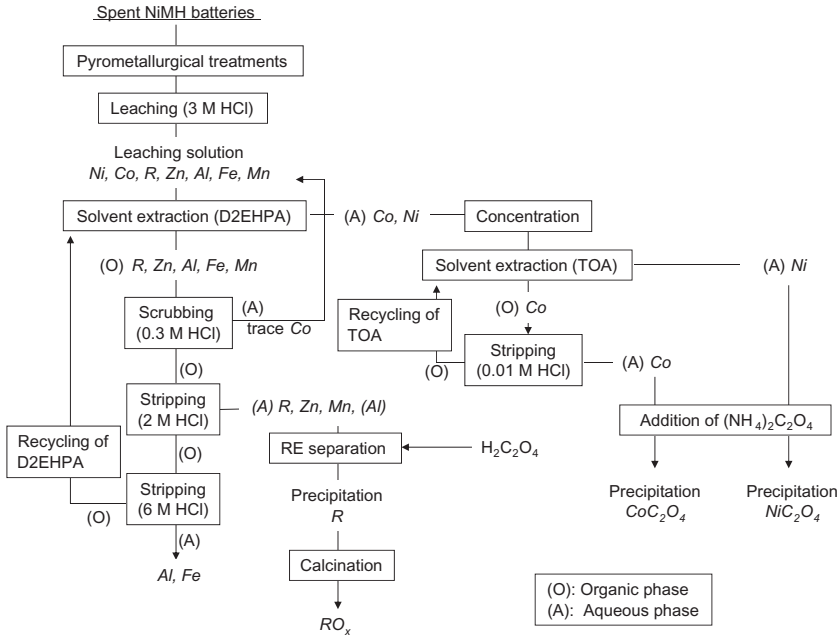

FIGURE 17 A conceptual flow of the hydrometallurgical process focusing on solvent extraction methods from the HCl leaching solution (Zhang et al., 1998). "M" means kmol/m^3.

of solvent extraction (Fig. 17). The rare earths can be quantitatively extracted over nickel and cobalt in the HCl leaching solution with 25% D2EHPA in kerosene at an equilibrium pH of 2.0. After scrubbing cobalt with 0.3 kmol/m^3 HCl and stripping with 2.0 kmol/m^3 HCl, rare-earth oxides of over 99% purity were obtained by selective precipitation with oxalic acid followed by calcination. The total yield of rare earths was nearly 98% (Fig. 17).

Recovery of nickel and cobalt after the rare earth separation by selective extraction of cobalt over nickel with 25% TOA, followed by precipitation with ammonium oxalate (Zhang et al., 1998), and electrochemical process (Tzanetakis and Scott, 2004b) was also studied.

4.3. Molten Salt Electrolysis

Most of the recycling processes using molten salts mentioned in Section 2 seem to be applicable to other rare-earth scrap, if rare earths exist as metals or alloys, with or without certain modification. Hydrogen-absorbing alloys containing mischmetal used for NiMH batteries are one of the typical examples of such materials. Available literature concerning rare-earth recycling from hydrogen-absorbing alloys, however, is sparse, because much more attention is paid to rare-earth permanent magnet scraps at present. One of

the few papers was published by Matsuura et al. (2005). They proposed a process to recover rare-earth metals using molten salt via the following steps: (i) rare earth metals are anodically dissolved into molten salt from hydrogen-absorbing alloys, (ii) rare-earth ions are concentrated near the anode area by electromigration, and (iii) rare-earth metals are recovered from the rare-earth ions concentrated melt by electrodeposition, where three anode and cathode couples are employed individually in each step. Matsumiya et al. (2005, 2006) claimed that this electromigration step is also applicable for recycling of rare-earth metals from wasted catalysts for automobiles using room temperature molten salts or ionic liquids. In this case, however, certain modifications seem to be necessary for practical use in order to carry out a suitable anode reaction during the electrowinning step. Because of the lack of data through all steps, the effectiveness of these processes is unclear at present.

5. POLISHING POWDERS, OPTICAL GLASS, AND CATALYSTS

5.1. Polishing Powders

Ceria-based glass polishing powders are widely used for the final stage during the manufacturing process of (i) optical products such as lenses, prisms, and liquid display panels and (ii) electronic products such as IC photomasks and glass hard disks. The Japanese annual demand of the ceria-based glass polishing powders in 2006 was 5500 tons, which was the highest in the rare-earth products; however, the spent powders are not recycled (JOGMEC, 2008). During the actual polishing operation, ceria-based glass polishing powders are used as ca. 10% slurry with water. Currently, the spent powders are generally separated from the slurry by precipitation using a flocculant, dehydrated by a filter press, and discarded in a landfill; however, the cost of disposal cannot be neglected because of the required flocculant and insufficient dehydration of the precipitate. Recycling of the ceria-based glass polishing powders is considered to be easier than other rare-earth products used in commodities that are sold to consumers because the polishing companies are its final users (Sato and Kato, 2010). One example of the composition of new and spent polishing powder is shown in Table 10 (Kato et al., 2000a). In the waste powder, silica and alumina as impurities are present which come from fine glass powder and flocculants, respectively.

Liang et al. (2009) attempted the application of flotation using sodium dodecylsulfate as a collector. More than 99% recovery was achieved from the model spent powder with the composition of new polishing powder: glass containing no rare earths = 1:2. However, when the real sludge obtained by coagulation treatment of spent slurry was treated, the recovery of rare-earth oxides was only 40% with the purity of 44% (35% in feed sample).

Kato et al. (2000a,b,c, 2010) studied the recycling of ceria-based glass polishing powder via alkali treatment. The powder was regenerated after

TABLE 10 Typical Composition of the Polishing Powder and Its Waste (Mass%) (Kato et al., 2000a)

Oxide	Polishing powder	Polishing powder waste
La_2O_3	34.2	17.8
CeO_2	43.8	22.1
Pr_6O_{11}	3.4	2.3
Nd_2O_3	10.9	5.1
BaO	2.62	0.67
SiO_2		12.6
Al_2O_3		24.8

removing major impurities, that is, silica and alumina, at 50–60 °C in a 4 mol/kg NaOH solution within 1 h. After appropriately adjusting the solution composition, dissolved silica and alumina can be recovered as zeolite ($Na_8(AlSiO_4)_6$ $(OH)_2 \cdot 4H_2O$) at 80 °C (Kato et al., 2000a) or hydroxysodalite ($Na_8(AlSiO_4)_6(OH)_2 \cdot 4H_2O$) at 80–100 °C (Kato et al., 2000b). The polishing ability of the regenerated powder was shown to be the same as the new polishing powder by measuring the surface roughness after polishing (Kato et al., 2000a). A useful method based on the solubility curves of silica and alumina at 60 and 100 °C was proposed for appropriate adjustment of the solution composition (Kato et al., 2000c).

This method needs a relatively large-scale facility and generates alkaline waste water, which hampers actual implementation of the technique. Thus, Kato and Sato are now studying a simple elutriation method (Kato et al., 2011; Sato and Kato, 2010). They carried out the experiment using an apparatus with two settling tanks having maximum capacity of 50 dm^3 slurry. In the first tank, large particles such as glass fragments and solidified aggregates of the polishing powder rapidly sank after sufficient mixing. The supernatant solution was transferred to the second tank and settled for 3 days in order to sediment the polishing powder. They confirmed that the recovered polishing powder was reusable.

Liang's group is studying hydrometallurgical recovery of rare earths from the spent ceria-based glass polishing powder as well as the separation by flotation as mentioned earlier (Yamada et al., 2011). The leaching test with hydrochloric acid using the real spent polishing powder indicates that lanthanum is leached preferentially to cerium (Yamada et al., 2010). For example, using 1.4 $kmol/m^3$ HCl at 55 °C, 65% of Ce and only a few percent of La are dissolved within 60 min. Thus, selective leaching of cerium seems to be possible. Solvent extraction separation of rare earths from the acid leach liquor of spent ceria-based glass polishing powder is also being studied using acidic

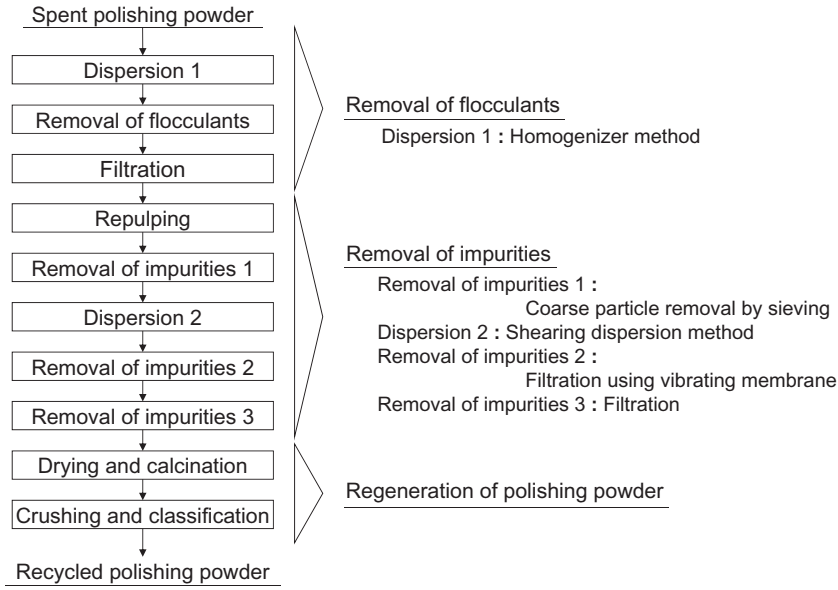

FIGURE 18 Basic flow of regeneration of polishing powders (JOGMEC, 2011).

organophosphorous reagents such as D2EHPA and PC-88A (Yamada et al., 2011). Cerium is extracted preferentially to lanthanum with these reagents. For example, the extraction efficiencies of cerium and lanthanum with 50% PC-88A at the after-extraction pH of 1.24 are 74% and 28%, respectively.

JOGMEC is managing a project of recycling polishing powders from 2009 (JOGMEC, 2011). At present, a basic flow sheet has been proposed as shown in Fig. 18. After specification of each step is established, a demonstration test will be conducted.

As a pyrometallurgical approach, Ozaki et al. (1999) studied the application of the chemical vapor transport method described in Section 2.3.1. Used polishing powder was chlorinated by chlorine gas at 1000 °C, and transported along the temperature gradient via gaseous complex with aluminum chloride. The rare-earth chlorides were mainly condensed over the temperature range of 457–947 °C. The purity of the rare-earth chlorides in this temperature range was about 95%.

5.2. Optical Glass

Lanthanum, yttrium, and gadolinium are used in optical glasses with high refractive index and low dispersion. The annual demand for La_2O_3 for this purpose in Japan was 502 tons in 2006; none of this glass is recycled (JOGMEC, 2008).

Jiang et al. (2004) developed a hydrometallurgical process to recover the rare earths from the spent optical glass containing lanthanum, yttrium, and

gadolinium that involves conversion of the rare earths to hydroxides with sodium hydroxide, leaching of the hydroxides by hydrochloric acid, purification of the leach liquor by selective precipitation followed by separation of rare earths using solvent extraction with D2EHPA. The composition and the process flow sheet are shown in Table 11 and Fig. 19, respectively. Laboratory-scale experiment showed that 99.95% pure lanthanum chloride solution containing 31.8 kg/m^3 La with a total recovery of 93.6%, 98.7% pure

TABLE 11 Typical Composition of Spent Optical Glass (Mass%) (Jiang et al., 2004)

Component	Content	Component	Content
La_2O_3	43.12	Sb_2O_3	0.13
Y_2O_3	9.37	BaO	1.25
Gd_2O_3	4.60	B_2O_3	24.50
ZrO_2	6.48	SiO_2	6.25
ZnO	0.25	Others	0.75
Nb_2O_5	3.30		

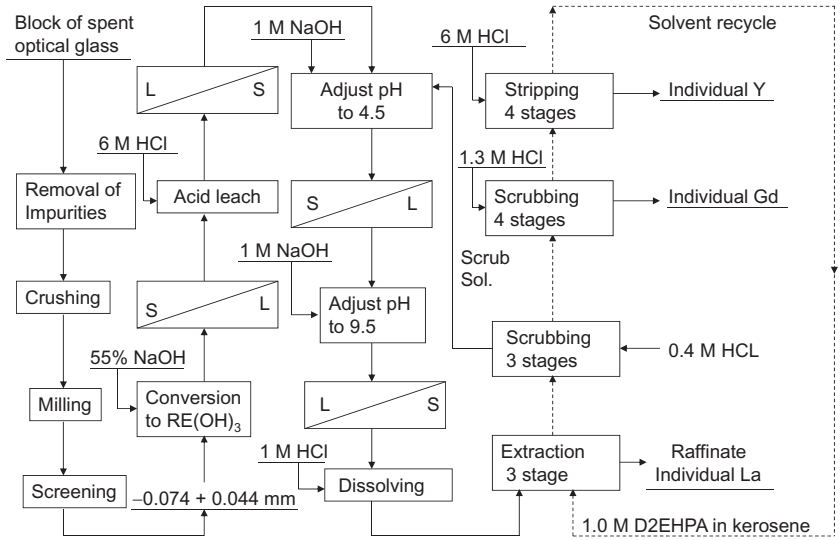

FIGURE 19 Schematic process flow sheet for recovery of rare earths from spent optical glass containing lanthanum, yttrium, and gadolinium. Reproduced from Jiang et al. (2004) after slight modification. "M" means kmol/m^3.

yttrium chloride solution containing 11.5 kg/m^3 Y with a total recovery of 97.6%, and 95.2% pure gadolinium chloride solution containing 5.6 kg/m^3 Gd with a total recovery of 93.6% were obtained.

5.3. Catalysts

Three-way catalysts used in exhaust-gas catalytic converters of automobiles contain platinum, palladium, rhodium, zirconium, and cerium. Oki et al. have developed a method which concentrates these metals by means of a two-step crushing procedure (Kim et al., 2010; Oki et al. 2010). The process makes it possible to increase concentration of rare-earth metals by a factor of five by first demolishing the honeycomb structure, and then peeling off the surface. To date, no process leading to recovery of individual rare-earth metals has been described.

6. CONCLUDING REMARKS

As the result of the literature survey of the rare-earth recycling studies, recycling of magnet scrap has received most of the attention. This is because of the large predicted growth of the demand for neodymium magnets and the presence of a highly critical rare earth element, dysprosium. The important points of the out-of-plant magnet recycling in physical separation are dismantling and demagnetization. At present, dismantling is mainly done manually, which implies high cost and limited productivity, while a few studies of successful automation have been reported. Although these examples certainly enhance the productivity, economic aspects of permanent magnet materials recycling remain somewhat uncertain. For demagnetization, heating has been a main method because of a relatively low Curie temperature of the Nd–Fe–B magnets, while athermal methods using magnetic field are also being developed. Hydrometallurigical methods are actively investigated. Separation of the rare earths from excess iron is prerequisite; thus, selective leaching is important. Separation of dysprosium from neodymium is relatively easy achieved by solvent extraction using acidic organophosphorous reagents such as PC-88A. For efficient separation, however, further studies are necessary to model various systems in order to quantitatively simulate the process. New extractant, DODGAA, is worthy of notice because of the rejection of iron and higher separation factor for Nd/Pr. Pyrometallurgical methods have an advantage in reaction kinetics over hydrometallurgical ones and are thus expected to treat bulky wastes. Wide variety of processes have been proposed, and high separation efficiencies of rare earths from iron were reported in laboratory-scale experiments. Although a few studies of the use of molten salts have been described, these studies are still at the fundamental stage

and have not been commercialized. This is because the physicochemical and electrochemical behaviors of rare earths in molten salts are already well known, and a simple application to recycling does not stimulate academic interest much. Thus, current research is predominantly to find novel methods based on less familiar principles. Although practical implementation of such methods in a short term is difficult, future developments are expected.

Phosphors are also receiving attention next to magnets. Physical separation, in contrast to the permanent magnet case, is based on fine particle separation techniques, which is a primary issue because particle size of common phosphors is around 5 μm. The application of HGMS is notable, and further studies are expected. Hydrometallurgical methods, such as leaching of yttrium and europium and their mutual separation are not difficult; however, similar to issues related to recycling of permanent magnets, further studies are necessary to model practical systems in order to quantitatively simulate processes potentially leading to high efficiency. In order to recover highly critical element, terbium, green phosphor should be targeted. Although it is possible to dissolve green phosphor either by concentrated sulfuric acid leaching, mechanochemical treatment, or alkaline fusion, cost effectiveness remains a formidable barrier for practical implementation.

There are many studies related to recycling of NiMH batteries. In this case, the main targets are nickel and cobalt, and the rare-earths recovery is only secondary. Nevertheless, it would be important to develop an efficient total process considering the recovery of both Ni/Co and the rare earths. Recycling of polishing powders is becoming more important because of the recent rapid price increase of ceria and cerium. Considering that spent polishing powders never leave the plant where polishing is performed, there would be little difficulty in collection of waste. Simple and effective processes are expected to be soon established.

Finally, it is doubtless that the rare-earth recycling should be promoted in order to stabilize the supply chain and save the limited natural resources. The rare-earth separation from the scrap would be possible in most cases; however, cost effectiveness is always a problem for practical implementation, as is the case in recycling of many post consumer products. This problem maybe overcome not only by pursuing the separation technologies but also by establishing sufficient collection and stockpiling systems together probably with some motivating framework established through legislation. Nonetheless, from the view point of separation technology, the integrated approach is necessary, and it should involve collaborations among experts in various fields, such as physical separation, hydrometallurgy, pyrometallurgy, chemical engineering, and analytical chemistry on the basis of the fundamental knowledge on the physics and chemistry of rare earths.

ABBREVIATIONS

Acorga M5640	2-hydroxy-5-nonylbenzaldehyde oxime with a fatty ester modifier
Cyanex 272	bis(2,4,4-trimethylpentyl)phosphinic acid
D	distribution ratio
D2EHPA	bis(2-ethylhexyl)phosphoric acid
DD	direct drive
DOE	United States Department of Energy
HDD	hard disk drive
HEV	hybrid electric vehicle
HGMS	high-gradient magnetic separator
JOGMEC	Japan Oil, Gas, and Metals National Corporation
LIX65N	2-hydroxy-5-nonylbenzophenone oxime
NiMH	nickel metal hydride
PC-88A	2-ethylhexylphosphinic acid mono-2-ethylhexyl ester
SLM	supported liquid membrane
TBP	tri-*n*-butylphosphate
TOA	tri-*n*-octylamine
TOPO	tri-*n*-octylphosphine oxide
VCM	voice coil motor
Versatic 10	2-ethyl-2-methylheptanoic acid
$\Delta pH_{1/2}$	difference in $pH_{1/2}$, in which $pH_{1/2}$ denotes the pH when 50% extraction takes place

REFERENCES

Akai, T., 2011a. Funct. Mater. 31 (7), 25.

Akai, T., 2011b. In: Proceedings of the 6th Rare Metals Symposium, October 24, 2011. National Institute of Advanced Industrial Science and Technology, Nagoya, pp. 125–134.

Akai, T., Yamashita, M., Oki, T., 2011. Rare Earths 58, 14.

Arai, Y., 2010. In: Symposium on Recycling of Rare Metals, July 9, 2010. Japan Society of Material Cycles and Waste Management, Tokyo (http://jsmcwm.or.jp/recycle/7_Arai_MMC.pdf, accessed on December 15, 2011).

Arai, Y., Koga, S., Hoshina, H., Yamaguchi, S., Kondo, H., 2011. Mater. Cycl. Waste Manag. Res. 22, 41.

Baba, K., Nemoto, T., Maruyama, H., Taketani, N., Itayagoshi, K., Hirose, Y., 2010. Hitachi Hyoron 92 (6), 74 [Hitachi Review 59, 180–187].

Baba, Y., Kubota, F., Kamiya, N., Goto, M., 2011. Solv. Extr. Res. Dev. Japan 18, 193.

Bard, A.J. (Ed.), 1976. In: Encyclopedia of Electrochemistry of Elements, vol. X. Marcel Dekker, New York, p. 68.

Bernards, A.M., Espinosa, D.C.R., Tenório, J.A.S., 2004. J. Power. Sources 130, 291.

Boghosian, S., Papatheodorou, G.N., 1996. In: Gschneidner Jr., K.A., Eyring, L. (Eds.), Handbook on the Physics and Chemistry of Rare Earths, vol. 23. Elsevier Science B.V., Amsterdam, pp. 435–496.

Bounds, C.O., 1994. In: Liddell, K.C., Bautista, R.G., Orth, R.J. (Eds.), Metals and Materials Waste Reduction, Recovery and Remediation. The Minerals, Metals & Materials Society, Warrendale, PA, pp. 173–186.

Cordier, D.J., 2011. Rare Earths: U.S. Geological Survey, Mineral Commodity Summaries 2011. U.S. Geological Survey p. 129.

Croat, J.J., Herbst, J.F., Lee, R.W., Pinkerton, F.E., 1984. J. Appl. Phys. 55, 2078.

DOE, Critical Materials Strategy, 2011.

Fujita, T., Dodbiba, G., Otsuki, A., 2009. Rare Earths 54, 28.

Goonan, T. G., Rare earth elements—End use and recyclability, Scientific Investigations Report *2011–5094*, U. S. Geological Survey, 2011.

Gschneidner Jr., K.A., Daane, A.H., 1988. In: Gschneidner Jr., K.A., Eyring, L. (Eds.), Handbook on the Physics and Chemistry of Rare Earths, vol. 11. Elsevier Science B.V., Amsterdam, pp. 409–484.

Heegn, H., Rutz, M., 2009. AT/Miner. Proce. 50 (6), 48.

Hirai, H., Hirajima, T., Tsunekawa, M., Hiroyoshi, N., Nakayama, K., Sasaki, K., Takahashi, T., Nagano, N., 2001. In: Proceedings of MMIJ Fall Meeting, September 24–26, 2001. The Mining and Materials Processing Institute of Japan, Tokyo, PY-27.

Hirajima, T., Hamada, N., Hirai, H., Tsunekawa, M., Hiroyoshi, N., Sasaki, K., Takahashi, T., Nagano, N., 2002. In: Proceedings of MMIJ Annual Meeting, March 28–30, 2002, II. The Mining and Materials Processing Institute of Japan, Tokyo, pp. 191–192.

Hirajima, T., Sasaki, K., Bissombolo, A., Hirai, H., Hamada, M., Tsunekawa, M., 2005a. Sep. Purif. Technol. 44, 197.

Hirajima, T., Bissombolo, A., Sasaki, K., Nakayama, K., Hirai, H., Tsunekawa, M., 2005b. Int. J. Miner. Process. 77, 187.

Horikawa, T., Machida, K., 2011. Mater. Integr. 24 (2), 37.

Hubbard, W.M., Adams, E., Gilfrich, J., 1960. J. Appl. Phys. 31, 368S.

Itakura, T., Sasai, R., Itoh, H., 2006. J. Alloys Compd. 408–412, 1382.

Ito, Y., 2011. In: Proceedings of the 43rd Symposium on Molten Salt Chemistry. Molten Salt Committee of the Electrochemical Society of Japan, Osaka, p. 52.

Ito, M., Kashiwaya, K., Sumiya, N., Furuya, H., Hiroyoshi, N., Tsunekawa, M., 2007. In: Proceedings of the 9th International Symposium on East Asian Resources Recycling Technology (EARTH 2007), October 29–November 2, 2007. The Mining and Materials Processing Institute of Japan, Tokyo, pp. 439–442.

Ito, M., Kashiwaya, K., Sumiya, N., Hiroyoshi, N., Tsunekawa, M., 2009. Sep. Purif. Technol. 69, 149.

Ito, M., Kashiwaya, K., Sumiya, N., Furuya, H., Hiroyoshi, N., Tsunekawa, M., 2010. Int. J. Miner. Process. 97, 92.

Itoh, M., Machida, K., 2011. Mater. Integr. 24 (2), 32.

Itoh, K., Nakamura, E., Sasaki, S., 1988. Sumitomo Light Met. Tech. Rep. 29, 127.

Itoh, M., Miura, K., Machida, K., 2007. J. Ceramic Soc. Jpn. 115, 628.

Itoh, M., Miura, K., Machida, K., 2009. J. Alloy Comp. 477, 484.

Jiang, Y., Shibayama, A., Liu, K., Fujita, T., 2004. Can. Metallur. Quart. 43, 431.

JOGMEC, 2011. Kinzoku Shigen Rep. 41, 309.

JOGMEC, Material Flow of Mineral Resources 2007, 2008, pp. 227–234.

JOGMEC, Material Flow of Mineral Resources 2010, 2011, pp. 383–403.

Katayama, Y., Kubo, K., Tanaka, T., Nakamoto, M., Yamamoto, T., 2010. CAMP-ISIJ 23, 898.

Kato, K., Tsuboi, T., Munakata, M., Gamo, K., Hattori, Y., Watanabe, T., Study for recycling of ceria-based glass polishing powder. In: Technical Reports of Fukushima Technology Center, 2010, pp. 5–13.

Kato, K., Yoshioka, T., Okuwaki, A., 2000a. Ind. Eng. Chem. Res. 39, 943.
Kato, K., Yoshioka, T., Okuwaki, A., 2000b. Ind. Eng. Chem. Res. 39, 4148.
Kato, K., Yoshioka, T., Okuwaki, A., 2000c. Nippon Kagaku Kaishi 2000, 725.
Kato, K., Tsuboi, T., Munakata, M., Gamo, K., Sato, M., 2011. Chem. Eng. 2011 (2), 156.
Kim, W.-T., Kim, B., Choi, D., Oki, T., Kim, S., 2010. J. Hazardous Mater. 183, 29.
Kobayashi, S., Kobayashi, K., Nohira, T., Hagiwara, R., Oishi, T., Konishi, H., 2011. J. Electrochem. Soc. 158, E142.
Konishi, H., Ono, H., Nohira, T., Oishi, T., 2011. Molten Salts 54, 21.
Koshimura, H., Recovery of samarium from scrap of samarium–cobalt alloy with double salt of samarium sulfate. In: Report of Tokyo Metropolitan Industrial Technology Center 1987, 16, pp. 113–118.
Koshimura, H., Recovery of samarium from scrap of samarium–cobalt alloy by a batch counter current extractor. In: Report of Tokyo Metropolitan Industrial Technology Center 1988, 17, pp. 83–88.
Koshimura, H., Yamamoto, S., 1983. In: Proceedings of Symposium of Solvent Extraction, Dec. 9–10, 1983. Japanese Association of Solvent Extraction, Hamamatsu, pp. 155–162.
Koshimura, H., Yamamoto, S., 1984. In: Proceedings of Symposium of Solvent Extraction, Dec. 7–8, 1984. Japanese Association of Solvent Extraction, Hamamatsu, pp. 115–120.
Koyama, K., Tanaka, M., 2009. In: Proceedings of MMIJ Fall Meeting, Sep 8–10, 2009. The Mining and Materials Processing Institute of Japan vol. 2, Tokyo, pp. 57–58.
Koyama, K., Tanaka, M., 2011a. In: Machida, K. (Ed.), The Latest Technology Trend and Resource Strategy of Rare Earths. CMC Press, Tokyo, pp. 127–131.
Koyama, K., Tanaka, M., 2011b. In: Proceedings of MMIJ Annual Meeting 2011. The Mining and Materials Processing Institute of Japan, Tokyo, No. 2411.
Koyama, K., Kitajima, A., Tanaka, M., 2009. Rare Earths 54, 36.
Kubo, K., Tanaka, T., Nakamoto, M., Yamamoto, T., 2009. CAMP-ISIJ 22, 118.
Kubo, T., Sekimoto, H., Kon, T., Yamaguchi, K., 2011. In: Proceedings of MMIJ Fall Meeting, Sep 26–29, 2011. The Mining and Materials Processing Institute of Japan, Tokyo, PY-35.
Kubota, F., Shiobori, Y., Koyanagi, Y., Shimojo, K., Kamiya, N., Goto, M., 2010. Anal. Sci. 26, 289.
Kubota, F., Shiobori, Y., Baba, Y., Koyanagi, Y., Shimojo, K., Kamiya, N., Goto, M., 2011. J. Chem. Eng. Japan 44, 307.
Lee, J.-c., Kim, W.-b., Jeong, J., Yoon, I.J., 1998. J. Korean Inst. Met. Mater. 36, 967.
Lee, M.-S., Lee, J.-Y., Kim, J.-S., Lee, G.-S., 2005. Sep. Purif. Technol. 46, 72.
Li, L., Xu, S., Ju, Z., Wu, F., 2009. Hydrometallurgy 100, 41.
Liang, R., Yamada, T., Kikuchi, E., Kawashima, H., Soma, T., 2009. In: Proceedings of MMIJ Annual Meeting, Mar 26–28, II. The Mining and Materials Processing Institute of Japan, Tokyo, pp. 181–182.
Lupi, C., Pilone, D., Cannavale, G., Pescetelli, A., 2000. In: Taylor, P.R. (Ed.), EPD Congress 2000. The Minerals, Metals & Materials Society, Warrendale, PA, pp. 257–270.
Lyman, J.W., Palmer, G.R., 1993a. High Temp. Mater. Process. 11, 175.
Lyman, J. W., Palmer, G. R., 1993b. Recycling of neodymium iron boron magnet scrap. In: Report of Investigations 9481: United States Bureau of Mines.
Machida, K., 2003. J. Magn. Soc. Japan 27, 793.
Machida, K., 2004. Kinzoku 74, 389.
Machida, K., 2009. Kinzoku 79, 705.
Matsumiya, M., Tokuraku, K., Matsuura, H., Hinoue, K., 2005. Electrochem. Commun. 7, 370.
Matsumiya, M., Tokuraku, K., Matsuura, H., Hinoue, K., 2006. J.Electroanal. Chem. 586, 12.
Matsuura, H., Numata, H., Fujita, R., Akatsuka, H., 2005. J. Phys. Chem. Solids 66, 439.

Minowa, T., 2011. Materials Integration 24 (2), 17.
Miura, K., 2011. Demagnetization of neodymium magnets at room temperature. In: Lecture in Tokyo on November 11, 2011: Japan Society of Material Cycles and Waste Management (Abstract available at: http://jsmcwm.or.jp/jimu/event/20111111-youshi.pdf, Accessed on December 15, 2011).
Miura, K., Itoh, M., Machida, K., 2008. J. Alloy Comp. 466, 228.
Morimoto, S., Daigo, I., Matsubae, K., 2011. Kinzoku 81, 117.
Murase, K., Machida, K., Adachi, G., 1995. J. Alloy Comp. 217, 218.
Nagai, H., 2010. Kinzoku Shigen Rep. 40, 493.
Naganawa, H., Shimojo, K., Mitamura, H., Sugo, Y., Noro, J., Goto, M., 2007. Solv. Extr. Res. Dev. Japan 14, 151.
Nakamura, E., 2011. Funct. Mater. 31, 25, No. 7.
Nakamura, T., Nishihama, S., Yoshizuka, K., 2007. Solv. Extr. Res. Dev. Japan 14, 105.
Nan, J., Han, D., Yang, M., Cui, M., 2006a. J. Electrochem. Soc. 153, A101.
Nan, J., Han, D., Yang, M., Cui, M., Hou, X., 2006b. Hydrometallurgy 84, 75.
Nash, K.L., 1994. In: Gschneidner Jr., K.A., Eyring, L., Choppin, G.R., Lander, G.H. (Eds.), Handbook on the Physics and Chemistry of Rare Earths, vol. 18. Elsevier Science B.V., Amsterdam, pp. 197–238.
Nemoto, T., Tanaka, Y., Tsujioka, S., Eryu, Y., Takada, T., 2011. Hitachi Hyoron 93 (5–6), 56 [Hitachi Review 2011, 60, 335].
Niinae, M., Yamaguchi, K., Ishida, N., Djohari, A., Nakahiro, Y., Wakamatsu, T., 1994. J. MMIJ 110, 981.
Ohta, A., 2003. Tech. Rep. Sumitomo Spec. Metals 14 (Mar), 20.
Oishi, T., Konishi, H., Nohira, T., Tanaka, M., Usui, T., 2010. Kagaku Kogaku Ronbunshu 36, 299.
Okabe, T.H., Takeda, O., Fukuda, K., Umetsu, U., 2003. Mater. Trans. 44, 798.
Oki, T., 2007. Advanced particle separation technology for rare metals recycling. In: Exhibitor Brochure at Hannover Messe 2007, April 16–20, 2007, Hannover.
Oki, T., 2010. Rare Earths 56, 198.
Oki, T., 2011. Rare Earths 58, 34.
Oki, T., Kobayashi, M., Int. Patent Appl. No. PCT/JP2008/066961; Publ. No. WO/2009/038163, March 26, 2009.
Oki, T., Kim, W.-T., Katsumata, T., Kobayashi, M., 2010. Japan Patent Appl. No. 2008-236137; 2010. Publ. No. 2010-069351, April 2.
Oki, T., Wada, N., Matsumoto, M., 2011. In: Proceedings of MMIJ Annual Meeting. The Mining and Materials Processing Institute of Japan, Tokyo, No. 2025.
Otsuki, A., Fujita, T., 2008. In: Proceedings of the 17th Symposium of Resources Processing Society of Japan, Sept. 18, 2008. The Resources Processing Society of Japan, Kyoto, pp. 8–10.
Otsuki, A., Dodbiba, G., Sadaki, J., Fujita, T., 2007. In: The 4th Korea/Japan International Symposium on Resources Recycling and Materials Science, March 8–10, 2007, Jeju 86–93.
Otsuki, A., Dodbiba, G., Shibayama, A., Sadaki, J., Mei, G., Fujita, T., 2008. Jpn. J. Appl. Phys. 47, 5093.
Ozaki, T., Machida, K., Adachi, G., 1999. Metall. Mater. Trans. B 30B, 45.
Pourbaix, M., 1966. Atlas of Electrochemical Equilibria in Aqueous Solutions. Pergamon Press, Oxford.
Provazi, K., Campos, B.A., Espinosa, D.C.R., Tenório, J.A.S., 2011. Waste Manag. 31, 59.
Rabah, M.A., 2008. Waste Manag. 28, 318.

Radeke, K.H., Riedel, V., Weiss, E., Kussin, P., Gosse, I., Reimer, B., 1998. Chem. Technik 50 (3), 126.

Rodrigues, L.E.O.C., Mansur, M.B., 2010. J. Power. Sources 195, 3735.

Sagawa, M., Fujimura, S., Togawa, N., Yamamoto, H., Matsuura, Y., 1984. J. Appl. Phys. 55, 2083.

Saguchi, A., Asabe, K., Fukuda, T., Takahoshi, W., Suzuki, R.O., 2006. J. Alloy Comp. 408, 1377.

Saito, T., Sato, H., Ozawa, S., Yu, J., Motegi, T., 2003. J. Alloys Compd. 353, 189.

Saito, T., Sato, H., Motegi, T., 2005a. J. Alloys Compd. 387, 274.

Saito, T., Sato, H., Motegi, T., Kobayashi, K., 2005b. J. Alloys Compd. 403, 341.

Sanuki, S., Sugiyama, A., Kadomachi, K., Miyata, K., Arai, K., 1995. J. Japan Inst. Metals 59, 169.

Sato, M., Kato, K., 2010. Chem. Eng. 2010 (5), 334.

Sato, N., Wei, Y., Nanjo, M., Tokuda, M., 1997. J. MMIJ 113, 1082.

Shimakage, K., Hirai, S., Sekii, M., Takahashi, T., Sakuta, Y., 1996. J. MMIJ 112, 953.

Shimizu, R., Sawada, K., Enokida, Y., Yamamoto, I., 2005. J. Supercrit. Fluids 33, 235.

Shimojo, K., Kubota, F., Oshima, T., Goto, M., Furusaki, S., 2000. Kagakukogaku Ronbunshu 26, 506.

Shimojo, K., Naganawa, H., Noro, J., Kubota, F., Goto, M., 2007. Anal. Sci. 23, 1427.

Shiratori, G., Minami, S., Murayama, N., Shibata, J., Kawakita, K., Kamiya, T., Nagai, H., Obara, M., 2010a. In: Preprint of the Society of Chemical Engineers Japan 75th Annual Meeting, Mar. 18–20, 2010. The Society of Chemical Engineers, Japan, Tokyo, p. 42.

Shiratori, G., Murayama, N., Shibata, J., Nagai, H., Obara, M., 2010b. In: Preprint of the Society of Chemical Engineers Japan 42nd Autumn Meeting, Sep 6–8, 2010. The Society of Chemical Engineers, Japan, Tokyo, p. 395.

Shirayama, S., Okabe, T.H., 2008. In: Proceeding of Annual Meeting of MMIJ, Mar. 27–29, 2008, II. The Mining and Materials Processing Institute of Japan, Tokyo, pp. 69–70.

Shirayama, S., Okabe, T.H., 2009. Molten Salts 52, 71.

Suzuki, R.O., Saguchi, A., Takahashi, W., Yagura, T., Ono, K., 2001. Mater. Trans. 42, 2492.

Takahashi, T., Tomita, K., Sakuta, Y., Takano, A., Nagano, N., 1996. Separation and recovery of rare earth elements from phosphors in waste fluorescent lamp (part II)—Separation and recovery of rare earth elements by chelate resin. In: Reports of the Hokkaido Industrial Research Institute, No. 295, pp. 37–44.

Takahashi, T., Takano, A., Saito, T., Nagano, N., 1999. Separation and recovery of rare earth elements from phosphors in waste fluorescent lamp (part III)—Separation and recovery of rare earth elements by multistage countercurrent extraction. In: Reports of the Hokkaido Industrial Research Institute, No. 298, pp. 37–47.

Takahashi, T., Takano, A., Saitoh, T., Nagano, N., 2003. Separation and recovery of rare earth phosphor from phosphor sludge in waste fluorescent lamp by multistage countercurrent solvent extraction. In: Reports of the Hokkaido Industrial Research Institute, No. 302, pp. 41–48.

Takahashi, T., Takano, A., Saitoh, T., Nagano, N., Hirai, S., Shimakage, K., 2001a. J. MMIJ 117, 579.

Takahashi, T., Takano, A., Saitoh, T., Nagano, N., Hirai, S., Shimakage, K., 2001b. In: Proceedings of the 6th International Symposium on East Asian Resources Recycling Technology (EARTH 2001), October 23–25, 2001. The Korean Institute of Resources Recycling, Seoul, pp. 421–426.

Takahashi, T., Takano, A., Saitoh, T., Nagano, N., 2001c. Synthesis of rare earth phosphor from phosphor sludge in processing plant of waste fluorescent lamp. In: Reports of the Hokkaido Industrial Research Institute, No. 300, pp. 1–8.

Takahashi, T., Tomita, K., Sakuta, Y., Takano, A., 1994. Separation and recovery of rare earth elements from phosphors in waste fluorescent lamp (part I). In: Reports of the Hokkaido Industrial Research Institute, No. 293, pp. 7–13.

Takeda, M., 2000. Molten Salts 43, 103.

Takeda, O., Okabe, T.H., Umetsu, U., 2004. J. Alloy Comp. 379, 305.

Takeda, O., Okabe, T.H., Umetsu, U., 2006. J. Alloy Comp. 408–412, 378.

Takeda, O., Nakano, K., Sato, Y., 2009. Molten Salts 52, 63.

Takeda, O., Nakano, K., Sato, Y., 2011. In: Symposium on Current Status Toward Stable Supply of Rare-Earth, 2011. The Mining and Materials Processing Institute of Japan, Tokyo, pp. 22–23.

Tanaka, M., Maruo, T., Japanese Patent. No. 3950968 (2007).

Tanaka, M., Sato, Y., Huang, Y., Narita, H., Koyama, K., 2009. In: Proceedings of the 10th International Symposium on East Asian Resources Recycling Technology (EARTH2009), Nov. 2–6, 2009. The Korean Institute of Resources Recycling, Seoul, pp. 200–203.

Tawara, Y., Strnat, K.J., 1976. IEEE Trans. Magn. 13, 954.

Terada, T., Onishi, H., Kawakami, T., 2001. J. Japan Inst. Metals 65, 627.

Toki, N., Takeda, K., Takahashi, J., 2007. In: Proceedings of the 9th International Symposium on East Asian Resources Recycling Technology (EARTH 2007), October 29–November 2, 2007. The Mining and Materials Processing Institute of Japan, Tokyo, pp. 424–427.

Toma, K., Kojima, Y., 1995. In: Proceedings of the MMIJ Fall Meeting, Sept. 18–20, 1995, N. The Mining and Materials Processing Institute of Japan, Tokyo, pp. 9–12.

Tzanetakis, N., Scott, K., 2004a. J. Chem. Technol. Biotechnol. 79, 919.

Tzanetakis, N., Scott, K., 2004b. J. Chem. Technol. Biotechnol. 79, 927.

Uda, T., 2002. Mater. Trans. 43, 55.

Uda, T., Jacob, K.T., Hirasawa, H., 2000. Science 289, 2326.

Wang, L.P., Dodbiba, G., Okaya, K., Fujita, T., Murata, K., Kawano, M., Fujigaki, Y., 2011. In: Proceedings of the MMIJ Annual Meeting. The Mining and Materials Processing Institute of Japan, Tokyo, pp. 43–44.

Wei, Y., Sato, N., Nanjo, M., 1989. J. MMIJ 105, 965.

Xu, Y., Chumbley, L.S., Laabs, F.C., 2000. J. Mater. Res. 15, 2296.

Yamada, T., Liang, R., Kikuchi, E., Kawashima, H., 2010. In: Proceedings of the MMIJ Annual Meeting 2010, Mar. 30–Apr. 1, 2010. The Mining and Materials Processing Institute of Japan, Tokyo, No. 1524.

Yamada, T., Liang, R., Kikuchi, E., Kawashima, H., 2011. In: Proceedings of the MMIJ Annual Meeting 2011. The Mining and Materials Processing Institute of Japan, Tokyo, No. 1114.

Yamashita, F., Terada, T., Onishi, H., 2001. J. Magn. Soc. Japan 25, 687.

Yoon, H.-S., Kim, C.-J., Lee, J.-Y., Kim, S.-D., Kim, J.-S., Lee, J.-C., 2003. J. Korean Inst. Resources Recycling 12, 57.

Yoshida, T., Ono, H., Shirai, R., 1995. In: Queneau, P.B., Peterson, R.D. (Eds.), Proceedings of the Third International Symposium, Recycling of Metals and Engineered Materials, Nov. 12–15, 1995. The Minerals, Metals & Materials Society. Warrendale, PA, pp. 145–152.

Zhang, Q., Saito, F., 1998. J. MMIJ 114, 253.

Zhang, P., Yokoyama, T., Itabashi, O., Wakui, Y., Suzuki, T.M., Inoue, K., 1998. Hydrometallurgy 50, 61.

Zhang, P., Yokoyama, T., Itabashi, O., Wakui, Y., Suzuki, T.M., Inoue, K., 1999. J. Power. Sources 77, 116.

Zhang, Q., Lu, J., Saito, F., 2000. J. MMIJ 116, 137.

Intentionally left as blank

Chapter 256

Ionic Liquids: New Hopes for Efficient Lanthanide/Actinide Extraction and Separation?

Isabelle Billard

Institut Pluridisciplinaire Hubert Curien, Groupe de Radiochimie, CNRS/IN2P3, Université de Strasbourg, Strasbourg cedex 2, France

Chapter Outline

Handbook on the Physics and Chemistry of Rare Earths, Vol. 43.
http://dx.doi.org/10.1016/B978-0-444-59536-2.00003-9

1. INTRODUCTION

Liquid–liquid extraction of rare earths (RE) and actinides (An) is of huge industrial importance. RE are used in a large variety of devices (bulb lamps, screens, batteries, magnets, etc.), and the cost pressure induced by the off-shoring of RE mining industries to China (Gschneidner, 2011a,b) has imposed a renewed interest in any liquid–liquid extraction method of these elements. On another hand, recycling of actinides, and in particular, of uranium and plutonium, by liquid–liquid extraction processes, is at the heart of the development of nuclear industry. Although the Fukushima accident has shed some serious doubts onto the security aspects of nuclear industry, even in well-developed countries, nuclear generation of electricity and heat will remain a major solution for a demanding world of possibly more than 9 billion inhabitants at the middle of this century, each of them aspiring to and deserving high living standards in terms of energy supply. According to the World Nuclear Association (http://www.world-nuclear.org/info), there were some 440 nuclear power plants operating in 2011 generating about 14% of the world's electricity and over 60 new reactors were under construction, mainly in Asia.

Besides these energetic and political aspects, there is a strong impulse toward "greener" industrial processes through the REACH regulation (entered into force in 2007), which will limit the future use of volatile organic compounds in use in nowadays liquid–liquid extraction systems. One possible alternative to these detrimental chemicals is the use of a new class of solvents, called ionic liquids (ILs). These solvents are usually presented as nonvolatile and nonflammable. Some of them are claimed to be nontoxic, biodegradable, and even edible. Although this enthusiasm should be somehow restrained, as will be detailed in the next section, ILs are nevertheless solvents displaying fantastic physicochemical properties allowing unusual chemistry to occur. ILs are studied for an increasing number of applications in various aspects of chemistry, such as organic synthesis (Wasserscheid and Welton, 2008), electrochemistry (Ohno, 2005), and, of course, liquid–liquid extraction. Recently, they have spread out of the laboratory shelves to enter the industrial world (Plechkova and Seddon, 2008).

An increased number of studies deal with the use of ILs for liquid–liquid extraction of RE and actinides. Although the field is not mature yet, as a lot is still to be understood and discovered, there are enough data available already to derive general rules and trends and also to envision future directions for IL uses in liquid–liquid extraction of these metallic ions. This chapter therefore presents an historical perspective and a critical review of current works on this topic. Two brief presentations of ILs and of traditional liquid–liquid extraction will be first given. Then, current results and ideas in the field of liquid–liquid extraction of RE and actinides by use of ILs will be reviewed. As much as possible, we limited ourselves to studies dealing with the metals of interest to the handbook (4f and 5f elements), but in some cases, we

extended the review to works devoted to other elements, owing to their general interest to the questions discussed. Note that solid–liquid extraction by use of ILs, although very interesting as such, is out of the scope of this chapter. Readers are referred to some recent papers on this rising subject (Myasodeova et al., 2008; Odinets et al., 2010; Olivier et al., 2011; Sun et al., 2009). Similarly, we will not present data on ILs/supercritical CO_2 systems, although this domain is presently deserving much attention (Dzyuba and Bartsch, 2003; Keskin et al., 2007; Mekki et al., 2005, 2006).

2. IONIC LIQUIDS: SOME FACTS AND FIGURES

The simplest and widest definition of ILs is "salts with melting temperature below 100 °C," and this will be used throughout this review. Many papers consider also a subclass of ILs, composed of those being liquid at room temperature (RTILs, room-temperature ILs), but this denomination will not be used in this review. We will not review data obtained with chloroaluminate ILs because this first generation of solvents is always highly sensitive to water and oxygen, thus rending them inadequate to solvent extraction from aqueous phases. According to their definition, ILs are media composed of ions. The discovery of such solvents can be traced back to the early beginning of the twentieth century, with the synthesis of ethylammonium nitrate in 1914, a salt with melting point equal to $T_m = 14$ °C. Despite this long history, IL studies really started with the synthesis of numerous air and water stable salts composed of an organic cation and an inorganic anion, and the reader is referred to the very good paper by Wilkes (2002) for an historical perspective on ILs. Since then, the number of new ILs has been rising tremendously and it is difficult to assess the number of all ILs described to date, although estimates have been proposed (Rodgers and Seddon, 2003). On a practical aspect, structure variations seem to be more in the cationic component of ILs, mainly because the organic skeleton allows any fantasy of the organist chemists, while anions belong to a somehow more restricted list. Scheme 1 presents the chemical structures of commonly used cations and anions in ILs. Most of the cations composing the ILs cited in this review belong to the *N*,*N*-dialkylimidazolium family and will thereafter be denoted as $C_nC_m im^+$ where *n* and *m* are the length of the alkyl chains. We would like also to point out dicationic ILs (Ito et al., 2000) and just a few other interesting compounds (Del Sesto et al., 2008; Yoshida and Saito, 2010) to give an idea of the versatility of ILs' world. Despite the fantastic variety of ILs chemical structures, RE/An liquid–liquid extraction studies with ILs deal with quite a limited list of ILs skeletons, mostly based on the imidazolium family, mainly because the wealth of data already accumulated for these ILs facilitates their use for liquid/liquid extraction studies. Recent papers start to investigate the physicochemical properties of other cationic families (Gerhard et al., 2005; Papaiconomou et al., 2010) that will certainly be of interest to the extraction field soon.

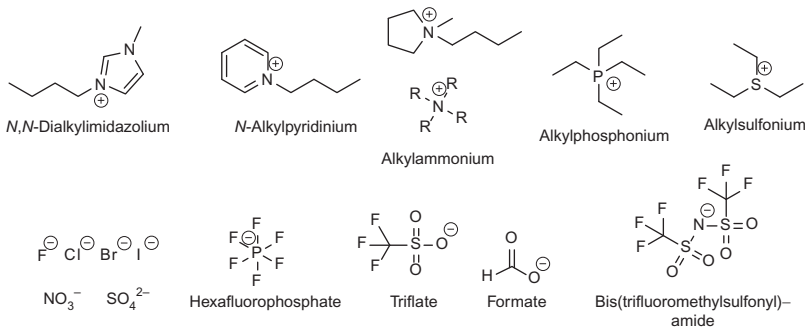

SCHEME 1 Chemical structures of the most common cationic and anionic parts of ILs.

Which properties render ILs so interesting that an increased number of publications, in all fields of chemistry and material science, are presenting them as the panacea for all encountered problems? Obviously, as pointed out above, this is not due to their chemical versatility as such. In fact, introductions of many papers present ILs as "nonvolatile, nonflammable solvents," thus "green media," which would be the rationale for the enthusiasm they generate. These common places have to be somehow moderated. Actually, it has been rapidly shown that although many ILs do not present noticeable vapor pressure, some are volatile and can be distilled (Wasserscheid, 2006). Some applications of ILs are for thermal liquid media or for explosives (Singh et al., 2006), and one can also synthesize highly flammable ILs (Smiglak et al., 2006). Finally, the claimed nontoxicity of ILs is at the moment mainly due to a lack of data (Wood and Stephens, 2010), although eco-friendly or biodegradable ILs appear to be within reach (Gathergood et al., 2006; Scammells et al., 2005). ILs properties are so diverse that they escape any classification attempts, besides that used for their definition, based on their melting point value.

Another, more reasonable, argument often put forward is the huge potential arising from their "tuneable physicochemical properties." Again, this is based on a large amount of data, as numerous excellent papers have demonstrated that slight changes in the chemical structures of both the anion and the cation of ILs induce significant changes in any physicochemical properties of ILs, such as viscosity, density, melting point, and conductivity (see Table 1 for some physicochemical properties of the most common ILs used in RE/An extraction studies). However, the term "tuneable" would indicate that one controls the relations between structures and properties *a priori* and that prediction of a given property is feasible, which is far from true unfortunately. At the moment, only empirical trends have been derived, which apply to rather limited series of ILs. More sophisticated attempts to link structures and

TABLE 1 Viscosity, η, Density, d, and Melting Temperature, T_m, of Some Common ILs

IL	η (cP)	d	T_m (°C)
$C_1C_2imPF_6$	19 (67)[a]		5[b]
$C_1C_2imTf_2N$	27 (30)[c]	1.51 (30)[c]	−18[c]
$C_1C_4imPF_6$	182 (30)[c]	1.37 (30)[c]	10[c]
$C_1C_4imTf_2N$	40 (30)[c]	1.43 (30)[c]	−3[c]
$C_1C_8imPF_6$	506 (25)[*,d]	1.16 (25)[*,d]	−70[e]
$C_1C_8imTf_2N$	71 (30)[c]	1.31 (30)[c]	−80[c]
$C_1C_{10}imTf_2N$	91 (25)[f]	1.27 (25)[f]	
Me_3BuNTf_2N	141 (21)[g]	1.39 (21)[g]	

The temperature at which η and d have been measured is indicated in parenthesis.
**Water equilibrated.*
[a] *McEwen et al. (1999).*
[b] *Ngo et al. (2000).*
[c] *Tokuda et al. (2006).*
[d] *Huddleston et al. (2001).*
[e] *Law and Watson (2001).*
[f] *Dzyuba and Bartsch (2002).*
[g] *Jacquemin et al. (2006).*

properties have been dealing mainly with melting points, with a rather limited success, as the series used to build models concerned only bromide-based ILs, thus seriously limiting the chemical diversity of the data set (Katritzky et al., 2002; Varnek et al., 2007). See also a discussion on the possibilities offered by *ab initio* methods for predicting properties (Izgorodina, 2011). In our opinion, mathematical approaches called QSPR (quantitative structure–property relationships), in large use in the pharmaceutical field for drug design, appear to be very promising. Although such mathematical empirical correlation searches cannot explain *why* one IL is liquid down to −10 °C or why another one displays a viscosity below 10 cP, for example, these mathematical methods will certainly, in the next future, be of great help for the rational design of ILs presenting a given set of desirable properties. Attempts have been already made in this direction, which focused so far on a single property, viscosity, demonstrating the feasibility of such investigations (Billard et al., 2011a). Thus, it would be more unbiased to state that ILs are so diverse that the IL you would like for a given application certainly exists, but so far, the disappointing and time-consuming trials-and-errors strategy is the only available way to search for it.

In our opinion, the major interest of ILs lies in their liquid structure and in the very few properties that can be directly inferred from their definition. First, ILs present polar and apolar parts in their cationic and/or anionic components. Molecular dynamic simulations have shown that in the liquid state, ILs thus display nanodomains of polar and apolar types, in dynamical equilibrium (Canongia Lopes and Padua, 2006; Jiang et al., 2007). These theoretical results sustain and complement many experimental indications (Chiappe, 2007; Jeon et al., 2008; Shigeto and Hamaguchi, 2006). The unusual liquid structure induces a dual solvating behavior of ILs toward molecular species and ions (Chaumont and Wipff, 2007). In case ILs also contain water, the nanodomains have been shown to be preserved up to very high water contents (Jiang et al., 2007), and conversely, fascinating structures have been calculated for ILs dissolved in water (Bhargava and Klein, 2011). It has also been demonstrated that the state of water in ILs is quite unusual (Cammarata et al., 2001), as H_2O most probably solvates the anion preferentially (Jiang et al., 2007). This is also confirmed experimentally, as An(IV) compounds are not hydrolyzed in ILs, while they are very sensitive to water in molecular solvents (Nikitenko and Moisy, 2006).

Another very specific advantage of ILs in view of nuclear fuel reprocessing is their stability toward radiolysis. Solvents in contact with highly radioactive ions arising from dissolution of fuel rods will suffer from high radiation intensities, mainly from α emitters but also from β, γ, and possibly neutron emitters. Subsequent radiolysis phenomena are occurring, particularly in highly concentrated solutions containing large amounts of nitric acid, which renders the study of such effects very complicated. Radiolysis of the solvent and of the solutes dissolved in them may lead to decreased efficiencies of the extraction process, owing to degradation of the solutions and appearance of undesired compounds that may be detrimental to the reprocessing chemistry. Gaseous compounds may also be problematic (H_2, for example). A recent series of review focuses on such problems in molecular solvents (Mincher et al., 2009, 2010). Some of the strategies envisioned to cope with this question are modification of the solutes, to make them more radio resistant, if possible, or to favor radiolysis degradation of deliberately added pendant arms, that would not lower the overall extraction efficiency, by preventing degradation of the complexing pattern. When designing new molecules for future extraction/partitioning processes, very strict radio resistance tests are performed that have been lethal to many molecules otherwise appealing on a purely extraction efficiency criterion. In this respect, ILs appear to be solvents with high potential. First, modification of their chemical structure, in order to introduce boron or other elements, could help improve the criticality limit of the solutions (Harmon et al., 2001), that is, the maximum concentration of actinides above which a nuclear reaction may diverge without human will and control. In this way, ILs would appear as intrinsically safer solvents than molecular

ones. Second, the radiolytic stability of the most common IL families has been proved to be comparable to that of molecular aromatic liquids (Berthon et al., 2006; Bossé et al., 2008; Huang et al., 2011; Le Rouzo et al., 2009). Even more interestingly, the damage to the IL solvent is greater than that to the solutes, a situation opposite to that observed in traditional extraction systems, where the solutes are highly sensitive to radiolysis. Excellent papers have appeared recently on this question (Shkrob et al., 2011a,b,c,d; Yuan et al., 2008, 2009). The extraction study by Bell and Ikeda (2011) is the first one for which ILs have been deliberately conceived considering this point.

It is, however, necessary to pinpoint some disadvantages of ILs. Owing to their large cations and anions, ILs are rather viscous solvents at room temperature, with typical viscosities in the range of 25–120 cP for the imidazolium and tetraalkylammonium families, thus at least one order of magnitude above viscosities of molecular solvents. This is of course a real problem in view of industrial implementation, where radius pipes and pump motors would have to be adapted to these viscous compounds. In many instances, fortunately, it is nevertheless possible to cope with viscosities below 50 cP. Another point is the cost of ILs. At the moment, in the academic world, these solvents are very expensive, reaching prices around 2000 €/kg for the imidazolium-Tf_2N family, with little hope these prices will decrease significantly in the next future, owing to the cost of the $LiTf_2N$ salt used for their synthesis. Although an increasing demand from the industry would certainly induce a price lowering, ILs still remain costly solvents, both for industrial applications and for academic studies. In this respect, ILs may reveal their real potential for the recovery of precious and rare metals, such as RE and actinides.

Finally, the reader is referred to some valuable review papers dealing with An and Ln chemistry in ILs (Billard and Gaillard, 2009; Binnemans, 2007; Mudring and Tang, 2010).

3. LIQUID–LIQUID EXTRACTION OF RARE EARTHS AND ACTINIDES

3.1. Traditional Organic Solvents: A Brief Overview

In this section, we present the basis of liquid–liquid extraction, focusing on results for metallic cations and in particular on RE and An. However, most information of this section can easily be adapted to the extraction of organic molecules. To get a deeper insight into the field of liquid–liquid extraction, especially from an applied viewpoint, the reader is referred to a recent book (Henley et al., 2011).

In the following, subscripts "aq," "org," and "IL" in the notation $[X]_{i,j}$ correspond to the aqueous, molecular organic, and IL phase concentrations,

respectively, while subscripts "init" and "eq" designate the initial and equilibrium concentrations, respectively. In the chemical equilibria, an upper bar corresponds to species present in the organic or IL phase.

The aim of liquid–liquid extraction is to extract one given species from a starting liquid phase, which is, most of the time, an aqueous phase into another liquid phase, usually an organic solvent forming a biphasic system with water. Most of the time, the aqueous phase also contains many other species (other ions, acids, etc.), sometimes in large excess as compared to the species to be extracted. Thus, "efficient" liquid–liquid extraction is to be understood in terms of high yields (i.e., the remaining amount in the aqueous phase after extraction is very low) and in terms of high separation factors (i.e., the extraction has been achieved without extracting the other species in noticeable amounts). Quantitatively speaking, one defines the distribution ratio, D_M, of species M as

$$D_M = \frac{[M]_{org,eq}}{[M]_{aq,eq}} \frac{V_{aq}}{V_{org}} \quad (1)$$

where V_{aq} and V_{org} are the volumes of the aqueous and organic phases, respectively. Most of the time, extraction experiments are performed with $V_{org} = V_{aq}$, leading to the usual equation:

$$D_M = \frac{[M]_{org,eq}}{[M]_{aq,eq}} \quad (2)$$

One may also define, E_M, the extraction efficiency of a species M, expressed in percentage; for $V_{org} = V_{aq}$, one gets

$$E_M = \frac{100\,[M]_{org,eq}}{[M]_{aq,init}} \quad (3)$$

D_M and E_M are related and, for equal volumes of aqueous and organic phases, the relationship is

$$E_M = \frac{100\,D_M}{1 + D_M} \quad (4)$$

Unless otherwise specified in the text, we will consider that Eqs. (2) and (3) apply (equal volumes of organic and aqueous phases).

An extraction is qualified as being "good" when D_M values are larger than 10 ($E_M > 90.9\%$), but in some cases, distribution ratios can reach values larger than 10^4 ($E_M > 99.99\%$). An extraction process is termed "inefficient" when D_M values are smaller than 1. For $D_M = 1$ ($E_M = 50\%$), half of the initial amount of M in water is transferred into the organic solvent. D_M values in the range of 10^4 are meaningful, owing to the very good detection limits of analytical techniques such as ICP-MS.

The separation factor, $SF_{M_1M_2}$, of M_1 with respect to M_2 is defined as

$$SF_{M_1M_2} = \frac{D_{M_1}}{D_{M_2}} \quad (5)$$

Depending on the systems, "good" separation factors can be in the range of 2–5000.

In general, metallic cations do not spontaneously transfer from an aqueous phase to an organic phase, because of the difference of solvation energy between the two solvents. In order to favor solubilization of the metal into the organic solvent, chelating agents, L, are to be used. Furthermore, to avoid hydrolysis and precipitation, aqueous phases are usually acidified by mineral acids such as HCl or HNO_3. Thus, a liquid–liquid extraction system is defined by the cation to be extracted, the chelating agent, and the receiving organic phase, while the starting phase is always an aqueous solution. In the following, systems of this type will be thus described as M^{m+}/HX//L/Org, where M^{m+} is the cation of interest, HX is the acid, L is the chelating agent, and Org is the organic molecular solvent. Cat^+ and A^- will designate the cationic and anionic component of an IL solvent.

In view of industrial applications, after extraction from water, the metallic cation has to be transferred from the organic extraction phase into a fresh aqueous phase (possibly acidified, to avoid precipitation) from which various hydrometallurgical processes can be easily implemented. This operation is called either back-extraction or stripping. This is of course an important industrial aspect which is nevertheless often neglected in academic studies, assuming reversibility of processes.

From a practical point of view, on a laboratory scale, extraction is usually performed following the batch technique, in two steps: First, during the pre-equilibration step, the aqueous acidified phase is put into contact by mechanical shaking ("contacted") with the organic phase containing the chelating agent, in order to ensure mutual saturation of the phases. Then, extraction is performed by either adding the metallic cation directly to the pre-equilibrated aqueous phase or separating this phase and contacting the pre-equilibrated organic phase with a fresh aqueous phase of same acidity containing the metallic cation. The second procedure is valid only if the organic phase does not dissolve too much in the aqueous one and also if volume changes by mutual solubilization are not too important. After mechanical shaking that can last from a few minutes to several hours, depending on systems and experimental procedures, the biphasic system is separated by centrifugation and D_M is determined by any suitable analytical method. To this aim, ICP-MS and ICP-AES are common but, in case of radioactive samples, α or γ counting can be preferred as experiments are usually performed at the trace level.

On an industrial scale, the batch method is usually replaced by continuous counterflow contactors, and to obtain high distribution ratios or separation

factors, several extraction stages can be implemented. Also, to ensure reproducible extracting performances, the ligand concentration is always in large excess as compared to the metallic species to be extracted.

Extraction mechanisms in molecular solvents have been studied for decades and are now well understood. They rely on one single, very easy to understand rule: ion pairing occurs, so the extracted species is always neutral, in order to accommodate it in the organic phase. Then, the exact description of the extraction process can be divided into three categories, depending on the ligand nature. Nonprotonated ligands, L, extract a metallic neutral entity under the form $\overline{MX_mL_p}$ (see Eq. 6), while protonated ligands, here denoted as HL, form the neutral species $\overline{ML_n}$, n protons being transferred to the aqueous phase to ensure electrical neutrality of both phases (Eq. 7). The third possibility, which is not as common as the previous two, arises from quaternary ammonium salts, denoted LB, that may extract negatively charged metallic ions of the form $\overline{MX_kL_p}$ (Eq. 8). In addition to these extraction equilibria, ligands are usually also extracting part of the acid dissolved in the aqueous phase, under the form of species with various stoichiometries (Eq. 9):

$$M^{m+} + p\overline{L} + mX^- \rightleftarrows \overline{MX_mL_p} \tag{6}$$

$$M^{m+} + m\overline{HL} \rightleftarrows \overline{ML_m} + mH^+ \tag{7}$$

$$[MX_k]^{p-} + p\overline{LB} \rightleftarrows \overline{MX_kL_p} + pB^- \tag{8}$$

$$i(H^+ + X^-) + jL \rightleftarrows \overline{HX_iL_j} \tag{9}$$

Acid extraction is competing with the extraction of the metallic cation at high acid concentration, thus lowering the extraction efficiency. This effect can be negligible or not, depending on the relative values of the equilibrium constants, which in turn depend on the ligand chemistry, and range of acid concentration. Finally, the complexing abilities of the acidic counteranion, X^-, have also to be taken into account to reach a comprehensive understanding of the extraction process. In keeping with common practice, when the acid extraction is competitive, a plot of D_M versus $[HX]_{aq,init}$ is preferred and displays a typical bell shape as illustrated in Fig. 1, while when the acid extraction can be neglected and the ligand is of the proton-dissociation type, the curve E_M versus pH is preferentially chosen, as illustrated in Fig. 2. Note that owing to Eq. (4), E_M and D_M vary similarly as a function of $[HX]_{aq,init}$. As illustrated in Fig. 1, ligands are not specific to one given element and can, under different chemical conditions, extract preferentially various ions. Thus the separation factor is also dependent on the chemical conditions. Modeling of extraction processes in molecular solvents is now well mastered, even to account for the complicated ionic strength effects in the aqueous and organic phases, and the reader is referred to two examples among many others that illustrate the excellent modeling abilities reached in this field for activity

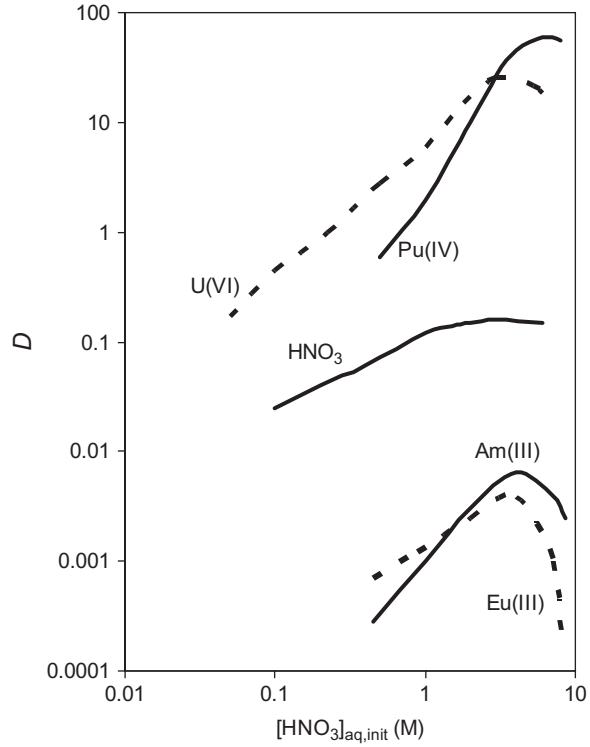

FIGURE 1 Typical D variation as a function of $[HNO_3]_{aq,init}$ for some radionuclides and HNO_3 by use of a malonamide dissolved in a molecular solvent.

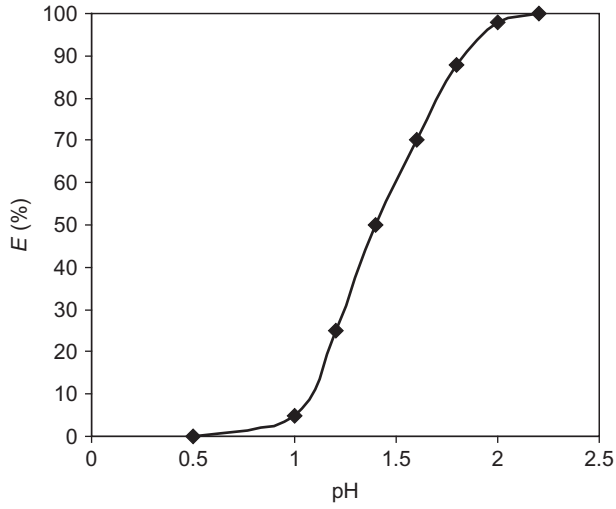

FIGURE 2 Typical E variation as a function of pH for a Ln(III) cation extracted by a protonated ligand toward a molecular solvent.

coefficients (Condamines et al., 1993) or for mass transfer kinetics (Geist et al., 2002).

In case a ligand L is considered not efficient enough for a given application, another ligand, L′, can be added: M^{m+}/HX//(L + L′)/Org. In favorable cases, this leads to an increased extraction, which is better than could be expected from the effect of each ligand alone. These are called synergistic systems, and the increased extraction efficiency is due to the formation of mixed complexes of the form $ML_iL'_j$, that are better extracted than either ML_i or ML'_j because the metallic core is better protected from interaction with water molecules. A typical synergistic system for nuclear waste management is operating in the TRUEX process (see Table 2), where 0.2 M CMPO is added to ca. 1.3 M TBP (tributylphosphate, acting as a phase modifier to avoid third phase formation), diluted in paraffinic hydrocarbons in view of extracting U, Np, Pu, and Am simultaneously. Some systems present an antisynergistic effect, but they will not be discussed here.

TABLE 2 List of the Main Extraction Processes Envisioned for Future Nuclear Fuel: Nicknames, Signification of Acronyms, Main General Composition of the Organic Phase, Purpose

Acronym and signification	Goal	Ligand/organic phase	References
PUREX	U, Pu extraction and partitioning Extension to Np partitioning	TBP/kerosene	Dileep et al. (2008)
UREX, UREX+ (Uranium Refinement by extraction)	No pure Pu stream (UREX); removal of Tc (UREX+)	TBP/dodecane	Mitchell et al. (2009)
TRUEX (TRans Uranium EXtraction)	U, Np, Pu, Am recovery	CMPO + TBP/ paraffinic hydrocarbon	Schulz and Horwitz (1988)
DIAMEX (DIAMide EXtraction)	An(III) and Ln(III) coextraction from high active raffinate	Malonamide/TPH	Modolo et al. (2007)
SANEX (Selective ActiNide Extraction)	An(III) recovery from DIAMEX raffinate (An in the organic phase)	BTBP/octanol	Magnusson et al. (2009)
GANEX (Group ActiNide EXtraction)	An(III) separation from Ln(III)	(BTBP + TBP)/ cyclohexanone	Aneheim et al. (2010)

TABLE 2 List of the Main Extraction Processes Envisioned for Future Nuclear Fuel: Nicknames, Signification of Acronyms, Main General Composition of the Organic Phase, Purpose—Cont'd

Acronym and signification	Goal	Ligand/organic phase	References
TALSPEAK (Trivalent Actinide–Lanthanide Separation by Phosphorus reagent Extraction from Aqueous Komplexes)	An(III) separation from Ln(III) (Ln in the organic phase)	$(RO)_2PO_2H$/ diisopropylbenzene	Nilsson and Nash (2007)
TRPO (TRialkyl Phosphine Oxide)	U, Np, Pu extraction	TRPO/kerosene	Liu et al. (2004)

Solutes added in some cases to the aqueous phases are not indicated.

3.2. Extraction Processes in Nuclear Industry

The choice of a chelating agent and an organic phase is strongly dependent on the cation to be extracted. The workhorse of the nuclear industry is TBP diluted in kerosene (30%, v/v, i.e., 1.1 M), in use in the PUREX process (plutonium–uranium refinement extraction), only slightly modified since its first implementation in the USA during WWII in order to obtain uranium and plutonium for the nuclear bombs launched over Japan. In the presently operating PUREX process, used nuclear fuels are dissolved in water acidified with large amounts of nitric acid (in the range of 4 M). Besides nitrates, such aqueous solutions contain mainly uranium, under its uranyl form UO_2^{2+}, a large variety of other metallic cations, arising from nuclear fission (main fission products: Zr, Nb, Ru, Sr, Eu, Tc, etc.) as well as minor actinides (Am, Cm, and Np) and plutonium (Pu), arising from neutron captures. Among the anionic metallic species, we note the presence of TcO_4^- and ReO_4^-. Such an aqueous soup is contacted with a mixture of TBP and kerosene to extract U and Pu. Slight modifications of the chemical conditions (e.g., increasing HNO_3 concentration to ca. 5 M) allow quantitative extraction of Np too, as TBP is not very specific to U and Pu. For a more detailed overview of the context of nuclear management and nuclear waste reprocessing, the reader is referred to various publications (Abu-Khader, 2009; Barré, 1998; Choppin, 2006).

Although very effective, the industrial PUREX process suffers from some drawbacks, among which the limited ease of recycling for TBP, because of its phosphorus content. Molecules that would be as efficient as TBP and that would comply with the CHON principle (i.e., containing only C, H, O, and N atoms in their chemical structure) would be highly desirable. In addition,

in view of transmutation, extraction and partitioning of minor actinides (Np, Am, Cm) and lanthanides are mandatory, which is impossible to perform with TBP. Depending on what will be the exact chemical composition of fuels for transmutation, separation may concern either all three minor actinides (Np, Am, and Cm) or only Np and Am. Cesium is also problematic in view of its specific storage needs. In the future, there may also be concerns about higher transuranic elements, such as Cf and Bk, now arising in noticeable amounts owing to higher burnups, increased operating times of fuels, and higher neutron fluxes. Protactinium may also be of some interest to the chemists in the future, owing to the molten salt reactors implementation envisioned in the fourth generation concept of nuclear plants (http://www.gen-4.org/). Furthermore, there will be great concern in remediation of possibly huge volumes of radioactive wastes that do not resemble basic nuclear fuels. The US government, for example, has launched a project for Hanford tank remediation, and one can also think of the wastes accumulated through the Fukushima accident. As a conclusion of this list of unresolved problems in the field of nuclear waste reprocessing, it is clear that the list of elements that will, should, or could be recycled at the middle of this century, besides U and Pu, is not fixed yet.

As pointed in the introduction, the recovery of RE, either from ore or from recycling of technological devices such as screens or bulb lamps, is becoming of tremendous importance to the industry. In this respect, liquid/liquid extraction processes are of interest, but the reader is referred to Chapter 255 for a review on the recycling of RE from various scraps.

Therefore, there is an active field of research and development aiming at finding new extraction agents for An/Ln partitioning, in particular, for the nuclear industry (see, e.g., the long-lasting ACSEPT program (actinide recycling by separation and transmutation), funded by the EU (actinide recycling by separation and transmutation, http://www.acsept.org/). This is a difficult task, because of the great similarities in the chemistry of An and Ln. To name just a few of the chelating agents of interest to the academic world at the moment, the following chemical families are worth mentioning: malonamides, BTP, CMPO, calixarenes, phosphine oxides, crown-ethers (see Table 2 for extraction purposes and names of processes in which they may be involved). Industrial extractants may also consist of mixtures of organic molecules of various similar chemical structures, having industrial nicknames such as Cyanex, A336, etc. A tremendous effort is under way in the academic world to propose new extracting systems, but the intrinsic complexity of the problem leads to rather intricate chemical systems, as illustrated in one publication chosen as a typical example (Geist et al., 2006).

3.3. Using ILs for RE/An Extraction and Partitioning

For all the pending questions cited above, ILs may provide unexpected answers, new ways, and original strategies, which prompted this review paper.

Academic research on liquid/liquid extraction by use of ILs is now well developed and can be divided into four distinct methodological categories that will be reviewed successively as follows:

(i) ILs are just considered as being new solvents, and the system is simply changed from M^{m+}/HX//L/Org to M^{m+}/HX//L/IL, where L is a traditional molecular extracting ligand. We also include in this category systems of the form M^{m+}/HX//(L + L′)/IL. This is certainly not an original way to use ILs, but the idea has proved to be quite fruitful. In addition to their extraction efficiency, the interest in using ILs relies on some of their "green" aspects, here limited to low volatility and nonflammability because in almost if not all published papers on this topic, the anionic part of the IL solvent does not comply with the CHON principle owing to the introduction of Tf_2N^- or PF_6^- anions, most of the time. Historically speaking, this is the first way ILs were used and this represents the largest number of publications. The wealth of work accumulated so far has allowed proposing general rules and schemes for metal extraction in such systems, and it is safe to state that extraction mechanisms are now well understood. Considering the rather limited time elapsed between the first publication evidencing efficient liquid/liquid extraction in ILs (1999) and the first comprehensive modeling of extraction systems with ILs (2010), this is quite remarkable.

(ii) ILs are used as new extracting agents, either dissolved in more classical ILs or dissolved in traditional solvents, leading to M^{m+}/HX//IL/Org or to M^{m+}/HX//IL_1/IL_2 systems. In order to distinguish between IL_1 (the solute) and IL_2 (the solvent), the terms solute-IL and solvent-IL will be used. In such systems, the versatility of the IL chemical structure is the impulse for their investigation. Such works are growing in number, but, as stressed before, unless some *in silico* design is applied in the future, this aspect will remain limited, because of the endless efforts needed to optimize such systems. Mechanistic understanding is not an issue so far, with very few publications on this point, while all other works focus on the originality and increased efficiency of the synthesized ILs.

(iii) ILs are used as pure solvent phases to form M^{m+}/HX//IL systems. In this case, no solute (i.e., no dedicated ligand) is added to the IL solvent to perform extraction. Mechanistic studies of such a surprising phenomenon are still very scarce, although the number of examples is rising in the literature. It is hoped that the experiments developed in view of mechanistic investigation in the case of (i) and (ii) could be easily adapted to help understanding such systems quite rapidly.

(iv) ILs are introduced as synergistic agents or additives into classical extraction systems to form M^{m+}/HX//(L + IL)/Org. All "green" aspects of ILs are lost, but the cost is lowered as compared to points (i) to (iii). Such studies have appeared only recently, and mechanistic knowledge is still in its infancy. More systematic experimental work is required to gain a fundamental understanding of these systems.

4. ILS AS REPLACEMENT SOLVENTS: M^{m+}/HX//L/IL SYSTEMS

As explained above, in this section, we review results concerning extraction systems in which the molecular solvent has been replaced by an IL phase, using a molecular well-known ligand for the extraction, and we include synergistic systems of the form M^{m+}/HX//(L + L′)/IL.

The results to be found in the literature are numerous; thus they can be divided into four categories without losing significance: systems where ILs induce a benefit, in terms of distribution ratio; systems where ILs do not bring any improvements; systems displaying a complete different behavior as compared to molecular solvents; and finally, systems apparently behaving similar to molecular ones.

4.1. ILs Extract Better

It would be important to define what "better" precisely means but this is an intricate question. One may consider that a system using IL as a solvent and displaying at least one D_M value above that of the molecular solvent used for comparison purpose, all other chemical conditions being equal, should be qualified as being "better" or "more efficient." However, there could be other criteria on which one can judge whether a system is "better" than another one. One may impose D_M values above those of the reference system for all chemical conditions, for example, which is clearly a more restrictive obligation. One may be interested in separation factors between two metals, even if extraction itself is not very high. One may also be looking at systems allowing extraction and stripping, therefore requesting D_M values ranging from below 1 to above 1, depending on the chemical conditions.

It is thus hard to define what "better" means but, despite these restrictions, one has to admit that, most of the time, ILs extract "better," most papers measuring the gain from molecular solvents to ILs by the fact that the IL system provides higher D_M values at least under one set of chemical conditions. The first paper demonstrating the fantastic potential of ILs for liquid/liquid extraction compared the D_M values for Sr^{2+} extracted by a crown-ether in various solvents (Dai et al., 1999). Table 3 gathers some of the most striking features of this seminal publication. Obviously, the D_{Sr} values in the range of 10^4 for some of the ILs investigated are surprisingly higher than those obtained in molecular solvents. This chapter is an excellent example of what can be expected with ILs as replacement solvents: huge extraction efficiencies as a whole, together with tremendous changes in D_M values upon slight changes in the ILs chemical structure.

Following this appealing publication, numerous papers have appeared testing various chemical families of extracting agents in ILs and comparing them to one molecular solvent chosen as a reference. Besides the very detailed paper of Turanov et al. (2008a), evidencing extraction efficiency of one to more than three orders of magnitude for Ln^{3+} (or Y^{3+})/HNO_3//diamide/

TABLE 3 Strontium(II) Distribution Ratio in Various Solvents, in the Absence or in the Presence of Dicyclohexyl-18-crown-6 (DCH18C6)

Solvent	D_{Sr} without DCH18C6	D_{Sr} with DCH18C6
$C_6H_5CH_3$	–[a]	0.76
$CHCl_3$	–[a]	0.77
$C_4C_1C_1imPF_6$	0.67	4.2
$C_4C_1imPF_6$	0.89	24
$C_2C_1C_1imTf_2N$	0.81	4.5×10^3
$C_2C_1imTf_2N$	0.64	1.1×10^4

[a]*Not measurable.*
Data from Dai et al. (1999).

$C_1C_4imTf_2N$ as compared to chloroform, dichloroethane, and nitrobenzene, one can now find comparisons of extraction results for Ce^{3+} (or Eu^{3+} or Y^{3+})/HNO_3//CMPO/C_1C_4-$imPF_6$ compared to dodecane (Nakashima et al., 2005), Ce^{3+} (or Sm^{3+}, Yb^{3+})/HNO_3//DEHPA/$C_1C_nimPF_6$ ($n = 2$, 4) compared to hexane (Yoon et al., 2010), or Eu^{3+} (or Y^{3+})/HNO_3//diglycolamic acid/$C_1C_4imTf_2N$ compared to dodecane (Kubota et al., 2011). Data for actinides are less numerous, with Am^{3+}/HNO_3//(CMPO + TBP)/$C_1C_4imTf_2N$ compared to dodecane (Rout et al., 2009) and Th^{4+}/HNO_3//diglycolamide/$C_1C_nimPF_6$ ($n = 4$, 6, 8) as compared to chloroform (Shen et al., 2011b). In all cases listed above, the system with the IL solvent extracts better. However, these results have to be put into perspective. Very high extraction distribution ratios are not necessarily requested in industrial processes. Actually, one needs to extract the metallic cation from the aqueous phase, and therefore, high D_M values are valuable, but one has also to back-extract it into another aqueous phase and, in this second step, too high D_M values are detrimental to the whole process. Note that the too high efficiency of TBP (which is a liquid at room temperature and thus could have been used as a pure liquid phase) toward uranyl extraction in the PUREX process has led to dilute it into dodecane (down to 1.1 M), to lower its efficiency! Being aware of this point, some authors noted that ILs would thus request less extracting agent to get the same distribution ratio, meaning extraction at a lower cost. This argument is not perfectly correct either, unfortunately. First, one has to include the ILs' price in the balance and, at the moment, ILs are still very costly solvents. Second, as quoted in Section 3.1, one needs to use a large excess of the ligand, so using less ligand would impose to lower the cation concentration, which is certainly not what an industrial process would be designed for. A possible counterexample to this remark is found in the

synergistic system $Am^{3+}/HNO_3//(CMPO+TBP)/C_1C_4imTf_2N$ (Rout et al., 2009), in which less CMPO than in the equivalent dodecane system is requested, with distribution values above 2×10^4 or equal to 16 ($[HNO_3]_{aq,init}=1$ M) in $C_1C_4imTf_2N$ and dodecane, respectively. In this case, saving the costly CMPO molecule might compensate using the costly IL. However, an effective balance of financial benefits and losses would be needed to definitively conclude.

4.2. ILs Extract Worse

Not surprisingly, there are few papers presenting data for which ILs appear less efficient than traditional extraction systems, as no one is eager to publish such disappointing data. It is also possible that the first systems for which the IL solvent appeared less effective were discovered and studied when it was already clear that extraction mechanisms were different in ILs and molecular solvents so that a comparison in terms of one single D value was actually meaningless.

Most of the systems $UO_2^{2+}/HNO_3//TBP/IL$which have been investigated extensively by various authors, would not be relevant for dodecane replacement in a "greener" PUREX process, as depicted in Fig. 3. As can be seen from this figure, the D values for the long-chain imidazolium ILs studied ($n=8$, 10) are lower than in dodecane from $[HNO_3]_{aq,init}=2\times10^{-2}$ M to 4 M, that is, in the range of the PUREX operations. For short-chain imidazolium ILs and the two tetraalkylammonium ILs, although D values seem to be competitive, D is never below 1, thus precluding the back-extraction process. Note that $C_1C_{10}imTf_2N$ is the IL in which the general feature of the D_M variations is closest to those in dodecane, a point to be discussed further below.

Furthermore, the advantages and disadvantages of an IL extraction system as compared to the well-known TBP/dodecane one do not simply refer to extraction efficiencies. In view of industrial applications, many other technical factors play an important role, for example, density (phase reversal during operation is a threat to mixer-settlers). In a very interesting and valuable paper, Giridhar and coworkers unambiguously demonstrated that $C_1C_4imTf_2N$ is by far not competitive compared to dodecane in the hypothesis of solvent replacement (Giridhar et al., 2004b). This is mainly due to density variation as a function of nitric acid concentration and also to the instability of the PF_6^- anion toward water (see also comments by Zuo et al., 2008 on this question and kinetics data on PF_6^- degradation in Shen et al., 2011b) so that this conclusion can apply to all PF_6-based ILs. In addition, catalytic effects have been shown to impact the stability of An(IV) in PF_6-based ILs (Nikitenko et al., 2007). Therefore, it is now very difficult to support the idea that PF_6-ILs may be used in the nuclear fuel cycle, although such a proposal is put forward in the still too many published studies using such ILs.

Another point for which ILs may be less interesting than molecular solvents is the question of kinetics, but at the moment, this question is almost

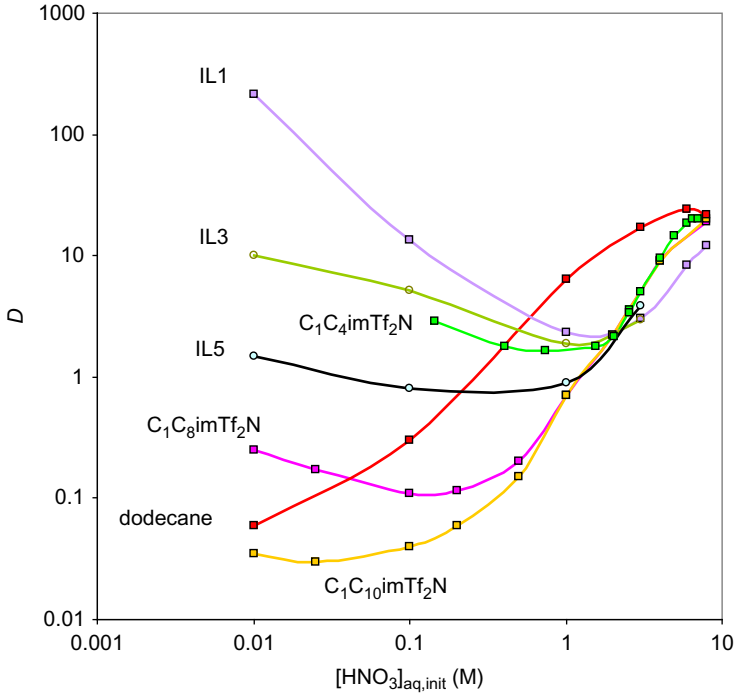

FIGURE 3 Comparison of the distribution ratio of UO_2^{2+} as a function of $[HNO_3]_{aq,init}$ in various ILs of the C_1C_nimTf$_2$N family, and in dodecane, by use of TBP. IL1, IL3, IL5, and dodecane data are from Bell and Ikeda (2011), C_1C_nimTf$_2$N data ($n = 5$, 8, 10) are redrawn after Dietz and Stepinski (2008), and C_1C_4imTf$_2$N data are redrawn after Billard et al. (2011c). IL1, $(CH_3)_3(CH_2CH_2OMe)NTf_2N$; IL3, $(CH_3)_3(CH_2CH_2Cl)NTf_2N$; IL5, $(CH_3)_3(CH_2C_6H_4NO_2)NTf_2N$.

not documented. ILs are rather viscous, with values in the range of 40 cP or above (see Table 1) so that mass transfer at the liquid/liquid interface may be slow, which would be detrimental to industrial applications. Very few papers so far indicate that kinetics investigations have been performed prior to extraction studies to check the time requested to reach equilibration of phases, which would be, however, a prerequisite and thus an important point to note. The kinetics appears to be very fast (below 1 min) for various $UO_2^{2+}/HNO_3//TBP/IL$ systems (Bell and Ikeda, 2011) but is quite slow (ca. 2 h) for Ce^{3+}/HNO_3//DEHPA/C_1C_4imPF$_6$ (Yoon et al., 2010), and there are indications that some systems lead to even slower kinetics, while equilibrium is reached within minutes in molecular solvents. Although very interesting on a fundamental point of view, such experimental constraints would considerably limit industrial applications, but this is not discussed in the abovementioned papers.

4.3. ILs Extract Differently

Apart from the question of higher or lower D_M values, the main general feature of extraction with ILs is a complete different mechanism as compared to molecular solvents, as illustrated for D_M variation as a function of the acidity of the aqueous phase (Fig. 3, compare the general trend for dodecane and ILs and compare with Fig. 1). In accord with what is known in molecular solvents, such a nonmonotonous variation is ascribable to (at least) two different competing mechanisms. Their relative strengths induce distortions of the generic curve. The characteristic boomerang shape of the D_M variation as a function of $[HX]_{aq,init}$ is now quite common in the literature. Besides the data of Bell and Billard illustrated in Fig. 3 for uranyl, boomerang-shaped curves of this kind can be found for several tetraalkylammonium ILs in systems such as $UO_2^{2+}/HNO_3//TBP/IL$ (Bell and Ikeda, 2011), for $UO_2^{2+}/HNO_3//diglycolamide/C_1C_nimPF_6$ ($n=4$, 6, 8) (Shen et al., 2011a), for Pu^{4+}/HNO_3//octyl-1,2-HOPO/$C_1C_8imTf_2N$ (Cocalia et al., 2006), for Th^{4+}/HNO_3//diglycolamide/$C_1C_nimPF_6$ ($n=4$, 6, 8) (Shen et al., 2011b), and for Am^{3+}/HNO_3//Cyanex-272/$C_1C_{10}imTf_2N$ (Cocalia et al., 2005). A plot of the D data listed in a table displayed in the paper by Rout et al. (2009) for the system $Am^{3+}/HNO_3/(TBP+CMPO)/C_1C_4imTf_2N$ and its dodecane equivalent also evidences an opposite trend between the two solvents, with the usual bell shape in dodecane and a decrease in IL, as illustrated in Fig. 4. However, in the IL system, the second mechanism is not competitive enough to increase D_{Am} above ca. $[HNO_3]_{aq,init}=2$ M and a decrease is observed instead.

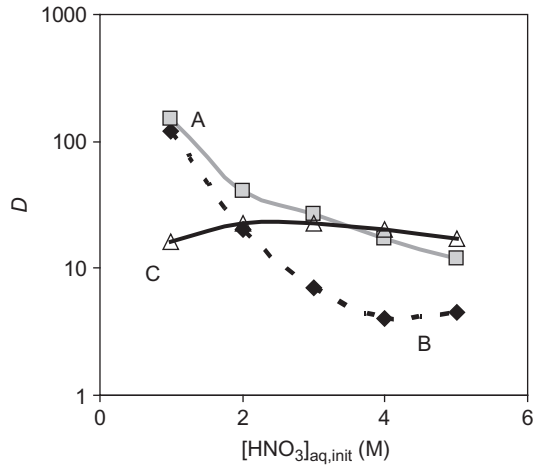

FIGURE 4 D as a function of $[HNO_3]_{aq,init}$ for (A) Am^{3+}/HNO_3//(0.05 M CMPO + 1.2 M TBP)/$C_1C_4imTf_2N$, drawn after data published in Rout et al. (2009). (B) Pu^{4+}/HNO_3//phosphonate-IL/$C_1C_4imTf_2N$, drawn after data published in Rout et al. (2010). (C) Am^{3+}/HNO_3//(0.2 M CMPO + 1.2 M TBP)/dodecane drawn after data published in Rout et al. (2009).

Such similarities in D_M variations, while the metallic cation, the ligand, and the IL phase are varied, are a strong indication that a general similar mechanism is at work in all these systems. This is not surprising, as ILs obviously impact the D_M variation features as a consequence of their ionic nature, so that the extraction mechanism could be quite different from that in molecular solvents, but quite similar from one IL to the other.

Another striking illustration of the differences between ILs and molecular solvents is the extraction of various lanthanides in $C_1C_n imTf_2N$ ($n = 2, 4, 6$) or isooctane by use of the TODGA molecule (Shimojo et al., 2008), as illustrated in Fig. 5. In isooctane, extraction of La^{3+}, Eu^{3+}, and Lu^{3+} occurs in the acidic range of 0.01–1 M, with the usual E (or D) increase as $[HNO_3]_{aq,init}$ increases, in the order: $Lu^{3+} > Eu^{3+} > La^{3+}$. By contrast, in $C_1C_2imTf_2N$, E is decreasing as a function of HNO_3 in the range of 0.01–1 M in the order $Lu^{3+} > La^{3+} > Eu^{3+}$. Note this is not a new feature of IL extraction systems with respect to what has been discussed above and presented in Fig. 3 for the IL systems. By using an E versus $[HNO_3]_{aq,int}$ plot for data of Fig. 3, in the range of 10^{-2}–1 M, one obtains a sigmoid decrease similar to that depicted in Fig. 5 for the IL case. Even more interestingly, the study of the complete lanthanide series (but Pm) showed that TODGA favors the extraction of the heavier Ln(III) ions in isooctane, while it favors that of the middle of the Ln series in $C_1C_2imTf_2N$. Other interesting results on the change of selectivity

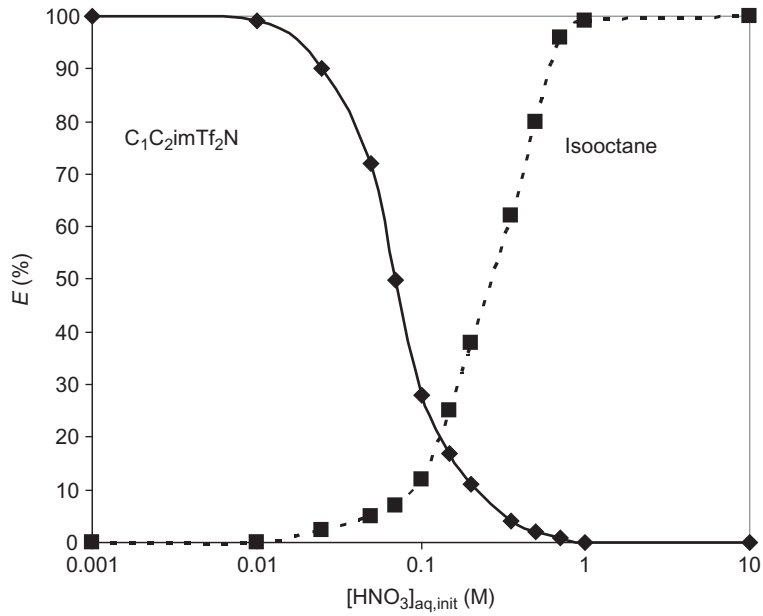

FIGURE 5 Schematic variation of E_{Ln} for Ln^{3+} ions as a function of $[HNO_3]_{aq,init}$ in $C_1C_2imTf_2N$ and isooctane, redrawn after Shimojo et al. (2008).

of DEHPA toward the Ln series by switching from hexane to ILs can be found in Yoon et al. (2010). Such differences have to do with differences in Ln solvation from one solvent to the other, but no detailed explanation of this phenomenon, on the basis of thermodynamic considerations for example, has been proposed yet.

These results are fascinating in the sense that, in addition to differences in extraction efficiencies from molecular solvents to ILs, they provide another handle for adjusting separation factors through a judicious choice of the solvent, and not solely of the ligand. Although such effects have not been evidenced for An(III) yet, this would be an elegant way to tune An(III)/Ln(III) separation factors.

The $UO_2^{2+}/HNO_3//TBP/IL$ systems are the most studied ones so far. The wealth of data accumulated by the various groups allows a deeper qualitative discussion on this system, as compared to the other ones. Data recorded in PF_6-based ILs (Giridhar et al., 2004a) have to be considered with caution, owing to the degradation of the IL anionic constituent and will not be included in the discussion. In fact, the D_U versus HNO_3 variations in Fig. 3 point to three different regimes independent of the IL: at low acidities, D_U is decreasing (regime I); at medium acidities, D_U is increasing (regime II); and at very high acidities (above ca. 6 M), D_U is either plateauing or slightly decreasing (regime III). The rather limited range of available acidities at which this third regime is evidenced justifies that the first publications did not discuss it (Billard et al., 2011c; Dietz and Stepinski, 2008; Giridhar et al., 2008). In their recent paper, Bell and Ikeda (2011) suggested that the decrease at very high acidities (regime III) is due to the competition between HNO_3 and metallic extraction by TBP. This would be in line with what is known in molecular solvents and with previous results evidencing HNO_3 extraction in the presence of TBP or other molecules in various ILs (Gaillard et al., 2012; Giridhar et al., 2004a; Rout et al., 2009). From Fig. 3 and comparison with the other data gathered in Bell and Ikeda (2011), it is obvious that the change in the IL component of the system has a strong impact onto the nitric acid concentration at which D changes from the first to the second regime, from ca. 0.01 M for $C_1C_{10}imTf_2N$ to ca. 3 M for $(CH_3)_3(CH_2CH_2OMe)NTf_2N$. It is hard to figure out if the slope of the decrease under regime I is similar for all ILs and so is it difficult to link the IL chemical structures to the limit between regimes I and II, but under regime II, similarities between all investigated ILs are striking. Therefore, one can expect that the extraction mechanism in region II does not imply the cationic part of the IL. Although many publications have studied extraction, none of them have been focusing on the optimization of a given system, but the data gathered on the $UO_2^{2+}/HNO_3//TBP/IL$ system show that such an optimization is rather limited: varying the IL (or, at least its cationic part) does not seem to enhance the maximum D_U value at high acidities, which are of interest to the nuclear fuel cycle.

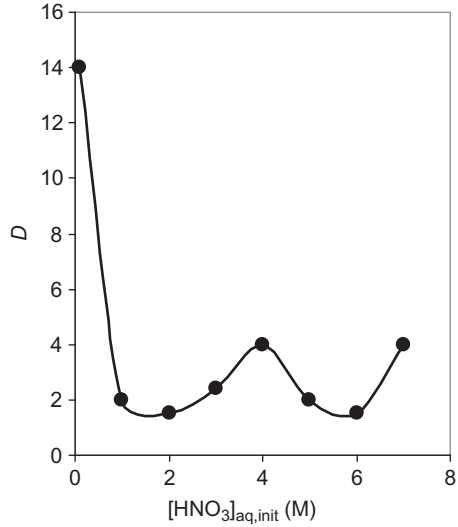

FIGURE 6 Schematic variation of D_{Th} as a function of $[HNO_3]_{aq,init}$ (M) for Th^{4+}/HNO_3//diglycolamide/C_1C_nimPF_6 redrawn after Shen et al. (2011b).

Finally, in the system Th^{4+}/HNO_3/diglycolamide/C_1C_nimPF_6 ($n=4$, 6, 8) (Shen et al., 2011b), the D_{Th} variations as a function of $[HNO_3]_{aq,init}$ display a rather complicated W form, as schematically presented in Fig. 6. These data should be considered with caution for two reasons. First, the authors have been using PF_6-based ILs, which they also show to be highly sensitive to HNO_3 above 3 M, with degradation of the PF_6^- anion being dependent of both acid concentration and contact time, and second, no indication of uncertainties and the rather limited number of data points could shed some doubts onto the reality of such a curve. Nevertheless, these variations that more or less parallel data obtained in a very recent publication concerning alkaline and alkaline-earth elements (Hawkins et al., 2012) are worth mentioning. They will be discussed further in Section 8.2, together with the data for alkaline and alkaline-earth elements.

4.4. ILs Extract Similarly

In two cases, a similar extraction behavior has been evidenced in ILs and a molecular solvent (Cocalia et al., 2005; Kubota et al., 2011), and these two very interesting examples will also be discussed in details in Section 8.

The extraction ability of DODGAA, a compound of the malonamide family, which is known to be a proton-dissociation-type extractant in molecular solvents, has been investigated in dodecane and various ILs of the C_1C_nimTf_2N ($n=4$, 8, 12) family (Kubota et al., 2011). For Y^{3+} and Eu^{3+}, the E_M versus pH variations in dodecane and in all three ILs parallel the

typical sigmoid shape in the pH range of 0.5–3, although the pH value at which $E_M = 50\%$ is shifted from 1 ($n = 4$) to 2.4 ($n = 12$), while $E_M = 50\%$ at pH 1.8 in dodecane.

The second example concerns $UO_2^{2+}(\text{or } Am^{3+})/HNO_3//\text{Cyanex} - 272/C_1C_{10}imTf_2N$ in comparison with the dodecane equivalent system (Cocalia et al., 2005). Cyanex-272 is a commercial mixture of phosphinic acids, similar to the pure compound HDEHP, used for comparison purposes in this work. The D_M variations for UO_2^{2+} and Am^{3+} as a function of $[HNO_3]_{aq,init}$ displayed the same boomerang shape in $C_1C_{10}imTf_2N$ and dodecane. Note that this IL is also providing D_U variations close to those for U(VI) extraction in dodecane by use of TBP (see Section 4.2 and Fig. 3).

From the various examples presented above, one may have the feeling that extraction mechanisms in $M^{m+}/HX//L/IL$ present a large diversity of patterns, and this might be considered as confusing. It is our opinion, however, that extraction in ILs is as simple (although not identical) to understand as extraction in molecular solvents, which has been studied for more than 50 years. We think that the apparent complexity of the phenomenon described above is just a matter of novelty. Very simple ideas with which one can describe these extraction data are detailed in Section 8.

5. ILS AS NEW EXTRACTING AGENTS: $M^{m+}/HX//IL/ORG$ OR $M^{m+}/HX//IL_1/IL_2$ SYSTEMS

The versatility of the IL structures prompted studies aiming at the synthesis of new ILs specifically designed to extract metallic ions. This very good idea is the basis on which the field of task-specific ILs (TSILs) has emerged because ILs could be, in principle, tailored for various purposes, such as metal extraction but also catalysis or chiral synthesis, among other applications. However, as already stressed, the fundamental understanding of the relations between IL structures and IL properties is still very limited so that most of these synthetic works aimed at metal extraction tend to apply good old recipes to ILs, by simply grafting well-known complexing patterns to the cationic part of the IL, such as carboxylate (Kogelnig et al., 2008); phosphonate (Rout et al., 2010); phosphoryl (Ouadi et al., 2007); phosphine oxides (Miroshnichenko et al., 2011); hydroxylamine (Ouadi et al., 2006); terpyridine (Olivier et al., 2009); malonamide (Bonnaffé-Moity et al., 2012); thiourea, thioether, and urea (Visser et al., 2001); aza-crown-ether (Luo et al., 2006); CMPO (Odinets et al., 2010); etc. Furthermore, the choice of the IL skeleton is rather limited with a wide majority of works dedicated to the functionalization of the sole imidazolium cation. Despite these limitations, the number of possible so-called TSIL is tremendous. The reader is referred to some reviews specifically focused on these topics for further information (Davis, 2004; Giernoth, 2010). It is only recently that more original syntheses appeared, in particular, by grafting complexing patterns on the anion (Sun et al., 2010) or by

preparing multiply charged cations (Miroshnichenko et al., 2011), that although very viscous are liquid at room temperature.

The term "task specific," by opposition to "generic," "basic," or "classical," is quite appealing, in the sense that it highlights the purpose and attracts attention onto the synthetic work which obviously deserves consideration, but, to our opinion, it is meaningless. First, TSILs are ILs, by definition, and the question raised whether they should be considered as a new class of solvents is inaccurate (Visser et al., 2002). Terms as dual-functionalized (Zhao et al., 2004) or multitask-specific ILs (Tindale et al., 2010) are just vocabulary rushing ahead for very interesting compounds. Second, any IL, even a "basic" one, is intrinsically designed for the physicochemical properties it displays and also for its own extracting properties, even if they are, most of the time, not interesting but may also be astonishingly efficient (this point will be reviewed and discussed in Section 6). To further pinpoint how vague the task-specific notion is, let us consider the recent three papers presenting new ILs containing a diketonate functionality. In the work of Olivier et al. (2011), the diketonate moiety is grafted onto an imidazolium structure, in line with the common acceptance of TSILs. In the other two publications, the diketonate structure is not grafted on the cation, nor is it grafted onto the anion but constitutes the anionic IL component itself (Bell et al., 2011; Mehdi et al., 2010). Therefore, although the idea behind the three syntheses is the same (use of an efficient diketonate complexing pattern), the last two examples do not correspond strictly to the task-specific notion because nothing new, in terms of functionality, is added to the "basic" constituents of the IL.

We now turn to a review of extraction results for An and Ln by use of ILs being considered as ligands. This means that such compounds are dissolved in a solvent and are thus considered as solutes. Although many reports have appeared with solute-ILs in view of the extraction of transition metals, in particular Hg(II) (Visser et al., 2002), the number of works devoted to An and Ln is very limited so far. This could be a consequence of the very active research for molecular ligands in the field of nuclear waste reprocessing, which renders the search for new ligands that would also be new ILs an endless task. Obviously, for any neutral ligand, there are plenty of ILs bearing the same complexing pattern. Whatever the reason, it is thus difficult to derive general observations from such a limited bibliographical content but, as is expected in rising fields, the number of pending questions raised by the experimental results is by far exceeding the number of publications.

Because the new ligands under consideration in this section are ILs and have been conceived in the IL frame of thinking, extraction studies are most of the time performed using another IL as solvent, and a single publication uses a traditional molecular solvent instead. This is also due to the difficulty of dissolving ILs in some molecular solvents. For instance, $C_1C_4imTf_2N$ is well soluble in cyclohexanone and nitrobenzene, but poorly soluble in

1-octanol, toluene, dodecane, or *tert*-butylbenzene, while solute-ILs easily dissolve in many solvents. A clear added interest of these solute-ILs is that they avoid or displace toward higher concentrations the technical problem of third phase formation, a pin in the neck of all industrial extraction systems (Rao and Kolarik, 1996). Note that formation of crud is observed in Eu^{3+}/HNO_3//(CMPO-TBP)/$C_1C_4imTf_2N$, at higher concentrations than in the traditional system (Rout et al., 2011a).

Grafting an extracting pattern onto an IL structure is not benign to the general properties of the ligand, and two studies have evidenced changes in the pK_a or protonation ability when going from a molecular ionizable ligand to its IL analogue (Bonnaffé-Moity et al., 2012; Ouadi et al., 2006).

One of the first examples of such systems is interesting because it presents data clearly not suitable for An recovery from fuels, as the solute-IL is efficient at basic pH (Ouadi et al., 2006). Despite many other problems of this system, it is one of the very rare examples of extraction under basic conditions.

Not surprisingly, plotting the data displayed in a table in Rout et al. (2010) evidences a clear boomerang shape for $Pu^{4+}/HNO_3//ImPTf_2N/C_1C_4imTf_2N$, where $ImPTf_2N$ is an IL ligand displaying a phosphonate part on the imidazolium cation (see Fig. 4). This characteristic boomerang curve is also obtained for $UO_2^{2+}/HNO_3//malonamide-IL/C_1C_4im\ Tf_2N$ (Bonnaffé-Moity et al., 2012). On the other hand, the only paper presenting data for solute-ILs dissolved in classical molecular solvents (cyclohexane, chloroform, and toluene) evidences an increase of the europium distribution ratio as a function of HNO_3 (Sun et al., 2010), a trend perfectly in agreement with the usual bell shape displayed in molecular solvents with neutral ligands. Detailed comparisons between the IL-solute and its molecular equivalent have been performed in a single publication (Bonnaffé-Moity et al., 2012) so far and are evidencing a higher extraction efficiency of the solute-IL as compared to its neutral analogue. Another paper simply reports higher distribution ratio for U(VI), Eu(III), and Am(III) in case of a calixarene-IL, as compared to a traditional phosphine oxide, although D_M values are above 1 for U(VI) only (Miroshnichenko et al., 2011). The sensitivity of D to the exact structure of the solute-IL is exemplified in Ouadi et al. (2007) for $UO_2^{2+}/HNO_3/IL/Me_3BuNTf_2N$, where the IL is based on a quaternary ammonium cation bearing various phosphoryl groups. Huge changes in D_U, from 0.63 up to surprisingly high values of 170, are obtained, following the trend phosphate < phosphonate < phosphoramidate. Again, disappointing D_U values are obtained for the phosphate-IL, as is the case for TBP.

Although not very common to the field of Ln/An extraction, as pinpointed above, many solute-ILs have been used to recover transition metals and the amount of work accumulated so far for these elements allowed some authors to consider that "none have proven to be exceptionally better than neutral extractants" (Bell et al., 2011). Again, it would be desirable to exactly define what "exceptionally" means, and actually, some of these solute-ILs are more

efficient than their neutral analogue. This might be an indication that we are on the way to obtain higher efficiencies.

Open questions remain numerous and can be divided into three main topics: questions related to liquid structures and questions related to processes. They are briefly exposed below:

(i) Can we always conceive at least one solute-IL being more efficient than the molecular analogue? What would be the reasons for such an increased efficiency? Could it be linked to the intrinsic ionic nature of solvent-ILs, to their polar and nonpolar nanodomains, that would accommodate solute-ILs better than molecular entities, possibly restricted to and experiencing a smaller bulk volume, thus being less efficient?

(ii) What are the effects of the solubilization of ionic or neutral ligands on the solvent-IL structure? Is the preorganization of the solvent of any help to the extraction? Actually, it has been known for some time that the preorganization of the extractant in molecular solvents is providing better efficiencies, as compared to more flexible ligands. This is typically illustrated by the calixarene family, as compared to the lower efficiency of the monomer they are composed of.

(iii) The design of most solute-ILs is based on the functionalization of the cationic part, because of its organic structure, but the fact that these positively charged ligands are efficient at extracting cations is rather counterintuitive. Considering the large flexible structures of solute-ILs, is it possible that the charge borne by the IL function, either positive or negative, is not the main parameter driving extraction?

In order to answer these questions, it would be needed to perform many systematic studies, comparing extraction efficiencies of various extracting patterns either under a neutral or an IL form, in both ILs and molecular solvents. Molecular extractants have been conceived for decades for solubilization in molecular solvents. Are we now facing a drastic change in paradigm, with solute-ILs perfectly adapted to be dissolved in solvent-ILs?

6. ILS AS PURE EXTRACTING PHASES: M^{m+}/HX//IL SYSTEMS

In molecular solvents, the difficulty to directly extract metallic species from an aqueous phase has been the basis for the search of extracting ligands to help metallic transfer into the organic phase. Conversely, as ILs contain, most of the time, very weakly coordinating anions (especially the Tf_2N^- entity, but also triflate), it was assumed from the start that extraction in IL could not be carried out without ligands. Therefore, most of the extraction studies with ILs did not even measure extraction efficiencies without ligand, although the data from Dai et al. (1999) for Sr^{2+} extraction in the presence of DCH18C6 (see Table 3) gave some indications that something unusual was happening. Indeed, extraction of Sr^{2+} in all the four pure ILs investigated was not

negligible, although low, with the largest distribution ratio $D_{Sr} = 0.89$ ($E_{Sr} \approx 47\%$) for $C_1C_4imPF_6$, a very common IL, while it is below the detection limit for the two molecular solvents of the comparison study. Although Sr^{2+} extraction efficiencies with the pure IL phases are by far not interesting for real application, the result by itself is quite surprising at first glance and can be analyzed in two ways. It would first suggest that a ligand is not really needed to obtain high extraction efficiencies, assuming the large IL chemical database available most probably contains an IL yielding adequate D_M values. This is a complete renewal of the philosophy of extraction studies, which puts more energy and ideas in ligand design than in solvent control. Second, this result can also be considered under the light of our previous discussion about TSILs (see Section 5), as these data show that even basic ILs are, as a matter of fact, surprisingly "task specific."

Since the work on Sr^{2+}, many more data have appeared in the literature on the extraction efficiencies of pure IL phases. Unfortunately for this review paper, most of the metals investigated do not belong to the RE or An series (for a recent list of involved metals, see Billard et al., 2011b). It is important to note that such experiments require IL phases that are fluid enough at the temperature of the study, to act as extracting phases. In principle, data could be collected above room temperature, to decrease IL's viscosity, but all works have been performed at room temperature. Table 5 gathers some of these results, highlighting the capacity of very simple ILs to efficiently extract Pu(IV), Th(IV), Ce(IV), and La(III). Note a contradictory result for the system $Th^{4+}/HNO_3//C_1C_8imPF_6$, which hardly extracts Th(IV) up to 7 M, according to a recently published work (Shen et al., 2011b). No explanation is proposed for this discrepancy, which could be ascribed to the inherent instability of PF_6-based ILs.

Data listed in Table 5 are collected from various publications so that the majority of the results gathered are not for competitive experiments, and it would be interesting to measure the maximum loading capacities of these ILs, by increasing the metal content of the aqueous phase, and to confirm their selectivity by extraction experiments performed with aqueous phases containing a large variety of cations and anions. Some published results are already quite encouraging in this matter, demonstrating that some pure IL phases can efficiently discriminate UO_2^{2+} from other divalent cations such as Ca^{2+} and Mg^{2+} (Srncik et al., 2009). Similarly, Ce(IV) is efficiently extracted, while Ce(III) and Th(IV) are not, for example (see Table 4).

Despite the limited amount of data reported in Table 5, it is clear that high nitric acid concentrations favor the extraction of Pu(IV) and Ce(IV) (and possibly Th(IV)). This might be an indication that nitrato complexes are extracted but no firm conclusion can be obtained from the available data. This would mean poor or no selectivity in mixtures of Pu(IV) and Ce(IV), while no conclusion can be drawn for La(III) and Sr(II) because experiments were performed at a single nitric acid concentration. On the other hand, the exact nature of the IL has a great effect onto Pu(IV) extraction ability.

TABLE 4 Values of the Pu Distribution Ratio, D_{Pu}, as a Function of $[HNO_3]_{aq,init}$, for (a) $Pu^{4+}/HNO_3//(CMPO+TBP)/C_1C_4imTf_2N$ or (b) $Pu^{4+}/HNO_3//(CMPO+TBP)/dodecane$

$[HNO_3]_{aq,init}$ (M)	(a) [CMPO] = 0.02 M	(b) [CMPO] = 0.2 M
1	7.7	16.1
2	3.3	22.7
3	2.2	22.6
4	1.8	20.4
5	1.5	17.3

TBP concentration is 1.2 M; data from Rout et al. (2009).

The data in Table 5 have been intentionally restricted to "simple" IL phases, that is, IL phases that were not intended (or designed) to extract metallic ions. However, more sophisticated ILs do also extract metallic cations and one can find extraction studies for various systems displaying a rather fancy (i.e., not commercially available at the moment) pure IL phase. Within this frame, the result for $UO_2^{2+}/HNO_3//phosphate-IL$ (Ouadi et al., 2007) is again less good than that for $UO_2^{2+}/HNO_3//TBP/dodecane$, at the single nitric acid concentration examined (3 M). A very impressive list of 18 La^{3+}/H_2O//diketonate-IL systems provides distribution ratios in the range of 48 up to 10^4 (Bell et al., 2011), $Pu^{4+}/HNO_3//CH_3(C_8H_{17})NNO_3$ leads to distribution ratios of 48 (Rout et al., 2011b), and a proof of concept (no D_{Nd} values are reported, but convincing pictures of the extraction process are shown) is also found for Nd^{3+}/HTf_2N//diketonate-IL (Mehdi et al., 2010). The diketone pattern is obviously an interesting one, with Eu^{3+}/H_2O (pH 8)//diketone-IL evidencing extraction by use of ILs grafted onto their cationic part (Olivier et al., 2011).

Now that extraction evidences with pure IL phases are becoming more common, in the course of classical extraction studies of $M^{m+}/HX//L/IL$ as discussed in Section 4, authors take care to indicate that extraction has been tested without introduction of the ligand, and a striking result can be found as a by-side aspect in the study of the system Pu(IV)/HNO_3//phosphonate-IL/$C_1C_nimTf_2N$ ($n = 4$, 8) (Rout et al., 2010). The specifically designed phosphonate-IL, used as a ligand, appears rather efficient at low acidities ($D_{Pu} = 240$ for $[HNO_3]_{aq,init} = 1$ M and an IL-solute concentration of 0.5 M) with no contribution to Pu(IV) extraction of the pure solvents $C_1C_4imTf_2N$ and $C_1C_8imTf_2N$ (D_{Pu} below 0.05 for both solvent-ILs), but at the highest acidities tested in this work ($[HNO_3]_{aq,init} > 3$ M), Pu is better extracted ($D_{Pu} = 6.62$ at $[HNO_3]_{aq,init} = 5$ M) by pure $C_1C_4imTf_2N$ than by the phosphonate-IL diluted in it ($D_{Pu} = 4.1$ for $[HNO_3]_{aq,init} = 5$ M and a ligand

TABLE 5 Extraction Efficiencies of Some ILs as Pure Liquid Phases

IL	Extracted ion (D or E (%) values), $[HX]_{aq,init}$ or pH value	References
$C_1C_2imTf_2N$	Sr(II) (0.64), pH 4.1	Dai et al. (1999)
$C_1C_4imPF_6$	Sr(II) (0.89), pH 4.1	Dai et al. (1999)
	Pu(IV) (1.6); $[HNO_3]_{aq,init} = 5$ M	Rout et al. (2010)
$C_1C_4imTf_2N$	Pu(IV) (6.62); $[HNO_3]_{aq,init} = 5$ M	Rout et al. (2010)
$C_1C_8imTf_2N$	Pu(IV) (37.5); $[HNO_3]_{aq,init} = 5$ M	Rout et al. (2010)
$C_1C_6imTf_2N$	Pu(IV) ($\approx$18); $[HNO_3]_{aq,init} = 5$ M	Rout et al. (2012)
$C_1C_8imPF_6$	Ce(IV) (65); Th(IV) (0.75); Ce(III), Gd(III), Yb (III) (0); $[HNO_3]_{aq,init} = 3.0$ M	Zuo et al. (2008)
	Pu(IV) (7.8) $[HNO_3]_{aq,init} = 5$ M	Lohithakshan and Aggarwal (2008)
C_1C_4imNfO	La(III) (95.5%)[a]	Kozonoi and Ikeda (2007)

NfO, nonafluorobutanesulfonate.
[a]*The pH value is not specified.*

concentration of 0.5 M). This disappointing (in term of the IL design) or interesting (in term of efficient pure common IL) result is not put into perspective by the authors, unfortunately. In addition, these data raise the question of the mechanism, which should be properly addressed to separate the mixed contributions of the solvent-IL and the solute-IL. As a by-side effect, it could be envisioned that a constant D_{Pu} value can be achieved in the range of 0.1–5 M of nitric acid, by properly adjusting the composition of the IL phase through the variation of its solute-IL content. This may not have any utility in the nuclear fuel cycle problematic but may reveal some potential for environmental studies where samples of various pHs have to be treated with high and similar efficiencies.

Apart from two publications, to be discussed below, mechanistic studies have not appeared yet but two main ideas can be put forward. As common ILs are known to accept very large amount of acidic water in their bulk structure, at least part of the extraction could be related to a physical phenomenon of ion dragging caused by water solubilization in the IL phase. This may have some implications onto the IL structure, and this fascinating point would deserve more studies in the future. Another possibility would be an ion-exchange mechanism, both processes possibly occurring at the same time. Attempts to understand the extraction mechanism in the system

Ce(IV)/HNO_3//$C_1C_8imPF_6$ have been performed by Zuo et al. (2008), but unfortunately, $C_1C_8imPF_6$ is very sensitive to water, as pointed by the authors, so that the conclusions to be drawn from their experiments have to be taken with great caution. Furthermore, although the authors state that an ion-exchange mechanism is at work in the system, all the proposed equilibria they wrote present a neutral extracted species. Despite these restrictions, this work presents a fascinating result. By dissolving the water-soluble C_1C_8imCl IL in an aqueous solution of Ce(IV) acidified with large amounts of nitric acid (>7 M), the authors unexpectedly obtained a biphasic system, with the newly formed bottom phase displaying a strong red color, characteristic of tetravalent cerium salts. Although a deeper investigation would be required to characterize this new phase, it is clear that Ce(IV) extraction from the aqueous phase has been successfully obtained without the help of any ligand but also without the help of a water-immiscible IL as starting materials. The mechanism is most probably ascribable to precipitation of a new compound which may be an IL phase, immiscible with water and liquid at room temperature. This process is formally identical to the metathesis process used to synthesize many ILs by exchange of an ion. Again, studies of this type will certainly increase in number in a near future because metathesis is a very common way to synthesize ILs. The second publication dealing with mechanistic investigations concerns Pu(IV)/HNO_3//$C_1C_n imTf_2N$ ($n=4$, 8) (Rout et al., 2010). Addition of $LiTf_2N$ to the aqueous phase, a method which has proven efficient for mechanistic understanding (see Section 8.1), leads to a decrease in D_{Pu}, which is consistent with anionic exchange. Slope analysis (see Section 8.3 for a detailed description and comment on this data treatment) allows one to conclude that one Tf_2N^- has been exchanged for $(Pu(NO_3)_5)^-$ in $C_1C_4imTf_2N$. For the other IL studied, $C_1C_8imTf_2N$, the slope has a noninteger value of -1.43 which could be interpreted as reflecting two anion exchange processes, one identical to the preceding one and the other involving two Tf_2N^- exchanged with $(Pu(NO_3)_6)^{2-}$.

It would be desirable to perform systematic studies aiming at evidencing extraction efficiencies of pure IL phases. These would provide the database needed to understand the extraction mechanism at work and, possibly, would help to derive QSPR approaches for further extraction enhancements that would be more detailed than the very basic comments we proposed above from the examination of the limited data presented in Table 4.

We would like to stress the mesmerizing underlying implications of the results discussed in this section. Efficient extraction of pure IL phases opens the route to totally new systems, purely (and simply) discarding the notion of ligand which has been in use for decades in the field of metallic ion extraction. On a more classical approach, selective successive extractions could be envisioned, some elements being extracted by the pure IL phase, and once these have been back extracted, the now clean pure IL phase could act as a solvent for a ligand able to extract the remaining elements of interest from

the aqueous phase. This principle is far from a proof of concept, but it will certainly develop in the future.

7. ILS AS ADDITIVES TO TRADITIONAL SYSTEMS: M^{m+}/HX//(L + IL)/ORG

In this section, we review the yet to be explored field of ILs used as additives to traditional extraction systems, that is, M^{m+}/HX//(L + IL)/Org. The situation is different from the one described in Section 5, where ILs are used as ligands, without any other solute and resembles more that of a traditional synergistic system (see Section 3).

As a matter of fact, various tetraalkylammonium salts, the most famous one being the commercial Aliquat 336 (a 2:1 mixture of methyl trioctyl and methyl tridecylammonium chloride), are used as synergistic agents for Ln (III) extraction in traditional solvents (Atanassova, 2009; Atanassova and Dukov, 2010), and we would like to recall that many tetraalkylammonium salts are, in fact, ILs: for example, tetraoctylammonium bromide melts at ca. 95 °C. On the other hand, new routes for the synthesis of ammonium-type ILs have been proposed (Mikkola et al., 2006; Sun et al., 1998). However, it is out of the scope of this work to review all literature involving Aliquat salts, especially because, being commercial mixtures, their chemical and physical properties are difficult to determine. Therefore, we will restrict ourselves to systems in which the additive was clearly considered by the authors as an IL.

This fourth way to use ILs in the field of liquid–liquid extraction of metallic ions has just been developing recently, most probably because it seems at first glance in total disagreement with all the arguments put forward in favor of ILs over conventional solvents. This is in contradiction with the environmental need to discard molecular volatile and flammable solvents, and it may be also a way to render these systems even more complex than they already are. However, one can argue that it is a way to save costly compounds and one can also pinpoint the mostly unknown but sometimes yet doubtful benign environmental impact of ILs. In case of RE, data are provided by one Russian group (Turanov et al., 2008a,b) (from the same group, see also solid–liquid extraction of RE with the same ideas (Turanov et al., 2008c)). There are no data for actinides, but one publication from another group deals with fission products such as TcO_4^- and ReO_4^-(Stepinski et al., 2010).

Turanov et al. (2008a) have performed an impressive work on RE/HX//(diamide + IL)/Org. Organic solvents are 1,2-dichloroethane, nitrobenzene, and chloroform; a comparison has been made with C_1C_4im Tf_2N as a solvent; HX are $HC1O_4$, HPF_6, HTfO (TfO^-stands for the triflate anion, $CF_3SO_3^-$), and HTf_2N; the added ILs are C_1C_4im Tf_2N and C_1C_4imPf_6, and the metallic elements cover the entire Ln series but Pm, plus Y. The very interesting idea in this work is based on the observation of ion exchange as a preferred mode of extraction in IL solvents. Therefore, the authors simply consider the IL as a reservoir for

ion exchange, since it is in large excess as compared to the metallic ion when it acts as solvent. It thus appears clever to use only a limited amount of IL, by diluting it in a more common (and cheap) solvent.

This extensive work first presents a comprehensive study of the systems RE/HX/diamide/Org that all behave traditionally with bell-shaped variations of the distribution ratios. The extracted species are of the form $[EuX_3L_3]$, the extraction efficiency being dependent on the nature of HX, with extraction following the trend: $HTf_2N > HPF_6 > HClO_4$ for all of the REs. As a consequence, the authors enhance RE extraction from HNO_3 solutions by adding $LiPF_6$ or $LiTf_2N$ to the aqueous phase, the extracted species being now $EuX_2NO_3L_2$. In a third step, a comparison has been performed between RE/HX//diamide/Org and RE/HX//diamide/$C_1C_4imTf_2N$. A dramatic increase in the distribution ratio of more than two orders of magnitude is obtained in the IL system, as compared to the three molecular solvents, for the investigated RE (Y, La, Ce, Pr, Nd). Finally, ILs have been diluted together with the diamide in 1,2-dichloroethane. At a fixed nitric acid concentration of the aqueous phase (3 M), the europium distribution ratio is increasing as the amount of added IL increases, up to a plateau value at ca. 1 M of added IL. Again, the Tf_2N^- anion appears to be more efficient than PF_6^- and the extracted species is $EuX_2NO_3L_2$ (derived from a slope analysis, see Section 8.1). As a last result of this work, the D variations as a function of $[HNO_3]_{aq,init}$ (from 0.1 to 1 M) for Lu, Ho, Tb, Sm, Nd, and Pr in the system Ln^{3+}/HNO_3//(diamide + $C_1C_4imTf_2N$)/1,2-dichloroethane display decreasing trends, similar to what is observed in IL solvents (region I, see Section 4). As a complement, Turanov et al. (2008b) studied the effect of the same added ILs in the systems Ln^{3+}/HCl//(phosphine oxide + IL)/dichloroethane. Similar to their work on diamides, at a fixed HCl concentration equal to 3 M, they demonstrate for all Ln (but Pm) and Y a huge increase in D (almost three orders of magnitude) when 0.45 M $C_1C_4imPF_6$ is added as a synergistic agent to CMPO dissolved in dichloroethane. Finally, the variation of D_{Eu} for the Eu^{3+}/HCl//(phosphine oxide + IL)/dichloroethane systems presents a striking boomerang shape in the acidity range of 0.1–8 M. Similar results for Sr, Cs, and Ba by the same group (Turanov et al., 2010) demonstrate that this astonishing effect of added ILs is not restricted to REs.

The authors make several qualitative remarks in an attempt to relate the hydrophobicity of the IL cations or anions, the dielectric constant of the organic solvents, or other solvent properties to their experimental results. Although interesting as such, these qualitative comments have their limits and we would like also to commend the efforts of the authors to analyze their data with the slope-analysis method, taking into account more than one equilibrium (see Section 8.3 for a discussion on this method).

Considering that this single work is quite unusual, we do not discuss the proposed interpretation in Section 8, devoted to modeling, but in this section instead.

As far as mechanistic approaches are concerned, the authors suggest the following equilibrium to account for their boomerang-shaped data in the organic solvents:

$$Ln^{3+} + (3-n)X^- + n\overline{A^-} + p\overline{L} \rightleftarrows \overline{LnX_{3-n}A_nL_p} \quad (10)$$

The decrease observed at low acidities would be a consequence of an increased concomitant extraction of HX that would lower the availability of the ligand, while the increase in D at high acidities would be due to an increase in $[X^-]$. Although in qualitative agreement with the data, additional experiments would be required to fully assess such a hypothesis.

Turanov and coworkers quoted their results as a synergistic effect of IL onto the diamide or phosphine oxide ligands. It would be desirable to further investigate this idea, by answering the following pending questions:

- **(i)** In order to get a parallel between synergism as already known in molecular solvents between two effective ligands (see Section 3) and the synergistic effect observed here, what about the extraction efficiency of the added IL alone in Ln/HX//IL/Org? This question actually relates the aspects described in Section 5 (Table 5) to those presented in this section. Are some ILs acting as antisynergistic components?
- **(ii)** What is the optimized concentration of the IL additive for a given system? Does it depend on the concentration of the other ligand or on the concentration of the metallic ion (or on both parameters)?
- **(iii)** Above which concentration of the IL additive does the system switch from an extraction typical of molecular solvents (bell shape) to an extraction typical of ILs (boomerang shape)?
- **(iv)** Is the synergistic effect equivalent to what could be obtained by grafting the ligand molecular pattern onto the ILs used as additive, in order to minimize the number of components of the systems? In other words, is the effect of added IL related or not to the fact that the IL is an independent constituent of the system?

8. TOWARD A MECHANISTIC UNDERSTANDING OF EXTRACTION IN ILS

In this section, we review and discuss papers presenting a mechanistic approach of liquid–liquid extraction by use of ILs. In principle, it could be envisioned that different mechanisms are occurring depending on the way ILs are used: as replacement solvents (Section 4), as solutes (Section 5), as pure phases (Section 6), or as additives to molecular solvents (Section 7). Surprisingly enough, almost all mechanistic studies published so far focused solely on ILs as replacement solvents. Only two attempts to understand extraction of M^{m+}/HX//IL systems are published (Rout et al., 2010; Zuo et al., 2008), and considering the rather mitigated results obtained, these were

discussed in Section 6, while one proposal for M^{m+}/HX//(L + IL)/Org systems is presented in Section 7. The reasons of such an unbalanced situation may be first found in the recent discovery of the efficiency of ILs as additive to molecular solvents or as pure phases and second in the complexity of some of the systems (ILs as additives).

These mechanistic attempts can be classified into qualitative and quantitative approaches. In this chapter, the term "qualitative" corresponds to publications in which mechanisms are proposed, on the basis of the collected experimental data, through chemical equilibria solely, while the term "quantitative" corresponds to papers in which such chemical equilibria are then used to derive mathematical expressions of the experimentally measured quantities (typically: D vs. $[HX]_{aq,init}$) in order to perform curve fitting for deriving conditional equilibrium constants. The qualitative approach is, by far, the dominant way mechanistic studies have been performed so far for IL extraction systems, with only one group performing extensive curve fitting, while such mathematical treatments are more common for the study of extraction systems implying molecular solvents. This is ascribed to the novelty of IL systems, and curve fitting of IL extraction systems will certainly expand in the future.

Chemical models describing metal extraction toward IL phases can be categorized into two groups: mechanisms involving solely ion exchanges, either cationic or anionic, depending on systems and chemical conditions, and thereafter denoted IX, or mixed mechanisms (MM) comprising a contribution of ion-pairing equilibria, in addition to ion exchange. In this frame, MM would appear as a complement to IX but such a distinction is very important. Since a wealth of data has been acquired on IL extraction systems, it may be timely to propose a generalization of such phenomena, if possible, in terms of a comprehensive synthetic model comprising a limited number of basic equations, as has been done years ago for metal extraction into molecular solvents, and summarized through Eqs. (6)–(9). What is at stake is the demonstration that we are now mastering extraction mechanisms, as the first step toward rational optimization of extraction systems.

In the field of RE/An liquid–liquid extraction, the overdominating situation is that of IX, as proposed and substantiated worldwide, and detailed in Section 8.1. MM (i.e., with both ion exchange and ion pairing) has been seldom proposed for An extraction by use of ILs, while it has been intensively developed for extraction of some fission products (Sr and Cs). Although these elements do not enter in the scope of the handbook, we nevertheless present this model in details in Section 8.2 because confronting both views is important for gaining a deeper insight into the question of metal extraction in IL phases. Then we will discuss the quantitative approach of extraction and we will conclude on what can be inferred from the wealth of data accumulated for M^{m+}/HX/L/IL system and their corresponding qualitative and quantitative modeling.

8.1. The IX Qualitative Approach

As already highlighted in Section 4.3, the boomerang shape observed for the dependence of D_M upon the acidity and its variations, with a well-pronounced decrease or a smoother one, depending on the cationic component of the IL (see Fig. 3) allows one to deduce some facts. For instance, it is obvious that two different mechanisms are in competition (notwithstanding of the further decrease or leveling off at very high acidities). Whatever these are, if the first one (at low acidities) is highly dependent on the IL structure, while the second one (at high acidities) is not, by changing the cationic part of the IL one will observe a series of curves similar to those plotted in Fig. 3. The HNO_3 concentration at which the change from one mechanism to the other one becomes noticeable will then shift along the HNO_3 axis. In other words, taking into account the relative equilibrium constants of the two different mechanisms, one leading to a decrease in D_M and the other one to an increase, one can qualitatively describe all variations displayed in Fig. 3. Therefore, there is no need to imagine a third mechanism. This, however, does not prove that another mechanism is not playing a role in the variations observed in Fig. 3, but looking for only two mechanisms corresponds to the Ockham razor principle.

In the case of ionic exchange, the question is not only what is the exact nature of the extracted metallic species but also what is the exact nature of the species back transferred into the aqueous phase to ensure electrical neutrality, as both cationic and anionic exchanges can be envisioned. Although of course ILs used for extraction are forming biphasic systems with aqueous phases, there are nevertheless partly soluble in water, and similarly, water is partly soluble in ILs to an extend largely dependent on the IL chemical structure and on the composition of the aqueous phase. In fact, ILs in equilibrium with aqueous phases have been proven to also dissolve large amounts of water, together with large amounts of many ions, introduced as either acids (Billard et al., 2011c; Gaillard et al., 2012; Rout et al., 2009) or neutral salts (Freire et al., 2007, 2009; Tomé et al., 2009). Therefore, it is possible that cationic exchange proceeds through the back transfer of both IL cations and H^+ or, possibly, of other additional "spectator" cations introduced. On the other hand, starting from M^{n+}, anionic exchange may imply either the negatively charged species $[MX_{n+p}]^{p-}$ if the acid counteranion is complexing (NO_3^-, Cl^-, etc.) or $[MA_{n+p}]^{p-}$ if the IL anionic component is complexing. The case of mixed complexes between M^{n+}, X^-, and A^- is not considered further. In common practice, X^- is most of the time a stronger complexing anion than A^-, as Tf_2N^- is a very weak complexing anion, but PF_6^- and BF_4^- display some affinities toward UO_2^{2+} (Gaillard et al., 2005a) and thus could be envisioned for anionic exchange from aqueous solutions acidified by $HClO_4$ or HTf_2N. Such experimental conditions are not documented yet.

As a consequence, IX extraction mechanism in ILs can be understood with the help of two equilibria, as proposed under a less synthetic form in Billard et al. (2011c):

$$M^{m+} + p\overline{L} + i\overline{Cat^+} + (m-i)\overline{H^+} \rightleftarrows \overline{ML_p^{m+}} + iCat^+ + (m-i)H^+ \quad (11)$$

$$M^{m+} + (m+p)X^- + q\overline{L} + p\overline{A^-} \rightleftarrows \overline{MX_{m+p}L_q^{p-}} + pA^- \quad (12)$$

Equation (11) should be the dominating process at low acidities, while Eq. (12) is the major process at high acidities. Although quite an unusual situation, values of p in Eq. (12) can be larger than 1, for example, in the case of Pu complexes which can bear a -1 or -2 charge in ILs (Rout et al., 2010). It is important to note that in this model, by contrast to the molecular organic systems described through Eqs. (6)–(9), no distinction is made between nonprotonated and protonated ligands and the origin of the H^+ involved in the ion exchange is not specified. This is in part due to the ionic nature of ILs and to our incomplete knowledge of the associated or dissociated state of molecules in such solvents. This does not mean, however, that molecular ligands cannot protonate or deprotonate in ILs but, if needed, such a process can be described simply according to an additional equilibrium:

$$\overline{L} + \overline{H^+} \rightleftarrows \overline{LH^+} \quad (13)$$

Let us remind the reader that the availability of H^+ in the IL phase has been ascertained by several authors.

Qualitative arguments are in favor of the double mechanism depicted in Eqs. (11) and (12). They will be presented first and then chemical evidences will be discussed.

At low acidities, should X^-, the anionic counterpart of the acid used, be a complexing agent of the metal cation studied, as is the case for Cl^- or NO_3^-, an increase in HX concentration will lead to a decrease in D_M values because the metal is locked up in a nonextractable form through complexation. On the other hand, at high acidities of the aqueous phase, an increase in HX concentration should lead to an increase in D_M according to Eq. (12). This perfectly corresponds to the boomerang shape experimentally observed in so many cases. Furthermore, the first chemical equilibrium (Eq. 11) relates to Cat^+ solubility in the aqueous phase. Obviously, this is highly dependent on the cationic chemical structure of the IL and may vary tremendously from one IL to the other, all other chemical conditions being equal. Conversely, the second equilibrium (Eq. 12) involves the A^- aqueous solubility. Although the solubility of the two extracted species may differ from one IL to the other, it can be expected that increasing the Cat^+ hydrophobicity in the system M^{n+}/HX//L/IL will lead to a decrease in extraction efficiencies at low acidities and to identical D_M values at high acidities with a subsequent shift toward lower $[HNO_3]_{aq,init}$ values of the boomerang curvature. This is in very good agreement with the variations shown in Fig. 3.

There are many ways to experimentally demonstrate the mechanism depicted in Eqs. (11) and (12). The easiest and more elegant way is to add the IL cation to the aqueous phase, in the form of its chloride salt, for example, at a fixed low acidity or to add the IL anion, in the form of its lithium salt, at fixed high acidities, as this should induce a decrease in D_M in both cases. However, four important aspects of these experiments have to be stressed. First, note that in the case where $i=0$ in Eq. (11), addition of the CatCl salt does not induce any change in the D_M values. Second, in the case where $i=n$, D_M should be constant as a function of HX at low acidities, apart from variations ascribed to ionic strength effects or to ongoing complexation with X^-. Third, this qualitative demonstration of the ion exchange does not give access to the exact values of i by itself. For example, in the case of a $+3$ charged metal cation ($m=3$ in Eq. 11), one can envision either one H^+ and two Cat^+ ($i=2$) or two H^+ and one Cat^+ ($i=1$) to be exchanged, and these two different chemical equilibria would both lead to D_M decrease as a function of CatCl added. Similarly, a decrease in D_M as a function of LiA added to the aqueous phase does not provide information on the exact charge of the extracted anionic complex. Finally, it is important to be aware that $H_2O/HTf_2N//C_1C_4imTf_2N$ is no more biphasic above $[HTf_2N]_{aq,init}=3$ M (Gaillard et al., 2012) (see also the noticeable increase in volume observed in Mehdi et al., 2010 for $Nd^{3+}/HTf_2N//IL$) and this could also be the case for other ILs based on the Tf_2N^- anion. Thus, caution should be paid to intricate effects that may impact the D_M values when large amounts of $LiTf_2N$ are added at already high acidic acid concentrations, in an attempt to confirm Eq. (12). More complicated ways to demonstrate parts of Eq. (11) or (12) can be found in Billard et al. (2011c). Another procedure which does not appear easy to interpret is the addition of $CatNO_3$ to the aqueous phase. This salt simultaneously brings two ions potentially involved in the extraction process, with opposite effects. Furthermore, experiments in our laboratory have shown that $C_1C_4imNO_3$ transfers substantially to the IL phase so that the equilibrium concentration in the aqueous phase is far from the initial value, rendering qualitative discussions rather hazardous. As a matter of fact, in the $Am^{3+}/HNO_3//(CMPO+TBP)/C_1C_4imTf_2N$ system (Rout et al., 2009), addition of $C_1C_4imNO_3$ (from 0.1 to 1 M) to the aqueous phase leads to almost constant D_M values, which could be due either to massive transfer of this salt to the IL phase or to opposite effects almost exactly compensating one another.

Most of the relevant experimental data concern cationic exchange described by Eq. (11), and one of the first papers using this convincing and simple method for mechanistic understanding fortunately could conclude to $i=m$ in two systems (Nakashima et al., 2005). Exchange of at least one $C_1C_4im_+$ is proved for Ce^{3+} (or Eu^{3+})$/H_2O/HNO_3//CMPO/C_1C_4imPF_6$ because D_{Ln} is sharply decreasing as a function of $C_1C_4im_+$ added to the aqueous phase. The authors also observed a constant D_{Ln} value as a function

of [HNO_3] for Eu^{3+} and Ce^{3+} and thus concluded to the exchange of three $C_1C_4im^+$. Another study also suggested the exchange of three Cat^+ to counterbalance extraction of Sc^{3+}, but the absence of H^+ effect was not demonstrated (Sun et al., 2007). For Eu^{3+}/HNO_3/TODGA/$C_1C_2imTf_2N$ (Shimojo et al., 2008), the addition of Cat^+ to the aqueous phase leads to a clear decrease in the extractability but the exchange of three Cat^+ to account for these data is not convincing, a question that will be detailed in Section 8.2. Apart from the exchange of Cat^+ alone, demonstrations of mixed Cat^+/H^+ exchanges can be found in the literature (Bell and Ikeda, 2011) together with exchanges of H^+ alone (Bonnaffé-Moity et al., 2012; Kubota et al., 2011).

Another rather convincing way to prove part of Eq. (11) is to perform extraction experiments with another acid. Similar D_M values as a function of [HNO_3] and [HX] would demonstrate that no NO_3^- or X^- is involved, in agreement with Eq. (11). However, caution should be paid to the effect of side reactions that may also have a great impact on the D_M values, for example, partial dissociation of the weak biacid H_2SO_4 (Shimojo et al., 2008) or M^{n+}/X^- complexation, that may differ between NO_3^- and X^-. Therefore, experiments with $HClO_4$, a fully dissociated acid with a more or less noncoordinating anion (at least in water), would suppress these two by-side effects in the aqueous phase. Nevertheless, it has been recently shown that weakly coordinating anions in water become rather strong ligands in ILs (Chaumont et al., 2012) so that it might be possible that any counteranion X^- (ClO_4^- or triflate, among the weakest known) will participate in the extraction of the metallic entity at high acid concentration. In case HTf_2N is used, as indicated above, the system is no more biphasic above 3 M of acid.

It is now possible to consider the mechanistic aspects of the system $Y^{3+}\left(\text{or}\,Eu^{3+}\right)/HNO_3//$DODGAA/IL (Kubota et al., 2011) that behaves identically to its molecular analogue (see Section 4.4). The authors observed that the $Y^{3+}Y^{3+}$ and Eu^{3+}extraction performance of DODGAA in ILs was not affected by the addition of Cat^+ to the aqueous phase, while a classical slope analysis (see Section 8.2) allowed them to conclude that the extraction mechanism involves three H^+ ions, released to the aqueous phase. As a consequence, they proposed the following mechanism to occur in the IL media:

$$M^{3+} + 3\overline{HL} \rightleftarrows \overline{ML_3} + 3H^+ \tag{14}$$

This equilibrium is formally identical to Eq. (11) with $i = 0$, assuming the ligand can be deprotonated (thus including Eq. 13).

Evidences for anionic exchange through Eq. (12) are uncommon and concern $UO_2^{2+}/HNO_3//$TBP/IL (Bell et al., 2011; Billard et al., 2011c) or $UO_2^{2+}/HNO_3//$malonamide/$C_1C_4im\,Tf_2N$ (Bonnaffé-Moity et al., 2012), by use of two different methods. Addition of $LiTf_2N$ to the aqueous phases at high nitric concentrations leads to a decrease in D_M, in agreement with Eq. (11) (Bonnaffé-Moity et al., 2012). Titration of $[Tf_2N^-]_{aq,eq}$ as a function of the mole number of uranium transferred to the IL phase evidences a linear

dependence with slope 1, in perfect agreement with the suspected anionic exchange (Bell et al., 2011).

Finally, one publication evidences an anion exchange of a particular type. In the system Nd^{3+} (or Eu^{3+})/HNO_3//HTTA/$C_1C_4imTf_2N$ (Jensen et al., 2003), the extracted species has been characterized by UV–vis (Nd), EXAFS (Eu), and luminescence (Eu). All these spectroscopic data and the results of the slope analysis support the existence of the $(Ln(TTA)_4)^-$ species in the IL phase, arising from to the following equilibrium:

$$Ln^{3+} + 4\overline{HTTA} + \overline{C_1C_4im^+Tf_2N^-} \rightleftarrows \overline{Ln(TTA)_4^-} + 4H^+ + \overline{C_1C_4im^+} + Tf_2N^- \quad (15)$$

This chemical equation can also be written in a more synthetic form as follows:

$$Ln^{3+} + 4\overline{HTTA} + \overline{Tf_2N^-} \rightleftarrows \overline{Ln(TTA)_4^-} + 4H^+ + Tf_2N^- \quad (16)$$

Although it involves the back transfer of A^-, as in Eq. (12), no X^- is included in the extracted species.

An important point concerns the characterization of the extracted species in order to confirm (or invalidate) the mechanism described through Eqs. (11) and (12), but a very limited number of studies have dealt with this question so far. This is in part due to the difficulty in adapting analytical tools to ILs, such as capillary electrophoresis, while EXAFS and other related techniques are easily implemented in ILs (Carmichael et al., 1999; Gaillard et al., 2005b; Nockemann et al., 2009).

IR (Quasch et al., 2010) has been used to study the speciation of uranyl in IL samples mimicking extraction phases. UV–vis is a powerful technique to study uranyl complexation in IL (Chaumont et al., 2012; Georg et al., 2010) and so is luminescence, in the case of Eu(III) and other Ln(III) and Cm(III) (Billard, 2003; Binnemans, 2007; Stumpf et al., 2007, 2008). However, the concentrations of the metallic ions that are required to perform either EXAFS, UV–vis, Raman, or IR experiments are around 10^{-2} M or above, which is most of the time much larger than the usual metal concentrations in extraction experiments, especially in the case of heavier actinides. It would thus be necessary to assess that a similar mechanism is at work over a wide range of metal concentrations for any of the studied elements. Such a positive result has only been obtained in the range of uranium(VI) concentrations from traces to 10^{-2} M by comparing data from different publications (Billard et al., 2011c). Development of sensitive analytical techniques for ILs is mandatory to improve our knowledge of extracted species and requires adjustments to comply with the ionic solvent nature of ILs. In this respect, microcalorimetric studies could be of some interest, provided that the impact of radioactivity and thus of the internal heat added to the system is properly and precisely taken into account.

Again, the system $UO_2^{2+}/HNO_3//TBP/IL$ provides most of the spectroscopic studies aiming at characterizing the extracted species. By comparison of UV–vis spectra, two papers have clearly demonstrated that the extracted species at low and high acidities are different from one another and are not identical to that extracted in the dodecane system (Bell and Ikeda, 2011; Billard et al., 2011c). It is a deceptive result, in the sense that it does not provide information on the exact structure of the uranyl complex. In particular, the number of coordinated TBP molecules remains unclear, with a TBP stoichiometry equal to 3 at $[HNO_3]_{aq,init} = 0.01$ M and equal to 1 at $[HNO_3]_{aq,init} = 6$ M in ammonium-based ILs, while TBP stoichiometry was found equal to 2, whatever the acidity, for the data in $C_1C_4im\,Tf_2N$. Interestingly, the UV–vis data recorded in ILs of the imidazolium and tetraalkylammonium families are very similar, if not identical, thus pointing to the existence of a general extraction mechanism. Furthermore, the UV–vis spectra recorded in the $C_1C_4im\,Tf_2NN$ extraction phase at several of acidities (Billard et al., 2011c) evidence a change from one dominant species to another, thus confirming the change in extraction mechanism as the HNO_3 concentration is increased. ESI-MS and other techniques have been used to get insight into the speciation of uranyl in $TBP/C_1C_4im\,Tf_2N$ extracting phases (Murali et al., 2010), as compared to dodecane. Unfortunately, measurements were performed at $[HNO_3]_{aq,init} = 1$ M, the turnover HNO_3 concentration of this system (see Fig. 3), so that whatever the exact uranyl speciation, a mixture of species is expected. The authors concluded that the most abundant species is $[UO_2(NO_3)(TBP)_2]^+$, while they observed the neutral $[UO_2(NO_3)_2(TBP)_2]$ species in dodecane.

Other systems have also been spectroscopically investigated. EXAFS and UV–vis measurements performed for $UO_2^{2+}/HNO_3//(CMPO + TBP)/C_1C_4im\,PF_6$, and $C_1C_8im\,Tf_2N$ systems evidenced a differently extracted species as compared to the dodecane equivalent system (Visser et al., 2003), and the authors concluded to the formation of $[UO_2(NO_3)CMPO]^+$ in the extracted IL phases, arising from cationic exchange with Cat^+, to be compared to the $[UO_2(NO_3)_2(CMPO)_2]$ species present in dodecane. Finally, as noted above, EXAFS was successfully used to ascertain the $[Ln(TTA)_4]^-$ structure in the $Nd3^+\left(\text{or } Am^{3+}\right)/HNO_3//HTTA/C_1C_4imTf_2N$ systems (Jensen et al., 2003).

8.2. The MM Qualitative Approach

In addition to cationic exchange, a nonnegligible contribution of ion pairing to metal extraction is proposed by a very limited number of groups. The most important work based on this assumption is that of Dietz and coworkers, who rationalize a wealth of data accumulated over the last 10 years or so for rather similar systems of the general type $Sr^{2+}(\text{or } Na^+, Ca^{2+}, Ba^{2+})/HX//DCH18C6/C_1C_nim\,Tf_2N$ ($n = 2$–10), where DCH18C6 is a crown-ether (Dietz and Dzielawa, 2001; Dietz

and Stepinski, 2005; Dietz et al., 2003, 2008; Hawkins et al., 2012; Heitzman et al., 2006; Jensen et al., 2002). A few years ago, this group has also published a very interesting paper on their views on the question of metal extraction in IL phases (Dietz, 2006) and has conducted one study on the $UO_2^{2+}/HNO_3//TBP/C_1C_n imTf_2N$ ($n = 5$, 8, 10) systems (Dietz and Stepinski, 2008) (see Fig. 3 for the data), again proposing a MM mechanism. We will thus summarize these experimental results, focusing on the typical examples of Sr^{2+}, Ca^{2+}, and K^+, and we will then discuss the MM model.

The D_M variations for Sr^{2+} and Ca^{2+} as a function of $[HNO_3]_{aq,init}$ in the presence of DCH18C6 dissolved in $C_1C_5imTf_2N$ display the typical boomerang shape (Hawkins et al., 2012; Fig. 7). For example, D_{Ca} decreases from 0.3 at $[HNO_3]_{aq,init} = 10^{-2}$ M down to ca. 0.015 at $[HNO_3]_{aq,init} \approx 3$ M and then increases to 0.06 at the highest nitric acid concentration, while D_{Sr} decreases from ca. 110 to 3 and then further increases up to ca. 7 at the same acidities. In the case of K^+, only a decrease in D_K is observed in $C_1C_5imTf_2N$ (Fig. 8). In the ILs bearing a longer alkyl chain ($n = 6$, 8, 10), for Sr^{2+} and Ca^{2+}, the D_M variations display a complex behavior, as schematically illustrated in Fig. 7 for Ca^{2+} (Hawkins et al., 2012). This behavior is more or less similar to that already pinpointed in Section 4.3 for Th^{4+}/HNO_3//diglycolamide/

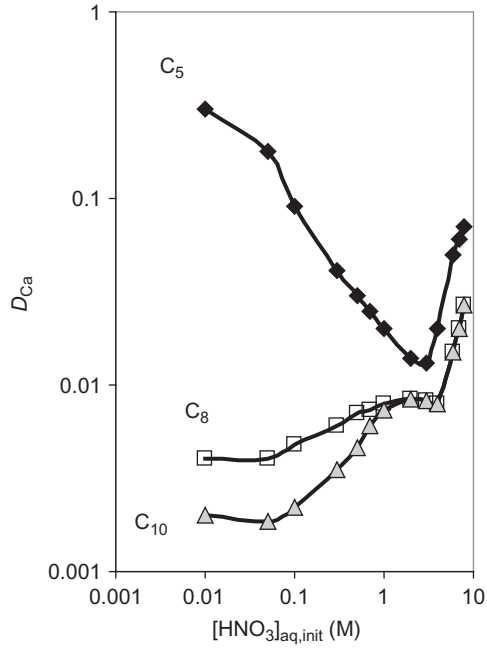

FIGURE 7 Schematic variations of D_{Ca} as a function of $[HNO_3]_{aq,init}$ for several systems Ca^{2+}/HNO_3//DCH18C6/$C_1C_n imTf_2N$ redrawn after Hawkins et al. (2012).

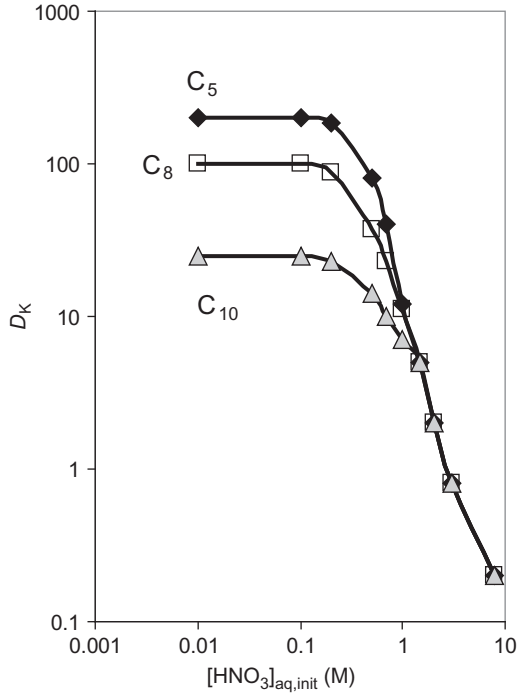

FIGURE 8 Schematic variations of D_K as a function of $[HNO_3]_{aq,init}$ for several systems K^+/HNO_3//DCH18C6/C_1C_nimTf_2N redrawn after Hawkins et al. (2012).

C_1C_nimPF_6 ($n=4$, 6, 8) (Fig. 6). It was also quoted that the acid dependencies of D_{Sr} in C_1C_2imTf_2N using HCl or H_2SO_4 differ little from the one observed with HNO_3 (Dietz and Dzielawa, 2001). Finally, EXAFS data acquired in several extracted IL phases (C_1C_nimTf_2N, $n=5$, 6, 8, 10) could not evidence any nitrate ions in the first Sr^{2+} coordination sphere, while two nitrates are detected in 1-octanol extraction phase (Dietz et al., 2003). Unfortunately, no indication on the nitric acid concentration at which the EXAFS data have been recorded is given in this paper.

The model proposed by Dietz and coworkers to account for their data evolved along the years and will be thus presented and discussed in a chronological way. It is important to remember that although we have summarized the whole set of data available today, the earlier stages of the model proposed have been based on a more limited data set and that the model evolved naturally as additional data became available.

In the first stage of the model (Dietz and Dzielawa, 2001), the similar D_{Sr} variations obtained for HNO_3, HCl, and H_2SO_4 prompted the authors to suggest a unique equilibrium, based on cation exchange according to

$$\mathrm{SrDCH18C6^{2+}} + 2\overline{\mathrm{C_1C_nim^+}} \rightleftarrows \overline{\mathrm{SrDCH18C6^{2+}}} + 2\mathrm{C_1C_nim^+} \quad (17)$$

In this first publication, the following equilibrium was ruled out:

$$\mathrm{Sr^{2+}} + \overline{\mathrm{DCH18C6}} + 2\overline{\mathrm{Tf_2N^-}} \rightleftarrows \overline{\mathrm{Sr(Tf_2N)_2DCH18C6}} \quad (18)$$

In the next paper (Jensen et al., 2002), EXAFS data were performed for one IL and 1-octanol, demonstrating that two nitrate ions are present in the Sr^{2+} first coordination sphere when 1-octanol is the solvent, while no nitrate can be detected in the first coordination sphere when $C_1C_5imTf_2N$ is the solvent. However, the authors noted that it does not prove unambiguously that nitrate ions are not coextracted with Sr^{2+} because EXAFS cannot detect NO_3^- in an outer-sphere complex. This is perfectly right, but we would like to stress that it does not prove either that nitrates are coextracted with Sr^{2+} in an outer-sphere complex. In fact, in this case, EXAFS does not help identifying the extracted species. Consequently, Dietz and coworkers performed nitrate titration of the IL phase and wrote that "the amounts of anion coextracted into the IL are vastly insufficient to produce neutral Sr^{2+} complexes," so they concluded that the phase transfer reaction proceeds primarily through cation exchange as described by Eq. (17). As can be clearly seen, this model is identical to the IX model.

The third paper focuses on the change in D_{Sr} variation as the alkyl chain length of the IL is varied and leads to the introduction of the MM hypothesis (Dietz et al., 2003). Starting from the result of Sr^{2+} extraction by cation exchange of two Cat^+ in $C_1C_5imTf_2N$, as demonstrated in their previous papers (Dietz and Dzielawa, 2001; Jensen et al., 2002), the authors postulated that an increase in the alkyl chain of Cat^+, and thus a decrease in Cat^+ solubility in water, would induce a change in the extraction mechanism, from cation exchange to ion pairing. It is important to note that all extraction experiments in this paper have been performed in a limited acidic range, with no data above $[HNO_3]_{aq,init} = 1$ M. Actually, the data recorded in $C_1C_{10}imTf_2N$ display an increase in D_{Sr} as a function of $[HNO_3]_{aq,init}$ (see Fig. 7 for the similar case of Ca^{2+}). The MM hypothesis thus relies on two experimental results. First, EXAFS data performed in several imidazolium ILs ($n = 5$, 6, 8, 10) could not evidence any nitrate in the first Sr^{2+} coordination sphere, so the authors concluded to an outer-sphere complex. We already pinpointed that this is not a convincing argument. Second, they observed by titration experiments that NO_3^- extraction is increasing from $C_1C_5imTf_2N$ to $C_1C_{10}imTf_2N$, from 9% to 20%, while Sr^{2+} extraction decreases from 96.5% to 20.2% for one set of (identical) chemical conditions that are nevertheless not specified. The authors then concluded that this is ascribable to a change from cation exchange to ion pairing, which would be the dominating (but not very efficient) process in all the acidic range investigated in $C_1C_{10}imTf_2N$ and would be always negligible in $C_1C_5imTf_2N$. Thus, the MM assumption relies solely on the coincidental values of the Sr^{2+} and

NO_3^- extraction in $C_1C_{10}imTf_2N$ for one single $[HNO_3]_{aq,init}$ value. As already stressed above, ILs can dissolve large quantities of water and nitric acid, depending on their chemical structure, so it would have been necessary to check the amount of nitrates partitioning to the IL phase in the absence of Sr^{2+} and the DCH18C6 and to confirm the equality of E_{Sr} and $E_{NO_3^-}$ in a wider acidic range to derive firm conclusions. Despite these restrictions, it is clear that the proposed mechanism is in qualitative agreement with the data displayed in both Figs. 3 and 7, just as the IX model is, by the way. Subsequently, the same authors published one paper on $UO_2^{2+}/HNO_3//TBP/C_1C_nimTf_2N$ ($n=5$, 8, 10) systems (Dietz and Stepinski, 2008), proposing a cation exchange at low acidities and ion pairing with extraction of the neutral $[UO_2(NO_3)_2(TBP)_2]$ species at higher acidities. In this case however, as detailed in Section 8.1, UV–vis spectra performed by two other groups have demonstrated that this neutral species is not present in the IL extraction phases (Bell and Ikeda, 2011; Billard et al., 2011a,b,c), thus ruling out the MM hypothesis for the uranyl system.

The final stage (so far) of the model appeared already in 2005, in a publication dealing with the study of $Na^+/HNO_3//DCH18C6/C_1C_nimTf_2N$ ($n=5$–10) (Dietz and Stepinski, 2005). Starting from the observation that D_{Na} decreases as a function of increasing acidities for $Na^+/HNO_3//DCH18C6/C_1C_5imTf_2N$, while it is increasing for $Na^+/HNO_3//DCH18C6/$1-octanol, a behavior identical to that of Sr^{2+} in the same two systems, the authors performed extraction experiments in $C_1C_{10}imTf_2N$, hoping that the change in the cation hydrophobicity would be accompanied by an increase in D_{Na}, as was the case for D_{Sr} (Dietz et al., 2003). This foreseen change was ascribed to ion pairing becoming a predominant mode of Na^+ extraction. By contrast to their expectations, D_{Na} is decreasing as a function of $[HNO_3]_{aq,init}$ in both IL solvents, $C_1C_{10}imTf_2N$ being less efficient than $C_1C_5imTf_2N$, under the same chemical conditions. Slope analysis evidenced that the transfer of Na^+ was concomitant with the back transfer of one H^+. This cationic exchange was ascribed to the formation of a DCH18C6-H_3O^+ adduct according to

$$Na^+ + \overline{H_3ODCH18C6^+} \rightleftarrows \overline{NaDCH18C6^+} + H_3O^+ \qquad (19)$$

This corresponds to Eqs. (11) and (13) (with $i=0$). In addition to this dominant process, as the authors observed some extraction of nitrates to the IL phase, they concluded that the overall process should be described according to a ternary mechanism, comprising cation exchange with either Cat^+ or H^+ (mediated by DCH18C6) and, finally, ion pairing (MM hypothesis). We note, however, that this last mechanism, if present, cannot be dominating the chemistry under the chemical conditions of the work, as D_{Na} is always decreasing sharply as a function of $[HNO_3]_{aq,init}$. We also recall that the exact contribution of natural solubility of nitrates in the IL phase in the absence of Sr^{2+} and DCH18C6 should be precisely accounted for before assuming any

significant contribution of ion pairing to the Sr^{2+} extraction process, a measurement that has not been performed in this work.

In their most recent available paper, Dietz and coworkers (Hawkins et al., 2012) are presenting new experimental data for $M^{m+}/HNO_3/DCH18C6/C_1C_n imTf_2N$ ($n = 5$, 8, 10) and M = Ca, Sr, Ba, Na, K, and Cs (see Figs. 7 and 8 for schematic variations for Ca^{2+} and K^+, chosen as typical examples). In particular, the data discussed in one of their previous publication (Dietz et al., 2003) have been extended up to $[HNO_3]_{aq,init} \approx 8$ M. Considering the very different behaviors of the D_M versus $[HNO_3]_{aq,init}$ variations for Ca and K, we will first discuss K^+ data (Fig. 8) and second, Ca^{2+} data (Fig. 7), together with the data of Shen et al. (2011b) (see Fig. 6).

According to the authors, Fig. 8 points to two types of ion exchanges occurring. At low acidities, D_M strongly depends on Cat^+ and does not seem to vary much as a function of H^+, while at high acidities, all curves converge, indicating an identical process in all ILs, thus a mechanism independent of Cat^+. This is ascribed to IL cation exchange (Eq. 11 with $i = m = 1$), followed by H^+ exchange (Eq. 11, with $i = 0$). These data are thus easily qualitatively described with the IX model.

By contrast, data plotted in Figs. 6 and 7 present an intricate behavior. Purely phenomenological considerations about the shape of these curves would suggest at least three different mechanisms in the case of Ca^{2+} and four different ones to account for the W shape for Th^{4+}. For the Ca^{2+} data, one mechanism is dominating below 1 M and is highly dependent on the cationic structure of the IL, one is dominating in the limited concentration range of 1–3 M and, above ca. 3 M, a third mechanism occurs, being almost independent of the cationic IL component. Other points that should be accounted for are the possible differences between the charges of the metallic cations of concern (Th^{4+} and Ca^{2+}) that may render the overall chemical problem even more complicated.

In line with previous reports on Sr^{2+} extraction in ILs by use of DCH18C6, the model proposed to describe the data schematically presented in Fig. 7 is based on a ternary extraction process, involving contributions of Cat^+ exchange, H^+ exchange, and extraction of a neutral species. Similarly, to account for their data, Shen and coworkers propose four equilibria (Shen et al., 2011b), involving successively $[ThL]^+$, $[ThL_2]^{4+}$, $[Th(NO_3)_nL_2]^{4-n}$ ($n < 4$), and finally the neutral species $[Th(NO_3)_4L_2]$. The first one is assumed to be exchanged with four Cat^+, but this stoichiometry, as compared to mixed $xH^+/yCat^+$ exchange ($x + y = 4$) is not proved or disproved. Again, the important point is the proposal of a neutral species at the highest acidic conditions of the work. Although interesting and in qualitative agreement with the data, no spectroscopic or additional extraction experiments in the forms discussed in Section 8.1 have been performed to substantiate this model. Despite the lack of experimental proofs, we, however, think that the partially nitrated thorium species proposed above are realistic.

Finally, MM is also considered in view of describing extraction data in $Am^{3+}/HNO_3//Cyanex/C_1C_{10}imTf_2N$ (Cocalia et al., 2005). In order to account for the boomerang shape observed, the authors proposed the following set of equilibria, on the basis of data in a variety of dialkyl-phosphoric and phosphinic acids in nonpolar molecular organic solvents, in which the ligands are known to form dimers:

$$M^{m+} + m\overline{(HL)_2} \rightleftarrows \overline{M(HL_2)_m} + mH^+ \tag{20}$$

$$M^{m+} + mNO_3^- + p\overline{(HL)_2} \rightleftarrows \overline{M(NO_3)_m \cdot p(HL)_2} \tag{21}$$

Equation (20) is based on the partial deprotonation of a dimeric extracting moiety and is formally identical to Eq. (11) with $i=0$. By contrast, the extracted species in Eq. (21) differs from that in Eq. (12) by one X^- entity, although these two equilibria are in qualitative agreement with the increase in D_M experimentally observed for the highest acidities in the two types of solvents. In order to support their proposed mechanism and to prove it is identical in both types of solvents, the authors collected and compared spectroscopic data (UV–vis and EXAFS) for the U(VI) and Nd(III) extracted species in dodecane and $C_1C_{10}imTf_2N$ at low acidities ($[HNO_3]_{aq, init}=0.25$ M). Actually, the match between UV–vis spectra in dodecane and $C_1C_{10}imTf_2N$ is very good, as is the agreement for the EXAFS data. Thus, the authors concluded that some extraction systems involving ILs can behave identically to traditional ones based on molecular solvents, with respect to both distribution features and environment of the metal ion complexes. However, as the spectroscopic data have been collected at low acidities only, the envisioned extracted species obtained at higher nitric acid concentration was not scrutinized and thus their experiments cannot confirm or rule out any of Eq. (21) or (12), while confirming Eq. (20) or (11). In order to discriminate between the two equilibria proposed at high acidic concentrations, it would be necessary to examine the effect of added Tf_2N^- anions to the aqueous phase in both systems. Again, let us stress that EXAFS data, such as those collected by the authors, are not precise enough to unambiguously discriminate between n and $(n+1)$ nitrates in the first coordination sphere of U(VI) or Eu(III). Similarly, UV–vis data for U(VI) complexed by nitrates are known to display very similar shapes as soon as the first nitrato complex is formed, whatever the solvent (Georg et al., 2010; Ikeda et al., 2008), rending precise speciation determination quite difficult in ILs (Georg et al., 2010).

To conclude on the IX and MM modeling, we would like first to insist on the complementary aspects of the two models, as all authors agree on a cationic exchange mechanism at low acidities, involving possibly both Cat^+ and H^+, although it can be expressed in various ways (Eq. 11 or Eqs. 11 and 13, depending on the nature of the ligand). The main difference between IX and MM relies on the exact contribution of ion pairing and anionic

exchange at high acidities, as both models are in qualitative agreement with all data collected so far. Spectroscopic results have proved that anionic exchange is dominating in $UO_2^{2+}/HNO_3//TBP/IL$, but this is not enough to assess it is a general rule. However, it is important to remember that ion pairing has not been convincingly proved in any system so far. In this respect, as stressed above, there is an urgent need for deeper spectroscopic investigations of the extracted species in many systems, in order to settle this question.

8.3. IX Quantitative Description

Besides the mechanistic qualitative understanding of extraction discussed in the above sections, it is possible to reach quantitative aspects through modeling and/or data fitting and this section presents some recent advances in this field together with more usual ways. Then, two examples are described and critically assessed.

The classical fitting technique is the so-called slope-analysis method. It is easy to perform "by hand" and has been widely used for years for molecular solvent studies. It is also used for ILs nowadays because it can be applied without the help of computers. Taking Eq. (6) as an example, one can express the mass action law as follows:

$$K = \frac{\overline{[MX_mL_p]}}{[M]\overline{[L]}^p[X^-]^m} \tag{22}$$

where K is the equilibrium constant. One easily derives

$$\log D = p\log\overline{[L]} + m\log[X^-] + \log K \tag{23}$$

As a consequence, a plot of $\log D$ as a function of $\log\overline{[L]}$ or $\log[X^-]$ should give a straight line, with slope p or m, respectively. Many examples of the successful use of the slope-analysis method can be found in the literature. However, in several cases, both in molecular solvents or ILs, the slope derived is not an integer (2.67 in *n*-octanol (Geist et al., 2006), 1.68 in dodecane (Murali et al., 2010), 1.6 in $C_1C_{10}imTf_2N$ (Jensen et al., 2003), rounded to ≈ 2, or -2.5 in $C_1C_4imTf_2N$ (Rout et al., 2010), for example), while the regression coefficient are very good, indicating the data do follow a linear empirical law. Values as far as 0.5 above (or below) an integer are difficult to reconcile with the mathematical treatment detailed above. In fact, such noninteger values are a consequence of the numerous approximations contained in Eq. (22). From a mathematical point of view, the approximation that all equilibrium concentrations in the equation can be approximated to their initial values is always made. From a chemical point of view, Eq. (22) assumes a single equilibrium, thus neglecting competitive extraction of HX, complexation of M^{n+} with X^-, and, in the case of liquid/liquid extraction in IL solvents, the presence of two competitive extraction mechanisms, as depicted by Eqs. (11) and (12), for example. It also assumes that HNO_3 is

fully dissociated, which is known not to be the case above 3 M (Ruas et al., 2010). Finally, Eq. (22) assumes that ionic strength effects are negligible, which is most of the time hard to reconcile with the experimental reality.

These hypotheses will now be discussed.

The approximation of equilibrium and initial concentrations being equal is usually valid because most of the time, the ligand and the acid are in large excess as compared to the metal ion. However, it implies that competitive extraction of the acid by the ligand is negligible, which has to be properly addressed. Clearly, assuming more than one dominant equilibrium immediately renders the mathematical system quite tricky to solve (although analytical expressions can be obtained in most cases, possibly with the help of mathematical softwares as Maple® or Matlab®), the consequence being that the expression of D_M as a function of $[HNO_3]_{aq,init}$ or $[L]_{org,init}$ cannot be linearized anymore. Thus, a graphical approach by hand is no more possible. Similarly, considering the partial dissociation of HNO_3, one always derives nonlinear equations. Again, however, the mathematical system obtained can be solved, at the price of rather complex polynomial expressions that can be nevertheless easily handled with the help of computers.

The question of activity coefficients is of a deeper theoretical importance and difficulty. For the aqueous phase, beside the Debye–Hückel treatment which is limited to ionic strengths below ca. 0.1 M, many theoretical approaches have tried to tackle the question of modeling activity coefficients: SIT (specific interaction theory) (Guillaumont et al., 2003), Pitzer (Pitzer, 1973), MSA (mean spherical approximation) (Simonin et al., 1996), and its recent improvement, BiMSA (binding mean spherical approximation) (Simonin et al., 1998). The first two are empirical approaches which contain a large number of parameters and thus do not allow for any predictions. In the case of SIT, the required so-called interaction parameters are not tabulated for any of the IL cations present in rather large amounts in the equilibrated aqueous phases nor are they tabulated for most of the actinides complexes (Guillaumont et al., 2003). The same remarks hold for Pitzer's method so that these two empirical approaches are of little help for modeling and predictions. By contrast, MSA and BiMSA are analytical mathematical approaches allowing predictions and requiring a very limited number of parameters, to be fitted independently. Unfortunately, this rigorous method is at the cost of intricate transcendental equations, hard to introduce in computer software. For activity coefficients in the organic phase, either a molecular solvent or an IL phase, almost no theoretical approach is available at present. MSA and BiMSA have not been applied to IL phases so far, one of the reasons being the nonspherical nature of most of IL components. Another interesting approach is developed in Condamines et al. (1993) but is valid only for constant ionic strength. This publication presents also a very detailed and interesting discussion on the validity and shortcuts of the slope-analysis method, demonstrating that neglecting activity coefficients may lead to slope values significantly either above or below the

expected integer value, which renders the determination of the exact stoichiometry of the complex rather risky.

For all the above reasons, and especially those pertaining to the question of competitive equilibria that are not taken into account, it would be better, now that computer modeling is widely available, to go beyond the slope-analysis method.

Although far from perfect, a detailed modeling approach has been attempted recently and proved to be very successful (Billard et al., 2011c; Bonnaffé-Moity et al., 2012). It is based on the use of the mass action law, applied to all the equilibria needed to describe extraction: successive complexation reactions between M^{n+} and X^- in the aqueous phase, possible protonation of the ligand (Eq. 13) and the two competitive extraction processes (Eqs. 11 and 12). The solubilization of HX in the IL phase is also taken into account. Some basic assumptions have been made, in order to render the system mathematically tractable (the ligand is supposed to be in excess compared to the metal, for example), and all the activity coefficients have been considered to be equal to unity. Thus, the unique (but major) improvement as compared to the slope-analysis method described above is to be found in the inclusion of all the equilibria, and the last development includes the partial dissociation of HNO_3 (Bonnaffé-Moity et al., 2012). Although this method has been applied to the IX model, it can of course be applied in the same way to the MM hypothesis.

The unknown parameters are the equilibrium constants, and these can be fitted to the D_M values, by use of least square adjustment routines, as a function of either $[HNO_3]_{aq,eq}$ or $[L]_{IL,eq}$ but data about D_M variation as a function of $[Cat^+]_{aq,eq}$ or $[A^-]_{aq,eq}$ can also be included in the fits. Thus, it is a way to determine the values of i and m in Eqs. (11) and (12). However, in order to do so, the concentration values to be included in the fits are the equilibrium ones, which may noticeably differ from the initial ones, especially for HNO_3 (partial dissociation of the acid), A^-, Cat^+, and L, as already explained. These values can be accounted for by precise measurements of all the related quantities. NMR has been used for $[C_1C_4im^+]$ and $[Tf_2N^-]$ determination in aqueous samples (Bell and Ikeda, 2011), while $[H^+]_{aq,eq}$ is routinely measured by titration and ion chromatography can be applied for nitrate determination, for example.

We now want to illustrate, on the basis of two examples, the interest and limitations of the slope-analysis and modeling methods.

The first examples is based on the data of Eu^{3+}/HNO_3//TODGA/$C_1C_2imTf_2N$ (Shimojo et al., 2008). As briefly presented in Section 4.3, the addition of Cat^+ to the aqueous phase induces a decrease in E_{Eu}, and the authors thus proposed a cation exchange mechanism with three Cat^+ back transferred into the aqueous phase for each extracted Eu^{3+}, on the sole basis of the observed decrease. We have to remember that other extraction mechanisms, involving either (one H^+, two Cat^+) or (two H^+, one Cat^+) would also

induce a decrease in E_{Eu}. Let us apply the slope-analysis method to the data displayed in this work, assuming only the general cationic exchange described by Eq. (11). One easily derives

$$\log D_M = -i\log[Cat^+] + (m-i)(\log[\overline{H^+}] - \log[H^+]) + \log K + i\log[\overline{Cat^+}] + p\log[\overline{L}] \quad (24)$$

Thus, plotting $\log D_{Eu}$ versus $\log[Cat^+]$ should give a straight line of slope $-i$. This analysis has not been performed in the work of Shimojo and coworkers, but we took advantage of their graphical display (E_{Eu} vs. $[Cat^+]_{aq,init}$) to obtain the plot according to Eq. (24). The variation is linear, with a slope equal to -1.42, far from the value of three Cat^+ assumed by the authors. Another way to use the slope analysis is to consider D_{Eu} instead of $\log D_{Eu}$ as

$$D_M = \frac{K[\overline{L}]^p[\overline{H^+}]^{m-i}[\overline{Cat^+}]^i}{[H^+]^{m-i}} \frac{1}{[Cat^+]^i} \quad (25)$$

As $[Cat^+]_{IL,eq}$ can reasonably be assumed to be a constant, a plot of D_M as a function of $1/[Cat^+]^i$ should give a straight line only for the exact stoichiometry involved. Such a plot is displayed in Fig. 9. As can be seen, a cubic dependency of $1/[Cat^+]$ is far from linear, while powers of 2 and 1 give rather linear variations. This is of course in line with the value of -1.42 obtained

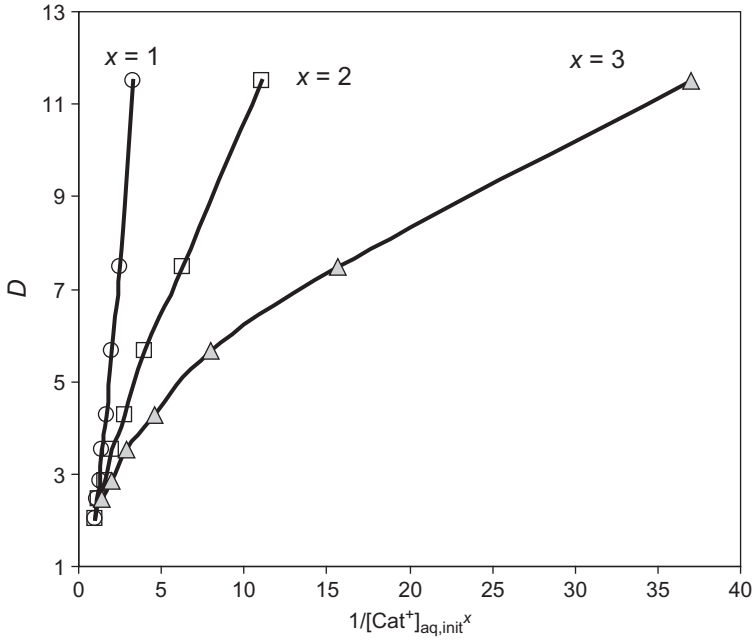

FIGURE 9 Variations of D_{Eu}, as derived from Shimojo et al. (2008), as a function of several reversal powers of $[Cat^+]_{aq,init}$. Solid lines are guide for the eye only.

otherwise. We would therefore conclude that the extraction mechanism in $Eu^{3+}/HNO_3//TODGA/C_1C_4im\ Tf_2N$ involves both Cat^+ and H^+, with possibly two different i values ($i=1$ and 2) of almost identical importance, to account for the noninteger values.

The second example is discussed at length in Billard et al. (2011c) and concerns the use of modeling in $UO_2^{2+}/HNO_3//TBP/C_1C_4im\ Tf_2N$. Fitting the experimental data gives access to the conditional equilibrium constants associated to Eqs. (11) and (12), but another interest of this mathematical treatment is to be found in the predictive abilities of such approaches. By neglecting one or the other of the conditional equilibrium constants of the model, one can have access to the specific contributions of each extraction mechanism to the overall variation in D_U. One can also compare various models, as illustrated in Fig. 10. The variations in D_U have been simulated assuming either extraction of $[UO_2(NO_3)(TBP)_2]^+$, $[UO_2(NO_3)_2(TBP)_2]$, or $[UO_2(NO_3)_3(TBP)_2]^-$. As can be seen, the three models lead to very distinct variations and, on this basis,

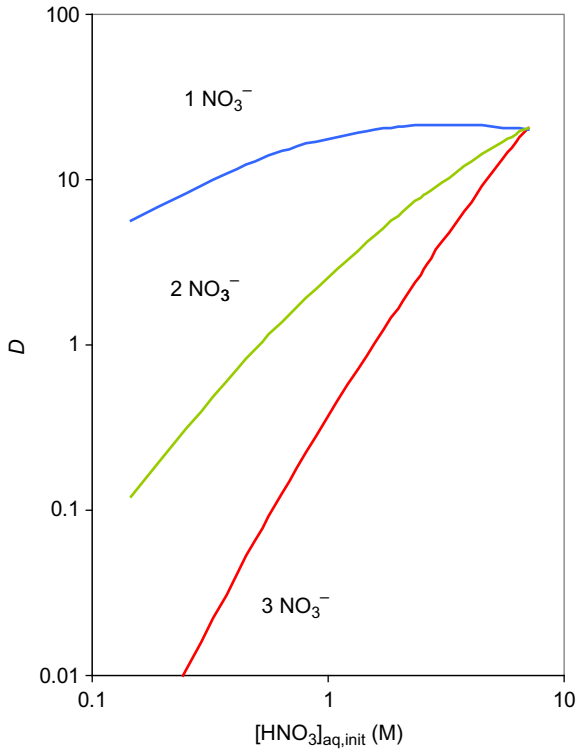

FIGURE 10 Calculated D_M values on the basis of uranyl complexes comprising 1, 2, or 3 nitrate entities redrawn after Billard et al. (2011c).

the only suitable species to allow a simulation of the experimental data appears to be the negatively charged complex.

8.4. Implications for RE/An Recovery and Separation

Soon after the enthusiasm raised by the fantastic distribution ratio obtained by Dai et al. (1999), the cationic exchange mechanism at work in ILs has been rapidly considered as a major drawback for industrial applications of ILs. Obviously, no one is interested in the leaching in the aqueous phase of costly IL cations and anions and some authors repeatedly thus argued against the greenness of ILs (Dietz, 2006; Dietz and Dzielawa, 2001; Jensen et al., 2003) or considered this leaching to be a major limitation for practical applications of ILs in separations (Cocalia et al., 2006). In our opinion, ILs, as replacement solvents, are nevertheless offering extended possibilities for the extraction of RE and An and the difference in extraction mechanisms is not an intrinsic advantage or disadvantage of ILs as compared to molecular solvents, but one may take advantage of such differences in order to solve a precise problem.

In particular, the cationic exchange described by Eq. (11) is quite encouraging, by contrast to what has been first thought. In the case, this cationic exchange proceeds through H^+ alone, as already observed in some systems (Bonnaffé-Moity et al., 2012; Kubota et al., 2011), the loss of IL cations in the aqueous phase as part of the extraction process is no longer a problem. Of course, all investigated ILs so far appear to be partly soluble in the aqueous phase during the pre-equilibration step, but other ILs, that are less soluble, are now synthesized and investigated (Papaiconomou et al., 2007, 2008), while the control of IL aqueous solubility is under study (Gutowski et al., 2003). It would be important to understand why some IL systems exchange preferentially Cat^+, while others favor H^+ exchange. The number of systems studied so far is unfortunately too limited to even derive some trends related to either the IL solvent, the ligand, or the metallic entity.

Whatever the reasons for the H^+ or Cat^+ exchange are, these may take time to be understood and mastered at our will. Efforts toward the suppression of such detrimental effect have been attempted, not all being successful, unfortunately. Under the frame of the MM hypothesis (see Section 8.2), Dietz and coworkers tried to promote ion pairing by modifications of the IL solvents. Using fluorinated ILs did not appear convincing, with ion transfer being the predominant mode of extraction in these solvents, that yielded Sr^{2+} distribution ratios as much as an order of magnitude lower than in the corresponding $C_1C_n imTf_2N$ ILs (Heitzman et al., 2006). The use of a synergistic system $Sr^{2+}/HNO_3//(TBP + DCH18C6)/C_1C_5 imTf_2N$ did not offer better results, with cation exchange being the dominating process over the range of 10–90% (v/v) TBP (as a synergistic agent to DCH18C6) (Stepinski et al., 2005). These negative results might be an indication that ion pairing is not

a usual process in ILs. Another interesting idea is the use of sacrificial ions, dissolved in the IL phase, and intended to preferentially exchange with the metallic entity instead of the IL constituents. In this frame, the goal is not to avoid ion exchange but to take advantage of it to control exchanged ions. This has been investigated in Cs^+/HNO_3//calixarene/$C_1C_4imTf_2N$, using sodium tetraphenylborate, dissolved in the IL, as a sacrificial agent (Luo et al., 2004). The authors showed that part of the cationic exchange does occur through the back transfer of Na^+ instead of Cat^+, reducing the solubilization of Cat^+ by 24%. This is far from perfect, but the idea is worth mentioning. Note that a cation exchange occurring through the sole exchange of H^+ is the most elegant process involving a sacrificial agent, as H^+ arises from the acidic aqueous phase and is thus back transferred to it. In this case, H^+, which is mandatory to prevent metal hydrolysis, also plays the role of the sacrificial ion, with no need to specifically dissolve it in the IL phase because it naturally dissolves in it.

9. CONCLUSION

ILs are so numerous and appear to be of such a wide interest in all fields of chemistry and material science that one could wonder why they were not discovered and studied before. From the examples discussed in this review, we hope to have shown that ILs provide so many distinctive features that they should be considered as being more than solvents, more than solutes, and more than additives. Although their definition is rather vague, their properties are unique. ILs push usual ways of thinking to their limits, as in the case of M^{m+}/HX//IL, a situation merely envisioned for molecular solvents.

From a fundamental point of view, it would be desirable to be able to decide between IX and MM models, or to prove that both ideas can prevail, depending on the system. As has been shown, spectroscopic studies may provide answers to that question and there is no doubt that this problem will be solved in the future. Other fundamental advances in the field of extraction by use of ILs will benefit future studies hopefully filling the gap of thermodynamic investigations, at present very scarce (Kobrak, 2008; Yoon et al., 2010).

In the near future, we expect extraction studies with the help of ILs to develop. Studies of M^{m+}/HX//L/IL systems will grow in number, but it is our hope that pragmatic studies, contenting themselves to the measurements of (possibly high) extraction ratios, will be replaced by mechanistic (and kinetic) studies of more fundamental interest. It is our opinion that the most fascinating studies and results will come from M^{m+}/HX//IL and M^{m+}/HX//(L + IL)/Org systems. Other fascinating results may also arise from triphasic systems, as recently illustrated (Takata and Hirayama, 2009).

In view of nuclear applications of ILs for the extraction and separation of metal ions, we think there is little hope that UO_2^{2+}/HNO_3//L/IL systems will

be largely used as replacement of $UO_2^{2+}/HNO_3//TBP/dodecane$, most probably because of cost and viscosity concerns, unless breakthroughs could be found on the latter problem. Nevertheless, ILs, in any of their uses (solvents, pure phases, new ligands, or additives), will certainly find various niches for the recovery of valuable metals from very specific contaminated samples. In this respect, the recent increase of studies involving ILs in view of determining natural or accidental levels of radionuclides (Jie et al., 2008; Srncik et al., 2009) (see also the general discussion in Heitzman et al., 2006) is an indication of future IL potential in the medium term. In the far future, one may reasonably envision using edible ILs in view of decorporation of contaminated human beings. Toward this end, the synthesis of aspirin-IL is an interesting beginning (Bica et al., 2010).

ACKNOWLEDGMENTS

The author is indebted to Prof. Y. Ikeda and Dr. T. Bell for sharing their experimental data prior to the publication of this review.

LIST OF ABBREVIATIONS

An	actinide
BiMSA	binding mean spherical approximation
BTBP	2,2′-bis(triazinyl-6,6′-bipyridine)
BTP	2,6-bis(triazinyl pyridine)
CMPO	octyl(phenyl)-*N*,*N*-diisobutylcarbamoylmethyl(phosphine oxide)
D_M	distribution ratio of a species M
DEHPA	di-(2-ethylhexyl)phosphoric acid
DCH18C6	dicyclohexano-18-crown-6 ether
DODGAA	*N*,*N*-dioctyldiglycol amic acid
E_M	extraction efficiency of a species M
EU	European Union
EXAFS	extended X-ray fine structure spectroscopy
HOPO	2-hydroxypyridine-*N*-oxide
HTTA	2-thenoyltrifluoroacetone
ICP-AES	inductively coupled plasma atomic emission spectroscopy
ICP-MS	inductively coupled plasma mass spectrometry
IL	ionic liquid
IX	ion-exchange mechanism
Ln	lanthanoid or lanthanide
MM	mixed mechanism
MSA	mean spherical approximation
PUREX	plutonium–uranium refinement extraction
QSPR	quantitative structure–property relationship

RE	rare earth
REACH	registration, evaluation, authorization, and restriction of chemical substances
RTIL	room-temperature ionic liquid
SF	separation factor
SIT	specific interaction theory
TBP	tributylphosphate
TfO^-	triflate (trifluoromethanesulfonate)
Tf_2N^-	bis(trifluoromethanesulfonyl)amide
TODGA	tetraoctyldiglycolamide
TPH	hydrogenated tetrapropylene
TSIL	task-specific ionic liquid

REFERENCES

Abu-Khader, M.M., 2009. Prog. Nucl. Energy 51, 225.

Aneheim, E., Ekberg, C., Fermvik, A., Foreman, M.R.S., Retegan, T., Skarnemark, G., 2010. Solv. Extr. Ion Exchange 28, 437.

Atanassova, M., 2009. Solv. Extr. Ion Exchange 27, 159.

Atanassova, M., Dukov, I., 2010. Sep. Purif. Technol. 74, 300.

Barré, B., 1998. J. Alloys Compd. 271/273, 1.

Bell, T.J., Ikeda, Y., 2011. Dalton Trans. 40, 10125.

Bell, J.R., Luo, H., Dai, S., 2011. Tetrahedron Lett. 52, 3723.

Berthon, L., Nikitenko, S.I., Bisel, I., Berthon, C., Faucon, M., Saucerotte, B., Zorz, N., Moisy, P., 2006. Dalton Trans. 2526.

Bhargava, B.L., Klein, M.L., 2011. J. Phys. Chem. B 115, 10439.

Bica, K., Rijksen, C., Nieuwenhuyzen, M., Rodgers, R.D., 2010. Phys. Chem. Chem. Phys. 12, 2011.

Billard, I., 2003. Lanthanide and actinide solution chemistry studied by time-resolved emission spectroscopy. In: Gschneidner Jr., K.A., Bünzli, J.-C.G., Pecharsky, V. (Eds.), Handbook on the Physics and Chemistry of Rare Earths, vol. 33. Elsevier Science, Amsterdam, pp. 465–514 (Chapter 216).

Billard, I., Gaillard, C., 2009. Radiochim. Acta 97, 355.

Billard, I., Marcou, G., Ouadi, A., Varnek, A., 2011a. J. Phys. Chem. B 93, 115.

Billard, I., Ouadi, A., Gaillard, C., 2011b. Anal. Bioanal. Chem. 400, 1555.

Billard, I., Ouadi, A., Jobin, E., Champion, J., Gaillard, C., Georg, S., 2011c. Solv. Extr. Ion Exchange 29, 577.

Binnemans, K., 2007. Chem. Rev. 107, 2592.

Bonnaffé-Moity, M., Ouadi, A., Mazan, V., Miroshnichenko, S., Ternova, D., Georg, S., Sypula, M., Gaillard, C., Billard I., 2012. Dalton Trans. 41, 7526.

Bossé, E., Berthon, L., Zorz, N., Monget, J., Berthon, C., Bisel, I., Legand, S., Moisy, P., 2008. Dalton Trans. 924.

Cammarata, L., Kazarian, S.G., Salter, P.A., Welton, T., 2001. Phys. Chem. Chem. Phys. 3, 5192.

Canongia Lopes, J.N., Padua, A.A.H., 2006. J. Phys. Chem. B 110, 3330.

Carmichael, A.J., Hardacre, C., Holbrey, J.D., Nieuwenhuyzen, M., Seddon, K.R., 1999. Anal. Chem. 71, 4572.

Chaumont, A., Wipff, G., 2007. J. Mol. Liquids 131/132, 36.

Chaumont, A., Klimchuk, O., Gaillard, C., Billard, I., Ouadi, A., Hennig, C., Wipff, G., 2012. J. Phys. Chem. B 116, 3205.
Chiappe, C., 2007. Monatsh. Chem. 138, 1035.
Choppin, G., 2006. Sep. Sci. Technol. 41, 1955.
Cocalia, V.A., Jensen, M.P., Holbrey, J.D., Spear, S.K., Stepinski, D.C., Rogers, R.D., 2005. Dalton Trans. 1966.
Cocalia, V.A., Holbrey, J.D., Gutowski, K.E., Bridges, N.J., Rogers, R.D., 2006. Tsinghua Sci. Technol. 11, 188.
Condamines, N., Turq, P., Musikas, C., 1993. Solv. Extr. Ion Exchange 11, 187.
Dai, S., Ju, Y.H., Barnes, C.E., 1999. J. Chem. Soc. Dalton Trans. 1201.
Davis, J.H., 2004. Chem. Lett. 33, 1072.
Del Sesto, R.E., McCleskey, T.M., Burrell, A.K., Baker, G.A., Thompson, J.D., Scott, B.L., Wilkes, J.S., Williams, P., 2008. Chem. Commun. 447.
Dietz, M.L., 2006. Sep. Sci. Technol. 41, 2047.
Dietz, M.L., Dzielawa, J.A., 2001. Chem. Commun. 2124.
Dietz, M.L., Stepinski, D.C., 2005. Green Chem. 7, 747.
Dietz, M.L., Stepinski, D.C., 2008. Talanta 75, 598.
Dietz, M.L., Dzielawa, J.A., Laszak, I., Young, B.A., Jensen, M.P., 2003. Green Chem. 5, 682.
Dietz, M.L., Jakab, S., Yamato, K., Bartsch, R.A., 2008. Green Chem. 10, 174.
Dileep, C.S., Jagasia, P., Dhami, P.S., Achuthan, P.V., Dakshinamoorthy, A., Tomar, B.S., Munshi, S.K., Dey, P.K., 2008. Desalination 232, 157.
Dzyuba, S., Bartsch, R.A., 2002. Chemphyschem 3, 161.
Dzyuba, S.V., Bartsch, R.A., 2003. Angew. Chem. Int. Ed. Engl. 42, 148.
Freire, M.G., Santos, L.M.N.B.F., Fernandes, A.M., Coutinho, J.A.P., Marrucho, I.M., 2007. Fluid Phase Equilib. 261, 449.
Freire, M.G., Carvalho, P.J., Silva, A.M.S., Santos, L.M.N.B.F., Rebelo, L.P.N., Marrucho, I.M., Coutinho, J.A.P., 2009. J. Phys. Chem. B 113, 202.
Gaillard, C., El Azzi, A., Billard, I., Bolvin, H., Hennig, C., 2005a. Inorg. Chem. 44, 852.
Gaillard, C., Billard, I., Chaumont, A., Mekki, S., Ouadi, A., Denecke, M., Moutiers, G., Wipff, G., 2005b. Inorg. Chem. 44, 8355.
Gaillard, C., Mazan, V., Georg, S., Klimchuk, O., Sypula, M., Billard, I., Schurhammer, R., Wipff, G., 2012. Phys. Chem. Chem. Phys. 14, 5187.
Gathergood, N., Scammells, P.J., Garcia, M.T., 2006. Green Chem. 8, 156.
Geist, A., Weigl, M., Gompper, K., 2002. Sep. Sci. Technol. 37, 3369.
Geist, A., Hill, C., Modolo, G., Foreman, M.R.S., Gompper, K., Weigl, M., Hudson, M.J., Madic, C., 2006. Solv. Extr. Ion Exchange 24, 463.
Georg, S., Billard, I., Ouadi, A., Gaillard, C., Petitjean, L., Picquet, M., Solov'ev, V., 2010. J. Phys. Chem. B 114, 4276.
Gerhard, D., Alpaslan, S.C., Gores, H.J., Uerdingen, M., Wasserscheid, P., 2005. Chem. Commun. 5080.
Giernoth, R., 2010. Angew. Chem. Int. Ed. Engl. 49, 2834.
Giridhar, P., Venkatesan, K.A., Srinivasan, T.G., Vasudeva Rao, P.R., 2004a. J. Nucl. Radiochem. Sci. 5, 21.
Giridhar, P., Venkatesan, K.A., Srinivasan, K.V., Vasudeva Rao, P.R., 2004b. J. Nucl. Radiochem. Sci. 5, 17.
Giridhar, P., Venkatesan, K., Subramaniam, S., Srinivasan, T.G., Vasudeva Rao, P.R., 2008. J. Alloys Compd. 448, 104.
Gschneidner, K.A., 2011a. Mater. Matters 6, 32.

Gschneidner, K.A., 2011b. Magn. Bus. Technol. 6–8, Spring.
Guillaumont, R., Fanghanel, T., Fuger, J., Grenthe, I., Neck, V., Palmer, D.A., Rand, M.H., 2003. Update on the Chemical Thermodynamics of Uranium, Neptunium, Plutonium, Americium and Technetium. Elsevier, Amsterdam.
Gutowski, K.E., Broker, G.A., Willauer, H.D., Huddleston, J.G., Swatloski, R.P., Holbrey, J.D., Rogers, R.D., 2003. J. Am. Chem. Soc. 125, 6632.
Harmon, C., Smith, W., Costa, D., 2001. Radiat. Phys. Chem. 60, 157.
Hawkins, C.A., Garvey, S.L., Dietz, M., 2012. Sep. Purif. Technol. 89, 31.
Heitzman, H., Young, B.A., Rausch, D.J., Rickert, P., Stepinski, D.C., Dietz, M.L., 2006. Talanta 69, 527.
Henley, E.J., Seader, J.D., Roper, D.K., 2011. Separation Process Principles. John Wiley, Hoboken, NJ.
Huang, W., Chen, S., Liu, Y., Fu, H., Wu, G., 2011. Radiat. Phys. Chem. 80, 573.
Huddleston, J.G., Visser, A.E., Reichert, W.M., Willauer, H., Broker, G., Rogers, R.D., 2001. Green Chem. 3, 156.
Ikeda, A., Hennig, C., Rossberg, A., Tsushima, S., Scheinost, A.C., Bernhard, G., 2008. Anal. Chem. 80, 1102.
Ito, K., Nuishina, N., Ohno, H., 2000. Electrochim. Acta 45, 1295.
Izgorodina, E.I., 2011. Phys. Chem. Chem. Phys. 13, 4189.
Jacquemin, J., Husson, P., Padua, A.A.H., Majer, V., 2006. Green Chem. 8, 172.
Jensen, M.P., Dzielawa, J.A., Rickert, P., Dietz, M.L., 2002. J. Am. Chem. Soc. 124, 10664.
Jensen, M.P., Neuefeind, J., Beitz, J.V., Skanthakumar, S., Soderholm, L., 2003. J. Am. Chem. Soc. 125, 15466.
Jeon, Y., Sung, J., Seo, C., Lim, H., Cheong, H., Kang, M., Moon, B., Ouchi, Y., Kim, D., 2008. J. Phys. Chem. B 112, 4735.
Jiang, W., Wang, Y., Voth, G.A., 2007. J. Phys. Chem. B 111, 4812.
Jie, C., Zaijun, L., Ming, L., 2008. Int. J. Environ. Anal. Chem. 583–590, 88.
Katritzky, A.R., Jain, R., Lomaka, A., Petrukhin, R., Karelson, M., Visser, A.E., Rogers, R.D., 2002. J. Chem. Inf. Comput. Sci. 42, 225.
Keskin, S., Kayrac-Talay, D., Akman, U., Hortaçsu, O., 2007. J. Supercrit. Fluids 43, 150.
Kobrak, M.N., 2008. Solv. Extr. Ion Exchange 26, 735.
Kogelnig, D., Stojanovic, A., Galanski, M., Groessl, M., Jirsa, F., Krachler, R., Keppler, B.K., 2008. Tetrahedron Lett. 49, 2782.
Kozonoi, N., Ikeda, Y., 2007. Monatsh. Chem. 138, 1145.
Kubota, F., Shimobori, Y., Baba, Y., Koyanagi, Y., Shimojo, K., Kamiya, N., Goto, M., 2011. J. Chem. Eng. Jpn. 44, 307.
Law, G., Watson, P.R., 2001. Langmuir 17, 6138.
Le Rouzo, G., Lamouroux, C., Dauvois, V., Dannoux, A., Legand, S., Durand, D., Moisy, P., Moutiers, G., 2009. Dalton Trans. 6175–6184.
Liu, X., Liang, J., Xu, J., 2004. Solv. Extr. Ion Exchange 22, 163.
Lohithakshan, K.V., Aggarwal, S.K., 2008. Radiochim. Acta 96, 93.
Luo, H., Dai, S., Bonnesen, P.V., Buchanan, A.C., Holbrey, J.D., Bridges, N.J., Rogers, R.D., 2004. Anal. Chem. 76, 3078.
Luo, H., Dai, S., Bonnesen, P.V., Buchanan, A.C., 2006. J. Alloys Compd. 418, 195.
Magnusson, D., Christiansen, B., Foreman, M.R.S., Geist, A., Glatz, J.P., Malmbeck, R., Modolo, G., Serrano-Purroy, D., Sorel, C., 2009. Solv. Extr. Ion Exchange 27, 97.
McEwen, A.B., Ngo, H.L., LeCompte, K., Goldman, J.L., 1999. J. Electrochem. Soc. 146, 1687.

Mehdi, H., Binnemans, K., Van Hecke, K., Van Meervelt, L., Nockemann, P., 2010. Chem. Commun. 46, 234.
Mekki, S., Wai, C.M., Billard, I., Moutiers, G., Yen, C.H., Wang, J.S., Ouadi, A., Gaillard, C., Hesemann, P., 2005. Green Chem. 7, 421.
Mekki, S., Wai, C.M., Billard, I., Moutiers, G., Burt, J., Yen, C.H., Wang, J.S., Gaillard, C., Ouadi, A., Hesemann, P., 2006. Chem. Eur. J. 12, 1760.
Mikkola, J.P., Virtanen, P., Sjöholm, R., 2006. Green Chem. 8, 250.
Mincher, B.J., Modolo, G., Mezyk, S.P., 2009. Solv. Extr. Ion Exchange 27, 331.
Mincher, B.J., Modolo, G., Mezyk, S.P., 2010. Solv. Extr. Ion Exchange 28, 415.
Miroshnichenko, S., Ternova, D., Billard, I., Ouadi, A., Klimchuk, O., Kalchenko, V., 2011. Phosphorus Sulfur Silicon Relat. Elem. 186, 903.
Mitchell, J.A., Counce, R.M., Watson, J.S., Spencer, B.B., Del Cul, G.D., 2009. Nucl. Technol. 165, 360.
Modolo, G., Vijgen, H., Serrano-Purroy, D., Christiansen, B., Malmbeck, R., Sorel, C., Baron, P., 2007. Sep. Sci. Technol. 42, 439.
Mudring, A.V., Tang, S., 2010. Eur. J. Inorg. Chem. 2569.
Murali, M.S., Bonville, N., Choppin, G.R., 2010. Solv. Extr. Ion Exchange 28, 495.
Myasoedova, G., Molochnikova, N.P., Mokhodoeva, O.B., Myasoedov, B., 2008. Anal. Sci. 24, 1351.
Nakashima, K., Kubota, F., Maruyama, T., Goto, M., 2005. Ind. Eng. Chem. Res. 44, 4368.
Ngo, H.L., LeCompte, K., Hargens, L., McEwen, A.B., 2000. Thermochim. Acta 357/358, 97.
Nikitenko, S., Moisy, P., 2006. Inorg. Chem. 45, 1235.
Nikitenko, S., Berthon, C., Moisy, P., 2007. C. R. Chim. 10, 1122.
Nilsson, M., Nash, K., 2007. Solv. Extr. Ion Exchange 25, 665.
Nockemann, P., Thijs, B., Lunstroot, K., Parac-Vogt, T., Görller-Walrand, C., Binnemans, K., Van Hecke, K., Van Meervelt, L., Nikitenko, S., Daniels, J., Hennig, C., Van Deun, R., 2009. Chem. Eur. J. 15, 1449.
Odinets, I.L., Sharova, E.V., Artyshin, O.I., Lyssenko, K.A., Nelyubina, Y.V., Myasoedova, G.V., Molochnikova, N.P., Zakharchenro, E.A., 2010. Dalton Trans. 39, 4170.
Ohno, H., 2005. Electrochemical Aspects of Ionic Liquids. Wiley, Hoboken, NJ.
Olivier, J.H., Camerel, F., Selb, J., Retailleau, P., Ziessel, R., 2009. Chem. Commun. 1133.
Olivier, J.H., Camerel, F., Ziessel, R., 2011. Chem. Eur. J. 17, 9113.
Ouadi, A., Gadenne, B., Hesemann, P., Moreau, J.J.E., Billard, I., Gaillard, C., Mekki, S., Moutiers, G., 2006. Chem. Eur. J. 12, 3074.
Ouadi, A., Klimchuk, O., Gaillard, C., Billard, I., 2007. Green Chem. 9, 1160.
Papaiconomou, N., Salminen, J., Lee, J.M., Prausnitz, J.M., 2007. J. Chem. Eng. Data 52, 833.
Papaiconomou, N., Lee, J.M., Salminen, J., von Stosch, M., Prausnitz, J.M., 2008. Ind. Eng. Chem. Res. 47, 5080.
Papaiconomou, N., Estager, J., Traore, Y., Bauduin, P., Bas, C., Legeai, S., Viboud, S., Draye, M., 2010. J. Chem. Eng. Data 55, 1971.
Pitzer, K.S., 1973. J. Phys. Chem. 77, 268.
Plechkova, N., Seddon, K.R., 2008. Chem. Soc. Rev. 37, 123.
Quasch, D.L., Wai, C.M., Pasilis, S.P., 2010. Inorg. Chem. 49, 8568.
Rao, P.R.V., Kolarik, Z., 1996. Solv. Extr. Ion Exchange 14, 955.
Rodgers, R.D., Seddon, K., 2003. Science 302, 792.
Rout, A., Venkatesan, K.A., Srinivasan, T.G., Vasudeva Rao, P.R., 2009. Radiochim. Acta 97, 719.
Rout, A., Venkatesan, K., Srinivasan, T.G., Vasudeva Rao, P.R., 2010. Radiochim. Acta 98, 459.

Rout, A., Venkatesan, K.A., Srinivasan, T.G., Vasudeva Rao, P.R., 2011a. Sep. Purif. Technol. 76, 238.
Rout, A., Venkatesan, K.A., Srinivasan, T.G., Vasudeva Rao, P.R., 2011b. Solv. Extr. Ion Exchange 29, 602.
Rout, A.,Venkatesan, K.A., Srinivasan, T.G., 2012. Sep. Purif. Technol. 97, 164.
Ruas, A., Pochon, P., Simonin, J.P., Moisy, P., 2010. Dalton Trans. 39, 10148.
Scammells, P.J., Scott, J.L., Singer, R.D., 2005. Aust. J. Chem. 58, 155.
Schulz, W.W., Horwitz, E.P., 1988. Sep. Sci. Technol. 23, 1191.
Shen, Y., Tan, X., Wang, L., Wu, W., 2011a. Sep. Purif. Technol. 78, 298.
Shen, Y., Wang, S., Zhu, L., Wang, J., Wu, W., 2011b. Ind. Eng. Chem. Res. 50, 13990.
Shigeto, S., Hamaguchi, H., 2006. Chem. Phys. Lett. 427, 329.
Shimojo, K., Kurahashi, K., Naganawa, H., 2008. Dalton Trans. 37, 5083.
Shkrob, I.A., Marin, T.W., Chemerisov, S.D., Hatcher, J.L., Wishart, J.F., 2011a. J. Phys. Chem. B 115, 3889.
Shkrob, I.A., Marin, T.W., Chemerisov, S.D., Wishart, J.F., 2011b. J. Phys. Chem. B 115, 10927.
Shkrob, I.A., Marin, T.W., Chemerisov, S.D., Wishart, J.F., 2011c. J. Phys. Chem. B 115, 3872.
Shkrob, I.A., Marin, T.W., Dietz, M., 2011d. J. Phys. Chem. B 115, 3903.
Simonin, J.P., Blum, L., Turq, P., 1996. J. Phys. Chem. 100, 7704.
Simonin, J.P., Bernard, O., Blum, L., 1998. J. Phys. Chem. B 102, 4411.
Singh, R.P., Verma, R.D., Meshri, D.T., Shreeve, J.M., 2006. Angew. Chem. Int. Ed. Engl. 45, 3584.
Smiglak, M., Reichert, W.M., Holbrey, J.D., Wilkes, J.S., Sun, L., Thrasher, J.S., Kirichenko, K., Singh, S., Katritsky, A.R., Rogers, R.D., 2006. Chem. Commun. 2554.
Srncik, M., Kogelnig, D., Stojanovic, A., Korner, W., Krachler, R., Wallner, G., 2009. Appl. Radiat. Isotopes 67, 2146.
Stepinski, D.C., Jensen, M.P., Dzielawa, J.A., Dietz, M.L., 2005. Green Chem. 7, 151.
Stepinski, D.C., Vandegrift, G.F., Shkrob, I.A., Wishart, J.F., Kerr, K., Dietz, M., Qadah, D.T.D., Garvey, S.L., 2010. Ind. Eng. Chem. Res. 49, 5863.
Stumpf, S., Billard, I., Panak, P.J., Mekki, S., 2007. Dalton Trans. 240.
Stumpf, S., Billard, I., Gaillard, C., Panak, P., Dardenne, K., 2008. Radiochim. Acta 96, 1.
Sun, J., Forsyth, M., MacFarlane, D.R., 1998. J. Phys. Chem. B 102, 8858.
Sun, X., Wu, D., Chen, J., Li, D., 2007. J. Chem. Technol. Biotechnol. 82, 267.
Sun, X., Ji, Y., Chen, J., Ma, J., 2009. J. Rare Earths 27, 932.
Sun, X., Ji, Y., Hu, F., He, B., Chen, J., Li, D., 2010. Talanta 81, 1877.
Takata, T., Hirayama, N., 2009. Anal. Sci. 25, 1269.
Tindale, J.J., Hartlen, K.D., Alizadeh, A., Workentin, M.S., Ragogna, P.J., 2010. Chem. Eur. J. 16, 9068.
Tokuda, H., Tsuzuki, S., Susan, A.B.H., Hayamizu, K., Watanabe, M., 2006. J. Phys. Chem. B 110, 19593.
Tomé, L.I.N., Varanda, F.R., Freire, M.G., Marrucho, I.M., Coutinho, J.A.P., 2009. J. Phys. Chem. B 113, 2815.
Turanov, A.N., Karandashev, V.K., Baulin, V.E., 2008a. Solv. Extr. Ion Exchange 26, 77.
Turanov, A.N., Karandashev, V.K., Baulin, V.E., 2008b. Russ. J. Inorg. Chem. 53, 970.
Turanov, A.N., Karandashev, V.K., Baulin, V.E., 2008c. Radiochemistry 50, 266.
Turanov, A.N., Karandashev, V.K., Baulin, V.E., 2010. Solv. Extr. Ion Exchange 28, 367.
Varnek, A., Kireeva, N., Tetko, I.V., Baskin, I.I., Solov'ev, V.P., 2007. J. Chem. Inf. Model. 47, 1111.

Visser, A.E., Swatloski, R.P., Reichert, W.M., Mayton, R., Sheff, S., Wierzbicki, A., Davis, J.H., Rogers, R.D., 2001. Chem. Commun. 135.
Visser, A.E., Swatloski, R.P., Reichert, W.M., Mayton, R., Sheff, S., Wierzbicki, A., Davis, J.H., Rogers, R.D., 2002. Environ. Sci. Technol. 36, 2523.
Visser, A.E., Jensen, M.P., Laszak, I., Nash, K.L., Choppin, G.R., Rogers, R.D., 2003. Inorg. Chem. 42, 2197.
Wasserscheid, P., 2006. Nature 439, 797.
Wasserscheid, P., Welton, T., 2008. Ionic Liquids in Synthesis. Wiley-VCH, Weinheim.
Wilkes, J.S., 2002. Green Chem. 4, 73.
Wood, N., Stephens, G., 2010. Phys. Chem. Chem. Phys. 12, 1670.
Yoon, S.J., Lee, J.G., Tajima, H., Yamasaki, A., Kiyono, F., Nakazato, T., Tao, H., 2010. J. Ind. Eng. Chem. 16, 350.
Yoshida, Y., Saito, G., 2010. Phys. Chem. Chem. Phys. 12, 1675.
Yuan, L., Peng, J., Xu, L., Zhai, M., Li, J., Wei, G., 2008. Dalton Trans. 6358.
Yuan, L., Xu, C., Peng, J., Xu, L., Zhai, M., Li, J., Wei, G., Shen, X., 2009. Dalton Trans. 7873.
Zhao, D., Fei, Z., Ohlin, C.A., Laurenczy, G., Dyson, P.J., 2004. Chem. Commun. 2500.
Zuo, Y., Liu, Y., Chen, J., Li, D.Q., 2008. Ind. Eng. Chem. Res. 47, 2349.

Intentionally left as blank

Chapter 257

Structural Properties of Lanthanides at Ultra High Pressure

Gopi K. Samudrala and Yogesh K. Vohra
Department of Physics, College of Arts and Sciences, University of Alabama at Birmingham (UAB), Birmingham, Alabama, USA

Chapter Outline

1. INTRODUCTION

The nature of the 4f electrons in lanthanides and their compounds may be broadly characterized as being either "localized" or "itinerant" and is held responsible for a wide range of physical and chemical properties of both the elements and compounds. The localized states are marked by tightly bound shells or narrow bands of highly correlated electrons near the Fermi level and are observed at ambient conditions for all of the lanthanide elements. The pressure variable has a dramatic effect on the electronic structure of lanthanides, which in turn, drives a sequence of structural phase transitions under pressure. A very important manifestation of this change is the pressure-induced *s* to *d* electron transfer that is known to give rise to the

Handbook on the Physics and Chemistry of Rare Earths, Vol. 43.
http://dx.doi.org/10.1016/B978-0-444-59536-2.00004-0

well-known lanthanide crystal structure sequence. At extreme compressions, 4f shell is expected to delocalize and participate in bonding, and hence, influence crystal structures. Over the past few years, modern diamond anvil cell techniques coupled with the synchrotron sources and advanced structural refinement techniques have led to the identification of new crystalline phases of the rare-earth metals at pressures in excess of 200 GPa and documenting reduction in volume of 70% (volume compression $V/V_0 = 0.3$).

In this chapter, we focus on the structural studies of lanthanides carried out under high static pressure over the past decade. The block of lanthanides in the periodic table consists of the elements lanthanum ($z = 57$) through lutetium ($z = 71$). Progressive filling of 4f shell is observed from Ce to Lu. It is the filling of these 4f electrons that gives rise to the interesting material properties for lanthanides. Barring the divalent europium and ytterbium metals (classified as irregular members of lanthanides for this reason), all other lanthanide metals are trivalent (we note that elemental cerium at ambient conditions adopts intermediate valence state that only slightly exceeds 3+, and therefore, can also be classified as a regular lanthanide). With decreasing atomic number or under the application of pressure, the regular trivalent lanthanides show the structural sequence $hcp \rightarrow Sm\text{-}type \rightarrow dhcp \rightarrow fcc$. This sequence has been seen under application of modest pressure (Jayaraman, 1964) and it was initially thought that face-centered cubic (*fcc*) is the ultimate high pressure phase for all lanthanides. However, it was later shown that distortions occur in the *fcc* phase upon further compression and if still more pressure is applied, low symmetry structures are observed in these regular trivalent lanthanides with unfilled f shell. It is not prudent to discuss the structural transitions of all lanthanides together. Instead, high-pressure structural transitions of individual lanthanides are discussed.

Whereas Ce through Lu are characterized by filling of 4f shell, actinide elements thorium to lawrencium are characterized by filling of 5f shells. The major difference in bonding behavior in the solid state between these two series of elements is that 5f elements have delocalized f electrons whereas 4f electrons are localized in lanthanides and do not readily participate in bonding. This is where pressure plays an important role at room temperature. High pressure can delocalize the 4f shell and it can cause electron transfer between various subbands in the conduction electrons such as $sp \rightarrow d$ and $spd \rightarrow f$. Participation of f electrons in bonding is accompanied by a volume collapse in various lanthanides.

2. LANTHANUM

Lanthanum (La) is the first element of the lanthanide series. Like other light lanthanide elements, La crystallizes in the double hexagonal close-packed (*dhcp*) phase at ambient conditions. Crystal structure studies under high pressure on La show that it follows the "regular" trivalent lanthanide structure

sequence *dhcp* → *fcc* → *dfcc*. When the light lanthanides such as cerium and praseodymium were compressed to higher pressures, additional low symmetry structure has been seen in these elements, and it was thought that these low symmetry structures result from the participation of f electrons in bonding (Wittig, 1980). Lanthanum, however, does not have any electrons in the 4f shell. Theoretical studies by Herbst (1992) suggested that, around 1100 GPa, some electron occupancy in the 4f band of La, can be expected.

The initial *dhcp* to *fcc* transition in La is around 2.5 GPa, and a second transition to a distorted fcc (*dfcc*) phase occurs around 7 GPa (Grosshans et al., 1982). It was also noted that the intensity of superlattice reflections of *dfcc* phase increased continuously with increasing pressure. In a study of La by Porsch and Holzapfel (1993), it was shown that these superstructure reflections disappear and the diffraction pattern of the undistorted *fcc* structure is seen again above 60 GPa (Fig. 1). The effect was experimentally reproduced by these authors and they conclude this not to be a texturing effect. Band structure calculations by Pickett et al. (1980) and McMahan et al. (1981) show that for the *fcc* La, up to four Lifshitz singularities are passed when lanthanum is compressed to V/V_0 of 0.5. The authors speculate that the structural instability of *fcc* lanthanum could be related to these singularities where the Fermi surface topology changes.

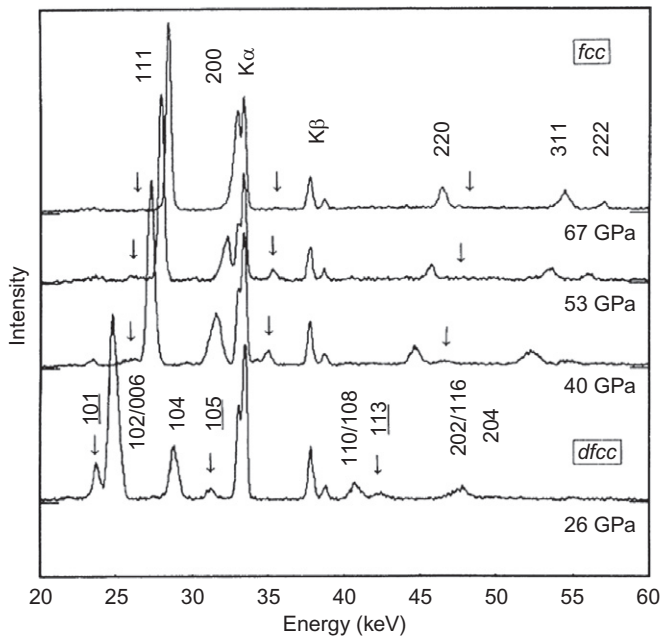

FIGURE 1 EDXD spectra of La under pressure. Arrows indicate the positions of superstructure reflections (Porsch and Holzapfel, 1993).

3. CERIUM

Cerium (Ce) with a single electron in the 4f shell [Xe] $6s^2 5d^1 4f^1$ is a classic example of the element that shows electronic transitions that can be induced by pressure and/or temperature. The crystallographic changes and the electronic phenomena associated with this transition have been the focus of intense experimental and theoretical research. Cerium is unique in the 4f element series because of the proximity of the f shell to the Fermi energy and related phase transformations induced by pressure. Ce crystallizes in the *fcc* lattice (γ phase) at ambient pressure and temperature. The single 4f electron in Ce is localized at ambient conditions and does not participate in bonding.

The isostructural volume collapse transition ($\gamma \rightarrow \alpha$) occurs at 0.7 GPa at ambient temperature with a volume discontinuity of about 16%. This volume collapse transition is associated with a change in the f-electron character from a localized shell to an electronic state strongly hybridizing with the conduction band. In the Mott transition model given by Johansson (1974), the ($\gamma \rightarrow \alpha$) transition is interpreted as a transition from a state with localized nonbonding 4f electrons to a state with delocalized 4f electrons that participate in solid state bonding. Alternatively, in the Kondo volume collapse model, Allen and Martin (1982), the transition is merely viewed as a transition from essentially unscreened localized moments to a phase consisting of screened moments.

Above 10 GPa, 4f electrons are expected to participate in bonding in Ce and crystal structures characteristic of 4f bonding are expected. Endo et al. (1977) showed that Ce transforms to a body-centered tetragonal (*bct*) structure at a pressure of 13 GPa. Cerium has since been studied at different pressure ranges to observe the stability of its phases by Olsen et al. (1985), McMahon and Nelmes (1997), and eventually to 208 GPa by Vohra et al. (1999). Similarities between structures of the lanthanides and actinides under pressure have always been a very important driving point in studying these elements at high pressures. In that regard, it is important to mention that the light actinide metal thorium has been shown to transform from an *fcc* phase to a *bct* phase at 60 GPa, and the *bct* phase is known to be stable even at ultrahigh pressure of 300 GPa (Vohra and Akella, 1991). A detailed discussion of the complicated crystallographic phases like face-centered monoclinic and orthorhombic α-uranium phases that are known to exist between 5 and 13 GPa could be found in McMahon and Nelmes (1997). The theoretical investigations of the high-pressure crystal structures of Ce and Th at ultra high pressures by Soderlind et al. (1995) predict a wide range of stability for the *bct* structure in Ce and Th, and also predict additional transformation to the hexagonal close-packed (*hcp*) structure at 1600 GPa for Ce at room temperature.

The energy dispersive X-ray diffraction (EDXD) pattern of cerium at 208 GPa is shown in Fig. 2. The lattice parameters for the *bct* phase of Ce at 208 GPa are $a = 2.476 \pm 0.001$ Å, $c = 4.161 \pm 0.002$ Å with $c/a = 1.680$. Figure 3 shows the pressure variation of the axial ratio (c/a) for the *bct* phase of Ce between 14 and

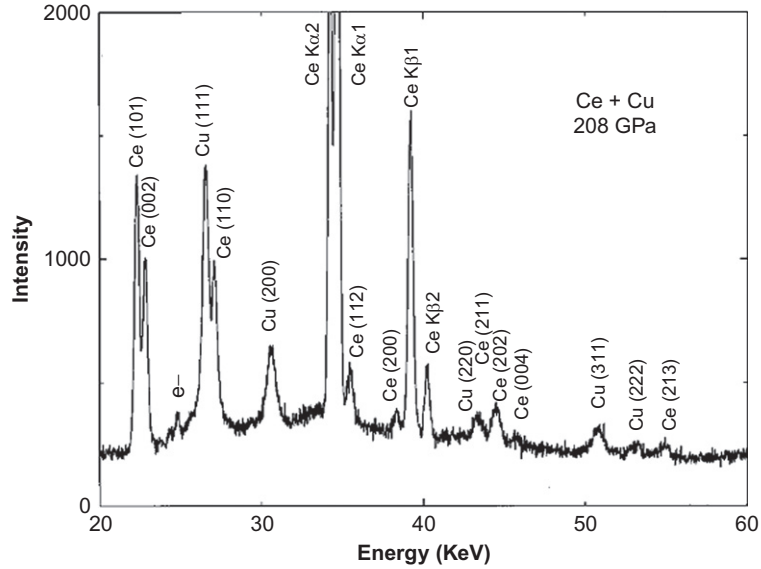

FIGURE 2 EDXD pattern of Ce at 208 GPa (Vohra et al., 1999).

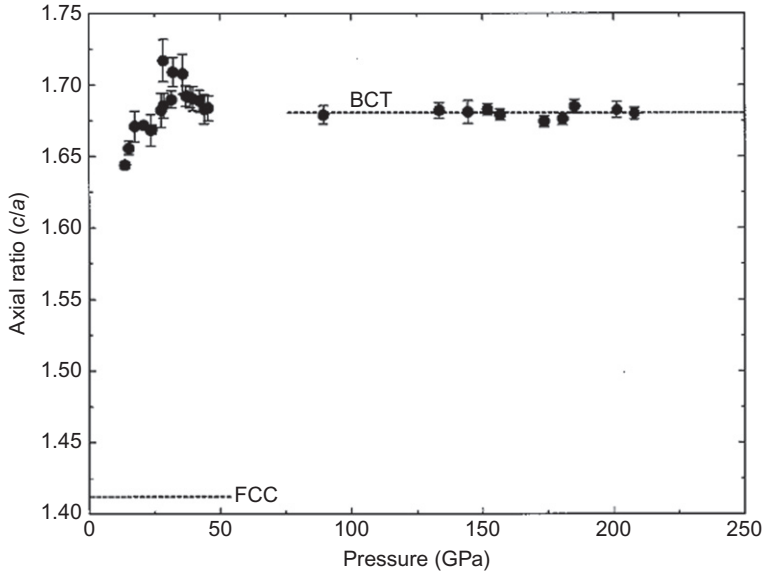

FIGURE 3 The variation of the axial ratio (c/a) for the *bct* phase as a function of pressure in the pressure range of 14–208 GPa. The ideal value for the *fcc* lattice of 1.414 is also indicated. At ultrahigh pressures, *bct* phase assumes a constant value of $c/a = 1.680$ as indicated by the dashed line (Vohra et al., 1999).

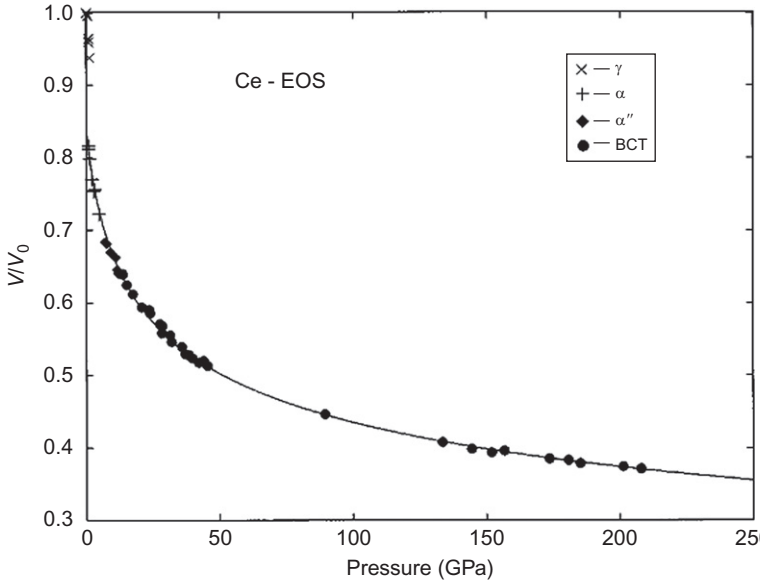

FIGURE 4 The measured equation of state of cerium metal to 208 GPa at room temperature. The solid curve drawn through the collapsed phases above 1 GPa is the MUEOS fit (Vohra et al., 1999).

208 GPa at room temperature. Also shown in Fig. 3 is the ideal *c*/*a* value of 1.414 for the undistorted *fcc* phase. The *c*/*a* ratio increases first above the transition pressure of 13 GPa and then attains a constant value of 1.680 ± 0.006 at ultrahigh pressures between 90 and 208 GPa. A similar behavior is observed in the 5f metal Th, where the *c*/*a* for the *bct* phase first increases beginning from the transition pressure of 60 GPa and then reaches a plateau with $c/a = 1.65$ above 200 GPa. Figure 4 shows the measured equation of state (EOS) for cerium based on the experimental data from the works of Olsen et al. (1985) and Vohra et al. (1999), with ambient pressure volume V_0 (*fcc* phase) = 34.363 Å^3/atom. The fit parameters for this entire pressure range between 0 and 208 GPa are given as $B_0 = 23.08$ GPa, its pressure derivative $B_0{}^1 = 4.945$ and ambient pressure volume V_0 (collapsed *fcc* phase) of 28.88 Å^3/atom (Vohra et al., 1999).

4. PRASEODYMIUM

Praseodymium (Pr), along with the other light lanthanide cerium, has been subject of intense research given the low pressures at which the electronically driven structural transitions can be seen. Whereas in cerium the 4f shell delocalization accompanied by a volume collapse is seen at 0.7 GPa, in Pr it occurs around 20 GPa. There is a lot of debate as to which "precollapse" structure is the correct assignment for Pr since depending on this factor volume collapses

in the range of 8.3–16.7% have been reported. Pr crystallizes in *dhcp* structure at ambient conditions and undergoes the following structural sequence with increasing pressure: *dhcp* → *fcc* → *dfcc* (*hR24*) → *monoclinic* → *α-uranium* → *primitive orthorhombic* ($P2_12_12_1$). The presence of the monoclinic phase has been reported by Chesnut and Vohra (2000a) but later it has been questioned by Cunningham et al. (2005) and Evans et al. (2009). A high value for volume collapse 16.7% has been a result of assuming the presence of *monoclinic* (*C2/m*) phase by Chesnut and Vohra (2000a).

The *fcc* phase of Pr transforms into the *dfcc* phase (*hR24*) (Hamaya et al., 1993) around 7 GPa. The *fcc* → *hR24* has no detectable discontinuity in the atomic volume. Upon further compression, the *hR24* structure undergoes a transition to *Pr-VII* beginning near 13.7 GPa (Evans et al., 2009). This transition occurs over a wide pressure range and single-phase patterns of *Pr-VII* are obtained only above 18 GPa. The structure of *Pr-VII* is proposed as body-centered orthorhombic with space group *Ibam* with 16 atoms/cell or a very small distortion of the same. Phase transition of *Pr-VII* to the orthorhombic *α-uranium* phase has been seen around 20 GPa, with an accompanying volume change of 8.3%, and this phase is stable up to 147 ± 5 GPa (Velisavljevic and Vohra, 2004), where it undergoes a transition to a primitive orthorhombic structure ($P2_12_12_1$). Furthermore, studies of Pr metal also show crystalline grain growth at the point of transition to *α-U* structure (20 GPa) indicating reconstructive nucleation and growth processes coinciding with delocalization of the 4f shell (Cunningham et al., 2005). Praseodymium has been compressed to 313 GPa by Velisavljevic and Vohra (2004) and they first reported the transition around 147 GPa and also investigated the stability of the primitive orthorhombic phase. This primitive orthorhombic phase has been reported to have an unusual anisotropic compressibility, which leads to the formation of a pseudotetragonal phase at 260 ± 7 GPa. The *bct* phase predicted by theory (Soderlind, 2002) was not observed in this study.

Figure 5 shows the evolution of raw image plate data in Pr across the volume collapse (Cunningham et al., 2005). Debye rings with nearly even distribution of Bragg intensity for *dfcc*, redistribution of Bragg intensity indicating grain growth in *α-U*, and return to a uniform distribution of the Bragg intensity along the Debye rings can be seen. The Rietveld refinements from this study are shown in Fig. 6. The EOS figures from the studies of Cunningham et al. (2005), Evans et al. (2009), and Velisavljevic and Vohra (2004) are presented in Figs. 7–9. The EDXD patterns from Velisavljevic et al. (2004) showing the phase transitions at ultra high pressures in Pr are also presented in Fig. 10.

5. NEODYMIUM

Neodymium (Nd), the fourth member of the lanthanide series, which is also light lanthanide, has electronic configuration of $4f^3$ $(spd)^3$ and crystallizes in

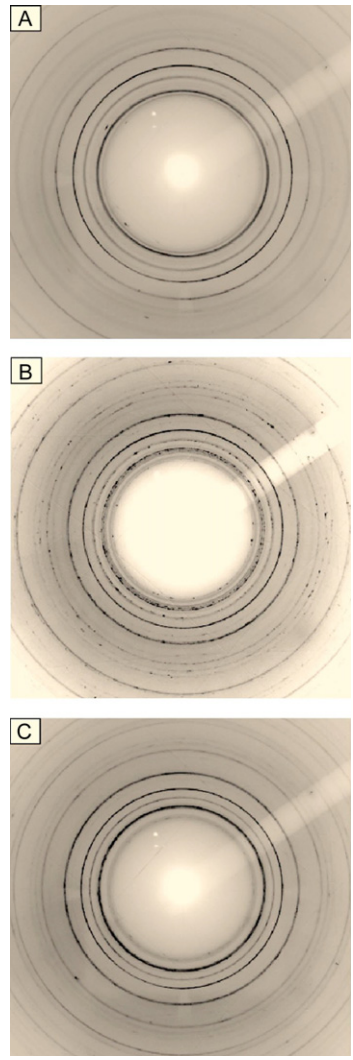

FIGURE 5 Evolution of the image plate raw data across the volume collapse in Pr. (A) Smooth diffraction rings for the *hR24* phase at 16.0 GPa. (B) Dramatic grain growth at 18.9 GPa showing a spotty pattern. (C) A return to continuous diffraction rings showing near random distribution of small grains at a higher pressure of 28.5 GPa (Cunningham et al., 2005).

the *dhcp* structure at ambient conditions. As with other lanthanides, pressure driven electronic and structural changes are seen in Nd. What prompted a number of studies on this element is the low number of f electrons in its configuration and the anticipation that low symmetry structures resulting from delocalization of f electrons could be seen at moderately high pressures. Early

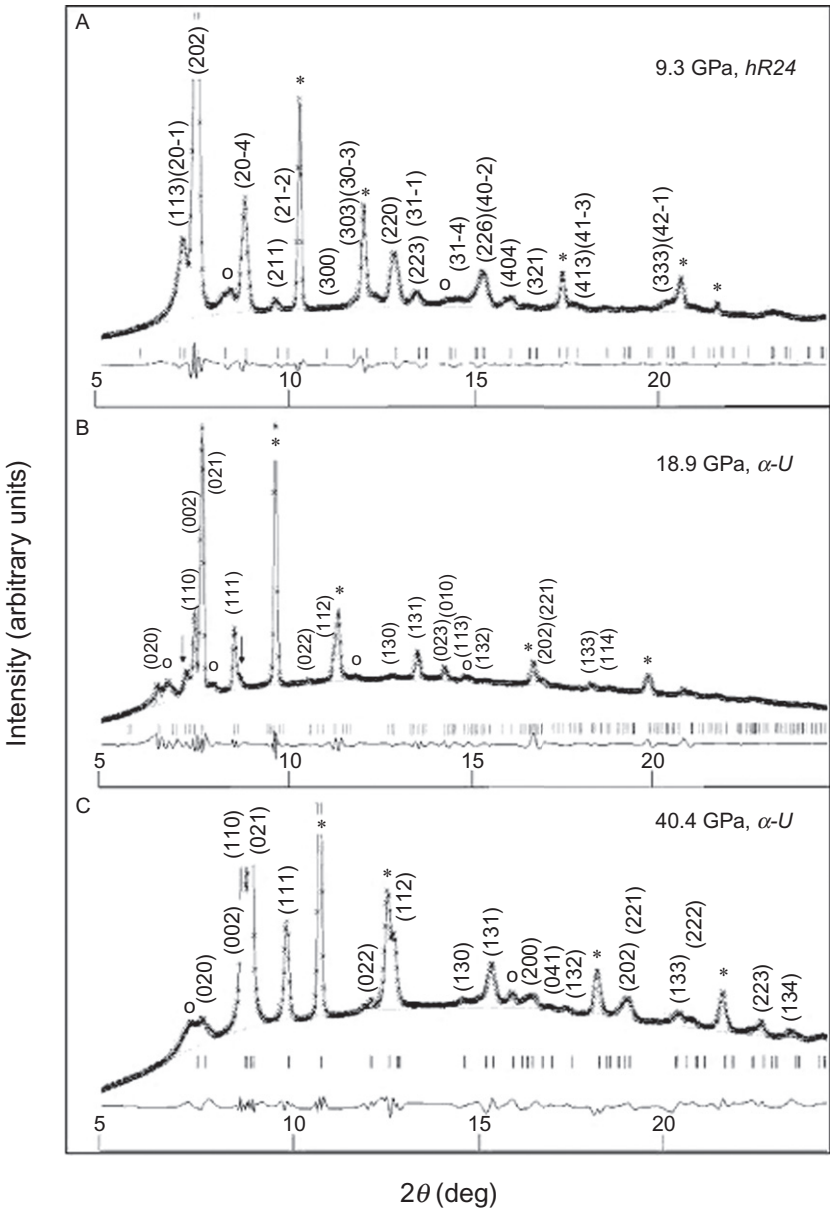

FIGURE 6 Refined praseodymium X-ray spectra showing the emergence of the low symmetry α-*U* phase. Copper pressure marker peaks are denoted by an asterisk and oxide peaks with "o." (A) *hR24* phase at 9.3 GPa. (B) α-*U* phase at 18.9 GPa, slightly above the transition pressure. Residual *hR24* peaks are marked with arrows. (C) Pure α-*U* phase at 40.4 GPa (Cunningham et al., 2005).

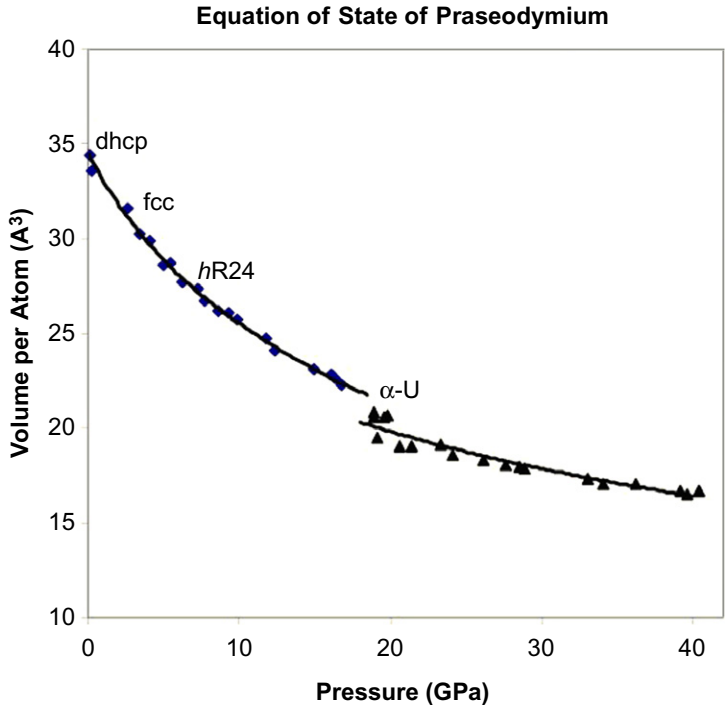

FIGURE 7 Equation of state of Pr to 40 GPa (Cunningham et al., 2005). Note that these authors assumed the presence of only *hR24* phase between *fcc* and α-*U* phases. Volume collapse is calculated as 9.1%. The bulk modulus and its first derivative are given as 21.70 GPa and 3.03 for the precollapse phases and 27.69 GPa and 3.44 for the α-*U* structure, respectively.

studies by Akella et al. (1986) and Zhao et al. (1994a) established the crystal structure sequence $dhcp \rightarrow fcc \rightarrow dfcc \rightarrow hP3$ in neodymium below 60 GPa. These phase transitions were observed around 9, 18, and 40 GPa, respectively. Later studies by Akella et al. (1999) observed another phase transition from *hP3* to a monoclinic *C2/m* phase around 75 GPa. In this study, the authors proposed that this monoclinic phase in Nd persists to a pressure of 153 GPa and that no further phase transitions were observed. Later, examination of these data and further independent experimental studies by Chesnut and Vohra (2000b), however, showed that there is indeed yet another phase transition that Akella et al. failed to observe. Chesnut and Vohra (2000a) showed that the monoclinic phase in Nd transitions to the α-*U* structure, which is also observed in Ce and Pr, around 113 ± 6 GPa. The α-*U* phase is shown to be stable to 155 GPa. This places the entire structure sequence of light lanthanides at $dhcp \rightarrow fcc \rightarrow dfcc \rightarrow hP3 \rightarrow C2/m \rightarrow \alpha\text{-}U$. Figures 11 and 12 show the EDXD patterns and the EOS from this study. The following modified universal equation of state (MUEOS) fits for Nd were obtained using ambient pressure

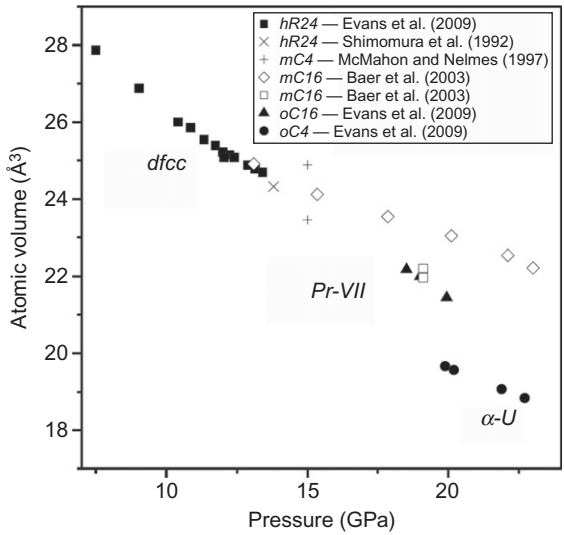

FIGURE 8 The measured compressibility of Pr from 7 to 23 GPa (Evans et al., 2009). *Pr-VII → α-uranium* volume change is given as 8.3%.

volumes of V_0 (*dhcp*) = 34.165 Å^3/atom: (i) $B_0 = 25.38$ GPa and $B_0{}^1 = 3.119$, for $0 < P < 80$ GPa; (ii) $B_0 = 24.05$ GPa and $B_0{}^1 = 3.225$, for $80 < P < 119$ GPa; and (iii) $B_0 = 6.141$ GPa and $B_0{}^1 = 7.351$, for $119 < P < 155$ GPa.

As discussed earlier, the phase transitions in Ce and Pr are accompanied by large volume collapses indicating abrupt change in behavior of 4f electrons in these materials. However, in case of Nd, there are no such volume collapses as shown in the work of Chesnut and Vohra (2000b). In another study by Velisavljevic et al. (2005), simultaneous electrical and structural studies were carried out on Nd to 152 GPa to confirm this phenomenon. It was indeed shown that in contrast to the abrupt pressure-induced 4f electron transitions seen in cerium and praseodymium, the α-*U* structure undergoes a continuous evolution in neodymium. Electrical resistivity measurements confirmed the gradual nature of the 4f delocalization process in this element. The authors present the argument that the decrease of 38% in the electrical resistivity of Nd above 100 GPa is similar in magnitude to the 50% drop in the electrical resistivity of Pr at 20 GPa (Velisavljevic et al., 2004) where its α-*U* phase is first observed, thus leading them to believe that 4f electrons in Nd become itinerant at pressures exceeding 100 GPa. Further, the continuous nature of this phase change is supported by the image plate studies conducted by the authors as part of this study where they have not observed the crystal grain growth effects that have been seen in Ce and Pr at high pressures during the transformation to the α-*U* phase. Figures 13 and 14 show the continuous evolution of the α-*U* structure in Nd and the results from the electrical resistivity studies carried out by designer diamond anvils.

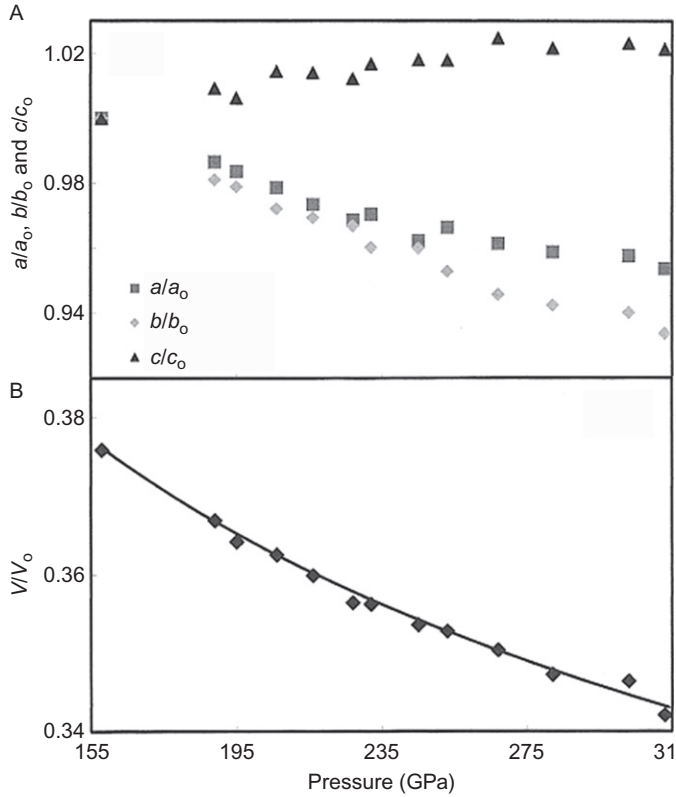

FIGURE 9 Linear compression of the three axes normalized to lattice parameters at 158 GPa, a/a_0, b/b_0, and c/c_0, where $a_0 = 2.434 \pm 0.008$ Å, $b_0 = 4.813 \pm 0.001$ Å, and $c_0 = 4.433 \pm 0.001$ Å are values obtained at 158 GPa. The *c*-axis shows negative compressibility while the compressions of the *a*-axis and *b*-axis are nearly similar. (B) The measured EOS of Pr in the 155–315 GPa pressure range at room temperature. The measured compression of Pr at 313 GPa is $V/V_0 = 0.343$, where $V_0 = 34.538$ Å^3/atom for the ambient pressure *dhcp* phase of Pr (Velisavljevic and Vohra, 2004). The following values were obtained by the fit $V_0(P2_12_12_1) = 30.19$ Å^3/atom, $B_0 = 177.07$ GPa, and $B_0{}^1 = 0.349$.

6. PROMETHIUM

Promethium (Pm) is the last element in the lanthanides to assume *dhcp* structure at ambient conditions. It is also the only radioactive element besides technetium with stable neighboring elements. The work of Haire et al. (1990), where they obtained Pm-147 as a reactor byproduct is summarized here. An extended discussion on the comparison of Pm with that of Sm, Nd, and actinide materials is given in this work. Pm has been compressed to 60 GPa in a diamond anvil cell and EDXD was employed in observing the structural changes in Pm. The lattice parameters of this Pm sample at ambient conditions are given as $a = 0.364$ nm, $c = 1.180$ nm.

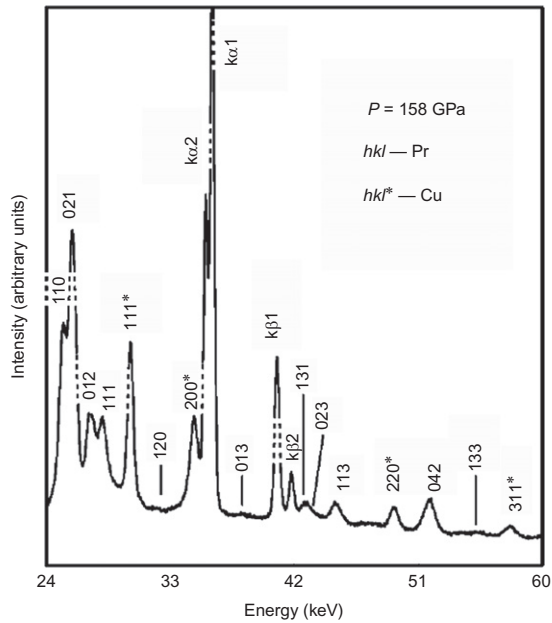

FIGURE 10 The full EDXD pattern for the Pr sample and Cu pressure marker at 158 GPa. The diffraction angle $2\theta = 13^\circ$. The 11 diffraction peaks from the Pr sample are indexed to the $P2_12_12_1$ phase and the 4 Cu diffraction peaks denoted by asterisk are indexed to the *fcc* phase. Kα and Kβ are the fluorescence peaks from the Pr sample (Velisavljevic and Vohra, 2004).

The first phase transition in Pm from *dhcp* to *fcc* has been reported at 10 GPa. The next transition occurred around 18 GPa and Pm is shown to exhibit a *dfcc* structure which in this study has been stable at 60 GPa. The authors point out changes in diffraction patterns between 50 and 60 GPa and attribute them to a possible indication of further phase change. Upon releasing the pressure, the *dfcc* structure reverted to *fcc* and with some hysteresis, back to *dhcp*. Figures 15 and 16 show the diffraction patterns at various pressures and EOS of Pm to 60 GPa, respectively. The authors point out the smooth nature of the fit and the absence of large discontinuities in the volume to come to the conclusion that the f-electron delocalization that is seen in the neighboring elements of Pm is not seen in its case up to 60 GPa.

7. SAMARIUM

Samarium (Sm) has been studied extensively as the low number of 4f electrons in its configuration prompted the researchers to speculate that their participation in bonding, and thus the appearance of low-symmetry crystal structures, could be seen at moderately high pressures, as seen in Ce, Pr, and Nd. The low pressure transitions are well documented by Zhao et al. (1994a), where they proposed a hexagonal structure *hP3* for the post-*dfcc*

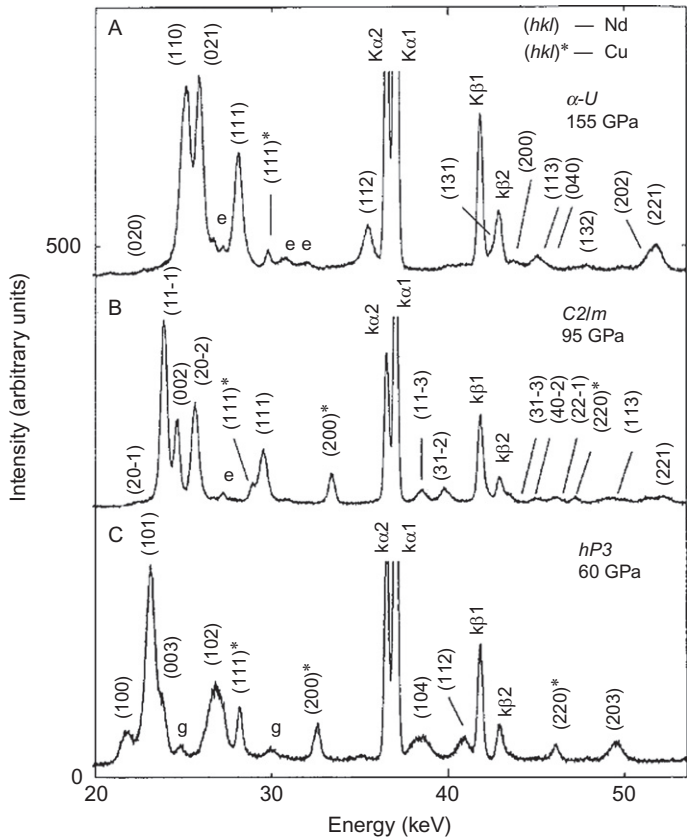

FIGURE 11 EDXD spectra of Nd ($Ed = 54.795$ keV Å) at various pressures showing the structural transitions. The peaks labeled "e" are escape peaks from the germanium detector, and Kα and Kβ lines are fluorescence emission from the neodymium sample (Chesnut and Vohra, 2000a).

phase. Additional phase transitions were first reported by Vohra et al. (1991) to 189 GPa, where the transition near 91 GPa was temporarily assigned to a *bct* phase. Chesnut in his dissertation work 2001, examined Sm to 205 GPa and found the monoclinic *C2/m* phase to be a more suitable assignment for this structure.

Sm crystallizes in the *Sm-type* structure at ambient conditions with lattice parameters $a = 3.626$ Å and $c = 26.222$ Å. Under high pressure, *Sm-type* to *dhcp* transition has been seen around 1 GPa, *dhcp* to *fcc* transition has been seen around 14 ± 3 GPa. Distortion in the *fcc* phase persists in the pressure range of 20–35 GPa. A further phase transition from this *dfcc* phase to *hP3* phase has been reported around 36 ± 4 GPa by Zhao et al. (1994a) and Chesnut (2001). A low symmetry structure *C2/m* has been reported by Chesnut (2001) around 103 ± 5 GPa, and the appearance of this low symmetry

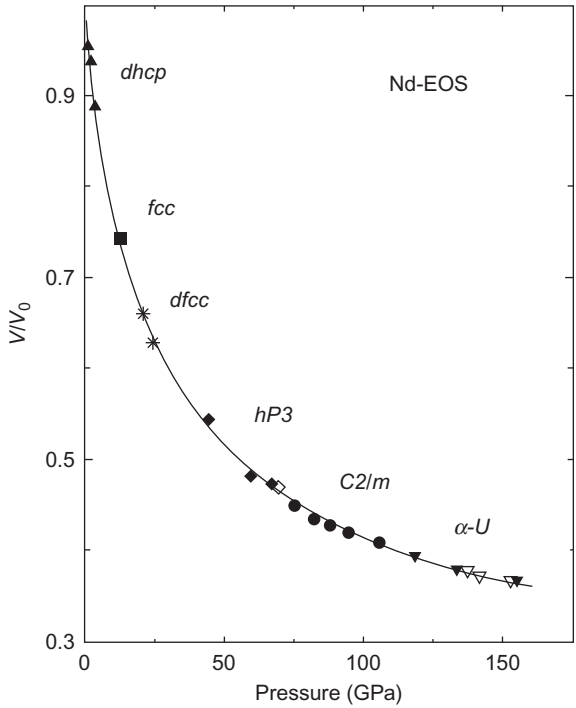

FIGURE 12 Measured EOS of Nd to 155 GPa (Chesnut and Vohra, 2000a). The fit parameters are given in text.

structure prompted the speculation about the participation of 4f electrons in bonding. The *C2/m* phase of Sm is stable at a pressure of 205 GPa ($V/V_0 = 0.37$) and no further transition to *bct* phase was observed. Figures 17 and 18 show the EDXD patterns of Sm at various pressures and Fig. 19 shows the EOS fit to the measured volumes vs. pressure. The reported bulk modulus and its pressure derivative are 33 ± 2 GPa and 1.5 ± 0.5, respectively.

8. EUROPIUM

Europium (Eu) and ytterbium (Yb) are the only two elements in the lanthanide series that show divalent electronic character. This divalent character manifests as larger atomic volume compared to their neighboring elements. Also, the structures of these two elements do not fit into the structure sequence (*hcp* → *Sm-type* → *dhcp* → *fcc* → *dfcc*) seen with either increasing pressure or decreasing atomic number. As such, there is lot of interest to see if pressure can cause change in Eu electronic character. A great deal of theoretical and experimental work has been done on europium to see if it would exhibit the same behavior as its trivalent neighbors under the application of pressure.

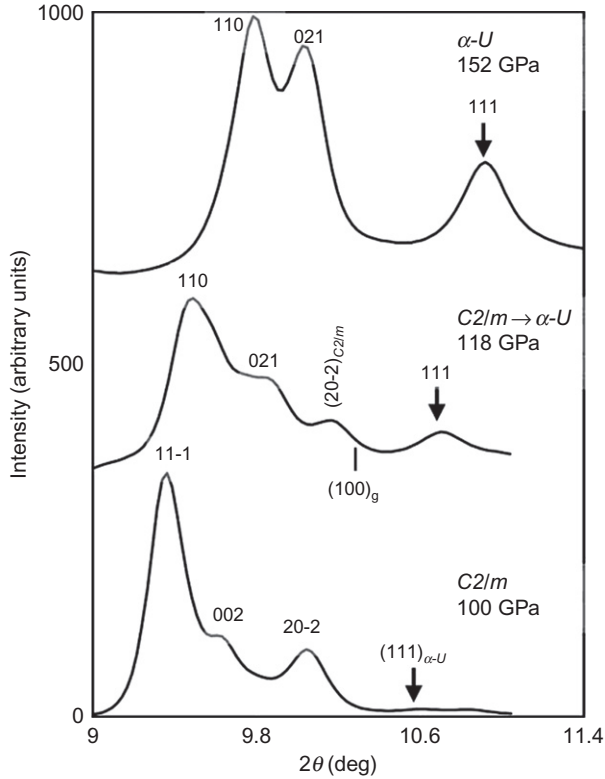

FIGURE 13 A continuous evolution of the α-*U* phase in Nd. At 100 GPa, the (111) peak of α-*U* appears (marked with an arrow). The (111) diffraction peak of α-*U* phase continues to increase in intensity up to the highest pressure of 152 GPa (Velisavljevic et al., 2005).

Under atmospheric conditions, Eu crystallizes in a body-centered cubic (*bcc*) structure. Earlier studies by Takemura and Syassen (1985) and Grosshans and Holzapfel (1992) have shown a phase transition from *bcc* to *hcp* around 12 GPa, accompanied by a volume collapse of 4%. Upon further compression, a new close-packed structure has been observed in Eu around 17 GPa. Takemura and Syassen (1985) termed this *Eu-III*, a multiple of *hcp* cell with 36 atoms. In the same work, the authors show that the EOS of Eu approaches that of gadolinium near 20 GPa and argue that a change in its valence (not completely trivalent, rather a mixed valent state) must be the reason for it. However, in both aforementioned studies, Eu did not show structures seen in its neighboring elements.

In the latest study by Bi et al. (2011), the authors tried to answer the question of whether or not europium achieves fully trivalent state and to see if under extreme pressures Eu takes on the structures shown by its neighboring elements by compressing it to 92 GPa in a diamond anvil cell. This work and

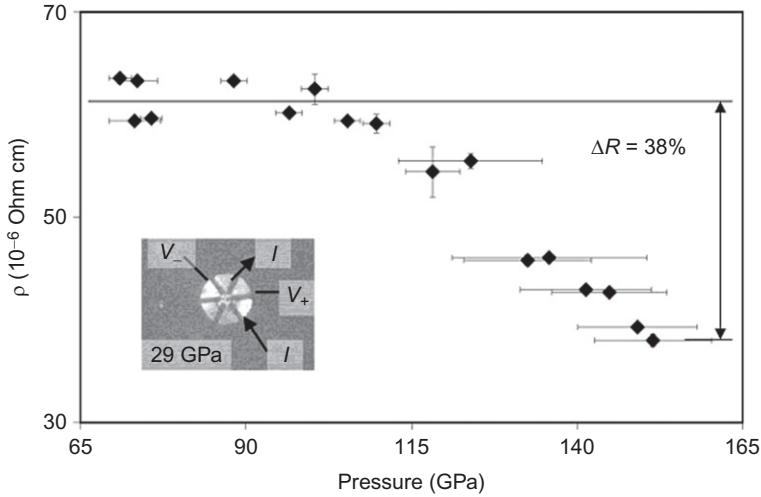

FIGURE 14 Change in electrical resistivity in Nd metal with increasing pressure. A steady decrease of 38% in resistivity is seen at 152 GPa. The insert shows an optical micrograph of the designer diamond anvil with Nd sample in the gasket hole of a spring steel gasket (Velisavljevic et al., 2005).

the references therein provide an extended discussion on the previous and present theoretical work done on europium. The authors show that there are three phase regions in Eu when compressed to 92 GPa. The *bcc* to *hcp* transitions seen in earlier works is observed, a mixed phase region between 18 and 62 GPa, followed by a transition to orthorhombic *Pnma* structure at 66 GPa which persists to 92 GPa. The X-ray diffraction spectra from this study at various pressures along with the Rietveld refinements are shown in Figs. 20 and 21. Bi et al. (2011) also see the *bcc* to *hcp* transition near 12 GPa. Above 18 GPa, a sluggish transition is seen. The authors claim they are able to fit the *hcp* structure at 28 GPa by ignoring weak Bragg reflections. As seen from the figures, they indexed the diffraction spectra between 18 and 35 GPa as a mixture of *hcp* and a monoclinic *C2/c* structure. Above 42 GPa, they claim a mixed phase of *C2/c* and *Pnma* is seen until 66 GPa. From 66 to 92 GPa, a pure *Pnma* phase is seen. In producing an EOS for Eu, these authors obtained the lattice parameters between 12 and 35 GPa by assuming the *hcp* phase. Above 35 GPa, the orthorhombic *Pnma* has been used. The EOS figure presented and the bulk modulus of 10.9 ± 0.6 GPa and its derivative of 3.0 ± 0.2 calculated from it shows their data to be consistent with earlier works.

The authors also point out that a fully trivalent Eu state does not appear likely at pressures as high as 92 GPa, since none of the structures observed under pressure in the present experiment (*bcc* → *hcp* → *mixed phase* → *primitive orthorhombic* (*Pnma*)) have been observed at pressures exceeding 1 Mbar

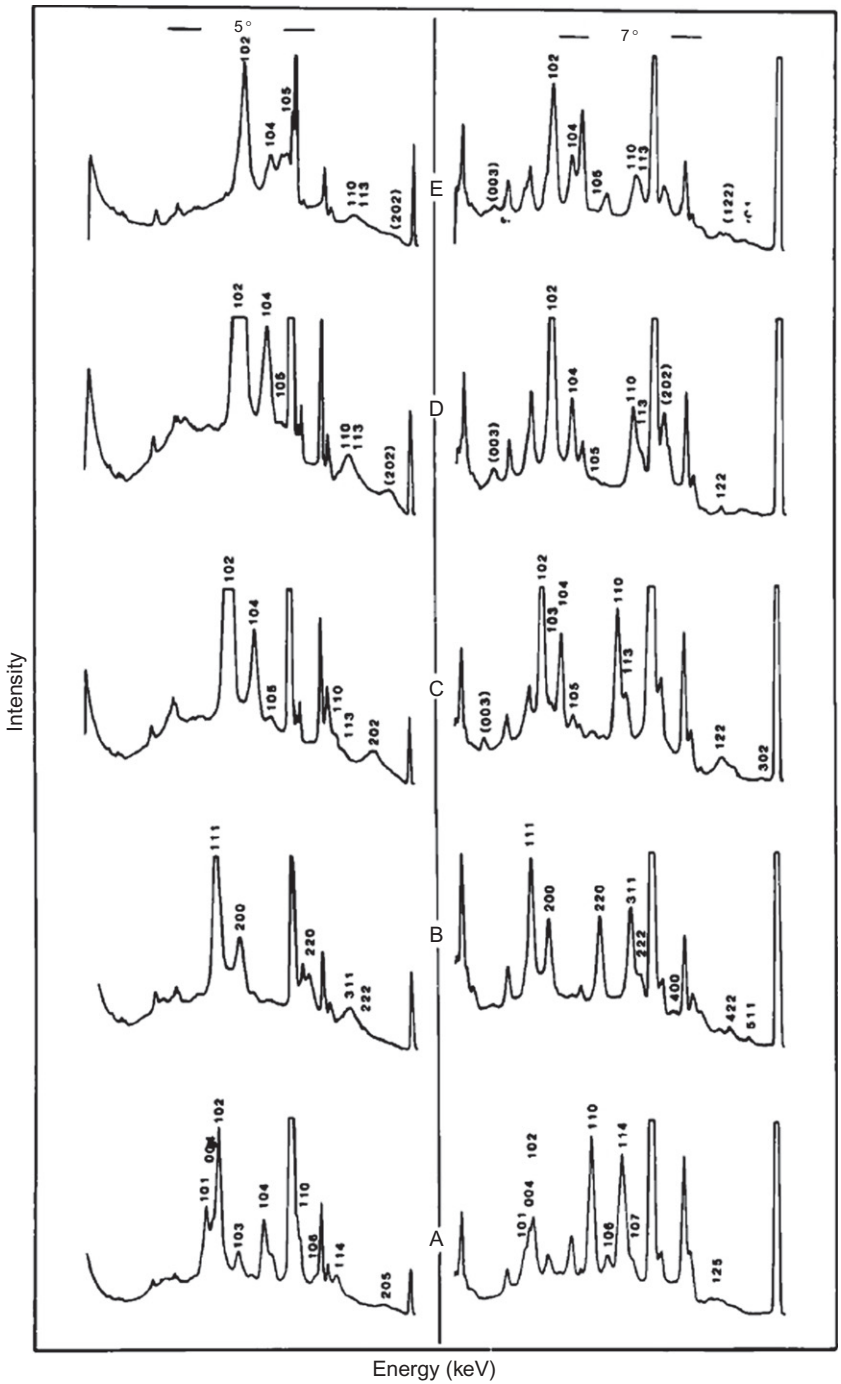

FIGURE 15 Sequence of diffraction spectra of Pm representative of various structures (A) *dhcp* spectrum below 10 GPa, (B) *fcc* spectra between 10 and 18 GPa, (C) spectra at 29 GPa, (D) spectra at 50 GPa, and (E) spectra at 60 GPa (Haire et al., 1990).

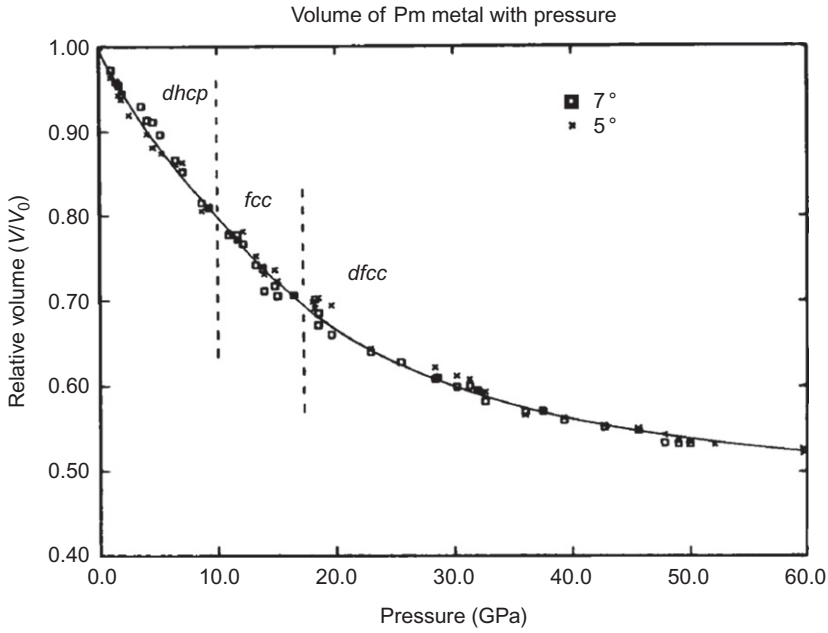

FIGURE 16 Relative volume of the three forms of Pm as a function of pressure. Bulk modulus and its pressure derivative are calculated to be 38 GPa and 1.4, respectively (Haire et al., 1990).

for the neighboring trivalent lanthanides Nd, Sm, Gd, and Tb or for any of the other trivalent rare-earth metals (Fig. 22).

9. GADOLINIUM

Gadolinium (Gd) has half-filled 4f shell. Thus it is a unique element in the lanthanide series as general interest immediately arises as to whether or not 4f electron participation in bonding can be seen in this element under the influence of pressure. As such, Gd has been extensively studied over the decades. In case of gadolinium, there are conflicting assignments of structures in various pressure ranges. Although universal agreement exists that the lanthanide crystal structure sequence of *hcp* → *Sm-type* → *dhcp* → *dfcc* can be seen in Gd and that a low symmetry structure appears upon further compression, there are widely conflicting reports on the pressure regions where the *dfcc* and *post-dfcc* structures appear and are stable. Possible reasons suggested by researchers for such disagreements include possibilities of impurities in samples, sample preparation itself, use or non use of pressure medium in high pressure experiments, etc.

Gadolinium crystallizes in the *hcp* structure at ambient conditions with the lattice parameters $a = 3.633$ Å and $c = 5.779$ Å. As mentioned earlier, elements like Gd with half-filled shell are thought to be relatively stable and the phenomenon of 4f-shell delocalization can only be expected under very

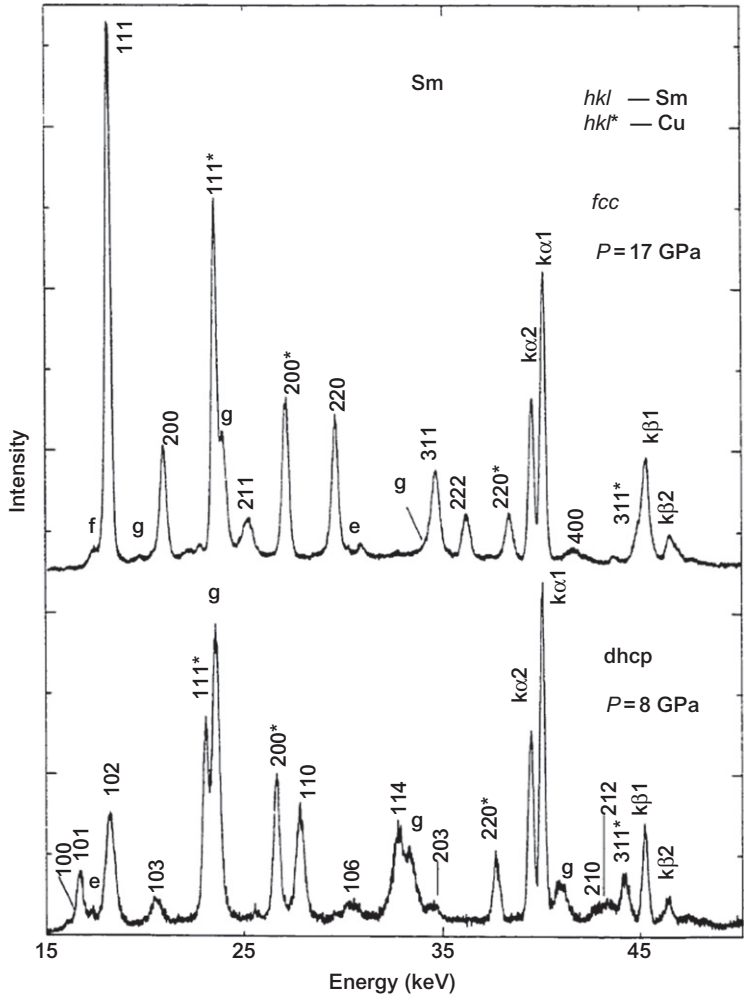

FIGURE 17 EDXD spectra of Sm at low pressures (Chesnut, 2001).

high compression. Work done by Hua et al. (1998) and the references therein suggest that the first transition in Gd, *hcp* to *Sm-type* structure is seen at 0.8 ± 0.5 GPa. The second transition to *dhcp* is seen at 6 ± 1 GPa. Hua et al. (1998) suggested that this *dhcp* phase persists to 36 GPa and that a *dfcc* phase appears after this pressure, and labeled it as six-layer hexagonal. The authors claim this phase persists until 61 ± 1 GPa and the next transition is to a body-centered monoclinic (*bcm*) structure, which persists to a pressure of 118 GPa. Figure 23 shows the EDXD patterns from their work. It is to be pointed out that the EOS fit parameters presented by these authors for the *bcm* phase appears quite unreal. In conclusion, Hua et al. (1998) offer that gadolinium

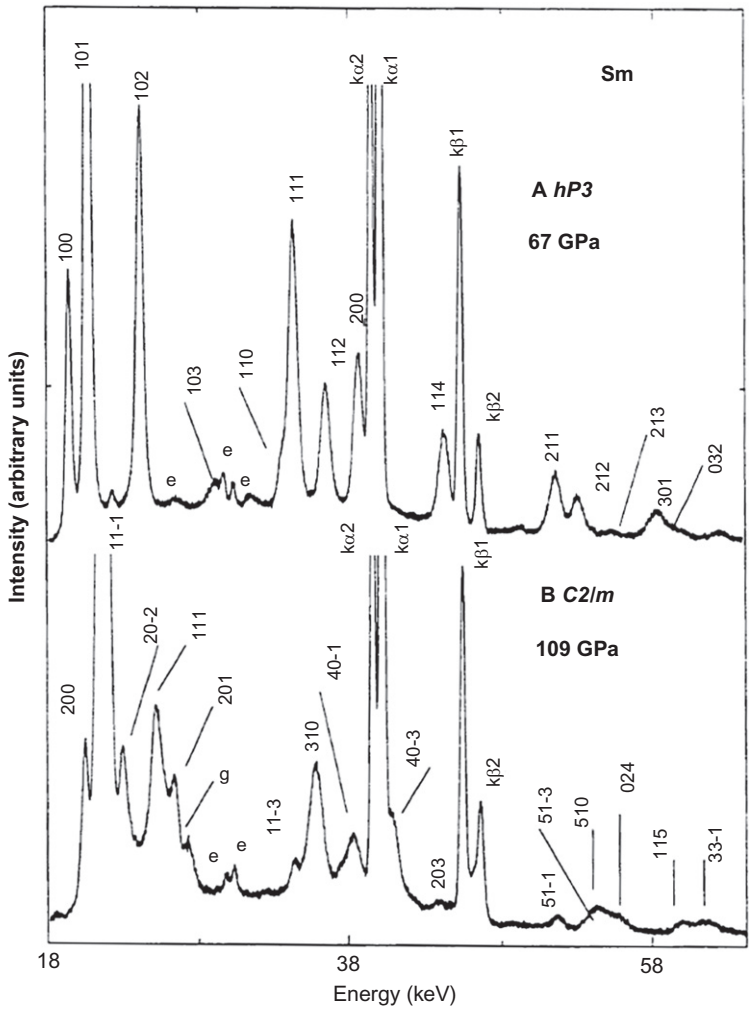

FIGURE 18 Post-*dfcc* phase and the low symmetry phase in Sm at high pressures (Chesnut, 2001).

follows the crystal structure sequence *hcp* → *Sm-type* → *dhcp* → *dfcc* below 57 GPa and labeled the low symmetry phase that appears after 60 GPa as *bcm*, which is shown to be stable to a pressure of 118 GPa.

Chesnut (2001) claims that the phase seen after transition around 29 GPa, which Hua et al. (1998) labeled as six-layer hexagonal is in fact a monoclinic *C2*/*m* phase. He maintains that this phase is stable to a pressure of 59 ± 2 GPa. In the same work, it is noted that upon further compression, gadolinium transitions to *bcm* phase as proposed by Hua et al. (1998). The EDXD spectra he presented supporting his claim are shown in Figs. 24 and 25.

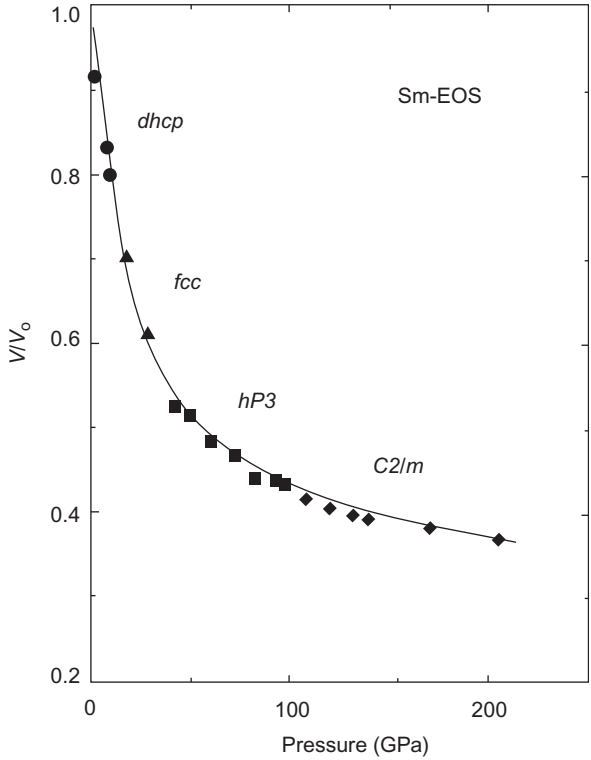

FIGURE 19 The measured EOS of Sm to 205 GPa at room temperature (Chesnut, 2001).

These are very different results for the same element. It must be noted that the aforementioned two studies did not employ a pressure medium. The sample preparation methods (which in itself can impart additional energy to the material) in both cases are unknown. The latest study of Gd by Errandonea et al. (2007) tried to answer these conflicting reports by employing argon as pressure medium and using angle dispersive X-ray diffraction (ADXD), which allowed them to Rietveld refine their observed diffraction patterns. In this study, Gd has been compressed to 93 GPa at room temperature. In the same work, novel phases observed in gadolinium under heating are discussed. The sample in this study has been compressed starting from a pressure of 10 GPa. At 10 GPa, the sample has been identified to be in *dhcp* phase with the lattice parameters of $a = 3.415$ Å and $c = 10.864$ Å. The *dhcp* to *fcc* transition was found at 26 GPa and the *fcc–dfcc* transition at 33 GPa. Another phase transition was observed at 60.5 GPa, which is in agreement with the works of Grosshans and Holzapfel (1992) and Hua et al. (1998). This phase, which the authors termed *Gd-VIII*, is shown to be stable to a pressure of 93 GPa. Through Rietveld refinements, the authors support their claim that

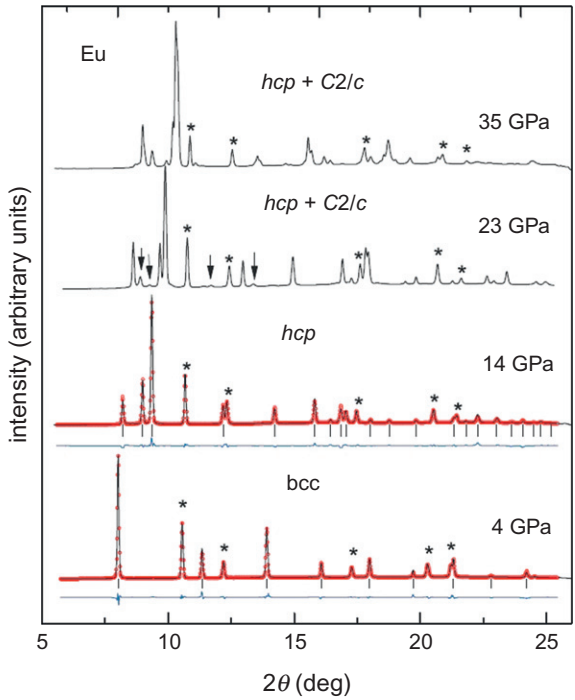

FIGURE 20 X-ray diffraction spectra of Eu from 4 to 35 GPa with Rietveld full-profile refinements (red lines) for *bcc* and *hcp* phases. Pt pressure marker peaks are identified by asterisks in all spectra (Bi et al., 2011).

the *dfcc* phase observed between 33 and 60 GPa is *hR24* phase, seen in Pr by Hamaya et al. (1993). The authors also show that the low-symmetry crystal structure observed between 60 and 93 GPa is *C2/m* and suggest that as both the *dfcc* and *C2/m* structures are closely related to the *fcc* structure, the $fcc \rightarrow dfcc \rightarrow C2/m$ structural sequence is quite possible on geometrical grounds. The EOS data and the fits are shown in Fig. 26. The fit gives the atomic volume, the bulk modulus, and its pressure derivative for Gd: $V_0 = 31.3(3)$ Å^3/atom, $B_0 = 34(3)$ GPa, and $B_0{}^1 = 4.2(2)$, respectively. For the high pressure phase, the B_0 and $B_0{}^1$ values are given as 45(3) and 4(fixed), respectively.

10. TERBIUM

Terbium (Tb) with electronic configuration of [Xe] $6s^2 5d^1 4f^8$ is the first 4f-shell element past half-filling. It is the second of the "heavy" lanthanides (gadolinium being the first). The nominal filling of its 4f shell consists of seven electrons forming a spherically symmetric half-shell and one

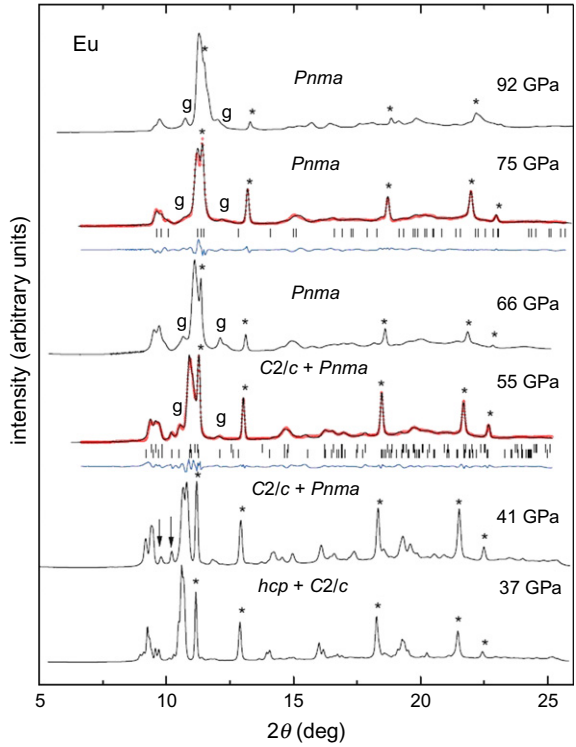

FIGURE 21 X-ray diffraction spectra of Eu from 37 to 92 GPa including refinements (red lines) at 55 and 75 GPa showing the sluggish transition from *C2/c* to *Pnma* (Bi et al., 2011).

additional electron with the opposite spin. Terbium follows the same structural sequence under pressure as cerium, albeit without the isostructural collapse, and at higher pressures with much broader regions of stability for each phase. The observed similarities in structure between terbium and cerium may be attributed to the presence of a single unpaired 4f electron.

A reversible initial phase transition from terbium's atmospheric *hcp* to a *Sm-type* structure α-*Sm* has been reported at 2.5–3.5 GPa. Further, compression is shown to produce the hexagonal packed structure *dhcp* around 16 GPa. At 30 ± 3 GPa, a *dfcc* phase *hR24* is reported. The transition from the *dfcc* structure *hR24* to the monoclinic *C2/m* as seen in cerium is reported at 51 ± 2 GPa, accompanied by a volume collapse of 5%. The *C2/m* monoclinic phase was found to be stable to a pressure of 155 GPa or a volume compression $V/V_0 = 0.39$. The high pressure phase *C2/m* is analogous to the "α" phase of cerium, providing evidence for 4f-electron delocalization in Tb and

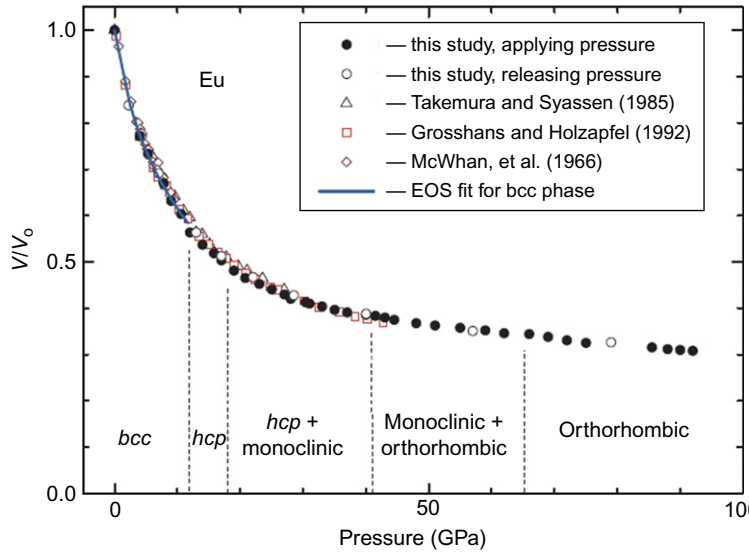

FIGURE 22 EOS for Eu at ambient temperature to 92 GPa from Bi et al. (2011) and previous works.

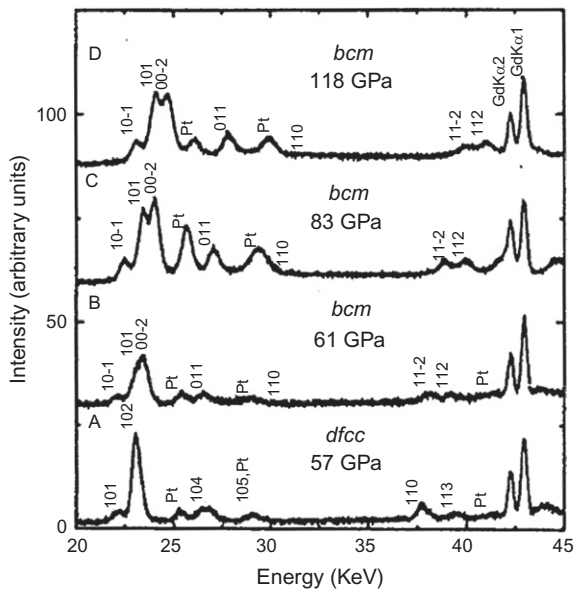

FIGURE 23 EDXD patterns of Gd at high pressures showing the phase transition between 57 and 61 GPa. Subsequent compression to 118 GPa does not show further phase transitions (Hua et al., 1998).

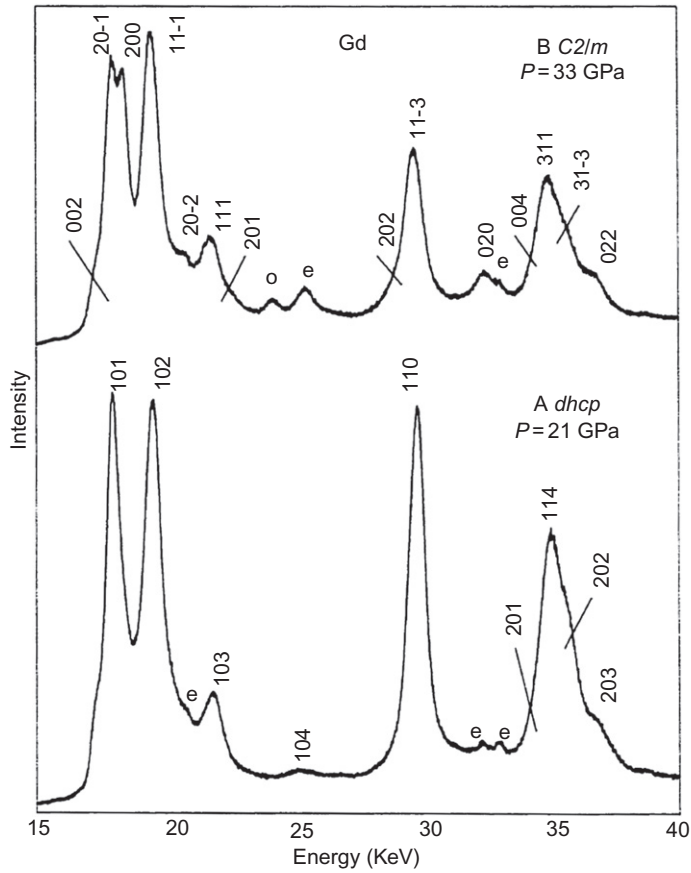

FIGURE 24 EDXD spectra of Gd showing the phase transition around 29 GPa from *dhcp* to *C2/m*. Peaks labeled as "e" and "o" are escape peaks and oxide peaks, respectively (Chesnut, 2001).

arguing for the thermodynamic stability of that phase in a light lanthanide metal Ce. The presence of the body-centered tetragonal phase at extreme compressions in both cerium, which has one 4f electron, and thorium, which has one 5f electron, indicates the possibility of observing a similar phase in terbium at ultrahigh pressures.

ADXD spectra of terbium at 40 and 155 GPa obtained at a synchrotron source by Cunningham et al. (2007) are shown in Figs. 27 and 28. In both figures, sample peaks are labeled by their fitted *hkl* values and reflections from the copper pressure marker are marked with asterisks. The EOS for terbium up to a pressure of 155 GPa from their work is also presented in Fig. 29.

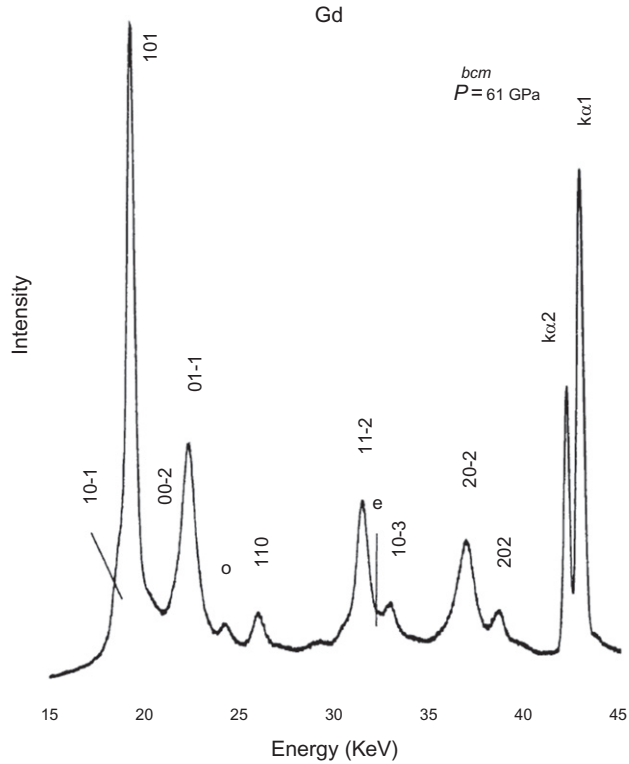

FIGURE 25 EDXD spectrum of Gd indexed as *bcm* at 61 GPa (Chesnut, 2001).

11. DYSPROSIUM

Dysprosium (Dy) has electronic configuration of [Xe] $6s^2 5d^1 4f^9$. The complete trivalent lanthanide crystal structure sequence can also be accessed in Dy with the application of pressure. Dysprosium has been extensively studied to various pressure ranges (Patterson et al., 2004; Samudrala and Vohra, 2012; Shen et al., 2007).

At ambient conditions, dysprosium is in *hcp* structure and the *hcp* → *Sm-type* phase transition is reported starting at 7 GPa at ambient temperature. The phase transformation from *Sm-type* → *dhcp*, another hexagonal packed structure, is reported to be around 17 GPa. Above 42 GPa, *dhcp* phase is shown to transform to the *dfcc* phase (*hR24* phase) proposed by Hamaya et al. (1993). It should be noted that the structure of this *dfcc* phase has also been claimed as orthorhombic *Cmmm* by Shen et al. (2007). The *dfcc* phase is observed between 42 and 80 GPa. Beyond 82 ± 2 GPa, a phase transition was observed that was attributed to a monoclinic (*C2/m* phase). It has been

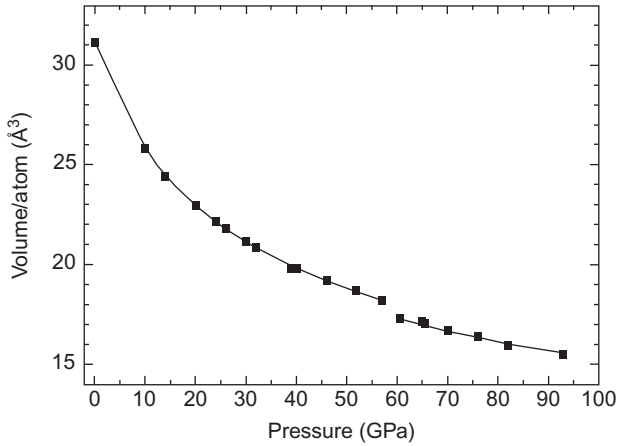

FIGURE 26 Volume–pressure data of Gd. Solid squares: experimental data. Solid curve: fitted EOSs (Errandonea et al., 2007).

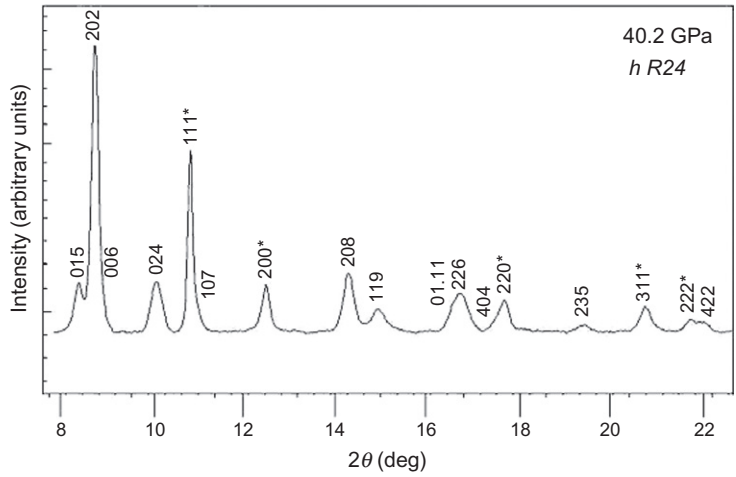

FIGURE 27 ADXD spectrum of terbium showing the *hR*24 phase at 40.2 GPa (Cunningham et al., 2007).

suggested that this high pressure phase could have a *bcm* structure by Patterson et al. (2004). However, as explained by McMahon and Nelmes (1997), the *bcm* structure which has also been proposed for Gd by Hua et al. (1998) is a special case of *C*2/*m* and both are closely related to the *fcc* phase. Figure 30 shows all five phases observed in dysprosium at different pressures. Upon compression to 210 GPa, dysprosium has a V/V_0 of 0.35 (Samudrala and Vohra, 2012).

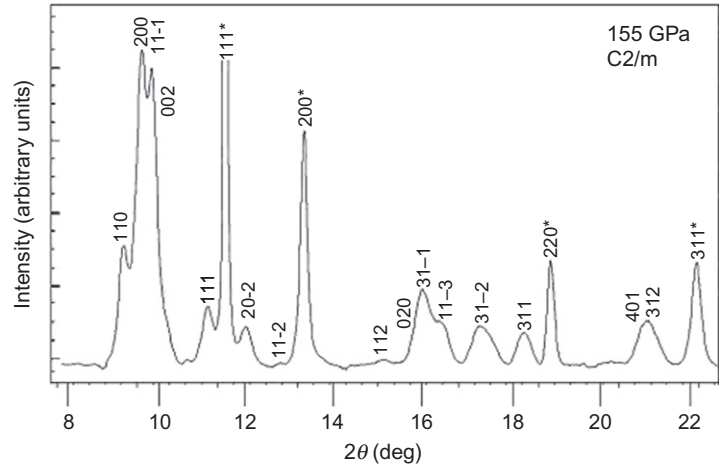

FIGURE 28 ADXD spectrum of terbium at the highest pressure of 155 GPa in the *C*2/*m* phase (Cunningham et al., 2007).

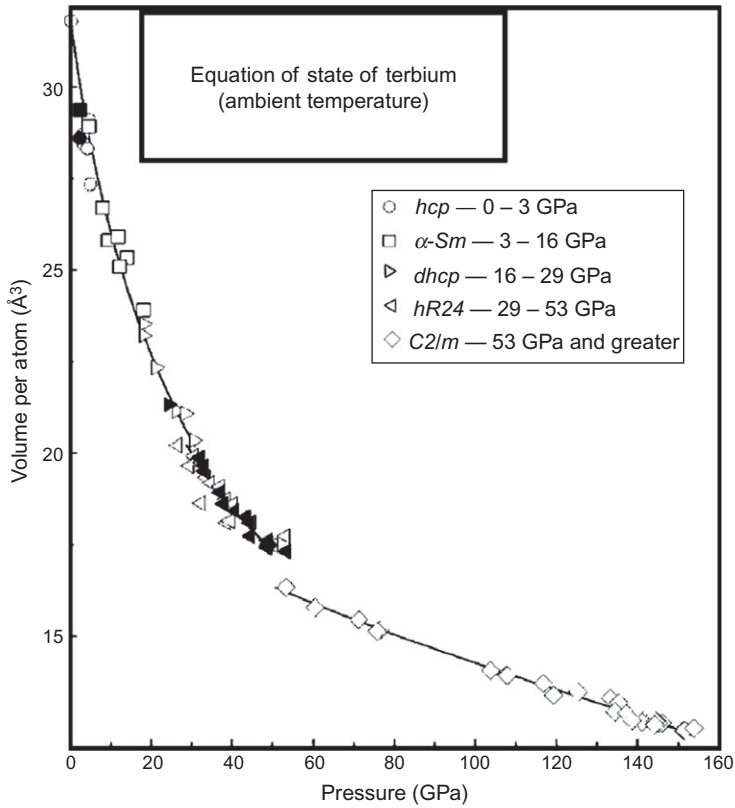

FIGURE 29 Equation of state fit for terbium to 155 GPa. At 51 ± 2 GPa, a 5% volume collapse is observed as the structure transforms to the open, low symmetry *C*2/*m* phase. The sharp decrease in compressibility of this low symmetry phase is argued as an indication of change in character of metallic bonds, that is, onset of 4f electron participation in bonding (Cunningham et al., 2007).

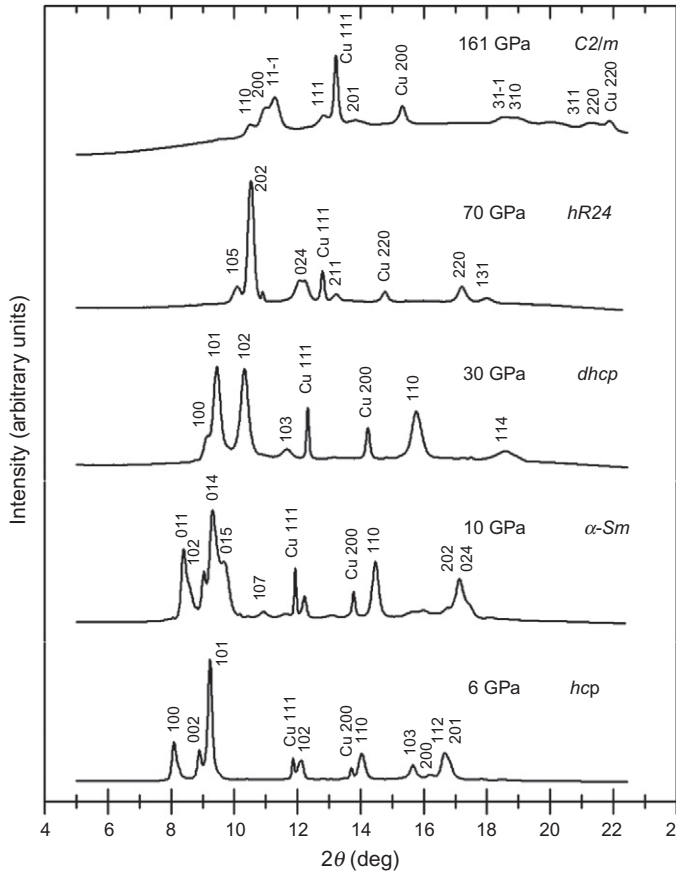

FIGURE 30 The ADXD spectra of dysprosium at various pressures showing all five phases seen in it when compressed to 210 GPa (Samudrala and Vohra, 2012).

From the studies conducted on dysprosium, the average bulk modulus is calculated to be 36 ± 2 GPa and the pressure derivative of bulk modulus is given as 3.5 ± 0.5. The third order Birch–Murnaghan fit is given by Eq. (1), where $X = (V_0/V)$.

$$P = \frac{3}{2} B_0 (X^{7/3} - X^{5/3}) \left[1 + \frac{3}{4} ({B_0}^1 - 4)(X^{2/3} - 1) \right]. \tag{1}$$

The Vinet EOS used by Patterson et al. (2004) is given by Eq. (2), where $H = PX^2/3(1-X), \eta = 1.5({B_0}^1 - 1)$, and $X = (V/V_0)^{1/3}$.

$$\ln H = \ln B_0 + \eta(1-X) + \beta(1-X)^2. \tag{2}$$

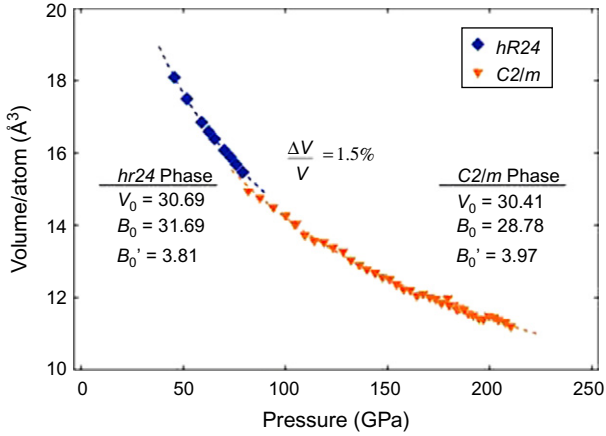

FIGURE 31 Volume per atom as a function of pressure for dysprosium; the Birch–Murnaghan equation of state fits from Samudrala and Vohra (2012).

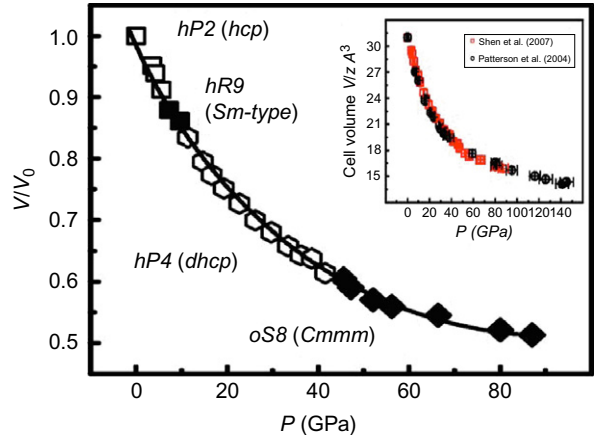

FIGURE 32 Equation of state fit for Dy from Shen et al. (2007) where the *dfcc* phase is assumed to be orthorhombic *Cmmm*.

The equations of state figures from the works of Patterson et al. (2004), Shen et al. (2007) and Samudrala and Vohra (2012) are presented in Figs. 31–33. Again, it is to be noted that these values are in agreement with one another even though the *dfcc* phase has been assumed to be different structures by different researchers.

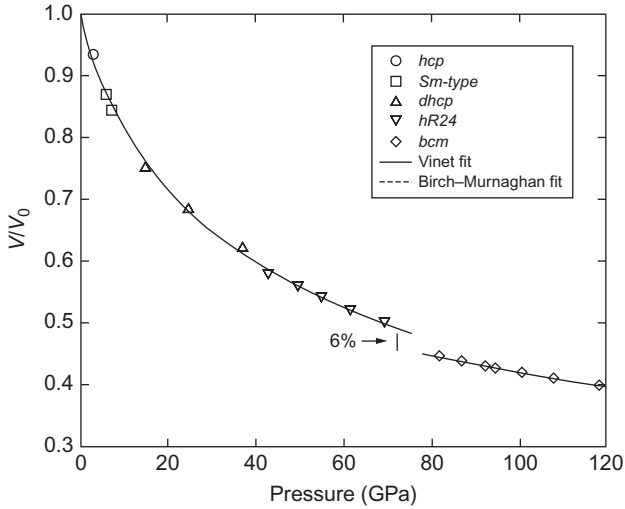

FIGURE 33 Equation of state fit for Dy where the low symmetry phase under high pressures is assumed to be body-centered monoclinic (Patterson et al., 2004).

12. HOLMIUM

Holmium (Ho) has electronic configuration of [Xe] $6s^2 5d^1 4f^{10}$. Holmium crystallizes under ambient conditions as an *hcp* structure with $a = 3.5778$ Å, $c = 5.6178$ Å, and axial ratio $c/a = 1.5702$, lower than the ideal close-packing ratio of 1.6333. At low pressures, the lanthanide structure sequence caused by the transfer of sp electrons to d band has been reported in holmium (Cunningham et al., 2006). The authors suggest that owing to polytypism and the broad overlap between energetically quite similar phases, a pure *fcc* phase is never observed in their study. Participation of 4f electrons in bonding at ultra high pressures has also been observed in holmium (Vohra et al., 2008).

The *hcp* → *Sm-type* phase transition is observed in Ho at 10 GPa at ambient temperature. This is followed by a phase transformation from *Sm-type* → *dhcp* phase transition at 19 GPa. Cunningham et al. (2006) found in their study that the nine layer *Sm-type* structure continues to be observed until 22.0 GPa, but beginning at 19.5 GPa, it is in coexistence with *dhcp*. The four layer *dhcp* structure persists until 55 ± 2 GPa. The *dfcc* phase *hR24* is observed after this pressure. Upon further compression, holmium is shown to have a low symmetry structure *C2/m*, typical when the 4f electrons participate in bonding, starting at 103 GPa. This is accompanied by a small volume collapse. This low symmetry structure is shown to be stable to 137 GPa (Vohra et al., 2008). Figures 34 and 35 show the structures of holmium at various pressures after phase transitions and Fig. 36 shows the EOS fit for holmium up to 137 GPa ($V/V_0 = 0.41$).

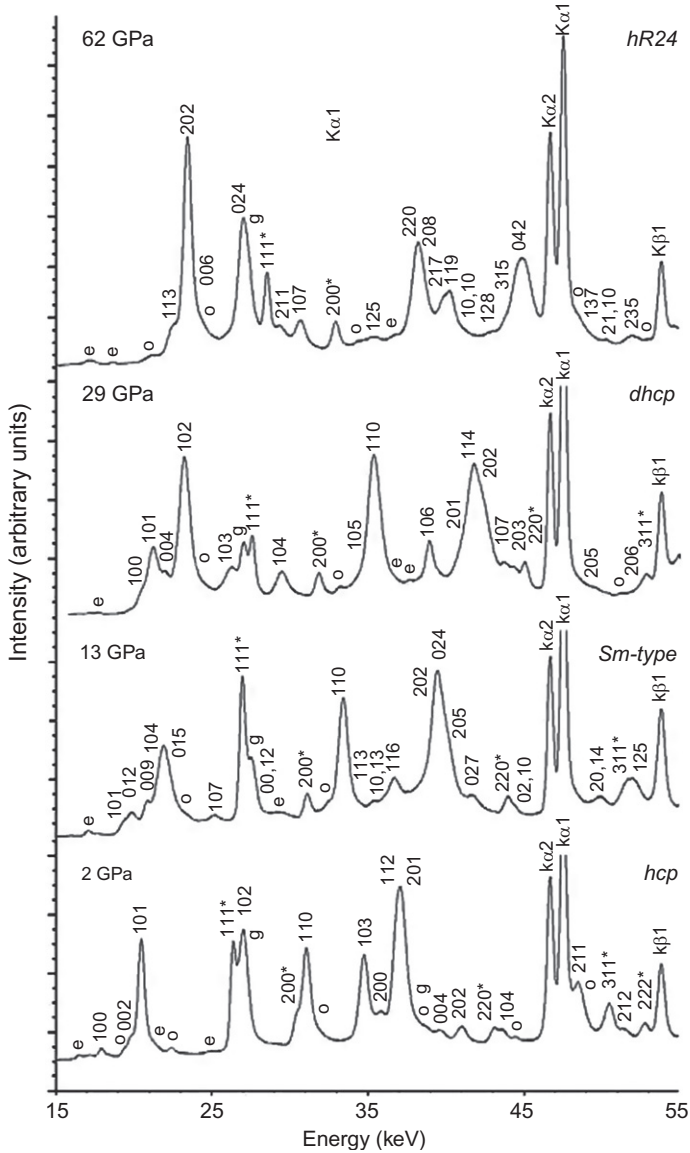

FIGURE 34 EDXD spectra of Ho in various phases to 62 GPa at ambient temperature (Cunningham et al., 2006).

13. ERBIUM

Erbium has a total of 11 electrons in its 4f shell. The crystal structure sequence $hcp \rightarrow Sm\text{-}type \rightarrow dhcp \rightarrow dfcc$ seen in lanthanide metals with decreasing atomic number and increasing pressure is also observed in erbium.

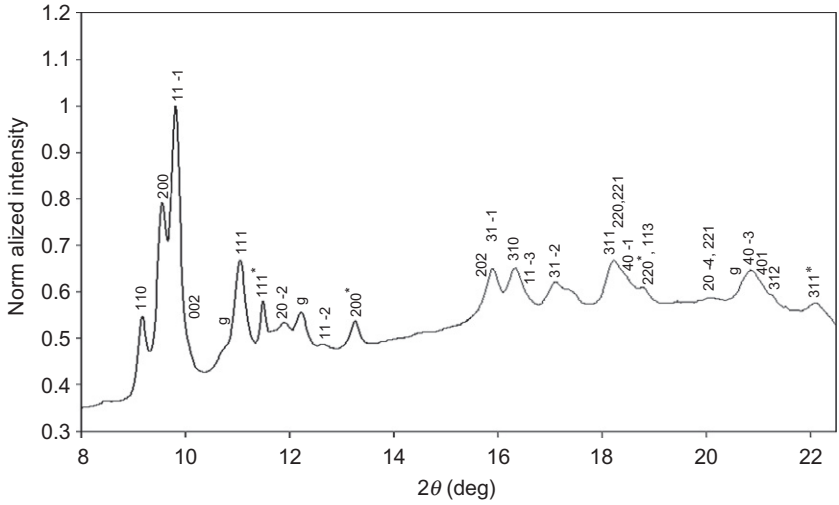

FIGURE 35 ADXD spectrum of holmium at 137 GPa. The *hkl* assignment is done assuming the low symmetry structure to be *C2/m* (Vohra et al., 2008).

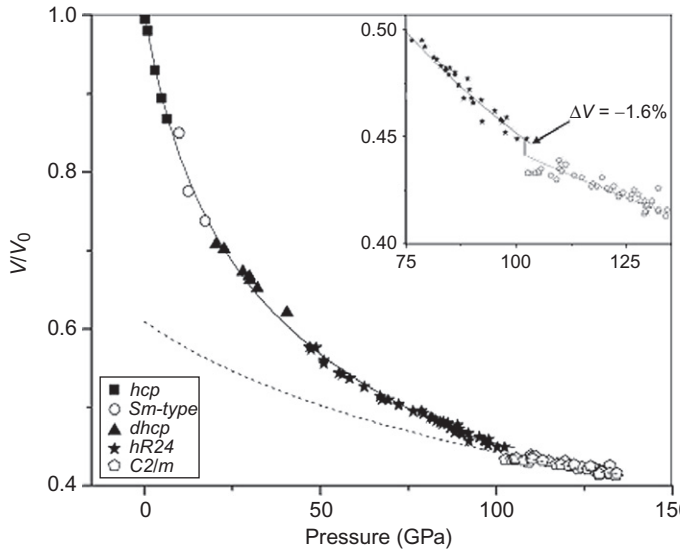

FIGURE 36 Equation of state fit showing the volume collapse after 4f-electron participation in bonding in holmium (Vohra et al., 2008).

The first phase transition under compression, *hcp* → *Sm-type*, is observed in erbium starting at 9 GPa at ambient temperature. This is followed by a phase transformation from *Sm-type* → *dhcp* starting at 29 GPa. The *dhcp* phase is observed between 29 and 58 GPa. Above 60 ± 2 GPa, *dhcp* phase transforms

TABLE 1 Structural Data for the Five Different Phases Observed in Erbium to 151 GPa

hcp Phase (P=Ambient)	$a=3.553\pm0.003$ Å; $c=5.564\pm0.002$ Å 2 Atoms/unit cell. Hexagonal stacking *AB* $A=(0, 0, 0)$; $B=(1/3,2/3,1/2)$
Sm-type phase (P=12 GPa)	$a=3.280\pm0.003$ Å; $c=23.236\pm0.002$ Å 9 Atoms/unit cell. Hexagonal stacking *ABCBCACAB* $A=(0, 0, z)$; $B=(1/3, 2/3, z)$; $C=(2/3, 1/3, z)$ $z=n/9$, $n=0, 1, \ldots, 8$
dhcp phase (P=32 GPa)	$a=3.043\pm0.002$ Å; $c=9.904\pm0.003$ Å 4 Atoms/unit cell. Hexagonal stacking *ABAC* $A=(0, 0, z)$; $B=(1/3, 2/3, z)$; $C=(2/3, 1/3, z)$ $z=n/4$, $n=0, 1, \ldots, 3$
hR24 phase (P=80 GPa)	$a=5.5412\pm0.0011$ Å; $c=13.5788\pm0.0065$ Å 24 Atoms/unit cell. Atom positions 6c $(0, 0, z_1)$; 18h $(x, -x, z_2)$ $z_1=0.2918\pm0.0008$; $x=0.5038\pm0.0016$; $z_2=0.2454\pm0.0008$
C2/m phase (P=151 GPa)	$a=4.5402\pm0.0013$ Å; $b=2.6670\pm0.0006$ Å; $c=4.3553\pm0.0028$ Å $\beta=105.77°\pm0.025°$ 4 atoms/unit cell. Atom positions 4i $(x, 0, z)$ $x=0.2986\pm0.0022$; $z=0.0793\pm0.0042$

to the *dfcc* phase (Pravica et al., 2005; Samudrala et al., 2011). The *dfcc* phase is observed between 58 and 118 GPa. Beyond 118 ± 2 GPa, a phase transition was observed that was attributed to a monoclinic $C2/m$ phase (Samudrala et al., 2011).

The structural data for the five different phases observed in erbium are given in Table 1. Pravica et al. (2006) also suggested that the *dfcc* phase could be assigned an orthorhombic *Cmmm* structure with lattice parameters of $a=8.042\pm0.017$ Å, $b=5.748\pm0.014$ Å, and $c=2.989\pm0.011$ Å at a pressure of 70 GPa. The diffraction patterns from the five phases observed in erbium under compression are shown in Fig. 37. Also, EOS fit (Samudrala et al., 2011) of erbium to 151 GPa is presented in Fig. 38. The fit parameters in the pressure range $0<P<118$ GPa, $B_0=45.7$ GPa and $B_0{}^1=2.253$, given by Samudrala et al. (2011) are in general agreement with previous works. In the pressure range $118<P<151$ GPa, the fit parameters are given as $B_0=154.8$ and $B_0{}^1=4.876$, indicating that erbium is becoming incompressible as it transforms to low symmetry structures.

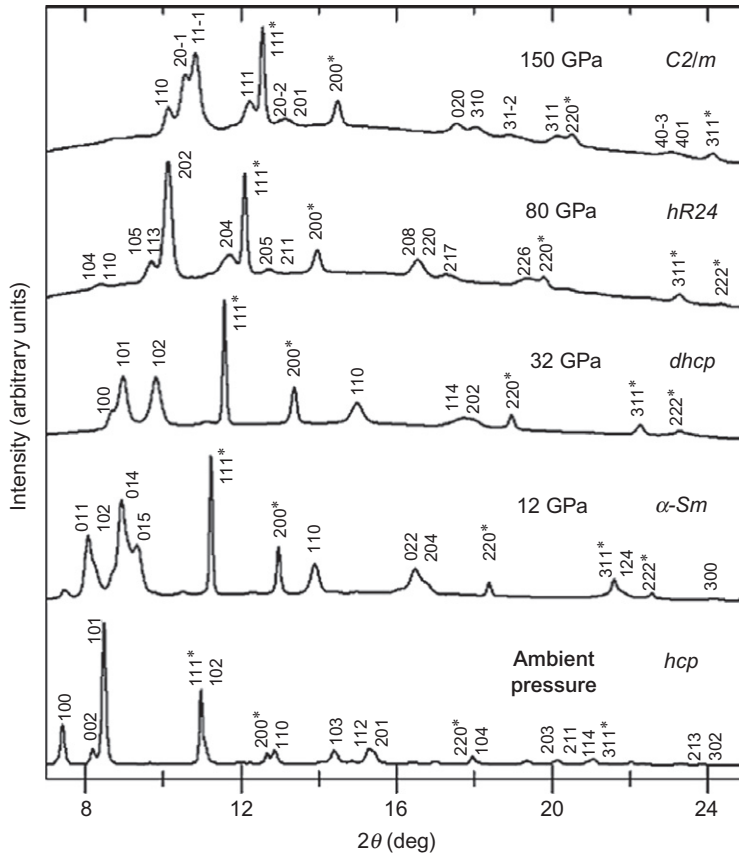

FIGURE 37 The ADXD spectra of the five phases observed in erbium under high pressure (Samudrala et al., 2011).

14. THULIUM

Thulium (Tm) is a unique heavy lanthanide element. It is the last heavy lanthanide with an incomplete 4f shell. In the lanthanide series, thulium is followed by ytterbium, which has a divalent electronic character and does not show the typical structural changes observed in other trivalent lanthanide elements. And the last element in the lanthanide series lutetium also has a completely filled 4f shell, and therefore is not expected to exhibit low symmetry structures at ultra high pressures.

The structural phase transitions in thulium have been studied to 195 GPa (Montgomery et al., 2011). The lanthanide crystal structure sequence, *hcp* → *Sm-type* → *dhcp* → *dfcc*, is observed below 70 GPa. It is to be noted that the pure *fcc* phase is not seen in this study. The hexagonal *hR24* phase (Montgomery et al., 2011) and orthorhombic *Cmmm* (Pravica et al., 2006) are used

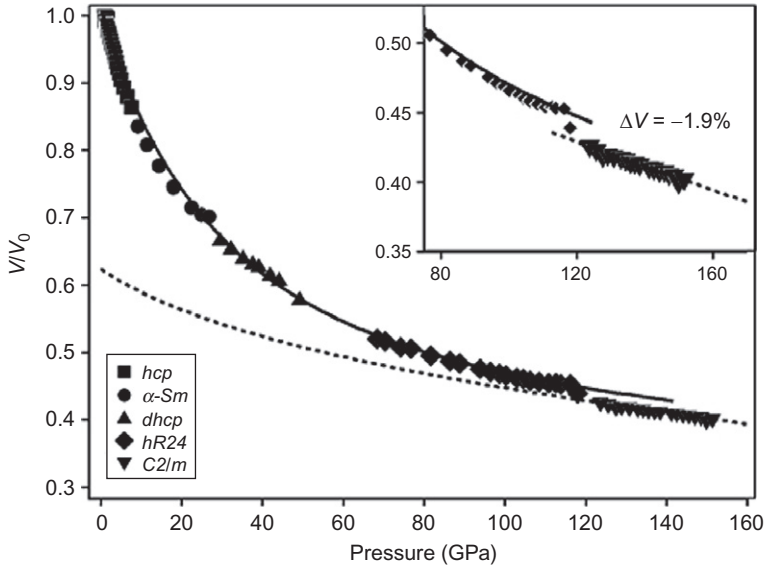

FIGURE 38 The measured equation of state for Er to 151 GPa at room temperature (Samudrala et al., 2011).

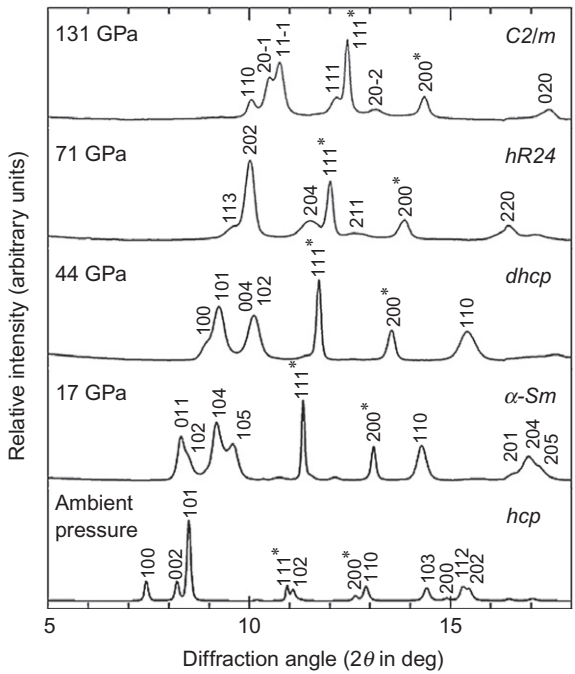

FIGURE 39 ADXD spectra of thulium at different pressures showing the five phases observed under compression to 195 GPa (Montgomery et al., 2011).

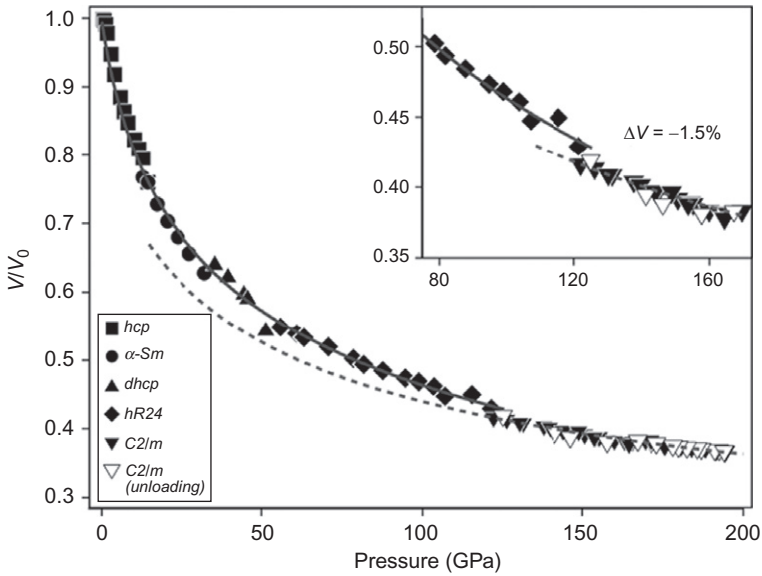

FIGURE 40 The measured pressure–volume curve or equation of state for Tm to 195 GPa at room temperature (Montgomery et al., 2011).

to describe the *dfcc* phase between 70 and 124 GPa. Above 124 ± 4 GPa, a structural transformation from *hR*24 phase to a monoclinic *C*2/*m* phase is observed with a volume change of -1.5% (Montgomery et al., 2011). Figure 39 shows the five phases seen in thulium under compression. The EOS data from this study are also presented in Fig. 40. The fit parameters are given as $B_0 = 32.11$ GPa and $B_0{}^1 = 3.865$, in the pressure range $0 < P < 124$ GPa; and $B_0 = 58.09$ GPa and $B_0{}^1 = 3.086$, in the pressure range $124 < P < 195$ GPa.

15. YTTERBIUM

Ytterbium (Yb) is another element in the lanthanides that garnered lot of interest because of its electronic structure. It shows a different behavior under pressure in comparison with the regular (trivalent) lanthanides. Yb is divalent with an electronic configuration of [Xe] $6s^2$ $4f^{14}$. The divalent character manifests in a higher atomic volume and Yb has an ambient volume which is 41% larger than the neighboring element lutetium. Early work by Syassen et al. (1982) and Grosshans and Holzapfel (1985) on Yb metal demonstrated that a gradual valence transition with increasing pressure from $4f^{14}$ $(spd)^2$ to $4f^{13}$ $(spd)^3$ or from 2^+ to 3^+ is observed at high pressures to 30 GPa. In a study of Yb to 90 GPa by Zhao et al. (1994b), it was found that the structural sequence of this metal with pressure is highly irregular and no similarities

with other lanthanide metals could be discerned. There are additional predictions of further electronic transition in Yb near 300 GPa by Herbst and Wilkins (1984).

The phase transformation sequence of *fcc* (*I*) → *bcc* → *hcp* → *fcc* (*II*) is reported by Zhao et al. (1994b) in Yb to 90 GPa. The *fcc* (I) to *bcc* transition occurs at 4 GPa, the *bcc* to *hcp* transition occurs at 26 GPa, and the *hcp* to *fcc* (II) transition occurs at 53 GPa. The two *fcc* phases are labeled as I and II to discriminate the pressure range over which they occur. Otherwise, crystallographically they are the same phase. Chesnut and Vohra (1999) reported a new phase transition in Yb at 98 ± 5 GPa, which has been indexed as a hexagonal unit cell with 3 atoms/cell referred to as *hP3* structure. The measured lattice parameters for the *hP3* phase at 202 GPa are $a = 2.522$ Å, $c = 5.908$ Å. Figure 41 shows the EDXD spectra of Yb at various pressures (Chesnut and Vohra, 1999). The EOS fit presented in this work, which includes data from the earlier works of Takemura and Syassen (1985), Grosshans and Holzapfel (1985), and Zhao et al. (1994b), is shown in Fig. 42. A global fit ignoring the small volume changes of 1–3% by the authors yielded a bulk modulus of 14.6 GPa and a pressure derivative of bulk modulus of 1.205. This low value of B_0^1 is argued as being indicative

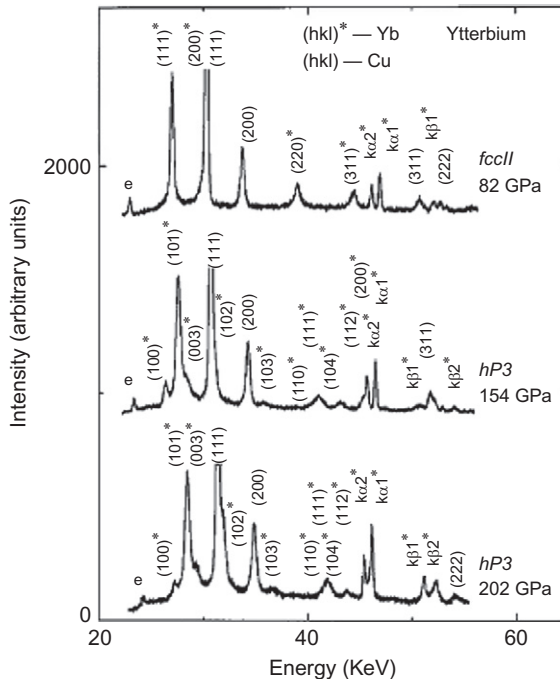

FIGURE 41 Energy dispersive X-ray diffraction spectrum of the ytterbium sample mixed with a copper pressure standard at various pressures (Chesnut and Vohra, 1999).

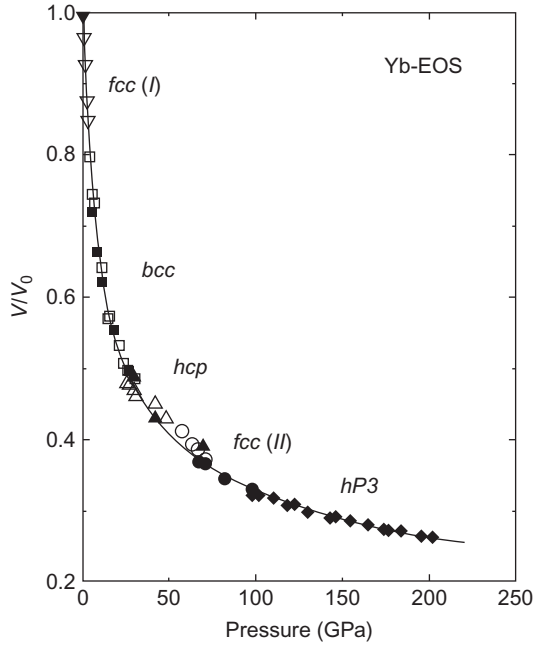

FIGURE 42 The measured equation of state of ytterbium to 202 GPa at room temperature (Chesnut and Vohra, 1999). Open symbols represent data from Takemura and Syassen (1985), Grosshans and Holzapfel (1985), and Zhao et al. (1994b).

of unusual compressibility associated with gradual divalent to trivalent electronic transition at ultra high pressures.

It is a general trend in divalent 4f materials that the application of pressure will cause a configurational crossover from an initial $4f^n$ configuration to a $4f^{n-1}$ configuration at high pressures. Chesnut and Vohra (1999) argue that the $4f^{14}$ to $4f^{13}$ transition in Yb proceeds in a rather continuous manner and that there are no large volume discontinuities of magnitude greater than 3% based on their EOS data. The measured compression for Yb at 202 GPa is $V/V_0 = 0.26$, and the extrapolated value for lutetium at the same pressure is $V/V_0 = 0.37$ from the work of Chesnut and Vohra (1998). It is clear that Yb is much more compressible than the neighboring lanthanide metals. It has been speculated that Yb ions undergo rapid interconfigurational fluctuation ($4f^{14}$ to $4f^{13}$) in the pressure range below 100 GPa and the unusually high compressibility is related to these fluctuations. Yb is thus shown to be isostructural with trivalent Sm and neodymium under high pressures.

16. LUTETIUM

Lutetium is the last element in the lanthanide series. It has a completely filled 4f shell. As such, it has been the subject of intense study. In lanthanides, participation of 4f electrons in bonding is suggested and generally accepted as a

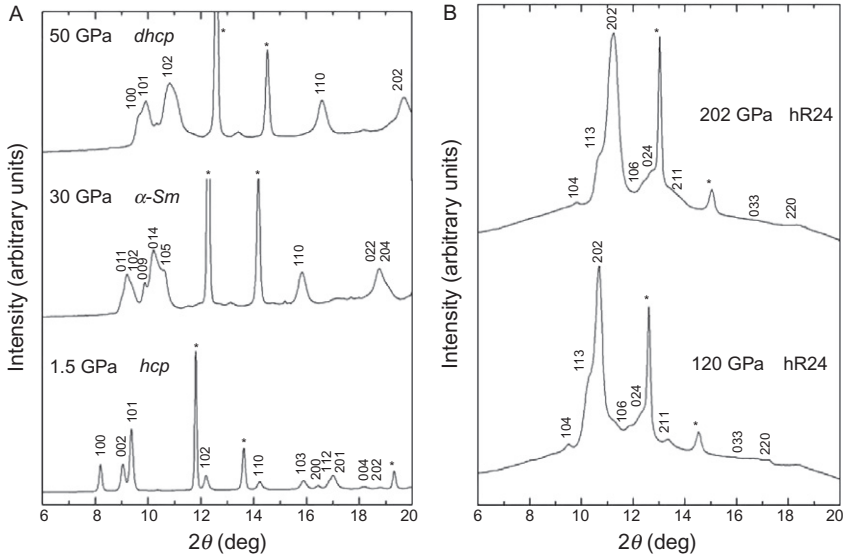

FIGURE 43 (A) ADXD spectra of pre-*dfcc* phases of lutetium under pressure, and (B) ADXD spectra of Lu in *dfcc* phase under high pressures (Samudrala et al., 2012).

cause for the appearance of low symmetry structures under extreme compression. However, a fully filled f shell element like lutetium is not expected to show such phases. So far, when compressed to 202 GPa, where V/V_0 of Lu is 0.39, it is still seen in the *dfcc* phase (Samudrala et al., 2012). Lutetium shows the structural sequence observed in other trivalent lanthanide metals under compression due to changes in the *d* band occupancy. Figure 43A shows the diffraction patterns of the low pressure phases (*hcp*, *Sm-type*, and *dhcp*). Figure 43B shows the *dfcc* phase assigned as *hR24*. The *hcp* to *Sm-type* transition has been noticed at 24 GPa, *Sm-type* to *dhcp* transition has been noticed at 45 GPa. Upon further compression, a phase transition into *hR24* has been noticed starting around 90 ± 4 GPa (Chesnut and Vohra, 1998; Samudrala and Vohra, 2012). As noted previously by Chesnut and Vohra (1998), the phase transition into *hR24* takes place over a long range of pressures and a clear transition into *hR24* has been observed at 102 GPa. This phase has been noticed to be stable to a pressure of 202 GPa. The EOS data for lutetium up to 202 GPa are presented in Fig. 44.

17. SUMMARY AND OUTLOOK

It is clear from the data presented in this chapter that the trivalent lanthanide metals show the following structural sequence *hcp* → *Sm-type* → *dhcp* → *fcc* → *dfcc* (*hR24 phase—hexagonal with 24 atoms/cell*) with increasing pressure. The long standing debate on the structure of the *dfcc* phase now appears to be settled with

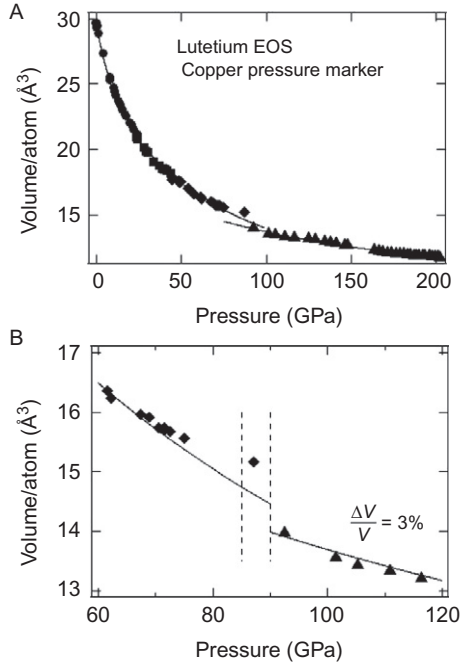

FIGURE 44 (A) Equation of state for lutetium to 202 GPa, (B) volume collapse at transition region from *dhcp* to *hR24* phase (Samudrala et al., 2012).

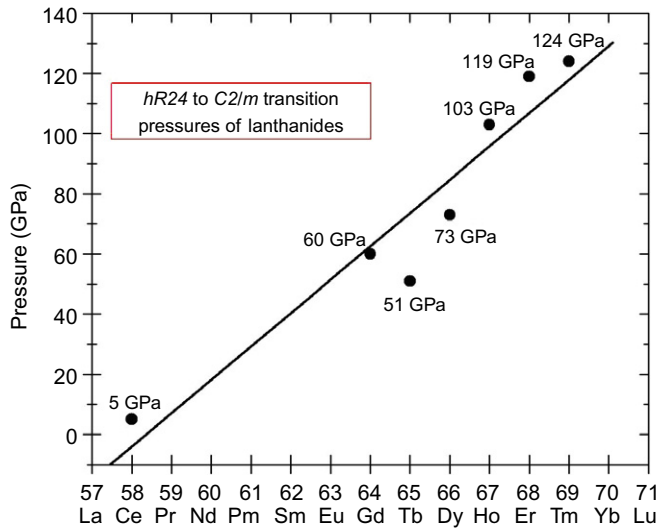

FIGURE 45 The transition pressures for selected lanthanides which exhibit monoclinic (*C2/m*) structure as a post-*dfcc* phase. The solid line is only a guide to the eye and it indicates that the pressure needed to delocalize 4f electrons increases with increasing atomic number. Terbium is an exception (see text and summary).

the detailed structural refinements where *hR24* phase provides the best fit to the available X-ray data. The stability field of *fcc* phase is rather limited in some of the heavy lanthanides (Ho–Tm) at room temperature and the *dhcp* phase directly transforms to the *dfcc* phase with increasing pressure. It is generally observed that the *dfcc* phase further transforms to a new phase at higher pressure, however, there does not appear to be a consistent structural trend in the post-*dfcc* phases at high pressures.

The most common post-*dfcc* phase appears to be the monoclinic *C2/m* phase with 4 atoms/cell. This low-symmetry monoclinic *C2/m* phase, first seen in cerium near 5 GPa, was also observed in heavy lanthanides (Gd–Tm) at high pressures. The appearance of this low-symmetry monoclinic structure signals 4f electron participation in bonding and is accompanied by a volume change at the transition. Figure 45 shows the transition pressure for *dfcc* → *monoclinic C2/m* phase transition for lanthanides. The solid line in Fig. 45 is only a guide to the eye; there is a clear trend of this transition pressure increasing with increasing atomic number of the lanthanide metal. Of course, terbium transition pressure deviates from this linear behavior as it has only one electron past a half-filled shell and it closely imitates cerium in its behavior under compression. Although, the monoclinic *C2/m* phase is stable in Tb to 155 GPa, a transformation to a *bct* phase is anticipated under further compression similar to Ce and Th under extreme conditions. Future research on extending high pressure studies to 300–400 GPa on heavy lanthanides may clarify these trends. Further, in this chapter we have not covered the other extreme that is high pressures and low temperatures where magnetic phase transitions are expected in heavy lanthanide metals and can be investigated by neutron diffraction techniques. The high pressure–low temperature investigations of the rare-earth metals may be very fruitful in that regard.

ACKNOWLEDGMENTS

This work was supported by the Department of Energy (DOE)—National Nuclear Security Administration (NNSA) under Grant No. DE-FG52-10NA29660. Portions of this work were performed at HPCAT (Sector 16), Advanced Photon Source (APS), Argonne National Laboratory. Authors acknowledge contributions from several of the past and present members of the high pressure research group at the University of Alabama at Birmingham (UAB).

ABBREVIATIONS

ADXD	angle dispersive X-ray diffraction
B_0	bulk modulus
B_0^1	pressure derivative of bulk modulus
bcc	body-centered cubic
bct	body-centered tetragonal

dfcc	distorted face-centered cubic
dhcp	double hexagonal close-packed
EDXD	energy dispersive X-ray diffraction
EOS	equation of state
fcc	face-centered cubic
hcp	hexagonal close packed
MUEOS	modified universal equation of state
Sm type	Samarium type

REFERENCES

Akella, J., Xu, J., Smith, G.S., 1986. Physics B&C 139B/140B, 285.

Akella, J., Weir, S.T., Vohra, Y.K., Prokop, H., Catledge, S.A., Chesnut, G.N., 1999. J. Phys. Condens. Matter 11, 6515.

Allen, J.W., Martin, R.M., 1982. Phys. Rev. Lett. 49, 1106.

Baer, B.J., Cynn, H., Iota, V., Yoo, C.S., Shen, G., 2003. Phys. Rev. B 67, 134115.

Bi, W., Meng, Y., Kumar, R.S., Cornelius, A.L., Tipton, W.W., Hennig, R.G., Zhang, Y., Chen, C., Schilling, J.S., 2011. Phys. Rev. B 83, 104106.

Chesnut, G.N., (2001). Ultra-high pressure phase transitions in light rare earth metals. Ph.D. dissertation.

Chesnut, G.N., Vohra, Y.K., 1998. Phys. Rev. B 57, 10221.

Chesnut, G.N., Vohra, Y.K., 1999. Phys. Rev. Lett. 82, 1712.

Chesnut, G.N., Vohra, Y.K., 2000a. Phys. Rev. B 62, 2965.

Chesnut, G.N., Vohra, Y.K., 2000b. Phys. Rev. B 61, R3768.

Cunningham, N.C., Velisavljevic, N., Vohra, Y.K., 2005. Phys. Rev. B 71, 012108.

Cunningham, N.C., Qiu, W., Vohra, Y.K., 2006. High Pres. Res. 26, 43.

Cunningham, N.C., Qiu, W., Hope, K.M., Liermann, H.P., Vohra, Y.K., 2007. Phys. Rev. B 76, 121101.

Endo, S., Sasaki, H., Mitsui, T., 1977. J. Phys. Soc. Jpn 42, 282.

Errandonea, D., Boehler, R., Schwager, B., Mezouar, M., 2007. Phys. Rev. B 75, 014103.

Evans, S.R., Loa, I., Lundegaard, L.F., McMahon, M.I., 2009. Phys. Rev. B 80, 134105.

Grosshans, W.A., Holzapfel, W.B., 1985. J. Magn. Magn. Mater. 47 & 48, 295.

Grosshans, W.A., Holzapfel, W.B., 1992. Phys. Rev. B 45, 1571.

Grosshans, W.A., Vohra, Y.K., Holzapfel, W.B., 1982. Phys. Rev. Lett. 49, 1572.

Haire, R.G., Heathman, S., Benedict, U., 1990. High Pres. Res. 2, 273.

Hamaya, N., Sakamoto, Y., Fujihisa, H., Fujii, Y., Takemura, K., Kikegawa, T., Shimomura, O., 1993. J. Phys. Condens. Matter 5, L369.

Herbst, J.F., 1992. Phys. Rev. B 46, 6665.

Herbst, J.F., Wilkins, J.W., 1984. Phys. Rev. B 29, 5992.

Hua, H., Vohra, Y.K., Akella, J., Weir, S.T., Ahuja, R., Johansson, B., 1998. Rev. High Pressure Sci. Technol. 7, 233.

Jayaraman, A., 1964. Phys. Rev. A 135, 1056.

Johansson, B., 1974. Philos. Mag. 30, 469.

McMahan, A.K., Skriver, H.L., Johansson, B., 1981. Phys. Rev. B 23, 5016.

McMahon, M.I., Nelmes, R.J., 1997. Phys. Rev. Lett. 78, 3884.

McWhan, D.B., Souers, P.C., Jura, G., 1966. Phys. Rev. 143, 385.

Montgomery, J.M., Samudrala, G.K., Tsoi, G., Vohra, Y.K., 2011. J. Phys. Condens. Matter 23, 155701.
Olsen, J.S., Gerward, L., Benedict, U., Itie, J.P., 1985. Phys. B 133, 129.
Patterson, R., Saw, C.K., Akella, J., 2004. J. Appl. Phys. 95, 5443.
Pickett, W.E., Freeman, A.J., Koelling, D.D., 1980. Phys. Rev. B 22, 2695.
Porsch, F., Holzapfel, W.B., 1993. Phys. Rev. Lett. 70, 4087.
Pravica, M.G., Romano, E., Quine, Z., 2005. Phys. Rev. B 72, 214122.
Pravica, M., Quine, Z., Romano, E., 2006. Phys. Rev. B 74, 104107.
Samudrala, G.K., and Vohra, Y.K., (2012). J. Phys.: Conf. Ser. 377, 012111.
Samudrala, G.K., Thomas, S.A., Montgomery, J.M., Vohra, Y.K., 2011. J. Phys. Condens. Matter 23, 315701.
Samudrala G.K., Montgomery, J.M., and Vohra, Y.K. (2012). Compression of Lu to 202 GPa, unpublished.
Shen, Y.R., Kumar, R.S., Cornelius, A.L., Nicol, M.F., 2007. Phys. Rev. B 75, 064109.
Shimomura, O., Takemura, K., Fujihisa, H., Fujii, Y., Ohishi, Y., Kikegawa, T., Amemiya, Y., Matsushita, T., 1992. Rev. Sci. Instrum. 63, 967.
Soderlind, P., 2002. Phys. Rev. B 65, 115105.
Soderlind, P., Eriksson, O., Johansson, B., Wills, J.M., 1995. Phys. Rev. B 52, 13169.
Syassen, K., Wortmann, G., Feldhaus, J., Frank, K.H., Kaindl, G., 1982. Phys. Rev. B 26, 4745.
Takemura, K., Syassen, K., 1985. J. Phys. F 15, 543.
Velisavljevic, N., Vohra, Y.K., 2004. High Pres. Res. 24, 295.
Velisavljevic, N., MacMinn, K.M., Vohra, Y.K., Weir, S.T., 2004. Appl. Phys. Lett. 84, 927.
Velisavljevic, N., Vohra, Y.K., Weir, S.T., 2005. High Pres. Res. 25, 137.
Vohra, Y.K., Akella, J., 1991. Phys. Rev. Lett. 67, 3563.
Vohra, Y.K., Akella, J., Weir, S.T., Smith, G.S., 1991. Phys. Lett. A 158, 89.
Vohra, Y.K., Beaver, S.L., Akella, J., Ruddle, C.A., Weir, S.T., 1999. J. App. Phy. 85, 2451.
Vohra, Y.K., Sangala, B.R., Stemshorn, A.K., Hope, K.M., 2008. Mater. Res. Soc. Symp. Proc. 1104, 1104-NN01-04.
Wittig, J., 1980. Z. Phys. B 38, 11.
Zhao, Y.C., Porsch, F., Holzapfel, W.B., 1994a. Phys. Rev. B 50, 6603.
Zhao, Y.C., Porsch, F., Holzapfel, W.B., 1994b. Phys. Rev. B 49, 815.

Intentionally left as blank

Chapter 258

Selected Values of the Thermodynamic Properties of Scandium, Yttrium, and the Lanthanide Elements

John W. Arblaster
Poolhouse Farm, West Midlands, United Kingdom

Chapter Outline

Handbook on the Physics and Chemistry of Rare Earths, Vol. 43.
http://dx.doi.org/10.1016/B978-0-444-59536-2.00005-2

1. INTRODUCTION

1.1. The Rare Earths

Scandium, yttrium, and the lanthanides represent 17% of all of the elements that can be obtained in coherent form. In view of their similar chemical behavior separation of these elements proved to be formidable (Szabadvary, 1988) but all of the metals have now been obtained in relatively high purity and, except for promethium, their thermodynamic properties have been measured with varying degrees of quality. Based on the interpolation of the properties of neighboring elements, it has also been possible to estimate the thermodynamic properties of promethium in order to complete this review. Because of the radioactive nature of this element and the fact that the most stable isotope has half-life of only 17.7 years, it is unlikely that further measurements will be carried out beyond the very basic properties which have already been determined.

1.2. Previous Reviews

When Stull and Sinke (1956) reviewed the thermodynamic properties of the elements, data available for scandium, yttrium, and the lanthanides were meager and most values were estimated. However, by the time of the review by Hultgren et al. (1973), much new data had become available and this review became the most comprehensive for all of these elements except promethium. Contemporary to this review, Holley et al. (1968) reviewed the thermodynamic properties of the condensed phases except promethium using basically the same input data. Gurvich et al. (1982) reviewed scandium, yttrium, and lanthanum; Cordfunke and Konings (1990) reviewed lanthanum, europium, and neodymium; and Shen et al. (1995) reviewed yttrium, gadolinium, and dysprosium. Stull and Sinke (1956) and Hultgren et al. (1973) only gave tabulated data, but the remainder gave both tabulated data and representative equations. Therefore in all of these reviews, there was a significant amount of redundancy so that any errors tended to be revealed. However, in the latest review by Konings and Beneš (2010), a minimalist approach was used in which only the entropies at 298.15 K, enthalpies of fusion, and transition and heat capacity equations were used to represent the data. Therefore, if there were errors in any of the equations, there was no redundancy to reveal these errors. Because the approach used by Konings and Beneš (2010) may represent an unfortunate modern trend in reviewing thermodynamic data, then in this review, the data have been deliberately given in explicit detail to avoid this trend. Further differences from the recent review by Konings and Beneš (2010) include the following:

a. the present acceptance of the upper transition temperatures and melting points selected by Gschneidner (1990);
b. the input of a significant amount of unpublished data supplied by Ames Laboratory staff (Gschneidner, 1991; Pecharsky, 2006);
c. the addition of a major number of new energy levels for calculating the thermodynamic properties of the gas phases beyond those originally given by Martin et al. (1978).

2. THE CALCULATION OF THERMODYNAMIC DATA

2.1. Fixed Values

The melting points and upper transition temperatures are those selected by Gschneidner (1990) as being the best values obtained in the Ames Laboratory and are therefore the most representative of the pure metals. The only exception is for neodymium where the later Ames Laboratory values of Gschneidner and Beaudry (1991) were accepted. However, these agree with the selected values of Gschneidner (1990) to within 1 K.

Wherever possible, values have been corrected to the 2009 atomic weights (Wieser and Coplen, 2011) except for ^{147}Pm where the atomic mass value of 146.9151385 was selected (Audi et al., 2003b). Although attempts were made to correct to the ITS-90 temperature scale (Douglas, 1969; Weir and Goldberg, 1996) because of a lack of detail at to what temperature scales had been used, these corrections could only be applied in a very limited number of cases. In particular, for this reason, no corrections were applied to any of the vapor pressure measurements.

2.2. Analytical Expressions

$$
\begin{aligned}
&C^\circ{}_p(T) = a_1 + a_2T + a_3T^2 + a_4T^3 + a_5/T^2\\
&H^\circ(T) - H^\circ(298) = a_1T + (a_2/2)T^2 + (a_3/3)T^3 + (a_4/4)T^4 - a_5/T + a_6\\
&S^\circ(T) = a_1\ln(T) + a_2T + (a_3/2)T^2 + (a_4/3)T^3 - (a_5/2)/T^2 + a_7\\
&\qquad -[G^\circ(T) - H^\circ(298)]/T = a_1\ln(T) + a_7 - a_1 + (a_2/2)T + (a_3/6)T^2\\
&\qquad +(a_4/12)T^3 + (a_5/2)/T^2 - a_6/T\\
&G^\circ(T) - H^\circ(298) = -a_1T\ln(T) + T(a_1 - a_7) - (a_2/2)T^2 - (a_3/6)T^3\\
&\qquad\qquad -(a_4/12)T^4 - (a_5/2)/T + a_6
\end{aligned}
$$

2.3. Calculation of the Thermodynamic Properties of an Ideal Monatomic Gas

The thermodynamic properties of the gases were calculated using the method of Kolsky et al. (1957). All values given correspond to the 2010 Fundamental Constants (Mohr et al., 2011) and to one bar standard state pressure:

$$
\begin{aligned}
&\text{Gas constant} = R = 8.3144621 \pm 0.0000075\,\text{J/(mol K)}\\
&\text{Second radiation constant} = c_2 = 0.014387770 \pm 0.000000013\,\text{m K}\\
&\alpha = 100c_2 = 1.4387770\,\text{cm K}\\
&K1 = R\alpha = 11.96265684\,\text{J cm/mol}\\
&K2 = 2.5R = 20.78615525\,\text{J/(mol K)}\\
&K3 = R\alpha^2 = 17.21159552\,\text{J cm}^2\,\text{K/mol}\\
&K4 = 1.5R = 12.47169315\,\text{J/(mol K)}\\
&K5 = S_0 = \text{Sackur} - \text{Tetrode constant} = -9.57583085\,\text{J/(mol K)}\\
&K6 = K5 - 2.5R = -30.36198610\,\text{J/(mol K)}
\end{aligned}
$$

2.3.1. Partition Functions

$$\text{Atomic weight} = A_r$$
$$\text{Energy level of } i\text{th electronic state} = \varepsilon_i\ \text{cm}^{-1}$$
$$\text{Degeneracy(statistical weight)of } i\text{th electronic state} = g_i$$
$$Q = \Sigma(2g_i+1)\exp(-\alpha\varepsilon_i/T);\quad Q1 = \Sigma(2g_i+1)\varepsilon_i\exp(-\alpha\varepsilon_i/T);$$
$$Q2 = \Sigma(2g_i+1)\varepsilon_i^2\exp(-\alpha\varepsilon_i/T)$$

2.3.2. Thermodynamic Equations

$$C^\circ{}_p(T)(\text{J/(mol K)}) = (K3/T^2)\left(Q2/Q1 - (Q1/Q)^2\right) + K2$$
$$H^\circ(T) - H^\circ(0)(\text{J/mol}) = K1(Q1/Q) + K2T$$
$$S^\circ(T)(\text{J/(mol K)}) = (K1/T)(Q1/Q) + R\ln(Q) + K4\ln(A_r) + K2\ln(T) + K5$$
$$-[G^\circ(T) - H^\circ(0)]/T(\text{J/(mol K)}) = R\ln(Q) + K4\ln(A_r) + K2\ln(T) + K6$$
$$= S^\circ(T) - [H^\circ(T) - H^\circ(0)]/T$$
$$H^\circ(T) - H^\circ(298) = [H^\circ(T) - H^\circ(0)] - [H^\circ(298) - H^\circ(0)]$$
$$-[G^\circ(T) - H^\circ(298)]/T = -[G^\circ(T) - H^\circ(0)]/T + [H^\circ(298) - H^\circ(0)]/T$$

2.3.3. Vapor Pressure

$$\Delta H^\circ(T) = \Delta_{\text{sub}} H^\circ(298) - \delta[H^\circ(T) - H^\circ(298)]$$
$$\Delta G^\circ(T) = \Delta_{\text{sub}} H^\circ(298) - T\delta\{-[G^\circ(T) - H^\circ(298)]/T\}$$
$$\ln(p,\text{bar}) = -\Delta G^\circ/RT$$
$$\delta[H^\circ(T) - H^\circ(298)] = H^\circ(T) - H^\circ(298)(g) - H^\circ(T) - H^\circ(298)(\text{cr,liq})$$
$$\delta\{-[G^\circ(T) - H^\circ(298)]/T\} = -[G^\circ(T) - H^\circ(298)]/T(g) - [G^\circ(T) - H^\circ(298)]/T(\text{cr,liq})$$

Vapor pressure is expressed by the equation

$$\ln(p,\text{bar}) = b_1 + b_2/T + b_3\ln(T) + b_4T + b_5T^2$$

The derivation of this equation is explained by Arblaster (2007).

2.3.4. Enthalpy of Sublimation

Third Law

$$\Delta_{\text{sub}}H^\circ(298,\text{III law}) = T\delta\{-[G^\circ(T) - H^\circ(298)]/T\} - R\ln(p,\text{bar})$$

Revised Second Law

$$\delta\{-[G^\circ(T) - H^\circ(298)]/T\} - R\ln(p,\text{bar}) = B + A/T$$

$$\Delta_{\text{sub}}H^\circ(298,\text{II law}) = A,\quad \text{while } B = \text{entropy drift} = \delta S^\circ(\text{III}) - \delta S^\circ(\text{II})$$

Ideally, B is zero and any deviation from zero may indicate the degree to which the vapor pressure measurements may be in error.

Traditional Second Law

$$\ln(p,\text{bar}) = B + A/T(\text{Clausius} - \text{Clapeyron equation})$$

$$\Delta_{\text{sub}}H^{\circ}(298,II\text{law}) = -\delta[H^{\circ}(T) - H^{\circ}(298)] - RA$$

For vapor pressure values given only in the form of the Clausius–Clapeyron equation a "pseudo" Third Law value is calculated by evaluating the enthalpy of sublimation at the temperature extremes and averaging. The value obtained gives a reasonable estimate compared to the value that would have been obtained if all the data had been available. For vapor pressure measurements, the Revised method is used to calculate the Second Law enthalpy of sublimation, but for mass spectrographic measurements fitted to the Clausius–Clapeyron equation, the Traditional method is used.

2.4. The Calculation of the Nuclear Heat Capacity

The nuclear contribution to the heat capacity can be respresented by:

$$C^{\circ}{}_{N}(T) = X\left(A/T^2 + B/T^3 + C/T^4 + \text{L}\right)$$

where X is the atomic fraction of the isotope.

If a' is the magnetic interaction parameter, P is the quadrupole coupling constant, I is the nuclear spin, and R is the gas constant, then

$$A/R = 1/3a'^2 I(I+1) + 1/45P^2 I(I+1)(2I-1)(2I+3) + \text{L}$$
$$B/R = -1/15a'^2 PI(I+1)(2I-1)(2I+3) + \text{L}$$
$$C/R = -1/30a'^2 I(I+1)(2I^2+2I+1) + \text{L}$$

It is considered that the additional terms contribute negligibly to the heat capacity, and therefore, the calculations are restricted to the following terms.

$$I = 1/2 : A/R = a'^2/4 : B/R = 0 : C/R = -a'^4/16$$
$$I = 3/2 : A/R = 5/4a'^2 + P^2 : B/R = -3a'^2 P : C/R = -17/16a'^4$$
$$I = 5/2 : A/R = 35/12a'^2 + 56/9P^2 : B/R = -56/3a'^2 P : C/R = -259/48a'^4$$
$$I = 7/2 : A/R = 21/4a'^2 + 21P^2 : B/R = -63a'^2 P : C/R = -273/16a'^4$$

3. THERMODYNAMIC FUNCTIONS OF SCANDIUM

3.1. Introduction

Gschneidner (1990) selected 1610 K for the alpha–beta transformation from a hexagonal close-packed to a body-centered cubic structure and 1814 K for the melting point.

3.2. Alpha Phase at Low Temperature

Below 4 K, the heat capacity can be represented by the electronic coefficient (γ) and the limiting Debye temperature (θ_D) (Table 1).

The values of Swenson (1996) are selected since in combination with the heat capacity measurements of Gerstein et al. (1971) (6–350 K), Swenson (1996) gives representative equations of up to 350 K. The above value for the Debye temperature may be compared to 354.2 K calculated by Pleschiutschnig et al. (1991) from inelastic neutron scattering measurements.

Heat capacity measurements of Tsang et al. (1976b, 1985) on average deviate from 1% low initially to 2% high at 11 K before converging to the selected values at 20 K. Above 4 K, the values were only shown graphically with actual data point being given by Gschneidner (1991).

The measurements of Flotow and Osborne (1967) are initially 15% higher and then converge to the selected values to become on average 1% lower above 15 K, while those of Weller and Kelley (1962) (53–296 K) are generally lower but agree to better than 1% above 150 K. The heat capacity measurements of Sirota and Kudel'ko (1973) (10–300 K) are generally higher than the selected curve but scatter 8% lower to 17% higher.

TABLE 1 Low-Temperature Heat Capacity Coefficients

Authors	Temperature range (K)	γ (mJ/(mol K^2))	θ_D (K)
Montgomery and Pells (1961)	1.7–4.2	11.3	470
Lyman et al. (1965)	0.15–3	10.9	344
Flotow and Osborne (1967)	0.9–22.6	10.66	359.5
Betterton and Scarbrough (1968)	1.1–4.2	10.717	425.6
Isaacs (1973)	0.5–4.2	10.72	359
Tsang et al. (1976a,b)	1–20	10.340	346.1
Tsang et al. (1985)	1–20	10.334	345.3
		10.33[a]	346.3[a]
Swenson (1996)	1–110	10.38	352.2
Selected		10.38	352.2

[a] *As corrected by Swenson (1996).*

3.3. Alpha Phase at High Temperature

Enthalpy measurements have been determined by Dennison et al. (1966a) (373–1810 K) and Lyapunov et al. (2001) (407–1782 K). The values of Dennison et al. (1966a) were given only in the form of an equation and tabulated values with actual data points being supplied by Gschneidner (1991). These measurements were corrected to ITS-90 and from a 273.15 to a 298.15 K base by subtracting 634.21 J/mol obtained from the low-temperature selected values. A Shomate plot indicates that the two sets of measurements do not agree and cannot be processed jointly. Therefore, the later measurements of Lyapunov et al. (2001) were selected in preference because of the much higher purity of the material used and in consideration of the likely improvements in techniques in the 35-year gap between the measurements. The Shomate plot also indicated that the two lowest measurements of Lyapunov et al. (2001) were incompatible with the remainder of the data and were rejected. The remaining data were then fitted to the following equation with an overall accuracy as a standard deviation of ±55 J/mol (0.20%):

$$H^{\circ}(T) - H^{\circ}(298)(\mathrm{J/mol}) = 29.1803T - 2.03166 \times 10^{-3}T^2 + 2.10347 \times 10^{-6}T^3 + 263{,}299/T - 9458.36$$

The measurements of Dennison et al. (1966a) are initially up to 5% lower than the selected values and then show a trend to become 4% higher at 1586 K.

3.4. Beta Phase

Enthalpy measurements were performed by Dennison et al. (1966a) (1610–1743 K) and Lyapunov et al. (2001) (1633–1782 K). After correction of the measurements of Dennison et al. (1966a) as described above, they were on average found to agree to better than 1% with the measurements of Lyapunov et al. (2001) where the latter can be represented by the following equation with an overall accuracy as a standard deviation of ±80 J/mol (0.15%):

$$H^{\circ}(T) - H^{\circ}(298)(\mathrm{J/mol}) = 44.1542T - 25{,}786.60$$

The derived heat capacity is 44.15 ± 0.47 J/(mol K), and the enthalpy of transition is 4105 ± 97 J/mol.

3.5. Liquid Phase

Only one enthalpy value was determined in the liquid phase, by Dennison et al. (1966a) at the melting point. After correction for tantalum contamination due to partial dissolution of the liquid scandium in the tantalum container following the method of Dennison et al. (1966b), the derived enthalpy of fusion is 14,096 J/mol which is considered to be intrinsic and independent of any

systematic errors in the measurements. Dennison et al. (1966a) suggested that the actual effect of the tantalum contamination may not have been properly accounted for and that the derived enthalpy of fusion could be too low. However, the equivalent entropy of fusion at 7.77 J/(mol K) is higher than an estimated value of 7.58 J/(mol K) calculated from a relationship between entropies of fusion and melting points by Chekhovskoi and Kats (1981), so it is possible that the value may be considered to be satisfactory. In agreement with Gurvich et al. (1982), it is assumed that the heat capacities of the solid and the liquid at the melting point are similar, and therefore, a value of 44 J/(mol K) is selected and the enthalpy of the liquid can be represented by

$$H^{\circ}(T) - H^{\circ}(298)(\mathrm{J/mol}) = 44.0000T - 11{,}410.86$$

3.6. Gas Phase

Values are based on one bar standard state pressure and are calculated from 288 energy levels below 50,000 cm^{-1} selected by Ralchenko et al. (2012) which include 33 levels measured by Garton et al. (1973b) which were not given degeneracy weighting (g_i) assignments by Ralchenko et al. (2012), but Garton et al. (1973a,b) suggested that the value could be either 3/2 or 5/2, so an average was taken. The thermodynamic properties were calculated using the method of Kolsky et al. (1957) and the 2010 Fundamental Constants (Mohr et al., 2011).

3.7. Enthalpy of Sublimation

TABLE 2 Enthalpy of Sublimation at 298.15 K

Authors	Methods	Temperature Range (K)	$\Delta_{sub}H^{\circ}$(298, II law) (kJ/mol)	$\Delta_{sub}H^{\circ}$(298, III law) (kJ/mol)	Notes
Vergen et al. (1965)	MS	1200–1500	380	–	–[a]
Ackermann and Rau (1962)	MS	1420–1720	336 ± 2	–	
	MS	1460–1845	349 ± 3	–	
DeMaria et al. (1963a)	MS	1255–1572	348 ± 2	–	
Spedding et al. (1960a)	KE	1340–1748	361 ± 5	376.3 ± 0.3	–[b]

TABLE 2 Enthalpy of Sublimation at 298.15 K—Cont'd

Authors	Methods	Temperature Range (K)	$\Delta_{sub}H°$(298, II law) (kJ/mol)	$\Delta_{sub}H°$(298, III law) (kJ/mol)	Notes
Ackermann and Rau (1962)	KE	1555–1760	349 ± 5	374.6 ± 0.6	
Karelin et al. (1962a)	KE	1301–1644	350 ± 4	371.1 ± 0.5	–[c]
Krikorian (1963)	KE	1477–1838	378 ± 2	380.8 ± 0.4	–[d]
Habermann (1963)	KE	1528–1797	391 ± 4	378.8 ± 0.2	–[e]
Habermann and Daane (1964)	KE	1521–1813	384 ± 2	378.7 ± 0.5	–[f]
Selected				379.0 ± 5.0	

MS, mass spectrometry; KE, Knudsen effusion.
[a]*Value quoted by Hultgren et al. (1973).*
[b]*Four discrepant data points at 1360, 1414, 1716, and 1748 K were rejected.*
[c]*One discrepant data point at 1574 K rejected.*
[d]*Four data points rejected by the author were not included.*
[e]*This is Run 2 of Habermann and Daane (1964) given in detail.*
[f]*Results given only in the form of the Clausius–Clapeyron equation.*

The selected value is based on a combination of the measurements of Spedding et al. (1960a), Krikorian (1963), Habermann (1963), and Habermann and Daane (1964). The two other Knudsen effusion experiments of Ackermann and Rau (1962) and Karelin et al. (1962a) showed marked differences between Second and Third Law-derived enthalpies of sublimation were not included.

3.8. Vapor Pressure

For the alpha phase, the vapor pressure equation was derived by evaluating the solid and gas free energy functions at 25 K intervals from 800 to 1600 K and the transition temperature; for the beta phase, at 20 K intervals from 1630 to 1810 K and the transition temperature and melting point; and for the liquid phase, at 50 K intervals from 1850 to 3200 K and the melting point (Table 3).

TABLE 3 Vapor Pressure Equations

$\ln(p, \text{bar}) = b_1 + b_2/T + b_3 \ln(T) + b_4 T + b_5 T^2$

Phase	Range (K)	b_1	b_2	b_3	b_4	b_5
Alpha	800–1610.15	22.16499	−45,850.00	−0.7651022	9.25454×10^{-5}	-1.08869×10^{-7}
Beta	1610.15–1814.15	38.13285	−47,940.93	−2.786040	0	0
Liquid	1814.15–3200	29.20997	−45,542.32	−1.645949	-6.33710×10^{-4}	6.11547×10^{-8}

3.9. Comparison of Selected Values at 298.15 K

Both Holley et al. (1968) and Hultgren et al. (1973) relied on the values of Weller and Kelley (1962) which included estimated values below 54 K. Gurvich et al. (1982) utilized the later heat capacity values of Gerstein et al. (1971), while in this review, values were calculated from the equations given by Swenson (1996) (Table 4).

TABLE 4 Comparison of Heat Capacity, Enthalpy, and Entropy Values at 298.15 K

Authors	$C°_p(298)$ (J/(mol K))	$H°(298) - H°(0)$ (J/mol)	$S°(298)$ (J/(mol K))
Holley et al. (1968)	25.52	5181	34.43
Hultgren et al. (1973)	25.52	5217	34.64
Gurvich et al. (1982)	25.51	5207	34.77
This work	25.57	5206	34.76

3.10. Summary of Representative Equations

TABLE 5 Representative Equations Above 298.15 K

Alpha phase: 298.15–1610.15 K
$C°_p(T)(\text{J/(mol K)}) = 29.1803 - 4.06332 \times 10^{-3} T + 6.31041 \times 10^{-6} T^2 - 263299/T^2$
$H°(T) - H°(298)(\text{J/mol}) = 29.1803T - 2.03166 \times 10^{-3} T^2 + 2.10347 \times 10^{-6} T^3 + 263299/T - 9458.36$

TABLE 5 Representative Equations Above 298.15 K—Cont'd

$S^\circ(T)(\text{J/(mol K)}) = 29.1083\ \ln(T) - 4.06332 \times 10^{-3} T + 3.155205 \times 10^{-6} T^2 + 131649.5/T^2 - 132.0449$
Beta phase: 1610.15–1814.15 K
$C^\circ_p(T)(\text{J/(mol K)}) = 44.1542$
$H^\circ(T) - H^\circ(298)(\text{J/mol}) = 44.1542T - 25,786.60$
$S^\circ(T)(\text{J/(mol K)}) = 44.1542\ \ln(T) - 238.3757$
Liquid phase: 1814.15–3200 K
$C^\circ_p(T)(\text{J/(mol K)}) = 44.0000$
$H^\circ(T) - H^\circ(298)(\text{J/mol}) = 44.0000T - 11,410.86$
$S^\circ(T)(\text{J/mol K}) = 44.0000\ \ln(T) - 229.4486$

TABLE 6 Free Energy Equations Above 298.15 K

Alpha phase: 298.15–1610.15 K
$G^\circ(T) - H^\circ(298)(\text{J/mol}) = 161.2252T + 2.03166 \times 10^{-3} T^2 - 1.051735 \times 10^{-6} T^3 + 131649.5/T - 29.1803T\ln(T) - 9458.36$
Beta phase: 1610.15–1814.15 K
$G^\circ(T) - H^\circ(298)(\text{J/mol}) = 282.5299T - 44.1542T\ln(T) - 25,786.60$
Liquid phase: 1814.15–3200 K
$G^\circ(T) - H^\circ(298)(\text{J/mol}) = 273.4486T - 44.0000T\ln(T) - 11,410.86$

TABLE 7 Transition Values Associated with the Free Energy Equations

Transition	T (K)	ΔH° (J/mol)	ΔS° (J/(mol K))
Alpha–beta	1610.15	4104.883	2.5494
Fusion	1814.15	10,496.000	7.7700

3.11. Thermodynamic Tables

TABLE 8 Low-Temperature Thermodynamic Data

T (K)	$C°_p(T)$ (J/(mol K))	$H°(T)-H°(0)$ (J/mol)	$S°(T)$ (J/(mol K))	$-[G°(T)-H°(0)]/T$ (J/(mol K))
5	0.0574	0.137	0.0537	0.0264
10	0.148	0.628	0.118	0.0555
15	0.316	1.742	0.206	0.0903
20	0.634	4.041	0.337	0.135
25	1.161	8.434	0.530	0.193
30	1.927	16.06	0.806	0.271
35	2.901	28.05	1.174	0.373
40	4.028	45.32	1.634	0.501
45	5.243	68.48	2.178	0.656
50	6.507	97.84	2.795	0.839
60	9.031	175.6	4.206	1.279
70	11.362	277.8	5.777	1.808
80	13.383	401.8	7.430	2.407
90	15.085	544.4	9.107	3.058
100	16.515	702.6	10.773	3.747
110	17.864	874.6	12.411	4.460
120	18.914	1059	14.012	5.190
130	19.806	1252	15.562	5.928
140	20.568	1454	17.058	6.670
150	21.226	1663	18.500	7.411
160	21.797	1879	19.889	8.148
170	22.296	2099	21.225	8.878
180	22.735	2324	22.512	9.600
190	23.124	2554	23.752	10.312
200	23.469	2787	24.947	11.014
210	23.776	3023	26.100	11.705

TABLE 8 Low-Temperature Thermodynamic Data—Cont'd

T (K)	$C^\circ_p(T)$ (J/(mol K))	$H^\circ(T)-H^\circ(0)$ (J/mol)	$S^\circ(T)$ (J/(mol K))	$-[G^\circ(T)-H^\circ(0)]/T$ (J/(mol K))
220	24.052	3262	27.212	12.385
230	24.301	3504	28.287	13.053
240	24.527	3748	29.326	13.710
250	24.734	3994	30.332	14.355
260	24.926	4243	31.306	14.980
270	25.106	4493	32.250	15.610
280	25.277	4745	33.166	16.211
290	25.440	4998	34.056	16.820
298.15	25.568	5206	34.763	17.301

TABLE 9 High-Temperature Thermodynamic Data

T (K)	$C^\circ_p(T)$ (J/(mol K))	$H^\circ(T)-H^\circ(298)$ (J/mol)	$S^\circ(T)$ (J/(mol K))	$-[G^\circ(T)-H^\circ(298)]/T$ (J/(mol K))
Alpha phase				
298.15	25.568	0	34.763	34.763
300	25.604	47	34.921	34.763
400	26.919	2682	42.490	35.786
500	27.673	5413	48.583	37.756
600	28.283	8212	53.683	39.997
700	28.891	11,070	58.088	42.274
800	29.557	13,992	61.988	44.499
900	30.310	16,984	65.512	46.641
1000	31.164	20,057	68.749	48.692
1100	32.219	23,221	71.764	50.654
1200	33.208	26,487	74.605	52.532

Continued

TABLE 9 High-Temperature Thermodynamic Data—Cont'd

T (K)	$C°_p(T)$ (J/(mol K))	$H°(T) - H°(298)$ (J/mol)	$S°(T)$ (J/(mol K))	$-[G°(T) - H°(298)]/T$ (J/(mol K))
1300	34.407	29,866	77.309	54.335
1400	35.726	33,372	79.907	56.069
1500	37.167	37,016	82.420	57.743
1600	38.731	40,809	84.868	59.362
1610.15	38.896	41,203	85.113	59.523
Beta phase				
1610.15	44.154	45,308	87.663	59.523
1700	44.154	49,276	90.060	61.075
1800	44.154	53,691	92.584	62.756
1814.15	44.154	54,316	92.930	62.990
Liquid phase				
1814.15	44.000	68,412	100.700	62.990
1900	44.000	72,189	102.734	64.740
2000	44.000	76,589	104.991	66.697
2100	44.000	80,989	107.138	68.572
2200	44.000	85,389	109.185	70.372
2300	44.000	89,789	111.141	72.102
2400	44.000	94,189	113.013	73.768
2500	44.000	98,589	114.809	75.374
2600	44.000	102,989	116.535	76.924
2700	44.000	107,389	118.196	78.422
2800	44.000	111,789	119.796	79.871
2900	44.000	116,189	121.340	81.275
3000	44.000	120,389	122.832	82.635
3100	44.000	124,989	124.274	83.955
3200	44.000	129,389	125.671	85.237

TABLE 10 Thermodynamic Properties of the Gas Phase

T (K)	$C^\circ_p(T)$ (J/(mol K))	$H^\circ(T) - H^\circ$ (298) (J/mol)	$S^\circ(T)$ (J/(mol K))	$-[G^\circ(T) - H^\circ(298)]/T$ (J/(mol K))
298.15	22.103	0	174.787	174.787
300	22.088	41	174.923	174.787
400	21.541	2219	181.193	175.646
500	21.273	4358	185.967	177.251
600	21.125	6477	189.832	179.036
700	21.035	8585	193.081	180.817
800	20.976	10,685	195.885	182.529
900	20.936	12,781	198.354	184.153
1000	20.908	14,873	200.558	185.685
1100	20.888	16,963	202.550	187.129
1200	20.875	19,051	204.366	188.491
1300	20.869	21,138	206.037	189.777
1400	20.873	23,225	207.584	190.995
1500	20.890	25,313	209.024	192.149
1600	20.923	27,403	210.373	193.246
1610.15	20.928	27,616	210.506	193.355
1700	20.979	29,498	211.643	194.292
1800	21.063	31,600	212.845	195.289
1814.15	21.077	31,898	213.010	195.427
1900	21.181	33,712	213.987	196.244
2000	21.338	35,837	215.077	197.158
2100	21.541	37,981	216.123	198.036
2200	21.796	40,147	217.130	198.882
2300	22.106	42,342	218.106	199.696
2400	22.476	44,571	219.054	200.483
2500	22.908	46,839	219.980	201.245
2600	23.404	49,154	220.888	201.983
2700	23.964	51,522	221.782	202.700

Continued

TABLE 10 Thermodynamic Properties of the Gas Phase—Cont'd

T (K)	$C^\circ_p(T)$ (J/(mol K))	$H^\circ(T)-H^\circ$ (298) (J/mol)	$S^\circ(T)$ (J/(mol K))	$-[G^\circ(T)-H^\circ(298)]/T$ (J/(mol K))
2800	24.588	53,949	222.664	203.397
2900	25.274	56,442	223.539	204.076
3000	26.019	59,006	224.408	204.740
3100	26.820	61,648	225.274	205.388
3200	27.670	64,372	226.139	206.023

$H^\circ(298)-H^\circ(0)=7002.2$ J/mol.

TABLE 11 Vapor Pressure Data

T (K)	p (bar)	$\Delta G^\circ(T)$ (J/mol)	$\Delta H^\circ(T)$ (J/mol)	p (bar)	T (K)
298.15	8.24×10^{-60}	337,252	379,000	10^{-15}	892
300	2.12×10^{-59}	336,993	378,994	10^{-14}	935
400	6.52×10^{-43}	323,056	378,537	10^{-13}	982
500	4.93×10^{-33}	309,252	377,945	10^{-12}	1034
600	1.85×10^{-26}	295,577	377,265	10^{-11}	1092
700	9.03×10^{-22}	282,020	376,515	10^{-10}	1157
800	2.91×10^{-18}	268,576	375,693	10^{-9}	1230
900	1.54×10^{-15}	255,239	374,797	10^{-8}	1314
1000	2.29×10^{-13}	242,007	373,816	10^{-7}	1409
1100	1.35×10^{-11}	228,877	372,742	10^{-6}	1521
1200	4.02×10^{-10}	215,850	371,564	10^{-5}	1653
1300	7.02×10^{-9}	202,925	370,272	10^{-4}	1813
1400	8.08×10^{-8}	190,105	368,853	10^{-3}	2019
1500	6.65×10^{-7}	177,390	367,297	10^{-2}	2283
1600	4.17×10^{-6}	164,785	365,594	10^{-1}	2633
1610.15	4.96×10^{-6}	163,511	365,413	1	3125
1610.15	4.96×10^{-6}	163,511	361,308	NBP	3129
1700	2.06×10^{-5}	152,531	359,222		

TABLE 11 Vapor Pressure Data—Cont'd

T (K)	p (bar)	$\Delta G°(T)$ (J/mol)	$\Delta H°(T)$ (J/mol)	p (bar)	T (K)
1800	8.41×10^{-5}	140,439	356,909		
1814.15	1.01×10^{-4}	138,739	356,582		
1814.15	1.01×10^{-4}	138,739	342,486		
1900	2.82×10^{-4}	129,143	340,523		
2000	8.25×10^{-4}	118,077	338,249		
2100	2.17×10^{-3}	107,124	335,992		
2200	5.18×10^{-3}	96,278	333,759		
2300	1.14×10^{-2}	85,533	331,553		
2400	2.35×10^{-2}	74,883	329,382		
2500	4.52×10^{-2}	64373	327,250		
2600	8.28×10^{-2}	53,847	325,165		
2700	0.144	43,450	323,133		
2800	0.241	33,128	321,160		
2900	0.387	22,875	319,253		
3000	0.601	12,686	317,617		
3100	0.906	2558	315,659		
3125.35	1	0	315,226		
3200	1.326	−7515	313,983		

NBP, normal boiling point at one atmosphere pressure (1.01325 bar).
$\Delta H°(0) = 377,204$ J/mol.

4. THERMODYNAMIC FUNCTIONS OF YTTRIUM

4.1. Introduction

Gschneidner (1990) selects 1751 K for the alpha–beta transformation from a hexagonal close-packed to a body-centered cubic structure and 1795 K for the melting point.

4.2. Alpha Phase—Low Temperature

The values given in Table 12 have been determined for the electronic coefficient (γ) and the limiting Debye temperature (θ_D).

The revised values of Tsang et al. were selected. The value of θ_D is in close agreement with the value of 245 K obtained by Sinha et al. (1970) from

TABLE 12 Low-Temperature Heat Capacity Coefficients

Authors	Temperature range (K)	γ (mJ/(mol K^2))	θ_D (K)
Montgomery and Pells (1961)	1.7–4.2	10.2	300
Morin and Maita (1963)	1.5–20	10.1	235
Bonneret et al. (1966)	2–40	9.4	232
Satoh and Ohtsuka (1966, 1967)	1.1–4.2	10.5	330
Ohtsuka and Sato (1966)			
Cetas et al. (1969)	1–26	8.75	276
Wells et al. (1976)	1.6–15	8.2	248
Tsang et al. (1985)	1.3–20.6	7.878	244.4
		7.851[a]	244.1[a]
Devyatykh et al. (2004)	2.0–15.1	7.92	243
Selected		7.851	244.1

[a]*Revised values from the present evaluation 1.3–4.9 K.*

neutron scattering measurements but in relatively poor agreement with the value of 255.2 K obtained by Palmer (1978) from elastic constant measurements on single crystals.

Up to 298.15 K selected values are based on a combination of the heat capacity values of Tsang et al. (1985) and Berezovskii et al. (1989) (8–296 K) because of the very high purity and precision of these two sets of measurements in comparison with other determinations. Above 4 K, the measurements of Tsang et al. were only shown graphically with actual data points being given by Gschneidner (1991).

Heat capacity measurements of Cetas et al. (1969) are initially 11% higher than the selected values but quickly fall to become lower with an average of 2% lower at 20 K and above, while the measurements of Wells et al. (1976) show some scatter but are generally much higher than the selected values and average at 3% higher over the whole temperature range. The measurements of Devyatykh et al. (2004) are initially higher than the selected value but then are generally lower above 3.6 K averaging 1% low. The smoothed values of Jennings et al. (1960) (5–340 K) are above 20 K up to 2% lower before tending to 1% higher in the room temperature region. The metal used was particularly impure containing 0.44% tantalum, 0.97% yttrium oxyfluoride, and 0.5% other metals. While attempts were made to correct for the tantalum and oxyfluoride contaminants, the heat capacity values of the oxyfluoride were unknown and were therefore

estimated so that the correction for the oxyfluoride could introduce considerable uncertainties in the corrected values.

Smooth values of Sirota and Tomilo (1982) (4–300 K) are initially nearly 25% higher than the selected values but above 30 K become lower by up to 4% in the 100-K region before converging to the selected values and are only 1% lower above 250 K.

Measurements of Shen (1994) (115–900 K) in this region are initially 7% lower but then become higher than the selected values above 173 K with an average of 2% higher from 213 to 300 K. Apart from the initial difference, these values are well within the 5% accuracy assigned to these values.

4.3. Alpha Phase—High Temperature

In spite of containing 1% of tantalum, in agreement with previous reviews, the enthalpy measurements of Berg et al. (1961) (373–1746 K in the alpha range) are preferred to those of Welty et al. (1963) (401–1301 K) because of the closer agreement with the value of heat capacity selected at room temperature. After correction for temperature scale and atomic weight and from a 273.15 to a 298.15 K base by subtracting 654.90 J/mol as determined from the low-temperature selected values, a Shomate plot indicates that the values below 772 K deviate and are therefore rejected. The remaining values 772–1746 K were fitted to the following equation which has an overall accuracy as a standard deviation of ±144 J/mol (0.32%):

$$H^\circ(T) - H^\circ(298)(\mathrm{J/mol}) = 24.1832T + 3.66724 \times 10^{-3}T^2 + 7412.44/T - 7561.08$$

The enthalpy measurements of Welty et al. (1963) disagree notably being initially 14% higher before falling to 1% higher at 800 K and then increasing again to 6% higher at 1300 K.

The heat capacity equation of Suganeyev et al. (1970) (293–673 K) deviates strongly giving an initial value 10% higher but then climbing to 168% higher at 673 K. In the high-temperature region, the measurements of Shen (1994) (115–900 K) are initially 2% higher but then become about 1% lower above 500 K. However, this is well within the accuracy of 5% assigned to these measurements. The heat capacity values of Novikov and Mardykin (1974) (1000–1700 K) were given only graphically with actual data points being given by Shen et al. (1995). Although initially agreeing with the selected values, they gradually deviate and reach 7% higher at 1698 K. However, the later measurements of Novikov et al. (1978) (1100–2100 K) differ considerably from these earlier measurements. After correction from heat capacity–density to heat capacity by using the density measurements of Stankus and Basin (1980), the values are on average 15% lower in the solid region than the selected values, while, in comparison, the older measurements are from 17% to 27% higher than the newer measurements. This indicates major

problems with this multiproperty-determining technique and on these grounds neither of the sets of measurements by Novikov and Mardykin (1974) or Novikov et al. (1978) should be considered for the evaluation.

4.4. Beta Phase

Berg et al. (1961) (1772–1786 K) determined the enthalpy at only three data points. After correction as described above, these values were fitted to the following equation with an overall accuracy as a standard deviation of ±101 J/mol (0.11%):

$$H^\circ(T) - H^\circ(298)(\mathrm{J/mol}) = 34.9108T - 10{,}082.20$$

The derived heat capacity is 34.9 ± 10.2 J/(mol K) and the enthalpy of transition 5015 ± 176 J/mol.

4.5. Liquid Phase

Enthalpy measurements were performed by Stretz and Bautista (1974) (1806–2360 K) using the levitation technique. However, the published paper contained several errors including the reporting of four different values for the liquid specific heat and three different sets of smoothed values. However, comparison with the measurements given in the original thesis of Stretz (1973) indicates that for the definitive values in Table III of Stretz and Bautista (1974), the reported experimental values at 2006 and 2360 K were incorrect and should have been 71,956 and 86,705 J/mol, respectively, and not 71,624 and 85,704 J/mol as reported. With these corrections and after also correcting for atomic weight, the enthalpy values can then be represented by the following equation which has an overall accuracy as a standard deviation of ±342 J/mol (0.42%):

$$H^\circ(T) - H^\circ(298)(\mathrm{J/mol}) = 39.5647T - 7119.04$$

The derived heat capacity is 39.56 ± 0.52 J/(mol K); the enthalpy of fusion, 11,318 ± 357 J/mol; and the entropy of fusion, 6.30 ± 0.20 J/(mol K).

Enthalpy measurements of Berg et al. (1961) (1828–1950 K) were corrected as described above. However, liquid yttrium is soluble in the tantalum containers used for carrying out the measurements. Assuming saturation, the experimental enthalpy measurements could be corrected for tantalum following the method of Dennison et al. (1966c), but since the base metal used already contained 1% of tantalum, then this complicates the interpretation of the results so that it is difficult to apply meaningful corrections and the quality of these measurements must be questioned. However, the values do on average appear to be 1% higher than the selected values due to Stretz and Bautista (1974).

After correction from heat capacity–density to heat capacity as above, the measurements of Novikov et al. (1978) over the range of 1800–2100 K show very poor agreement with the selected value and are on average 22% lower.

4.6. Gas Phase

Values are based on one bar standard state pressure and are calculated from 284 energy levels, including the ground state, listed in Table 13 using the method of Kolsky et al. (1957) and the 2010 Fundamental Constants (Mohr et al., 2011).

TABLE 13 Sources of Energy Level Data

Authors	Number of levels
Palmer (1977)	178
Moore (1971)	13
Garton et al. (1973a,b)	93

Seventy-two of the levels given by Garton et al. (1973a,b) could have degeneracy weighting (g_i) values of either 3/2 or 5/2 so an average was taken.

4.7. Enthalpy of Sublimation

TABLE 14 Enthalpy of Sublimation at 298.15 K

Authors	Methods	Range (K)	$\Delta_{sub}H^{\circ}$(298, II law) (kJ/mol)	$\Delta_{sub}H^{\circ}$(298, III law) (kJ/mol)	Notes
Ackermann and Rau (1962)	MS	1690–2020	413 ± 13	–	
	MS	1720–2050	418 ± 4	–	
DeMaria et al. (1963d)	MS	1331–1760	425 ± 10	–	
Ackermann et al. (1970)	MS	1336–1994	413 ± 6	–	–[a]
Karelin et al. (1962b)	KE	1405–1731	355 ± 3	403.8 ± 1.1	
Karelin et al. (1962c)	KE	1361–1761	314 ± 7	357.8 ± 1.3	
Nesmeyanov et al. (1962)					

Continued

TABLE 14 Enthalpy of Sublimation at 298.15 K—Cont'd

Authors	Methods	Range (K)	$\Delta_{sub}H°$(298, II law) (kJ/mol)	$\Delta_{sub}H°$(298, III law) (kJ/mol)	Notes
Ackermann and Rau (1962)	Eff	1774–2103	414 ± 1	423.3 ± 0.2	
Kruglykh et al. (1964)	KE	1433–1753	365 ± 16	419.7 ± 1.5	
Habermann (1963)	KE	1858–2178	433 ± 3	424.2 ± 0.2	–[b]
Habermann and Daane (1964)	KE	1780–2185	429 ± 2	423.4 ± 0.6	–[c]
Lundin and Yamamoto (1967)	KE	1867–2037	419 ± 23	424.9 ± 0.3	–[c]
Ackermann et al. (1970)	Eff	1789–2055	419 ± 8	420.5 ± 0.3	
Han et al. (2009)	KEMS	1423–1573	401 ± 3	418.9 ± 0.9	–[c]
Selected				423.3 ± 3.0	

MS, mass spectrometry; KE, Knudsen effusion; KEMS, Knudsen effusion mass spectrometry; Eff, effusion.
[a]*Unweighed average of seven runs.*
[b]*Run 4 of Habermann and Daane (1964) given in detail.*
[c]*Given only in the form of the Clausius–Clapeyron equation.*

The selected value is an average of the measurements of Ackermann and Rau (1962), Habermann (1963), Habermann and Daane (1964), Lundin and Yamamoto (1967), and Ackermann et al. (1970) which all show good agreement between Second- and Third Law-derived enthalpies of sublimation. The assigned accuracy takes into account the spread of these measurements.

4.8. Vapor Pressure

The vapor pressure equation for the alpha phase is derived by evaluating free energy functions for the solid and the gas at 25 K intervals from 1000 to 1750 K and the transition temperature. For the liquid phase, values are evaluated at 50 K intervals from 1800 to 3600 K and the melting point. For the beta phase, values were evaluated at the transition and melting point temperatures and fitted to the Clausius–Clapeyron equation (Table 15).

TABLE 15 Vapor Pressure Equations

$\ln(p, \text{bar}) = b_1 + b_2/T + b_3 \ln(T) + b_4 T + b_5 T^2$

Phase	Range (K)	b_1	b_2	b_3	b_4	b_5
Alpha	1000–1751.15	15.47523	−50,974.45	0.1938960	-7.82724×10^{-4}	3.69449×10^{-8}
Beta	1751.15–1795.15	14.35124	−48,672.32	0	0	0
Liquid	1795.15–2700	24.26207	−50,552.83	−1.050220	-6.75585×10^{-4}	6.78413×10^{-8}
	2700–3600	35.88096	−52,057.36	−2.604729	-1.40933×10^{-4}	3.72483×10^{-8}

4.9. Comparison of Selected Values at 298.15 K

Holley et al. (1968), Hultgren et al. (1973), and Gurvich et al. (1982) all based their selected values on Jennings et al. (1960), while Shen et al. (1995) used a combination of the measurements of Jennings et al. (1960) and Berezovskii et al. (1989). The present values are based on Berezovskii et al. (1989) and Tsang et al. (1985).

4.10. Summary of Representative Equations

TABLE 16 A Comparison of Heat Capacity, Enthalpy, and Entropy Values at 298.15 K

Authors	$C^\circ_p(298)$ (J/(mol K))	$H^\circ(298) - H^\circ(0)$ (J/mol)	$S^\circ(298)$ (J/(mol K))
Holley et al. (1968)	26.57	5962	44.43
Hultgren et al. (1973)	26.53	5966	44.43
Gurvich et al. (1982)	26.52	5965	44.43
Shen et al. (1995)	26.33	5983	44.79
Berezovskii et al. (1989)	26.28	5992	44.80
This work	26.29	5992	44.83

TABLE 17 Representative Equations above 298.15 K

Alpha phase: 298.15–1751.15 K
$C°_p(T)(\text{J/(mol K)}) = 24.1832 + 7.33448 \times 10^{-3} T - 7412.44/T^2$
$H°(T) - H°(298)(\text{J/mol}) = 24.1832T + 3.66724 \times 10^{-3} T^2 + 7412.44/T - 7561.08$
$S°(T)(\text{J/(mol K)}) = 24.1832 \ln(T) + 7.33448 \times 10^{-3} T + 3706.22/T^2 - 95.1882$
Beta phase: 1751.15–1795.15 K
$C°_p(T)(\text{J/(mol K)}) = 34.9108$
$H°(T) - H°(298)(\text{J/mol}) = 34.9108T - 10,082.20$
$S°(T)(\text{J/(mol K)}) = 34.9108 \ln(T) - 159.5936$
Liquid phase: 1795.15–3600 K
$C°_p(T)(\text{J/(mol K)}) = 39.5647$
$H°(T) - H°(298)(\text{J/mol}) = 39.5647T - 7119.04$
$S°(T)(\text{J/(mol K)}) = 39.5647 \ln(T) - 188.1600$

TABLE 18 Free Energy Equations Above 298.15 K

Alpha phase: 298.15–1751.15 K
$G°(T) - H°(298)(\text{J/mol}) = 119.3714T - 3.66724 \times 10^{-3} T^2 + 3706.22/T - 24.1832T \ln(T) - 7561.08$
Beta phase: 1751.15–1795.15 K
$G°(T) - H°(298)(\text{J/mol}) = 194.5044T - 34.9108T \ln(T) - 10,082.20$
Liquid phase: 1795.15–3600 K
$G°(T) - H°(298)(\text{J/mol}) = 227.7247T - 39.5647T \ln(T) - 7119.04$

TABLE 19 Transition Values Involved with the Free Energy Equations

Transition	T (K)	$\Delta H°$ (J/mol)	$\Delta S°$ (J/(mol K))
Alpha–beta	1751.15	5014.595	2.8636
Fusion	1795.15	11,317.608	6.3045

4.11. Thermodynamic Tables

TABLE 20 Low-Temperature Thermodynamic Data

T (K)	$C^\circ_p(T)$ (J/(mol K))	$H^\circ(T) - H^\circ(0)$ (J/mol)	$S^\circ(T)$ (J/(mol K))	$-[G^\circ(T) - H^\circ(0)]/$ T (J/(mol K))
5	0.0561	0.119	0.0448	0.0210
10	0.232	0.752	0.126	0.0508
15	0.769	3.035	0.304	0.102
20	1.891	9.418	0.664	0.193
25	3.502	22.81	1.254	0.342
30	5.314	44.78	2.051	0.558
35	7.220	76.11	3.013	0.838
40	9.098	116.9	4.100	1.177
45	10.860	166.9	5.275	1.566
50	12.457	225.3	6.503	1.998
60	15.131	363.7	9.021	2.959
70	17.230	526.0	11.517	4.004
80	18.827	706.7	13.928	5.095
90	20.035	901.2	16.218	6.205
100	20.995	1107	18.380	7.315
110	21.785	1321	20.420	8.415
120	22.445	1542	22.344	9.496
130	22.988	1769	24.163	10.555
140	23.425	2001	25.883	11.589
150	23.786	2237	27.512	12.597
160	24.131	2477	29.058	13.578
170	24.421	2720	30.530	14.532
180	24.673	2965	31.933	15.460
190	24.887	3213	33.273	16.362
200	25.070	3463	34.554	17.240
210	25.233	3714	35.781	18.094

Continued

TABLE 20 Low-Temperature Thermodynamic Data—Cont'd

T (K)	$C°_p(T)$ (J/(mol K))	$H°(T)-H°(0)$ (J/mol)	$S°(T)$ (J/(mol K))	$-[G°(T)-H°(0)]/T$ (J/(mol K))
220	25.391	3967	36.959	18.925
230	25.549	4222	38.091	19.734
240	25.695	4478	39.181	20.522
250	25.829	4736	40.233	21.289
260	25.950	4995	41.249	22.037
270	26.058	5255	42.230	22.767
280	26.152	5516	43.179	23.479
290	26.232	5778	44.099	24.175
298.15	26.287	5992	44.826	24.729

TABLE 21 High-Temperature Thermodynamic Data

T (K)	$C°_p(T)$ (J/(mol K))	$H°(T)-H°$ (298) (J/mol)	$S°(T)$ (J/(mol K))	$-[G°(T)-H°(298)]/T$ (J/(mol K))
Alpha phase				
298.15	26.287	0	44.826	44.826
300	26.301	49	44.989	44.827
400	27.071	2717	52.662	45.868
500	27.821	5462	58.783	47.859
600	28.563	8281	63.921	50.119
700	29.302	11,175	68.380	52.416
800	30.039	14,142	72.340	54.663
900	30.775	17,183	75.921	56.829
1000	31.510	20,297	79.202	58.905
1100	32.245	23,485	82.239	60.890
1200	32.979	26,746	85.076	62.788
1300	33.714	30,080	87.745	64.606
1400	34.448	33,488	90.271	66.350

TABLE 21 High-Temperature Thermodynamic Data—Cont'd

T (K)	$C°_p(T)$ (J/(mol K))	$H°(T) - H°$ (298) (J/mol)	$S°(T)$ (J/(mol K))	$-[G°(T) - H°(298)]/T$ (J/(mol K))
1500	35.182	36,970	92.672	68.026
1600	35.915	40,525	94.966	69.638
1700	36.649	44,153	97.166	71.193
1751.15	37.025	46,037	98.258	71.968
Beta phase				
1751.15	34.911	51,052	101.121	71.968
1795.15	34.911	52,588	101.988	72.693
Liquid phase				
1795.15	39.565	63,906	108.292	72.693
1800	39.565	64,097	108.399	72.789
1900	39.565	68,054	110.538	74.72
2000	39.565	72,010	112.567	76.562
2100	39.565	75,967	114.498	78.323
2200	39.565	79,923	116.338	80.01
2300	39.565	83,880	118.097	81.628
2400	39.565	87,836	119.781	83.182
2500	39.565	91,793	121.396	84.679
2600	39.565	95,749	122.948	86.121
2700	39.565	99,706	124.441	87.513
2800	39.565	103,662	125.88	88.858
2900	39.565	107,619	127.268	90.158
3000	39.565	111,575	128.61	91.418
3100	39.565	115,532	129.907	92.639
3200	39.565	119,488	131.163	93.823
3300	39.565	123,444	132.38	94.973
3400	39.565	127,401	133.562	96.091
3500	39.565	131,357	134.708	97.178
3600	39.565	135,314	135.823	98.236

TABLE 22 Thermodynamic Properties of the Gas Phase

T (K)	C°_p(T) (J/(mol K))	$H^\circ(T) - H^\circ(298)$ (J/mol)	S°(T) (J/(mol K))	$-[G^\circ(T) - H^\circ(298)]/T$ (J/(mol K))
298.15	25.860	0	179.475	179.475
300	25.860	48	179.635	179.475
400	25.293	2613	187.017	180.485
500	24.377	5096	192.563	182.370
600	23.589	7493	196.934	184.446
700	22.988	9820	200.523	186.494
800	22.542	12,095	203.562	188.443
900	22.210	14,332	206.197	190.272
1000	21.960	16,540	208.524	191.983
1100	21.770	18,726	210.607	193.583
1200	21.626	20,896	212.495	195.082
1300	21.521	23,053	214.222	196.489
1400	21.451	25,201	215.814	197.813
1500	21.416	27,344	217.292	199.063
1600	21.420	29,485	218.674	200.246
1700	21.465	31,629	219.974	201.369
1751.15	21.506	32,728	220.611	201.921
1795.15	21.552	33,675	221.145	202.386
1800	21.558	33,780	221.203	202.437
1900	21.702	35,942	222.372	203.455
2000	21.904	38,122	223.491	204.429
2100	22.168	40,325	224.565	205.363
2200	22.497	42,558	225.604	206.259
2300	22.895	44,827	226.612	207.122
2400	23.363	47,139	227.596	207.955
2500	23.903	49,502	228.561	208.760
2600	24.512	51,922	229.510	209.540
2700	25.190	54,407	230.448	210.297

TABLE 22 Thermodynamic Properties of the Gas Phase—Cont'd

T (K)	$C°_p$(T) (J/(mol K))	$H°(T) - H°(298)$ (J/mol)	$S°$(T) (J/(mol K))	$-[G°(T) - H°(298)]/T$ (J/(mol K))
2800	25.932	56,962	231.377	211.033
2900	26.734	59,595	232.301	211.751
3000	27.591	62,311	233.221	212.451
3100	28.496	65,115	234.141	213.136
3200	29.442	68,012	235.060	213.807
3300	30.420	71,005	235.981	214.465
3400	31.423	74,097	236.904	215.111
3500	32.441	77,290	237.830	215.747
3600	33.467	80,585	238.758	216.373

$H°(298) - H°(0) = 6857.0$ J/mol.

TABLE 23 Vapor Pressure

T (K)	p (bar)	$\Delta G°(T)$ (J/mol)	$\Delta H°(T)$ (J/mol)	p (bar)	T (K)
298.15	7.49×10^{-68}	383,155	423,300	10^{-15}	1007
300	2.15×10^{-67}	382,906	423,299	10^{-14}	1056
400	5.68×10^{-49}	369,461	423,196	10^{-13}	1109
500	6.38×10^{-38}	356,044	422,934	10^{-12}	1169
600	1.64×10^{-30}	342,703	422,512	10^{-11}	1235
700	2.61×10^{-25}	329,445	421,945	10^{-10}	1309
800	2.24×10^{-24}	316,276	421,254	10^{-9}	1393
900	2.53×10^{-18}	303,200	420,449	10^{-8}	1489
1000	6.93×10^{-16}	290,221	419,543	10^{-7}	1600
1100	6.77×10^{-14}	277,337	418,541	10^{-6}	1728
1200	3.05×10^{-12}	264,548	417,450	10^{-5}	1885
1300	7.60×10^{-11}	251,853	416,273	10^{-4}	2077
1400	1.18×10^{-9}	239,252	415,013	10^{-3}	2315

Continued

TABLE 23 Vapor Pressure—Cont'd

T (K)	p (bar)	$\Delta G^\circ(T)$ (J/mol)	$\Delta H^\circ(T)$ (J/mol)	p (bar)	T (K)
1500	1.27×10^{-8}	226,744	413,674	10^{-2}	2620
1600	1.01×10^{-7}	214,328	412,260	10^{-1}	3022
1700	6.21×10^{-7}	202,002	410,776	1	3581
1751.15	1.45×10^{-6}	195,732	409,991	NBP	3584
1751.15	1.45×10^{-6}	195,732	404,976		
1795.15	2.87×10^{-6}	190,482	404,387		
1795.15	2.87×10^{-6}	190,482	393,069		
1800	3.08×10^{-6}	189,935	392,983		
1900	1.22×10^{-5}	178,703	391,189		
2000	4.20×10^{-5}	167,566	389,412		
2100	1.28×10^{-4}	156,517	387,658		
2200	3.50×10^{-4}	145,550	385,935		
2300	8.75×10^{-4}	134,662	384,247		
2400	2.02×10^{-3}	123,846	382,603		
2500	4.34×10^{-3}	113,097	381,009		
2600	8.76×10^{-3}	102,411	379,473		
2700	1.68×10^{-2}	91,783	378,001		
2800	3.06×10^{-2}	81,208	376,600		
2900	5.33×10^{-2}	70,682	375,276		
3000	8.95×10^{-2}	60,200	374,036		
3100	0.145	49,758	372,883		
3200	0.228	39,352	371,824		
3300	0.348	28,977	370,861		
3400	0.517	18,631	369,996		
3500	0.752	8308	369,233		
3580.62	1.000	0	368,691		
3600	1.069	−1995	368,571		

NBP, normal boiling point at one atmosphere pressure (1.01325 bar).
$\Delta H^\circ(0) = 422,435$ J/mol.

5. THERMODYNAMIC FUNCTIONS OF LANTHANUM

5.1. Introduction

The low-temperature hexagonal close-packed alpha phase undergoes a superconducting transformation at 5.12 K (Legvold et al., 1976). The transformation from the alpha phase to the face-centered cubic beta phase shows significant hysteresis with transformation temperature varying between 583 K on heating and 533 K on cooling (Gschneidner, 1990). In agreement with Konings and Beneš (2010), the equilibrium value of 566 K determined by Spedding et al. (1961) from X-ray diffraction is accepted. Gschneidner (1990) selects 1138 K for the transformation from the beta phase to the body-centered gamma phase and 1191 K for the melting point.

5.2. Alpha Phase—Low Temperature

Many of the early measurements were carried out on samples containing a mixture of the alpha and beta phases with the beta phase being stabilized by the presence of impurities since Legvold et al. (1977) have shown that for pure samples, the beta phase cannot be retained below the transformation temperature. Earlier measurements of the heat capacity by Berman et al. (1958) were definitely on a mixture of phases as evidenced by the detection of anomalies corresponding to the superconducting transformation temperatures of both phases. Later measurements by Finnemore et al. (1965) on nearly pure alpha phase were succeeded by measurements of both Johnson and Finnemore (1967) and Pan et al. (1980). In the normal state, the values of the electronic coefficient (γ), the limiting Debye temperature (θ_D), and the superconducting transformation temperature (T_s) have been determined (Table 24).

For the last two determinations, the values of the Debye temperature agree satisfactorily with a value of 154 K obtained by Rosen (1967) from elastic

TABLE 24 Low-Temperature Heat Capacity Coefficients

Authors	Range (K)	γ (J/(mol K^2))	Θ_D (K)	T_s (K)
Berman et al. (1958)	1.6–6.5	10.1	142	4.8
Finnemore et al. (1965)	1.6–7.4	(10.0)	142	4.88
Bonneret et al. (1966)	2–40	(10.0)	140	4.5
Satoh and Ohtsuka (1966, 1967)	1.1–4.2	10	142	4.9
Sirota et al. (1983)	2.6–300	8.9	163	4.6
Johnson and Finnemore (1967)	1–10	9.4	152	4.87
Pan et al. (1980)	1–7	9.45	150	5.04

constant measurements. However, the measurements of both Johnson and Finnemore (1967) and Pan et al. (1980) were shown only in the form of graphs with actual values corresponding to those of Johnson and Finnemore (1967) being given by Johnson (1966) which are the selected values up to 10 K. Measurements were not corrected for a small percentage of the beta phase and possibly as a result the entropies of the two phases become equal at 4.92 K which is about 0.20 K lower than the value for the pure metal (Legvold et al., 1976). However, the transition temperature agrees with that determined by Johnson and Finnemore (1967) and also with 4.88 K determined by Lounasmaa and Sundström (1967). Below 10 K, the measurements of Lounasmaa and Sundström (3–25 K) tend from 3% low to 3% high in the superconducting region and in the normal region tend from 17% high before converging to the selected values and are selected above 10 K and up to 25 K. Below 30 K, the measurements of Parkinson et al. (1951) (4.5–180 K) scatter form 8% high to 9% low but are accepted above this temperature and up to the limit of 180 K. Measurements over the whole low-temperature range up to 300 K by Sirota et al. (1983) were unfortunately shown only in the form of a small graph. Therefore, the interval from 180 K to room temperature was estimated by fixing the values of heat capacity and their derivatives at 180 and 298.15 K and fitting to the equation

$$C^{\circ}{}_{\mathrm{p}}(T)(\mathrm{J}/(\mathrm{mol\,K})) = 15.12948 + 0.109140T - 3.35666 \times 10^{-4}T^2 + 3.50085 \times 10^{-7}T^3$$

5.3. Alpha Phase—High Temperature

Enthalpy measurements of Berg et al. (1961) (372–566 K in the alpha phase) were found to be incompatible with the low-temperature data, and values for the alpha phase were estimated by extrapolating the low-temperature measurements of Parkinson et al. (1951). Following this procedure, the estimated values of Holley et al. (1968), Hultgren et al. (1973), and Gurvich et al. (1982) show satisfactory agreement and the latter values were accepted:

$$H^{\circ}(T) - H^{\circ}(298)(\mathrm{J/mol}) = 26.411T + 1.1715 \times 10^{-3}T^2 - 7978.58$$

After correcting for temperature scale and from a 273.15 to a 298.15 K base by subtracting 650.88 J/mol from an internal fit, it was found that the enthalpy measurements of Berg et al. tend from 2% low to 0.7% high.

5.4. Beta Phase

After correcting as above, enthalpy measurements of Berg et al. (1961) (621–1128 K) were fitted to the following equation with an overall fit as a standard deviation of ± 1 J/mol ($<0.01\%$):

$$H^\circ(T) - H^\circ(298)(\text{J/mol}) = 33.5876T - 5.26848 \times 10^{-3}T^2 + 3.71827 \times 10^{-6}T^3 + 1299{,}390/T - 12{,}577.03$$

The derived enthalpy of transition is 370 J/mol.

Enthalpy measurements of Jaeger et al. (1938) (593–997 K) below 900 K trend from agreement with selected values up to 8% high but above 900 K increase sharply to 50% high. Heat capacity measurements of Akimov and Kraftmakher (1970) and Kraftmakher (1973) (636–1076 K) initially scatter from 2% high to 1% low but above 916 K show a trend to become 13% high. Heat capacity measurements of Kurichenko et al. (1986) (600–1080 K) tend from 7% to 23% high.

5.5. Gamma Phase

After correcting as above, the three enthalpy measurements of Berg et al. (1961) (1155–1170 K) were fitted to the following equation with an accuracy as a standard deviation of better than 1 J/mol (<0.01%):

$$H^\circ(T) - H^\circ(298)(\text{J/mol}) = 39.4844T - 16{,}354.32$$

The derived heat capacity is 39.48 ± 0.01 J/(mol K), and the enthalpy of transition is 3135 ± 1 J/mol.

5.6. Liquid Phase

After correction for atomic weight, enthalpy measurements of Stretz and Bautista (1975a) (1253–2419 K) were fitted to the following equation with an overall accuracy as a standard deviation of ±308 J/mol (0.55%):

$$H^\circ(T) - H^\circ(298)(\text{J/mol}) = 32.7730T - 2288.07$$

The derived heat capacity is 32.77 ± 0.18 J/(mol K); the enthalpy of fusion, 6072 ± 308 J/mol; and the entropy of fusion, 5.10 ± 0.26 J/(mol K).

After correction as above, enthalpy measurements of Berg et al. (1961) (1208–1374 K) can be considered to be 0.7% higher than the selected values, while heat capacity values of Novikov and Mardykin (1975) (1200–1550 K) tend from 38% high to 30% high. Heat capacity measurements of Mardykin et al. (1973) (1200–1600 K) and Banchila and Fillipov (1974) (1200–1900 K) were given only in the form of small graphs.

5.7. Gas Phase

Values are based on one bar standard state pressure and are calculated from the 384 energy levels, including the ground state, listed in Table 25 using the method of Kolsky et al. (1957) and the 2010 Fundamental Constants (Mohr et al., 2011).

TABLE 25 Sources of Energy Level Data

Authors	Number of levels
Ralchenko et al. (2012)	307
Furmann et al. (2009)	23
Furmann et al. (2010)	51
Nighat et al. (2010)	3

5.8. Enthalpy of Sublimation

TABLE 26 Enthalpy of Sublimation at 298.15 K

Authors	Methods	Range (K)	$\Delta_{sub}H^{\circ}$(298, II law) (kJ/mol)	$\Delta_{sub}H^{\circ}$(298, III law) (kJ/mol)	Notes
Ackermann and Rau 1962	MS	1655–2050	436 ± 4	–	
Chupka et al. (1956)	CMS	1723–1873	393 ± 29	420.6 ± 1.0	
Daane (1950, 1955)	KE	1614–1911	341 ± 13	415.0 ± 0.8	
Daane and Spedding (1958)	KE	1640–2017	405 ± 4	419.8 ± 1.5	–[a]
Ackermann and Rau (1962)	KE	1866–2167	425 ± 10	425.7 ± 0.5	
Habermann (1963)	KE	1939–2155	430 ± 4	430.9 ± 0.1	–[b]
Habermann and Daane (1964)	KE	1874–2182	434 ± 3	430.4 ± 0.3	–[a]
Shoji et al. (1997)	KEMS	1588–1797	434 ± 9	431.9 ± 0.1	–[a]
Selected				430.0 ± 5.0	

MS, mass spectrometry; CMS, calibrated mass spectrometry; KE, Knudsen effusion; KEMS, Knudsen effusion mass spectrometry.
[a] *Given only in the form of the Clausius–Clapeyron equation.*
[b] *Run 3 of Habermann and Daane (1964) given in detail.*

The selected value is based on the measurements of Ackermann and Rau (1962), Habermann and Daane (1964), and Shoji et al. (1997) but is biased toward the last two sets of measurements and agrees with the value selected by Gurvich et al. (1982) even though they did not have access to the later measurements of Shoji et al. (1997).

5.9. Vapor Pressure

The vapor pressure equation for the beta phase was obtained by evaluating the free energy functions of the solid and the gas at 10 K intervals from 1000 to 1130 K and the transition temperature; for the gamma phase, the extreme values were fitted to the Clausius–Clapeyron equation; and for the liquid phase, at 50 K intervals from 1200 to 3700 K and the melting point (Table 27).

TABLE 27 Vapor Pressure Equations

$\ln(p, \text{bar}) = b_1 + b_2/T + b_3 \ln(T) + b_4 T + b_5 T^2$

Phase	Range (K)	b_1	b_2	b_3	b_4	b_5
Beta	1000–1138.15	9.01656	−51,236.02	0.866692	-5.85004×10^{-4}	0
Gamma	1138.15–1191.15	14.29638	−51,061.42	0	0	0
Liquid	1191.15–2400	16.82108	−50,619.76	−0.43547	1.75102×10^{-4}	-1.39289×10^{-8}
	2400–3700	13.15331	−50,357.96	9.81549×10^{-2}	-1.44268×10^{-4}	1.59155×10^{-8}

5.10. Comparison of Selected Values at 298.15 K

Holley et al. (1968), Hultgren et al. (1973), and Gurvich et al. (1982) relied mainly on extrapolating the heat capacity measurements of Parkinson et al. (1951) from 180 K into the room temperature region. Cordfunke and Konings (1990) accepted the evaluation of Holley et al. (1968), while in this review, although the alpha phase evaluation of Gurvich et al. (1982) was accepted above 298.15 K, below this temperature, an independent interpolation was carried out between 180 and 298.15 K. Konings and Beneš (2010) also carried out an independent assessment to determine the entropy at 298.15 K (Table 28).

TABLE 28 Comparison of Heat Capacity, Enthalpy, and Entropy Values at 298.15 K

Authors	$C^\circ_p(298)$ (J/(mol K))	$H^\circ(298) - H^\circ(0)$ (J/mol)	$S^\circ(298)$ (J/(mol K))
Holley et al. (1968)	27.07	6644	56.57
Hultgren et al. (1973)	27.11	6665	56.9

Continued

TABLE 28 Comparison of Heat Capacity, Enthalpy, and Entropy Values at 298.15 K—Cont'd

Authors	$C°_p(298)$ (J/(mol K))	$H°(298) - H°(0)$ (J/mol)	$S°(298)$ (J/(mol K))
Gurvich et al. (1982)	27.11	6657	56.7
Cordfunke and Konings (1990)	27.11	–	56.6
Konings and Beneš (2010)	–	–	56.6
This work	27.11	6679	57.05

5.11. Summary of Representative Equations

TABLE 29 Representative Equations Above 298.15 K

Alpha phase: 298.15–566.15 K
$C°_p(T)(\text{J/(mol K)}) = 26.411 + 2.343 \times 10^{-3} T$
$H°(T) - H°(298)(\text{J/mol}) = 26.411T + 1.1715 \times 10^{-3} T^2 - 7978.58$
$S°(T)(\text{J/(mol K)}) = 26.411 \ln(T) + 2.343 \times 10^{-3} T - 94.1279$
Beat phase: 566.15–1138.15 K
$C°_p(T)((\text{J/mol K})) = 33.5876 - 1.053696 \times 10^{-2} T + 1.115511 \times 10^{-5} T^2 - 1,299,390/T^2$
$H°(T) - H°(298)(\text{J/mol}) = 33.5876T - 5.26848 \times 10^{-3} T^2 + 3.71873 \times 10^{-6} T^3 + 1299,390/T - 12,577.03$
$S°(T)(\text{J/(mol K)}) = 33.5876 \ln(T) - 1.053696 \times 10^{-2} T + 5.578095 \times 10^{-6} T^2 + 649,695/T^2 - 135.4880$
Gamma phase: 1138.15–1191.15 K
$C°_p(T)(\text{J/(mol K)}) = 39.4844$
$H°(T) - H°(298)(\text{J/mol}) = 39.4844T - 16,354.32$
$S°(T)(\text{J/(mol K)}) = 39.4844 \ln(T) - 178.4962$
Liquid phase: 1191.15–3700 K
$C°_p(T)(\text{J/(mol K)}) = 32.7730$
$H°(T) - H°(298)(\text{J/mol}) = 32.7730T - 2288.07$
$S°(T)(\text{J/mol K}) = 32.7730 \ln(T) - 125.8640$

TABLE 30 Free Energy Equations Above 298.15 K

Alpha phase: 298.15–566.15 K
$G^\circ(T) - H^\circ(298)(\text{J/mol}) = 120.5389T - 1.1715 \times 10^{-3}T^2 - 26.411T\ln(T) - 7978.58$
Beta phase: 566.15–1138.15 K
$G^\circ(T) - H^\circ(298)(\text{J/mol}) = 169.0756T + 5.26848 \times 10^{-3}T^2 - 1.859185 \times 10^{-6}T^3 + 649{,}695/T - 33.5876T\ln(T) - 12{,}577.03$
Gamma phase: 1138.15–1191.15 K
$G^\circ(T) - H^\circ(298)(\text{J/mol}) = 217.9806T - 39.4844T\ln(T) - 16{,}354.32$
Liquid phase: 1191.15–3700 K
$G^\circ(T) - H^\circ(298)(\text{J/mol}) = 158.6370T - 32.7730T\ln(T) - 2288.07$

TABLE 31 Transition Values Involved with the Free Energy Equations

Transition	T (K)	ΔH° (J/mol)	ΔS° (J/(mol K))
Alpha–beta	566.15	370.293	0.6541
Beta–gamma	1138.15	3135.044	2.7545
Fusion	1191.15	6071.966	5.0976

5.12. Thermodynamic Tables

TABLE 32 Thermodynamic Properties in the Superconducting Region

	Superconducting state			Normal state		
T (K)	C°_p(T) (mJ/ (mol K))	H°(T) − H° (0) (mJ/mol)	S°(T) (mJ/ (mol K))	C°_p(T) (mJ/ (mol K))	H°(T) − H° (0) (mJ/mol)	S°(T) (mJ/ (mol K))
1.0	0.99	0.42	1.09	10.2	5.01	9.95
1.5	4.70	1.66	2.05	16.2	11.6	15.2
2.0	13.6	6	4.48	23.5	21.5	20.8
2.5	28.4	16.2	8.99	32.5	35.4	27.0
3.0	49.5	35.4	15.9	43.7	54.3	33.9

Continued

TABLE 32 Thermodynamic Properties in the Superconducting Region—Cont'd

	Superconducting state			Normal state		
T (K)	$C°_p$(T) (mJ/(mol K))	$H°$(T) − H° (0) (mJ/mol)	$S°$(T) (mJ/(mol K))	$C°_p$(T) (mJ/(mol K))	$H°$(T) − H° (0) (mJ/mol)	$S°$(T) (mJ/(mol K))
3.5	78.1	66.9	25.6	57.6	79.5	41.6
4.0	115.4	115.0	38.4	75.1	112.5	50.4
4.5	160.7	183.8	54.5	97.1	155.5	60.5
4.92[a]	190.7	258.7	70.4	123.3	202.2	70.4

[a]*For an explanation of the difference between this value and the selected value of 5.12 K, see the text.*

TABLE 33 Low-Temperature Thermodynamic Data

T (K)	$C°_p(T)$ (J/(mol K))	$H°(T) - H°(0)$ (J/mol)	$S°(T)$ (J/(mol K))	$-[G°(T) - H°(0)]/T$ (J/(mol K))
5.12	0.137	0.228	0.0755	0.031
6	0.218	0.381	0.103	0.0394
8	0.552	1.112	0.206	0.0668
10	1.137	2.767	0.388	0.111
15	3.466	13.84	1.254	0.332
20	6.439	38.48	2.652	0.727
25	9.613	78.47	4.423	1.284
30	11.969	132.6	6.389	1.970
40	15.718	272.0	10.735	3.575
50	18.397	443.4	14.188	5.320
60	20.245	637.2	17.716	7.096
70	21.488	846.3	20.937	8.847
80	22.335	1066	23.865	10.544
90	22.979	1292	26.533	12.175
100	23.599	1525	28.986	13.735
110	24.101	2764	31.260	15.226

TABLE 33 Low-Temperature Thermodynamic Data—Cont'd

T (K)	$C^\circ_p(T)$ (J/(mol K))	$H^\circ(T) - H^\circ(0)$ (J/mol)	$S^\circ(T)$ (J/(mol K))	$-[G^\circ(T) - H^\circ(0)]/T$ (J/(mol K))
120	24.476	2007	33.374	16.651
130	24.771	2253	35.345	18.014
140	25.020	2507	37.190	19.319
150	25.252	2753	38.924	20.569
160	25.481	3007	40.561	21.768
170	25.712	3263	42.113	22.919
180	25.941	3521	43.589	24.027
190	26.150	3782	44.998	25.090
200	26.332	4045	46.344	26.119
210	26.488	4309	47.632	27.113
220	26.622	4548	48.868	28.074
230	26.734	4841	50.054	29.004
240	26.828	5109	51.193	29.905
250	26.905	5378	52.290	30.779
260	26.968	5647	53.347	31.627
270	27.019	5917	54.365	32.450
280	27.058	6188	55.349	33.250
290	27.089	6458	56.299	34.029
298.15	27.110	6679	57.050	34.648

TABLE 34 High-Temperature Thermodynamic Data

T (K)	$C^\circ_p(T)$ (J/(mol K))	$H^\circ(T) - H^\circ(298)$ (J/mol)	$S^\circ(T)$ (J/(mol K))	$-[G^\circ(T) - H^\circ(298)]/T$ (J/(mol K))
Alpha phase				
298.15	27.110	0	57.050	57.050
300	27.114	50	57.218	57.050
350	27.231	1409	61.406	57.381

Continued

TABLE 34 High-Temperature Thermodynamic Data—Cont'd

T (K)	$C°_p(T)$ (J/(mol K))	$H°(T) - H°(298)$ (J/mol)	$S°(T)$ (J/(mol K))	$-[G°(T) - H°(298)]/T$ (J/(mol K))
400	27.348	2773	65.050	58.117
450	27.465	4144	68.278	59.070
500	27.583	5520	71.178	60.138
550	27.700	6902	73.812	61.263
566.15	27.737	7350	74.614	61.633
Beta phase				
566.15	27.144	7720	75.268	61.633
600	27.672	8648	76.860	62.447
700	29.026	11,484	81.230	64.824
800	30.267	14,449	85.187	67.126
900	31.536	17,539	88.825	69.337
1000	32.906	20,760	92.217	71.457
1100	34.421	24,125	95.423	73.492
1138.15	35.042	25,450	96.607	74.247
Gamma phase				
1138.15	39.484	28,585	99.362	74.247
1191.15	39.484	30,678	101.159	75.404
Liquid phase				
1191.15	32.773	36,749	106.256	75.404
1200	32.773	37,040	106.499	75.633
1300	32.773	40,317	109.122	78.109
1400	32.773	43,594	111.551	80.412
1500	32.773	46,871	113.812	82.565
1600	32.773	50,149	115.927	84.584
1700	32.773	53,426	117.914	86.487
1800	32.773	56,703	119.787	88.286
1900	32.773	59,981	121.559	89.991
2000	32.773	63,258	123.240	91.611
2100	32.773	66,535	124.839	93.156

TABLE 34 High-Temperature Thermodynamic Data—Cont'd

T (K)	$C^\circ_p(T)$ (J/(mol K))	$H^\circ(T) - H^\circ(298)$ (J/mol)	$S^\circ(T)$ (J/(mol K))	$-[G^\circ(T) - H^\circ(298)]/T$ (J/(mol K))
2200	32.773	69,813	126.364	94.631
2300	32.773	73,090	127.821	96.046
2400	32.773	76,361	129.216	97.396
2500	32.773	79,644	130.553	98.696
2600	32.773	82,922	131.839	99.946
2700	32.773	86,199	133.076	101.150
2800	32.773	89,476	134.268	102.318
2900	32.773	92,754	135.418	103.434
3000	32.773	96,031	136.529	104.518
3100	32.773	99,308	137.603	105.568
3200	32.773	102,586	138.644	106.586
3300	32.773	105,863	139.652	107.753
3400	32.773	109,140	140.631	108.531
3500	32.773	112,417	141.581	109.461
3600	32.773	115,695	142.504	110.366
3700	32.773	118,972	143.402	111.247

TABLE 35 Thermodynamic Properties of the Gas Phase

T (K)	$C^\circ_p(T)$ (J/(mol K))	$H^\circ(T) - H^\circ(298)$ (J/mol)	$S^\circ(T)$ (J/(mol K))	$-[G^\circ(T) - H^\circ(298)]/T$ (J/(mol K))
298.15	22.754	0	182.382	182.382
300	22.790	42	182.522	182.382
350	23.775	1206	186.110	182.663
400	24.662	2418	189.344	183.299
450	25.406	3670	192.293	184.137
500	26.019	4956	195.003	185.090
550	26.540	6271	197.508	186.107
566.15	26.695	6700	198.278	186.443

Continued

TABLE 35 Thermodynamic Properties of the Gas Phase—Cont'd

T (K)	$C^\circ_p(T)$ (J/(mol K))	$H^\circ(T) - H^\circ(298)$ (J/mol)	$S^\circ(T)$ (J/(mol K))	$-[G^\circ(T) - H^\circ(298)]/T$ (J/(mol K))
600	27.008	7609	199.837	187.155
700	27.891	10,355	204.067	189.275
800	28.762	13,187	207.848	191.364
900	29.593	16,106	211.285	193.390
1000	30.326	19,103	214.442	195.339
1100	30.922	22,166	217.361	197.210
1138.15	31.109	23,350	218.419	197.903
1191.15	31.335	25,005	219.840	198.848
1200	31.369	25,282	220.072	199.004
1300	31.680	28,435	222.596	200.723
1400	31.880	31,614	224.952	202.370
1500	32.000	34,809	227.156	203.950
1600	32.064	38,012	229.223	205.465
1700	32.098	41,221	231.168	206.921
1800	32.117	44,432	233.003	208.319
1900	32.135	47,644	234.740	209.664
2000	32.162	50,859	236.389	210.960
2100	32.203	54,077	237.959	212.208
2200	32.264	57,300	239.459	213.413
2300	32.346	60,531	240.895	214.577
2400	32.450	63,770	242.273	215.703
2500	32.577	67,021	243.601	216.792
2600	32.727	70,286	244.881	217.848
2700	32.899	73,567	246.119	218.872
2800	33.092	76,867	247.319	219.867
2900	33.305	80,186	248.484	220.834
3000	33.536	83,528	249.617	221.774
3100	33.784	86,894	250.721	222.690
3200	34.048	90,286	251.798	223.583

TABLE 35 Thermodynamic Properties of the Gas Phase—Cont'd

T (K)	$C^\circ_p(T)$ (J/(mol K))	$H^\circ(T) - H^\circ(298)$ (J/mol)	$S^\circ(T)$ (J/(mol K))	$-[G^\circ(T) - H^\circ(298)]/$ T (J/(mol K))
3300	34.324	93,704	252.849	224.454
3400	34.613	97,151	253.878	225.305
3500	34.911	100,627	254.886	226.135
3600	35.218	104,133	255.874	226.948
3700	35.532	107,671	256.843	227.743

$H^\circ(298) - H^\circ(0) = 6313.7$ J/mol.

TABLE 36 Vapor Pressure

T (K)	p (bar)	$\Delta G^\circ(T)$ (J/mol)	ΔH°(T) (J/mol)	p *(bar)*	T *(K)*
298.15	1.63×10^{-69}	392,638	430,000	10^{-15}	1046
300	4.77×10^{-69}	392,401	429,992	10^{-14}	1098
350	2.35×10^{-58}	386,151	429,798	10^{-13}	1154
400	2.44×10^{-50}	379,927	428,274	10^{-12}	1218
450	4.17×10^{-44}	373,720	429,527	10^{-11}	1290
500	4.03×10^{-39}	367,524	429,437	10^{-10}	1371
550	4.83×10^{-35}	361,336	429,369	10^{-9}	1463
566.15	7.03×10^{-34}	359,339	429,351	10^{-8}	1568
566.15	7.03×10^{-34}	359,339	428,981	10^{-7}	1690
600	1.20×10^{-31}	355,175	428,962	10^{-6}	1831
700	2.60×10^{-26}	342,884	428,870	10^{-5}	1999
800	2.59×10^{-22}	330,609	428,738	10^{-4}	2201
900	3.34×10^{-19}	318,353	428,567	10^{-3}	2448
1000	1.02×10^{-16}	306,118	428,343	10^{-2}	2758
1100	1.11×10^{-14}	293,909	428,041	10^{-1}	3157
1138.15	5.31×10^{-14}	289,260	427,900	1	3691
1138.15	5.31×10^{-14}	289,260	424,765	NBP	3694
1191.15	3.91×10^{-13}	282,960	424,327		

Continued

TABLE 36 Vapor Pressure—Cont'd

T (K)	*p* (bar)	$\Delta G^\circ(T)$ (J/mol)	ΔH°(T) (J/mol)	p *(bar)*	T *(K)*
1191.15	3.91×10^{-13}	282,960	418,255		
1200	5.33×10^{-13}	281,955	418,243		
1300	1.34×10^{-11}	270,603	418,119		
1400	2.12×10^{-10}	259,260	418,020		
1500	2.33×10^{-9}	247,922	417,938		
1600	1.89×10^{-8}	236,590	417,864		
1700	1.20×10^{-7}	225,263	417,795		
1800	6.19×10^{-7}	213,939	417,728		
1900	2.69×10^{-6}	202,620	417,664		
2000	1.01×10^{-5}	191,303	417,601		
2100	3.33×10^{-5}	179,990	417,542		
2200	9.89×10^{-5}	168,679	417,488		
2300	2.67×10^{-4}	157,379	417,441		
2400	6.62×10^{-4}	146,064	417,403		
2500	1.53×10^{-3}	134,759	417,377		
2600	3.31×10^{-3}	123,455	417,365		
2700	6.77×10^{-3}	112,150	417,368		
2800	1.31×10^{-2}	100,845	417,391		
2900	2.44×10^{-2}	89,539	417,433		
3000	4.34×10^{-2}	78,232	417,497		
3100	7.45×10^{-2}	66,922	417,586		
3200	0.124	55,608	417,700		
3300	0.199	44,291	417,841		
3400	0.312	32,968	418,011		
3500	0.475	21,641	418,210		
3600	0.709	10,307	418,439		
3690.89	1	0	418,674		
3700	1.034	−1033	418,699		

NBP, normal boiling point at one atmosphere pressure (1.01325 bar).
$\Delta H^\circ(0) = 430,365$ J/mol.

6. THERMODYNAMIC FUNCTIONS OF CERIUM

6.1. Introduction

The low-temperature transformations in cerium show marked hysteresis with Koskenmaki and Gschneidner (1978) selecting 96 K for the equilibrium transformation from the collapsed face-centered cubic alpha phase to the double close-packed hexagonal beta phase, while Gschneidner et al. (1996) determined the equilibrium transformation from the beta phase to the normal face-centered cubic gamma phase to be at 283 K. Gschneidner (1990) selects 999 K for the transformation from the gamma phase to the body-centered cubic delta phase and 1071 K for the melting point.

6.2. Alpha Phase

Early heat capacity measurements by Parkinson et al. (1951) (20–200 K), Parkinson and Roberts (1957) (1.5–20 K), and Lounasmaa (1964c) (0.4–4 K) were made on mixed phases. Measurements on the fairly pure alpha phase by Panousis and Gschneidner (1970) (2.5–20 K) were superseded by measurements of Koskimaki and Gschneidner (1975) (1.6–22 K) from which an electronic coefficient (γ) of 12.8 mJ/(mol K^2) and limiting Debye temperature (θ_D) of 179 K were derived. The measurements were shown only graphically with actual data points being supplied by Gschneidner (1991). There are no heat capacity measurements above 22 K but based on the shape of the specific heat curve for the beta phase (q.v.) then a value for the alpha phase of between 25 and 26 J/(mol K) at 96 K would appear to be representative. Selecting a median value of 25.5 J/(mol K) then together with the heat capacity value at 22 K and its derivative the heat capacity curve from 22 to 96.15 K can be represented by

$$C^{\circ}{}_{p}(T)(\mathrm{J}/(\mathrm{mol\,K})) = -5.77516 + 0.591988T - 2.77393 \times 10^{-3}T^2$$

High-pressure measurements by Phillips et al. (1968) on commercial purity metal leads to a value of $\gamma = 11.3$ mJ/(mol K^2) in reasonable agreement with that obtained by Koskimaki and Gschneidner (1975).

6.3. Beta Phase

The alpha–beta transition shows marked hysteresis with transition temperatures varying from 125 K on heating to 45 K on cooling (Gschneidner, 1990) with an equilibrium transition temperature selected as 96 K (Koskenmaki and Gschneidner, 1978). Using the Clausius–Clapeyron equation, Gschneidner et al. (1962) estimated an enthalpy of transition from the alpha to the beta phases. Using the same procedure but with more recent values as selected by Gschneidner and Pecharsky (1999) of 96 K for the alpha–beta transition temperature and 185 K at 220 MPa for the alpha–beta–gamma triple point but retaining the volume change on transition at 3.20 cm^3/mol, then the derived enthalpy of transition is 761 J/mol.

Heat capacity measurements by Koskimaki and Gschneidner (1974) (1.5–23 K) established two Néel transitions with ordering on hexagonal sites at 13.7 K and on cubic sites at 12.45 K. These measurements were superseded by those of Tsang et al. (1976a,b) (1.0–20 K) who confirmed the Néel transition peaks. Assuming a simple Debye relationship, then Conway and Phillips (1972) suggested a very high electronic coefficient (γ) of 54 mJ/(mol K^2), while the measurements of Koskimaki and Gschneidner (1974) led to 46 mJ/(mol K^2). However, this was considered to be a misinterpretation due to the presence of a large magnetic contribution to the specific heat and both Koskimaki and Gschneidner (1974) and Tsang et al. (1976a,b) calculated this contribution by assuming the lanthanum values of electronic coefficient $\gamma = 9.4$ mJ/(mol K^2) and Debye temperature $\theta_D = 152$ K determined by Johnson and Finnemore (1967). The measurements of Koskimaki and Gschneidner (1974) and Tsang et al. (1976a,b) were shown graphically with actual data points being supplied by Gschneidner (1991).

Heat capacity measurements of Gschneidner et al. (1996) and Gschneidner and Pecharsky (1999) (39–330 K) were also only shown graphically with actual data points being supplied by Pecharsky (2006). Values in the range 221–252 K were not included in the fit since they were anomalously high, while values above 281 K were not included since the marked scatter in these values significantly affects the selected specific heat curve below the transition temperature at 283 K.

6.4. Gamma Phase

The beta–gamma transformation shows considerable hysteresis varying from 412 K on heating to 257 K on cooling (Gschneidner, 1990), while Gschneidner et al. (1996) determined the equilibrium transition temperature to be 283 ± 5 K and the enthalpy of transition as 181 ± 12 J/mol. In the high-temperature region, enthalpy measurements of Spedding et al. (1960b) (373–975 K in the alpha phase) were corrected for temperature scale and from a 273.15 to a 298.15 K base by subtracting 668.91 J/mol obtained from an internal fit to the data, as because of the sluggishness nature of the beta–gamma transition, it is likely that all of the drop calorimetry measurements were confined to the gamma phase. The enthalpy values were represented by the following equation with an overall accuracy as a standard deviation of ± 24 J/mol (0.14%):

$$H^\circ(T) - H^\circ(298)(\mathrm{J/mol}) = 23.4711T + 5.12320 \times 10^{-3}T^2 + 1.46311 \times 10^{-6}T^3 - 7492.10$$

The graphical representation of Gschneidner and Pecharsky (1999) confirms the room temperature-derived heat capacity value of 27 J/(mol K). Enthalpy measurements of Jaeger et al. (1938) (596–804 K) average 5% high up to 773 K and then increase sharply to 17% high. Heat capacity measurements of Kurichenko et al. (1986) (600–952 K) tend from 3% low up to 15% high.

6.5. Delta Phase

After correcting as above, enthalpy measurements of Spedding et al. (1960b) (1017–1064 K) were fitted to the following equation with an overall accuracy as a standard deviation of ±8 J/mol (0.02%):

$$H^{\circ}(T) - H^{\circ}(298)(\mathrm{J/mol}) = 37.7268T - 12,232.95$$

The derived heat capacity is 37.73 ± 0.24 J/(mol K), and enthalpy of transition is 2929 ± 25 J/mol. In order to preserve self-consistency between the gamma and delta phases, this value was preferred to the directly determined enthalpy of transition of 2992 ± 13 J/mol by Chiotti et al. (1966).

6.6. Liquid Phase

After correcting as above, enthalpy measurements of Spedding et al. (1960b) (1085–1375 K) lead to an enthalpy of fusion of 5174 ± 19 J/mol compared to a directly determined value of 5460 ± 222 J/mol obtained by Chiotti et al. (1966). Extrapolation of the enthalpy measurements of Kuntz and Bautista (1976) (1714–2494 K) and Dokko and Bautista (1980) (1530–2407 K) to the melting point leads to enthalpy of fusion values of 10,554 and 7732 J/mol, respectively, which are both considered to be erroneously high. Additional measurements by Kuntz and Bautista (1976) over the range of 1419–1677 K indicate that the derived specific heat values increase with decreasing temperature possibly due to the unusual formation of metal clusters within the liquid which are considered as having dispersed by 1600 K since above this temperature both the measurements of Kuntz and Bautista (1976) and Dokko and Bautista (1980) suggest that the derived specific heat value is constant. Different values of enthalpy were obtained but because of technical improvements, the measurements of Dokko and Bautista (1980) were preferred. In agreement with Hultgren et al. (1973), the enthalpy of fusion value as determined by Chiotti et al. (1966) and the equivalent entropy of fusion, 5.10 ± 0.21 J/(mol K), were selected and together with the criterion that $dC_p/dt = 0$ at 1600 K and then the measurements of Dokko and Bautista (1980) could be represented by the following equations where above 1600 K, the overall fit to the linear equation is ±523 J/mol (0.80%) and the derived heat capacity is 33.36 ± 0.45 J/(mol K):

$$H^{\circ}(T) - H^{\circ}(298)(\mathrm{J/mol}) = 151.3042T - 7.37170 \times 10^{-2}T^2 + 1.53577 \times 10^{-5}T^3 - 62,725.73 (1071.15 - 1600\mathrm{K})$$

$$H^{\circ}(T) - H^{\circ}(298)(\mathrm{J/mol}) = 33.3569T + 176.553 (1600 - 3700\mathrm{K})$$

The measurements of Kuntz and Bautista (1976) overall average 2% high, while because the enthalpy of fusion value of Chiotti et al. (1966) was selected, the enthalpy values of Spedding et al. (1960b) average 2% low.

Heat capacity measurements of Mardykin and Vertman (1972) (1150–1600 K), Atalla et al. (1972) (1100–2100 K), and Novikov and Mardykin (1973) (1100–1800 K) were only shown in the form of small graphs.

6.7. Gas Phase

Values are based on one bar standard state pressure and are calculated from the 1026 energy levels, including the ground state, listed in Table 37 using the method of Kolsky et al. (1957) and the 2010 Fundamental Constants (Mohr et al., 2011).

Where energy levels are given as having one of the two or three possible degeneracy weighting (g_i) values then an average was taken.

TABLE 37 Sources of Energy Level Data

Authors	Number of levels
Ralchenko et al. (2012)	943
Zh-Ming et al. (2002)	83

6.8. Enthalpy of Sublimation

TABLE 38 Enthalpy of Sublimation at 298.15 K

Authors	Methods	Range (K)	$\Delta_{sub}H^{\circ}$(298, II law) (kJ/mol)	$\Delta_{sub}H^{\circ}$(298, III law) (kJ/mol)	Notes
Ackermann et al. (1969)	MS	1527–1979	414 ± 2	–	
	MS	1543–2227	411 ± 2	–	
Ahmann (1950, 1953)	KE	1433–1712	457 ± 12	375.7 ± 1.1	
Jackson (1958)	KE	1715–1949	455 ± 25	423.7 ± 0.8	
Daane and Spedding (1958)	KE	1611–2038	397 ± 2	419.2 ± 2.6	–[a]
Kruglykh and Pavlov (1965)	KE	1573–1793	374 ± 18	376.8 ± 0.7	
	L	1568–1843	388 ± 14	376.7 ± 0.7	

TABLE 38 Enthalpy of Sublimation at 298.15 K—Cont'd

Authors	Methods	Range (K)	$\Delta_{sub}H°$(298, II law) (kJ/mol)	$\Delta_{sub}H°$(298, III law) (kJ/mol)	Notes
Habermann (1963)	KE	1861–2252	444 ± 3	431.0 ± 0.3	–[b]
Habermann and Daane (1964)	KE	1861–2292	447 ± 3	430.4 ± 1.7	–[a]
Ackermann et al. (1969)	KE	1849–2190	412 ± 4	433.5 ± 0.3	
Shevchenko et al. (1978)	KE	1830–1900	447 ± 7	430.5 ± 0.3	–[a]
Shoji et al. (1998)	KEMS	1592–1781	446 ± 13	433.1 ± 0.7	–[a]
Selected				431.9 ± 3.0	

MS, mass spectrometry; KE, Knudsen effusion; L, Langmuir; KEMS, Knudsen effusion mass spectrometry.
[a]*Given only in the form of the Clausius–Clapeyron equation.*
[b]*Run 2 of Habermann and Daane (1964) given in detail.*

The selected value is an average of the last four determinations with the assigned accuracy taking into account actual deviations of the Third Law-determined enthalpies of sublimation in the selected experiments.

6.9. Vapor Pressure

TABLE 39 Vapor Pressure Equations

$\ln(p, \text{bar}) = b_1 + b_2/T + b_3 \ln(T) + b_4 T + b_5 T^2$

Phase	Range (K)	b_1	b_2	b_3	b_4	b_5
Delta	999.15–1071.15	14.47713	−51,416.07	0	0	0
Liquid	1071.15–1600	123.0728	−58,542.43	−16.05605	1.06026×10^{-2}	-1.11978×10^{-6}
	1600–3700	2.01538	−49,111.98	1.535065	-3.60753×10^{-4}	2.15305×10^{-8}

The vapor pressure equation for the delta phase was obtained by evaluating the free energy functions of the solid and the gas at the transition temperature and the melting point and fitting to the Clausius–Clapeyron equation and for the liquid phase at 50 K intervals from 1100 to 3700 K and the melting point.

6.10. Comparison of Selected Values at 298.15 K

Holley et al. (1968), Hultgren et al. (1973), and this review selected heat capacity values at 298.15 K derived from the enthalpy measurements of Spedding et al. (1960b). The enthalpy and entropy values given by Holley et al. (1968) were those selected by Jennings (1960). Hultgren et al. (1973) accepted the estimates of Parkinson et al. (1951) after correcting from 300 K. Values selected by Konings and Beneš (2010) appear to be estimates from the graphical representation of heat capacity for the beta and gamma phases given by Gschneidner and Pecharsky (1999), while the present evaluation is based mainly on an estimate for the alpha phase above 22 K but with actual specific heat values for the beta and gamma phases as given by Gschneidner (1991) and Pecharsky (2006) (Table 40).

TABLE 40 Comparison of Heat Capacity, Enthalpy, and Entropy Values at 298.15 K

Authors	$C°_p(298)$ (J/(mol K))	$H°(298) - H°(0)$ (J/mol)	$S°(298)$ (J/(mol K))
Holley et al. (1968)	26.94	9518	75.81
Hultgren et al. (1973)	26.94	7280	69.45
Konings and Beneš (2010)	27.0	–	69.7
This work	26.92	7889	65.49

6.11. Summary of Representative Equations

TABLE 41 Representative Equations Above 298.15 K

Gamma phase: 298.15–999.15 K
$C°_p(T)(\text{J/(mol K)}) = 23.4711 + 1.02464 \times 10^{-2} T + 4.38933 \times 10^{-6} T^2$
$H°(T) - H°(298)(\text{J/mol}) = 23.4711\,T + 5.12320 \times 10^{-3} T^2 + 1.46311 \times 10^{-6} T^3 - 7492.10$
$S°(T)(\text{J/(mol K)}) = 23.4711\ \ln(T) + 1.02464 \times 10^{-2} T + 2.194665 \times 10^{-6} T^2 - 71.4885$

TABLE 41 Representative Equations Above 298.15 K—Cont'd

Delta phase: 999.15–1071.15 K
$C°_p(T)(\text{J/(mol K)}) = 37.7268$
$H°(T) - H°(298)(\text{J/mol}) = 37.7268T - 12,232.95$
$S°(T)(\text{J/(mol K)}) = 37.7268\ln(T) - 154.5913$
Liquid phase: 1071.15–1600 K
$C°_p(T)(\text{J/(mol K)}) = 151.3042 - 0.147434T + 4.60731 \times 10^{-5}T^2$
$H°(T) - H°(298)(\text{J/mol}) = 151.3042T - 7.37170 \times 10^{-2}T^2 + 1.53577 \times 10^{-5}T^3 - 62,725.73$
$S°(T)(\text{J/(mol K)}) = 151.3042\ln(T) - 0.147434T + 2.303655 \times 10^{-5}T^2 - 810.3726$
Liquid phase: 1600–3700 K
$C°_p(T)(\text{J/(mol K)}) = 33.3569$
$H°(T) - H°(298)(\text{J/mol}) = 33.3569T + 179.553$
$S°(T)(\text{J/(mol K)}) = 33.3569\ln(T) - 117.1067$

TABLE 42 Free Energy Equations Above 298.15 K

Gamma phase: 298.15–999.15 K
$G°(T) - H°(298)(\text{J/mol}) = 94.9596T - 5.12320 \times 10^{-3}T^2 - 7.31555 \times 10^{-7}T^3 - 23.4711T\ln(T) - 7492.10$
Delta phase: 999.15–1071.15 K
$G°(T) - H°(298)(\text{J/mol}) = 192.3181T - 37.7268T\ln(T) - 12,232.95$
Liquid phase: 1071.15–1600 K
$G°(T) - H°(298)(\text{J/mol}) = 961.6768T + 7.37170 \times 10^{-2}T^2 - 7.67885 \times 10^{-6}T^3 - 151.3042T\ln(T) - 62,725.73$
Liquid phase: 1600–3700 K
$G°(T) - H°(298)(\text{J/mol}) = 150.4636T - 33.3569T\ln(T) + 179.553$

TABLE 43 Transition Values Involved with the Free Energy Equations

Transition	T (K)	$\Delta H°$ (J/mol)	$\Delta S°$ (J/(mol K))
Gamma–delta	999.15	2928.861	2.9314
Fusion	1071.15	5460.120	5.0974

6.12. Thermodynamic Tables

TABLE 44 Low-Temperature Thermodynamic Data

T (K)	$C°_p$(T) (J/(mol K))	$H°(T) - H°(0)$ (J/mol)	$S°$(T) (J/(mol K))	$-[G°(T) - H°(0)]/T$ (J/(mol K))
Alpha phase				
5	0.114	0.217	0.0791	0.0357
10	0.826	2.119	0.316	0.104
15	2.681	10.54	0.974	0.271
20	5.038	30.10	2.082	0.578
25	7.291	60.83	3.445	1.012
30	9.488	102.8	4.970	1.542
40	13.466	218.1	8.258	2.806
50	16.889	370.3	11.641	4.235
60	19.758	554.0	14.982	5.749
70	22.072	763.6	18.209	7.300
80	23.831	993.6	21.277	8.857
90	25.035	1238	24.159	10.399
96.15	25.500	1394	25.830	11.333
Beta phase				
96.15	27.347	2154	33.74	11.333
100	27.394	2260	34.815	12.216
110	27.467	2534	37.43	14.392
120	27.485	2809	39.821	16.413
130	27.485	3084	42.021	18.299
140	27.485	3359	44.058	20.067
150	27.485	3634	45.954	21.73
160	27.485	3908	47.728	23.300
170	27.485	4183	49.394	24.787
180	27.493	4458	50.965	26.198
190	27.505	4733	52.452	27.541
200	27.520	5008	53.863	28.822

TABLE 44 Low-Temperature Thermodynamic Data—Cont'd

T (K)	$C°_p$(T) (J/(mol K))	$H°$(T) − $H°$(0) (J/mol)	$S°$(T) (J/(mol K))	−[$G°$(T) − $H°$(0)]/T (J/(mol K))
210	27.538	5284	55.206	30.047
220	27.560	5559	56.488	31.220
230	27.587	5835	57.713	32.345
240	27.616	6111	58.888	33.427
250	27.649	6387	60.016	34.468
260	27.686	6664	61.101	35.471
270	27.726	6941	62.147	36.440
280	27.770	7218	63.156	37.376
283.15	27.785	7306	63.467	37.665
Gamma phase				
283.15	26.724	7487	64.106	37.665
290	26.812	7670	64.746	38.297
298.15	26.916	7889	65.490	39.030

TABLE 45 Thermodynamic Properties of the Metastable Beta Phase

T (K)	$C°_p$(T) (J/(mol K))	$H°$(T) − $H°$(0) (J/mol)	$S°$(T) (J/(mol K))	−[$G°$(T) − $H°$(0)]/T (J/(mol K))
5	1.023	1.444	0.436	0.147
10	7.024	18.89	2.624	0.735
11	8.983	26.86	3.382	0.940
12	11.254	36.98	4.261	1.179
12.45	12.089	42.24	4.692	1.298
12.5	11.922	42.84	4.740	1.312
13	10.928	48.51	5.184	1.453
13.5	10.232	53.83	5.586	1.598
13.6	9.979	54.84	5.661	1.628
13.7	10.016	55.84	5.734	1.658

Continued

TABLE 45 Thermodynamic Properties of the Metastable Beta Phase—Cont'd

T (K)	$C°_p$(T) (J/(mol K))	$H°$(T) − $H°$(0) (J/mol)	$S°$(T) (J/(mol K))	−[$G°$(T) − $H°$(0)]/T (J/(mol K))
13.8	9.906	56.84	5.806	1.688
13.9	9.687	57.82	5.877	1.717
14.0	9.393	58.77	5.945	1.747
14.5	7.658	63.03	6.244	1.898
15	6.823	66.59	6.486	2.047
16	6.910	73.48	6.931	2.338
18	7.943	88.35	7.805	2.897
20	9.000	105.3	8.695	3.432
25	12.837	159.4	11.096	4.719
30	15.934	231.8	13.728	6.000
40	20.004	412.7	18.903	8.586
50	23.205	629.8	23.733	11.138
60	25.146	872.3	28.149	13.612
70	26.301	1130	32.122	15.977
80	26.922	1397	35.678	18.222
90	27.259	1668	38.871	20.342
96.15	27.347	1836	40.676	21.586

TABLE 46 High-Temperature Thermodynamic Data

T (K)	$C°_p$(T) (J/(mol K))	$H°$(T) − $H°$(298) (J/mol)	$S°$(T) (J/(mol K))	−[$G°$(T) − $H°$(298)]/T (J/(mol K))
Gamma phase				
298.15	26.916	0	65.490	65.490
300	26.940	50	65.657	65.491
400	28.272	2810	73.587	66.563
500	29.692	5707	80.047	68.633

TABLE 46 High-Temperature Thermodynamic Data—Cont'd

T (K)	$C°_p$(T) (J/(mol K))	$H°$(T) − $H°$(298) (J/mol)	$S°$(T) (J/(mol K))	−[$G°$(T) − $H°$(298)]/T (J/(mol K))
600	31.199	8751	85.592	71.008
700	32.794	11,950	90.520	73.499
800	34.477	15,313	95.008	75.867
900	36.248	18,848	99.171	78.228
999.15	38.091	22,533	103.053	80.501
Delta phase				
999.15	37.727	25,462	105.984	80.501
1000	37.727	25,494	106.016	80.522
1050	37.727	27,380	107.857	81.781
1071.15	37.727	28,178	108.609	82.303
Liquid phase				
1071.15	46.243	33,638	113.707	82.303
1100	44.875	34,952	114.917	83.143
1200	40.729	39,225	118.638	85.950
1300	37.514	43,129	121.764	88.588
1400	35.200	46,756	124.453	91.056
1500	33.818	50,200	126.830	93.363
1600	33.357	53,551	128.992	95.523
1700	33.357	56,886	131.015	97.552
1800	33.357	60,222	132.921	99.465
1900	33.357	63,558	134.725	101.273
2000	33.357	66,893	136.436	102.989
2100	33.357	70,229	138.063	104.621
2200	33.357	73,565	139.615	106.177
2300	33.357	76,901	141.098	107.663
2400	33.357	80,236	142.518	109.086
2500	33.357	83,572	143.879	110.450
2600	33.357	86,907	145.188	111.762

Continued

TABLE 46 High-Temperature Thermodynamic Data—Cont'd

T (K)	$C°_p$(T) (J/(mol K))	$H°$(T) − $H°$(298) (J/mol)	$S°$(T) (J/(mol K))	−[$G°$(T) − $H°$(298)]/T (J/(mol K))
2700	33.357	90,243	146.446	113.023
2800	33.357	93,579	147.660	114.238
2900	33.357	96,915	148.830	115.411
3000	33.357	100,250	149.961	116.544
3100	33.357	103,586	151.055	117.640
3200	33.357	106,922	152.114	118.701
3300	33.357	110,257	153.140	119.729
3400	33.357	113,593	154.136	120.726
3500	33.357	116,929	155.103	121.695
3600	33.357	120,264	156.043	122.636
3700	33.357	123,600	156.957	123.551

TABLE 47 Thermodynamic Properties of the Gas Phase

T (K)	$C°_p$(T) (J/(mol K))	$H°$(T) − $H°$(298) (J/mol)	$S°$(T) (J/(mol K))	−[$G°$(T) − $H°$(298)]/ T (J/(mol K))
298.15	23.075	0	191.771	191.771
300	23.092	43	191.913	191.771
400	24.584	2418	198.736	192.691
500	26.785	4983	204.451	194.485
600	29.186	7781	209.546	196.577
700	31.497	10,817	214.221	198.768
800	33.560	14,072	218.565	200.974
900	35.291	17,518	222.621	203.157
999.15	36.649	21,087	226.382	205.277
1000	36.660	21,118	226.413	205.295
1071.15	37.416	23,755	228.960	206.783

TABLE 47 Thermodynamic Properties of the Gas Phase—Cont'd

T (K)	$C°_p$(T) (J/(mol K))	$H°$(T) − $H°$(298) (J/mol)	$S°$(T) (J/(mol K))	−[$G°$(T) − $H°$(298)]/T (J/(mol K))
1100	37.674	24,838	229.958	207.378
1200	38.373	29,643	233.267	209.399
1300	38.806	32,504	236.358	211.355
1400	39.032	36,397	239.243	213.245
1500	39.101	40,305	241.939	215.069
1600	39.061	44,214	244.462	216.828
1700	38.948	48,115	246.827	218.524
1800	38.793	52,002	249.049	220.159
1900	38.619	55,873	251.142	221.735
2000	38.442	59,726	253.118	223.255
2100	38.274	63,561	254.990	224.722
2200	38.124	67,381	256.737	226.139
2300	37.996	71,187	258.458	227.508
2400	37.894	74,981	260.073	228.831
2500	37.820	78,767	261.618	230.112
2600	37.771	82,546	263.101	231.352
2700	37.748	86,322	264.526	232.555
2800	37.749	90,096	265.899	233.721
2900	37.771	93,872	267.223	234.854
3000	37.812	97,651	268.505	235.954
3100	37.869	101,435	269.745	237.024
3200	37.939	105,225	270.949	238.066
3300	38.020	109,023	272.117	239.080
3400	38.108	112,830	273.254	240.069
3500	38.202	116,645	274.360	241.033
3600	38.299	120,470	275.437	241.973
3700	38.396	124,305	276.488	242.892

$H°(298) - H°(0) = 6667.5$ J/mol.

TABLE 48 Vapor Pressure

T (K)	p (bar)	ΔG°(T) (J/mol)	ΔH°(T) (J/mol)	p (bar)	T (K)
298.15	8.52×10^{-70}	394,250	431,900	10^{-15}	1049
300	2.49×10^{-69}	394,016	431,993	10^{-14}	1101
400	1.54×10^{-50}	381,449	431,508	10^{-13}	1159
500	2.85×10^{-39}	368,974	431,176	10^{-12}	1223
600	9.11×10^{-32}	356,558	430,930	10^{-11}	1295
700	2.08×10^{-26}	344,177	430,767	10^{-10}	1377
800	2.16×10^{-22}	331,814	430,660	10^{-9}	1468
900	2.88×10^{-19}	319,464	430,570	10^{-8}	1573
999.15	8.68×10^{-17}	307,230	430,454	10^{-7}	1694
999.15	8.68×10^{-17}	307,230	427,526	10^{-6}	1834
1000	9.07×10^{-17}	307,127	427,525	10^{-5}	2000
1071.15	2.76×10^{-15}	298,563	427,477	10^{-4}	2197
1071.15	2.76×10^{-15}	298,563	422,016	10^{-3}	2438
1100	9.56×10^{-15}	295,241	421,785	10^{-2}	2737
1200	4.45×10^{-13}	283,762	421,318	10^{-1}	3118
1300	1.15×10^{-11}	272,303	421,275	1	3619
1400	1.85×10^{-10}	260,835	421,541	NBP	3622
1500	2.08×10^{-9}	249,341	422,005		
1600	1.72×10^{-8}	237,812	422,563		
1700	1.12×10^{-7}	226,248	423,128		
1800	5.90×10^{-7}	214,650	423,680		
1900	2.62×10^{-6}	203,023	424,215		
2000	1.00×10^{-5}	191,368	424,732		
2100	3.39×10^{-5}	179,687	425,232		
2200	1.03×10^{-4}	167,983	425,716		
2300	2.83×10^{-4}	156,257	426,186		
2400	7.16×10^{-4}	144,512	426,645		
2500	1.68×10^{-3}	132,747	427,095		
2600	3.71×10^{-3}	120,964	427,538		

TABLE 48 Vapor Pressure—Cont'd

T (K)	p (bar)	$\Delta G°(T)$ (J/mol)	$\Delta H°(T)$ (J/mol)	p (bar)	T (K)
2700	7.73×10^{-3}	109,164	427,979		
2800	1.53×10^{-2}	97,348	428,417		
2900	2.88×10^{-2}	85,517	428,858		
3000	5.22×10^{-2}	73,670	429,301		
3100	9.09×10^{-2}	61,808	429,749		
3200	0.153	49,932	430,204		
3300	0.250	38,041	430,666		
3400	0.397	26,136	431,137		
3500	0.614	14,218	431,617		
3600	0.927	2285	432,106		
3619.14	1.000	0	432,201		
3700	1.369	−9661	432,605		

NBP, normal boiling point at one atmosphere pressure (1.01325 bar).
$\Delta H°(0) = 433,122$ J/mol.

7. THERMODYNAMIC FUNCTIONS OF PRASEODYMIUM

7.1. Introduction

Gschneidner (1990) selects 1068 K for the transformation from the double-hexagonal close-packed structure to the body-centered cubic structure and 1204 K for the melting point. There is a second-order Néel transformation with ordering on hexagonal sites at 0.039 K (Colclough, 1986).

7.2. Alpha Phase—Low Temperature

Neutron diffraction measurements on polycrystalline samples suggested a Néel transformation at 25 K (Cable et al., 1964), but measurements on single crystals indicated that such an anomaly did not exist down to at least 0.4 K (Hounmann et al., 1975). A sharp rise in the heat capacity below 1 K was initially interpreted as being due to a nuclear contribution by Dreyfus et al. (1961a) (0.5–4 K), Dempesy et al. (1962) (0.3–4.2 K), Lounasmaa (1964a) (0.35–4 K), Holmström et al. (1969) (0.02–0.4 K), and Gregers-Hansen et al. (1972) (0.02–0.3 K), whereas measurements on single crystals by Lindelof et al. (1975) (0.03–0.3 K) showed that the heat capacity did not obey the expected Schottky nuclear heat capacity behavior. Measurements by Erikson

et al. (1983) (0.02–1 K) confirmed that there was no nuclear contribution to the heat capacity but instead a large lambda peak corresponding to a second-order Néel transformation with ordering on hexagonal sites at a critical temperature of 0.042 K, which Colclough (1986) refined to 0.039 K.

Heat capacity measurements in the lambda region by Lindelof et al. (1975) and Erikson et al. (1983) were only given in the form of small graphs. Measurements of Colclough (1986) (0.012–0.24 K) continued to rise below the critical temperature due to residual stress within the samples. Therefore, at temperatures below the maximum, the specific heat curve is assumed to be a mirror image of the measurements above the critical temperature. As a result up to 0.24 K, the lambda transition contributes 0.0522 J/mol to the enthalpy and 1.175 J/(mol K) to the entropy. Because the same purity of metal was used by both Lounasmaa (1964a) and Holmström et al. (1969), heat capacity measurements agree in the overlap region but are significantly higher than those of Colclough (1986). However, by using an electronic coefficient (γ) of 20 mJ/(mol K^2) (Erikson et al., 1983) and a lattice contribution to the heat capacity derived as 0.5535 mJ/(mol K^4) from the Debye temperature of 152 K obtained from elastic constant measurements by Greiner et al. (1973), it is possible to reconcile the measurements of Colclough (1986) and Lounasmaa (1964a) using the following equation valid from 0.32 to 2.7 K:

$$C^{\circ}{}_{\mathrm{p}}(T)(\mathrm{J}/(\mathrm{mol\,K})) = 2.0\times10^{-2}T + 5.535\times10^{-4}T^3 + 1.456\times10^{-2}T^{3/2} + 1.227\times10^{-4}T^5$$

where the third term can be considered to be a magnetic contribution and the fourth term a second lattice contribution.

Above 2.7 K selected values are based on a combination of the heat capacity measurements of Lounasmaa and Sundström (1967) (2.7–24 K) and Berezovskii et al. (1990) (5.9–314 K) except that anomalies in the values of the latter between 215 and 275 K were not included since they were considered as being an experimental artifact since exactly the same behavior was observed for thulium (Berezovskii et al., 1991).

Heat capacity measurements of Forgan (1981) (1–6 K) carried out on very high purity metal were unfortunately shown only in the form of a small graph, but estimated values appear to be significantly lower than those obtained by Lounasmaa (1964a) and Lounasmaa and Sundström (1967) in the overlap region. Above 15 K, measurements of Parkinson et al. (1951) (2.5–170 K) tend from 1% high to 1% low at 40 K before increasing to 2% high at 170 K, while those of Stein and Butera (1970) (1.2–4.2 K) tend from 60% to 8% high.

7.3. Alpha Phase—High Temperature

After correction for temperature scale and from a 273.15 to a 298.15 K base by subtracting 700.63 J/mol from the low-temperature data, the enthalpy

measurements of McKeown (1958) (374–1151 K in the alpha phase) and Berg et al. (1961) (373–1063 K in the alpha phase) agree satisfactorily. However, the enthalpy measurements of Baginskii et al. (1993) (688–1046 K in the alpha phase) are about 14% higher than the above measurements. These differences could be experimental or could be due to various impurity effects since the samples used by Berg et al. (1961) and Baginskii et al. (1993) were stated to be only greater than 99.2% pure, while the metal used by McKeown (1958) was given as possibly being of the order of 99.5% pure. The criterion as to which a set of measurements are to be preferred is by a comparison of the liquid enthalpy measurements in these experiments with those of Stretz and Bautista (1976) which are selected for the liquid range. It is found that the measurements of Berg et al. (1961) are on average only 0.8% lower than the selected values, while those of Baginskii et al. (1993) are on average 10% higher. On these grounds, the measurements of Berg et al. (1961), which are preferred to the earlier measurements of McKeown (1958), are selected for the solid range but like the measurements of McKeown (1958) are generally incompatible with the low-temperature data, almost certainly due to the presence of significant amounts of impurities in the samples used. In order to ensure compatibility with the low-temperature data and obtain a smooth specific heat curve, only the four highest measurements of Berg et al. (1961) in the alpha phase were accepted and combined with the selected specific heat at 298.15 K and its derivative to produce the equation:

$$H^\circ(T) - H^\circ(298)(\mathrm{J/mol}) = 32.0459T - 6.91525 \times 10^{-3}T^2 + 7.37484 \times 10^{-6}T^3 + 152{,}543/T - 9646.86$$

The actual measurements of McKeown (1958) and Berg et al. (1961) tend from 4% low to converge with the selected values. Heat capacity measurements of Kurichenko et al. (1986) (746–1031 K) tend from 3% low to 2% high and then 4% low but above 980 K increase sharply to 29% high.

7.4. Beta Phase

After correction as above, the measurements of Berg et al. (1961) (1083–1199 K) were fitted to the following equation with an overall accuracy as a standard deviation of ±17 J/mol (0.03%):

$$H^\circ(T) - H^\circ(298)(\mathrm{J/mol}) = 38.3826T - 11{,}990.24$$

The derived heat capacity is 38.38 ± 0.21 J/(mol K), and the enthalpy of transition is 3185 J/mol. After correction as above, the two measurements of McKeown (1958) at 1087 and 1151 K average 0.4% low, while the measurements of Baginskii et al. (1993) (1074–1174 K) tend from 11% to 14% high. In spite of the large differences in values, the enthalpy of transition derived by

Baginskii et al. (1993) from their own measurements gives 3182 ± 250 J/mol which agrees closely with the selected value.

7.5. Liquid Phase

After correction for atomic weight and a misprint (the value at 2099 K should have been 78,772 J/mol and not 78,722 J/mol), the enthalpy measurements of Stretz and Bautista (1976) (1460–2289 K) were fitted to the following equation with an overall accuracy as a standard deviation of ± 276 J/mol (0.39%):

$$H^{\circ}(T) - H^{\circ}(298)(\mathrm{J/mol}) = 41.5560T - 8458.83$$

The derived heat capacity is 41.56 ± 0.23 J/(mol K); the enthalpy of fusion, 7353 ± 277 J/mol; and the entropy of fusion, 6.11 ± 0.23 J/(mol K).

After correction as above, the enthalpy measurements of Berg et al. (1961) (1214–1375 K) tend from 1% to 0.5% low, and this explains their lower derived enthalpy of fusion of 6912 ± 12 J/mol. The measurements of Baginskii et al. (1993) (1239–1661 K) tend from 7% to 14% high, and the very different enthalpy of fusion of 5647 ± 400 J/mol determined from these measurements may be associated with the marked trends with temperature found for both their beta phase and liquid enthalpy measurements. Heat capacity measurements of Banchila and Fillipov (1974) (1210–2000 K) tend from 9% to 19% low, while those of Novikov and Mardykin (1975) (1200–1550 K) tend from 10% to 5% high. Measurements of Mardykin and Kashin (1973) (1210–1500 K) were shown only in the form of a small graph.

7.6. Gas Phase

Values are based on one bar standard state pressure and are calculated from the 877 energy levels, including the ground state, listed in Table 49

TABLE 49 Sources of Energy Level Data

Authors	Number of levels
Ralchenko et al. (2012)	412
Ginibre (1981)	15
Ruczkowski et al. (2003)	275
Furmann et al. (2006)	57
Gamper et al. (2011)	24
Shamim et al. (2011)	54
Syed et al. (2011)	40

using the method of Kolsky et al. (1957) and the 2010 Fundamental Constants (Mohr et al., 2011).

7.7. Enthalpy of Sublimation

TABLE 50 Enthalpy of Sublimation at 298.15 K

Authors	Methods	Range (K)	$\Delta_{sub}H^{\circ}$ 298, II law) (kJ/mol)	$\Delta_{sub}H^{\circ}$ (298, III law) (kJ/mol)	Notes
Johnson et al. (1956)	MS	1210–1440	350 ± 8	–	
White et al. (1961)	MS	1505–1797	321 ± 3	–	
Daane (1950, 1955)	KE	1425–1692	342 ± 13	338.6 ± 0.6	
Nachman et al. (1962)	KE	1724–1874	374 ± 8	353.6 ± 0.9	–[a]
Habermann (1963)	KE	1755–2120	366 ± 4	355.3 ± 0.2	–[b]
Habermann and Daane (1964)	KE	1644–2120	367 ± 1	355.3 ± 1.4	–[a]
Shevchenko et al. (1978)	KE	1723–1823	374 ± 4	358.5 ± 0.5	–[a]
Selected				355.8 ± 3.0	

MS, mass spectrometry; KE, Knudsen effusion.
[a]*Given only in the form of the Clausius–Clapeyron equation.*
[b]*This is Run 2 of Habermann and Daane (1964) given in detail.*

In agreement with Konings and Beneš (2010), the selected value is an average of the measurements of Nachman et al. (1962), Habermann and Daane (1964), and Shevchenko et al. (1978).

7.8. Vapor Pressure

The vapor pressure equation for the alpha phase was obtained by evaluating the free energy functions of the solid and the gas at 25 K intervals from 875 to 1050 K and the transition temperature and for the beta phase at 25 K intervals from 1075 to 1200 K and the transition and melting points and for the liquid at 50 K intervals from 1250 to 3550 K and the melting point (Table 51).

TABLE 51 Vapor Pressure Equations

$\ln(p, \text{bar}) = b_1 + b_2/T + b_3 \ln(T) + b_4 T + b_5 T^2$

Phase	Range (K)	b_1	b_2	b_3	b_4	b_5
Alpha	875–1068.15	7.472672	−42,357.90	0.963215	-1.15074×10^{-3}	0
Beta	1068.15–1204.15	19.79656	−42,607.89	−0.9359410	0	0
Liquid	1204.15–2500	40.47881	−43,885.64	−3.892187	1.02129×10^{-3}	1.34810×10^{-8}
	2500–3550	63.72916	−45,422.42	−7.280646	3.03558×10^{-3}	-1.69566×10^{-7}

7.9. Comparison of Selected Values at 298.15 K

Both Holley et al. (1968) and Hultgren et al. (1973) relied mainly on the heat capacity measurements of Parkinson et al. (1951) up to 170 K and an interpolation above this temperature. The values given by Holley et al. (1968) are for 300 K. Konings and Beneš (2010) accepted the evaluation of Berezovskii et al. (1990), and while the present review is based on the same measurements, the enthalpy value differs because the anomalous behavior in the region of 215–275 K was treated as being real by Berezovskii et al. (1990) but was considered as being an experimental artifact in the present evaluation. The difference in entropy can be traced almost entirely to the present inclusion of the contribution from the large lambda anomaly corresponding to the Néel transition at 0.039 K (Table 52).

TABLE 52 Comparison of Heat Capacity, Enthalpy, and Entropy Values at 298.15 K

Authors	C°_p (298) (J/(mol K))	$H^\circ(298) - H^\circ(0)$ (J/mol)	$S^\circ(298)$ (J/(mol K))
Holley et al. (1968)	27.03	7146	73.18
Hultgren et al. (1973)	27.45	7418	73.93
Berezovskii et al. (1990)	28.15	7421	73.74
This work	28.17	7415	74.93

7.10. Summary of Representative Equations

TABLE 53 Representative Equations Above 298.15 K

Alpha phase: 298.15–1068.15 K
$C°_p(T)(\text{J/(mol K)}) = 32.0459 - 1.38305 \times 10^{-2} T + 2.212452 \times 10^{-5} T^2 - 152,543/T^2$
$H°(T) - H°(298)(\text{J/mol}) = 32.0459T - 6.91525 \times 10^{-3} T^2 + 7.37484 \times 10^{-6} T^3 + 152,543/T - 9646.86$
$S°(T)(\text{J/(mol K)}) = 32.0459 \ln(T) - 1.38305 \times 10^{-2} T + 1.106226 \times 10^{-5} T^2 + 76271.5/T^2 - 105.3749$
Beta phase: 1068.15–1204.15 K
$C°_p(T)(\text{J/(mol K)}) = 38.3826$
$H°(T) - H°(298)(\text{J/mol}) = 38.3826T - 11,990.24$
$S°(T)(\text{J/(mol K)}) = 38.3826 \ln(T) - 148.6684$
Liquid phase: 1204.15–3600 K
$C°_p(T)(\text{J/(mol K)}) = 41.5560$
$H°(T) - H°(298)(\text{J/mol}) = 41.5560T - 8458.83$
$S°(T)(\text{J/(mol K)}) = 41.5560 \ln(T) - 165.0730$

TABLE 54 Free Energy Equations Above 298.15 K

Alpha phase: 298.15–1068.15 K
$G°(T) - H°(298)(\text{J/mol}) = 137.4208T + 6.91525 \times 10^{-3} T^2 - 3.68742 \times 10^{-6} T^3 + 76,271.5/T - 32.0459T \ln(T) - 9646.86$
Beta phase: 1068.15–1204.15 K
$G°(T) - H°(298)(\text{J/mol}) = 187.0510T - 38.3826T \ln(T) - 11,990.24$
Liquid phase: 1204.15–3600 K
$G°(T) - H°(298)(\text{J/mol}) = 206.6290T - 41.5560T \ln(T) - 8458.83$

TABLE 55 Transition Values Involved with the Free Energy Equations

Transition	T (K)	$\Delta H°$ (J/mol)	$\Delta S°$ (J/(mol K))
Alpha–beta	1068.15	3184.552	2.9814
Fusion	1204.15	7352.656	6.1061

7.11. Thermodynamic Tables

TABLE 56 Low-Temperature Thermodynamic Data

T (K)	$C°_p(T)$ (J/(mol K))	$H°(T) - H°(0)$ (J/mol)	$S°(T)$ (J/(mol K))	$-[G°(T) - H°(0)]/T$ (J/(mol K))
5	0.600	0.928	1.453	1.268
10	3.725	10.98	2.723	1.625
15	8.361	40.73	5.072	2.357
20	13.343	95.13	8.168	3.411
25	17.839	173.4	11.644	4.706
30	21.308	271.8	15.221	6.161
35	23.580	384.5	18.691	7.705
40	24.844	505.9	21.931	9.282
45	25.234	632	24.901	10.856
50	25.889	760.7	27.612	12.398
55	26.041	890.6	30.088	13.896
60	26.080	1021	32.356	15.341
65	26.069	1151	34.443	16.731
70	26.041	1282	36.374	18.066
75	26.005	1412	38.170	19.347
80	25.940	1542	39.846	20.577
90	25.939	1801	42.899	22.891
100	25.992	2060	45.635	25.031
110	26.045	2321	48.114	27.018
120	26.099	2581	50.383	28.872
130	26.164	2843	52.474	30.608
140	26.235	3105	54.416	32.240
150	26.333	3367	56.229	33.780
160	26.484	3631	57.933	35.237
170	26.635	3897	59.543	36.619
180	26.782	4164	61.070	37.936
190	26.927	4433	62.522	39.192
200	27.069	4703	63.907	40.393

TABLE 56 Low-Temperature Thermodynamic Data—Cont'd

T (K)	$C^\circ_p(T)$ (J/(mol K))	$H^\circ(T) - H^\circ(0)$ (J/mol)	$S^\circ(T)$ (J/(mol K))	$-[G^\circ(T) - H^\circ(0)]/T$ (J/(mol K))
210	27.209	4974	65.231	41.545
220	27.324	5247	66.499	42.650
230	27.432	5521	67.716	43.714
240	27.541	5795	68.886	44.739
250	27.650	6071	70.013	45.727
260	27.758	6348	71.099	46.682
270	27.867	6627	72.149	47.606
280	27.976	6906	73.164	48.501
290	28.084	7186	74.148	49.368
298.15	28.173	7415	74.927	50.056

TABLE 57 High-Temperature Thermodynamic Data

T (K)	$C^\circ_p(T)$ (J/(mol K))	$H^\circ(T) - H^\circ$ (298) (J/mol)	$S^\circ(T)$ (J/(mol K))	$-[G^\circ(T) - H^\circ(298)]/T$ (J/(mol K))
Alpha phase				
298.15	28.173	0	74.927	74.927
300	28.193	52	75.102	74.928
400	29.100	2918	83.341	76.045
500	30.052	5874	89.933	78.185
600	31.289	8938	95.516	80.619
700	32.894	12,144	100.455	83.106
800	34.903	15,531	104.974	85.561
900	37.331	19,139	109.221	87.956
1000	40.187	23,011	113.298	90.287
1068.15	42.382	25,824	116.018	91.842
Beta phase				
1068.15	38.383	29,008	119.000	91.842
1100	38.383	30,231	120.127	92.645

Continued

TABLE 57 High-Temperature Thermodynamic Data—Cont'd

T (K)	$C°_p(T)$ (J/(mol K))	$H°(T) - H°$ (298) (J/mol)	$S°(T)$ (J/(mol K))	$-[G°(T) - H°(298)]/T$ (J/(mol K))
1200	38.383	34,069	123.467	95.076
1204.15	38.383	34,228	123.600	95.174
Liquid phase				
1204.15	41.556	41,581	129.706	95.174
1300	41.556	45,564	132.888	97.839
1400	41.556	49,720	135.968	100.454
1500	41.556	53,875	138.835	102.918
1600	41.556	58,031	141.517	105.248
1700	41.556	62,186	144.036	107.456
1800	41.556	66,342	146.412	109.555
1900	41.556	70,498	148.658	111.555
2000	41.556	74,653	150.790	113.464
2100	41.556	78,809	152.818	115.290
2200	41.556	82,964	154.751	117.040
2300	41.556	87,120	156.598	118.720
2400	41.556	91,276	158.367	120.335
2500	41.556	95,431	160.063	121.891
2600	41.556	99,587	161.693	123.390
2700	41.556	103,742	163.261	124.838
2800	41.556	107,898	164.773	126.238
2900	41.556	112,054	166.231	127.592
3000	41.556	116,209	167.640	128.903
3100	41.556	120,365	169.002	130.175
3200	41.556	124,520	170.322	131.409
3300	41.556	128,676	171.600	132.608
3400	41.556	132,832	172.841	133.773
3500	41.556	136,987	174.045	134.906
3600	41.556	141,143	175.216	136.010

TABLE 58 Thermodynamic Properties of the Gas Phase

T (K)	$C°_p(T)$ (J/(mol K))	$H°(T) - H°$ (298) (J/mol)	$S°(T)$ (J/(mol K))	$-[G°(T) - H°(298)]/T$ (J/(mol K))
298.15	21.360	0	189.811	189.811
300	21.377	40	189.943	189.811
400	22.531	2232	196.241	190.662
500	23.854	4551	201.411	192.309
600	25.068	6998	205.870	194.206
700	26.132	9559	209.816	196.159
800	27.104	12,222	213.369	198.092
900	28.063	14,980	216.617	199.972
1000	29.071	17,836	219.625	201.789
1068.15	29.811	19,842	221.565	202.989
1100	30.177	20,797	222.447	203.540
1200	31.415	23,876	225.124	205.228
1204.15	31.469	24,006	225.233	205.297
1300	32.806	27,085	227.693	206.858
1400	34.360	30,442	230.180	208.435
1500	36.074	33,963	232.608	209.966
1600	37.932	37,662	234.995	211.456
1700	39.903	41,553	237.353	212.910
1800	41.947	45,645	239.691	214.333
1900	44.014	49,943	242.015	215.729
2000	46.048	54,447	244.324	217.101
2100	47.996	59,150	246.619	218.452
2200	49.086	64,041	248.894	219.784
2300	51.434	69,105	251.144	221.099
2400	52.848	74,321	253.364	222.397
2500	54.026	79,667	255.546	223.680
2600	54.957	85,118	257.684	224.946
2700	55.641	90,650	259.772	226.198

Continued

TABLE 58 Thermodynamic Properties of the Gas Phase—Cont'd

T (K)	$C°_p(T)$ (J/(mol K))	$H°(T) - H°$ (298) (J/mol)	$S°(T)$ (J/(mol K))	$-[G°(T) - H°(298)]/T$ (J/(mol K))
2800	56.088	96,238	261.804	227.433
2900	56.312	101,860	263.777	228.653
3000	56.335	107,494	265.687	229.856
3100	56.180	113,121	267.532	231.041
3200	55.875	118,725	269.311	232.210
3300	55.441	124,292	271.024	233.360
3400	54.903	129,810	272.672	234.492
3500	54.284	135,270	274.254	235.606
3600	53.603	140,665	275.774	236.701

$H°(298) - H°(0) = 6223.2$ J/mol.

TABLE 59 Vapor Pressure

T (K)	p (bar)	$\Delta G°(T)$ (J/mol)	$\Delta H°(T)$ (J/mol)	p (bar)	T (K)
298.15	4.65×10^{-57}	321,548	355,800	10^{-15}	891
300	1.13×10^{-56}	321,335	355,757	10^{-14}	937
400	3.35×10^{-41}	309,953	355,113	10^{-13}	987
500	6.19×10^{-32}	298,738	354,477	10^{-12}	1043
600	9.09×10^{-26}	287,648	353,860	10^{-11}	1107
700	2.27×10^{-21}	276,663	353,215	10^{-10}	1179
800	4.44×10^{-18}	265,775	352,491	10^{-9}	1263
900	1.59×10^{-15}	254,985	351,641	10^{-8}	1360
1000	1.74×10^{-13}	244,298	350,625	10^{-7}	1475
1068.15	2.55×10^{-12}	237,078	349,818	10^{-6}	1610
1068.15	2.55×10^{-12}	237,078	346,634	10^{-5}	1773
1100	7.89×10^{-12}	233,816	346,367	10^{-4}	1973
1200	1.85×10^{-10}	223,618	345,607	10^{-3}	2222

TABLE 59 Vapor Pressure—Cont'd

T (K)	p (bar)	$\Delta G°(T)$ (J/mol)	$\Delta H°(T)$ (J/mol)	p (bar)	T (K)
1204.15	2.08×10^{-10}	223,196	345,578	10^{-2}	2542
1204.15	2.08×10^{-10}	223,196	338,225	10^{-1}	2962
1300	2.50×10^{-9}	214,076	337,321	1	3533
1400	2.32×10^{-8}	204,626	336,523	NBP	3537
1500	1.59×10^{-7}	195,228	335,887		
1600	8.55×10^{-7}	185,867	335,431		
1700	3.77×10^{-6}	176,528	335,166		
1800	1.41×10^{-5}	167,200	335,103		
1900	4.57×10^{-5}	157,869	335,245		
2000	1.32×10^{-4}	148,525	335,593		
2100	3.46×10^{-4}	139,159	336,141		
2200	8.30×10^{-4}	129,762	336,877		
2300	1.85×10^{-3}	120,328	337,785		
2400	3.87×10^{-3}	110,851	338,845		
2500	7.64×10^{-3}	101,327	340,036		
2600	1.43×10^{-2}	91,754	341,331		
2700	2.58×10^{-2}	82,129	342,708		
2800	4.45×10^{-2}	72,452	344,140		
2900	7.42×10^{-2}	62,723	345,606		
3000	0.120	52,943	347,085		
3100	0.188	43,114	348,556		
3200	0.287	33,238	350,005		
3300	0.427	23,317	351,416		
3400	0.624	13,354	352,778		
3500	0.891	3352	354,039		
3533.43	1.000	0	354,504		
3600	1.250	−6687	355,267		

NBP, normal boiling point at one atmosphere pressure (1.01325 bar).
$\Delta H°(0) = 356,992$ J/mol.

8. THERMODYNAMIC FUNCTIONS OF NEODYMIUM

8.1. Introduction

Gschneidner and Beaudry (1991) determined 1135 K for the transition temperature from the double-hexagonal close-packed alpha phase to the body-centered cubic beta phase and 1295 K for the melting point. Values selected by Gschneidner (1990) based on earlier measurements agreed to within 1 K. In the low-temperature region, there is a Néel transition with ordering on hexagonal sites at 20.0 K (Zochowski and McEwen, 1986) and a second Néel transition with ordering on cubic sites at 8.3 K (Forgan et al., 1979).

8.2. Alpha Phase—Low Temperature

A nuclear contribution to the heat capacity arises from the two isotopes ^{143}Nd and ^{145}Nd. Heat capacity measurements by Anderson et al. (1969) (0.026–0.37 K) were used to derive values of the magnetic interaction parameters (a') and the quadrupole coupling constants (P) for both isotopes and following the procedure as given in Section 2.4, and in Part 8.11, the variation with temperature of the nuclear contribution was derived.

Colclough (1986) (0.016–0.81 K) derived values for the electronic specific heat coefficient (γ) and the magnetic contribution to the heat capacity. In combination with the nuclear contribution as derived in Part 8.11, the heat capacity up to 1 K can be represented by

$$C^{\circ}{}_{\mathrm{p}}(T)(\mathrm{mJ/(mol\,K)}) = 6.625/T^2 + 3.641\times10^{-2}/T^3 - 2.087\times10^{-2}/T^4 + 22T + 390T^3\exp(-1.06/T)$$

Between 1 and 2 K, a lattice contribution of 0.449 T^3 J/(mol K) was added based on a Debye temperature of 163 K determined by Rosen (1967) from elastic constant measurements. With this addition, heat capacity measurements of Lounasmaa (1964a) (0.40–3.8 K) were used to derive a different interpretation of the large magnetic contribution as $133.5T^{2.383}$ which extended representation of the low-temperature heat capacity to 3.8 K:

$$C^{\circ}{}_{p}(T)(\mathrm{mJ/(mol\,K)}) = 6.625/T^2 + 3.641\times10^{-2}/T^3 - 2.087\times10^{-2}/T^4 + 22T + 0.449T^3 + 133.5T^{2.383}$$

Between 5 and 20 K, the heat capacity shows complicated behavior. From thermal expansion measurements, Zochowski and McEwen (1986) determined the upper Néel transition with ordering on hexagonal sites to be 20.0 K and a second transition at 19.1 K described as being due to magnetic satellites split transversely as the modulation wavevectors tilt away from the ⟨100⟩ directions. Both transitions were apparently first order although from X-ray diffraction measurements Bulatov and Dolzhenko

(1989) suggested that the Néel transition was second order. From heat capacity measurements, Forgan et al. (1979) determined the lower Néel transition with ordering on cubic sites to be at 8.3 K and a second prominent peak at 6.3 K which is considered to be due to hexagonal satellites splitting into different components. X-ray diffraction measurements of Bulatov and Dolzhenko (1989) established that the Néel transition was second order and the 6.3-K transition to be first order. Additional anomalies in the heat capacity measurements were also observed at 7.8 and 5.8 K but not observed in the X-ray diffraction measurements. Unfortunately, these heat capacity measurements on very high purity metal were shown only in the form of small graphs, and therefore, the only values which could be used are those determined by Lounasmaa and Sundström (1967) (3.1–25 K) on metal of much lower purity. These indicate a heat capacity peak at 7.43 K which is considered to be a mixture of the enthalpy of transition at 6.3 K and the peak arising from the second-order transition at 8.3 K and a second peak at around 20 K, which is used to represent the upper Néel transition, as it has not been firmly established as being first order.

Above 23 K and up to 80 K, the heat capacity values of Parkinson et al. (1951) (2–160 K) were preferred but above this temperature begin to deviate higher such that they could not extrapolate to values of heat capacity selected in the room temperature region. Therefore, the three values of heat capacity estimated by Hultgren et al. (1973) at 150, 200, and 250 K were accepted together with the selected value at 298.15 K and with an interpolation between 80 and 150 K based on values of specific heat and their derivatives at these two temperatures. From 2 to 30 K, the measurements of Parkinson et al. (1951) tend from 21% low to converge to the selected values, but above 80 K, the trend is to a maximum of 8% high.

8.3. Alpha Phase—High Temperature

Enthalpy measurements of Spedding et al. (1960b) (372–1126 K in the alpha phase) were corrected for temperature scale and from a 273.15 to a 298.15 K base by subtracting 683.15 J/mol obtained from the low-temperature data and were fitted to the following equation with an overall accuracy as a standard deviation of ±20 J/mol (0.21%):

$$H^\circ(T) - H^\circ(298)(\mathrm{J/mol}) = 25.2203T + 1.89846 \times 10^{-3}T^2 + 4.24898 \times 10^{-6}T^3 - 7800.81$$

Enthalpy measurements of Jaeger et al. (1938) (575–881 K) average 14% higher than the selected values, while those of Spedding and Miller (1951) (297–632 K) average 6% higher to 525 K and then scatter 3% high to 2% low. Heat capacity measurements of Ivliev and Zinov'ev (1981)

(400–1000 K) and Kurichenko et al. (1985) (900–1295 K) are shown only in the form of small graphs.

8.4. Beta Phase

After correction as above, enthalpy measurements of Spedding et al. (1960b) (1147–1259 K) were fitted to the following equation with an overall accuracy as a standard deviation of ±4 J/mol (0.01%):

$$H^\circ(T) - H^\circ(298)(\mathrm{J/mol}) = 44.5172T - 18{,}008.44$$

The derived heat capacity is 44.52 ± 0.05 J/(mol K), and the enthalpy of transition is 3036 ± 20 J/mol. Faudot and Harmelin (1990) directly determined the enthalpy of transition value to be between 2467 and 3029 J/mol.

8.5. Liquid Phase

After correction for atomic weight, the enthalpy measurements of Stretz and Bautista (1975b) (1446–2246 K) were fitted to the following equation with an overall accuracy as a standard deviation of ±364 J/mol (0.47%):

$$H^\circ(T) - H^\circ(298)(\mathrm{J/mol}) = 44.0168T - 10{,}042.80$$

The derived heat capacity is 44.02 ± 0.33 J/(mol K); the enthalpy of fusion, 7318 ± 364 J/mol; and the entropy of fusion, 5.65 ± 0.28 J/(mol K). Faudot and Harmelin (1990) directly determined the enthalpy of fusion to be between 6303 and 6707 J/mol. After correction as above, the three enthalpy measurements of Spedding et al. (1960b) (1304–1368 K) tend from 0.5% low to 0.6% high. Heat capacity measurements of Mardykin et al. (1972) (1300–1600 K) and Atalla et al. (1972) were shown only in the form of small graphs.

8.6. Gas Phase

Values are based on one bar standard state pressure and are calculated from the 716 energy levels, including the ground state, listed in Table 60 using the method of Kolsky et al. (1957) and the 2010 Fundamental Constants (Mohr et al., 2011).

TABLE 60 Sources of Energy Level Data

Authors	Number of levels
Ralchenko et al. (2012)	709
Aufmuth et al. (1992)	7

8.7. Enthalpy of Sublimation

TABLE 61 Enthalpy of Sublimation at 298.15 K

Authors	Methods	Range (K)	$\Delta_{sub}H°$(298, II law) (kJ/mol)	$\Delta_{sub}H°$(298, III law) (kJ/mol)	Notes
Johnson et al. (1956)	MS	1170–1400	318 ± 10	–	
White et al. (1961)	MS	1381–1792	318 ± 4	–	
Spedding and Daane (1954)	KE	1340–1610	311 ± 8	–	–[a]
Nachman, et al. (1962, 1963)	KE	1638–1701	376 ± 10	317.7 ± 0.6	
Habermann (1963)	KE	1538–1923	338 ± 2	326.6 ± 0.2	–[b]
Habermann and Daane (1964)	KE	1528–1923	338 ± 1	326.6 ± 1.3	–[c]
Shevchenko, et al. (1978)	KE	1723–1823	320 ± 9	327.9 ± 0.2	–[c]
Selected				327.3 ± 2.0	

MS, mass spectrometry; KE, Knudsen effusion.
[a]*Hultgren et al. (1973) give 327.6 ± 2.1 kJ/mol for this value.*
[b]*This is Run 4 of Habermann and Daane (1964) given in detail.*
[c]*Given only in the form of the Clausius–Clapeyron equation.*

The selected value is an average of the measurements of Habermann and Daane (1964) and Shevchenko et al. (1978).

8.8. Vapor Pressure

The vapor pressure equation for the alpha phase was obtained by evaluating the free energy functions of the solid and the gas at 25 K intervals from 800 to 1125 K and the transition temperature; for the beta phase, at 20 K intervals from 1140 to 1280 K and the transition and melting points; and for the liquid phase, at 50 K intervals from 1300 to 3300 K and the melting point (Table 62).

TABLE 62 Vapor Pressure Equations

$\ln(p, \text{bar}) = b_1 + b_2/T + b_3 \ln(T) + b_4 T + b_5 T^2$

Phase	Range (K)	b_1	b_2	b_3	b_4	b_5
Alpha	800–1135.15	16.68294	−39,424.91	−0.4185192	3.78411×10^{-4}	-3.19033×10^{-7}
Beta	1135.15–1295.15	27.21944	−40,200.26	−1.816615	0	0
Liquid	1295.15–2300	18.52738	−38813.78	−0.6004901	-1.05234×10^{-3}	1.60535×10^{-7}
	2300–3300	85.48607	−46071.03	−9.818059	2.87414×10^{-3}	-1.20028×10^{-7}

8.9. Comparison of Selected Values at 298.15 K

All reviews depended on a compromise between the heat capacity measurements of Parkinson et al. (1951) up to 160 K and the selected value of the specific heat at 298.15 K from the high-temperature data (Table 63).

TABLE 63 Comparison of Heat Capacity, Enthalpy, and Entropy at 298.15 K

Authors	$C^\circ_p(298)$ (J/(mol K))	$H^\circ(298) - H^\circ(0)$ (J/mol)	$S^\circ(298)$ (J/(mol K))
Holley et al. (1968)	27.49	7573	73.22
Hultgren et al. (1973)	27.41	7134	71.09
Cordfunke and Konings (1990)	27.50	–	71.10
Konings and Beneš (2010)	–	–	72.40
This work	27.49	7144	71.84

8.10. Summary of Representative Equations

TABLE 64 Representative Equations Above 298.15 K

Alpha phase: 298.15–1135.15 K
$C^\circ_p(T)(\text{J/(mol K)}) = 25.2203 + 3.79692 \times 10^{-3} T + 1.274694 \times 10^{-5} T^2$
$H^\circ(T) - H^\circ(298)(\text{J/mol}) = 25.2203T + 1.89846 \times 10^{-3} T^2 + 4.24898 \times 10^{-6} T^3 - 7800.81$
$S^\circ(T)(\text{J/(mol K)}) = 25.2203 \ln(T) + 3.79692 \times 10^{-3} T + 6.37347 \times 10^{-6} T^2 - 73.5498$
Beta phase: 1135.15–1295.15 K
$C^\circ_p(T)(\text{J/(mol K)}) = 44.5172$
$H^\circ(T) - H^\circ(298)(\text{J/mol}) = 44.5172T - 18,008.44$
$S^\circ(T)(\text{J/(mol K)}) = 44.5172 \ln(T) - 194.0971$
Liquid phase: 1295.15–3300 K
$C^\circ_p(T)(\text{J/(mol K)}) = 44.0168$
$H^\circ(T) - H^\circ(298)(\text{J/mol}) = 44.0168T - 10,042.80$
$S^\circ(T)(\text{J/(mol K)}) = 44.0168 \ln(T) - 184.8611$

TABLE 65 Free Energy Equations Above 298.15 K

Alpha phase: 298.15–1135.15 K
$G^\circ(T) - H^\circ(298)(\text{J/mol}) = 98.7701T - 1.89846 \times 10^{-3} T^2 - 2.12449 \times 10^{-6} T^3 - 25.2203T \ln(T) - 7800.81$
Beta phase: 1135.15–1295.15 K
$G^\circ(T) - H^\circ(298)(\text{J/mol}) = 238.6143T - 44.5172T \ln(T) - 18,008.44$
Liquid phase: 1295.15–3300 K
$G^\circ(T) - H^\circ(298)(\text{J/mol}) = 228.8779T - 44.0168T \ln(T) - 10,042.80$

TABLE 66 Transition Values Involved with the Free Energy Equations

Transition	T (K)	ΔH° (J/mol)	ΔS° (J/(mol K))
Alpha–beta	1135.15	3035.905	2.6745
Fusion	1295.15	7317.544	5.6500

8.11. Nuclear Heat Capacity

The nuclear heat capacity $C^{\circ}{}_{N}$ can be correlated by an equation using inverse powers of temperature:

$$C^{\circ}{}_{N}(T) = X\left(A/T^2 + B/T^3 + C/T^4 + \cdots\right)$$

where X is the isotopic fraction for the isotope and if a' is the magnetic interaction parameter, P is the quadrupole coupling constant, R is the gas constant, and I is the nuclear spin then since both ^{143}Nd and ^{145}Nd have $I = 7/2$:

$$A/R = 21/4a'^2 + 21P^2; \quad B/R = -63a'^2P; \quad C/R = -273/16a'^4$$

From their heat capacity measurements, Anderson et al. (1969) were able to derive values of a' and P not only for the individual isotopes but also for individual hexagonal and cubic sublattices (Table 67):

$$^{143}\mathrm{Nd(hexagonal)} : C^{\circ}{}_{N}(T)(\mathrm{mJ/(mol\,K)}) = 58.52/T^2 + 0.3508/T^3 - 0.2546/T^4$$
$$^{143}Nd(\mathrm{cubic}) : C^{\circ}{}_{N}(T)(\mathrm{mJ/(mol\,K)}) = 27.54/T^2 + 0.1650/T^3 - 5.631 \times 10^{-2}/T^4$$
$$^{145}\mathrm{Nd(hexagonal)} : C^{\circ}{}_{N}(T)(\mathrm{mJ/(mol\,K)}) = 22.51/T^2 + 8.097 \times 10^{-2}/T^3 - 3.767 \times 10^{-2}/T^4$$
$$^{145}\mathrm{Nd(cubic)} : C^{\circ}{}_{N}(T)(\mathrm{mJ/(mol\,K)}) = 10.64/T^2 + 3.824 \times 10^{-2}/T^3 - 8.402 \times 10^{-3}/T^4$$

Anderson et al. (1969) selected 12.20% for the abundance of ^{143}Nd and 8.30% for the abundance of ^{145}Nd. Assuming 50% for each of the sublattices, then the combined nuclear contribution is given by

$$\mathrm{Combined} : C^{\circ}{}_{N}(T)(\mathrm{mJ/(mol\,K)}) = 6.625/T^2 + 3.641 \times 10^{-2}/T^3 - 2.087 \times 10^{-2}/T^4$$

TABLE 67 Summary of Determinations of a' and P

Isotope	Sublattice	a' (K)	P (K)
^{143}Nd	Hexagonal	-0.0366 ± 0.0005	-0.0005 ± 0.0004
	Cubic	-0.0251 ± 0.0004	-0.0005 ± 0.0007
^{145}Nd	Hexagonal	-0.0227 ± 0.0003	-0.0003 ± 0.0002
	Cubic	-0.0156 ± 0.0002	-0.0003 ± 0.0004

8.12. Thermodynamic Tables

TABLE 68 Low-Temperature Thermodynamic Data

T (K)	$C^\circ_p(T)$ (J/(mol K))	$H^\circ(T) - H^\circ(0)$ (J/mol)	$S^\circ(T)$ (J/(mol K))	$-[G^\circ(T) - H^\circ(0)]/T$ (J/(mol K))
5	4.255	7.19	2.140	0.701
6	5.408	12.12	3.034	1.015
7	6.475	17.96	3.932	1.367
7.43	7.150	20.89	4.338	1.527
8	6.540	24.80	4.846	1.746
9	5.568	30.72	5.545	2.131
10	5.487	36.21	6.124	2.502
12	6.210	47.78	7.176	3.194
15	8.085	69.10	8.754	4.147
18	10.564	97.01	10.443	5.053
19	11.354	108.0	11.035	5.353
20	12.123	119.7	11.637	5.652
21	10.769	130.8	12.179	5.950
22	11.050	141.7	12.685	6.245
25	12.211	176.6	14.170	7.107
30	14.184	242.5	16.569	8.485
35	16.208	318.5	18.907	9.808
40	18.284	404.9	21.206	11.089
45	20.094	500.8	23.468	12.339
50	21.589	605.1	25.665	13.563
60	23.640	832.3	29.801	15.930
70	25.062	1076	33.562	18.184
80	25.732	1331	36.961	20.323
90	25.998	1590	40.007	22.344
100	26.177	1851	42.755	24.250
110	26.311	2113	45.257	26.047
120	26.398	2377	47.550	27.745

Continued

TABLE 68 Low-Temperature Thermodynamic Data—Cont'd

T (K)	$C°_p(T)$ (J/(mol K))	$H°(T) - H°(0)$ (J/mol)	$S°(T)$ (J/(mol K))	$-[G°(T) - H°(0)]/T$ (J/(mol K))
130	26.449	2641	49.665	29.351
140	26.475	2906	51.627	30.873
150	26.485	3170	53.453	32.318
160	26.494	3435	55.163	33.693
170	26.511	3700	56.770	35.004
180	26.536	3965	58.286	36.255
190	26.569	4231	59.721	37.453
200	26.610	4497	61.085	38.601
210	26.660	4763	62.385	39.703
220	26.718	5030	63.626	40.762
230	26.785	5298	64.815	41.782
240	26.860	5566	65.957	42.766
250	26.945	5835	67.055	43.716
260	27.039	6105	68.114	44.634
270	27.142	6376	69.136	45.522
280	27.255	6648	70.125	46.384
290	27.378	6921	71.084	47.219
298.15	27.485	7144	71.844	47.882

TABLE 69 High-Temperature Thermodynamic Data

T (K)	$C°_p(T)$ (J/(mol K))	$H°(T) - H°$ (298) (J/mol)	$S°(T)$ (J/(mol K))	$-[G°(T) - H°(298)]/T$ (J/(mol K))
Alpha phase				
298.15	27.485	0	71.844	71.844
300	27.507	51	72.014	71.844
400	28.779	2863	80.095	72.938
500	30.305	5815	86.676	75.046
600	32.087	8933	92.355	77.468

TABLE 69 High-Temperature Thermodynamic Data—Cont'd

T (K)	$C°_p(T)$ (J/(mol K))	$H°(T) - H°$ (298) (J/mol)	$S°(T)$ (J/(mol K))	$-[G°(T) - H°(298)]/T$ (J/(mol K))
700	34.124	12,241	97.451	79.964
800	36.416	15,766	102.155	82.447
900	38.963	19,533	106.588	84.885
1000	41.764	23,567	110.836	87.269
1100	44.821	27,894	114.958	89.600
1135.15	45.956	29,489	116.386	90.407
Beta phase				
1135.15	44.517	32,525	119.060	90.407
1200	44.517	35,412	121.533	92.023
1295.15	44.517	39,648	124.930	94.318
Liquid phase				
1295.15	44.017	46,966	130.580	94.318
1300	44.017	47,179	130.745	94.453
1400	44.017	51,581	134.007	97.163
1500	44.017	55,982	137.043	99.722
1600	44.017	60,384	139.884	102.144
1700	44.017	64,786	142.553	104.443
1800	44.017	69,187	145.069	106.631
1900	44.017	73,589	147.449	108.717
2000	44.017	77,991	149.706	110.711
2100	44.017	82,392	151.854	112.619
2200	44.017	86,794	153.902	114.45
2300	44.017	91,196	155.858	116.208
2400	44.017	95,598	157.732	117.899
2500	44.017	99,999	159.528	119.529
2600	44.017	104,401	161.255	121.101
2700	44.017	108,803	162.916	122.619
2800	44.017	113,204	164.517	124.086
2900	44.017	117,606	166.061	125.508

Continued

TABLE 69 High-Temperature Thermodynamic Data—Cont'd

T (K)	$C^\circ_p(T)$ (J/(mol K))	$H^\circ(T) - H^\circ$ (298) (J/mol)	$S^\circ(T)$ (J/(mol K))	$-[G^\circ(T) - H^\circ(298)]/T$ (J/(mol K))
3000	44.017	122,008	167.554	126.884
3100	44.017	126,409	168.997	128.22
3200	44.017	130,811	170.394	129.516
3300	44.017	135,213	171.749	130.775

TABLE 70 Thermodynamic Properties of the Gas Phase

T (K)	$C^\circ_p(T)$ (J/(mol K))	$H^\circ(T) - H^\circ$ (298) (J/mol)	$S^\circ(T)$ (J/(mol K))	$-[G^\circ(T) - H^\circ(298)]/T$ (J/(mol K))
298.15	22.092	0	189.410	189.410
300	22.120	41	189.547	189.411
400	23.732	2333	196.130	190.297
500	25.176	4781	201.587	192.024
600	26.294	7257	206.280	194.018
700	27.132	10,030	210.400	196.070
800	27.766	12,777	214.066	198.095
900	28.258	15,579	217.666	200.056
1000	28.659	18,425	220.364	201.939
1100	29.014	21,309	223.113	203.741
1135.15	29.136	22,331	224.027	204.355
1200	29.366	24,228	225.652	205.462
1295.15	29.736	27,039	227.906	207.029
1300	29.756	27,184	228.018	207.107
1400	30.224	30,182	230.239	208.681
1500	30.804	33,232	232.344	210.189
1600	31.527	36,347	234.354	211.637
1700	32.411	39,543	236.291	213.030
1800	33.466	42,835	238.172	214.375

TABLE 70 Thermodynamic Properties of the Gas Phase—Cont'd

T (K)	$C^\circ_p(T)$ (J/(mol K))	$H^\circ(T) - H^\circ$ (298) (J/mol)	$S^\circ(T)$ (J/(mol K))	$-[G^\circ(T) - H^\circ(298)]/T$ (J/(mol K))
1900	34.693	46,242	240.014	215.676
2000	36.078	49,779	241.828	216.939
2100	37.601	53,462	243.625	218.167
2200	39.235	57,303	245.411	219.364
2300	40.942	61,311	247.193	220.536
2400	42.687	65,493	248.972	221.683
2500	44.429	69,849	250.750	222.810
2600	46.131	74,377	252.526	223.919
2700	47.757	79,072	254.298	225.012
2800	49.277	83,925	256.062	226.089
2900	50.666	88,923	257.816	227.153
3000	51.906	94,053	259.555	228.204
3100	52.984	99,299	261.275	229.243
3200	53.894	104,644	262.972	230.271
3300	54.635	110,072	264.642	231.287

$H^\circ(298) - H^\circ(0) = 6268.8$ J/mol.

TABLE 71 Vapor Pressure

T (K)	p (bar)	$\Delta G^\circ(T)$ (J/mol)	$\Delta H^\circ(T)$ (J/mol)	p (bar)	T (K)
298.15	6.32×10^{-52}	292,248	327,300	10^{-15}	813
300	1.43×10^{-51}	292,030	327,290	10^{-14}	854
400	2.45×10^{-37}	280,356	326,770	10^{-13}	899
500	8.28×10^{-29}	268,811	326,266	10^{-12}	950
600	3.93×10^{-23}	257,370	325,725	10^{-11}	1006
700	4.38×10^{-19}	246,026	325,090	10^{-10}	1070
800	4.68×10^{-16}	234,782	324,311	10^{-9}	1144
900	1.05×10^{-13}	223,647	232,346	10^{-8}	1229
1000	7.83×10^{-12}	212,630	322,158	10^{-7}	1329

Continued

TABLE 71 Vapor Pressure—Cont'd

T (K)	p (bar)	$\Delta G^\circ(T)$ (J/mol)	$\Delta H^\circ(T)$ (J/mol)	p (bar)	T (K)
1100	2.63×10^{-10}	201,745	320,715	10^{-6}	1449
1135.15	7.78×10^{-10}	197,953	320,142	10^{-5}	1594
1135.15	7.78×10^{-10}	197,953	317,106	10^{-4}	1776
1200	4.77×10^{-9}	191,173	316,116	10^{-3}	2000
1295.15	4.87×10^{-8}	181,322	314,691	10^{-2}	2294
1295.15	4.87×10^{-8}	181,322	307,374	10^{-1}	2692
1300	5.41×10^{-8}	180,850	307,305	1	3253
1400	4.10×10^{-7}	171,175	305,901	NBP	3257
1500	2.36×10^{-6}	161,600	304,550		
1600	1.08×10^{-5}	152,112	303,263		
1700	4.12×10^{-5}	142,702	302,057		
1800	1.35×10^{-4}	133,361	300,948		
1900	3.88×10^{-4}	124,078	299,953		
2000	1.00×10^{-3}	114,845	299,088		
2100	2.36×10^{-3}	105,651	298,370		
2200	5.12×10^{-3}	96,488	297,809		
2300	1.04×10^{-2}	87,346	297,416		
2400	1.98×10^{-2}	78,218	297,195		
2500	3.60×10^{-2}	69,096	297,150		
2600	6.24×10^{-2}	59,971	297,276		
2700	0.104	50,839	297,570		
2800	0.166	41,691	298,021		
2900	0.259	32,529	298,618		
3000	0.392	23,341	299,346		
3100	0.578	14,127	300,190		
3200	0.832	4885	301,132		
3252.72	1.000	0	301,665		
3300	1.174	−4389	302,160		

NBP, normal boiling point at one atmosphere pressure (1.01325 bar).
$\Delta H^\circ(0) = 328,175$ J/mol.

9. THERMODYNAMIC FUNCTIONS OF PROMETHIUM

9.1. Introduction

Angelini and Adair (1974, 1976) determined the transformation from the double-hexagonal close-packed alpha phase to the body-centered cubic beta phase to be 1163 ± 5 K and the melting point as 1315 ± 5 K. These values were accepted by Gschneidner (1990). Although the actual structure of the beta phase has not been confirmed, it is considered to be the same as that obtained for all neighboring elements.

Although ^{145}Pm has the longest half-life at 17.7 years (Audi et al., 2003a), nearly all significant measurements have been carried out on ^{147}Pm of half-life 2.623 years, and this isotope is selected for calculating the thermodynamic properties.

9.2. Condensed Phases

Unfortunately, the light lanthanides do not show satisfactory periodic trends in properties and even praseodymium and neodymium, which are isostructural with promethium, show relatively poor agreement as to their physical properties. However, the ratio of the enthalpies of transformation and melting for neodymium as selected in Section 8 above at 0.415 ± 0.021 agrees with the value of 0.415 obtained for promethium by Angelini and Adair (1974, 1976). Therefore, selecting the summation of the entropies of transition and fusion for neodymium at 8.325 J/(mol K) leads to an enthalpy of transition for promethium of 3090 J/mol and an enthalpy of fusion of 7450 J/mol.

Heat capacity values for the body-centered cubic and liquid phases for lanthanum to samarium show a poor correlation, but from these, a value of 44 J/(mol K) is selected for both phases for promethium. Based mainly on neodymium, a heat capacity value of 27.5 J/(mol K) is selected for the alpha phase at 298.15 K and 45.5 J/(mol K) at 1163 K based on a heat capacity difference of 1.5 J/(mol K) at the transition temperature. An intermediate value of 35.0 J/(mol K) at 750 K is also selected based on the neodymium specific heat curve. These three values were used to represent the heat capacity of the alpha phase as

$$C^{\circ}{}_{\mathrm{p}}(T)(\mathrm{J}/(\mathrm{mol\,K})) = 24.8302 + 5.91568 \times 10^{-3} T + 1.01920 \times 10^{-5} T^2$$

Ward and Hill (1976) estimate the entropy at 298.15 K to be 71.5 J/(mol K) which is accepted and agrees with a value of 71 J/(mol K) estimated by Morss (1976).

9.3. Gas Phase

Values are based on one bar standard state pressure and are calculated from 223 energy levels selected by Ralchenko et al. (2012) using the method of Kolsky et al. (1957) and the 2010 Fundamental Constants (Mohr et al., 2011).

9.4. Enthalpy of Sublimation

A value of 315 ± 3 kJ/mol is selected for the enthalpy of sublimation at 298.15 K based on estimated values of 312.5 kJ/mol by Johansson and Rosengren (1975) and 318 kJ/mol by Morss (1976). Johnson (1974) estimated a value of 301 ± 33 kJ/mol which encompasses the above values. These values suggest a close affinity between promethium and the lighter analogues praseodymium and neodymium, and the selected value is therefore preferred to a periodic trend of a value halfway between that of neodymium and samarium (270 kJ/mol).

9.5. Vapor Pressure

The vapor pressure equation for the alpha phase was obtained by evaluating the free energy functions of the solid and the gas at 25 K intervals from 775 to 1150 K and the transition temperature; for the beta phase, at 20 K intervals from 1170 to 1310 K and the transition and melting points; and for the liquid phase, at 50 K intervals from 1350 to 3200 K and the melting point (Table 72).

TABLE 72 Vapor Pressure Equations

$\ln(p, \text{bar}) = b_1 + b_2/T + b_3 \ln(T) + b_4 T + b_5 T^2$

Phase	Range (K)	b_1	b_2	b_3	b_4	b_5
Alpha	775–1163.15	13.95886	−37,860.68	-2.14537×10^{-2}	1.08159×10^{-4}	-2.55389×10^{-7}
Beta	1163.15–1315.15	25.95563	−38,722.18	−1.647180	0	0
Liquid	1315.15–2250	28.49664	−38,047.61	−2.123928	3.28028×10^{-4}	-3.55430×10^{-8}
	2250–3200	15.77826	−36,713.89	−0.3634505	-4.53437×10^{-4}	2.27967×10^{-8}

9.6. Summary of Representative Equations

TABLE 73 Representative Equations Above 298.15 K

Alpha phase: 298.15–1163.15 K
$C^\circ_p(T)(\text{J/(mol K)}) = 24.8302 + 5.91568 \times 10^{-3} T + 1.01920 \times 10^{-5} T^2$
$H^\circ(T) - H^\circ(298)(\text{J/mol}) = 24.8302T + 2.95784 \times 10^{-3} T^2 + 3.39733 \times 10^{-6} T^3 - 7756.10$
$S^\circ(T)(\text{J/(mol K)}) = 24.8302 \ln(T) + 5.91568 \times 10^{-3} T + 5.09600 \times 10^{-6} T^2 - 72.1892$
Beta phase: 1163.15–1315.15 K
$C^\circ_p(T)(\text{J/(mol K)}) = 44.0000$
$H^\circ(T) - H^\circ(298)(\text{J/mol}) = 44.0000T - 17,615.54$
$S^\circ(T)(\text{J/(mol K)}) = 44.0000 \ln(T) - 191.0748$
Liquid phase: 1315.15–3200 K
$C^\circ_p(T)(\text{J/mol K}) = 44.0000$
$H^\circ(T) - H^\circ(298)(\text{J/mol}) = 44.0000T - 10,165.54$
$S^\circ(T)(\text{J/mol K}) = 44.0000 \ln(T) - 185.4100$

TABLE 74 Free Energy Equations Above 298.15 K

Alpha phase: 298.15–1163.15 K
$G^\circ(T) - H^\circ(298)(\text{J/mol}) = 97.0194T - 2.95784 \times 10^{-3} T^2 - 1.69867 \times 10^{-6} T^3 - 24.8302T \ln(T) - 7756.10$
Beta phase: 1163.15–1315.15 K
$G^\circ(T) - H^\circ(298)(\text{J/mol}) = 235.0748T - 44.0000T \ln(T) - 17,615.54$
Liquid phase: 1315.15–3200 K
$G^\circ(T) - H^\circ(298)(\text{J/mol}) = 229.4100T - 44.0000T \ln(T) - 10,165.54$

TABLE 75 Transition Values Involved with the Free Energy Equations

Transition	T (K)	ΔH° (J/mol)	ΔS° (J/(mol K))
Alpha–beta	1163.15	3090.000	2.6566
Fusion	1315.15	7450.000	5.6648

9.7. Thermodynamic Tables

TABLE 76 Thermodynamic Properties of the Condensed Phases

T (K)	$C^\circ_p(T)$ (J/(mol K))	$H^\circ(T) - H^\circ$ (298) (J/mol)	$S^\circ(T)$ (J/(mol K))	$-[G^\circ(T) - H^\circ(298)]/T$ (J/(mol K))
Alpha phase				
298.15	27.500	0	71.500	71.500
300	27.522	51	71.670	71.501
400	28.827	2867	79.762	72.595
500	30.336	5823	86.352	74.706
600	32.049	8941	92.032	77.131
700	33.965	12,240	97.113	79.628
800	36.086	15,741	101.785	82.109
900	38.410	19,464	106.167	84.541
1000	40.938	23,429	110.343	86.914
1100	43.670	27,658	114.372	89.228
1163.15	45.500	30,473	115.860	90.661
Beta phase				
1163.15	44.000	33,563	119.516	90.661
1200	44.000	35,184	120.889	91.568
1300	44.000	39,584	124.410	93.961
1315.15	44.000	40,251	124.920	94.315
Liquid phase				
1315.15	44.000	47,701	130.585	94.315
1400	44.000	51,434	133.336	96.597
1500	44.000	55,834	136.372	99.149
1600	44.000	60,234	139.211	101.565
1700	44.000	64,634	141.879	103.859
1800	44.000	69,034	144.394	106.041
1900	44.000	73,434	146.773	108.123
2000	44.000	77,834	149.030	110.112
2100	44.000	82,234	151.176	112.017

TABLE 76 Thermodynamic Properties of the Condensed Phases—Cont'd

T (K)	$C°_p(T)$ (J/(mol K))	$H°(T) - H°$ (298) (J/mol)	$S°(T)$ (J/(mol K))	$-[G°(T) - H°(298)]/T$ (J/(mol K))
2200	44.000	86,634	153.223	113.844
2300	44.000	91,034	155.179	115.599
2400	44.000	95,434	157.052	117.287
2500	44.000	99,834	158.848	118.914
2600	44.000	104,234	160.574	120.484
2700	44.000	108,634	162.234	121.999
2800	44.000	113,034	163.834	123.465
2900	44.000	117,434	165.379	124.884
3000	44.000	121,834	166.870	126.259
3100	44.000	126,234	168.313	127.592
3200	44.000	130,634	169.710	128.887

TABLE 77 Thermodynamic Properties of the Gas Phase

T (K)	$C°_p(T)$ (J/(mol K))	$H°(T) - H°(298)$ (J/mol)	$S°(T)$ (J/(mol K))	$-[G°(T) - H°(298)]/T$ (J/(mol K))
298.15	24.257	0	187.103	187.103
300	24.299	45	187.254	187.104
400	26.181	2575	194.520	188.082
500	27.403	5259	200.503	189.985
600	28.203	8042	205.575	192.172
700	28.764	10,892	209.967	194.407
800	29.189	13,790	213.837	196.599
900	29.531	16,727	217.295	198.710
1000	29.817	19,695	220.622	200.727
1100	30.055	22,688	223.275	202.649
1163.15	30.181	24,591	224.956	203.815
1200	30.247	25,704	225.899	204.479

Continued

TABLE 77 Thermodynamic Properties of the Gas Phase—Cont'd

T (K)	$C^\circ_p(T)$ (J/(mol K))	$H^\circ(T) - H^\circ(298)$ (J/mol)	$S^\circ(T)$ (J/(mol K))	$-[G^\circ(T) - H^\circ(298)]/T$ (J/(mol K))
1300	30.391	28,736	228.326	206.221
1315.15	30.409	29,197	228.678	206.478
1400	30.487	31,781	230.582	207.881
1500	30.535	34,832	232.687	209.466
1600	30.536	37,886	234.658	210.979
1700	30.493	40,938	236.508	212.427
1800	30.411	43,983	238.249	213.814
1900	30.296	47,019	239.890	215.143
2000	30.152	50,042	241.441	216.420
2100	29.987	53,049	242.908	217.647
2200	29.807	56,038	244.299	218.827
2300	29.619	59,010	245.620	219.963
2400	29.428	61,962	246.876	221.059
2500	29.243	64,896	248.074	222.115
2600	29.068	67,811	249.217	223.136
2700	28.910	70,710	250.311	224.122
2800	28.775	73,594	251.360	225.077
2900	28.668	76,466	252.368	226.000
3000	28.594	79,329	253.338	226.896
3100	28.558	82,186	254.275	227.764
3200	28.563	85,041	255.182	228.606

$H^\circ(298) - H^\circ(0) = 6462.7$ J/mol.

TABLE 78 Vapor Pressure

T (K)	p (bar)	$\Delta G^\circ(T)$ (J/mol)	$\Delta H^\circ(T)$ (J/mol)	p (bar)	T (K)
298.15	7.12×10^{-50}	280,533	315,000	10^{-15}	784
300	1.56×10^{-49}	280,319	314,994	10^{-14}	824
400	7.91×10^{-36}	268,805	314,709	10^{-13}	867

TABLE 78 Vapor Pressure—Cont'd

T (K)	p (bar)	$\Delta G°(T)$ (J/mol)	$\Delta H°(T)$ (J/mol)	p (bar)	T (K)
500	1.30×10^{-27}	257,360	314,436	10^{-12}	916
600	3.86×10^{-22}	245,975	314,101	10^{-11}	971
700	3.09×10^{-18}	234,655	313,652	10^{-10}	1032
800	2.59×10^{-15}	223,408	313,050	10^{-9}	1103
900	4.80×10^{-13}	212,248	312,263	10^{-8}	1183
1000	3.10×10^{-11}	201,187	311,265	10^{-7}	1278
1100	9.26×10^{-10}	190,237	310,031	10^{-6}	1392
1163.15	5.82×10^{-9}	183,385	309,117	10^{-5}	1531
1163.15	5.82×10^{-9}	183,385	306,027	10^{-4}	1701
1200	1.54×10^{-8}	179,507	305,520	10^{-3}	1917
1300	1.61×10^{-7}	169,062	304,152	10^{-2}	2198
1315.15	2.23×10^{-7}	167,489	303,946	10^{-1}	2584
1315.15	2.23×10^{-7}	167,489	296,496	1	3152
1400	1.56×10^{-6}	159,202	295,346	NBP	3156
1500	6.21×10^{-6}	149,524	293,998		
1600	2.70×10^{-5}	139,937	292,652		
1700	9.83×10^{-5}	130,434	291,303		
1800	3.08×10^{-4}	121,010	289,949		
1900	8.52×10^{-4}	111,661	288,585		
2000	2.12×10^{-3}	102,385	287,207		
2100	4.81×10^{-3}	93,178	285,814		
2200	1.01×10^{-2}	84,038	284,404		
2300	1.98×10^{-2}	74,962	282,975		
2400	3.67×10^{-2}	65,949	281,528		
2500	6.44×10^{-2}	56,997	280,061		
2600	0.108	48,104	278,577		
2700	0.174	39,268	277,075		
2800	0.27	30,488	275,559		
2900	0.406	21,762	274,031		

Continued

TABLE 78 Vapor Pressure—Cont'd

T (K)	p (bar)	$\Delta G°(T)$ (J/mol)	$\Delta H°(T)$ (J/mol)	p (bar)	T (K)
3000	0.592	13,089	272,494		
3100	0.841	4468	270,951		
3152.05	1	0	270,147		
3200	1.167	−4104	269,407		

NBP, normal boiling point at one atmosphere pressure (1.01325 bar).

10. THERMAL FUNCTIONS OF SAMARIUM

10.1. Introduction

Beaudry and Gschneidner (1978b) select 1004 K for the equilibrium transformation from the alpha phase rhombohedral structure to the beta phase close-packed hexagonal structure, while Gschneidner (1990) selects 1195 K for the transformation from the beta phase to the body-centered cubic gamma phase and 1347 K for the melting point. There is a second-order Néel transition representing ordering on cubic sites at 13.25 K (Lounasmaa and Sundström, 1967) and a second-order Néel transition representing ordering on hexagonal sites at 105.2 K (Jennings et al., 1959).

10.2. Alpha Phase—Low Temperature

A nuclear contribution to the heat capacity arises from the two isotopes ^{147}Sm and ^{149}Sm. Heat capacity measurements by Anderson et al. (1969) (0.024–0.42 K) were used to derive values of the magnetic interaction parameters (a') and the quadrupole coupling constants (P) for both isotopes, and following the procedure as given in Section 2.4 and Part 10.12, the variation with temperature of the nuclear contribution was derived.

The heat capacity measurements of Lounasmaa (1962a) (0.4–4.0 K) were analyzed in terms of nuclear, electronic, and combined lattice-magnetic terms. Further to these measurements, a number of new determinations have helped to improve the fit. The measurements of Lounasmaa and Sundström (1967) showed that the discrepant Run III of Lounasmaa (1962a) was incorrect and therefore rejected. Rosen (1967) determined the Debye temperature from elastic constant measurements to be 169 K at 4.2 K, equivalent to a lattice contribution to the heat capacity as 0.403 mJ/(mol K^4). With the values of the nuclear and lattice contributions fixed, the heat capacity values of Lounasmaa (1962a) were used to derive the electronic

coefficient (γ), a magnetic contribution proportional to T^3, and a second lattice coefficient proportional to T^5. The heat capacity up to 4 K can then be represented by the following equation which has an overall accuracy as a standard deviation of ± 0.44 mJ/mol. The first three terms are the nuclear contribution as derived in Part 10.12, and the fourth terms is the electronic coefficient.

$$C^{\circ}{}_{\mathrm{p}}(T)(\mathrm{mJ}/(\mathrm{mol\,K})) = 8.55/T^2 + 0.0107/T^3 - 0.0195/T^4 + 12.34T + 0.198T^3 + 0.403T^3 + 0.0359T^5$$

The electronic coefficient is notably lower than the value of 13.7 mJ/(mol K) determined by Lounasmaa and Veuro (1972) for the even–even isotope ^{152}Sm which has no nuclear contribution. Although these measurements were carried out over the temperature range of 0.45–6 K and generally represent an improvement over the measurements of Lounasmaa (1962a), unfortunately, the results were only given in the form of a small graph.

Heat capacity measurements of Dreyfus (1961) and Dreyfus et al. (1961b, d) (0.4–2.0 K) were shown only in the form of small graphs. In this region, the measurements of Roberts (1957) are from 5% to 14% lower, while in this overlap region, the measurements of Lounasmaa and Sundström (1967) (3.0–24.8 K) are on average 1% lower than the selected curve but being determined later are probably superior, and this indicates the type of accuracy that must be applied to the measured values.

From 4 to 25 K, selected values are the heat capacity measurements of Lounasmaa and Sundström (1967) which identify the second-order Néel transition representing the magnetic ordering on cubic sites with a temperature determined to be 13.7 K by Stewart and Collocott (1989) from heat capacity measurements and as 12.7 K by Thompson et al. (1992) from electrical resistivity measurements. The measurements of Lounasmaa and Sundström (1967) can be extrapolated to a peak of 13.42 J/(mol K) at 13.25 K. A second peak at 9.6 K which was also observed by Roberts (1957) and Stewart and Collocott (1989) was shown by Thompson et al. (1992) to be due to oxide inclusions and was therefore ignored in the evaluation. In this region, the measurements of Roberts (1957) show a different peak for the ordering on cubic sites at 13.6 K, and therefore, the comparison is distorted close to this temperature. However, from 4 to 13 K, these measurements are on average 13% lower than the selected values, while from 15 to 20 K, they initially agree but then deviate to 4% higher. The heat capacity measurements of Stewart and Collocott (1989) (2–32 K) on much higher purity metal should be the definitive values up to 30 K but were unfortunately shown only in the form of small graphs which did, however, show an unconfirmed anomaly at 20.4 K.

The measurements of Lounasmaa and Sundström (1967) up to 20 K were combined with the measurements of Jennings et al. (1959) (13–350 K) which were given only in the form of smooth values 20–360 K. Because of this

combination, it was found that the enthalpy values of Jennings et al. were 0.46 J/mol too high and the entropy values were 0.032 J/(mol K) too low. These values were subtracted and added to the smooth values, respectively, which were also corrected for atomic weight as 150.36/150.35.

Jennings et al. (1959) identified the second-order Néel transition corresponding to magnetic ordering on hexagonal sites at a temperature of 105.2 K in relatively good agreement with the value of 105.8 ± 0.5 K obtained by Yao et al. (1980) from electrical resistivity measurements. Heat capacity measurements by Jayasuriya et al. (1986) (80–400 K) on metal of relatively high purity were shown only in the form of a small graphs. These measurements could not reproduce the lambda-like peak obtained by Jennings et al. (1959) but instead show a continuity of heat capacity up to the transition temperature and then a sharp drop above this which is more reminiscent of a first-order transition, although there is no suggestion of this. However, the suggestion is that impurities, particularly hydrogen, may have enhanced the peak as found by Jennings et al. (1959), but unfortunately, there are no other actual published measurements to replace the presently selected values.

10.3. Alpha Phase—High Temperature

Enthalpy values have been determined by both Spedding et al. (1960b) (375–1174 K in the alpha plus beta phases) and Baginskii et al. (1996) (392–977 K in the alpha phase). The latter measurements were selected since they were carried out on much purer metal but still showed a major anomaly at about 545 K and a transition temperature about 26 K lower than the selected value. These authors treated the anomaly at 545 K as being representative of the pure metal and developed two equations covering the data up to 545 K and a further equation covering the range of 545–978 K. However, a Shomate plot clearly indicates that all of the measurements below 723 K were affected by the anomaly and are to be rejected, and only the five measurements at 723–977 K were accepted and fitted to the following equation which has an overall accuracy as a standard deviation of ± 43 J/mol (0.09%):

$$H^\circ(T) - H^\circ(298)(\mathrm{J/mol}) = 28.5112T + 7.37573 \times 10^{-3}T^2 + 300399/T - 10,163.8$$

The rejected data points are from 2% lower to 1% higher than the selected curve.

The measurements of Spedding et al. (1960b) were corrected for both atomic weight and temperature scale and from a 273.15 to a 298.15 K base by subtracting 728.90 J/(mol K) from the low-temperature data. These authors attempted to represent the values for the alpha phase by a complex equation, but a Shomate plot clearly indicates slopes for two different phases with a

transition temperature of about 700 K in agreement with the eutectoid temperature of 703 K in the samarium–samarium hydride system (Beaudry and Gschneidner, 1978b), suggesting that the metal used was highly contaminated with hydrogen with only the four lowest data points representing the alpha phase and the five highest data points representing the beta phase stabilized to lower temperatures by the hydrogen contamination. The alpha phase values are from 2% lower to 8% higher than the selected values.

Heat capacity measurements of Polovov (1973) (300–950 K) are shown only in the form of a small graph, but they detect an anomaly at 694 K which may well correspond to the eutectoid in the samarium–samarium hydride system and they also detect a further anomaly at 830 K which may well be the reduced alpha–beta transformation temperature. Heat capacity measurements of Kurichenko et al. (1985) (900–1350 K) are also shown in the form of a small graph, but in particular, their thermal diffusivity measurements show an anomaly at 980 K which may also be associated with the alpha–beta transformation.

10.4. Beta Phase

Enthalpy measurements were performed by Baginskii et al. (1996) (979–1179 K). A discrepant value at 1071 K was rejected and the remaining data points were fitted to the following equation with a standard deviation of the fit of ±15 J/mol (0.04%):

$$H^\circ(T) - H^\circ(298)(\mathrm{J/mol}) = 7.15958T + 1.79675 \times 10^{-2}T^2 + 1296.12$$

The derived enthalpy of transition is 400 ± 46 J/mol. When extrapolated to the selected transition temperature, the evaluation of Baginskii et al. (1996) leads to 398 J/mol in satisfactory agreement, while Polovov (1973) estimates a value of 452 ± 37 J/mol from the observed transition at 830 K. The five data points of Spedding et al. (1960b) (774–1174 K), which are considered to be in the beta region but generally stabilized below the transition temperature, are from 1% to 6% higher than the selected values.

10.5. Gamma Phase

For enthalpy measurements of Baginskii et al. (1996) (1202–1343 K), the two lowest data points at 1205 and 1210 K and a further data point at 1335 K were rejected and the remaining values were fitted to the following equation which has an overall accuracy as a standard deviation of ± 84 J/mol (0.19%):

$$H^\circ(T) - H^\circ(298)(\mathrm{J/mol}) = 47.2787T - 17{,}892.2$$

The derived heat capacity is 47.28 ± 0.60 J/(mol K), and the enthalpy of transition is 3096 ± 85 J/mol.

After correction for temperature scale and atomic weight and from a 273.15 to a 298.15 K base as described above, the three measurements of Spedding et al. (1960b) (1202–1312 K) are on average 4% higher than the selected values. A direct determination of the enthalpy of transition at 3800 J/mol by Gibson and Haire (1992) is definitely too high when compared to the above values even though the transition temperature was reproduced.

10.6. Liquid Phase

It was found that a linear equation gave only a poor representation of the enthalpy measurements of Baginskii et al. (1996) (1369–1902 K) which were best fitted by the following quadratic equation with an overall accuracy as a standard deviation of ±90 J/mol (0.11%):

$$H^\circ(T) - H^\circ(298)(\mathrm{J/mol}) = 26.5315T + 9.21992 \times 10^{-3}T^2 + 2900.49$$

The derived enthalpy of fusion is 9576 ± 123 J/mol and the entropy of fusion 7.11 ± 0.09 J/(mol K).

The three data points in the liquid range obtained by Spedding et al. (1960b) (1353–1399 K), as corrected above, are 1–2% higher than the selected values.

10.7. Gas Phase

Values are based on one bar standard state pressure and are calculated from 1326 energy levels, including the ground state, which are listed in Table 79 using the method of Kolsky et al. (1957) and the 2010 Fundamental Constants (Mohr et al., 2011).

TABLE 79 Sources of Energy Level Data

Authors	References	Number of Levels
Ralchenko et al. (2012)	30	472
Jia et al. (1993)	31	7
Jayasekharan et al. (1996)	32	86
Jayasekharan et al. (2000a)	33	565
Jayasekharan et al. (2000b)	34	28
Gomonai and Kudelich (2002)	35	140
Gomonai and Pickan (2003)	36	4
Hong-Ying et al. (2009)	37	34

Eleven additional new levels given by Gomonai and Pickan (2003) were included in Gomonai and Kudelich (2002). All of the levels of Jia et al. (1993) and 10 of the levels of Jayasekharan et al. (1996) were revised by Jayasekharan et al. (2000a).

10.8. Enthalpy of Sublimation

TABLE 80 Enthalpy of Sublimation at 298.15 K

Authors	Methods	Range (K)	$\Delta_{sub}H^{\circ}$(298, II law) (kJ/mol)	$\Delta_{sub}H^{\circ}$(298, III law) (kJ/mol)	Notes
Savage et al. (1959)	MS	700–950	206 ± 2	–	
Polyachenko and Novikov (1963a,b)	BP	1373–1623	186	193.1 ± 0.6	–[a]
Habermann (1963)	KE	923–1208	215 ± 1	204.3 ± 0.2	–[b]
Habermann and Daane (1964)	KE	885–1222	212 ± 1	204.5 ± 1.2	–[a]
Herrick (1964)	TE	928–1160	207 ± 2	207.8 ± 0.1	–[c]
Yamamoto et al. (1965)	KE	1033–1302	232 ± 2	204.3 ± 0.6	
Kruglykh et al. (1965)	KE	757–994	161 ± 1	188.7 ± 0.7	
Lundin and Yamamoto (1967)	KE	1033–1073	215 ± 6	199.8 ± 1.0	–[a,d]
Fedechkin and Shmykov (1973)	Eff	1000–1150	211 ± 6	198.8 ± 0.9	–[a,d]
Desideri et al. (1973)	TE	800–998	179 ± 1	184.6 ± 0.6	–[a]
		1043–1179	207 ± 4	208.7 ± 0.1	
Selected				208.0 ± 2.0	

MS, mass spectrometry; BP, boiling points; KE, Knudsen effusion; TE, torsion effusion; Eff, effusion.
[a] *Given only in the form of the Clausius–Clapeyron equation.*
[b] *This is Run 4 of Habermann and Daane (1964) given in detail.*
[c] *Average of three runs—a fourth run was rejected by Herrick (1964).*
[d] *Both values were given since they were based on different sources of material from Ames and Lunex.*

Only the measurements of Herrick (1964) and Disideri et al. (1973) do not show trends with temperature, but in both cases, only metal of initial purity 99% was available although further refinement was carried out on the samples used by Herrick (1964) and therefore most weight is given to these measurements. The assigned error accounts for the spread in the values obtained from these two sets of measurements

10.9. Vapor Pressure

For the alpha phase, the vapor pressure equation was derived by evaluating the thermodynamic properties at 20 K intervals from 500 to 1000 K and the transition temperature; for the beta phase, at 20 K intervals from 1010 to 1190 K and the two transition temperatures; for the gamma phase, at 20 K intervals from 1200 to 1340 K and the transition temperature and the melting point; and for the liquid phase, at 50 K intervals from 1350 to 2100 K and the melting point (Table 81).

10.10. Comparison of Selected Values at 298.15 K

All reviews are based on the values determined by Jennings et al. (1959) but with small differences in interpretation leading to different values of entropy (Table 82).

TABLE 81 Vapor Pressure Equations

$\ln(p, \text{bar}) = b_1 + b_2/T + b_3 \ln(T) + b_4 T + b_5 T^2$

Phase	Range (K)	b_1	b_2	b_3	b_4	b_5
Alpha	500–1004.15	11.71085	−24,998.35	0.369143	-8.11931×10^{-4}	-3.65872×10^{-8}
Beta	1004.15–1195.15	−8.187788	−23,551.14	3.261838	-2.37918×10^{-3}	0
Gamma	1195.15–1347.15	24.55614	−25,792.94	−1.4507	-2.66278×10^{-4}	0
Liquid	1347.15–2100	−0.3830677	−22,089.01	2.012998	-2.02162×10^{-3}	7.18616×10^{-8}

TABLE 82 Comparison of Heat Capacity, Enthalpy, and Entropy Values at 298.15 K

Authors	$C°_p(298)$ (J/(mol K))	$H°(298) - H°(0)$ (J/mol)	$S°(298)$ (J/(mol K))
Holley et al. (1968)	29.53	7575	69.58
Hultgren et al. (1973)	29.53	7575	69.50
Konings and Beneš (2010)	29.53	–	69.60
This work	29.53	7575	69.64

10.11. Summary of Representative Equations

TABLE 83 Representative Equations Above 298.15 K

Alpha phase: 298.15–1004.15 K
$C°_p(T)(\text{J/(mol K)}) = 28.5112 + 1.475146 \times 10^{-2} T - 300,399/T^2$
$H°(T) - H°(298)(\text{J/mol}) = 28.5112T + 7.37573 \times 10^{-3} T^2 + 300,399/T - 10,163.8$
$S°(T)(\text{J/(mol K)}) = 28.5112 \ln(T) + 1.475146 \times 10^{-2} T + 150199.5/T^2 - 98.8931$
Beta phase: 1004.15–1195.15 K
$C°_p(T)(\text{J/(mol K)}) = 7.15958 + 3.59350 \times 10^{-2} T$
$H°(T) - H°(298)(\text{J/mol}) = 7.15958T + 1.79675 \times 10^{-2} T^2 + 1296.12$
$S°(T)(\text{J/(mol K)}) = 7.15958 \ln(T) + 3.59350 \times 10^{-2} T + 27.96334$
Gamma phase: 1195.15–1347.15 K
$C°_p(T)(\text{J/(mol K)}) = 47.2787$
$H°(T) - H°(298)(\text{J/mol}) = 47.2787T - 17,892.2$
$S°(T)(\text{J/(mol K)}) = 47.2787 \ln(T) - 210.7840$
Liquid phase: 1347.15–2100 K
$C°_p(T)(\text{J/(mol K)}) = 26.5315 + 1.843984 \times 10^{-2} T$
$H°(T) - H°(298)(\text{J/mol}) = 26.5315T + 9.21992 \times 10^{-3} T^2 + 2900.49$
$S°(T)(\text{J/(mol K)}) = 26.5315 \ln(T) + 1.843984 \times 10^{-2} T - 79.0182$

TABLE 84 Free Energy Equations Above 298.15 K

Alpha phase: 298.15–1004.15 K
$G^\circ(T) - H^\circ(298)(\text{J/mol}) = 127.4043T - 7.37573 \times 10^{-3}T^2 + 150,199.5/T - 28.5112T\ln(T) - 10,163.8$
Beta phase: 1004.15–1195.15 K
$G^\circ(T) - H^\circ(298)(\text{J/mol}) = -20.80376T - 1.79675 \times 10^{-2}T^2 - 7.15958T\ln(T) + 1296.12$
Gamma phase: 1195.15–1347.15 K
$G^\circ(T) - H^\circ(298)(\text{J/mol}) = 258.0627T - 47.2787T\ln(T) - 17,892.20$
Liquid phase: 1347.15–2100 K
$G^\circ(T) - H^\circ(298)(\text{J/mol}) = 105.5497T - 9.21992 \times 10^{-3}T^2 - 26.5315T\ln(T) + 2900.49$

TABLE 85 Transition Values Involved with the Free Energy Equations

Transition	T (K)	ΔH° (J/mol)	ΔS° (J/(mol K))
Alpha–beta	1004.15	400.397	0.3987
Beta–gamma	1195.15	3095.565	2.5901
Fusion	1347.15	9575.531	7.1080

10.12. Nuclear Heat Capacity

The nuclear heat capacity $C^\circ{}_N$ can be correlated by an equation using inverse powers of temperature:

$$C^\circ{}_N(T) = X\left(A/T^2 + B/T^3 + C/T^4 + \mathrm{L}\right)$$

where X is the isotopic fraction for the isotope and if a' is the magnetic interaction parameter, P is the quadrupole coupling constant, R is the gas constant, and I is the nuclear spin then since both ^{147}Sm and ^{149}Sm have $I = 7/2$ then

$$A/R = 21/4a'^2 + 21P^2;\ \ B/R = -63a'^2P;\ \ \ C/R = -273/16a'^4$$

Anderson et al. (1969) determined the heat capacity from 0.0241 to 0.4167 K and by ratioing the magnetic moments of the two even–odd isotopes which give rise to the nuclear heat capacity and selecting values for their atomic abundance they arrived at the following values for a' and P:

Isotope	X	a' (K)	P (K)
^{147}Sm	0.1507	-0.0283 ± 0.0008	-0.0002 ± 0.0003
^{149}Sm	0.1384	-0.0233 ± 0.0007	0.00005 ± 0.00008

Substituting these values into the above equations, then

$$^{147}\mathrm{Sm}: C^{\circ}{}_{\mathrm{N}}(T)(\mathrm{mJ}/(\mathrm{mol\,K})) = 34.97/T^2 + 0.08390/T^3 - 0.09100/T^4$$

$$^{149}\mathrm{Sm}: C^{\circ}{}_{\mathrm{N}}(T)(\mathrm{mJ}/(\mathrm{mol\,K})) = 23.70/T^2 - 0.01422/T^3 - 0.04181/T^4$$

$$\mathrm{Combined}: C^{\circ}{}_{\mathrm{N}}(T)(\mathrm{mJ}/(\mathrm{mol\,K})) = 8.55/T^2 + 0.0107/T^3 - 0.0195/T^4$$

10.13. Thermodynamic Tables

TABLE 86 Low-Temperature Thermodynamic Data

T (K)	$C^{\circ}{}_{\mathrm{p}}(T)$ (J/(mol K))	$H^{\circ}(T) - H^{\circ}(0)$ (J/mol)	$S^{\circ}(T)$ (J/(mol K))	$-[G^{\circ}(T) - H^{\circ}(0)]/T$ (J/(mol K))
5	0.257	0.350	0.111	0.0410
10	2.983	6.753	0.895	0.220
11	4.251	10.32	1.234	0.296
12	6.953	15.72	1.702	0.392
12.2	7.988	17.21	1.825	0.415
12.4	9.023	18.91	1.964	0.438
12.6	10.06	20.82	2.116	0.464
12.8	11.09	22.94	2.283	0.491
13.0	12.13	25.26	2.463	0.520
13.2	13.16	27.79	2.656	0.551
13.25	13.42	28.44	2.705	0.559
13.4	12.46	30.39	2.852	0.584
13.6	11.19	32.76	3.027	0.618
13.8	9.917	34.87	3.181	0.654
14.0	8.647	36.72	3.315	0.692
14.5	6.218	40.33	3.568	0.787
15	5.651	43.25	3.766	0.883

Continued

TABLE 86 Low-Temperature Thermodynamic Data—Cont'd

T (K)	$C°_p(T)$ (J/(mol K))	$H°(T) - H°(0)$ (J/mol)	$S°(T)$ (J/(mol K))	$-[G°(T) - H°(0)]/T$ (J/(mol K))
16	5.497	48.72	4.119	1.074
17	5.873	54.40	4.463	1.263
18	6.325	60.49	4.811	1.451
19	6.813	67.06	5.166	1.637
20	7.309	74.12	5.528	1.822
25	10.05	117.4	7.446	2.752
30	13.00	175.0	9.539	3.706
35	15.77	247.0	11.757	4.698
40	18.28	332.3	14.032	5.725
45	20.55	429.5	16.322	6.778
50	22.57	537.4	18.594	7.847
60	26.20	781.3	23.040	10.017
70	29.32	1060	27.317	12.179
80	32.21	1367	31.420	14.330
90	35.09	1704	35.384	16.450
100	37.98	2069	39.224	18.537
102	38.86	2146	39.984	18.949
104	40.33	2224	40.750	19.362
104.2	40.57	2232	40.827	19.402
104.4	40.82	2241	40.905	19.443
104.6	41.16	2249	40.984	19.485
104.8	41.68	2257	41.063	19.526
105.0	42.04	2265	41.143	19.567
105.2	42.17	2274	41.223	19.608
105.4	41.74	2282	41.303	19.649
105.6	39.98	2291	41.381	19.690
105.8	37.45	2298	41.454	19.732

TABLE 86 Low-Temperature Thermodynamic Data—Cont'd

T (K)	$C^\circ_p(T)$ (J/(mol K))	$H^\circ(T) - H^\circ(0)$ (J/mol)	$S^\circ(T)$ (J/(mol K))	$-[G^\circ(T) - H^\circ(0)]/T$ (J/(mol K))
106	34.14	2305	41.521	19.772
106.5	29.51	2321	41.668	19.875
107.0	28.43	2335	41.804	19.978
107.5	29.97	2350	41.935	20.079
108	27.66	2363	42.064	20.180
110	27.12	2418	42.566	20.583
115	26.61	2552	43.758	21.564
120	26.37	2685	44.885	22.513
130	26.23	2948	46.990	24.315
140	26.22	3210	48.933	26.005
150	26.29	3473	50.743	27.593
160	26.42	3736	52.444	29.094
170	26.57	4001	54.052	30.516
180	26.71	4268	55.574	31.865
190	26.86	4536	57.022	33.151
200	27.07	4805	58.406	34.380
210	27.27	5077	59.731	35.555
220	27.48	5351	61.005	36.684
230	27.71	5627	62.231	37.768
240	27.93	5905	63.415	38.811
250	28.22	6186	64.561	39.818
260	28.49	6469	65.674	40.791
270	28.70	6755	66.753	41.733
280	28.98	7044	67.802	42.645
290	29.28	7335	68.825	43.531
298.15	29.53	7575	69.640	44.233

TABLE 87 High-Temperature Thermodynamic Data

T (K)	$C°_p(T)$ (J/(mol K))	$H°(T) - H°(298)$ (J/mol)	$S°(T)$ (J/(mol K))	$-[G°(T) - H°(298)]/T$ (J/(mol K))
Alpha phase				
298.15	29.530	0	69.64	69.640
300	29.599	55	69.823	69.641
400	32.534	3172	78.770	70.841
500	34.685	6537	86.269	73.196
600	36.528	10,099	92.759	75.928
700	38.224	13,837	98.519	78.751
800	39.843	17,741	103.729	81.553
900	41.417	21,804	108.513	84.286
1000	42.962	26,024	112.957	86.933
1004.15	43.026	26,202	113.135	87.041
Beta phase				
1004.15	43.244	26,602	113.534	87.041
1100	46.688	30,912	117.631	89.529
1195.15	50.107	35,517	121.644	91.926
Gamma phase				
1195.15	42.279	38,613	124.334	91.926
1200	42.279	38,842	124.426	92.057
1300	42.279	43,570	128.210	94.694
1347.15	42.279	45,799	129.894	95.897
Liquid phase				
1347.15	51.373	55,375	137.002	95.897
1400	52.347	58,116	138.998	97.487
1500	54.191	63,443	142.672	100.377
1600	56.035	68,954	146.229	103.132
1700	57.879	74,650	149.681	105.769
1800	59.723	80,530	153.041	108.303
1900	61.567	86,594	156.320	110.744
2000	63.411	92,843	159.525	113.103
2100	65.255	99,276	162.663	115.389

TABLE 88 Thermodynamic Properties of the Gas Phase

T (K)	$C°_p(T)$ (J/(mol K))	$H°(T) - H°(298)$ (J/mol)	$S°(T)$ (J/(mol K))	$-[G°(T) - H°(298)]/T$ (J/(mol K))
298.15	30.354	0	183.046	183.046
300	30.354	56	183.234	183.046
400	30.471	3096	191.979	184.238
500	30.655	6153	198.798	186.493
600	30.830	9227	204.403	189.024
700	30.944	12,316	209.165	191.570
800	30.956	15,412	213.299	194.034
900	30.847	18,504	216.940	196.380
1000	30.620	21,578	220.179	198.601
1004.15	30.609	21,705	220.306	198.691
1100	30.295	24,624	223.083	200.697
1195.15	29.918	27,489	225.582	202.581
1200	29.898	27,635	225.703	202.674
1300	29.461	30,603	228.079	204.538
1347.15	29.248	31,987	229.125	205.380
1400	29.011	33,526	230.245	206.298
1500	28.575	36,405	232.232	207.962
1600	28.174	39,242	234.063	209.537
1700	27.828	42,042	235.760	211.030
1800	27.553	44,810	237.343	212.448
1900	27.362	47,555	238.827	213.798
2000	27.267	50,286	240.228	215.085
2100	27.276	53,012	241.558	216.314

$H°(298) - H°(0) = 8170.6$ J/mol.

TABLE 89 Vapor Pressure

T (K)	p (bar)	$\Delta G^\circ(T)$ (J/mol)	$\Delta H^\circ(T)$ (J/mol)	p (bar)	T (K)
298.15	3.04×10^{-31}	174,188	208,000	10^{-15}	519
300	5.11×10^{-31}	173,978	207,999	10^{-14}	546
400	5.78×10^{-22}	162,641	207,924	10^{-13}	575
500	1.54×10^{-16}	151,352	207,616	10^{-12}	607
600	6.31×10^{-13}	140,142	207,128	10^{-11}	643
700	2.36×10^{-10}	129,027	206,479	10^{-10}	683
800	1.97×10^{-8}	118,015	205,671	10^{-9}	730
900	6.07×10^{-7}	107,115	204,700	10^{-8}	783
1000	9.29×10^{-6}	96,332	203,554	10^{-7}	844
1004.15	1.03×10^{-5}	95,887	203,503	10^{-6}	917
1004.15	1.03×10^{-5}	95,887	203,103	10^{-5}	1003
1100	8.51×10^{-5}	85,714	201,712	10^{-4}	1108
1195.15	4.89×10^{-4}	75,751	199,972	10^{-3}	1240
1195.15	4.89×10^{-4}	75,751	196,876	10^{-2}	1416
1200	5.30×10^{-4}	75,260	196,793	10^{-1}	1667
1300	2.40×10^{-3}	65,203	195,033	1	2050
1347.15	4.51×10^{-3}	60,509	194,189	NBP	2053
1347.15	4.51×10^{-3}	60,509	184,613		
1400	8.38×10^{-3}	55,664	183,410		
1500	2.38×10^{-2}	46,623	180,962		
1600	5.85×10^{-2}	37,753	178,288		
1700	0.128	29,057	175,392		
1800	0.254	20,538	172,280		
1900	0.462	12,197	168,961		
2000	0.784	4037	165,443		
2050.31	1.000	0	163,601		
2100	1.253	−3943	161,736		

NBP, normal boiling point at one atmosphere pressure (1.01325 bar).
$\Delta H^\circ(0) = 207,404$ J/mol.

11. THERMODYNAMIC FUNCTIONS OF EUROPIUM

11.1. Introduction

The alpha phase exists in a body-centered tetragonal structure below the Néel type of magnetic transition, and the beta phase adopts a body-centered cubic structure above (Bulatov and Kovalev, 1988). Gschneidner (1990) selects 90.4 K for the alpha–beta transition temperature and 1095 K for the melting point.

11.2. Alpha Phase

Both naturally occurring isotopes ^{151}Eu and ^{153}Eu give a nuclear contribution to the heat capacity and measurements of Krusius et al. (1974) (0.03–0.8 K) were used to derive values of the magnetic interaction parameters (a') and the quadrupole coupling constants (P). These values are in excellent agreement with those obtained by Hüfner and Wernick (1968) using the Mössbauer effect. Following the procedure described in Section 2.4, the selected values given in Part 11.11 were used to calculate the variation of the nuclear heat capacity with temperature.

At the time of the heat capacity measurements of Lounasmaa (1964c) (0.4–4.0 K), the lattice and magnetic contributions could not be separated but later Rosen (1968a) determined the limiting Debye temperature from elastic constants measurements to be 118 K, equivalent to a lattice contribution to the heat capacity of 1.18 mJ/(mol K^4) so that the magnetic contribution could then be separately calculated from a reassessment of the measurements of Lounasmaa (1964c) over the temperature range of 0.50–1.25 K. When combined with the nuclear terms as determined in Part 11.11, results in a revised heat capacity equation valid to 1.25 K:

$$C^\circ_{\mathrm{p}}(T)(\mathrm{mJ/(mol\,K)}) = 2.456/T^2 + 1.221\times10^{-3}/T^3 - 6.789\times10^{-4}/T^4 + 5.624T + 1.18T^3 + 27.21T^3$$

where the first three terms are the nuclear contribution, the fourth the electronic contribution, the fifth the lattice contribution, and the sixth the magnetic contribution which dominates the heat capacity above 1 K. However, there is a deviation away from a T^3 representation above 1.2 K which is expected since the magnetic contribution expected to vary as $T^{3/2}$ or $T^{5/2}$ rather than T^3, but attempts to fit the data to these powers were unsuccessful, possibly because the quality of the heat capacity measurements should be questioned because of the high impurity levels in the samples used which amounted to 0.21 wt% (5.2 atm%).

An anomaly shown as a peak at 16.1 K in the measurements of Lounasmaa (1966) (3.0–24.8 K) was later shown by Lounasmaa and Kalvius (1967) to be impurity induced, possibly due to europium hydride since hydrogen alone accounts for 3.2 atm% of the nonmetallic impurities. A similar peak was not

found in the measurements of Gerstein et al. (1967) (5–324 K), possibly because of the much higher purity of the samples used which contained only 0.036 wt% (1.3 atm%) of hydrogen and oxygen. After correcting for atomic weight, these values were selected. With this selection, the measurements of Lounasmaa (1966) in the overlap region from 5 to 25 K are initially 159% too high falling to as low as 28% too high in the region of the spurious anomaly but above this temperature falls to 11% lower.

Above 82 K, the heat capacity measurements of Gerstein et al. (1967) increase sharply suggesting that the Néel type transition is a typical second-order lambda peak, whereas later measurements showed that the transition to be first order. These included the observation of a crystallographic change not only by Bulatov and Dolzhenko (1988) but also by the Mössbauer effect as observed by Cohen et al. (1969a,b,c), neutron diffraction measurements of Millhouse and McEwen (1973), and magnetization effects observed by McEwen et al. (1973) as well as measurement of the actual enthalpy of transition by Åström et al. (1992). Polovov and Maĭstrenko (1975) also observed a similar peak on metal of only 99.5% purity, suggesting that the behavior observed for the transition may be impurity induced. It is noted that the peak temperature observed by Gerstein et al. (1967) at 88.77 K is notably lower than the value of the transition at 90.4 K obtained for pure metal (Gschneidner, 1990). Therefore, the measurements of Gerstein et al. (1967) in the range of 82–98 K are not considered to be representative of the pure metal and are not included in the evaluation. Instead, only measurements up to 82 K were included and the fitted equation extrapolated to the transition temperature.

11.3. Beta Phase—Low Temperature

Enthalpy of a first-order transition of 61 ± 2J/mol is selected from the measurements of Åström et al. (1992). Above this transition, heat capacity measurements of Gerstein et al. (1967) from 99 to 164 K were fitted to an equation which is used to represent the heat capacity from 90.4 to 160 K. However, the measurements from 199 to 324 K show scatter and a poor agreement with the lower temperature measurements but were extrapolated to a selected value of 27.65 J/(mol K) at 298.15 K. In an attempt to accommodate these scattered measurements, Gerstein et al. (1967) selected values which did not show smooth behavior and which were incompatible with both the lower temperature and the higher temperature data. In order to obtain a smooth curve, the heat capacity values at 160 and 298.15 K were held fixed and combined with the derivative of the specific heat value at 298.15 K in order to ensure a smooth continuity with the high-temperature equation.

Heat capacity measurements in the low-temperature region were also carried out by Teaney and Moruzzi (1967) (13–300 K), but no actual values were

given although they did detect the spurious anomaly at 16.5 K reported by Lounasmaa (1966) and therefore these values would also have been suspect.

11.4. Beta Phase—High Temperature

In the high-temperature region, numerous anomalies have been reported which include, for example, observations of a heat capacity anomaly by Polovov and Maĭstrenko (1975) at 765 K, in direct density measurements by Stankus and Khairulin (1987) at 700 K, in enthalpy measurements by Berg et al. (1961) at 503 K, and in electrical resistivity measurements by Zinov'ev et al. (1976) at both 600 and 880 K. That such anomalies were likely to be impurity induced was suggested by the electrical resistivity measurements of Guntherodt et al. (1976) on metal of 99.99% purity which indicated no anomalies between room temperature and the melting point, with these findings being confirmed by similar measurements by Ten Cate et al. (1980) on metal of 99.9% purity.

Enthalpy measurements determined by Berg et al. (1961) (273–1075 K in the solid phase) were corrected for atomic weight and temperature scale and from a 273.15 to a 298.15 K base by subtracting 690.30 J/mol as obtained from the low-temperature data. The two lowest data points at 373 and 473 K behaved differently to the higher temperature data, and therefore, two different equations were originally given covering the ranges 273–503 and 503 K to the melting point. It is considered, however, that this behavior is due to impurities in view of the lack of anomalies found for pure europium from the electrical resistivity measurements and that the anomaly is spurious and not representative of the pure metal. Since the measurements above 503 K are self-consistent, the two data points at 373 and 473 K were rejected as were two of the high-temperature data points at 974 and 1075 K and the remaining values were fitted to the following equation which has an overall accuracy of ±16 J/mol (0.11%):

$$C^{\circ}_{\mathrm{p}}(T)(\mathrm{J}/(\mathrm{mol\,K})) = 27.8899T - 2.64063 \times 10^{-3}T^2 + 5.00497 \times 10^{-6}T^3 - 8213.29$$

11.5. Liquid Phase

After correction as described above, the four liquid enthalpy measurements of Berg et al. (1961) (1100–1374 K) were fitted to the following equation with an overall accuracy as a standard deviation of ±81 J/mol (0.14%):

$$C^{\circ}_{\mathrm{p}}(T)(\mathrm{J}/(\mathrm{mol\,K})) = 38.0588T - 6729.95$$

The derived heat capacity is 38.06 ± 0.39 J/mol; the enthalpy of fusion, 9213 ± 83 J/mol; and the entropy of fusion, 8.41 ± 0.08 J/mol.

11.6. Gas Phase

Values are based on one bar standard state pressure and are calculated from the 866 energy levels, including the ground state, listed in Table 90 using the method of Kolsky et al. (1957) and the 2010 Fundamental Constants (Mohr et al., 2011). In cases where the degeneracy weight (g_i) values could be one of two or three possible values, then an average was taken.

TABLE 90 Sources of Energy Level Data

Authors	Number of levels
Ralchenko et al. (2012)	496
Wyart (1985)	13
Nakhate et al. (1996)	54
Nakhate et al. (2000a)	81
Nakhate et al. (2000b)	178
Ying et al. (2009)	11
Ying et al. (2010)	9
Xie et al. (2011)	24

11.7. Enthalpy of Sublimation

TABLE 91 Enthalpy of Sublimation at 298.15 K

Authors	Methods	Range (K)	$\Delta_{sub}H^{\circ}$(298, II law) (kJ/mol)	$\Delta_{sub}H^{\circ}$(298, III law) (kJ/mol)	Notes
Trulson et al. (1961)	MS	650–820	179.6 ± 1.0	–	
DeMaria et al. (1963c)	MS	648–858	170.5	–	
Fedechkin and Shmykov (1973)	Eff	700–922	144.5 ± 0.7	166.2 ± 3.0	–[a]
Spedding et al. (1958)	KE	696–899	176.5 ± 0.4	177.8 ± 0.1	–[b]
Selected				177.8 ± 0.5	

[a] *Given only in the form of the Clausius–Clapeyron equation.*
[b] *The data were originally given only in the form of the Clausius–Clapeyron equation. Actual data points were supplied by Iowa State University Ames Laboratory staff.*

11.8. Vapor Pressure

For the solid phase, the vapor pressure was evaluated from the free energy functions at 25 K intervals from 400 to 1075 K and the melting point, and for the liquid phase, at 25 K intervals from 1100 to 1900 K and the melting point (Table 92).

11.9. Comparison of Selected Values at 298.15 K

In spite of the very different treatments of the data, the selected values of Gerstein et al. (1967) and the present evaluation show satisfactory agreement at 298.15 K. The review by Hultgren et al. (1973) dates from December 1966 and includes only an estimated value of the entropy $S°(298)$ which later measurements suggest is greatly in error. Holley et al. (1968) accepted prepublication values given by Gerstein which are close to the final values as given by Gerstein et al. (1967). Both Cordfunke and Konings (1990) and Konings and Beneš (2010) accepted the values given by Gerstein et al. (1967) (Table 93).

TABLE 92 Vapor Pressure Equations

$\ln(p, \text{bar}) = b_1 + b_2/T + b_3 \ln(T) + b_4 T + b_5 T^2$

Phase	Range (K)	b_1	b_2	b_3	b_4	b_5
Solid	400–1095.15	18.96252	−21,626.88	−0.8543599	3.17549×10^{-4}	-3.00968×10^{-7}
Liquid	1095.15–1900	26.36507	−21,385.17	−1.930161	-1.14161×10^{-4}	1.47683×10^{-8}

TABLE 93 Comparison of Heat Capacity, Enthalpy, and Entropy Values at 298.15 K

Authors	$C°_p(298)$ (J/(mol K))	$H°(298) - H°(0)$ (J/mol)	$S°(298)$ (J/(mol K))
Holley et al. (1968)	27.57	8000	78.49
Hultgren et al. (1973)	27.11	–	80.79
Gerstein et al. (1967)	27.65	8008	77.81
This work	27.65	8005	77.8

11.10. Summary of Representative Equations

TABLE 94 Low-Temperature Heat Capacity Equations

Measurement range (K)	Useful range (K)	Equation
15.7–39.4	15–30	$C^\circ_p(T)(\mathrm{J/(mol\,K)}) = 1.21185T - 9.65328\times10^{-3}T^2 - 9.19737$
30–81.75	30–90.4	$C^\circ_p(T)(\mathrm{J/(mol\,K)}) = 1.58153T - 1.99011\times10^{-2}T^2 + 8.22975\times10^{-5}T^3 + 2.28228\times10^{-7}T^4 - 13.4718$
98.6–163.9	90.4–160	$C^\circ_p(T)(\mathrm{J/(mol\,K)}) = 66.7257 - 0.713892T + 4.56268\times10^{-3}T^2 - 1.00789\times10^{-5}T^3$
160–298.15	160–298.15	$C^\circ_p(T)(\mathrm{J/(mol\,K)}) = 30.6619 - 2.38760\times10^{-2}T + 4.61985\times10^{-5}T^2$

TABLE 95 Representative Equations Above 298.15 K

Solid phase: 298.15–1095.15 K
$C^\circ_p(T)(\mathrm{J/(mol\,K)}) = 27.8899 - 5.28126\times10^{-3}T + 1.501491\times10^{-5}T^2$
$H^\circ(T) - H^\circ(298)(\mathrm{J/mol}) = 27.8899T - 2.64063\times10^{-3}T^2 + 5.00497\times10^{-6}T^3 - 8213.29$
$S^\circ(T)(\mathrm{J/(mol\,K)}) = 27.8899\ \ln(T) - 5.28126\times10^{-3}T + 7.507455\times10^{-6}T^2 - 80.1936$
Liquid phase: 1095.15–1900 K
$C^\circ_p(T)(\mathrm{J/(mol\,K)}) = 38.0588$
$H^\circ(T) - H^\circ(298)(\mathrm{J/mol}) = 38.0588T - 6729.95$
$S^\circ(T)(\mathrm{J/(mol\,K)}) = 38.0588\ \ln(T) - 139.7293$

TABLE 96 Free Energy Equations Above 298.15 K

Solid phase: 298.15–1095.15 K
$G^\circ(T) - H^\circ(298)(\mathrm{J/mol}) = 108.0835T + 2.64063\times10^{-3}T^2 - 2.502485\times10^{-6}T^3 - 27.8899T\ln(T) - 8213.29$
Liquid phase: 1095–1900 K
$G^\circ(T) - H^\circ(298)(\mathrm{J/mol}) = 177.7881T - 38.0588T\ln(T) - 6729.95$

TABLE 97 Transition Values Involved with the Free Energy Equations

Transition	T (K)	ΔH° (J/mol)	ΔS° (J/(mol K))
Fusion	1095.15	9212.972	8.4125

11.11. Nuclear Heat Capacity

The nuclear heat capacity $C^\circ{}_N$ can be correlated by an equation using inverse powers of temperature:

$$C^\circ{}_N(T) = X\left(A/T^2 + B/T^3 + C/T^4 + \mathrm{L}\right)$$

where X is the isotopic fraction for the isotope and if a' is the magnetic interaction parameter, P is the quadrupole coupling constant, R is the gas constant, and I is the nuclear spin, then since both isotopes of europium ^{151}Eu and ^{153}Eu have $I = 5/2$:

$$A/R = 35/12a'^2 + 56/9P^2\,;\quad B/R = -56/3a'^2P;\quad C/R = -259/48a'^4$$

The isotopes are assumed to have fractional isotope abundances of 0.4782 and 0.5218, respectively, based on 1961 values (Cameron and Wichers, 1962) which were currently at the time of the heat capacity measurements of Krusius et al. (1974) determined in the nuclear heat capacity region and the Mössbauer effect measurements by Hüfner and Wernick (1968) (Table 98).

Selecting the values of a' and P from the evaluation of Krusius et al. (1974) then

$$^{151}\mathrm{Eu}: C^\circ{}_N(T)(\mathrm{mJ/(mol\,K)}) = 4.226/T^2 + 1.673\times10^{-3}/T^3 - 1.362\times10^{-3}/T^4$$

$$^{153}\mathrm{Eu}: C^\circ{}_N(T)(\mathrm{mJ/(mol\,K)}) = 0.834/T^2 + 8.527\times10^{-4}/T^3 - 5.290\times10^{-5}/T^4$$

$$\mathrm{Combined}: C^\circ{}_N(T)(\mathrm{mJ/(mol\,K)}) = 2.456/T^2 + 1.221\times10^{-3}/T^3 - 6.789\times10^{-4}/T^4$$

TABLE 98 Summary of Determinations of a' and P

Isotope	Authors	a' (K)	P (K)
^{151}Eu	Krusius et al. (1974)	0.0132 ± 0.0001	−0.00006 ± 0.00006
	Hüfner and Wernick (1968)	0.0134 ± 0.0003	–
^{153}Eu	Krusius et al. (1974)	0.00586 ± 0.00005	−0.00016 ± 0.00016
	Hüfner and Wernick (1968)	0.00593 ± 0.00010	–

11.12. Thermodynamic Tables

TABLE 99 Low-Temperature Thermodynamic Data

T (K)	$C°_p(T)$ (J/(mol K))	$H°(T) - H°(0)$ (J/mol)	$S°(T)$ (J/(mol K))	$-[G°(T) - H°(0)]/T$ (J/(mol K))
Alpha phase				
5	0.425	0.565	0.170	0.057
10	2.664	7.308	1.019	0.288
15	6.808	30.68	2.856	0.811
20	11.178	75.85	5.425	1.632
25	15.065	141.7	8.346	2.679
30	18.470	225.7	11.401	3.878
35	21.374	325.5	14.473	5.172
40	23.799	438.6	17.490	6.524
45	25.833	562.9	20.414	7.906
50	27.566	696.5	23.228	9.298
60	30.510	987.2	28.520	12.067
70	33.428	1307	33.438	14.772
80	37.168	1658	38.131	17.400
90	42.636	2056	42.803	19.962
90.4	42.904	2073	42.993	20.664
Beta phase				
90.4	32.031	2134	43.668	20.664
100	30.884	2436	46.841	22.486
110	29.991	2740	49.741	24.834
120	29.345	3036	52.321	27.019
130	28.886	3327	54.651	29.057
140	28.553	3614	56.778	30.962
150	28.286	3898	58.739	32.749
160	28.024	4180	60.556	34.432
170	27.938	4460	62.253	36.019
180	27.861	4739	63.847	37.521

TABLE 99 Low-Temperature Thermodynamic Data—Cont'd

T (K)	$C^\circ_p(T)$ (J/(mol K))	$H^\circ(T) - H^\circ(0)$ (J/mol)	$S^\circ(T)$ (J/(mol K))	$-[G^\circ(T) - H^\circ(0)]/T$ (J/(mol K))
190	27.793	5017	65.352	38.947
200	27.735	5295	66.776	40.303
210	27.685	5572	68.128	41.596
220	27.645	5848	69.415	42.832
230	27.614	6125	70.643	44.014
240	27.593	6401	71.818	45.149
250	27.580	6676	72.944	46.238
260	27.577	6952	74.026	47.286
270	27.583	7228	75.066	48.296
280	27.599	7504	76.070	49.270
290	27.623	7780	77.039	50.211
298.15	27.650	8005	77.805	50.955

TABLE 100 High-Temperature Thermodynamic Data

T (K)	$C^\circ_p(T)$ (J/(mol K))	$H^\circ(T) - H^\circ(298)$ (J/mol)	$S^\circ(T)$ (J/(mol K))	$-[G^\circ(T) - H^\circ(298)]/T$ (J/(mol K))
Solid phase				
298.15	27.650	0	77.805	77.805
300	27.657	51	77.976	77.805
400	28.180	2840	85.996	78.895
500	29.003	5697	92.367	80.973
600	30.127	8651	97.750	83.332
700	31.550	11,732	102.497	85.737
800	33.274	14,971	106.819	88.105
900	35.299	18,397	110.852	90.411
1000	37.624	22,041	114.689	92.648
1095.15	40.114	25,737	118.218	94.717

Continued

TABLE 100 High-Temperature Thermodynamic Data—Cont'd

T (K)	$C°_p(T)$ (J/(mol K))	$H°(T) - H°(298)$ (J/mol)	$S°(T)$ (J/(mol K))	$-[G°(T) - H°(298)]/T$ (J/(mol K))
Liquid phase				
1095.15	38.059	34,950	126.631	94.717
1100	38.059	35,135	126.799	94.858
1200	38.059	38,941	130.111	97.660
1300	38.059	42,746	133.157	100.275
1400	38.059	46,552	135.977	102.726
1500	38.059	50,358	138.603	105.031
1600	38.059	54,164	141.059	107.207
1700	38.059	57,970	143.367	109.267
1800	38.059	61,776	145.542	111.222
1900	38.059	65,582	147.600	113.083

TABLE 101 Thermodynamic Properties of the Gas Phase

T (K)	$C°_p(T)$ (J/(mol K))	$H°(T) - H°(298)$ (J/mol)	$S°(T)$ (J/(mol K))	$-[G°(T) - H°(298)]/T$ (J/(mol K))
298.15	20.786	0	188.798	188.798
300	20.786	38	188.927	188.799
400	20.786	2117	194.906	189.614
500	20.786	4196	199.545	191.153
600	20.786	6274	203.335	192.877
700	20.786	8353	206.539	194.606
800	20.786	10,432	209.314	196.275
900	20.786	12,510	211.763	197.862
1000	20.786	14,589	213.953	199.364
1095.15	20.787	16,567	215.842	200.715
1100	20.787	16,667	215.934	200.782
1200	20.788	18,746	217.743	202.121

TABLE 101 Thermodynamic Properties of the Gas Phase—Cont'd

T (K)	$C°_p(T)$ (J/(mol K))	$H°(T) - H°$ (298) (J/mol)	$S°(T)$ (J/(mol K))	$-[G°(T) - H°(298)]/T$ (J/(mol K))
1300	20.792	20,825	219.407	203.387
1400	20.801	22,905	220.948	204.587
1500	20.819	24,986	222.383	205.726
1600	20.853	27,069	223.728	206.810
1700	20.910	29,157	224.994	207.843
1800	20.999	31,252	226.191	208.829
1900	21.132	33,358	227.330	209.773

$H°(298) - H°(0) = 6197.4$ J/mol.

TABLE 102 Vapor Pressure

T (K)	p (bar)	$\Delta G°(T)$ (J/mol)	$\Delta H°(T)$ (J/mol)	p (bar)	T (K)
298.15	4.45×10^{-26}	144,707	177,800	10^{-15}	447
300	6.93×10^{-26}	144,502	177,787	10^{-14}	470
400	3.68×10^{-18}	133,513	177,071	10^{-13}	495
500	1.52×10^{-13}	122,710	176,299	10^{-12}	523
600	1.75×10^{-10}	112,072	175,422	10^{-11}	555
700	2.63×10^{-8}	101,591	174,420	10^{-10}	591
800	1.10×10^{-6}	91,264	173,260	10^{-9}	631
900	1.97×10^{-5}	81,094	171,912	10^{-8}	678
1000	1.94×10^{-4}	71,085	170,348	10^{-7}	733
1095.15	1.14×10^{-3}	61,717	168,630	10^{-6}	797
1095.15	1.14×10^{-3}	61,717	159,416	10^{-5}	874
1100	1.23×10^{-3}	61,284	159,322	10^{-4}	969
1200	5.21×10^{-3}	52,447	157,605	10^{-3}	1088
1300	1.75×10^{-2}	43,754	155,878	10^{-2}	1252
1400	4.86×10^{-2}	35,194	154,152	10^{-1}	1481
1500	0.117	26,757	152,430	1	1826

Continued

TABLE 102 Vapor Pressure—Cont'd

T (K)	p (bar)	$\Delta G°(T)$ (J/mol)	$\Delta H°(T)$ (J/mol)	p (bar)	T (K)
1600	0.250	18,435	150,704	NBP	1829
1700	0.485	10,221	148,986		
1800	0.869	2108	147,276		
1826.17	1.000	0	146,830		
1900	1.454	−5911	145,576		

NBP, normal boiling point at one atmosphere pressure (1.01325 bar).
$\Delta H°(0) = 179,608$ J/mol.

12. THERMODYNAMIC FUNCTIONS OF GADOLINIUM

12.1. Introduction

Dankov et al. (1998) selected 294 ± 1 K for the Curie temperature, while Gschneidner (1990) selected 1508 K for the transformation from the hexagonal close-packed structure to the body-centered cubic structure and 1586 K for the melting point. It is noted that the transition temperature, which was determined on the purest samples available at Iowa State University by both Beaudry and Daane (1964) and Beaudry and Spedding (1974), is notably lower than a consensus value of 1534 ± 5 K obtained on materials of commercial purity (Konings and Beneš, 2010).

12.2. Alpha Phase—Low Temperature

Heat capacity measurements of Kurti and Safrata (1958) (0.2–6 K), Crane (1962) (1.3–5 K), and Lounasmaa (1963) (0.4–4 K) were all performed on samples which were significantly contaminated with oxygen and showed peaks corresponding to the effects of Gd_2O_3. Very low-temperature measurements by Dreyfus et al. (1967) (0.023–0.6 K) suggested the presence of a nuclear contribution to the heat capacity which has not been confirmed. Wells et al. (1974) (1.5–14 K) and Lounasmaa and Sundström (1966) (3–25 K) both suggested a significant magnetic contribution to the heat capacity which was also found in later measurements on much purer samples by Hill et al. (1987) (0.47–20 K) but was not found on metal of similar high purity by Tsang et al. (1985) (1–20 K) who pointed out that a theoretical approach by Rao and Narayana Murty (1978) suggested that the magnetic contribution should be negligible below 15 K.

TABLE 103 Low-Temperature Specific Heat Coefficients

Authors	γ (mJ/(mol K^2))	θ_D (K)	B (mJ/(mol K$^{(n+1)}$))	n
Wells et al. (1974a,b)	3.7	187	1.94	1.75
Lounasmaa and Sundström (1967)	11.27	195	0.19	2.7
Hill et al. (1987)	4.48	169	1.37	1.5
Tsang et al. (1985)	6.38	163	0	0
Selected	6.38	163	0	0

Values of the electronic, lattice, and magnetic contribution were fitted to the equation $C^\circ_p = \gamma T + AT^3 + BT^n$ where in Table 103, the constant A is given as the equivalent limiting Debye temperature (θ_D).

The values obtained for θ_D for the purest samples are notably different from the values of 184 K obtained from elastic constant measurements by Rosen (1967) and from 180.2 K obtained by Palmer (1978) from similar measurements on single crystals. At 4 K, the equation of Wells et al. (1974a,b) leads to a heat capacity value 0.75% greater than that obtained from the measurements of Tsang et al. (1985), but the latter are given preference and up to 350 K selected values are based on a combination of these measurements and the heat capacity values of Dankov et al. (1998) (4.2–351 K) since in both cases the samples used were of very high purity. Also in both cases, the results were shown only graphically with actual data points being supplied by Gschneidner (1991) and Pecharsky (2006), respectively. However, in the region of 290–298 K, the measurements of Bednarz et al. (1993) were also included in which the heat capacity above and below the Curie temperature was represented by power series with confluent corrections to the scaling terms. They also obtained a Curie temperature of 294.5 K which is within the range of 294 ± 1 K proposed by Dankov et al. (1998).

Of other measurements in the low-temperature region, all of which are heat capacity determinations, those of Lounasmaa and Sundström (1966) (3–25 K) are above 5 K—to avoid the abnormal peak at 3 K which is due to Gd_2O_3—initially 100% high but gradually converge to the selected values being only 2% high above 20 K. The values of Jelinek et al. (1966) (15–355 K), which revise early measurements of Griffel et al. (1954), are initially up to 2% low and then scatter 0.4% low to 0.4% high above 100 K before tending to 4% high above 300 K. Results on the low-temperature measurements of Shen (1994) (213–423 K) scatter from 0.2% to 14% high.

12.3. Alpha Phase—High Temperature

High-temperature enthalpy measurements of Dennison et al. (1966a) (302–1520 K for the alpha phase) were given only in the form of equations and smooth values with actual data points being supplied by Gschneidner (1991). The normal procedure was initially adopted in that values were corrected for temperature scale and from a 273.15 to a 298.15 K basis by subtracting the experimental value $H^\circ(298) - H^\circ(273) = 1269.45$ J/mol. After rejecting discrepant values at 302, 1517, and 1520 K, the data were fitted to a cubic equation. However, because of the large abnormality caused by the Curie temperature, it is suggested that equilibrium corrections to the enthalpy may not have applied in the drop calorimetry experiments. It was found that the derived heat capacity curve from the enthalpy equation initially did not match that obtained from the actual heat capacity curve but that they could be joined smoothly at 380 K. At 380 K, the enthalpy difference $H^\circ(380) - H^\circ(298)$ calculated from the heat capacity data was 115.13 J/mol higher than that obtained from the enthalpy equation. This amount was therefore added to the enthalpy equation in order to ensure a match at this temperature, but this equation then only applies above 380 K but joins smoothly with the heat capacity-derived values below this temperature. With this correction, the enthalpy values can now be represented by the following equation with an overall fit as a standard deviation of ±129 J/mol (1.17%):

$$H^\circ(T) - H^\circ(298)(\mathrm{J/mol}) = 31.9577T - 5.15961 \times 10^{-3}T^2 + 3.52016 \times 10^{-6}T^3 - 9047.70$$

In the high-temperature region of the alpha phase, heat capacity measurements of Shen (1994) (323–1073 K), above 373 K, scatter 1% high to 1% low before becoming 2% high at 873 K and above, but this is well within the expected accuracy of ±5.6%. Determinations of Novikov et al. (1977) (1100–2100 K) tend from 4% to 7% lower than the selected values in the solid phase, while those of Kurichenko et al. (1986) (672–1502 K) initially agree with the selected values then rise to 45% high at 900 K before decreasing to 15% high at 1100 K and then tend upward to 60% high. Measurements of Pozdeyev et al. (1990) (400–1550 K) in the alpha region scatter 4% low to 0.1% high.

12.4. Beta Phase

Dennison et al. (1966a) determined the enthalpy at three temperatures between 1545 and 1588 K (after correcting the temperatures to ITS-90) with the actual data points being given by Gschneidner (1991). For the correction from a 273.15 to a 298.15 K base a working value of 1154.32 J/mol was selected which is the experimental value of 1269.45 J/mol corrected by 115.13 J/mol to account for the mismatch between derived enthalpy values at 380 K. The three data points were fitted to the following equation with an overall accuracy as a standard deviation of ±103 J/mol (0.13%):

$$H^\circ(T) - H^\circ(298)(\mathrm{J/mol}) = 28.1790T - 898.902$$

However, the derived heat capacity of 28.2 ± 3.4 J/(mol K) is considered to be far too low when compared to values for neighboring phases and a more likely value would be 39 J/(mol K) which is similar to the value selected by Shen et al. (1995) and agrees with a value of 39.3 J/(mol K) determined by Pozdeyev et al. (1990) at 1550 K. Combining this selected heat capacity with the enthalpy value of 44,496.04 J/mol obtained from the above equation at the mid-point temperature of 1547.15 K, then the revised enthalpy for the beta phase is

$$H^\circ(T) - H^\circ(298)(\mathrm{J/mol}) = 39.0000T - 15,842.81$$

The derived enthalpy of transition is 3486 ± 165 J/mol where the accuracy is derived from a combination of the standard deviations of the fits obtained for both phases.

12.5. Liquid Phase

Dennison et al. (1966a) determined the enthalpy at four temperatures between 1610 and 1771 K (after correcting the temperatures to ITS-90) with the actual data points being given by Gschneidner (1991). Because gadolinium is soluble in the tantalum containers used in the experiments, the enthalpy values were corrected for tantalum saturation following the method of Dennison et al. (1966b), and after correction from a 273.15 to a 298.15 K base as described above, then the four data points were fitted to the following equation with an overall accuracy as a standard deviation of ± 122 J/mol (0.15%):

$$H^\circ(T) - H^\circ(298)(\mathrm{J/mol}) = 37.0179 - 3076.59$$

The derived heat capacity is 37.02 ± 0.99 J/(mol K); enthalpy of fusion, 9622 ± 160 J/mol; and entropy of fusion, 6.07 ± 0.10 J/(mol K). Measurements of Novikov and Mardykin (1974) (1600–1800 K) were given as heat capacity–density and were corrected to heat capacity using the liquid density values of Stankus and Khairulin (1991). The corrected values lead to an almost constant heat capacity value which is 6% higher than the selected value. Similarly, Novikov et al. (1977) (1100–2100 K) obtained heat capacity values in the liquid phase which are also 6% higher than the selected value. Although Shen et al. (1995) included the latter measurements in arriving at a heat capacity value for the liquid phase, the very poor agreement with selected values for the alpha phase suggests that these measurements should be rejected.

12.6. Gas Phase

Values are based on one bar standard state pressure and are calculated from the 661 energy levels, including the ground state, listed in Table 104 using the method of Kolsky et al. (1957) and the 2010 Fundamental Constants (Mohr et al., 2011).

TABLE 104 Sources of Energy Level Data

Authors	Number of levels
Ralchenko et al. (2012)	614
Hayman et al. (1993)	1
Miyabe et al. (1996)	38
Khim et al. (2000)	8

Seven of the levels determined by Miyabe et al. (1996) had degeneracy weight (g_i) values amended by Miyabe et al. (1998).

12.7. Enthalpy of Sublimation

TABLE 105 Enthalpy of Sublimation at 298.15 K

Authors	Methods	Range (K)	$\Delta_{sub}H^{\circ}$(298, II law) (kJ/mol)	$\Delta_{sub}H^{\circ}$(298, III law) (kJ/mol)	Notes
Trulson et al. (1961)	MS	1214–1500	334 ± 1	–	
White et al. (1961)	MS	1685–2044	348 ± 4	–	
Yamamoto et al. (1965)	KE	1623–1784	307 ± 8	369.5 ± 0.6	
Kovtun et al. (1964)	KE	1393–1580	440 ± 6	374.7 ± 0.8	
Lundin and Yamamoto (1967)	KE	1649–1939	368 ± 14	387.6 ± 1.6	–[a]
Habermann (1963)	KE	1760–2070	402 ± 2	395.3 ± 0.1	–[b]
Habermann and Daane (1964)	KE	1620–2097	401 ± 2	396.8 ± 0.6	–[a]
Hoenig et al. (1967)	KE	1574–2057	407 ± 4	396.3 ± 0.3	
Shoji et al. (1997)	KEMS	1588–1797	403 ± 8	394.5 ± 0.5	–[a]
Selected				396.0 ± 2.0	

MS, mass spectrometry; KE, Knudsen effusion; KEMS, Knudsen effusion mass spectrometry.
[a] *Given only in the form of the Clausius–Clapeyron equation.*
[b] *Run 9 of Habermann and Daane (1964).*

Additional measurements by Bronin et al. (1989) were not reported as actual data. The selected enthalpy value is based on the measurements of Habermann and Daane (1964), Hoenig et al. (1967), and Shoji et al. (1997).

12.8. Vapor Pressure

The vapor pressure equation for the alpha phase was evaluated at 25 K intervals from 950 to 1500 K and the transition temperature, and for the liquid phase, at 50 K intervals from 1600 to 3600 K and the melting point. The values for the beta phase were obtained by calculating the vapor pressure values at the transition temperature and the melting point and fitting to the Clausius–Clapeyron equation (Table 106).

12.9. Comparison of Selected Values at 298.15 K

Holley et al. (1968) selected the revised values given by Jelinek et al. (1966), while Hultgren et al. (1973) selected the original measurements of Griffel et al. (1954). Shen et al. (1995) based their selected entropy on a value calculated by Gerstein and Jelinek (1966) from the raw specific heat measurements of Griffel et al. (1954) and selected the enthalpy value as given by Hultgren et al. (1973), while Konings and Beneš (2010) selected the entropy value as given by Jelinek et al. (1966). The present evaluation is based on a combination of the heat capacity measurements of Tsang et al. (1985), Dankov et al. (1998), and Bednarz et al. (1993) (Table 107).

TABLE 106 Vapor Pressure Equations

$\ln(p, \text{bar}) = b_1 + b_2/T + b_3 \ln(T) + b_4 T + b_5 T^2$

Phase	Range (K)	b_1	b_2	b_3	b_4	b_5
Alpha	950–1508.15	13.81535	−47,538.31	0.2012880	-2.74256×10^{-4}	-9.38022×10^{-8}
Beta	1508.15–1586.15	13.70051	−46,088.95	0	0	0
Liquid	1586.15–2600	27.23630	−47,548.11	−1.699176	-1.23626×10^{-4}	4.03714×10^{-8}
	2600–3600	40.01176	−49,017.16	−3.441833	5.71666×10^{-4}	-6.25986×10^{-9}

TABLE 107 Comparison of Heat Capacity, Enthalpy, and Entropy Values at 298.15 K

Authors	C°_p (J/(mol K))	$H^\circ_{298.15} - H^\circ_0$ (J/mol)	$S^\circ_{298.15}$ (J/(mol K))
Holley et al. (1968)	37.03	9113	68.07
Hultgren et al. (1973)	37.07	9088	67.95
Shen et al. (1995)	39.76	9088	68.09
Konings and Beneš (2010)	–	–	68.06
This work	37.65	9167	68.53

12.10. Summary of Representative Equations

TABLE 108 Representative Equations Above 380 K

Alpha phase: 370–1508.15 K
$C^\circ_p(T)(\text{J/(mol K)}) = 31.9577 - 1.031922 \times 10^{-2} T + 1.056048 \times 10^{-5} T^2$
$H^\circ(T) - H^\circ(298)(\text{J/mol}) = 31.9577T - 5.15961 \times 10^{-3} T^2 + 3.52016 \times 10^{-6} T^3 - 9047.70$
$S^\circ(T)(\text{J/(mol K)}) = 31.9577 \ln(T) - 1.031922 \times 10^{-2} T + 5.28024 \times 10^{-6} T^2 - 110.5730$
Beta phase: 1508.15–1586.15 K
$C^\circ_p(T)(\text{J/(mol K)}) = 39.0000$
$H^\circ(T) - H^\circ(298)(\text{J/mol}) = 39.0000T - 15,842.81$
$S^\circ(T)(\text{J/(mol K)}) = 39.0000 \ln(T) - 163.3545$
Liquid phase: 1586.15–3600 K
$C^\circ_p(T)(\text{J/(mol K)}) = 37.0179$
$H^\circ(T) - H^\circ(298)(\text{J/mol}) = 37.0179T - 3076.59$
$S^\circ(T)(\text{J/(mol K)}) = 37.0179 \ln(T) - 142.6818$

TABLE 109 Free Energy Equations Above 380 K

Alpha phase: 370–1508.15 K
$G^\circ(T) - H^\circ(298)(\text{J/mol}) = 142.5307T + 5.15961 \times 10^{-3} T^2 - 1.76008 \times 10^{-6} T^3 - 31.9577T \ln(T) - 9047.70$
Beta phase: 1508.15–1586.15 K
$G^\circ(T) - H^\circ(298)(\text{J/mol}) = 202.3545T - 39.0000T \ln(T) - 15,842.81$
Liquid phase: 1586.15–3600 K
$G^\circ(T) - H^\circ(298)(\text{J/mol}) = 179.6997T - 37.0179T \ln(T) - 3076.59$

TABLE 110 Transition Values Involved with the Free Energy Equations

Transition	T (K)	ΔH° (J/mol)	ΔS° (J/(mol K))
Alpha–beta	1508.15	3486.108	2.3115
Fusion	1586.15	9622.314	6.0665

12.11. Thermodynamic Tables

TABLE 111 Low-Temperature Thermodynamic Data

T (K)	$C^\circ_p(T)$ (J/(mol K))	$H^\circ(T) - H^\circ(0)$ (J/mol)	$S^\circ(T)$ (J/(mol K))	$-[G^\circ(T) - H^\circ(0)]/T$ (J/(mol K))
5	0.0865	0.148	0.0502	0.0205
10	0.543	1.461	0.215	0.0689
15	1.907	7.133	0.657	0.181
20	4.247	22.17	1.506	0.397
25	7.095	50.41	2.754	0.738
30	10.081	93.35	4.312	1.201
40	15.538	222.4	7.987	2.426
50	19.665	399.6	11.924	3.931
60	22.585	611.4	15.778	5.587
70	24.978	849.7	19.446	7.307

Continued

TABLE 111 Low-Temperature Thermodynamic Data—Cont'd

T (K)	$C°_p(T)$ (J/(mol K))	$H°(T) - H°(0)$ (J/mol)	$S°(T)$ (J/(mol K))	$-[G°(T) - H°(0)]/T$ (J/(mol K))
80	26.743	1109	22.903	9.043
90	28.095	1383	26.314	10.765
100	29.113	1670	29.149	12.454
110	30.009	1965	31.966	14.101
120	30.808	2269	34.613	15.701
130	31.465	2581	37.105	17.253
140	32.145	2899	39.462	18.756
150	32.790	3224	41.702	20.211
160	33.440	3555	43.838	21.622
170	34.141	3893	45.887	22.989
180	34.772	4237	47.856	24.317
190	35.478	4588	49.754	25.606
200	36.279	4947	51.593	26.859
210	37.126	5313	53.380	28.080
220	38.123	5689	55.130	29.270
230	39.053	6075	56.846	30.432
240	40.106	6471	58.529	31.567
250	41.615	6879	60.196	32.679
260	43.521	7304	61.863	33.769
270	45.949	7751	63.549	34.841
280	49.601	8227	65.278	35.897
285	52.039	8481	68.177	36.420
290	56.114	8750	67.114	36.941
291	57.283	8807	67.309	37.045
292	58.628	8865	67.507	37.149
293	60.320	8924	67.711	37.253
294	62.987	8985	67.920	37.357
294.1	63.418	8992	67.942	37.368
294.2	63.935	8998	67.963	37.378

TABLE 111 Low-Temperature Thermodynamic Data—Cont'd

T (K)	$C°_p(T)$ (J/(mol K))	$H°(T) - H°(0)$ (J/mol)	$S°(T)$ (J/(mol K))	$-[G°(T) - H°(0)]/T$ (J/(mol K))
294.3	64.599	9005	67.985	37.389
294.4	65.600	9011	68.007	37.399
294.5	102.000	9018	68.030	37.409
294.6	47.068	9023	68.047	37.420
294.7	45.845	9027	68.063	37.435
294.8	45.080	9032	68.078	37.441
294.9	44.513	9036	68.093	37.451
295	44.056	9041	68.108	37.461
295.5	42.252	9062	68.181	37.513
296	40.818	9083	68.251	37.565
297	38.855	9123	68.385	37.669
298	37.761	9161	68.514	37.772
298.15	37.647	9167	68.533	37.787

TABLE 112 High-Temperature Thermodynamic Data

T (K)	$C°_p(T)$ (J/(mol K))	$H°(T) - H°(298)$ (J/mol)	$S°(T)$ (J/(mol K))	$-[G°(T) - H°(298)]/T$ (J/(mol K))
Alpha phase				
298.15	37.647	0	68.533	68.533
300	36.553	69	68.762	68.534
305	34.337	245	69.345	68.542
310	33.299	414	69.895	68.560
320	31.765	738	70.925	68.618
330	30.683	1050	71.884	68.702
340	30.180	1355	72.794	68.809
350	29.842	1655	73.664	68.936
360	29.680	1952	74.502	69.079

Continued

TABLE 112 High-Temperature Thermodynamic Data—Cont'd

T (K)	$C^\circ_p(T)$ (J/(mol K))	$H^\circ(T) - H^\circ(298)$ (J/mol)	$S^\circ(T)$ (J/(mol K))	$-[G^\circ(T) - H^\circ(298)]/T$ (J/(mol K))
380	29.561	2544	76.102	69.407
400	29.520	3135	77.618	69.780
450	29.452	4609	81.090	70.847
500	29.438	6081	84.192	72.029
600	29.568	9030	89.568	74.518
700	29.909	12,002	94.148	77.003
800	30.461	15,019	98.176	79.403
900	31.224	18,101	101.806	81.693
1000	32.199	21,271	105.144	83.873
1100	33.385	24,548	108.267	85.950
1200	34.782	27,955	111.230	87.935
1300	36.390	31,511	114.076	89.837
1400	38.209	35,240	116.838	91.667
1500	40.240	39,160	119.542	93.435
1508.15	40.415	39,489	119.761	93.577
Beta phase				
1508.15	39	42,975	122.072	93.577
1586.15	39	46,017	124.039	95.027
Liquid phase				
1586.15	37.018	55,639	130.106	95.027
1600	37.018	56,152	130.427	95.332
1700	37.018	59,854	132.672	97.463
1800	37.018	63,555	134.787	99.479
1900	37.018	67,257	136.789	101.390
2000	37.018	70,959	138.688	103.208
2100	37.018	74,661	140.494	104.941
2200	37.018	78,363	142.216	106.596
2300	37.018	82,065	143.861	108.181
2400	37.018	85,766	145.437	109.701

TABLE 112 High-Temperature Thermodynamic Data—Cont'd

T (K)	$C^\circ_p(T)$ (J/(mol K))	$H^\circ(T) - H^\circ(298)$ (J/mol)	$S^\circ(T)$ (J/(mol K))	$-[G^\circ(T) - H^\circ(298)]/T$ (J/(mol K))
2500	37.018	89,468	146.948	111.161
2600	37.018	93,170	148.400	112.565
2700	37.018	96,872	149.797	113.918
2800	37.018	100,574	151.143	115.224
2900	37.018	104,275	152.442	116.485
3000	37.018	107,977	153.697	117.705
3100	37.018	111,679	154.911	118.885
3200	37.018	115,381	156.086	120.030
3300	37.018	119,082	157.225	121.140
3400	37.018	122,784	158.330	122.217
3500	37.018	126,486	159.403	123.265
3600	37.018	130,188	160.446	124.283

TABLE 113 Thermodynamic Properties of the Gas Phase

T (K)	$C^\circ_p(T)$ (J/(mol K))	$H^\circ(T) - H^\circ(298)$ (J/mol)	$S^\circ(T)$ (J/(mol K))	$-[G^\circ(T) - H^\circ(298)]/T$ (J/(mol K))
298.15	27.549	0	194.317	194.317
300	27.546	51	194.487	194.317
400	27.288	2794	202.380	195.395
500	26.906	5504	208.430	197.422
600	26.438	8172	213.295	199.675
700	25.930	10,791	217.333	201.917
800	25.433	13,359	220.762	204.064
900	24.990	15,879	223.732	206.088
1000	24.632	18,359	226.345	207.986
1100	24.380	20,809	228.680	209.763

Continued

TABLE 113 Thermodynamic Properties of the Gas Phase—Cont'd

T (K)	$C°_p(T)$ (J/(mol K))	$H°(T) - H°(298)$ (J/mol)	$S°(T)$ (J/(mol K))	$-[G°(T) - H°(298)]/T$ (J/(mol K))
1200	24.244	23,239	230.795	211.429
1300	24.227	25,662	232.734	212.994
1400	24.327	28,089	234.532	214.469
1500	24.535	30,531	236.217	215.863
1508.15	24.557	30,731	236.350	215.974
1586.15	24.794	32,655	237.594	217.006
1600	24.842	32,999	237.810	217.186
1700	25.237	35,502	239.327	218.444
1800	25.707	38,049	240.783	219.645
1900	26.241	40,646	242.187	220.794
2000	26.828	43,299	243.548	221.898
2100	27.461	46,013	244.872	222.961
2200	28.129	48,792	246.164	223.986
2300	28.828	51,640	247.430	224.978
2400	29.549	54,558	248.672	225.940
2500	30.288	57,550	249.893	226.873
2600	31.040	60,616	251.096	227.782
2700	31.801	63,758	252.282	228.667
2800	32.569	66,977	253.452	229.532
2900	33.338	70,272	254.608	230.376
3000	34.106	73,644	255.751	231.203
3100	34.870	77,093	256.882	232.013
3200	35.627	80,618	258.002	232.808
3300	36.375	84,218	259.109	233.588
3400	37.111	87,893	260.206	234.355
3500	37.832	91,640	261.292	235.109
3600	38.537	95,459	262.368	235.852

$H°(298) - H°(0) = 7637.0$ J/mol.

TABLE 114 Vapor Pressure

T (K)	p (bar)	$\Delta G°(T)$ (J/mol)	$\Delta H°(T)$ (J/mol)	p (bar)	T (K)
298.15	1.56×10^{-63}	358,497	396,000	10^{-15}	963
300	4.19×10^{-63}	358,265	395,982	10^{-14}	1010
400	7.08×10^{-46}	345,754	395,659	10^{-13}	1062
500	1.52×10^{-35}	333,304	395,423	10^{-12}	1120
600	1.16×10^{-28}	320,906	395,142	10^{-11}	1185
700	9.45×10^{-24}	308,560	394,789	10^{-10}	1258
800	4.53×10^{-20}	296,271	394,340	10^{-9}	1341
900	3.27×10^{-17}	284,045	393,778	10^{-8}	1436
1000	6.29×10^{-15}	271,888	393,089	10^{-7}	1546
1100	4.60×10^{-13}	259,806	392,261	10^{-6}	1678
1200	1.63×10^{-11}	247,807	391,285	10^{-5}	1837
1300	3.33×10^{-10}	235,895	390,151	10^{-4}	2030
1400	4.36×10^{-9}	224,077	388,849	10^{-3}	2271
1500	4.03×10^{-8}	212,358	387,371	10^{-2}	2578
1508.15	4.76×10^{-8}	211,408	387,242	10^{-1}	2984
1508.15	4.76×10^{-8}	211,408	383,756	1	3545
1586.15	2.14×10^{-7}	202,523	382,638	NBP	3548
1586.15	2.14×10^{-7}	202,523	373,016		
1600	2.74×10^{-7}	201,035	372,847		
1700	1.42×10^{-6}	190,334	371,649		
1800	6.10×10^{-6}	179,701	370,493		
1900	2.24×10^{-5}	169,132	369,388		
2000	7.20×10^{-5}	158,620	368,340		
2100	2.06×10^{-4}	148,158	367,352		
2200	5.37×10^{-4}	137,742	366,429		
2300	1.28×10^{-3}	127,367	365,575		
2400	2.84×10^{-3}	117,027	364,792		
2500	5.89×10^{-3}	106,718	364,082		
2600	1.16×10^{-2}	96,437	363,447		

Continued

TABLE 114 Vapor Pressure—Cont'd

T (K)	p (bar)	$\Delta G°(T)$ (J/mol)	$\Delta H°(T)$ (J/mol)	p (bar)	T (K)
2700	2.15×10^{-2}	86,178	362,887		
2800	3.83×10^{-2}	75,939	362,404		
2900	6.55×10^{-2}	65,715	361,997		
3000	0.109	55,504	361,668		
3100	0.172	45,304	361,415		
3200	0.267	35,109	361,238		
3300	0.403	24,920	361,136		
3400	0.594	14,732	361,109		
3500	0.855	4544	361,154		
3544.59	1.000	0	361,198		
3600	1.208	−5647	361,271		

NBP, normal boiling point at one atmosphere pressure (1.01325 bar).
$\Delta H°(0) = 397,530$ J/mol.

13. THERMODYNAMIC FUNCTIONS OF TERBIUM

13.1. Introduction

Jayasuriya et al. (1983) selected 221.45 K for the first-order Curie-like transformation from the alpha phase orthorhombic structure to the beta phase hexagonal closed-packed structure, while Jayasuriya et al. (1984) selected 229.95 K for the second-order Néel transformation. Gschneidner (1990) selected 1562 K for the transformation to the gamma phase body-centered cubic structure and 1629 K for the melting point.

13.2. Alpha Phase

Very low-temperature calorimetry measurements of Lounasmaa and Roach (1962) (0.37–4.2 K), Van Kempen et al. (1964) (0.05–0.89 K), Anderson et al. (1968), and Krusius et al. (1969) (0.03–0.5 K) as well as nuclear magnetic resonance (NMR) measurements by Kobayashi et al. (1967) and Sano and Itoh (1972) were used to derive the nuclear contribution to the heat capacity by determining the magnetic interaction parameter a' and the quadrupole coupling constant P. Following the procedure described in Section 2.4, the selected values given in Part 13.12 were used to calculate the variation of the nuclear heat capacity with temperature.

TABLE 115 Low-Temperature Heat Capacity Coefficients

Authors	Range (K)	γ (mJ/(mol K^2))	θ_D (K)
Lounasmaa and Roach (1962)	0.37–4.2	9.05	150
Hill et al. (1974)	1.5–4.0	4.35	174
Wells et al. (1976)	1.5–16	4.4	178
Ikeda et al. (1985)	1.3–20	3.71	169.6

The values given in Table 115 were obtained for the electronic coefficient (γ) and the limiting Debye temperature (θ_D). In each case, the nuclear contribution to the heat capacity has been subtracted. In the case of the measurements of Lounasmaa and Roach (1962) and Hill et al. (1974), no magnetic contribution was considered, but both Wells et al. (1976) and Ikeda et al. (1985) included a magnetic term $9.5T^{3/2}\exp(-14.8/T)$.

While the value of θ_D obtained by Wells et al. (1976) agrees with a value of 177 K obtained by Rosen (1968b) from elastic constant measurements, the measurements of neither Wells et al. (1976) nor Ikeda et al. (1985) agree with a value of 185.6 K obtained by Palmer (1978) also from elastic constant measurements. In view of the very high purity of the samples used by Ikeda et al., the selection of these values and the inclusion of the nuclear contribution obtained from Part 13.12 lead to the heat capacity up to 4 K being represented by

$$C^\circ{}_p(T)(\text{mJ}/(\text{mol K})) = 235/T^2 - 9.0/T^3 - 4.4/T^4 + 3.71T + 0.3985T^3 + 9.5T^{3/2}\exp(-14.8/T)$$

Smoothed values of Lounasmaa and Roach (1962) are initially only 0.6% higher than the selected values and then show a trend to be 55% higher at 4 K. Heltemes and Swenson (1961) (0.25–1.0 K) gave the nuclear heat capacity coefficient of 233 mJ/(mol K) which agrees with the first term in the above equation. Earlier heat capacity measurements of Kurti and Safrata (1958) (0.6–6.0 K), Stanton et al. (1960) (1.4–4.0 K) and Bailey (1962) (1.7–4.1 K) are all difficult to interpret since all show a spike in the specific heat curve at about 2.4 K which is consistent with antiferromagnetic ordering at this temperature in Tb_2O_3 (Gerstein et al., 1962).

Above 4 K, heat capacity measurements of Wells et al. (1976) (1.6–16 K) were combined with the values of Jennings et al. (1957) (15–347 K) to represent the thermodynamic properties of the alpha phase up to the Curie temperature. Measurements of Lounasmaa and Sundström (1966) (3.1–24 K) show anomalies but can be considered as being 60% high at 4 K converging to the selected values to be only 3% high.

13.3. Beta Phase—Low Temperature

The crystallographic transition at the Curie temperature is first order with the values given in Table 116 being obtained for the enthalpy of transition:

The calorimetric value obtained by Jayasuriya et al. (1983) is selected. Between the Curie and Néel transitions, the heat capacity values determined by Jennings et al. (1957) are from 5% to 14% higher than those calculated from the power law fit equations given by Jayasuriya et al. (1984). This can be traced to the fact that Jennings et al. (1957) obtained a maximum in their heat capacity curve at 227.7 K which is 2.25 K lower than the value determined by Jayasuriya et al. and is probably indicative of actual impurity levels in the sample used. The two sets of measurements cannot be reconciled, and therefore, the values of Jayasuriya et al. are selected to cover this range.

Above the Néel temperature, the heat capacity discrepancies continue to exist but can be resolved if the temperature value obtained by Jennings et al. (1957) at 230.4 K (the lowest temperature measured above 230 K) is considered to be displaced by 1.2 K low but that the displacement at 237.5 K is negligible so that the temperature values between these two temperature limits could be corrected by the difference $\Delta T\,(\mathrm{K}) = 40.14 - 0.1690T$ and a smooth heat capacity curve is then obtained reconciling the heat capacity values obtained from the power law equation of Jayasuriya et al. (1984) with those obtained from the measurements of Jennings et al. (1957). Jayasuriya et al. (1984) give heat capacity measurements up to 400 K but only in the form of a small graph.

13.4. Beta Phase—High Temperature

Enthalpy measurements of Dennison et al. (1966a) (373–1535 K in the alpha range) are given only in the form of equations and tabulated values with actual measured values being supplied by Gschneidner (1991). The measurements were corrected from 273.15 to a 298.15 K base by subtracting 730.27 J/mol

TABLE 116 Alpha–Beta Transformation Enthalpy

Authors	Methods	Enthalpy of transformation (J/mol)	Notes
Hegland et al. (1963)	Magnetization	11 ± 5	–[a]
Feron (1969)	Magnetization	15 ± 5	–[a]
Greenough and Hettiarachchi (1983)	Magnetization	17 ± 3	–[b]
Jayasuriya et al. (1983)	Calorimetry	13.6 ± 0.6	

[a] *As calculated by Jayasuriya et al. (1983).*
[b] *As calculated by Jayasuriya et al. (1985a,b).*

as determined from the low-temperature data. After rejection of the two lowest data points, then the remainder were fitted to the following equation with an overall accuracy as a standard deviation of ±152 J/mol (0.54%):

$$H^\circ(T) - H^\circ(298)(\text{J/mol}) = 17.9254T + 8.74703 \times 10^{-3}T^2 - 515{,}918/T - 4391.614$$

Heat capacity measurements of Pozdeyev et al. (1990) (400–1600 K) are initially 5% higher than the selected values and then show a trend to 16% lower.

13.5. Gamma Phase

Enthalpy measurements of Dennison et al. (1966a) (1554–1619 K) as given by Gschneidner (1991) were corrected as above, and after rejection of the lowest and the two highest data points, the remaining four values were fitted to the following equation with an overall accuracy as a standard deviation of ±10 J/mol (0.014%):

$$H^\circ(T) - H^\circ(298)(\text{J/mol}) = 27.6809T + 6453.642$$

However, the derived heat capacity at 27.68 ± 0.33 J/(mol K) is considered to be far too low when compared to values obtained for neighboring phases, and therefore, a more likely value of 46 J/(mol K) is selected to agree with values for the beta and the liquid phases. If the enthalpy value is assumed to be identical to that obtained from the above equation at the median temperature of 1595.65 K based on the range of stability for this phase, then the enthalpy equation becomes revised to

$$H^\circ(T) - H^\circ(298)(\text{J/mol}) = 46.0000T - 22{,}777.23$$

At the transition temperature at 1562.15 K, the derived enthalpy of transition is 4456 ± 152 J/mol.

A single measurement of the heat capacity in the gamma region at 1600 K by Pozdeyev et al. (1990) is 22% lower than the selected value.

13.6. Liquid Phase

Enthalpy measurements of Dennison et al. (1966a) (1635–1955 K) as given by Gschneidner (1991) were as corrected as above and then for saturation with tantalum due to the solubility of the metal in the tantalum container used for the measurements by following the method of Dennison et al. (1966b). The resultant corrected data were fitted to the following equation with an overall accuracy as a standard deviation of ±931 J/mol (1.15%):

$$H^\circ(T) - H^\circ(298)(\text{J/mol}) = 46.1815T - 12{,}879.94$$

The derived heat capacity is 46.2 ± 2.5J/(mol K); the enthalpy of fusion, 10,193 ± 931 J/mol; and the entropy of fusion, 6.26 ± 0.57 J/(mol K).

13.7. Gas Phase

Values are based on one bar standard pressure and are calculated from 599 energy levels, including the ground state, listed in Table 117 using the method of Kolsky et al. (1957) and the 2010 Fundamental Constants (Mohr et al., 2011).

TABLE 117 Sources of Energy Level Data

Authors	Number of levels
Ralchenko et al. (2012)	590
Gottwald et al. (2009)	9

Thirty-six of the levels selected by Ralchenko et al. (2012) were revised by Blaise (2005).

13.8. Enthalpy of Sublimation

TABLE 118 Enthalpy of Sublimation at 298.15 K

Authors	Methods	Range (K)	$\Delta_{sub}H^{\circ}$(298, II law) (kJ/mol)	$\Delta_{sub}H^{\circ}$(298, III law) (kJ/mol)	Notes
Jackson et al. (1961)	MS	1437	382 ± 2	–	
White et al. (1961)	MS	1492–1644	372 ± 7	–	
		1655–1967	369 ± 3	–	
Habermann (1963)	KE	1598–1918	398 ± 4	387.8 ± 0.3	–[a]
Habermann and Daane (1964)	KE	1625–2043	397 ± 3	386.7 ± 1.2	–[b,c]
Zaitsev et al. (1982)	KE	1262–1619	389 ± 1	386.4 ± 0.1	
Zaitsev et al. (1989)	KE	1435–1626	402 ± 4	386.2 ± 0.3	
Selected				386.5 ± 1.5	

MS, mass spectrometry; KE, Knudsen effusion.
[a] *This is Run 5 of Habermann and Daane (1964) given in detail.*
[b] *Given only in the form of the Clausius–Clapeyron equation.*
[c] *Note that Run 5 as given by Habermann (1963) is given to lower temperatures than the apparent complete range as given by Habermann and Daane (1964).*

The selected value is based on the excellent agreement between the last three sets of measurements with the accuracy assigned so as to take into account the individual results on Run 5 as given by Habermann (1963).

13.9. Vapor Pressure

The vapor pressure equation for the beta phase was evaluated at 25 K intervals from 900 to 1550 K and the transition temperature and for the liquid phase at 50 K intervals from 1650 to 3500 K and the melting point. The constants for the gamma phase was obtained by calculating the vapor pressure values at the transition temperature, the melting point, and 1600 K (Table 119).

13.10. Comparison of Selected Values at 298.15 K

Holley et al. (1968), Hultgren et al. (1973), and Konings and Beneš (2010) all based their selected values mainly on the heat capacity measurements of Jennings et al. (1957) although the entropy value selected by Konings and Beneš (2010) is clearly a misprint since the actual value from Jennings et al. (1957) is 73.24 J/(mol K). The present value is also based mainly on Jennings et al. (1957) but includes the enthalpy and entropy of the first-order transition from the alpha to the beta phases and the equations given by Jayasuriya et al. (1984) to represent the specific heat in the region of the Néel transition (Table 120).

TABLE 119 Vapor Pressure Equations

$\ln(p, \text{bar}) = b_1 + b_2/T + b_3 \ln(T) + b_4 T + b_5 T^2$

Phase	Range (K)	b_1	b_2	b_3	b_4	b_5
Beta	900–1562.15	15.63014	−46,556.94	4.05427×10^{-2}	-5.80744×10^{-4}	-1.45715×10^{-8}
Gamma	1562.15–1629.15	30.67849	−47,729.80	−2.031893	0	0
Liquid	1629.15–2500	39.08202	−47,452.75	−3.288692	4.71707×10^{-4}	-1.77148×10^{-8}
	2500–3500	35.52177	−47,045.57	−2.802756	2.77239×10^{-4}	-4.66562×10^{-9}

TABLE 120 Comparison of Heat Capacity, Enthalpy, and Entropy Values at 298.15 K

Authors	$C°_p(298)$ (J/(mol K))	$H°(298) - H°(0)$ (J/mol)	$S°(298)$ (J/(mol K))
Holley et al. (1968)	28.95	9414	73.22
Hultgren et al. (1973)	28.91	9427	73.30
Konings and Beneš (2010)	28.95	–	72.24
This work	28.95	9459	73.38

13.11. Summary of Representative Equations

TABLE 121 Representative Equations Above 298.15 K

Beta phase: 298.15–1562.15 K
$C°_p(T)(\text{J/(mol K)}) = 17.9254 + 1.749406 \times 10^{-2} T + 515,918/T^2$
$H°(T) - H°(298)(\text{J/mol}) = 17.9254T + 8.74703 \times 10^{-3} T^2 - 515,918/T - 4391.614$
$S°(T)(\text{J/(mol K)}) = 17.9254 \ln(T) + 1.749406 \times 10^{-2} T - 257,959/T^2 - 31.0616$
Gamma phase: 1562.15–1629.15 K
$C°_p(T)(\text{J/(mol K)}) = 46.0000$
$H°(T) - H°(298)(\text{J/mol}) = 46.0000T - 22,777.23$
$S°(T)(\text{J/(mol K)}) = 46.0000 \ln(T) - 207.4132$
Liquid phase: 1629.15–3500 K
$C°_p(T)(\text{J/(mol K)}) = 46.1815$
$H°(T) - H°(298)(\text{J/mol}) = 46.1815T - 12,879.94$
$S°(T)(\text{J/(mol K)}) = 46.1815 \ln(T) - 202.5278$

TABLE 122 Free Energy Equations Above 298.15 K

Beta phase: 298.15–1562.15 K
$G°(T) - H°(298)(\text{J/mol}) = 48.9870T - 8.74703 \times 10^{-3}T^2 - 257{,}959/T - 17.9254T\ln(T) - 4391.614$
Gamma phase: 1562.15–1629.15 K
$G°(T) - H°(298)(\text{J/mol}) = 253.4421T - 46.0000T\ln(T) - 22{,}777.23$
Liquid phase: 1629.15–3500 K
$G°(T) - H°(298)(\text{J/mol}) = 248.7093T - 46.1815T\ln(T) - 12{,}879.94$

TABLE 123 Transition Values Involved with the Free Energy Equations

Transition	T (K)	$\Delta H°$ (J/mol)	$\Delta S°$ (J/(mol K))
Beta–gamma	1562.15	4455.912	2.8524
Fusion	1629.15	10,192.98	6.2566

13.12. Nuclear Heat Capacity

The nuclear heat capacity $C°_N$ can be correlated by an equation using inverse powers of temperature:

$$C°_N(T) = X\left(A/T^2 + B/T^3 + C/T^4 + \text{L}\right)$$

where X is the isotopic fraction for the isotope and if a' is the magnetic interaction parameter, P is the quadrupole coupling constant, R is the gas constant, and I is the nuclear spin, and since ^{159}Tb has $I = 3/2$, the constants can be defined as

$$A/R = 5/4a'^2 + P^2; \quad B/R = -3a'^2P; \quad C/R = -17/16a'^4$$

The values of a' and P given in Table 124 were either given or derived using heat capacity (HC) and NMR methods.

TABLE 124 Summary of the Determinations of a' and P

Authors	Methods	a' (K)	P (K)
Lounasmaa and Roach (1962)	HC	0.15	0.021
Van Kempen et al. (1964)	HC	0.152	0.013
Krusius et al. (1969)	HC	0.149	0.0158
Kobayashi, et al. (1967)	NMR	0.1492	0.016
Sano and Itoh (1972)	NMR	0.1497	0.0162
Selected		0.1497	0.0161

a' and P are selected so that the derived constants conform with the rounded values selected by Wells et al. (1976) and since $X=1$, then $C^{\circ}_{N}(T)(\text{mJ/(mol K)}) = 235.1/T^2 - 9.00/T^3 - 4.44/T^4$.

13.13. Thermodynamic Tables

TABLE 125 Low-Temperature Thermodynamic Data

T (K)	$C^{\circ}_{p}(T)$ (J/(mol K))	$H^{\circ}(T) - H^{\circ}(0)$ (J/mol)	$S^{\circ}(T)$ (J/(mol K))	$-[G^{\circ}(T) - H^{\circ}(0)]/T$ (J/(mol K))
Alpha phase				
5	0.0793	0.112	0.0359	0.0136
10	0.506	1.270	0.180	0.0533
15	1.904	6.792	0.609	0.157
20	4.489	22.38	1.488	0.369
25	7.706	52.72	2.829	0.720
30	11.048	99.64	4.531	1.209
40	16.943	240.8	8.551	2.531
50	21.359	433.5	12.832	4.163
60	24.594	664.1	17.027	5.960
70	27.026	922.7	21.010	7.828
80	28.919	1203	24.747	9.712
90	30.426	1500	28.243	11.579
100	31.631	1810	31.513	13.411

TABLE 125 Low-Temperature Thermodynamic Data—Cont'd

T (K)	$C^\circ_p(T)$ (J/(mol K))	$H^\circ(T) - H^\circ(0)$ (J/mol)	$S^\circ(T)$ (J/(mol K))	$-[G^\circ(T) - H^\circ(0)]/T$ (J/(mol K))
110	32.763	2132	34.581	15.197
120	33.863	2465	37.479	16.934
130	34.949	2809	40.233	18.621
140	36.054	3164	42.863	20.260
150	37.232	3531	45.390	21.851
160	38.550	3910	47.834	23.399
170	40.093	4303	50.216	24.907
180	41.880	4712	52.557	26.378
190	44.058	5142	54.878	27.817
200	46.837	5595	57.205	29.228
210	50.979	6083	59.582	30.617
220	59.789	6630	62.126	31.990
221.45	60.801	6717	62.522	32.189
Beta phase				
221.45	57.195	6731	62.584	32.189
225	60.771	6940	63.519	32.676
226	62.395	7001	63.792	32.813
227	64.618	7065	64.072	32.950
228	68.028	7131	64.362	33.087
229	74.733	7202	64.673	33.224
229.5	82.884	7241	64.843	33.293
229.6	85.926	7249	64.882	33.307
229.7	90.257	7258	64.918	33.220
229.8	97.435	7267	64.958	33.334
229.9	115.636	7274	64.992	33.348
229.95	282.181	7284	65.033	33.355
230	75.474	7293	65.072	33.362
230.1	64.508	7300	65.102	33.375
230.2	60.133	7306	65.129	33.389

Continued

TABLE 125 Low-Temperature Thermodynamic Data—Cont'd

T (K)	$C°_p(T)$ (J/(mol K))	$H°(T) - H°(0)$ (J/mol)	$S°(T)$ (J/(mol K))	$-[G°(T) - H°(0)]/T$ (J/(mol K))
230.3	57.475	7312	65.156	33.403
230.4	55.594	7318	65.179	33.417
230.5	54.152	7323	65.203	33.431
231	49.837	7349	65.315	33.500
232	45.124	7397	65.519	33.637
233	41.816	7440	65.706	33.774
234	39.539	7481	65.880	33.911
235	37.976	7569	66.045	34.048
240	34.187	7698	66.799	34.722
250	31.577	8025	68.134	36.032
260	30.402	8335	69.347	37.291
270	29.745	8635	70.481	38.499
280	29.336	8930	71.555	39.661
290	29.088	9222	72.580	40.778
298.15	28.945	9459	73.384	41.659

TABLE 126 High-Temperature Thermodynamic Data

T (K)	$C°_p(T)$ (J/(mol K))	$H°(T) - H°(298)$ (J/mol)	$S°(T)$ (J/(mol K))	$-[G°(T) - H°(298)]/T$ (J/(mol K))
Beta phase				
298.15	28.945	0	73.384	73.384
300	28.906	54	73.563	73.385
350	28.260	1480	77.961	73.733
400	28.148	2888	81.723	74.502
500	28.736	5726	88.053	76.601
600	29.855	8653	93.386	78.964
700	31.224	11,705	98.088	81.367

TABLE 126 High-Temperature Thermodynamic Data—Cont'd

T (K)	$C°_p(T)$ (J/(mol K))	$H°(T) - H°(298)$ (J/mol)	$S°(T)$ (J/(mol K))	$-[G°(T) - H°(298)]/T$ (J/(mol K))
800	32.727	14,902	102.355	83.728
900	34.307	18,253	106.300	86.019
1000	35.935	21,765	109.999	88.234
1100	37.595	25,441	113.501	90.373
1200	39.277	29,285	116.845	92.441
1300	40.973	33,297	120.055	94.442
1400	42.680	37,480	123.154	96.383
1500	44.396	41,833	126.157	98.268
1562.15	45.465	44,626	127.981	99.414
Gamma phase				
1562.15	46.000	49,082	130.834	99.414
1600	46.000	50,823	131.935	100.171
1629.15	46.000	52,164	132.765	100.746
Liquid phase				
1629.15	46.181	62,357	139.022	100.746
1700	46.181	65,629	140.988	102.383
1800	46.181	70,247	143.628	104.602
1900	46.181	74,865	146.124	106.722
2000	46.181	79,483	148.493	108.752
2100	46.181	84,101	150.746	110.698
2200	46.181	88,719	152.895	112.568
2300	46.181	93,338	154.948	114.366
2400	46.181	97,956	156.913	116.098
2500	46.181	102,574	158.798	117.769
2600	46.181	107,192	160.610	119.382
2700	46.181	111,810	162.353	120.941
2800	46.181	116,428	164.032	122.451
2900	46.181	121,046	165.653	123.912

Continued

TABLE 126 High-Temperature Thermodynamic Data—Cont'd

T (K)	$C°_p(T)$ (J/(mol K))	$H°(T) - H°(298)$ (J/mol)	$S°(T)$ (J/(mol K))	$-[G°(T) - H°(298)]/T$ (J/(mol K))
3000	46.181	125,665	167.218	125.330
3100	46.181	130,283	168.733	126.706
3200	46.181	134,901	170.199	128.042
3300	46.181	139,519	171.620	129.341
3400	46.181	144,137	172.998	130.605
3500	46.181	148,755	174.337	131.836

TABLE 127 Thermodynamic Properties of the Gas Phase

T (K)	$C°_p(T)$ (J/(mol K))	$H°(T) - H°(298)$ (J/mol)	$S°(T)$ (J/(mol K))	$-[G°(T) - H°(298)]/T$ (J/(mol K))
298.15	26.882	0	202.096	202.096
300	26.853	50	202.263	202.097
350	26.092	1373	206.344	202.421
400	25.464	2661	209.785	203.132
500	24.707	5164	215.374	205.045
600	24.485	7620	219.852	207.151
700	24.608	10,073	223.632	209.243
800	24.936	12,549	226.938	211.252
900	25.381	15,064	229.900	213.162
1000	25.889	17,627	232.600	214.973
1100	26.428	20,243	235.093	216.690
1200	26.978	22,913	237.416	218.322
1300	27.529	25,639	239.597	219.875
1400	28.072	28,419	241.657	221.358
1500	28.603	31,253	243.612	222.777
1562.15	28.926	33,040	244.780	223.630
1600	29.118	34,139	245.475	224.138

TABLE 127 Thermodynamic Properties of the Gas Phase—Cont'd

T (K)	$C^\circ_p(T)$ (J/(mol K))	$H^\circ(T) - H^\circ(298)$ (J/mol)	$S^\circ(T)$ (J/(mol K))	$-[G^\circ(T) - H^\circ(298)]/T$ (J/(mol K))
1629.15	29.265	34,990	246.002	224.524
1700	29.616	37,076	247.255	225.446
1800	30.094	40,061	248.961	226.705
1900	30.552	43,094	250.601	227.920
2000	30.992	46,171	252.179	229.094
2100	31.412	49,292	253.702	230.229
2200	31.816	52,453	255.172	231.330
2300	32.203	55,654	256.595	232.398
2400	32.577	58,893	257.974	233.435
2500	32.938	62,169	259.311	234.443
2600	33.288	65,480	260.610	235.425
2700	33.629	68,826	261.872	236.381
2800	33.963	72,206	263.101	237.313
2900	34.291	75,619	264.299	238.223
3000	34.613	79,064	265.467	239.112
3100	34.932	82,541	266.607	239.981
3200	35.246	86,050	267.721	240.830
3300	35.558	89,591	268.810	241.662
3400	35.866	93,162	269.876	242.476
3500	36.171	96,764	270.921	243.274

$H^\circ(298) - H^\circ(0) = 7455.7$ J/mol.

TABLE 128 Vapor Pressure

T (K)	p (bar)	$\Delta G^\circ(T)$ (J/mol)	$\Delta H^\circ(T)$ (J/mol)	p (bar)	T (K)
298.15	1.03×10^{-61}	348,124	386,500	10^{-15}	933
300	2.68×10^{-61}	347,886	386,497	10^{-14}	979
350	1.10×10^{-51}	341,459	386,393	10^{-13}	1029

Continued

TABLE 128 Vapor Pressure—Cont'd

T (K)	p (bar)	$\Delta G^\circ(T)$ (J/mol)	$\Delta H^\circ(T)$ (J/mol)	p (bar)	T (K)
400	1.77×10^{-44}	335,048	386,273	10^{-12}	1085
500	2.15×10^{-34}	322,278	385,939	10^{-11}	1148
600	1.12×10^{-27}	309,588	385,468	10^{-10}	1218
700	6.90×10^{-23}	296,987	384,868	10^{-9}	1298
800	2.67×10^{-19}	284,480	384,147	10^{-8}	1389
900	1.62×10^{-16}	272,071	383,311	10^{-7}	1495
1000	2.70×10^{-14}	259,761	382,362	10^{-6}	1619
1100	1.76×10^{-12}	247,551	381,302	10^{-5}	1722
1200	5.64×10^{-11}	235,443	380,128	10^{-4}	1959
1300	1.05×10^{-9}	223,437	378,842	10^{-3}	2193
1400	1.28×10^{-8}	211,535	377,439	10^{-2}	2493
1500	1.11×10^{-7}	199,737	375,919	10^{-1}	2896
1562.15	3.67×10^{-7}	192,457	374,915	1	3463
1562.15	3.67×10^{-7}	192,457	370,459	NBP	3467
1600	7.20×10^{-7}	188,152	369,816		
1629.15	1.18×10^{-6}	184,847	369,326		
1629.15	1.18×10^{-6}	184,847	359,133		
1700	3.57×10^{-6}	177,293	357,947		
1800	1.45×10^{-5}	166,714	356,315		
1900	5.07×10^{-5}	156,224	354,729		
2000	1.56×10^{-4}	145,816	353,188		
2100	4.27×10^{-4}	135,485	351,690		
2200	1.06×10^{-3}	125,224	350,234		
2300	2.44×10^{-3}	115,028	348,817		
2400	5.21×10^{-3}	104,893	347,438		
2500	1.04×10^{-2}	94,814	346,095		
2600	1.98×10^{-2}	84,789	344,789		
2700	3.57×10^{-2}	74,814	343,516		
2800	6.16×10^{-2}	64,884	342,278		
2900	0.102	54,998	341,073		

TABLE 128 Vapor Pressure—Cont'd

T (K)	p (bar)	$\Delta G°(T)$ (J/mol)	$\Delta H°(T)$ (J/mol)	p (bar)	T (K)
3000	0.164	45,154	339,900		
3100	0.254	35,348	338,759		
3200	0.382	25,578	337,649		
3300	0.561	15,842	336,571		
3400	0.805	6140	335,525		
3463.44	1.000	0	334,877		
3500	1.129	−3534	334,508		

NBP, normal boiling point at one atmosphere pressure (1.01325 bar).
$\Delta H°(0)$=388,503 J/mol.

14. THERMODYNAMIC FUNCTIONS OF DYSPROSIUM

14.1. Introduction

Dysprosium exists in three allotropic modifications—an orthorhombic alpha phase transforming at 90.5 K to a close-packed hexagonal beta phase. The alpha phase is ferromagnetic and initially undergoes a first-order transition to the beta phase as an incommensurate helical antiferromagnetic state before undergoing a second-order transformation to a paramagnetic state at Néel temperature of 180.0 K. Gschneidner (1990) selects 1654 K for the transformation of the beta phase to the body-centered cubic gamma phase and 1685 K for the melting point.

14.2. Alpha Phase

^{161}Dy and ^{163}Dy give a nuclear contribution to the heat capacity. Values for the magnetic interaction parameter, a', and the quadrupole coupling constant, P, were obtained for both isotopes by Anderson et al. (1969) (0.025–0.4 K) using heat capacity measurements and by Kobayashi et al. (1966), Sano et al. (1970), and Berthier et al. (1975) using NMR. Based on the procedure as given in Section 2.4, the variation of the nuclear heat capacity with temperature derived from these measurements is given in Part 14.12.

Hill and Gschneidner (1988) (0.5–20 K) gave the heat capacity up to 6 K in the form of an equation with the nuclear contribution subtracted. If this contribution as derived in Part 14.12 is added, then the specific heat up to 6 K can be represented by the equation

$$C°_p(T)(\mathrm{mJ/(mol\,K)}) = 28.14/T^2 - 1.611/T^3 - 0.1295/T^4 + 4.86T + 0.282T^3 + 0.00145T^5$$

where the first three terms are the nuclear contribution, the fourth term is the electronic coefficient, and the fifth and sixth terms are the lattice contribution since it is assumed that a magnetic contribution would be negligible. The derived limited Debye temperature of 190 K is in exact agreement with the value obtained by Rosen and Klimker (1970) from elastic constant measurements but is notably higher than the value of 182.6 K derived by Scott (1978) from the elastic constant measurements of Palmer and Lee (1972) and the even lower value of 180.7 K obtained by Palmer (1978).

Other measurements of heat capacity in this region are on samples of much lower purity. As a result, those of Dash et al. (1961) (0.25–2 K) are from 16% lower than the selected values climbing to 64% higher. Those of Dreyfus et al. (1961c) (0.4–4 K) are on average 34% higher, while the measurements of Parks (1962) (0.4–4.2 K) are initially 2% lower and then rapidly increase to 535% higher. The measurements of Lounasmaa and Guenther (1962a,b) (0.4–4.0 K) were made on metal that was later shown to contain 6.1 atm% of nonmetallic elements and 0.43 wt% of metallic elements. The values obtained varied from 4% lower up to 300% higher than the selected values.

Above 6 K, selected heat capacity values are based on the measurements obtained on very high purity metal by Pecharsky et al. (1996) (3.5–325 K) which were given only in the form of a graph with actual values being supplied by Pecharsky (2006). Measurements of Hill and Gschneidner (1988) from 6 to 20 K were given only in the form of an equation with actual values supplied by Hill (1991), and on average, these show a bias of 1% greater than the selected values. Measurements of Flotow and Osborne (1964) (4–28 K) made on the same impure metal as used by Lounasmaa and Guenther (1962a,b) are initially 230% higher than the selected values but then converge to agree. Similarly, measurements by Lounasmaa and Sundström (1966) (3–25 K) on the same metal are initially up to 260% high and then converge to within 1% of the selected values.

In this region, the smooth values of Griffel et al. (1956) (14–304 K) vary from 1% low at 45 K and then deviate rapidly to be 11% high at 85 K, while those of Amitin et al. (1983) (5–300 K) in this region are initially 9% high at 10 K but then fall to an average of 1% high from 25 to 85 K. The measurements of Nikitin et al. (1991) (4–300K) are only given in the form of a small graph.

14.3. Beta Phase—Low Temperature

A selected equilibrium transition temperature of 90.5 K is based on the value of 90.54 K obtained by Pecharsky et al. (1996) which was confirmed by values of 90.7 K from the measurements of Jayasuriya et al. (1985b) and 90.4 K from the measurements of Åström and Benediktsson (1988). The values given in Table 129 have been obtained for the enthalpy of transition.

TABLE 129 Enthalpy of Transition Between the Alpha and Beta Phases

Authors	Methods	Enthalpy of transformation (J/mol)	Notes
Behrendt et al. (1958)	Magnetization	48 ± 6	–[a]
Feron (1969)	Magnetization	55 ± 8	–[a]
Fort et al. (1981)	Magnetization	57 ± 6	–[a]
Amitin et al. (1983)	Calorimetry	41 ± 1	–[b]
Jayasuriya et al. (1985b)	Calorimetry	39.1 ± 1.5	
Åström and Benediktsson (1988)	Calorimetry	35 ± 2	
Pecharsky et al. (1996)	Calorimetry	50.7 ± 1.2	

[a]*As calculated by Jayasuriya et al. (1985b).*
[b]*As calculated by Åström and Benediktsson (1988).*

The value determined by Pecharsky et al. (1996) on very high purity metal is selected to be consistent with the selected heat capacity measurements.

Below the Néel temperature, the beta phase is in an incommensurate helical antiferromagnetic state in which the helical turn angle varies from 24.0° at the Curie temperature to 42.9° at the Néel temperature (Greenhough et al., 1981). However, various turn angles are commensurate with the basal plane of the hexagonal crystal structure and nine such transitions have been definitely identified and the results are summarized in Part 14.13. Using sensitive calorimetry, Åström and Benediktsson (1988) were able to confirm only two of these transitions at 166 and 173 K and measured the enthalpies of transition to be 2 ± 1 J/mol in both cases, but this is considered to be within experimental noise and therefore these transitions were not considered in the evaluation of the thermodynamic data.

Although Åström and Benediktsson (1988) suggested that the Néel transition could be very weak first order and even measured an enthalpy of transition of 6.8 ± 1.0 J/mol, Chernyshov et al. (2005) showed from a consideration of the magnetic phase diagram that the transition must be second order. A transition temperature of 180.0 K is selected from values of 180.04 K obtained by both Pecharsky et al. (1996) as the maximum in their heat capacity values and Jayasuriya et al. (1985b) from a power law fit to their measurements and 179.90 ± 0.18 K directly obtained by Jayasuriya et al. (1985b) as an equilibrium transition temperature. Measurements that lead to Néel temperatures significantly different from the above value must be considered to be made on metals with notable impurity levels, for example, Amitin et al.

(1970) (148–202 K) obtained a maximum in the heat capacity at only 177.5 K while using a power law fit to their heat capacity measurements Lederman and Salamon (1974) obtained a Néel temperature of 183.15 K.

From 90.5 to 298.15 K, the selected values of heat capacity are generally those determined by Pecharsky et al. (1996), as given by Pecharsky (2006), because of the very high purity of the metal used. However, in the region of the Néel transition, Pecharsky et al. determined insufficient measurements to allow characterization of the heat capacity behavior and therefore the power law equations of Jayasuriya et al. (1985b) were used in the range of 179–181 K and joined smoothly with the measurements of Pecharsky et al. (1996) either side of this range. Above 280 K, the latter measurements show scatter but a heat capacity value of 26.56 ± 0.12 J/(mol K) at 298.15 K was calculated.

In this region, the smoothed values of Griffel et al. (1956) (14–304 K) are initially about 1% high but then gradually increase to be 6% high in the room temperature region. The metal used contained 0.6% of tantalum and almost certainly several atomic percentages of nonmetallic impurities which were typical of metal available at that time although no values were reported. The smooth values of Amitin et al. (1983) (5–300 K), when considered outside the range of the anomalies at the Curie and Néel transitions, and specifically above 200 K, increase from 1% to 4% above the selected values. Although stated to be of high purity, no hydrogen value or the possible presence of other lanthanides was given for the sample analysis and this may explain the difference from the selected values. Other measurements such as those of Jayasuriya et al. (1985b) (75–400), Nikitin et al. (1991) (4–300 K), and Chernyshov et al. (2005) (4–350 K) were given only in the form of small graphs.

14.4. Beta Phase—High Temperature

Enthalpy measurements were determined by both Dennison et al. (1966a) (273–1646 K in the beta phase) and Baginskii et al. (1997) (446–1650 K in the beta phase). In view of the increase in purity, the measurements of Baginskii et al. were selected but a Shomate-type plot indicated that in order to be compatible with the selected specific heat at 298.15 K, then all values up to 591 K were not included in the fit, while values at 788, 1329, 1502, and 1650 K all showed marked deviations and were similarly excluded. The remaining data points were fitted to the following equation with an overall accuracy of ± 65 J/mol (0.22%):

$$H^\circ(T) - H^\circ(298)(\mathrm{J/mol}) = 26.5476T - 1.24878 \times 10^{-3}T^2 + 2.83867 \times 10^{-6}T^3 - 7879.39$$

The enthalpy values of Dennison et al. (1966a) were given only in the form of an equation and smooth values with actual data points being given by Gschneidner (1991). After correction for temperature scale and from a

273.15 to a 298.15 K base by subtracting 665.0 J/mol obtained from the low-temperature data, the measurements scatter from 2% lower to 4.0% higher than the selected values for the beta phase but overall average at 1% higher.

Other measurements were all heat capacity determinations. Those of Banchila and Fillipov (1974) (1200–2000 K) were given as heat capacity–density and were corrected to heat capacity using the density values of Stankus and Tyagel'skii (2000) (293–1912 K) and as corrected are initially 10% high but then converge to the selected values. Measurements of Kurichenko et al. (1986) (697–1510 K) are initially 13% high but then diverge to become 66% higher above 1400 K, while the values of Pozdeyev et al. (1990) (400–1600 K) are initially 1% high and then deviate to a maximum of 12% low at 1400 K. The measurements of Shen (1994) (113–1073 K) are initially 6% high but above 373 K scatter within the 5% accuracy assigned to these values.

14.5. Gamma Phase

Dennison et al. (1966a) obtained only two successful measurements in this region at 1655 and 1658 K, while a third determination at 1679 K appeared to be on contaminated metal. They therefore ignored these measurements and from enthalpy values of the beta phase at the transition temperature and that of the liquid at the melting point and estimated values of the entropies of transition and fusion were able to estimate corresponding enthalpy values. However, their selected heat capacity of the gamma phase at 28.0 J/(mol K) is much too low when compared to values obtained for neighboring phases.

If the two highest data points of the enthalpy measurements of Baginskii et al. (1997) (1657–1686 K) are rejected, then the remainder can be fitted to the following equation with an overall fit as a standard deviation of ±203 J/mol (0.37%):

$$H^{\circ}(T) - H^{\circ}(298)(\mathrm{J/mol}) = 109.2675T - 31{,}541.86$$

The extraordinarily high derived heat capacity value of 109 ± 7 J/(mol K) is considered to be unrealistic and is rejected. Baginskii et al. appear to ignore their own measurements and instead select a heat capacity value of 84.75 J/(mol K) which also appears to be too high, and instead, a value of 50 J/(mol K) is selected as being consistent with the values obtained for neighboring phases and this value agrees with that selected by both Dinsdale (1991) and Huasen et al. (1995). Using the mid-point enthalpy of 50,897 J/mol at 1669.65 K obtained from the above equation, then the enthalpy can be represented by

$$H^{\circ}(T) - H^{\circ}(298)(\mathrm{J/mol}) = 50.0000T - 32{,}585.88$$

The derived enthalpy of transition is 4656 ± 213 J/mol. Using this equation, the actual enthalpy values obtained by Baginskii et al. (1997) tend from 1% lower to 1% higher than the selected values.

14.6. Liquid Phase

Enthalpy values have been determined by both Dennison et al. (1966a) (1700–2002 K) and Baginskii et al. (1997) (1706–2050 K). The liquid metal is soluble in the tantalum containers used to carry out the enthalpy measurements, and in both cases, the metal is assumed to be saturated with tantalum and enthalpy values were corrected following the method of Dennison et al. (1966b). Again the measurements of Baginskii et al. (1997) are selected, and after discarding two discrepant data points at 1842 and 1940 K, the remaining corrected values can be fitted to the following equation with an overall accuracy of ±123 J/mol (0.16%):

$$H^{\circ}(T) - H^{\circ}(298)(\mathrm{J/mol}) = 50.3049T - 21{,}838.88$$

The derived heat capacity is 50.30 ± 0.28 J/(mol K), the enthalpy of fusion is 11,261 ± 237 J/mol, and the entropy of fusion is 6.68 ± 0.14 J/(mol K).

Enthalpy measurements of Dennison et al. (1966a) were given only in the form of an equation with actual data points being given by Gschneidner (1991). After correction for temperature scale, from a 273.15 to a 298.15 K base, and for tantalum saturation, then these measurements average 1% lower than the selected values but the derived heat capacity of 49.8 ± 1.2 J/(mol K) agrees satisfactorily.

Heat capacity–density measurements of Banchila and Fillipov (1974) over the range of 1700–2000 K were corrected for density using the measurements of Stankus and Tyagel'skii (2000), and they tend from 13% to 25% lower than the selected value.

14.7. Gas Phase

Values are based on one bar standard state pressure and are calculated from the 763 energy levels, including the ground state, listed in Table 130 using the method of Kolsky et al. (1957) and the 2010 Fundamental Constants (Mohr et al., 2011).

TABLE 130 Sources of Energy Level Data

Authors	Number of levels
Ralchenko et al. (2012)	720
Nave and Griesmann (2000)	43

Thirty-one of the levels selected by Ralchenko et al. (2012) were revised by Nave (2005).

14.8. Enthalpy of Sublimation

TABLE 131 Enthalpy of Sublimation at 298.15 K

Authors	Methods	Range (K)	$\Delta_{sub}H^{\circ}$(298, II law) (kJ/mol)	$\Delta_{sub}H^{\circ}$(298, III law) (kJ/mol)	Notes
Savage et al. (1959)	MS	1080–1400	298 ± 3	–	
White et al. (1961)	MS	1278–1566	263 ± 1	–	
Spedding and Daane (1954)	KE	1245	297 ± 8	–	
Kovtun et al. (1964)	KE	1125–1346	306 ± 4	283.2 ± 0.4	
Habermann (1963)	KE	1339–1666	301 ± 3	291.2 ± 0.3	–[a]
Habermann and Daane (1964)	KE	1257–1690	301 ± 1	290.4 ± 1.6	–[b]
McCormack, et al. (1971)	KE	1239–1534	303 ± 2	292.1 ± 0.3	
Zaitsev et al. (1982)	KE	1043–1380	289 ± 1	290.6 ± 0.1	
Zaitsev et al. (1989)	KE	1248–1507	284 ± 2	286.3 ± 0.1	
Selected				288.0 ± 4.0	

MS, mass spectrometry; KE, Knudsen effusion.
[a]*This is Run 3 of Habermann and Daane (1964).*
[b]*Given only in the form of the Clausius–Clapeyron equation.*

The selected value is based on the good agreement between the Second and Third Law values obtained from the measurements of both Zaitsev et al. (1982) and Zaitsev et al. (1989), even though the former measurements were made on samples which may have been exposed to air for a long period of time prior to the experiments. The other Knudsen effusion measurements were not included because of the relatively poorer agreement between Second and Third Law values. In the case of McCormack et al. (1971), the samples appear to have been partially oxidized during the experiments. The assigned accuracy encompasses these other measurements.

14.9. Vapor Pressure

The vapor pressure equation for the beta phase was evaluated at 25 K intervals from 700 to 1650 K and the transition temperature and for the liquid phase at 25 K intervals from 1700 to 2800 K and the melting point. The constants for the gamma phase were obtained by calculating the vapor pressure

TABLE 132 Vapor Pressure Equations

$\ln(p, \text{bar}) = b_1 + b_2/T + b_3 \ln(T) + b_4 T + b_5 T^2$

Phase	Range (K)	b_1	b_2	b_3	b_4	b_5
Beta	700–1654.15	18.56553	−34,823.68	−0.5882662	-5.30118×10^{-5}	-1.05778×10^{-7}
Gamma	1654.15–1685.15	12.20723	−32,141.46	0	0	0
Liquid	1685.15–2800	40.01335	−36,453.04	−3.369664	-2.39989×10^{-4}	6.76147×10^{-8}

values at the transition temperature and the melting point and fitting to the Clausius–Clapeyron equation (Table 132).

14.10. Comparison of Selected Values at 298.15 K

Holley et al. (1968), Hultgren et al. (1973), and Shen et al. (1995) based their selected values mainly on the heat capacity measurements of Griffel et al. (1956), while Amitin et al. (1983) selected their own measurements. Konings and Beneš (2010) selected their entropy value based on a correction to the measurements of Amitin et al. (1983). The present evaluation is based mainly on the measurements of Pecharsky et al. (1996) and Jayasuriya et al. (1985b) (Table 133).

TABLE 133 Comparison of Heat Capacity, Enthalpy, and Entropy Values at 298.15 K

Authors	$C^\circ_p(298)$ (J/(mol K))	$H^\circ(298) - H^\circ(0)$ (J/mol)	$S^\circ(298)$ (J/(mol K))
Holley et al. (1968)	28.16	8853	74.77
Hultgren et al. (1973)	28.12	8866	74.89
Shen et al. (1995)	27.84	8866	74.96
Amitin et al. (1983)	27.73	8973	75.55
Konings and Beneš (2010)	27.73	–	77.81
This work	26.56	8842	74.78

14.11. Summary of Representative Equations

TABLE 134 Representative Equations Above 298.15 K

Beta phase: 298.15–1654.15 K
$C°_p(T)(\text{J/(mol K)}) = 26.5476 - 2.49756 \times 10^{-3} T + 8.51601 \times 10^{-6} T^2$
$H°(T) - H°(298)(\text{J/mol}) = 26.5476T - 1.24878 \times 10^{-3} T^2 + 2.83867 \times 10^{-6} T^3 - 7879.39$
$S°(T)(\text{J/(mol K)}) = 26.5476 \ln(T) - 2.49756 \times 10^{-3} T + 4.258005 \times 10^{-6} T^2 - 76.1153$
Gamma phase: 1654.15–1685.15 K
$C°_p(T)(\text{J/(mol K)}) = 50.0000$
$H°(T) - H°(298)(\text{J/mol}) = 50.0000T - 32,585.88$
$S°(T)(\text{J/(mol K)}) = 50.0000 \ln(T) - 239.5878$
Liquid phase: 1685.15–2800 K
$C°_p(T)(\text{J/(mol K)}) = 50.3049$
$H°(T) - H°(298)(\text{J/mol}) = 50.3049T - 21,838.88$
$S°(T)(\text{J/(mol K)}) = 50.3049 \ln(T) - 235.1707$

TABLE 135 Free Energy Equations Above 298.15 K

Beta phase: 298.15–1654.15 K
$G°(T) - H°(298)(\text{J/mol}) = 102.6629T + 1.24878 \times 10^{-3} T^2 - 1.419335 \times 10^{-6} T^3 - 26.5476T \ln(T) - 7879.39$
Gamma phase: 1654.15–1685.15 K
$G°(T) - H°(298)(\text{J/mol}) = 289.5878T - 50.0000T \ln(T) - 32,585.88$
Liquid phase: 1685.15–2800 K
$G°(T) - H°(298)(\text{J/mol}) = 285.4756T - 50.3049T \ln(T) - 21,838.88$

TABLE 136 Transition Values Involved with the Free Energy Equations

Transition	T (K)	$\Delta H°$ (J/mol)	$\Delta S°$ (J/(mol K))
Beta–gamma	1654.15	4656.105	2.8148
Fusion	1685.15	11,260.8	6.6824

14.12. Nuclear Heat Capacity

The nuclear contribution to the heat capacity can be represented by

$$C^{\circ}{}_{\mathrm{N}}(T) = X\left(A/T^2 + B/T^3 + C/T^4 + \mathrm{L}\right)$$

where X is the atomic fraction of the nuclide and if a' is the magnetic interaction parameter, P is the quadrupole coupling constant, R is the gas constant, and I is the nuclear spin, then since both the two isotopes ^{161}Dy and ^{163}Dy have $I = 5/2$

$$A/R = 35/12a'^2 + 56/9P^2; \quad B/R = -56/3a'^2P; \quad C/R = -259/48a'^4$$

The values of a' and P given in Table 137 were either given or derived using HC and NMR methods.

Selecting $X = 0.1889$ for ^{161}Dy and $X = 0.2490$ for ^{163}Dy (Berglund and Wieser, 2011), then

$$^{161}Dy : C^{\circ}{}_{\mathrm{N}}(T)(\mathrm{mJ}/(\mathrm{mol\,K})) = 42.89/T^2 - 2.286/T^3 - 0.1126/T^4$$

$$^{163}\mathrm{Dy} : C^{\circ}{}_{\mathrm{N}}(T)(\mathrm{mJ}/(\mathrm{mol\,K})) = 80.48/T^2 - 4.736/T^3 - 0.4349/T^4$$

$$\mathrm{Combined} : C^{\circ}{}_{\mathrm{N}}(T)(\mathrm{mJ}/(\mathrm{mol\,K})) = 28.14/T^2 - 1.611/T^3 - 0.1295/T^4$$

14.13. Commensurate Turn Angles

The beta phase below the Néel temperature at 180 K exists in an incommensurate helical antiferromagnetic state in which the helical turn angle varies from 24.0° at the Curie temperature to 42.9° at the Néel temperature (Greenhough et al., 1981). However, various turn angles are commensurate with the

TABLE 137 Summary of the Determinations of a' and P

		^{161}Dy		^{163}Dy	
Authors	Methods	a' (K)	P (K)	a' (K)	P (K)
Anderson et al. (1969)	HC	−0.0396	0.009	0.0554	0.01
Kobayashi et al. (1966)	NMR	0.0399	0.0093	0.0559	0.0098
Sano et al. (1970)	NMR	0.0399	0.0093	0.0558	0.0098
Berthier et al. (1975)	NMR	0.0398	0.0093	0.0558	0.0098
Selected		−0.0398	0.0093	0.0558	0.0098

TABLE 138 Summary of the Determination of Critical Turn Angle Temperatures

M:N	3:20	1:06	2:11	3:16	4:21	1:05	4:19	2:09	4:17
$\omega_c{}^\circ$	27.0	30.0	32.7	33.8	34.3	36.0	37.9	40.0	42.4
	T (K)								
A	97.5	113.7	127.5	130.5	137.0	147.0	152.5	166.5	173.0
B	97.9	113.0	–	130.3	137.0	147.0	151.2	161.8	173.2
C	101.5	111.7	124.8	131.0	140.6	144.9	153.3	161.2	173.1
D	101.9	113.2	122.5	129.9	139.9	147.6	151.9	162.6	173.7
E	98.5	114	128	134	137	147	156	167	175
F	–	114	–	–	–	–	156	–	–
G	–	116	–	132	–	145	156	–	–
Selected	99	113	126	131	138	147	153	164	173

basal plane of the hexagonal crystal structure. The commensurate structure is given by $\tau_m = M/N$ where the basal plane moment rotates by $M\pi$ for every N atomic planes or for every plane the turn angle is given as $\omega_c = (M\pi/N)\,\text{rad} = (180M/N)^\circ$ (Table 138).

The following measurements determined the commensurate turn angles:

A. Wilkinson et al. (1961): neutron diffraction
B. Greenhough et al. (1981): c-axis thermal expansion
C. Greenhough et al. (1981): measurement of elastic constant c_{44}
D. Mito et al. (2011): AC magnetic response
E. Blinov et al. (1991): magnetic susceptibility
F. Bulatov et al. (1996): measurement of elastic constant c_{33}
G. Bulatov et al. (1996): measurement of ultrasonic attenuation a_{33}

The selected values are suggested as consensus values rather than average values. In addition, Blinov et al. (1991) have also found other possible commensurate transitions:

1:7 93.9K; 2:13 102K; 3:19 105K; 3:17 122 K; 3:14 159K; 3:13 172K

The two commensurate transitions on which Åström and Benediktsson (1988) were able to determine enthalpies of transition at 2 ± 1 J/mol appear to be 2:9 and 4:17.

14.14. Thermodynamic Tables

TABLE 139 Low-Temperature Thermodynamic Data

T (K)	$C^\circ_p(T)$ (J/(mol K))	$H^\circ(T) - H^\circ(0)$ (J/mol)	$S^\circ(T)$ (J/(mol K))	$-[G^\circ(T) - H^\circ(0)]/T$ (J/(mol K))
Alpha phase				
5	0.0652	0.109	0.037	0.0152
10	0.546	1.272	0.181	0.0535
15	2.376	7.937	0.696	0.167
20	5.507	27.20	1.783	0.423
25	9.205	63.92	3.406	0.849
30	12.774	119.0	5.405	1.438
35	15.970	191.0	7.619	2.161
40	18.812	278.2	9.942	2.988
45	21.932	378.5	12.302	3.892
50	23.272	489.9	14.647	4.850
60	26.558	739.8	19.196	6.865
70	29.100	1019	23.488	8.936
80	31.105	1320	27.509	11.010
90	32.902	1640	31.276	13.054
90.5	32.999	1656	31.458	13.155
Beta phase				
90.5	32.999	1707	32.018	13.155
95	33.712	1857	33.637	14.087
100	34.554	2028	35.387	15.109
110	36.251	2382	38.758	17.107
120	38.046	2753	41.990	19.047
130	39.947	3143	45.110	20.932
140	42.201	3553	48.149	22.768
150	44.930	3989	51.150	24.560
160	48.489	4455	54.158	26.316
170	53.471	4963	57.239	28.044

TABLE 139 Low-Temperature Thermodynamic Data—Cont'd

T (K)	$C^\circ_p(T)$ (J/(mol K))	$H^\circ(T) - H^\circ(0)$ (J/mol)	$S^\circ(T)$ (J/(mol K))	$-[G^\circ(T) - H^\circ(0)]/T$ (J/(mol K))
175	57.303	5240	58.843	28.901
176	58.553	5298	59.173	29.072
177	60.067	5357	59.509	29.243
178	62.337	5418	59.854	29.414
179	67.274	5483	60.214	29.585
179.5	73.867	5518	60.410	29.670
179.6	76.213	5525	60.451	29.687
179.7	79.376	5533	60.494	29.705
179.8	84.037	5541	60.540	29.722
179.9	92.204	5550	60.588	29.739
180	116.395	5560	60.645	29.756
180.1	53.151	5568	60.688	29.773
180.2	45.719	5573	60.715	29.790
180.3	42.667	5577	60.739	29.808
180.4	40.825	5581	60.763	29.825
180.5	39.538	5585	60.785	29.842
181	36.144	5604	60.889	29.927
182	34.377	5639	61.082	30.098
183	33.150	5673	61.267	30.268
184	32.463	5706	61.446	30.437
185	31.827	5728	61.620	30.605
190	30.012	5892	62.441	31.432
200	28.535	6183	63.937	33.021
210	27.852	6465	65.311	34.526
220	27.448	6741	66.596	35.955
230	27.267	7015	67.813	37.314
240	27.101	7287	68.970	38.609
250	26.950	7557	70.073	39.846

Continued

TABLE 139 Low-Temperature Thermodynamic Data—Cont'd

T (K)	$C°_p(T)$ (J/(mol K))	$H°(T) - H°(0)$ (J/mol)	$S°(T)$ (J/(mol K))	$-[G°(T) - H°(0)]/T$ (J/(mol K))
260	26.814	7826	71.128	41.029
270	26.692	8093	72.137	42.162
280	26.620	8360	73.107	43.250
290	26.576	8626	74.040	44.296
298.15	26.560	8842	74.776	45.119

TABLE 140 High-Temperature Thermodynamic Data

T (K)	$C°_p(T)$ (J/(mol K))	$H°(T) - H°(298)$ (J/mol)	$S°(T)$ (J/(mol K))	$-[G°(T) - H°(298)]/T$ (J/(mol K))
Beta phase				
298.15	26.560	0	74.776	74.776
300	26.565	49	74.940	74.777
400	26.911	2722	82.626	75.822
500	27.428	5437	88.683	77.809
600	28.115	8213	93.742	80.054
700	28.972	11,066	98.138	82.330
800	30.000	14,013	102.072	84.556
900	31.198	17,071	105.673	86.705
1000	32.566	20,258	109.029	88.771
1100	34.105	23,590	112.204	90.758
1200	35.814	27,085	115.244	92.673
1300	37.693	30,759	118.183	94.523
1400	39.742	34,629	121.051	96.316
1500	41.962	38,713	123.867	98.059
1600	44.352	43,027	126.651	99.759
1654.15	45.718	45,466	128.150	100.664

TABLE 140 High-Temperature Thermodynamic Data—Cont'd

T (K)	$C°_p(T)$ (J/(mol K))	$H°(T) - H°(298)$ (J/mol)	$S°(T)$ (J/(mol K))	$-[G°(T) - H°(298)]/T$ (J/(mol K))
Gamma phase				
1654.15	50.000	50,122	130.964	100.664
1685.15	50.000	51,672	131.893	101.230
Liquid phase				
1685.15	50.305	62,932	138.575	101.230
1700	50.305	63,679	139.016	101.558
1800	50.305	68,710	141.892	103.720
1900	50.305	73,740	144.612	105.801
2000	50.305	78,771	147.192	107.806
2100	50.305	83,801	149.646	109.741
2200	50.305	88,832	151.986	111.608
2300	50.305	93,862	154.223	113.413
2400	50.305	98,993	156.364	115.158
2500	50.305	103,923	158.417	116.848
2600	50.305	108,954	160.390	118.485
2700	50.305	113,984	162.289	120.072
2800	50.305	119,015	164.118	121.613

TABLE 141 Thermodynamic Properties of the Gas Phase

T (K)	$C°_p$ (J/(mol K))	$H°_T - H°_{298.15}$ (J/mol)	$S°_T$ (J/(mol K))	$-(G°_T - H°_{298.15})/T$ (J/(mol K))
298.15	20.786	0	195.901	195.901
300	20.786	38	196.030	195.902
400	20.787	2117	202.010	196.717
500	20.793	4196	206.649	198.257
600	20.822	6276	210.442	199.981
700	20.895	8362	213.656	201.711

Continued

TABLE 141 Thermodynamic Properties of the Gas Phase—Cont'd

T (K)	C°_p (J/(mol K))	$H^\circ_T - H^\circ_{298.15}$ (J/mol)	S°_T (J/(mol K))	$-(G^\circ_T - H^\circ_{298.15})/T$ (J/(mol K))
800	21.031	10,458	216.455	203.383
900	21.237	12,570	218.943	204.976
1000	21.514	14,707	221.194	206.487
1100	21.859	16,875	223.260	207.919
1200	22.268	19,081	225.179	209.278
1300	22.741	21,331	226.980	210.571
1400	23.275	23,631	228.684	211.805
1500	23.870	25,988	230.310	212.985
1600	24.528	28,407	231.871	214.117
1654.15	24.910	29,746	232.694	214.711
1685.15	25.138	30,522	233.158	215.046
1700	25.249	30,896	233.380	215.206
1800	26.033	33,459	234.845	216.256
1900	26.883	36,105	236.275	217.272
2000	27.799	38,838	237.677	218.257
2100	28.782	41,667	239.056	219.215
2200	29.833	44,597	240.419	220.148
2300	30.953	47,636	241.770	221.059
2400	32.140	50,790	243.112	221.950
2500	33.395	54,066	244.449	222.823
2600	34.715	57,471	245.785	223.680
2700	36.097	61,011	247.120	224.524
2800	37.537	64,692	248.459	225.355

$H^\circ(298) - H^\circ(0) = 6197.4$ J/mol.

TABLE 142 Vapor Pressure

T (K)	p (bar)	$\Delta G^\circ(T)$ (J/mol)	$\Delta H^\circ(T)$ (J/mol)	p (bar)	T (K)
298.15	7.44×10^{-45}	251,887	288,000	10^{-15}	708
300	1.52×10^{-44}	251,662	287,989	10^{-14}	744

TABLE 142 Vapor Pressure—Cont'd

T (K)	p (bar)	$\Delta G^\circ(T)$ (J/mol)	$\Delta H^\circ(T)$ (J/mol)	p (bar)	T (K)
400	5.09×10^{-32}	239,642	287,395	10^{-13}	783
500	1.60×10^{-24}	227,776	286,759	10^{-12}	827
600	1.56×10^{-19}	216,044	286,063	10^{-11}	875
700	5.56×10^{-16}	204,434	285,296	10^{-10}	930
800	2.53×10^{-13}	192,939	284,445	10^{-9}	993
900	2.90×10^{-11}	181,556	283,499	10^{-8}	1065
1000	1.27×10^{-9}	170,285	282,449	10^{-7}	1148
1100	2.78×10^{-8}	159,124	281,285	10^{-6}	1246
1200	3.59×10^{-7}	148,074	279,996	10^{-5}	1362
1300	3.09×10^{-6}	137,137	278,572	10^{-4}	1504
1400	1.94×10^{-5}	126,315	277,002	10^{-3}	1681
1500	9.42×10^{-5}	115,611	275,275	10^{-2}	1927
1600	3.73×10^{-4}	105,028	273,380	10^{-1}	2266
1654.15	7.29×10^{-4}	99,348	272,280	1	2771
1654.15	7.29×10^{-4}	99,348	267,624	NBP	2774
1685.15	1.04×10^{-3}	96,202	266,850		
1685.15	1.04×10^{-3}	96,202	255,589		
1700	1.22×10^{-3}	94,799	255,217		
1800	3.32×10^{-3}	85,434	252,749		
1900	8.04×10^{-3}	76,204	250,365		
2000	1.77×10^{-2}	67,098	248,067		
2100	3.59×10^{-2}	58,104	245,866		
2200	6.79×10^{-2}	49,213	243,768		
2300	0.121	40,414	241,774		
2400	0.204	31,700	239,797		
2500	0.330	23,062	238,143		
2600	0.512	14,491	236,517		
2700	0.766	5981	235,029		
2770.65	1.000	0	234,061		
2800	1.112	−2477	233,677		

NBP, normal boiling point at one atmosphere pressure (1.01325 bar).
$\Delta H^\circ(0)$=290, 645 J/mol.

15. THERMODYNAMIC FUNCTIONS OF HOLMIUM

15.1. Introduction

In the low-temperature region, a value of 17.8 K was determined by Bates et al. (1988) for the first-order Curie temperature (T_C), while Jayasuriya et al. (1985a,b) determined the second-order Néel temperature (T_N) to be 132.26 K. In spite of these transitions, holmium retains a close-packed hexagonal structure up to the melting point which is selected as 1747 K by Gschneidner (1990). In contrast to gadolinium, terbium, and dysprosium, Spedding et al. (1973) proved that the pure metal does not transform to a body-centered cubic structure close to the melting point.

15.2. Solid Phase—Low Temperature

There is a large nuclear contribution to the low-temperature heat capacity. Measurements of the heat capacity were carried out by Dreyfus et al. (1961a) (1.4–4 K), Lounasmaa (1962b) (0.38–4.2 K), Van Kempen et al. (1964) (0.06–0.71 K), and Krusius et al. (1969) (0.03–0.5 K); neutron transmission measurements by Postma et al. (1962) (0.95 K), Sailor et al. (1962) (0.07–4.225 K), and Brunhart et al. (1965) (0.05–4 K); and NMR measurements by Mackenzie et al. (1974) and McCausland (1976). As summarized in Part 15.10, these measurements were used to determine the magnetic interaction parameter, a', and the quadrupole coupling constant, P, and following the procedure as given in Section 2.4 were then used to determine the variation of the nuclear heat capacity with temperature.

Additional contributions to the total heat capacity with the nuclear contribution omitted were fitted to the equation $C^\circ_p(T) = \gamma T + BT^3$, where γ is the electronic coefficient and B is a combination of the lattice and magnetic contributions to the heat capacity. From elastic constant measurements on single crystals, Rosen et al. (1974) determined a limiting Debye temperature of 191.5 K, equivalent to a lattice contribution of 0.28 mJ/(mol K^4), while similar measurements by Palmer (1978) determined 186.8 K, equivalent to 0.30 mJ/(mol K^4). Averaging these values to 0.29 mJ/(mol K^4), then the magnetic contribution to the heat capacity is given by the subtraction is $\mu = B - 0.29$ mJ/(mol K^4) (Table 143).

Selecting the later measurements of Collocott et al. (1988), then the total heat capacity up to 4.6 K can be represented by

$$C^\circ_p(\mathrm{mJ/(mol\,K)}) = 4182/T^2 - 125.4/T^3 - 1302/T^4 + 2.1T + 0.29T^3 + 1.01T^3$$

where the first three terms are the nuclear contribution as derived in Part 15.10.

Above 0.7 K, the heat capacity measurements of Lounasmaa (1962b) vary from initially 60% high compared to selected values and converge to be only about 3% high at 1.5 K before increasing rapidly to be 30% high at 4 K.

TABLE 143 Low-Temperature Heat Capacity Coefficients

Authors	Temperature range (K)	γ (mJ/(mol K^2))	B (mJ/(mol K^4))	μ (mJ/(mol K^4))
Hill et al. (1976)	0.8–4	6	1.1	0.81
Collocott et al. (1988)	0.6–5	2.1	1.3	1.01

Bates et al. (1988) obtained 17.8 K for the Curie temperature which is in agreement with heat capacity anomalies observed at 19.4 K determined by Gerstein et al. (1957) and 17.5 K determined by Lounasmaa and Sundström (1966). Using calorimetric and dilatometric measurements, Steinitz et al. (1987) determined the transition temperature to be between 18.2 and 18.7 K and also suggested that it could be first order with an enthalpy of transition of 7 J/mol. White (1989) confirmed the first-order nature from dilatometric measurements with a transition temperature of 19.5 K, while Stewart and Collocott (1989) measured the enthalpy of transition to be 2.7 ± 0.3 J/mol at 19.46 K. The Curie temperature determined by Bates et al. is selected, but there appears to be a sensitivity of the Curie temperature to impurity effects since it is noted that Willis and Ali (1992) obtained a much lower value of 13 K.

The transformation at the Curie temperature involves the formation of an incommensurate helical antiferromagnetic state up to the Néel temperature. However, at certain temperatures, the turn angle is commensurate with the basal plane and Bates et al. (1988) selected 19.8, 24.5, 40.5, and 97.4 K for these temperatures although Blinov et al. (1991) identified a further nine transitions above 50 K. Although Jayasuriya et al. (1985a) did notice an inflection in the heat capacity curve corresponding to the transition at 97.4 K, there does not appear to be any quantitative values given which could be associated with these anomalies. The details of the commensurate transitions are given in Section 15.11.

Unfortunately, although carried out on high purity metal, the heat capacity values of Stewart and Collocott (1989) (2–32 K) were shown only in the form of small graphs. Similarly, measurements of Gordon et al. (1962) (0.95–14 K) and Dempesy et al. (1966) (4–40 K) were also only given in the form of graphs. Therefore, above 5 K, the evaluation is based on heat capacity measurements of Gerstein et al. (1957) (13–301 K) and Lounasmaa and Sundström (1966) (3.1–25 K) except in the region of the Néel transition where the power law equations of Jayasuriya et al. (1985a) were given preference. Unfortunately, the values of Lounasmaa and Sundström (1966) tend from 12% to 50% higher than the selected values in the overlap region from 3 to 5 K, but the two sets of measurements were reconciled by interpolating between the low-temperature value at 4.58 K (the minimum in dC_p/dT for the selected

heat capacity curve) and the high-temperature value at 8 K. Because of the heat capacity anomalies observed by both Gerstein et al. (1957) and Lounasmaa and Sundström (1966), values were used only above 20.1 K and below 17.2 K, respectively.

Thermal expansion measurements by White (1989) and heat capacity measurements by Jayasuriya et al. (1985a) confirmed that the Néel transition was second order. The latter directly determined the transition temperature to be 132.245 ± 0.08 K, but a temperature of 132.268 K corresponds to the maximum in the power law equations and therefore suggesting a compromise value of 132.26 K. The power law equations were accepted from 124 to 132.4 K and could be joined smoothly with the heat capacity values of Gerstein et al. (1957) either side of this range. Jayasuriya et al. (1985a) determined values up to 400 K, but unfortunately, the results were reported only in the form of small graphs.

15.3. Solid Phase—High Temperature

Enthalpy measurements have been determined by both Dennison et al. (1966a) (373–1736 K for the solid region) and Baginskii et al. (1997) (390–1743 K for the solid region). The latter values were selected because of the much higher purity of the material used. However, in order to obtain a smooth continuity with the selected low-temperature heat capacity curve, the four lowest and the two highest enthalpy values were excluded and the following equation was then selected since this gives a minimum in the standard deviation of the fit at ± 82 J/mol (0.26%):

$$H^\circ(T) - H^\circ(298)(\mathrm{J/mol}) = 32.8494T - 9.18819 \times 10^{-3}T^2 + 7.42124 \times 10^{-6}T^3 - 1.27678 \times 10^{-9}T^4 + 183{,}852/T - 9780.52$$

The measurements of Dennison et al. (1966a) were given in the form of equations and tabulated values with actual data points being given by Gschneidner (1991). After correction for temperature scale and from a 273.15 to a 298.15 K base by subtracting 676.43 J/mol obtained from the low-temperature data, the measurements were found to deviate from the selected values by tending from 1.5% low at 473 K to 7% high at 1700 K before increasing sharply to 41% high at 1736 K.

Heat capacity measurements of Novikov et al. (1978) (1100–1700 K in the solid region) were given only in the form heat capacity–density. After correction for density using the density equations given by Stankus and Khairulin (1991), then the derived heat capacity values tended from 6% low to 25% high. Heat capacity measurements of Pozdeyev et al. (1990) (400–1600 K) tended from initially 0.7% low to 9% low at 1100 K before increasing to 4.5% low at 1500 K, while the value at 1600 K was 4.5% high. Measurements

of Novikov and Mardykin (1976) (1000–1700 K) were given only in the form of a small graph.

15.4. Liquid Phase

Enthalpy measurements of Baginskii et al. (1997) (1751–2094 K) were independently corrected for tantalum saturation following the method given by Dennison et al. (1966b) and after rejection of the lowest data point were fitted to the following equation with an overall accuracy as a standard deviation of ±200 J/mol (0.27%):

$$H^{\circ}(T) - H^{\circ}(298)(\mathrm{J/mol}) = 45.1139T - 15,600.52$$

The derived heat capacity is 45.11 ± 0.49 J/(mol K); the enthalpy of fusion, 15,868 ± 216 J/mol; and the entropy of fusion, 9.08 ± 0.12 J/(mol K).

After correction as above and for tantalum saturation, the two enthalpy data points determined by Dennison et al. (1966a) at 1750 and 1763 K are 6% higher than the selected values. Heat capacity values of Novikov et al. (1978) (1800–2100 K) were again only given in the form heat capacity–density and were corrected to heat capacity using the liquid density equations given by Stankus and Khairulin (1991). With this correction, the values tended from 2.5% higher to 6.5% lower than the selected value.

15.5. Gas Phase

Values are based on one bar standard state pressure and are calculated from the 381 energy levels, including the ground state, listed in Table 144 using the method of Kolsky et al. (1957) and the 2010 Fundamental Constants (Mohr et al., 2011).

TABLE 144 Sources of Energy Level Data

Authors	Number of levels
Ralchenko et al. (2012)	235
Wyart et al. (1977)	44
Child et al. (1983)	3
Kröger et al. (1997b)	99

15.6. Enthalpy of Sublimation

TABLE 145 Enthalpy of Sublimation at 298.15 K

Authors	Methods	Range (K)	$\Delta_{sub}H^{\circ}$(298, II law) (kJ/mol)	$\Delta_{sub}H^{\circ}$(298, III law) (kJ/mol)	Notes
Trulson et al. (1961)	MS	1194–1294	314 ± 2	–	
White et al. (1961)	MS	1253–1566	295 ± 5	–	
DeMaria et al. (1963b)	KEMS	1250–1500	342	311.9 ± 2.7	–[a]
Wakefield et al. (1967)	KE	1264–1874	300 ± 1	300.7 ± 0.1	
	L	947–1284	294 ± 1	299.5 ± 0.1	
	M	1435–2055	301 ± 2	300.4 ± 0.1	
Selected				300.2 ± 2.0	

MS, mass spectrometry; KEMS, Knudsen effusion mass spectrometry; KE, Knudsen effusion; L, Langmuir; M, modified Knudsen cell for higher pressure measurements.
[a]*Given only in the form of the Clausius–Clapeyron equation.*

The selected value is an average of the three techniques used by Wakefield et al. (1967) with the assigned accuracy representing the spread of individual values.

15.7. Vapor Pressure

The vapor pressure equation for the solid phase was obtained by evaluating the free energy functions of the solid and the gas at 25 K intervals from 725 to 1725 K and the melting point, and for the liquid phase, at 50 K intervals from 1750 to 3000 K and the melting point (Table 146).

15.8. Comparison of Selected Values at 298.15 K

Holley et al. (1968), Hultgren et al. (1973), and Konings and Beneš (2010) as well as the present review all essentially relied on low-temperature heat capacity values of Gerstein et al. (1957) except that in the present evaluation, the behavior in the region of the second-order Néel transition takes into account the power law equations of Jayasuriya et al. (1985a) (Table 147).

TABLE 146 Vapor Pressure Equations

$\ln(p, \text{bar}) = b_1 + b_2/T + b_3 \ln(T) + b_4 T + b_5 T^2$

Phase	Range (K)	b_1	b_2	b_3	b_4	b_5
Solid	725.15–1747.15	14.81062	−36,086.53	-3.30897×10^{-2}	-6.29679×10^{-4}	4.62182×10^{-9}
Liquid	1747.15–3000	39.35126	−37,734.31	−3.339629	-1.14463×10^{-4}	6.62641×10^{-8}

TABLE 147 Comparison of Heat Capacity, Enthalpy, and Entropy Values at 298.15 K

Authors	$C^\circ_p(298)$ (J/(mol K))	$H^\circ(298) - H^\circ(0)$ (J/mol)	$S^\circ(298)$ (J/(mol K))
Holley et al. (1968)	27.15	7996	75.02
Hultgren et al. (1973)	27.15	8004	75.65
Konings and Beneš (2010)	27.15	–	75.19
This work	27.15	8018	75.76

15.9. Summary of Representative Equations

TABLE 148 Representative Equations Above 298.15 K

Solid phase: 298.15–1747.15 K
$C^\circ_p(T)(\text{J/(mol K)}) = 32.8494 - 1.837638 \times 10^{-2} T + 2.226372 \times 10^{-5} T^2 - 5.10712 \times 10^{-9} T^3 - 183,852/T^2$
$H^\circ(T) - H^\circ(298)(\text{J/mol}) = 32.8494T - 9.18819 \times 10^{-3} T^2 + 7.42124 \times 10^{-6} T^3 - 1.27678 \times 10^{-9} T^4 + 183,852/T - 9780.52$
$S^\circ(T)(\text{J/(mol K)}) = 32.8494 \ln(T) - 1.837638 \times 10^{-2} T + 1.113186 \times 10^{-5} T^2 \left(\frac{\pi}{2} - \theta\right) - 1.70237333 \times 10^{-9} T^3 + 91,926/T^2 - 107.9046$
Liquid phase: 1747.15–3000 K
$C^\circ_p(T)(\text{J/(mol K)}) = 45.1139$
$H^\circ(T) - H^\circ(298)(\text{J/mol}) = 45.1139T - 15,600.52$
$S^\circ(T)(\text{J/(mol K)}) = 45.1139 \ln(T) - 197.5611$

TABLE 149 Free Energy Equations Above 298.15 K

Solid phase: 298.15–1747.15 K
$G^\circ(T) - H^\circ(298)(\text{J/mol}) = 140.7541\,T + 9.18819 \times 10^{-3}\,T^2 - 3.71062 \times 10^{-6}\,T^3 + 4.25593333 \times 10^{-10}\,T^4 + 91{,}926/T - 32.8494\,T\ln(T) - 9780.52$
Liquid phase: 1747.15–3000 K
$G^\circ(T) - H^\circ(298)(\text{J/mol}) = 242.6750\,T - 45.1139\,T\ln(T) - 15{,}600.52$

TABLE 150 Transition Values Involved with the Free Energy Equations

Transition	T (K)	ΔH° (J/mol)	ΔS° (J/(mol K))
Fusion	1747.15	15,867.730	9.0821

15.10. Nuclear Heat Capacity

The nuclear heat capacity $C^\circ{}_N$ can be correlated by an equation using inverse powers of temperature:

$$C^\circ{}_N(T) = X\left(A/T^2 + B/T^3 + C/T^4 + \mathrm{L}\right)$$

where X is the isotopic fraction for the isotope, and if a' is the magnetic interaction parameter, P is the quadrupole coupling constant, R is the gas constant, and I is the nuclear spin, then since ^{165}Ho has $I = 7/2$:

$$A/R = 21/4a'^2 + 21P^2;\quad B/R = -63a'^2P;\quad C/R = -273/16a'^4$$

The values of a' and P given in Table 151 were either given or derived using HC, neutron transmission (NT), and NMR methods.

TABLE 151 Summary of Determinations of a' and P

Authors	Methods	a' (K)	P (K)
Dreyfus et al. (1961b)	HC	0.302	–
Lounasmaa (1962b)	HC	0.32	0.007
van Kempen et al. (1964)	HC	0.32	0.008
Krusius et al. (1969)	HC	0.319	0.004

TABLE 151 Summary of Determinations of a' and P—Cont'd

Authors	Methods	a' (K)	P (K)
Postma et al. (1962)	NT	0.325	–
Sailor et al. (1962)	NT	0.29	–
Brunhart et al. (1965)	NT	0.305	0.002
Mackenzie et al. (1974)	NMR	0.3095	0.0025
McCausland (1976)	NMR	0.3095	0.0025
Selected		0.3095	0.0025

a' and P are selected so as to conform with the values selected by Hill et al. (1976). Since $X=1$ then $C°_N(T)(\text{mJ/(mol K)}) = 4182/T^2 - 25.4/T^3 - 1302/T^4$.

TABLE 152 Temperatures Corresponding to Magnetic and Critical Turn Angle Transitions

T (K)	17.8 (T_C)	19.8	24.5	40.5	97.4
M:N	1:6	2:11	5:27[a]	1:5	2:9[b]
$\omega_c°$	30	32.5	33.5	36	40

[a] *Blinov et al. (1991) do not give 5:27 but instead give 3:16 at 24 K and 4:21 at 25 K.*
[b] *Blinov et al. (1991) give 1:4 for this temperature and suggest that 2:9 occurs at 70 K.*

15.11. Commensurate Turn Angles

Between the Curie temperature at 17.8 K and the Néel temperature at 132.26 K, the structure is in an incommensurate helical antiferromagnetic state in which various turn angles are commensurate with the basal plane of the hexagonal crystal structure. The commensurate structure is given by $\tau_m = M/N$, where the basal plane moment rotates by $M\pi$ for every N atomic planes, or for every plane, the turn angle is given as $\omega_c = (M\pi/N)\,\text{rad} = (180M/N)°$. The temperatures given in Table 152 were determined by Bates et al. (1988), and values of τ_m are due to Willis and Ali (1992).

Above 50 K, Blinov et al. (1991) have also found other possible commensurate transitions:

4:19 at 54K; 3:14 at 60K; 2:9 at 70K; 3:13 at 79K; 4:17 at 83K;
5:19 at 108K; 4:15 at 113K; 3:11 at 117K; 5:18 at 129K

15.12. Thermodynamic Tables

TABLE 153 Low-Temperature Thermodynamic Data

T (K)	$C^\circ_p(T)$ (J/(mol K))	$H^\circ(T) - H^\circ(0)$ (J/mol)	$S^\circ(T)$ (J/(mol K))	$-[G^\circ(T) - H^\circ(0)]/T$ (J/(mol K))
5	0.358	0.232	0.0653	0.0188
10	2.739	6.66	0.855	0.190
15	6.603	29.49	2.654	0.688
17.8	8.827	51.15	3.973	1.099
17.8	8.827	53.85	4.124	1.099
20	10.179	74.79	5.232	1.492
25	12.678	132.0	7.775	2.495
30	15.370	202.1	10.322	3.587
40	20.425	381.7	15.456	5.913
50	24.525	607.1	20.468	8.326
60	27.976	870.3	25.257	10.752
70	31.086	1165	29.798	13.151
80	34.058	1491	34.137	15.505
90	36.980	1846	38.321	17.809
100	39.181	2227	42.337	20.063
110	40.595	2627	46.143	22.263
120	41.926	3039	49.732	24.404
125	42.897	3251	51.462	25.451
128	43.871	3381	52.489	26.073
129	44.381	3425	52.833	26.279
130	45.117	3470	53.178	26.485
131	46.404	3516	53.528	26.690
131.5	47.650	3539	53.702	26.792
132.0	50.846	3563	53.887	26.895
132.1	52.560	3568	53.926	26.915
132.2	56.541	3574	53.967	26.935
132.25	64.432	3576	53.988	26.946
132.26	70.821	3577	53.993	26.948

TABLE 153 Low-Temperature Thermodynamic Data—Cont'd

T (K)	$C°_p(T)$ (J/(mol K))	$H°(T) - H°(0)$ (J/mol)	$S°(T)$ (J/(mol K))	$-[G°(T) - H°(0)]/T$ (J/(mol K))
132.265	80.660	3577	53.996	26.949
132.27	90.480	3578	54.000	26.950
132.28	58.862	3579	54.005	26.952
132.29	51.295	3579	54.009	26.954
132.30	47.236	3580	54.013	26.956
132.32	42.595	3581	54.020	26.960
132.35	38.812	3582	54.029	26.966
132.4	35.784	3584	54.043	26.976
132.5	34.252	3587	54.069	26.997
133	30.040	3603	54.190	27.099
134	28.382	3632	54.404	27.302
135	27.956	3660	54.613	27.503
140	27.032	3797	55.610	28.489
150	26.497	4064	57.451	30.360
160	26.456	4328	59.159	32.107
170	26.411	4593	60.762	33.746
180	26.417	4857	62.270	35.289
190	26.450	5121	63.700	36.747
200	26.498	5386	65.058	38.729
210	26.558	5651	66.352	39.442
220	26.627	5917	67.589	40.694
230	26.700	6184	68.774	41.889
240	26.770	6451	69.912	43.033
250	26.831	6719	71.006	44.130
260	26.889	6988	72.059	45.184
270	26.952	7257	73.075	46.199
280	27.018	7527	74.057	47.176
290	27.087	7797	75.006	48.120
298.15	27.146	8018	75.758	48.865

TABLE 154 High-Temperature Thermodynamic Data

T (K)	$C°_p(T)$ (J/(mol K))	$H°(T) - H°(298)$ (J/mol)	$S°(T)$ (J/(mol K))	$-[G°(T) - H°(298)]/T$ (J/(mol K))
Solid phase				
298.15	27.146	0	75.758	75.758
300	27.160	50	75.926	75.758
400	27.585	2791	83.807	76.830
500	27.853	5563	89.991	78.866
600	28.225	8365	95.100	81.158
700	28.768	11,213	99.489	83.470
800	29.495	14,125	103.376	85.720
900	30.394	17,118	106.900	87.880
1000	31.446	20,209	110.156	89.947
1100	32.625	23,412	113.207	91.924
1200	33.905	26,737	116.100	93.819
1300	35.257	30,195	118.867	95.640
1400	36.652	33,790	121.531	97.395
1500	38.060	37,526	124.108	99.091
1600	39.452	41,402	126.609	100.733
1700	40.797	45,415	129.041	102.327
1747.15	41.406	47,353	130.165	103.063
Liquid phase				
1747.15	45.114	63,220	139.476	103.063
1800	45.114	65,605	140.592	104.145
1900	45.114	70,116	143.031	106.128
2000	45.114	74,627	145.345	108.032
2100	45.114	79,139	147.546	109.861
2200	45.114	83,650	149.645	111.622
2300	45.114	88,161	151.650	113.319
2400	45.114	92,673	153.570	114.957
2500	45.114	97,184	155.412	116.538

TABLE 154 High-Temperature Thermodynamic Data—Cont'd

T (K)	$C°_p(T)$ (J/(mol K))	$H°(T) - H°(298)$ (J/mol)	$S°(T)$ (J/(mol K))	$-[G°(T) - H°(298)]/T$ (J/(mol K))
2600	45.114	101,696	157.181	118.068
2700	45.114	106,207	158.884	119.548
2800	45.114	110,718	160.525	120.983
2900	45.114	115,230	162.108	122.373
3000	45.114	119,741	163.637	123.724

TABLE 155 Thermodynamic Properties of the Gas Phase

T (K)	$C°_p(T)$ (J/(mol K))	$H°(T) - H°(298)$ (J/mol)	$S°(T)$ (J/(mol K))	$-[G°(T) - H°(298)]/T$ (J/(mol K))
298.15	20.786	0	195.582	195.582
300	20.786	38	195.711	195.583
400	20.786	2117	201.691	196.398
500	20.786	4196	206.329	197.938
600	20.789	6274	210.119	199.662
700	20.800	8354	213.324	201.390
800	20.828	10,435	216.103	203.060
900	20.888	12,520	218.560	204.648
1000	20.991	14,614	220.765	206.151
1100	21.152	16,721	222.773	207.572
1200	21.382	18,847	224.623	208.917
1300	21.694	21,000	226.346	210.192
1400	22.097	23,188	227.968	211.405
1500	22.600	25,422	229.509	212.561
1600	23.210	27,712	230.986	213.666
1700	23.930	30,068	232.414	214.727
1747.15	24.308	31,205	233.074	215.214
1800	24.761	32,502	233.805	215.749

Continued

TABLE 155 Thermodynamic Properties of the Gas Phase—Cont'd

T (K)	$C°_p(T)$ (J/(mol K))	$H°(T) - H°(298)$ (J/mol)	$S°(T)$ (J/(mol K))	$-[G°(T) - H°(298)]/T$ (J/(mol K))
1900	25.702	35,024	235.169	216.735
2000	26.749	37,646	236.513	217.690
2100	27.894	40,377	237.846	218.619
2200	29.131	43,228	239.172	219.523
2300	30.449	46,206	240.495	220.406
2400	31.837	49,320	241.820	221.270
2500	33.286	52,575	243.149	222.119
2600	34.783	55,978	244.484	222.953
2700	36.316	59,533	245.825	223.776
2800	37.873	63,242	247.174	224.587
2900	39.444	67,108	248.530	225.389
3000	41.015	71,131	248.894	226.183

$H°(298) - H°(0) = 6197.4$ J/mol.

TABLE 156 Vapor Pressure

T (K)	p (bar)	$\Delta G°(T)$ (J/mol)	$\Delta H°(T)$ (J/mol)	p (bar)	T (K)
298.15	4.64×10^{-47}	264,474	300,200	10^{-15}	742
300	9.79×10^{-47}	264,253	300,188	10^{-14}	779
400	1.11×10^{-33}	252,373	299,526	10^{-13}	820
500	7.22×10^{-26}	240,664	298,833	10^{-12}	866
600	1.14×10^{-20}	229,098	298,109	10^{-11}	917
700	5.74×10^{-17}	217,656	297,340	10^{-10}	975
800	3.38×10^{-14}	206,328	296,510	10^{-9}	1041
900	4.75×10^{-12}	195,109	295,602	10^{-8}	1117
1000	2.45×10^{-10}	183,996	294,605	10^{-7}	1205
1100	6.11×10^{-9}	172,987	293,509	10^{-6}	1309
1200	8.81×10^{-8}	162,083	292,309	10^{-5}	1433
1300	8.35×10^{-7}	151,282	291,005	10^{-4}	1583

TABLE 156 Vapor Pressure—Cont'd

T (K)	p (bar)	$\Delta G°(T)$ (J/mol)	$\Delta H°(T)$ (J/mol)	p (bar)	T (K)
1400	5.69×10^{-6}	140,587	289,598	10^{-3}	1773
1500	2.97×10^{-5}	129,995	288,097	10^{-2}	2033
1600	1.25×10^{-4}	119,506	286,510	10^{-1}	2392
1700	4.44×10^{-4}	109,119	284,854	1	2917
1747.15	7.64×10^{-4}	104,256	284,053	NBP	2921
1747.15	7.64×10^{-4}	104,256	268,185		
1800	1.31×10^{-3}	99,313	267,097		
1900	3.35×10^{-3}	90,047	265,108		
2000	7.72×10^{-3}	80,882	263,218		
2100	1.64×10^{-2}	71,810	261,438		
2200	3.22×10^{-2}	62,819	259,778		
2300	5.97×10^{-2}	63,901	258,245		
2400	0.105	45,047	256,847		
2500	0.175	36,249	255,591		
2600	0.280	27,498	254,483		
2700	0.433	18,786	253,526		
2800	0.648	10,107	252,724		
2900	0.941	1454	252,079		
2916.83	1.000	0	251,985		
3000	1.334	−7180	251,590		

NBP, normal boiling point at one atmosphere pressure (1.01325 bar).
$\Delta H(0)$=302,021 J/mol.

16. THERMODYNAMIC FUNCTIONS OF ERBIUM

16.1. Introduction

As selected in the text, in the low-temperature region, there is a second-order upper Néel transition at 87 K with ordering on hexagonal sites and a first-order lower Néel transition at 52 K with ordering on cubic sites. There is also a first-order Curie-type transformation at 18.7 K. In spite of undergoing this series of magnetic transitions, erbium retains a close-packed hexagonal structure up to the melting point selected by Gschneidner (1990) as 1802 K.

16.2. Solid Phase—Low Temperature

The isotope ^{167}Er gives a nuclear contribution to the heat capacity. Earlier low-temperature heat capacity measurements such as those of Dreyfus et al. (1961a) (0.5–3 K), Dreyfus et al. (1961d) (0.3–1.2 K), and Parks (1962) (0.4–4.2 K) all suffered from marked impurity levels so that only the heat capacity measurements of Krusius et al. (1974) (0.03–0.8 K) and the NMR measurements of Sano et al. (1972) could be used to determine the magnetic interaction parameter, a', and the quadrupole coupling constant, P, which following the procedure as given in Section 2.4 were then used to determine the variation of the nuclear heat capacity with temperature as summarized in Part 16.10.

With the nuclear contribution removed heat capacity values were fitted to the equation $C^\circ_p = \gamma T + \beta T^3 + \mu T^3 \exp(-\Delta/T)$, where the first term is the electronic contribution; the second, the lattice contribution; and the third, the magnetic contribution. The lattice contribution gives rise to an equivalent Debye temperature (Θ_D) (Table 157).

The Debye temperature selected by Pecharsky et al. (1993) is notably lower than the experimental values obtained from elastic constant measurements at 192 K determined by Rosen (1968b) and 187.8 K determined by Palmer (1978). The selected values are basically those determined by Pecharsky et al. (1996) but adjusted so that the first term in the nuclear contribution is restored to the value of 19.45 mJ/(mol K) obtained from the NMR measurements of Sano et al. (1972) rather than the value of 18.0 mJ/(mol K) determined by Pecharsky et al. (1996) during the fitting process. The total heat capacity up to 6 K can then be represented by

$$C^\circ_p(\mathrm{mJ/(mol\,K)}) = 19.45/T^2 + 0.585/T^3 - 0.120/T^4 + 8.6T + 0.351T^3 + 8.8T^3\exp(-11.52/T)$$

Above 6 K, heat capacity measurements determined by Hill et al. (1984) were given only in the form of graphs with actual data points being supplied

TABLE 157 Low-Temperature Heat Capacity Coefficients

Authors	Range (K)	γ (mJ/(mol K^2))	β (mJ/mol^4)	μ (mJ/(mol K^4))	Δ	Θ_D (K)
Hill et al. (1984)	0.4–23	10	0.275	9.3	11.2	192
Schmitzer et al. (1987)	1.5–70	10.4	0.264	9.4	11.0	194.5
Pecharsky et al. (1996)	1.5–82	8.7	0.351	8.9	11.6	176.9
Selected		8.6	0.351	8.8	11.52	176.9

by Hill (1991). Similarly, the measurements of Pecharsky et al. (1996) (3.5–82 K) and Gschneidner et al. (1997) (3.4–102 K) were only shown in the form of graphs with actual data points being given by Pecharsky (2006). Measurements were also determined by both Berezovskii et al. (1993) (5.6–306 K) and Skochdopole et al. (1955) (15–325 K) although the latter were probably carried out on metal which was significantly impure compared to that available for the more recent measurements. Although the determinations of both Gschneidner et al. (1997) and Berezovskii et al. (1993) were carried out on metal of high purity, the derived heat capacity values differ notably as indicated in Table 158. Because of an apparent increased sensitivity in detecting the various specific heat anomalies and a correlation with the transition temperatures determined by Pecharsky et al. (1996), then preference was given to the measurements of Gschneidner et al. (1997) up to the upper Néel transition at 87 K and to those of Berezovskii et al. (1993) above this temperature. Above the upper Néel transition, the derived values of enthalpy and entropy differ significantly to those determined by Berezovskii et al. (1993), but this can be traced mainly to the accumulation of the selected transition enthalpies and entropies below this temperature when compared to those actually determined by Berezovskii et al. (1993). The heat capacity values in the ranges of 174–203 and 225–257 K showed anomalous behavior and were not included in the fit but apparently were included by Berezovskii et al. There was also notable scatter in the data above 260 K, and interpretation leads to the derivation of a different heat capacity at 298.15 K at 26.58 J/(mol K) compared to that selected by Berezovskii et al. at 26.61 J/(mol K).

The transformation at the Curie temperature involves the formation of an incommensurate helical antiferromagnetic state up to the lower Néel

TABLE 158 Summary of Enthalpy and Entropy Values Obtained at the Critical Turn Angle Temperatures

Transition	T_C	T_α	T_β	$\tau_m = 1/4$	$\tau_m = 6/23$	$\tau_m = 5/19$
T (K)	18.7	21.6	23.3	25.5	26.5	29
ΔH (J/mol)	35	0.5	0.5	?	3.1	1.6
ΔS (J/(mol K))	1.874	0.023	0.021	?	0.116	0.056

Transition	$\tau_m = 4/15$	$\tau_m = 3/11$	$\tau_m = 2/7$	$T_{N\perp}$	$T_{N\parallel}$
T (K)	35	42	50	52	87
ΔH (J/mol)	?	2.2	4.2	8.8	–[a]
ΔS (J/(mol K))	?	0.052	0.085	0.17	–[a]

[a] *Using sensitive dilatometry, Gonossar et al. (1984) confirmed that* $T_{N\parallel}$ *is second order.*

temperature. However, at certain temperatures, the turn angle is commensurate with the basal plane and consensus values from various determinations of these temperatures are summarized in Part 16.11 and in Table 158 including selected values for the Curie temperature (T_C), the lower Néel temperature ($T_{N\perp}$) involving ordering on cubic sites, and the upper Néel temperature ($T_{N\parallel}$) involving ordering on hexagonal sites. Many of the transitions are first order, and corresponding enthalpy and entropy values as selected in Part 16 are listed in Table 158 where a question mark indicates that it is uncertain if the transition is first order or second order. For the definition of τ_m, see Part 16.11.

Because of the presence of these anomalies, it is difficult to compare the selected heat capacity curves with the experimental values, but in the case of Skochdopole et al. (1955), the data above 60 K can be considered as showing a trend from 4% low increasing to 6% high in the room temperature region The measurements of Hill et al. (1984) below the Curie temperature tend from 5% high at 6 K to 1% low at 13 K and 5% high at 16 K before increasing rapidly to 50% high close to the transition temperature. Above 20 K, the measurements bias 0.7% low. The measurements of Pecharsky et al. (1996) tend from 1% high to 2% low below the Curie temperature and tend from 2% to 7% low between 20 and 50 K. However, above the lower Néel temperature, the values average 13% low. The measurements of Berezovskii et al. (1993) below the Curie temperature tend from an initial average of 18% high tending to 0.6% low at 10.5 K before then increasing rapidly to 85% high close to the transition temperature. From 20 to 50 K, the values vary from 10% high tending to 2% low, while between the lower and upper Néel transitions, the trend is from 6% high to 2% low. Above the upper Néel temperature, the measurements of Gschneidner et al. (1997) in the range of 89–101 K bias 2.5% higher than the selected values.

16.3. Solid Phase—High Temperature

Enthalpy measurements have been measured by both Dennison et al. (1966a) (373–1762 K in the solid phase) and Stankus et al. (1995/1996) (400–1802 in the solid phase). The measurements of Stankus et al. were selected because of the much high purity samples available. The results were shown only in the form of an equation which had to be increased to higher order in order to accommodate both the values of the specific heat at 298.15 K and the slope of the specific heat curve.

$$H^\circ(T) - H^\circ(298)(\mathrm{J/mol}) = 25.2737T + 2.64698 \times 10^{-3}T^2 - 3.55548 \times 10^{-7}T^3 + 4.80249 \times 10^{-10}T^4 + 20141.0/T - 7832.58$$

The measurements of Dennison et al. (1966a) were given only in the form of equations and tabulated values with actual data points being given by Gschneidner (1991). After correction for temperature scale and from a 273.15 to a 298.15 K base by subtracting 662.45 J/mol as derived in the

low-temperature fit, the resultant values are on average 3% higher than the selected values up to 1700 K and then increase rapidly to be 20% higher at the temperature extreme.

Heat capacity measurements of Pozdeyev et al. (1990) (400–1500 K) tend from 1% higher to 13% lower.

16.4. Liquid Phase

Enthalpy measurements of Stankus et al. (1995/1996) (1802–2100 K) were given only in the form of equations with and without correction for tantalum saturation. An independent evaluation of the effects of tantalum saturation was determined based on the uncorrected equation following the method of Dennison et al. (1966b) and which leads to

$$H^{\circ}(T) - H^{\circ}(298)(\mathrm{J/mol}) = 46.6660T - 18{,}712.43$$

The derived enthalpy of fusion is $16{,}080 \pm 215$ J/mol, and the entropy of fusion at 8.92 ± 0.12 J/(mol K) appears to be low when compared to the neighboring elements holmium and thulium which have values of 9.08 ± 0.12 and 9.18 ± 0.27 J/(mol K), respectively, from this evaluation. However, a strict periodic trend need not necessarily be followed. The decision by Stankus et al. (1995/1996) to average the enthalpies of fusion obtained from the original and corrected equations appears to have no justification.

Enthalpy measurements by Dennison et al. (1966a) (1774–1917 K) were corrected as above and also for tantalum saturation. The derived values are on average 7% higher than the selected values, while the derived specific heat at 38.6 ± 8.0 J/(mol K) is of relatively low accuracy and abnormally high entropy of fusion of 11.1 J/(mol K) was obtained from these measurements.

16.5. Gas Phase

Values are based on one bar standard pressure and were calculated from 670 energy levels selected by Ralchenko et al. (2012) using the method of Kolsky et al. (1957) and the 2010 Fundamental Constants (Mohr et al., 2011).

16.6. Enthalpy of Sublimation

TABLE 159 Enthalpy of Sublimation at 298.15 K

Authors	Methods	Range (K)	$\Delta_{sub}H^{\circ}$(298, II law) (kJ/mol)	$\Delta_{sub}H^{\circ}$(298, III law) (kJ/mol)	Notes
White et al. (1961)	MS	1349–1743	282 ± 3	–	
Trulson et al. (1961)	MS	1092–1342	314 ± 1	–	

Continued

TABLE 159 Enthalpy of Sublimation at 298.15 K—Cont'd

Authors	Methods	Range (K)	$\Delta_{sub}H^{\circ}$(298, II law) (kJ/mol)	$\Delta_{sub}H^{\circ}$(298, III law) (kJ/mol)	Notes
Mar and Bedford (1980)	MS	1165–1385	302 ± 9	–	
Ignatov and Lebedev (1960,1961)	KE	1373–1573	282 ± 41	333.6 ± 2.1	–[a]
Habermann (1963)	KE	1443–1859	346 ± 1	314.3 ± 0.6	–[b]
Habermann and Daane (1964)	KE	1392–1859	346 ± 1	314.6 ± 4.6	–[c]
Kruglykh et al. (1965)	KE	1188–1453	261 ± 3	300.5 ± 0.8	
McCormack et al. (1971)	KE	1352–1587	319 ± 5	313.7 ± 0.3	
Mar and Bedford (1980)	TE	1435–1575	311 ± 4	309.1 ± 0.1	
Selected				311.0 ± 4.0	

MS, mass spectrometry; KE, Knudsen effusion; TE, torsion effusion.
[a]*Also reported by Savitskii et al. (1960)*
[b]*This is Run 5 of Habermann and Daane (1964) given in detail.*
[c]*Given only in the form of the Clausius–Clapeyron equation.*

Only the Knudsen effusion values of McCormack et al. (1971) and the torsion effusion values of Mar and Bedford (1980) show good agreement between the Second and Third Law values, and the selected value is an average of these but with a slight bias toward the measurement of Mar and Bedford (1980). The suggested accuracy attempts to take into account Second Law deviations.

16.7. Vapor Pressure

The vapor pressure equation for the solid phase was obtained by evaluating the free energy functions of the solid and the gas at 25 K intervals from 750 to 1800 K and the melting point and for the liquid phase at 50 K intervals from 1850 to 3100 K and the melting point (Table 160).

16.8. Comparison of Selected Values at 298.15 K

Holley et al. (1968) and Hultgren et al. (1973) both relied mainly on the heat capacity measurements of Skochdopole et al. (1955), while Konings and Beneš (2010) accepted the values of Berezovskii et al. (1993). The present review is

TABLE 160 Vapor Pressure Equations

$\ln(p, \text{bar}) = b_1 + b_2/T + b_3 \ln(T) + b_4 T + b_5 T^2$

Phase	Range (K)	b_1	b_2	b_3	b_4	b_5
Solid	750–1802.15	17.05902	−37,547.55	−0.3909206	-4.29182×10^{-4}	1.51597×10^{-9}
Liquid	1802.15–2450	46.36946	−39,879.75	−4.315924	2.69589×10^{-4}	4.74242×10^{-8}
	2450–3100	69.69986	−42,440.73	−7.520382	1.61038×10^{-3}	-4.63633×10^{-8}

TABLE 161 Comparison of Heat Capacity, Enthalpy, and Entropy Values at 298.15 K

Authors	$C^\circ_p(298)$ (J/(mol K))	$H^\circ(298) - H^\circ(0)$ (J/mol)	$S^\circ(298)$ (J/(mol K))
Holley et al. (1968)	28.12	7376	73.14
Hultgren et al. (1973)	28.07	7392	73.18
Berezovskii et al. (1993)	26.61	7372	74.52
This work	26.58	7421	75.86

based on a combination of the entropies of transition determined by Pecharsky et al. (1996) and the heat capacity values of Gschneidner et al. (1997) and Berezovskii et al. (1993). The difference between $S^\circ(298)$ obtained in the present evaluation and that obtained by Berezovskii et al. (1993) can be traced almost entirely to the accumulation of the various entropies of transition below 87 K less those actually obtained by Berezovskii et al. (1993) (Table 161).

16.9. Summary of Representative Equations

TABLE 162 Representative Equations Above 298.15 K

Solid phase: 298.15–1802.15 K

$$C^\circ_p(T)(\text{J/(molK)}) = 25.2737 + 5.29396 \times 10^{-3} T - 1.066644 \times 10^{-6} T^2 + 1.920996 \times 10^{-9} T^3 - 20,141.0/T^2$$

$$H^\circ(T) - H^\circ(298)(\text{J/mol}) = 25.2737T + 2.64698 \times 10^{-3} T^2 - 3.55548 \times 10^{-7} T^3 + 4.80249 \times 10^{-10} T^4 + 20141.0/T - 7832.58$$

Continued

TABLE 162 Representative Equations Above 298.15 K—Cont'd

$S^\circ(T)(\mathrm{J/(mol\,K)}) = 25.2737\ln(T) + 5.29396\times10^{-3}T - 5.33322\times10^{-7}T^2 + 6.40332\times10^{-10}T^3 + 10070.5/T^2 - 69.8019$
Liquid phase: 1802.15–3200 K
$C^\circ_p(T)(\mathrm{J/(mol\,K)}) = 46.6660$
$H^\circ(T) - H^\circ(298)(\mathrm{J/mol}) = 46.6660T - 18,712.43$
$S^\circ(T)(\mathrm{J/(mol\,K)}) = 46.6660\ln(T) - 209.6924$

TABLE 163 Free Energy Equations Above 298.15 K

Solid phase: 298.15–1802.15 K
$G^\circ(T) - H^\circ(298)(\mathrm{J/mol}) = 95.0756T - 2.64698\times10^{-3}T^2 + 1.77774\times10^{-7}T^3 - 1.60083\times10^{-10}T^4 + 10,070.5/T - 25.2737T\ln(T) - 7832.58$
Liquid phase: 1802.15–3200 K
$G^\circ(T) - H^\circ(298)(\mathrm{J/mol}) = 256.3584T - 46.6660T\ln(T) - 18,712.43$

TABLE 164 Transition Values Involved with the Free Energy Equations

Transition	T (K)	ΔH° (J/mol)	ΔS° (J/(mol K))
Fusion	1802.15	16,079.793	8.9226

16.10. Nuclear Heat Capacity

The nuclear heat capacity C_N can be correlated by an equation using inverse powers of temperature:

$$C^\circ{}_N(T) = X\left(A/T^2 + B/T^3 + C/T^4 + \mathrm{L}\right)$$

where X is the isotopic fraction for the isotope, and if a' is the magnetic interaction parameter, P is the quadrupole coupling constant, R is the gas constant, and I is the nuclear spin, then as ^{167}Er has $I = 7/2$,

$$A/R = 21/4a'^2 + 21P^2;\quad B/R = -63a'^2P;\quad C/R = -273/16a'^4$$

The values of a' and P given in Table 165 were either given or derived using HC and NMR methods:

TABLE 165 Summary of the Determinations of a' and P

Authors	Methods	a' (K)	P (K)
Krusius et al. (1974)	HC	0.0423	−0.0027
Sano et al. (1972)	NMR	0.04385	0.00256
Selected		0.04385	−0.00256

$$^{167}\mathrm{Er}: C^{\circ}{}_{\mathrm{N}}(T)(\mathrm{mJ}/(\mathrm{mol\,K})) = 85.08/T^2 + 2.578/T^3 - 0.5245/T^4$$

Since $X = 0.22869$ (Berglund and Wieser, 2011), then the contribution to the heat capacity to conform with the values given by Hill et al. (1984):

$$C^{\circ}{}_{N}(T)(\mathrm{mJ}/(\mathrm{mol\,K})) = 19.45/T^2 + 0.585/T^3 - 0.120/T^4$$

16.11. Commensurate Turn Angles and Other Low-Temperature Transitions

Between the Curie temperature at 18.7 K and the lower Néel temperature at 52 K, the structure is in an incommensurate helical antiferromagnetic state in which various turn angles are commensurate with the basal plane of the hexagonal crystal structure. The commensurate structure is given by $\tau_{\mathrm{m}} = M/N$, where the basal plane moment rotates by $M\pi$ for every N atomic planes or for every plane the turn angle is given as $\omega_{\mathrm{c}} = (M\,\pi/N)\,\mathrm{rad} = (180M/N)^{\circ}$. The values of τ_{m} given in Table 166 are due to Watson and Ali (1995).

A significant number of techniques, magnetization, AC susceptibility, electrical resistivity, thermal expansion, calorimetry, and elasticity measurements, have been used to determine the transition temperatures. In particular, Watson and Ali (1995) used the first four techniques and the values quoted in Table 167 are an average of these determinations. Many of the transitions are first order, and entropies of transition as determined by Pecharsky et al. (1996) are selected except for T_{α} and T_{β} which are due to Åström and Benediktsson (1989). A question mark indicates that it is unknown as to whether or not the transition is first order or second order.

TABLE 166 Critical Turn Angles

M:N	5:21 (T_{C})	1:4	6:23	5:19	4:15	3:11	2:7
$\omega_{\mathrm{c}}{}^{\circ}$	43	45	47	47.5	48	49	51.5

TABLE 167 Temperatures and Entropies Corresponding to Magnetic and Critical Turn Angle Transitions

References Temperature	A T (K)	B	C	D	E	Selected	ΔS (J/(mol K))
T_C	19	19.2	18.74	18.7	19.1 ± 0.5	18.7	1.874
T_α	–	21.6	–	–	21.6 ± 0.6	21.6	0.023
T_β	–	23.3	–	–	23.3 ± 0.3	23.3	0.021
$\tau_m = 1/4$	–	25.3?	–	–	25.7 ± 0.8	25.5	?
$\tau_m = 6/23$	–	–	25.8	25.1	26.5 ± 0.8	26.5	0.116
$\tau_m = 5/19$	–	–	–	27.5	28.7 ± 0.7	29	0.056
$\tau_m = 4/15$	–	–	–	–	34.6 ± 1.0	35	?
$\tau_m = 3/11$	–	–	–	42	41.4 ± 1.0	42	0.052
$\tau_m = 2/7$	–	50.8	–	48.9	50.2 ± 1.0	50	0.085
$T_{N\perp}$	55	53.4	52.5	51.4	52.2 ± 0.9	52	0.170
$T_{N\parallel}$	88	85.6	85.7	–	87.1 ± 0.9	87	Second

The columns are for references: (A) Maezawa et al. (1985); (B) Åström and Benediktsson (1989); (C) Berezovskii et al. (1993); (D) Pecharsky et al. (1996); and (E) Watson and Ali (1995). Further temperatures were also determined by Blinov et al. (1991) (Table 167).

16.12. Thermodynamic Tables

TABLE 168 Low-Temperature Thermodynamic Data

T (K)	$C^\circ_p(T)$ (J/(mol K))	$H^\circ(T) - H^\circ(0)$ (J/mol)	$S^\circ(T)$ (J/(mol K))	$-[G^\circ(T) - H^\circ(0)]/T$ (J/(mol K))
5	0.198	0.245	0.0767	0.0278
10	2.443	5.683	0.743	0.175
15	6.611	27.89	2.487	0.628
18.7	12.451	60.87	4.430	1.175
18.7	12.418	95.92	6.303	1.175
20	12.704	112.2	7.146	1.536

TABLE 168 Low-Temperature Thermodynamic Data—Cont'd

T (K)	$C^\circ_p(T)$ (J/(mol K))	$H^\circ(T) - H^\circ(0)$ (J/mol)	$S^\circ(T)$ (J/(mol K))	$-[G^\circ(T) - H^\circ(0)]/T$ (J/(mol K))
21.6	13.526	133.1	8.152	1.989
21.6	13.526	133.6	8.175	1.989
23.3	14.867	157.7	9.247	2.479
23.3	14.867	158.2	9.268	2.479
25	16.472	184.9	10.373	2.978
26.5	17.665	210.5	11.368	3.425
26.5	17.665	213.6	11.484	3.425
29	19.347	259.9	13.154	4.191
29	19.347	261.5	13.210	4.191
30	19.952	281.2	13.876	4.503
35	22.767	388.1	17.165	6.078
40	25.459	508.7	20.384	7.666
42	26.399	560.6	21.649	8.301
42	26.399	562.8	21.701	8.301
45	27.890	644.2	23.573	9.257
50	30.595	790.2	26.647	10.843
50	30.000	794.5	26.732	10.843
52	30.000	854.5	27.909	11.477
52	28.693	863.3	28.079	11.477
55	29.066	949.9	29.698	12.427
60	29.938	1097	32.263	13.974
65	30.977	1250	34.700	15.475
70	32.020	1407	37.034	16.932
75	32.902	1570	39.274	18.348
80	33.838	1736	41.428	19.723
85	35.303	1909	43.518	21.062
86	35.747	1944	43.933	21.325
86.5	35.995	1962	44.141	21.457

Continued

TABLE 168 Low-Temperature Thermodynamic Data—Cont'd

T (K)	$C°_p(T)$ (J/(mol K))	$H°(T) - H°(0)$ (J/mol)	$S°(T)$ (J/(mol K))	$-[G°(T) - H°(0)]/T$ (J/(mol K))
87	36.261	1980	44.349	21.588
87.5	26.746	1995	44.517	21.718
88	25.740	2008	44.665	21.848
88.5	25.365	2029	44.810	21.977
89	25.133	2033	44.952	22.106
90	24.970	2058	45.232	22.361
100	24.762	2306	47.846	24.782
110	24.896	2555	50.212	26.988
120	25.010	2804	52.384	29.015
130	25.127	3055	54.389	30.890
140	25.272	3307	56.257	32.636
150	25.364	3560	58.004	34.270
160	25.465	3814	59.644	35.805
170	25.622	4070	61.192	37.253
180	25.727	4326	62.660	38.624
190	25.826	4584	64.053	39.926
200	25.918	4843	65.380	41.166
210	26.003	5102	66.647	42.350
220	26.082	5363	67.858	43.482
230	26.154	5624	69.019	44.567
240	26.219	5886	70.134	45.609
250	26.278	6148	71.205	46.612
260	26.330	6411	72.237	47.578
270	26.393	6675	73.232	48.510
280	26.460	6939	74.193	49.410
290	26.527	7204	75.123	50.280
298.15	26.582	7421	75.858	50.970

TABLE 169 High-Temperature Thermodynamic Data

T (K)	$C°_p(T)$ (J/(mol K))	$H°(T) - H°(298)$ (J/mol)	$S°(T)$ (J/(mol K))	$-[G°(T) - H°(298)]/T$ (J/(mol K))
Solid phase				
298.15	26.582	0	75.859	75.859
300	26.594	49	76.023	75.859
400	27.218	2740	83.761	76.910
500	27.814	5492	89.898	78.914
600	28.425	8307	95.023	81.184
700	29.075	11,178	99.453	83.484
800	29.778	14,120	103.380	85.730
900	30.550	17,136	106.932	87.892
1000	31.402	20,333	110.194	89.961
1100	32.347	23,420	113.230	91.940
1200	33.396	26,706	116.089	93.834
1300	34.562	30,103	118.807	95.651
1400	35.856	33,622	121.415	97.399
1500	37.289	37,278	123.937	99.085
1600	38.874	41,085	126.393	100.715
1700	40.622	45,059	128.801	102.964
1800	42.554	49,215	131.177	103.835
1802.15	42.587	49,307	131.228	103.868
Liquid phase				
1802.15	46.666	65,387	140.15	103.868
1900	46.666	69,953	142.618	105.800
2000	46.666	74,620	145.011	107.702
2100	46.666	79,286	147.288	109.533
2200	46.666	83,953	149.459	111.299
2300	46.666	88,619	151.533	113.003
2400	46.666	93,286	153.52	114.650
2500	46.666	97,953	155.425	116.244

Continued

TABLE 169 High-Temperature Thermodynamic Data—Cont'd

T (K)	$C°_p(T)$ (J/(mol K))	$H°(T) - H°(298)$ (J/mol)	$S°(T)$ (J/(mol K))	$-[G°(T) - H°(298)]/T$ (J/(mol K))
2600	46.666	102,619	157.255	117.786
2700	46.666	107,286	159.016	119.281
2800	46.666	111,952	160.713	120.730
2900	46.666	116,619	162.351	122.137
3000	46.666	121,286	163.933	123.504
3100	46.666	126,952	165.463	124.833

TABLE 170 Thermodynamic Properties of the Gas Phase

T (K)	$C°_p(T)$ (J/(mol K))	$H°(T) - H°$ (298) (J/mol)	$S°(T)$ (J/(mol K))	$-[G°(T) - H°(298)]/T$ (J/(mol K))
298.15	20.786	0	194.031	194.031
300	20.786	38	194.159	194.031
400	20.786	2117	200.139	194.847
500	20.787	4196	204.778	196.386
600	20.791	6275	208.568	198.110
700	20.808	8354	211.774	199.839
800	20.851	10,437	214.555	201.508
900	20.940	12,526	217.015	203.097
1000	21.095	14,627	219.229	204.602
1100	21.337	16,748	221.250	206.024
1200	21.686	18,898	223.121	207.372
1300	22.158	21,089	224.874	208.652
1400	22.765	23,334	226.538	209.870
1500	23.513	25,647	228.133	211.035
1600	24.403	28,042	229.678	212.152
1700	25.430	30,532	231.188	213.228

TABLE 170 Thermodynamic Properties of the Gas Phase—Cont'd

T (K)	$C^\circ_p(T)$ (J/(mol K))	$H^\circ(T) - H^\circ$ (298) (J/mol)	$S^\circ(T)$ (J/(mol K))	$-[G^\circ(T) - H^\circ(298)]/T$ (J/(mol K))
1800	26.583	33,132	232.673	214.267
1802.15	26.609	33,189	232.705	214.289
1900	27.846	35,852	234.144	215.274
2000	29.201	38,704	235.606	216.254
2100	30.627	41,695	237.065	217.211
2200	32.104	44,831	238.524	218.146
2300	33.611	48,117	239.984	219.064
2400	35.128	51,554	241.447	219.966
2500	36.638	55,142	242.911	220.855
2600	38.125	58,881	244.377	221.731
2700	39.578	62,766	245.844	222.597
2800	40.988	66,795	247.309	223.453
2900	42.348	70,962	248.771	224.301
3000	43.653	75,263	250.229	225.141
3100	44.901	79,691	251.681	225.974

$H^\circ(298) - H^\circ(0) = 6197.4$ J/mol.

TABLE 171 Vapor Pressure

T (K)	p (bar)	$\Delta G^\circ(T)$ (J/mol)	$\Delta H^\circ(T)$ (J/mol)	p (bar)	T (K)
298.15	4.87×10^{-49}	275,767	311,000	10^{-15}	771
300	1.06×10^{-48}	275,548	310,989	10^{-14}	810
400	3.54×10^{-35}	263,825	310,377	10^{-13}	854
500	4.43×10^{-27}	252,264	309,704	10^{-12}	902
600	1.08×10^{-23}	240,844	308,968	10^{-11}	956
700	7.43×10^{-18}	229,552	308,176	10^{-10}	1016

Continued

TABLE 171 Vapor Pressure—Cont'd

T (K)	p (bar)	$\Delta G^\circ(T)$ (J/mol)	$\Delta H^\circ(T)$ (J/mol)	p (bar)	T (K)
800	5.52×10^{-15}	218,377	307,317	10^{-9}	1086
900	9.29×10^{-13}	207,315	306,390	10^{-8}	1165
1000	5.54×10^{-11}	196,359	305,394	10^{-7}	1258
1100	1.55×10^{-9}	185,507	304,329	10^{-6}	1367
1200	2.47×10^{-8}	174,754	303,192	10^{-5}	1497
1300	2.55×10^{-7}	164,100	301,987	10^{-4}	1657
1400	1.87×10^{-6}	153,540	300,712	10^{-3}	1859
1500	1.04×10^{-5}	143,074	299,369	10^{-2}	2135
1600	4.65×10^{-5}	132,700	297,956	10^{-1}	2515
1700	1.73×10^{-4}	122,417	296,474	1	3071
1800	5.54×10^{-4}	112,223	294,917	NBP	3074
1802.15	5.67×10^{-4}	112,005	294,882		
1802.15	5.67×10^{-4}	112,005	278,802		
1900	1.47×10^{-3}	103,000	276,300		
2000	3.53×10^{-3}	93,894	275,084		
2100	7.74×10^{-3}	84,877	273,409		
2200	1.57×10^{-2}	75,936	271,879		
2300	3.00×10^{-2}	67,061	270,498		
2400	5.40×10^{-2}	58,242	269,268		
2500	9.25×10^{-2}	49,472	268,190		
2600	0.152	40,742	267,262		
2700	0.240	32,046	266,480		
2800	0.366	23,375	265,843		
2900	0.543	14,725	265,343		
3000	0.783	6089	264,977		
3070.59	1.000	0	264,796		
3100	1.103	−2536	264,739		

NBP, normal boiling point at one atmosphere pressure (1.01325 bar).
$\Delta H(0) = 312,224$ J/mol.

17. THERMODYNAMIC FUNCTIONS OF THULIUM

17.1. Introduction

Using calorimetry, Berezovskii et al. (1991) determined the second-order Néel transition to be at 56.6 K and the first-order Curie-type transition to be at 32.6 K. These values were satisfactorily confirmed by Åström et al. (1991) using a combination of magnetization, AC susceptibility, and calorimetry. In spite of these transitions, thulium exists in a close-packed hexagonal structure up to the melting point selected by Gschneidner (1990) as 1818 K.

17.2. Solid Phase—Low Temperature

Low-temperature heat capacity measurements determined by Dreyfus et al. (1961a) (0.5–4 K) and Lounasmaa (1964d) (0.4–4 K) were initially represented by equations in terms of nuclear, electronic, and combined lattice and magnetic terms. However, Lounasmaa (1964d) estimated the limiting Debye temperature θ_D to be 200 K, which was later confirmed by Rosen (1971) from elastic constant measurements, and this allowed the separation of the lattice and magnetic terms as well as a revision of the electronic term. However, the revised equation contained three nuclear terms as $1/T^2$, $1/T^3$, and $1/T^4$ which is incorrect since ^{169}Tb has a nuclear spin 1/2 and can therefore only be represented by even inverse values of temperature (see Part 17.10). Lounasmaa (1964d) tried to explain this anomaly as possibly being due to a strong additional magnetic term contributing to heat capacity in the low-temperature region, but it is much more likely to be due to the exceptionally impure samples used which were later shown to contain 2.0 wt% tantalum, 0.25 wt% other metallic elements, and 0.34 wt% (3.9 atm%) nonmetallic elements. Further, extrapolation of the selected values, those of Berezovskii et al. (1991) because they were extremely pure and contained only 0.1 atm% of impurities, below the experimental limit of 8 K indicates that the measurements of both Dreyfus et al. (1961a) and Lounasmaa (1964d) were much too high and that the results obtained as well as the corrections must be considered to be unreliable.

Heat capacity measurements of Holmström et al. (1969) (0.02–0.4 K), superseding earlier measurements of Anderson et al. (1968), used the same samples as Lounasmaa and, in spite of the impurity problem, by following the procedure outlined in Section 2.4 obtained a value for the magnetic interaction parameter, a', in excellent agreement with values obtained by Kalvius et al. (1963) from Mössbauer effect measurements and by Al-Kital et al. (1967) from neutron resonance measurements. The values are summarized in Part 17.10 and those of Holmström et al. (1969) would lead to the following two-term expression for the nuclear heat capacity:

$$C^{\circ}{}_{N}(T)(\mathrm{mJ/mol\,K}) = 23.89/T^2 - 0.06863/T^4$$

These may be the only realistic measurements of heat capacity in this region, as, for example, the heat capacity measurements of Lounasmaa and Sundström (1966) (3.1–24.5 K) carried out on the same samples as used for the low-temperature measurements of Lounasmaa are also much too high when compared with the measurements of Berezovskii et al. (1991) (8–325 K) in the overlap region of 8–25 K, being 190% high at 8.2 K but then converging toward the selected values and until they are only 2% high at 24.5 K.

Lattice parameter measurements of Bulatov and Dolzhenko (1988) directly establish that the Curie transition at 32.6 K is first order with a jump in the c-lattice parameter value with increasing temperature. Neutron diffraction measurements of Brun et al. (1970) confirms that below this transition, the magnetic structure locks into a 2/7 commensurate structure consisting of a 2π turn angle over a seven-layer repeat distance with the magnetic moments in three layers parallel to the c-axis and four layers antiparallel. The enthalpy of transition was measured by Åström et al. (1991) at only 0.8 ± 0.2 J/mol, whereas in their heat capacity measurements, Berezovskii et al. (1991) obtained a value of 8.2 J/mol and it is this latter value which is accepted to form a self-consistent set of low-temperature measurements. Jennings et al. (1961) (15–360 K) reported anomalies in their heat capacity measurements at 88, 162, and 180 K which could well be impurity effects since although they did not mention possible nonmetallic impurities, typical values at this time would have been between 2 and 5 atm%. However, Berezovskii et al. (1991) also obtained anomalous changes in heat capacity in spite of the very high purity of the metal used. Although they offered no explanation for these anomalies, which may be evidence of experimental difficulties, they appeared to treat them as being real and above 100 K their "smoothed" values to a large extent followed these anomalies. Therefore in order to obtain a revised smooth curve, selected experimental values from 110 to 321 K were fitted to the following equation which has an overall accuracy of ± 0.05 J/(mol K):

$$C^{\circ}{}_{\mathrm{p}}(\mathrm{J}/(\mathrm{mol\,K})) = 23.3298 + 2.42883 \times 10^{-2} T - 5.07687 \times 10^{-5} T^2 + 4.90293 \times 10^{-8} T^3$$

Even with the corrections, this equation gives values at 298.15 K which agree closely with those calculated by Berezovskii et al. (1991).

In comparison with the selected values, the earlier heat capacity measurements of Jennings et al. (1961) are 9% high at 15 K falling to 3% high at 20 K and 0.7% high at 25 K after which there is a gradual decrease to 1% low in the room temperature region. In the region from 50 to 60 K, a comparison was not considered since different values obtained for the second-order Néel temperature lead to unrealistic percentage differences between the two sets of measurements.

17.3. Solid—High Temperature

Enthalpy measurements of Dennison et al. (1966a) (373–1801 K in the solid region) were only given in the form of an equation and smooth values with actual data points being given by Gschneidner (1991). After correction to the ITS-90 temperature scale and from a 273.15 to a 298.15 K base by subtracting 681.7 J/mol from the selected low-temperature data, then a Shomate-type plot indicates that the three lowest data points at 373–573 K are incompatible with the selected value of the heat capacity at 298.15 K and were therefore rejected as were two further data points at 1642 and 1711 K which were also discrepant. The remaining data points were fitted to the following equation which has an overall accuracy as a standard deviation of ±428 J/mol (1.03%):

$$H^\circ(T) - H^\circ(298)(\mathrm{J/mol}) = 27.4061T - 7.60560 \times 10^{-4}T^2 + 1.52770 \times 10^{-6}T^3 - 8144.01$$

Heat capacity measurements of Pozdeyev et al. (1990) (400–1600 K) scatter but are up to 7% lower than the selected values.

17.4. Liquid Phase

Enthalpy measurements of Dennison et al. (1966a) (1818–1865 K) were corrected as above, and because liquid thulium is soluble in the tantalum container used, they were also corrected for the saturation with tantalum following the method of Dennison et al. (1966b). The two lowest data points were rejected, and the three remaining data points were fitted to the following equation with an accuracy as a standard deviation of ±231 J/mol (0.20%):

$$H^\circ(T) - H^\circ(298)(\mathrm{J/mol}) = 41.4756T - 10,374.8$$

Because of the scatter in the three experimental values, the derived heat capacity is poorly determined as 41.5 ± 11.1 J/(mol K), the derived enthalpy of fusion is 16,682 ± 486 J/mol, and the entropy of fusion is 9.18 ± 0.27 J/(mol K).

17.5. Gas Phase

Values are based on one bar standard state pressure and are calculated from 588 energy levels selected by Ralchenko et al. (2012) and a single energy level at 27,509.40 cm^{-1} discovered by Kröger et al. (1997a) using the method of Kolsky et al. (1957) and the 2010 Fundamental Constants (Mohr et al., 2011).

17.6. Enthalpy of Sublimation

TABLE 172 Enthalpy of Sublimation at 298.15 K

Authors	Methods	Range (K)	$\Delta_{sub}H^{\circ}$(298, II law) (kJ/mol)	$\Delta_{sub}H^{\circ}$(298, III law) (kJ/mol)	Notes
Savage et al. (1959)	MS	810–1070	240 ± 2	–	
Fedechkin and Shmykov (1973)	Eff	928–1131	230 ± 1	219.1 ± 1.1	–[a]
Spedding et al. (1957)	KE	809–1219	246 ± 2	232.9 ± 0.3	–[b]
Zaitsev and Mogutnov (1988/1989)	KEMS	821–1080	232 ± 2	232.9 ± 0.1	–[a,c]
		851–1085	233 ± 2	232.9 ± 0.1	–[a,c]
		830–1080	232 ± 2	233.0 ± 0.1	–[c]
Selected				233.0 ± 4.0	

MS, mass spectrometry; Eff, effusion; KE, Knudsen effusion; KEMS, Knudsen effusion mass spectrometry.
[a] *Given only in the form of the Clausius–Clapeyron equation.*
[b] *Combination of three series.*
[c] *Since the first two series were only given in the form of the Clausius–Clapeyron equation and the third series were given in complete detail then all were evaluated separately.*

The selected value is based on the last four sets of measurements with the accuracy assigned to the selected value being that suggested by Zaitsev and Mogutnov (1988/1989).

17.7. Vapor Pressure

The vapor pressure equation for the solid phase was obtained by evaluating the free energy functions for the solid and the gas at 50 K intervals from 600 to 1800 K and the melting point, and for the liquid phase, at 20 K intervals from 1820 to 2300 K and the melting point (Table 173).

17.8. Comparison of Selected Values at 298.15 K

Both Holley et al. (1968) and Hultgren et al. (1973) relied mainly on the heat capacity measurements of Jennings et al. (1961). Konings and Beneš (2010) accepted the evaluation of Berezovskii et al. (1991), while the present values are an interpretation of these measurements (Table 174).

TABLE 173 Vapor Pressure Equations

$\ln(p,\text{bar}) = b_1 + b_2/T + b_3 \ln(T) + b_4 T + b_5 T^2$

Phase	Range (K)	b_1	b_2	b_3	b_4	b_5
Solid	600–1818.15	19.14477	−28,247.65	−0.7624104	5.39581×10^{-5}	-8.50421×10^{-8}
Liquid	1818.15–2300	26.77979	−28,089.00	−1.725776	-4.58107×10^{-4}	4.78672×10^{-8}

TABLE 174 Comparison of Heat Capacity, Enthalpy, and Entropy Values at 298.15 K

Authors	$C^\circ_p(298)$ (J/(mol K))	$H^\circ(298) - H^\circ(0)$ (J/mol)	$S^\circ(298)$ (J/(mol K))
Holley et al. (1968)	27.03	7397	74.48
Hultgren et al. (1973)	27.03	7397	74.01
Berezovskii et al. (1991)	27.36	7441	73.26
This work	27.36	7440	73.26

17.9. Summary of Representative Equations

TABLE 175 Representative Equations Above 298.15 K

Solid phase: 298.15–1818.15 K
$C^\circ_p(T)(\text{J/(mol K)}) = 27.4061 - 1.52112 \times 10^{-3} T + 4.58310 \times 10^{-6} T^2$
$H^\circ(T) - H^\circ(298)(\text{J/mol}) = 27.4061\,T - 7.60560 \times 10^{-4} T^2 + 1.52770 \times 10^{-6} T^3 - 8144.01$
$S^\circ(S)(\text{J/(mol K)}) = 27.4061 \ln(T) - 1.52112 \times 10^{-3} T + 2.29155 \times 10^{-6} T^2 - 82.6391$
Liquid phase: 1818.15–2300 K
$C^\circ_p(T)(\text{J/(mol K)}) = 41.4756$
$H^\circ(T) - H^\circ(298)(\text{J/mol}) = 41.4756\,T - 10,374.8$
$S^\circ(T)(\text{J/(mol K)}) = 41.4756 \ln(T) - 174.2540$

TABLE 176 Free Energy Equations Above 298.15 K

Solid phase: 298.15–1818.15 K
$G^\circ(T) - H^\circ(298)(\text{J/mol}) = 110.0452T + 7.60560 \times 10^{-4}T^2 - 7.63850 \times 10^{-7}T^3 - 27.4061T\ln(T) - 8144.01$
Liquid phase: 1818.15–2300 K
$G^\circ(T) - H^\circ(298)(\text{J/mol}) = 215.7296T - 41.4756T\ln(T) - 10,374.8$

TABLE 177 Transition Values Involved with the Free Energy Equations

Transition	T (K)	ΔH° (J/mol)	ΔS° (J/(mol K))
Fusion	1818.15	16,682.040	9.1753

17.10. Nuclear Heat Capacity

The nuclear contribution to the heat capacity can be represented by

$$C^\circ{}_N(T) = X\left(A/T^2 + B/T^3 + C/T^4 + \text{L}\right)$$

where X is the atomic fraction of the nuclide, and with a' as the magnetic interaction parameter, P as the quadrupole coupling constant, I as the nuclear spin, and R as the gas constant, then since ^{169}Tm has $I = 1/2$, $P = 0$, and $X = 1$:

$$A/R = a'^2/4; \quad B/R = 0; \quad C/R = -a'^4/16$$

The magnetic interaction parameter, a, as determined by Holmström et al. (1969) to be -0.1072 ± 0.0008 K is in excellent agreement with values of 0.106 ± 0.003 K obtained by Kalvius et al. (1963) from Mössbauer effect measurements and 0.103 ± 0.015 K obtained by Al-Kital et al. (1967) from neutron resonance measurements. Since $X = 1$, the value of a' determined by Holmström et al. (1969) leads to

$$C^\circ{}_N(T)(\text{mJ/(mol K)}) = 23.89/T^2 - 0.06863/T^4$$

17.11. Thermodynamic Tables

TABLE 178 Low-Temperature Thermodynamic Data

T (K)	$C^\circ_p(T)$ (J/(mol K))	$H^\circ(T) - H^\circ(0)$ (J/mol)	$S^\circ(T)$ (J/(mol K))	$-[G^\circ(T) - H^\circ(0)]/T$ (J/(mol K))
8	0.399	0.792	0.132	0.0331
10	0.850	1.988	0.264	0.065
15	4.003	12.71	1.091	0.244
20	9.678	46.27	2.983	0.669
25	16.13	110.8	5.837	1.404
30	22.03	206.4	9.306	2.426
32.6	24.70	267.1	11.25	3.054
32.6	24.70	275.3	11.50	3.054
35	27.10	337.5	13.34	3.697
40	31.58	484.4	17.26	5.148
45	35.40	652.1	21.20	6.713
50	38.62	837.4	25.10	8.356
55	41.43	1038	28.92	10.04
56.6	42.60	1122	30.42	10.74
58	26.00	1156	31.02	11.09
59	24.75	1181	31.45	11.43
60	24.50	1206	31.87	11.77
70	24.52	1446	35.65	14.99
80	24.86	1693	38.95	17.79
90	25.12	1943	41.89	20.30
100	25.30	2195	44.55	22.60
110	25.45	2449	46.97	24.71
120	25.60	2704	49.19	26.66
130	25.74	2961	51.24	28.47

Continued

TABLE 178 Low-Temperature Thermodynamic Data—Cont'd

T (K)	$C°_p(T)$ (J/(mol K))	$H°(T) - H°(0)$ (J/mol)	$S°(T)$ (J/(mol K))	$-[G°(T) - H°(0)]/T$ (J/(mol K))
140	25.87	3219	53.16	30.17
150	26.00	3478	54.95	31.76
160	26.12	3739	56.63	33.26
170	26.23	4000	58.21	34.68
180	26.34	4263	59.72	36.03
190	26.45	4527	61.14	37.32
200	26.55	4792	62.50	38.54
210	26.65	5058	63.80	39.71
220	26.74	5325	65.04	40.84
230	26.83	5593	66.23	41.92
240	26.91	5862	67.38	42.95
250	26.99	6131	68.48	43.95
260	27.07	6402	69.54	44.92
270	27.15	6673	70.56	45.85
280	27.23	6945	71.55	46.75
290	27.30	7217	72.50	47.62
298.15	27.36	7440	73.26	48.31

TABLE 179 High-Temperature Thermodynamic Data

T (K)	$C°_p(T)$ (J/(mol K))	$H°(T) - H°$ (298) (J/mol)	$S°(T)$ (J/(mol K))	$-[G°(T) - H°(298)]/T$ (J/(mol K))
Solid phase				
298.15	27.360	0	73.260	73.260
300	27.362	51	73.429	73.261
400	27.531	2795	81.322	74.335
500	27.791	5560	87.491	76.372
600	28.143	8356	92.588	78.662

TABLE 179 High-Temperature Thermodynamic Data—Cont'd

T (K)	$C°_p(T)$ (J/(mol K))	$H°(T) - H°$ (298) (J/mol)	$S°(T)$ (J/(mol K))	$-[G°(T) - H°(298)]/T$ (J/(mol K))
700	28.587	11,192	96.959	80.971
800	29.122	14,076	100.810	83.214
900	29.749	17,019	104.275	85.365
1000	30.468	20,029	107.446	87.417
1100	31.278	23,116	110.387	89.373
1200	32.180	26,288	113.147	91.240
1300	33.174	29,555	115.761	93.027
1400	34.259	32,926	118.259	94.740
1500	35.436	36,410	120.662	96.389
1600	36.705	40,016	122.989	97.979
1700	38.065	43,754	125.255	99.517
1800	39.517	47,632	127.471	101.009
1818.15	39.791	48,352	127.869	101.275
Liquid phase				
1818.15	41.476	65,034	137.044	101.275
1900	41.476	68,429	138.871	102.855
2000	41.476	72,576	140.998	104.710
2100	41.476	76,724	143.022	106.486
2200	41.476	80,872	144.951	108.191
2300	41.476	85,019	146.795	109.830

TABLE 180 Thermodynamic Properties of the Gas Phase

T (K)	$C°_p(T)$ (J/(mol K))	$H°(T) - H°(298)$ (J/mol)	$S°$(T) (J/(mol K))	$-[G°(T) - H°(298)]/T$ (J/(mol K))
298.15	20.786	0	190.118	190.118
300	20.786	38	190.247	190.119
400	20.786	2117	196.227	190.934

Continued

TABLE 180 Thermodynamic Properties of the Gas Phase—Cont'd

T (K)	$C°_p(T)$ (J/(mol K))	$H°(T) - H°(298)$ (J/mol)	$S°$(T) (J/(mol K))	$-[G°(T) - H°(298)]/T$ (J/(mol K))
500	20.786	4196	200.865	192.474
600	20.786	6274	204.655	194.198
700	20.786	8353	207.859	195.926
800	20.786	10,432	210.635	197.595
900	20.787	12,510	213.083	199.183
1000	20.789	14,589	215.273	200.684
1100	20.795	16,668	217.255	202.102
1200	20.805	18,748	219.065	203.441
1300	20.824	20,830	220.731	204.708
1400	20.852	22,913	222.275	205.908
1500	20.894	25,000	223.715	207.048
1600	20.953	27,093	225.065	208.132
1700	21.033	29,192	226.338	209.166
1800	21.137	31,300	227.543	210.154
1818.15	21.160	31,684	227.755	210.328
1900	21.273	33,420	228.689	211.099
2000	21.444	35,556	229.785	212.006
2100	21.659	37,710	230.836	212.878
2200	21.925	39,889	231.849	213.718
2300	22.251	42,098	232.831	214.527

$H°(298) - H°(0) = 6197.4$ J/mol.

TABLE 181 Vapor Pressure

T (K)	p (bar)	$\Delta G°(T)$ (J/mol)	$\Delta H°(T)$ (J/mol)	p (bar)	T (K)
298.15	1.92×10^{-35}	198,159	233,000	10^{-14}	608
300	3.43×10^{-35}	197,943	232,988	10^{-13}	640
400	4.62×10^{-25}	186,361	232,323	10^{-12}	676

TABLE 181 Vapor Pressure—Cont'd

T (K)	p (bar)	$\Delta G°(T)$ (J/mol)	$\Delta H°(T)$ (J/mol)	p (bar)	T (K)
500	5.29×10^{-19}	174,949	231,636	10^{-11}	716
600	5.63×10^{-15}	163,678	230,918	10^{-10}	761
700	4.15×10^{-12}	152,531	230,161	10^{-9}	813
800	5.77×10^{-10}	141,495	229,355	10^{-8}	872
900	2.64×10^{-8}	130,564	228,491	10^{-7}	941
1000	5.57×10^{-7}	119,733	227,560	10^{-6}	1022
1100	6.67×10^{-6}	108,998	226,552	10^{-5}	1118
1200	5.23×10^{-5}	98,359	225,460	10^{-4}	1235
1300	2.96×10^{-4}	87,814	224,275	10^{-3}	1381
1400	1.30×10^{-3}	77,365	222,987	10^{-2}	1568
1500	4.64×10^{-3}	67,011	221,591	10^{-1}	1817
1600	1.40×10^{-2}	56,755	220,076	1	2210
1700	3.70×10^{-2}	46,597	218,438	NBP	2212
1800	8.70×10^{-2}	36,539	216,668		
1818.15	0.101	34,724	216,332		
1818.15	0.101	34,724	199,266		
1900	0.177	27,336	197,991		
2000	0.331	18,407	195,979		
2100	0.578	9577	193,987		
2200	0.955	842	192,018		
2209.69	1.000	0	191,828		
2300	1.504	−7804	190,078		

NBP, normal boiling point at one atmosphere pressure (1.01325 bar).
$\Delta H°(0) = 234,243$ J/mol.

18. THERMODYNAMIC FUNCTIONS OF YTTERBIUM

18.1. Introduction

For pure ytterbium, Kayser (1970) found a martensitic transition between the low-temperature close-packed hexagonal alpha phase and the high-temperature face-centered cubic beta phase with the transition on cooling starting at 260 K and the reverse on heating at 280 K with the conversion of

the alpha phase being completed at 365 K. The average of heating and cooling, 270 K, is taken as being the "equilibrium" transition temperature. For the transition from the beta phase to the body-centered cubic gamma phase, Gschneidner (1990) selects 1068 K and for the melting point 1092 K.

18.2. Alpha Phase

The values given in Table 182 have been obtained for the electronic coefficient (γ) and the limiting Debye temperature (θ_D).

The measurements of Bucher et al. (1970) were carried out using pure alpha phase and indicate that the metal used by Lounasmaa (1963) must have also been very rich in this phase. Both values of θ_D are in excellent agreement with the value of 117.5 K obtained by Rosen (1971) from elastic constant measurements.

Heat capacity measurements of Lounasmaa (1966) (3–25 K) and Gerstein et al. (1964) (13–341 K) differ in the overlap region with those of the former being from 3% to 1% lower. This may be an impurity effect since the metal used by Lounasmaa (1966) contained 0.17 wt% (7.8 atm%) of nonmetallic impurities, while the metal used by Gerstein et al. (1964) was much purer and contained only 0.04 wt% (1.5 atm%) of hydrogen and oxygen. The measurements of Gerstein et al. (1964) are therefore selected in the overlap region and up to the transition temperature in order to have a consistent set of measurements. However, Gerstein et al. (1964) did accept the lower temperature values of Lounasmaa (1963) and interpolated between 4 and 13 K.

18.3. Beta Phase

In the region of the alpha–beta transition at 270 K, the measurements of Gerstein et al. (1964) show a considerable scatter and no firm evidence of a transition, possibly because the samples consisted of a mixture of both phases and the transition would be smeared out. Based on a measurement of the volume difference between the two phases and the slope of the pressure curve, Bucher et al. (1970) used the Clausius–Clapeyron equation to calculate an enthalpy of transition of 25.8 J/mol which is accepted.

TABLE 182 Low-Temperature Heat Capacity Coefficients

Authors	Temperature range (K)	γ (mJ/(mol K^2))	Θ_D (K)
Lounasmaa (1963)	0.4–4	2.90	118.1
Bucher et al. (1970)	<5.3	3.30	117.6

In the high-temperature region, Spedding et al. (1961) found that for hydrogen-contaminated ytterbium, there was a transition to a close-packed hexagonal structure between 533 and 993 K but that purer samples showed only the face-centered structure up to the beta–gamma transition temperature. Previously, the same intermediate phase had been found for the similar metals calcium and strontium but again was not found in the pure metals (Katerberg et al., 1975; Peterson and Colburn, 1966; Peterson and Fattore, 1961). While this would appear to be definite proof as to the origin of the intermediate phase, these findings appeared to have been ignored later with Hurd and Alderson (1973) reporting anomalies in electrical resistivity measurements at 560 and 970 K; Vedinikov et al. (1974, 1977) finding a break in electrical resistivity, thermopower, and Hall effect measurements at 590 K; and Zinov'ev et al. (1975) using electrical resistivity, thermal diffusivity, and thermal conductivity measurements to find an anomaly at 600 K. Hurd and Alderson (1973) stated that their samples were of high purity, although no analytical data was given, and that their results proved that the intermediate phase did exist in the pure metal contrary to previous findings, and a similar conclusion was later reached by Vedinikov et al. (1974, 1977). This prompted Beaudry and Gschneidner (1974) to carry out measurements on very pure ytterbium, and they found only thermal arrests corresponding to the beta–gamma transition and the melting point. However, when they saturated their samples with hydrogen, they were able to reproduce the transition temperatures reported by Hurd and Alderson (1973). Perhaps final proof that the intermediate phase was impurity induced was from electrical resistivity measurements of both Guntherodt et al. (1976) and Ten Cate et al. (1980) who found no anomalies at all between room temperature and the beta–gamma transition temperature on metal that in both cases was definitely known to be 99.9% pure.

Although initial analysis suggested an hydrogen impurity of only 35 ppm for the samples used for enthalpy measurements by Berg et al. (1961) (273–1024 K in the beta phase), they obtained a beta–gamma transition temperature some 35 K lower than that obtained for the pure metal (Gschneidner, 1990), and a Shomate plot clearly indicated two different slopes above and below 553 K in agreement with the lower transition temperature found above for hydrogen-contaminated samples. Analysis treating the data above and below 553 K separately also suggested an enthalpy difference of 113 ± 25 J/mol at the transition temperature. However, the electrical resistance measurements alone would indicate that a transition is completely unrepresentative of the pure metal. Therefore, in order to obtain a continuously smooth heat capacity curve compatible with the low-temperature data, it was found that this could be achieved if only the four highest enthalpy measurements were considered together with the selected values of the specific heat at 298.15 K and its derivative. Enthalpy values were corrected for temperature scale and atomic weight and from a 273.15 to a 298.15 K base by subtracting 663.89 J/mol from the low-temperature data. The resultant equation is

$$H^\circ(T) - H^\circ(298)(\mathrm{J/mol}) = 19.1147T + 1.37035 \times 10^{-2}T^2 - 5.08815 \times 10^{-6}T^3 - 70298.5/T - 6546.56$$

Heat capacity measurements in the beta region by Pozdeyev et al. (1990) (400–1000 K) varied from 1% to 4% lower before tending to 2% higher than the selected values.

18.4. Gamma Phase

Enthalpy measurements of Berg et al. (1961) (1048–1088 K) were corrected as above and fitted to the following equation with an overall accuracy as a standard deviation of ±5 J/mol although this is considered to be unrealistically low and based on the estimated reproducibility of each data point at 0.05%, then a more realistic representation is considered to be ±13 J/mol:

$$H^\circ(T) - H^\circ(298)(\mathrm{J/mol}) = 36.0110T - 13{,}309.20$$

The derived heat capacity is 36.01 ± 0.17 J/(mol K), and the enthalpy of transition is at 1917 J/mol. The enthalpy value is notably different to the value of 1749 ± 13 J/mol at 1033 K obtained by Berg et al., but their value is transition temperature dependent and at 1068.15 K their value would have been 1918 J/mol in almost exact agreement with the selected value even though different approaches were used in processing the data.

18.5. Liquid Phase

Enthalpy measurements of Berg et al. (1961) (1105–1374 K) were corrected as above. After rejecting the lowest data point, the three remaining values were fitted to the following equation with an overall accuracy as a standard deviation of ±10 J/mol which is again considered to be unrealistically low, and again based on the reproducibility of 0.05% for individual values, this is equal to ±17 J/mol at the melting point which is considered to be a more satisfactory representation:

$$H^\circ(T) - H^\circ(298)(\mathrm{J/mol}) = 36.7164T - 6418.99$$

The derived heat capacity is 36.72 ± 0.07 J/(mol K), the enthalpy of fusion is 7661 ± 21 J/mol, and the entropy of fusion is 7.01 ± 0.02 J/(mol K). It is noted that Berg et al. (1961) gave an incorrect equation for calculating the enthalpy of the liquid in that their constant 1452.9 should have been 1542.9.

18.6. Gas Phase

Values are based on one bar standard state pressure and are calculated from the 287 energy levels, including the ground state, which are below

TABLE 183 Sources of Energy Level Data

Authors	Number of levels
Ralchenko et al. (2012)	171
Wyart and Camus (1979)	51
Camus et al. (1980)	26
Aymar et al. (1984)	7
Wu Bi-ru et al. (1991)	11
Ali et al. (1999)	21

50,000 cm^{-1} as listed in Table 183 using the method of Kolsky et al. (1957) and the 2010 Fundamental Constants (Mohr et al., 2011).

18.7. Enthalpy of Sublimation

TABLE 184 Enthalpy of Sublimation at 298.15 K

Authors	Methods	Range (K)	$\Delta_{sub}H^{\circ}$ (298, II law) (kJ/mol)	$\Delta_{sub}H^{\circ}$ (298, III law) (kJ/mol)	Notes
Savage et al. (1959)	MS	600–740	168 ± 2	–	
Guido and Balducci (1972)	KEMS	620–820	154 ± 3	–	–[a]
Habermann (1963)	KE	679–914	151 ± 1	152.0 ± 0.1	–[b]
Habermann and Daane (1964)	KE	623–931	151 ± 1	152.5 ± 0.2	–[c]
Kruglykh et al. (1965), Kruglykh and Pavlov (1966)	KE	663–767	169 ± 3	150.6 ± 0.4	
Bohdansky and Schins (1967)	BP	1185–1760	162 ± 1	153.4 ± 0.3	
Kulifeev et al. (1971)	Eff	683–823	146	150.6 ± 0.4	–[c]
Fedechkin and Shmykov (1973)	Eff	651–775	151 ± 1	139.2 ± 1.0	–[c]

Continued

TABLE 184 Enthalpy of Sublimation at 298.15 K—Cont'd

Authors	Methods	Range (K)	$\Delta_{sub}H^{\circ}$ (298, II law) (kJ/mol)	$\Delta_{sub}H^{\circ}$ (298, III law) (kJ/mol)	Notes
Disideri et al. (1973)	TE	775–907	156 ± 2	154.8 ± 0.1	–[d]
Zaitsev and Mogutnov (1988/1989)	KEMS	669–782	152 ± 1	151.5 ± 0.1	–[e]
	KEMS	689–761	152 ± 2	151.3 ± 0.1	–[c,e]
Selected				151.8 ± 2.0	

MS, mass spectrometry; KE, Knudsen effusion; BP, boiling points; Eff, effusion; KEMS, Knudsen effusion mass spectrometry; TE, torsion effusion.
[a]*Only the second law enthalpy of sublimation at 0 K was given.*
[b]*This is Run 13 of Habermann and Daane (1964).*
[c]*Given only in the form of the Clausius–Clapeyron equation.*
[d]*The metal used was only 99% pure.*
[e]*Series I and II are distinguished since only series I was given in detail.*

Zaitsev and Mogutnov (1988/1989) criticized the measurements of Habermann and Daane (1964) on the grounds that derived vapor pressures substantially exceeded the limit for the Knudsen effusion method so that the backward stream owing to the collision of vapor molecules in the zone of the effusion orifice would lead to lower measured vapor pressures and therefore higher calculated enthalpies of sublimation. However, the close agreement between the Second and Third Law values obtained from the measurements of Habermann and Daane (1964) would suggest that the existence of nonequilibrium conditions in these experiments would appear to be speculative. Therefore, the selected value is taken as an average of the measurements of Habermann and Daane (1964) and Zaitsev and Mogutnov (1988/1989) with the uncertainty attached to the value being that suggested by the latter.

18.8. Vapor Pressure

For the beta phase, the vapor pressure was evaluated by calculating the free energy functions of the solid and the gas at 20 K intervals from 360 to 1060 K and the transition temperature, and for the liquid phase, at 20 K intervals from 1100 to 1500 K and the melting point. For the gamma phase, the vapor pressures were evaluated at the extreme temperatures and the derived values fitted to the Clausius–Clapeyron equation (Table 185).

18.9. Comparison of Selected Values at 298.15 K

Both Holley et al. (1968) and Hultgren et al. (1973) generally accept the evaluation of Gerstein et al. (1964). Konings and Beneš (2010) corrected the

TABLE 185 Vapor Pressure Equations

$\ln(p, \text{bar}) = b_1 + b_2/T + b_3 \ln(T) + b_4 T + b_5 T^2$

Phase	Range (K)	b_1	b_2	b_3	b_4	b_5
Beta	400–1068.15	13.99744	−18,355.85	6.43149×10^{-2}	-1.50623×10^{-3}	2.79281×10^{-7}
Gamma	1068.15–1092.15	12.01274	−17,134.96	0	0	0
Liquid	1092.15–1500	26.46870	−18,283.99	−1.915962	0	0

TABLE 186 A Comparison of Heat Capacity, Enthalpy, and Entropy Values at 298.15 K

Authors	$C°_p(298)$ (J/(mol K))	$H°(298) - H°(0)$ (J/mol)	$S°(298)$ (J/(mol K))
Holley et al. (1968)	26.72	6712	59.88
Hultgren et al. (1973)	26.72	6712	59.83
Konings and Beneš (2010)	26.72	–	59.94
This work	26.72	6738	59.98

entropy value of Gerstein et al. (1964) by modifying the selected heat capacity values below 15 K. The present evaluation modifies the selected values of Gerstein et al. (1964) to include the enthalpy and entropy of the alpha–beta transition (Table 186).

18.10. Summary of Representative Equations

TABLE 187 Representative Equations Above 298.15 K

Beta phase: 298.15–1068.15 K
$C°_p(T)(\text{J/(mol K)}) = 19.1147 + 2.74070 \times 10^{-2}\, T - 1.526445 \times 10^{-5} T^2 + 70,298.5/T^2$
$H°(T) - H°(298)(\text{J/mol}) = 19.1147T + 1.37035 \times 10^{-2} T^2 - 5.08815 \times 10^{-6} T^3 - 70,298.5/T - 6546.56$

$S^\circ(T)(\mathrm{J/(mol\,K)}) = 19.1147\ln(T) + 2.74070\times10^{-2}T - 7.632225\times10^{-6}T^2 - 35,149.25/T^2 - 56.0254$
Gamma phase: 1068.15–1092.15 K
$C^\circ_p(T)(\mathrm{J/(mol\,K)}) = 36.0110$
$H^\circ(T) - H^\circ(298)(\mathrm{J/mol}) = 36.0110T - 13,309.20$
$S^\circ(T)(\mathrm{J/(mol\,K)}) = 36.0110\ln(T) - 151.5242$
Liquid phase: 1092.15 –1500 K
$C^\circ_p(T)(\mathrm{J/(mol\,K)}) = 36.7164$
$H^\circ(T) - H^\circ(298)(\mathrm{J/mol}) = 36.7164T - 6418.99$
$S^\circ(T)(\mathrm{J/(mol\,K)}) = 36.7164\ln(T) - 149.4448$

TABLE 188 Free Energy Equations Above 298.15 K

Beta phase: 298.15–1068.15 K
$G^\circ(T) - H^\circ(298)(\mathrm{J/mol}) = 75.1401T - 1.37035\times10^{-2}T^2 + 2.544075\times10^{-6}T^3 - 35,149.25/T - 19.1147T\ln(T) - 6546.56$
Gamma phase: 1068.15–1092.15 K
$G^\circ(T) - H^\circ(298)(\mathrm{J/mol}) = 187.5352T - 36.0110T\ln(T) - 13,309.20$
Liquid phase: 1092.15–1500 K
$G^\circ(T) - H^\circ(298)(\mathrm{J/mol}) = 186.1612T - 36.7164T\ln(T) - 6418.99$

TABLE 189 Transition Values Involved with the Free Energy Equations

Transition	T (K)	ΔH° (J/mol)	ΔS° (J/(mol K))
Beta–gamma	1068.15	1916.952	1.7946
Fusion	1092.15	7660.613	7.0142

18.11. Thermodynamic Tables

TABLE 190 Low-Temperature Thermodynamic Data

T (K)	$C^\circ_p(T)$ (J/(mol K))	$H^\circ(T) - H^\circ(0)$ (J/mol)	$S^\circ(T)$ (J/(mol K))	$-[G^\circ(T) - H^\circ(0)]/T$ (J/(mol K))
Alpha phase				
5	0.160	0.228	0.063	0.054
10	1.46	3.523	0.468	0.116
15	4.55	18.08	1.601	0.396
20	8.11	49.76	3.392	0.904
25	11.34	98.38	5.539	1.604
30	13.99	161.7	7.840	2.450
35	16.13	237.0	10.158	3.386
40	17.76	321.7	12.420	4.377
45	19.00	413.6	14.586	5.394
50	20.02	511.2	16.641	6.418
60	21.48	718.9	20.429	8.447
70	22.44	938.8	23.818	10.407
80	23.16	1167	26.863	12.279
90	23.70	1401	29.627	14.057
100	24.01	1640	32.141	15.742
110	24.32	1882	34.447	17.342
120	24.57	2126	36.576	18.860
130	24.80	2373	38.553	20.301
140	24.98	2622	40.399	21.673
150	25.12	2872	42.129	22.981
160	25.25	3124	43.755	24.320
170	25.38	3377	45.291	25.425
180	25.50	3631	46.747	26.571
190	25.60	3887	48.129	27.670
200	25.70	4144	49.444	28.726

Continued

TABLE 190 Low-Temperature Thermodynamic Data—Cont'd

T (K)	$C°_p(T)$ (J/(mol K))	$H°(T) - H°(0)$ (J/mol)	$S°(T)$ (J/(mol K))	$-[G°(T) - H°(0)]/T$ (J/(mol K))
210	25.79	4401	50.702	29.744
220	25.89	4660	51.904	30.724
230	25.97	4919	53.058	31.671
240	26.06	5179	54.165	32.585
250	26.15	5440	55.231	33.470
260	26.25	5702	56.259	34.327
270	26.36	5965	57.252	35.158
Beta phase				
270	26.36	5991	57.348	35.158
280	26.48	6255	58.309	35.968
290	26.61	6521	59.240	36.755
298.15	26.72	6738	59.980	37.380

TABLE 191 High-Temperature Thermodynamic Data

T (K)	$C°_p(T)$ (J/(mol K))	$H°(T) - H°(298)$ (J/mol)	$S°(T)$ (J/(mol K))	$-[G°(T) - H°(298)]/T$ (J/(mol K))
Beta phase				
298.15	26.720	0	59.980	59.980
300	26.744	49	60.145	59.980
350	27.411	1403	64.318	60.309
400	28.074	2790	68.022	61.045
450	28.704	4210	71.365	62.009
500	29.283	5660	74.420	63.100
550	29.803	7137	77.236	64.258
600	30.259	8639	79.849	65.450
650	30.646	10,162	82.287	66.523
700	30.963	11,703	84.570	67.852
750	31.209	13,257	86.715	69.038

TABLE 191 High-Temperature Thermodynamic Data—Cont'd

T (K)	$C°_p(T)$ (J/(mol K))	$H°(T) - H°(298)$ (J/mol)	$S°(T)$ (J/(mol K))	$-[G°(T) - H°(298)]/T$ (J/(mol K))
800	31.381	14,822	88.735	70.207
850	31.479	16,394	90.641	71.353
900	31.504	17,969	92.441	72.475
950	31.453	19,543	94.143	73.571
1000	31.228	21,113	95.754	74.641
1050	31.127	22,675	97.278	75.683
1068.15	31.035	23,239	97.811	76.054
Gamma phase				
1068.15	36.011	25,156	99.605	76.054
1092.15	36.011	26,020	100.405	76.581
Liquid phase				
1092.15	36.716	33,681	107.420	76.581
1100	36.716	33,969	107.682	76.802
1150	36.716	35,805	109.315	78.180
1200	36.716	37,641	110.877	79.510
1250	36.716	39,477	112.376	80.795
1300	36.716	41,312	113.816	82.037
1350	36.716	43,148	115.202	83.240
1400	36.716	44,984	116.537	84.406
1450	36.716	46,820	117.826	85.536
1500	36.716	48,656	119.070	86.633

TABLE 192 Thermodynamic Properties of the Gas Phase

T (K)	$C°_p(T)$ (J/(mol K))	$H°(T) - H°(298)$ (J/mol)	$S°(T)$ (J/(mol K))	$-[G°(T) - H°(298)]/T$ (J/(mol K))
298.15	20.786	0	173.129	173.129
300	20.786	38	173.258	173.130

Continued

TABLE 192 Thermodynamic Properties of the Gas Phase—Cont'd

T (K)	$C°_p(T)$ (J/(mol K))	$H°(T) - H°(298)$ (J/mol)	$S°(T)$ (J/(mol K))	$-[G°(T) - H°(298)]/T$ (J/(mol K))
350	20.786	1078	176.462	173.383
400	20.786	2117	179.238	173.945
450	20.786	3156	181.686	174.672
500	20.786	4196	183.876	175.485
550	20.786	5235	185.857	176.339
600	20.786	6274	187.666	177.209
650	20.786	7314	189.330	178.078
700	20.786	8353	190.870	178.937
750	20.786	9392	192.304	179.781
800	20.786	10,432	193.646	180.606
850	20.786	11,471	194.906	181.411
900	20.786	12,510	196.094	182.194
950	20.786	13,549	197.218	182.955
1000	20.786	14,589	198.284	183.695
1050	20.786	15,628	199.298	184.414
1068.15	20.786	16,005	199.654	184.670
1092.15	20.786	16,504	200.116	185.005
1100	20.786	16,667	200.265	185.113
1150	20.786	17,707	201.189	185.792
1200	20.786	18,746	202.074	186.452
1250	20.786	19,785	202.923	187.094
1300	20.786	20,825	203.738	187.719
1350	20.786	21,864	204.522	188.327
1400	20.786	22,903	205.278	188.919
1450	20.786	23,943	206.008	188.495
1500	20.787	24,982	206.712	190.058

$H°(298) - H°(0) = 6197.4$ J/mol.

TABLE 193 Vapor Pressure

T (K)	p (bar)	$\Delta G°(T)$ (J/mol)	$\Delta H°(T)$ (J/mol)	p (bar)	T (K)
298.15	2.07×10^{-21}	118,064	151,800	10^{-15}	379
300	3.02×10^{-21}	117,855	151,789	10^{-14}	398
350	1.79×10^{-17}	112,224	151,475	10^{-13}	420
400	1.19×10^{-14}	106,640	151,127	10^{-12}	443
450	1.84×10^{-12}	101,102	150,746	10^{-11}	470
500	1.03×10^{-10}	95,607	150,336	10^{-10}	500
550	2.74×10^{-9}	90,156	149,898	10^{-9}	534
600	4.19×10^{-8}	84,745	149,435	10^{-8}	573
650	4.18×10^{-7}	79,373	148,951	10^{-7}	618
700	2.99×10^{-6}	74,040	148,450	10^{-6}	671
750	1.63×10^{-5}	68,743	147,935	10^{-5}	735
800	7.17×10^{-5}	63,481	147,409	10^{-4}	812
850	2.63×10^{-4}	58,251	146,877	10^{-3}	908
900	8.34×10^{-4}	53,053	146,341	10^{-2}	1032
950	2.33×10^{-3}	47,885	145,806	10^{-1}	1204
1000	5.85×10^{-3}	42,745	145,276	1	1462
1050	1.34×10^{-2}	37,632	144,753	NBP	1464
1068.15	1.78×10^{-2}	35,782	144,566		
1068.15	1.78×10^{-2}	35,782	142,649		
1092.15	2.53×10^{-2}	33,385	142,284		
1092.15	2.53×10^{-2}	33,385	134,623		
1100	2.81×10^{-2}	32,657	134,498		
1150	5.32×10^{-2}	28,046	133,702		
1200	9.52×10^{-2}	23,470	132,905		
1250	0.162	18,926	132,109		
1300	0.264	14,415	131,312		
1350	0.413	9934	130,516		
1400	0.624	5482	129,719		
1450	0.916	1059	128,923		

Continued

TABLE 193 Vapor Pressure—Cont'd

T (K)	p (bar)	$\Delta G^\circ(T)$ (J/mol)	$\Delta H^\circ(T)$ (J/mol)	p (bar)	T (K)
1462.02	1.000	0	128,731		
1500	1.307	−3336	128,126		

NBP, normal boiling point at one atmosphere pressure (1.01325 bar).
$\Delta H^\circ(0) = 152,341$ J/mol.

19. THERMODYNAMIC FUNCTIONS OF LUTETIUM

19.1. Introduction

Lutetium exists in a close-packed hexagonal structure up to the melting point selected by Gschneidner (1990) as 1936 K.

19.2. Solid Phase—Low Temperature

The values given in Table 194 have been determined for the electronic coefficient (γ) and limiting Debye temperature (θ_D).

The values of Swenson (1996) are selected not only because of a very close agreement with the revised values of Thome et al. (1978) but also because Swenson (1996) represented the heat capacity curve by means of four equations covering the range 1–305 K based on his own measurements 1–110 K and the measurements of Gerstein et al. (1969) (6–300 K) after

TABLE 194 Low-Temperature Heat Capacity Coefficients

Authors	γ (mJ/(mol K^2))	θ_D (K)
Lounasmaa (1964b)	11.27	210
Stevens et al. (1971)	8.937	196
Wells et al. (1976)	6.8	205
Taylor et al. (1978)	8.30	185
Thome et al. (1978)	8.194	183.2
	8.305 [a]	190.3 [a]
Swenson (1996)	8.299	189.9
Devyatykh et al. (2004)	8.38	183
Selected	8.299	189.9

[a] *As revised by Swenson (1996).*

correction of the latter to ITS-90. The values of θ_D from the last four sets of heat capacity measurements are in satisfactory agreement with a value of 184.5 K determined from elastic constant measurements by Tonnies et al. (1971) and 186 K calculated by Swenson from the elastic constant measurements of Greiner et al. (1987).

Measurements of Lounasmaa (1964b) (0.4–3.9 K) above 1 K are 31% higher falling to 11% higher than the selected curve, while those of Stevens et al. (1971) for which no temperature range was given but was considered to be from 1 to 4 K are initially 7% higher but converge to the selected curve at 4 K. The measurements of Wells et al. (1976a,b) (1.5–13.8 K) are on average 21% lower than the selected curve, while those of Taylor et al. (1978) (2.3–19.7 K), representing the first determination on higher purity metal, are on average 1% higher. The measurements of Thome et al. (1978) (1.1–19.1 K), which were also selected by Tsang et al. (1985), vary 1% lower to 2% higher at 4 K where the values were only shown graphically with actual data points being given by Gschneidner (1991). The measurements of Devyatykh et al. (2004) (2.0–15.0 K) are initially 4% higher but converge toward the selected values at 10 K and then deviate to an average value of 1% higher above 14 K, while those of Culbert (1967) (3.0–24.7 K) are initially up to 20% higher and then gradually fall to an average value of 1% lower above 12 K. The smoothed values of Jennings et al. (1960) (5–340 K) are, over the actual temperature range of 15–350 K, initially 2% lower increasing to an average of 1% higher above 180 K.

19.3. Solid Phase—High Temperature

Enthalpy measurements of Dennison et al. (1966a) (273–1907 K in the solid range) were given only in the form of an equation and tabulated values with actual data points being given by Gschneidner (1991). After correction to ITS-90 and for atomic weight and from a 273.15 to a 298.15 K base by subtracting 660.35 J/mol obtained from the low-temperature data, it was found that the heat capacity curve derived from the enthalpy data was incompatible with the low-temperature selected values (a sharp change in slope at 298.15 K). Therefore in order to obtain a continuous smooth heat capacity curve, the enthalpy measurements between 1501 and 1907 K were combined with the selected heat capacity value at 298.15 K and its derivative leading to the following equation with an overall accuracy as a standard deviation of ±343 J/mol (0.71%):

$$H^\circ(T) - H^\circ(298)(\mathrm{J/mol}) = 32.5178T - 6.32019 \times 10^{-3}T^2 + 3.53959 \times 10^{-6}T^3 + 277{,}723/T - 10{,}158.66$$

It is noted that equations selected in the previous reviews all lead to a sharp change in the heat capacity slope dC°_p/dT at 298.15 K, and therefore, these selected values do not account for the incompatibility between the low- and high-temperature data.

The heat capacity measurements of Pozdeyev et al. (1990) (400–1700 K) showed a trend from 1% low to 7% low at 1300 K before increasing to 1% high at 1700 K. Values of Novikov et al. (1978) (1100–2100 K) are given in the form heat capacity–density. Corrections for density using values of Khairulin and Stankus (1989) lead to heat capacity values which are 1–8% lower than the selected values in the solid range.

19.4. Liquid Phase

Enthalpy measurements of Dennison et al. (1966a) over the range of 1921–2005 K do not show a sharp change consistent with the onset of melting but a gradual increase consistent with the dissolution of the tantalum container since tantalum is much more soluble in liquid lutetium than the other heavy lanthanide elements, and this solubility is clearly effecting the results far more than would be expected from the solubility equation of Dennison et al. (1966b). As a result, Dennison et al. (1966a) rejected all of the measurements relating to the liquid. For those heavy lanthanide elements which do not show high-temperature allotropic modifications, similar entropies of fusion of 9.1 J/(mol K) for holmium, 8.9 J/(mol K) for erbium, and 9.2 J/(mol K) for thulium are obtained in the present evaluation. However, for lutetium which has a closed electronic shell, it is considered that it would behave in a manner more typical of other close-packed structures for which Gschneidner (1964) estimates entropy of fusion of 9.6 ± 1.0 J/(mol K) as an average for 14 metals. If this value is applied to lutetium, then the equivalent enthalpy of fusion is $18{,}587 \pm 1936$ J/mol. For the heat capacity, a value of 48 J/(mol K) is selected so that the heat capacities of the solid and the liquid at the melting point are similar. The enthalpy of the liquid can then be represented by

$$H^\circ(T) - H^\circ(298)(\mathrm{J/mol}) = 48.0000T - 19{,}406.04$$

Heat capacity measurements of Novikov et al. (1978) (2000–2100 K) average to a value of 47 J/(mol K) in agreement with the selected value; this cannot be considered as being of high quality in view of the values obtained for the solid.

19.5. Gas Phase

Values are based on one bar standard state pressure and are calculated from 436 energy levels, including the ground state, as listed in Table 195 using the method of Kolsky et al. (1957) and the 2010 Fundamental Constants (Mohr et al., 2011).

The levels of Maeda et al. (1989) were given in terms of four Rydberg series. Vergès and Wyart (1978) corrected 36 of the levels selected by Ralchenko et al. (2012). For two levels selected by Ralchenko et al. (2012) and one level given by Vergès and Wyart (1978), two possible degeneracy weighting (g_i) were given in each case so average values was used.

TABLE 195 Sources of Energy Level Data

Authors	Number of levels
Ralchenko et al. (2012)	186
Vergès and Wyart (1978)	9
Maeda et al. (1989)	241

19.6. Enthalpy of Sublimation

TABLE 196 Enthalpy of Sublimation at 298.15 K

Authors	Methods	Range (K)	$\Delta_{sub}H^{\circ}$(298, II law) (kJ/mol)	$\Delta_{sub}H^{\circ}$ (298, III law) (kJ/mol)	Notes
White et al. (1961)	MS	1691–1937	398 ± 7	–	
Jackson et al. (1961)	MS	1758	424 ± 2	–	
Habermann (1963)	KE	1651–1930	433 ± 2	426.8 ± 0.1	–[a]
Habermann and Daane (1964)	KE	1651–1932	427 ± 3	427.2 ± 0.1	–[b]
Selected				427.2 ± 3.0	

MS, mass spectrometry; KE, Knudsen effusion.
[a]*This is Run 3 of Habermann and Daane (1964) as given in detail.*
[b]*Given only in the form of the Clausius–Clapeyron equation.*

As the selected value is based only on one set of measurements, the assigned accuracy is considered to be typical of that obtained for the lanthanides, in general.

19.7. Vapor Pressure

The vapor pressure equation for the solid phase was obtained by evaluating the free energy functions of the solid and the gas at 25 K intervals from 1000 to 1925 K and the melting point, and for the liquid phase, at 50 K intervals from 1950 to 3700 K and the melting point (Table 197):

$$\ln(p,\text{bar}) = A + B/T + C\ln(T) + DT + CT^2$$

TABLE 197 Vapor Pressure Equations

$\ln(p, \text{bar}) = b_1 + b_2/T + b_3 \ln(T) + b_4 T + b_5 T^2$

Phase	Range (K)	b_1	b_2	b_3	b_4	b_5
Solid	1000–1936.15	22.15068	−51,480.08	−1.025362	1.01972×10^{-3}	-2.48418×10^{-7}
Liquid	1936.15–2800	31.53732	−52,126.85	−2.027009	-2.49379×10^{-4}	1.44753×10^{-8}
	2800–3700	25.51241	−51,368.33	−1.217022	-5.39111×10^{-4}	3.18337×10^{-8}

TABLE 198 Comparison of Heat Capacity, Enthalpy, and Entropy Values at 298.15 K

Authors	$C^\circ_p(298)$ (J/(mol K))	$H^\circ(298) - H^\circ(0)$ (J/mol)	$S^\circ(298)$ (J/(mol K))
Holley et al. (1968)	26.86	6372	50.96
Hultgren et al. (1973)	26.78	6389	50.96
Konings and Beneš (2010)	26.85	–	50.98
Gerstein et al. (1969)	26.51	6348	51.17
This work	26.57	6347	51.15

19.8. Comparison of Selected Values at 298.15 K

Holley et al. (1968), Hultgren et al. (1973), and Konings and Beneš (2010) all relied on the obsolete low-temperature heat capacity values of Jennings et al. (1960) which were superseded by later measurements of Gerstein et al. (1969). The present results are based on the equations derived by Swenson (1996) (Table 198).

19.9. Summary of Representative Equations

TABLE 199 Representative Equations Above 298.15 K

Solid phase: 298.15–1936.15 K

$C^\circ_p(T)(\text{J/(mol K)}) = 32.5178 - 1.264038 \times 10^{-2} T + 1.061877 \times 10^{-5} T^2 - 277,723/T^2$

$H^\circ(T) - H^\circ(298)(\text{J/mol}) = 32.5178T - 6.32019 \times 10^{-3} T^2 + 3.53959 \times 10^{-6} T^3 + 277,723/T - 10,158.66$

$S^\circ(T)(\text{J/(mol K)}) = 32.5178\ln(T) - 1.264038\times10^{-2}T + 5.309385\times10^{-6}T^2 + 138,861.5/T^2 - 132.3897$
Liquid phase: 1936.15–3700 K
$C^\circ_p(T)(\text{J/(mol K)}) = 48.0000$
$H^\circ(T) - H^\circ(298)(\text{J/mol}) = 48.0000T - 19,406.04$
$S^\circ(T)(\text{J/mol K}) = 48.0000\ln(T) - 244.4995$

TABLE 200 Free Energy Equations Above 298.15 K

Solid phase: 298.15–1936.15 K
$G^\circ(T) - H^\circ(298)(\text{J/mol}) = 164.9075T + 6.32019\times10^{-3}T^2 - 1.769795\times10^{-6}T^3 + 138,861.5/T - 32.5178T\ln(T) - 10,158.66$
Liquid phase: 1936.15–3700 K
$G^\circ(T) - H^\circ(298)(\text{J/mol}) = 292.4995T - 48.0000T\ln(T) - 19,406.04$

TABLE 201 Transition Values Involved with the Free Energy Equations

Transition	T (K)	ΔH° (J/mol)	ΔS° (J/(mol K))
Fusion	1936.15	18,587.040	9.6000

19.10. Thermodynamic Tables

TABLE 202 Low-Temperature Thermodynamic Data

T (K)	$C^\circ_p(T)$ (J/(mol K))	$H^\circ(T) - H^\circ(0)$ (J/mol)	$S^\circ(T)$ (J/(mol K))	$-[G^\circ(T) - H^\circ(0)]/T$ (J/(mol K))
5	0.0799	0.159	0.0539	0.0238
10	0.481	1.306	0.199	0.0686
15	1.708	6.385	0.595	0.169
20	3.748	19.76	1.350	0.362
25	6.201	44.55	2.446	0.664
30	8.685	81.81	3.798	1.071

Continued

TABLE 202 Low-Temperature Thermodynamic Data—Cont'd

T (K)	$C°_p(T)$ (J/(mol K))	$H°(T) - H°(0)$ (J/mol)	$S°(T)$ (J/(mol K))	$-[G°(T) - H°(0)]/T$ (J/(mol K))
35	10.979	131.1	5.312	1.567
40	13.005	191.1	6.913	2.135
45	14.716	260.6	8.547	2.756
50	16.156	337.9	10.174	3.417
60	18.391	511.2	13.328	4.808
70	19.992	703.6	16.291	6.240
80	21.165	909.6	19.041	7.670
90	22.053	1126	21.587	9.077
100	22.721	1350	23.947	10.447
110	23.244	1580	26.138	11.775
120	23.679	1815	28.179	13.058
130	24.033	2053	30.089	14.296
140	24.326	2295	31.881	15.488
150	24.573	2540	33.568	16.638
160	24.788	2786	35.161	17.746
170	24.979	3035	36.670	18.816
180	25.152	3286	38.102	19.848
190	25.312	3538	39.467	20.845
200	25.460	3792	40.769	21.808
210	25.598	4047	42.014	22.741
220	25.727	4304	43.208	23.645
230	25.846	4562	44.354	24.520
240	25.956	4821	45.457	25.370
250	26.058	5081	46.518	26.195
260	26.155	5342	47.542	26.996
270	26.249	5604	48.531	27.776
280	26.348	5867	49.488	28.534
290	26.460	6131	50.414	29.273
298.15	26.569	6347	51.149	29.861

TABLE 203 High-Temperature Thermodynamic Data

T (K)	$C°_p(T)$ (J/(mol K))	$H°(T) - H°(298)$ (J/mol)	$S°(T)$ (J/(mol K))	$-[G°(T) - H°(298)]/T$ (J/(mol K))
Solid phase				
298.15	26.569	0	51.149	51.149
300	26.596	49	51.313	51.149
400	27.425	2758	59.101	52.206
500	27.741	5518	65.258	54.222
600	27.985	8304	70.337	56.497
700	28.306	11,118	74.674	58.791
800	28.768	13,970	78.482	61.019
900	29.400	16,877	81.905	63.153
1000	30.218	19,856	85.043	65.187
1100	31.233	22,927	87.969	67.126
1200	32.448	26,109	90.737	68.980
1300	33.867	29,423	93.389	70.756
1400	35.492	32,890	95.957	72.465
1500	37.326	36,529	98.467	74.115
1600	39.369	40,362	100.940	75.714
1700	41.621	44,410	103.394	77.270
1800	44.084	48,693	105.841	78.790
1900	46.758	53,233	108.296	80.278
1936.15	47.776	54,942	109.186	80.809
Liquid phase				
1936.15	48.000	73,529	118.787	80.809
2000	48.000	76,594	120.344	82.047
2100	48.000	81,394	122.686	83.927
2200	48.000	86,194	124.919	85.740
2300	48.000	90,994	127.052	87.490
2400	48.000	95,794	129.095	89.181
2500	48.000	100,594	131.055	90.817

Continued

TABLE 203 High-Temperature Thermodynamic Data—Cont'd

T (K)	$C^\circ_p(T)$ (J/(mol K))	$H^\circ(T) - H^\circ(298)$ (J/mol)	$S^\circ(T)$ (J/(mol K))	$-[G^\circ(T) - H^\circ(298)]/T$ (J/(mol K))
2600	48.000	105,394	132.937	92.401
2700	48.000	110,194	134.749	93.936
2800	48.000	114,994	136.494	95.425
2900	48.000	119,744	138.179	96.871
3000	48.000	124,594	139.806	98.275
3100	48.000	129,394	141.380	99.640
3200	48.000	134,194	142.904	100.968
3300	48.000	138,994	144.381	102.262
3400	48.000	143,794	145.814	103.522
3500	48.000	148,594	147.205	104.750
3600	48.000	153,394	148.558	105.948
3700	48.000	158,194	149.873	107.118

TABLE 204 Thermodynamic Properties of the Gas Phase

T (K)	$C^\circ_p(T)$ (J/(mol K))	$H^\circ(T) - H^\circ(298)$ (J/mol)	$S^\circ(T)$ (J/(mol K))	$-[G^\circ(T) - H^\circ(298)]/T$ (J/(mol K))
298.15	20.863	0	184.802	184.802
300	20.866	39	184.931	184.802
400	21.278	2142	190.979	185.624
500	22.100	4308	195.809	187.193
600	23.137	6569	199.929	188.980
700	24.155	8935	203.574	190.809
800	25.008	11,395	206.857	192.614
900	25.645	13,929	209.842	194.365
1000	26.073	16,517	212.567	196.051
1100	26.324	19,138	215.065	197.667

TABLE 204 Thermodynamic Properties of the Gas Phase—Cont'd

T (K)	$C^\circ_p(T)$ (J/(mol K))	$H^\circ(T) - H^\circ(298)$ (J/mol)	$S^\circ(T)$ (J/(mol K))	$-[G^\circ(T) - H^\circ(298)]/T$ (J/(mol K))
1200	26.442	21,777	217.361	199.214
1300	26.463	24,423	219.480	200.693
1400	26.419	27,068	221.439	202.105
1500	26.335	29,706	223.260	203.456
1600	26.226	32,334	224.956	204.747
1700	26.104	34,950	226.542	205.983
1800	25.979	37,555	228.031	207.167
1900	25.854	40,146	229.432	208.302
1936.15	25.811	41,080	229.919	208.701
2000	25.735	42,726	230.755	209.392
2100	25.623	45,293	232.008	210.440
2200	25.521	47,851	233.197	211.447
2300	25.430	50,398	234.330	212.418
2400	25.352	52,937	235.410	213.353
2500	25.290	55,469	236.444	214.256
2600	25.245	57,996	237.435	215.129
2700	25.220	60,519	238.387	215.973
2800	25.216	63,040	239.304	216.790
2900	25.235	65,563	240.189	217.582
3000	25.281	68,088	241.046	218.350
3100	25.353	70,620	241.876	219.095
3200	25.456	73,160	242.682	219.820
3300	25.590	75,712	243.467	220.524
3400	25.757	78,279	244.234	221.211
3500	25.958	80,864	244.983	221.879
3600	26.195	83,472	245.718	222.531
3700	26.468	86,105	246.439	223.168

$H^\circ(298) - H^\circ(0) = 6199.8$ J/mol.

TABLE 205 Vapor Pressure

T (K)	p (bar)	$\Delta G^\circ(T)$ (J/mol)	$\Delta H^\circ(T)$ (J/mol)	p (bar)	T (K)
298.15	1.38×10^{-68}	387,351	427,200	10^{-15}	1022
300	3.99×10^{-68}	387,104	427,189	10^{-14}	1072
400	1.53×10^{-49}	373,833	426,584	10^{-13}	1126
500	2.08×10^{-38}	360,715	425,990	10^{-12}	1187
600	5.37×10^{-31}	347,710	425,465	10^{-11}	1254
700	1.04×10^{-25}	334,787	425,017	10^{-10}	1330
800	9.57×10^{-22}	321,925	424,625	10^{-9}	1415
900	1.15×10^{-18}	309,109	424,252	10^{-8}	1512
1000	3.32×10^{-16}	296,336	423,861	10^{-7}	1625
1100	3.41×10^{-14}	283,605	423,411	10^{-6}	1755
1200	1.61×10^{-12}	270,919	422,868	10^{-5}	1910
1300	4.19×10^{-11}	258,282	422,200	10^{-4}	2104
1400	6.81×10^{-10}	245,703	421,378	10^{-3}	2347
1500	7.58×10^{-9}	233,189	420,377	10^{-2}	2660
1600	6.22×10^{-8}	220,747	419,172	10^{-1}	3079
1700	3.95×10^{-7}	208,389	417,741	1	3677
1800	2.04×10^{-6}	196,121	416,062	NBP	3682
1900	8.77×10^{-6}	183,954	414,113		
1936.15	1.43×10^{-5}	179,582	413,338		
1936.15	1.43×10^{-5}	179,582	394,751		
2000	3.12×10^{-5}	172,509	393,332		
2100	9.60×10^{-5}	161,523	391,110		
2200	2.65×10^{-4}	150,643	388,856		
2300	6.66×10^{-4}	139,866	386,604		
2400	1.54×10^{-3}	129,187	384,343		
2500	3.33×10^{-3}	118,602	382,075		
2600	6.73×10^{-3}	108,108	379,802		
2700	1.29×10^{-2}	97,701	377,525		
2800	2.34×10^{-2}	87,379	375,246		

TABLE 205 Vapor Pressure—Cont'd

T (K)	p (bar)	$\Delta G^\circ(T)$ (J/mol)	$\Delta H^\circ(T)$ (J/mol)	p (bar)	T (K)
2900	4.08×10^{-2}	77,138	372,969		
3000	6.82×10^{-2}	66,976	370,694		
3100	0.110	56,889	368,426		
3200	0.172	46,876	366,166		
3300	0.260	36,933	363,918		
3400	0.384	27,058	361,685		
3500	0.553	17,248	359,471		
3600	0.778	7501	357,278		
3677.39	1.000	0	355,598		
3700	1.074	−2185	355,111		

NBP, normal boiling point at one atmosphere pressure (1.01325 bar).
$\Delta H(0) = 427,347$ J/mol.

20. SUMMARY OF SELECTED THERMODYNAMIC FUNCTIONS

20.1. Summary of Heat Capacity, Enthalpy, and Entropy Values at 298.15 K

	Solid phase			Gas phase		
Symbol	$C^\circ_p(298)$ (J/(mol K))	$H^\circ(298) - H^\circ(0)$ (J/mol)	$S^\circ(298)$ (J/(mol K))	$C^\circ_p(298)$ (J/(mol K))	$H^\circ(298) - H^\circ(0)$ (J/mol)	$S^\circ(298)$ (J/(mol K))
Sc	25.57	5206	54.76	22.103	7002.2	174.787
Y	26.29	5992	44.83	25.860	6857.0	179.475
La	27.11	6679	57.05	22.754	6313.7	182.382
Ce	26.92	7889	65.49	23.075	6667.5	191.771
Pr	28.17	7415	74.93	21.360	6223.2	189.811
Nd	27.49	7144	71.84	22.092	6268.8	189.410
Pm	(27.50)	–	(71.50)	24.257	6462.7	187.103
Sm	29.53	7575	69.64	30.354	8170.6	183.046
Eu	27.65	8005	77.80	20.786	6197.4	188.798
Gd	37.65	9167	68.53	27.549	7637.0	194.317
Tb	28.95	9459	73.38	26.882	7455.7	202.096
Dy	26.56	8842	74.78	20.786	6197.4	195.901
Ho	27.15	8018	75.96	20.786	6197.4	195.582
Er	26.58	7421	75.86	20.786	6197.4	194.031
Tm	27.36	7440	73.26	20.786	6197.4	190.118
Yb	26.72	6738	59.98	20.786	6197.4	173.129
Lu	25.57	6347	51.15	20.863	6199.8	184.802

20.2. Enthalpy of Sublimation and Summary of Transition Temperature Properties

The melting points are those selected by Gschneidner (1990) except for Nd which is the later Ames Laboratory value of Gschneidner and Beaudry (1991). Although one bar is the standard state pressure, T_b are the "normal" boiling points at one atmosphere (1.01325 bar) pressure.

Symbol	T_m (K)	$\Delta_m H°$ (kJ/mol)	$\Delta_m S°$ (J/(mol K))	$\Delta_{sub} H°$(298, III law) (kJ/mol)	T_b (K)
Sc	1814	10.50	7.77	379.0	3129
Y	1795	11.32	6.30	423.3	3584
La	1191	6.07	5.10	430.0	3694
Ce	1071	5.46	5.10	431.9	3622
Pr	1204	7.35	6.11	355.8	3537
Nd	1295	7.32	5.65	327.3	3257
Pm	1315	(7.45)	(5.66)	(315.0)	(3156)
Sm	1347	9.58	7.11	208.0	2053
Eu	1095	9.21	8.41	177.8	1829
Gd	1586	9.62	6.07	396.0	3548
Tb	1629	10.19	6.26	386.5	3467
Dy	1685	11.26	6.68	288.0	2774
Ho	1747	15.87	9.08	300.2	2921
Er	1802	16.08	8.92	311.0	3074
Tm	1818	16.68	9.18	233.0	2212
Yb	1092	7.66	7.01	151.8	1464
Lu	1936	(18.59)	(9.60)	427.2	3682

21. CONCLUSIONS AND PERSPECTIVE

21.1. The Improvement in the Measurement of Thermodynamic Properties

The significant diversity that appears to exist between earlier measurements of the condense phase thermodynamic properties of these metals and more recent measurements is due almost entirely to the marked improvement in quality. However, as recently as 1980, lanthanide metals were still being supplied containing several thousand parts per million atomic of nonmetallic impurities (Gschneidner, 1980). By using a number of different techniques as described by Beaudry and Gschneidner (1978a), it has now become possible to produce ultra high purity metals both in the Ames Laboratory and by David Fort at the University of Birmingham, England, to the point where, as pointed out by Gschneidner (1990), lanthanide impurities in lanthanide metals may now amount to less than 10 ppm atomic, while nonmetallic impurities have been reduced to less than 300 ppm atomic. This has led to a greater confidence in the quality of measurements especially in the low-temperature region, so it can perhaps be considered that realistic values are now being obtained for these quantities.

For the gas phase, the publication by Martin et al. (1978) of energy levels for the lanthanides proved to be a landmark in that prior to that for five of the elements, praseodymium, dysprosium, holmium, erbium, and ytterbium, the thermodynamic properties calculated by Hultgren et al. (1973) were based on less than 15 energy levels in each case so that it is hardly surprising that the calculated values differ so significantly from the current values. It is also not surprising that in Section 20.2, the calculated boiling points differ from the familiar values calculated by Hultgren et al. (1973).

21.2. Areas Where Further Measurements Are Required

For the two common lanthanides lanthanum and neodymium that there are no quality heat capacity measurements available between 20 and 298 K and the selected entropy values at 298 K are therefore little more than educated guesses. Further measurements are also required on alpha cerium between 20 and 96 K in order to obtain a precision value for the entropy at 298 K. What is worryingly being shown up by these reviews is that for many of these elements, selected values in a particular region are generally based on only one set of measurements since other measurements differ so significantly that they cannot be considered. It is possible that measurements on the pure metals will become fewer and fewer as there is a concentration on commercially exploiting the many extraordinary properties of lanthanide compounds.

REFERENCES

Ackermann, R.J., Rau, E.G., 1962. J. Chem. Phys. 36, 448.
Ackermann, R.J., Kojima, M., Rauh, E.G., Walters, R.R., 1969. J. Chem. Thermodyn. 1, 527.
Ackermann, R.J., Rau, E.G., Walters, R.R., 1970. J. Chem. Thermodyn. 2, 139.
Ahmann, D.H., 1950. U.S. Atomic Energy Commission Rept. AECD-3205 (ISC 68).
Ahmann, D.H., 1953. Iowa State College J. Sci. 27, 120.
Akimov, A.I., Kraftmakher, Ya.A., 1970. Phys. Stat. Sol. 42, K41.
Ali, R., Yaseen, M., Nadeem, A., Bhatti, S.A., Baig, M.A., 1999. J. Phys. B Atom. Mol. Opt. Phys. 32, 953.
Al-Kital, R.A., Brünhart, G., Malik, S.S., Roberge, J.P., Sailor, V.L., 1967. Nucl. Phys. A91, 644.
Amitin, E.B., Kovalevskaya, Yu.A., Rakhmenkulov, F.S., Paukov, I.E., 1970. Fiz. Tverd. Tela 12, 774 (Sov. Phys. Solid State 12, 599–604).
Amitin, E.B., Bessergenev, W.G., Kovalevskaya, Yu.A., Paukov, I.E., 1983. J. Chem. Thermodyn. 15, 181.
Anderson, A.C., Holmström, B., Krusius, M., 1968. Phys. Rev. Lett. 20, 154–157.
Anderson, A.C., Holmström, B., Krusius, M., Pickett, G.R., 1969. Phys. Rev. 183, 546.
Angelini, P., Adair, H.L., 1974. Haschke, J.M., Eick, H.A. (Eds.), Proceedings of the 11th Rare Earth Research Conference, Traverse City, Michigan, 7–10 October 1974, U.S. Atomic Energy Commission Technical Information Center Publ. CONF-741002-P2, vol. II662.
Angelini, P., Adair, H. L., 1976. U.S. Atomic Energy Commission Rept. ORNL TM-4975.
Arblaster, J.W., 2007. Platinum Metals Rev. 51, 130.
Åström, H.U., Benediktsson, G., 1988. J. Phys. F Met. Phys. 18, 2113.

Åström, H.U., Benediktsson, G., 1989. J. Phys. Condens. Matter 1, 4381.
Åström, H.U., Nogues, J., Nicolaides, G.K., Rao, K.V., Benediktsson, G., 1991. J. Phys. Condens. Matter 3, 7395.
Åström, H.U., Nickolaides, G.K., Benediktsson, G., Rao, K.V., 1992. J. Magn. Magn. Mater. 104–107, 1507.
Atalla, S.R., Banchila, S.N., Filippov, L.P., 1972. Teplofiz. Vys. Temp. 10, 72 (High Temp. 10, 60–63).
Audi, G., Bersillon, O., Blachot, J., Wapstra, A.H., 2003a. Nucl. Phys. A729, 3.
Audi, G., Wapstra, A.H., Thibault, C., 2003b. Nucl. Phys. A729, 337.
Aufmuth, P., Bernard, A., Kopp, E.-G., 1992. Z. Phys. D23, 15.
Aymar, M., Champeau, R.J., Delsart, C., Robaux, O., 1984. J. Phys. B Atom. Mol. Phys. 17, 3645.
Baginskii, A.V., Stankus, S.V., Lyapunov, K.M., 1993. Sib. Fiz-Tekh. Zh. (4), 3.
Baginskii, A.V., Lyapunov, K.M., Stankus, S.V., 1996. Teplofiz. Vys. Temp. 34, 536 (High Temp. 34, 530–534).
Baginskii, A.V., Lyapunov, K.M., Stankus, S.V., 1997. Zh. Fiz. Khim. 71, 2138 (Russ. J. Phys. Chem. 71, 1931–1934).
Bailey, C.A., 1962. Private Communication quoted by Lounasmaa and Roach (1962).
Banchila, S.N., Fillipov, L.P., 1974. Inzh. Fiz. Zh. 27, 68 (J. Eng. Phys. 27, 839–841).
Bates, S., Patterson, C., McIntrye, G.J., Palmer, S.B., Mayer, A., Cowley, R.A., Melville, R., 1988. J. Phys. C Solid State Phys. 21, 4125.
Beaudry, B.J., Daane, A.H., 1964. J. Less Common Metals 6, 322.
Beaudry, B.J., Gschneidner Jr., K.A., 1974. Solid State Commun. 15, 791.
Beaudry, B.J., Gschneidner Jr., K.A., 1978a. Gschneidner Jr., K.A., Eyring, L. (Eds.), Handbook of the Physics and Chemistry of Rare Earths, Vol. 1: Metals. North Holland Publishing Co., Amsterdam, pp. 173–232.
Beaudry, B.J., Gschneidner Jr., K.A., 1978b. McCarthy, G.J., Rhyne, J.J. (Eds.), The Rare Earths in Modern Science and Technology. Plenum Press, New York, pp. 303–307.
Beaudry, B.J., Spedding, F.H., 1974. Metall. Trans. 5, 1631.
Bednarz, G., Gelart, D.J.W., White, M.A., 1993. Phys. Rev. B47, 14247.
Behrendt, D.R., Legvold, S., Spedding, F.H., 1958. Phys. Rev. 109, 1544.
Berezovskii, G.A., Paukov, I.E., Burkhanov, G.S., Chistyakov, O.D., 1989. Zh. Fiz. Khim. 63, 3141 (Russ. J. Phys. Chem. 63, 1730–1731).
Berezovskii, G.A., Burkhanov, G.S., Kal'chugina, N.B., Paukov, I.E., Tagaev, A.B., Chistyakov, O.D., 1990. Zh. Fiz. Khim. 64, 2636 (Russ. J. Phys. Chem. 64, 1419–1421).
Berezovskii, G.A., Burkhanov, G.S., Il'yasov, S.Sh., Kol'chugina, N.B., Chistyakov, O.D., Paukov, I.E., Tagaev, A.B., 1991. Zh. Fiz. Khim. 65, 1698 (Russ. J. Phys. Chem. 65, 905).
Berezovskii, G.A., Boyarski, L.A., Burkhanov, G.S., Kazakov, A.M., Kol'chugina, N.B., Paukov, I.E., Chistyakov, O.D., 1993. Zh. Fiz. Khim. 67, 2153 (Russ. J. Phys. Chem. 67, 1938).
Berg, J.R., Spedding, F.H., Daane, A.H., 1961. U.S. Atomic Energy Commission Rept. IS-327.
Berglund, M., Wieser, M.E., 2011. Pure Appl. Chem. 83, 397.
Berman, A., Zemansky, M.W., Daane, A.H., 1958. Phys. Rev. 109, 70.
Berthier, Y., Barak, J., Barrara, R., 1975. Solid State Commun. 17, 153.
Betterton, J.O., Scarbrough, J.O., 1968. Phys. Rev. 168, 715.
Bi-ru, Wu, You-feng, Zheng, Yun-fei, Xu, Li-gang, Pan, Ju, Li, Jian-wei, Zhong, 1991. J. Phys. B Atom. Mol. Opt. Phys. 24, 49.
Blaise, J., 2005. Private Communication (2001) to Sansonetti, J.E., Martin, W.C. J. Phys. Chem. Ref. Data 34, 1559.

Blinov, A.G., Boyarsky, L.A., Burkhanov, G.S., Kolchugina, N.B., Chystyakov, O.D., 1991. Vysokochistye Vestchestva (6), 197.
Bohdansky, J., Schins, K.E.J., 1967. J. Less Common Metals 13, 248.
Bonneret, J., Carol, B., Coqblin, B., 1966. Ann. Acad. Sci. Fenn. Ser. A6 (210), 120.
Bronin, S.Ya, Polishchuk, V.P., Sychev, P.E., Shabashov, V.I., Yartsev, I.M., 1989. Teplofiz. Vys. Temp. 27, 863 (High Temp. 27, 677–681).
Brun, T.O., Synha, S.K., Wakabayashi, N., Lander, G.H., Edwards, L.R., Spedding, F.H., 1970. Phys. Rev. B 1, 1251.
Brunhart, G., Postma, H., Sailor, V.L., 1965. Phys. Rev. B1484–B1490, 137.
Bucher, E., Schmidt, P.H., Jayaraman, A., Andres, K., Maita, J.P., Nassau, K., Dernier, P.D., 1970. Phys. Rev. B2, 3911.
Bulatov, O.S., Dolzhenko, V.F., 1988. Dop. Akad. Nauk SSSR A Fiz. Mat. Tekh. (11), 60.
Bulatov, A.S., Dolzhenko, V.F., 1989. Fiz. Nizk. Temp. 15, 1187 (Sov. J. Low Temp. Phys. 15, 655–658).
Bulatov, A.S., Klocho, V.S., Kornietz, A.V., Lisichkin, V.I., 1996. Czech. J. Phys. 46 (Suppl. 4), 2121.
Bulatov, A.S., Kovalev, O.V., 1988. Fiz. Tverd Tela 30, 471 (Sov.Phys.-Solid State, 30, 266–269).
Cable, J.W., Moon, R.M., Koehler, W.C., Wollan, E.O., 1964. Phys. Rev. Lett. 12, 553.
Cameron, A.E., Wichers, E., 1962. J. Am. Chem. Soc. 84, 4175.
Camus, P., Débarre, A., Morillon, C., 1980. J. Phys. B Atom. Mol. Phys. 13, 1073.
Cetas, T.C., Holste, J.C., Swenson, C.A., 1969. Phys. Rev. 182, 679.
Chekhovskoi, V.Ya., Kats, S.A., 1981. High. Temp. High Pressures 13, 611.
Chernyshov, A.S., Tsokol, A.O., Tishin, A.M., Gschneidner Jr., K.A., Pecharsky, V.K., 2005. Phys. Rev. B 71, Art. Nr. 184410 17pp.
Child, W.J., Cok, D.R., Goddman, L.S., 1983. J. Opt. Soc. Am. 73, 151.
Chiotti, P., Gartner, G.J., Stevens, E.R., Saito, Y., 1966. J. Chem. Eng. Data 11, 571.
Chupka, W.A., Inghram, M.G., Porter, R.F., 1956. J. Chem. Phys. 24, 792.
Cohen, R.L., Hüfner, S., West, K.W., 1969a. Phys. Rev. 184, 263.
Cohen, R.L., Hüfner, S., West, K.W., 1969b. Phys. Lett. 28A, 582.
Cohen, R.L., Hüfner, S., West, K.W., 1969c. J. Appl. Phys. 40, 1366.
Colclough, M.S., 1986. Ph.D. Thesis, University of Birmingham, Birmingham, England.
Collocott, S.J., Hill, R.W., Stewart, A.M., 1988. J. Phys. F Met. Phys. L223–L227, 18.
Conway, M.M., Phillips, N.E., 1972. Timmerhaus, K.D., O'Sullivan, W.J., Hammell, E.F. (Eds.), Low Temperature Physics—LT13: Quantum Crystals and Magnetism. Plenum Press, New York, London, pp. 629–632.
Cordfunke, E.H.P., Konings, R.J.M., 1990. Thermochemical Data for Reactor Materials and Fission Products, North Holland. Elsevier Science Publishers B.V, Amsterdam.
Crane, L.T., 1962. J. Chem. Phys. 36, 10.
Culbert, H.V., 1967. Phys. Rev. 156, 701.
Daane, A.H., 1950. Ph.D. Thesis, Iowa State College, AECD-3209 (ISC-121).
Daane, A.H., 1955. Iowa State College J. Sci. 29, 400.
Daane, A.H., Spedding, F.H., 1958. Am. Chem. Soc. 134, 25S (Abstracts of Papers Meeting).
Dankov, S.Yu, Tishin, A.M., Pecharsky, V.K., Gschneidner, K.A., 1998. Phys. Rev. B57, 3478.
Dash, J.G., Taylor, R.D., Craig, P.P., 1961. Graham, G.M., Hollis Hallet, A.C. (Eds.), Proceedings of the VIIth International Conference on Low Temperature Physics, University of Toronto, Canada, 29 August–3 September 1960. University of Toronto Press and North Holland Publishing Co., Amsterdam, pp. 705–706.

DeMaria, G., Gigli, R., Malaspina, L., 1963a. Soc. Ital. Progr. Sci. Sci. Technol. 7 (1–2), 26.
DeMaria, G., Guido, M., Malaspina, L., 1963b. Ann. Chim. (Rome) 53, 1044.
DeMaria, G., Malaspina, L., Piacente, V., 1963c. Soc. Ital. Progr. Sci. Sci. Technol. 7 (1-2), 11.
DeMaria, G., Malaspina, L., Piacente, V., 1963d. Soc. Ital. Progr. Sci. Sci. Technol. 7 (1–2), 33.
Dempesy, C.W., Gordon, J.F., Soller, T., 1962. Bull. Am. Phys. Soc. 7, 309.
Dempesy, C.W., Gordon, J.F., Soller, T., 1966. Ann. Acad. Sci. Fenn. A 6 (210), 204.
Dennison, D.H., Gschneidner Jr., K.A., Daane, A.H., 1966a. J. Chem. Phys. 44, 4273.
Dennison, D.H., Tschetter, M.J., Gschneidner Jr., J.A., 1966b. J. Less Common Metals 10, 108.
Dennison, D.H., Tschetter, M.J., Gschneidner Jr., J.A., 1966c. J. Less Common Metals 11, 423.
Desideri, A., Piacente, V., Nobili, S., 1973. J. Chem. Eng. Data 18, 140.
Devyatykh, G.G., Gusev, A.G., Gibin, A.M., Kabanov, A.V., Kupriyanov, V.F., Burkhanov, G.S., Kol'chugina, N.B., Chistyakov, O.D., 2004. Neorgan. Mater. 40, 174 (Inorg. Mater. 40, 130–133).
Dinsdale, A.T., 1991. Calphad 15, 317.
Disideri, A., Piacente, V., Nobili, S., 1973. J. Chem. Eng. Data 18, 140.
Dokko, W., Bautista, R.G., 1980. Met. Trans. B11, 511.
Douglas, T.B., 1969. J. Res. Nat. Bur. Stand. 73A, 451.
Dreyfus, M., 1961. J. Phys. Radium 22, 838.
Dreyfus, M., Goodman, B.B., Lacaze, A., Trolliet, G., 1961a. Compt. Rend. 253, 1764.
Dreyfus, M., Goodman, B.B., Trolliet, G., Weil, L., 1961b. Compt. Rend. 252, 1743.
Dreyfus, M., Goodman, B.B., Trolliet, G., Weil, L., 1961c. Compt. Rend. 253, 1085.
Dreyfus, M., Trolliet, G., Lacaze, A., 1961d. J. Phys. Radium 22, 66S.
Dreyfus, B., Michel, J.C., Thoulouze, D., 1967. Phys. Lett. 24A, 457.
Erikson, M., Forgan, E.M., Muirhead, C.M., Young, R.C., 1983. J. Phys. F Met. Phys. 13, 929.
Faudot, F., Harmelin, M., 1990. Scr. Metall. Mater. 24, 91.
Fedechkin, G.M., Shmykov, A.A., 1973. Izv. Vyssh. Ucheb. Zaved. Tsvet. Met. 16 (4), 109.
Feron, J.L., 1969. Ph.D. Thesis, University of Grenoble, France. Quoted by Coqblin, B. (1977), The Electronic Structure of Rare Earth Metals and Alloys: The Magnetic Heavy Rare Earths. Academic Press, London, pp. 451–457.
Finnemore, D.K., Johnson, D.L., Ostenson, J.E., Spedding, F.H., Beaudry, B.J., 1965. Phys. Rev. 137, A550–A556.
Flotow, H.E., Osborne, D.W., 1964. Vorres, K.S. (Ed.), Rare Earth Research II. Proceedings of the Third Conference on Rare Earth Research, Clearwater, Florida, 21–24 April 1963. Gordon and Breach, New York, pp. 233–243.
Flotow, H.E., Osborne, D.W., 1967. Phys. Rev. 160, 467.
Forgan, E.M., 1981. Physica B107, 65.
Forgan, E.M., Muirhead, C.M., Jones, D.W., Gschneidner Jr., K.A., 1979. J. Phys. F Met. Phys. 9, 651.
Fort, D., Jones, D.W., Greenhough, E.D., Hettiarachchi, N.F., 1981. J. Magn. Magn. Mater. 23, 1.
Furmann, B., Krzykowski, A., Stefańska, D., Dembczyński, J., 2006. Phys. Scr. 74, 658.
Furmann, B., Stefańska, D., Dembczyński, J., 2009. J. Phys. B Atom. Mol. Opt. Phys. 42, Art. Nr. 175005 (18pp).
Furmann, B., Stefańska, D., Dembczyński, J., 2010. J. Phys. B Atom. Mol. Opt. Phys. 43, Art. Nr. 115001 (8pp).
Gamper, B., Uddin, Z., Jahangir, M., Allard, O., Knöckel, H., Tiemann, E., Windholz, L., 2011. J. Phys. B Atom. Mol. Opt. Phys. 44, Art. Nr. 045003 (7pp).
Garton, W.R.S., Reeves, E.M., Tomkins, F.S., Ercoli, B., 1973a. Proc. R. Soc. Lond. A333, 17.
Garton, W.R.S., Reeves, E.M., Tomkins, F.S., Ercoli, B., 1973b. Proc. R. Soc. Lond. A333, 1.

Gerstein, B.C., Jelinek, F.J., 1966. Private Communication quoted by Dennison et al. (1966).
Gerstein, B.C., Griffel, M., Jennings, L.D., Miller, R.E., 1957. J. Chem. Phys. 27, 394.
Gerstein, B.C., Jelinek, F.J., Spedding, F.H., 1962. Phys. Rev. Lett. 8, 425.
Gerstein, B.C., Mullaly, J.L., Phillips, E., Miller, R.E., Spedding, F.H., 1964. J. Chem. Phys. 41, 883.
Gerstein, B.C., Jelinek, F.J., Mullaly, J.R., Schickell, W.D., Spedding, F.H., 1967. J. Chem. Phys. 47, 5194.
Gerstein, B.C., Taylor, W.A., Shickell, W.D., Spedding, F.H., 1969. J. Chem. Phys. 51, 2924.
Gerstein, B.C., Taylor, W.A., Schickell, W.D., Spedding, F.H., 1971. J. Chem. Phys. 54, 4723.
Gibson, J.K., Haire, R.G., 1992. J. Nucl. Mater. 195, 156.
Ginibre, A., 1981. Phys. Scr. 23, 260.
Gomonai, A.I., Kudelich, O.I., 2002. Opt. Spekstrosk. 93, 212 (Opt. Spectrosc. 93, 198–207).
Gomonai, A.I., Pickan, O.I., 2003. J. Phys. B Atom. Mol. Opt. Phys. 36, 4155.
Gonossar, J., Steinitz, M.O., Fawcett, E., 1984. Can. J. Phys. 62, 823.
Gordon, J.E., Dempesy, C.W., Soller, T., 1962. Nachman, J.F., Lundin, C.E. (Eds.), Proceedings of the Second Conference on Rare Earth Research, Glenwood Springs, Colorado, 24–27 September 1961. Gordon and Breach, New York, pp. 203–212.
Gottwald, T., Lassen, J., Liu, Y., Mattolat, C., Raeder, S., Wendt, K., 2009. Iguchi, T., Watanabe, K. (Eds.), 4th International Conference on Laser Probing—LAP 2008, Nagoya, Japan, 6–10 October 2008, AIP Conference Proceedings 1104, 138.
Greenhough, R.D., Blackie, G.N., Palmer, S.B., 1981. J. Phys C Solid State Phys. 14, 9.
Greenough, R.O., Hettiarachchi, N.F., 1983. J. Magn. Magn. Mater. 31–34, 178.
Gregers-Hansen, P.E., Krusisus, M., Pickett, G.R., 1972. Phys. Rev. Lett. 29, 420.
Greiner, J.D., Schiltz, R.J., Tonnies, J.J., Spedding, F.H., Smith, J.F., 1973. J. Appl. Phys. 44, 3862.
Greiner, J.D., Beaudry, B.J., Spedding, F.H., 1987. J. Appl. Phys. 62, 1220.
Griffel, M., Skochdopole, R.E., Spedding, F.H., 1954. Phys. Rev. 93, 657.
Griffel, M., Skochdopole, R.E., Spedding, F.H., 1956. J. Chem. Phys. 25, 75.
Gschneidner Jr., K.A., 1964. Solid State Phys. 16, 275.
Gschneidner Jr., K.A., 1980. Subbaras, E.C., Wallace, W.E. (Eds.), Science and Technology of Rare Earth Materials. Academic Press, New York, pp. 25–47.
Gschneidner Jr., K.A., 1990. Bull. Alloy Phase Diag. 11, 216.
Gschneidner Jr., K.A., 1991. Private Communication (June).
Gschneidner Jr., K.A., Beaudry, B.J., 1991. Scr. Metall. Mater. 25, 745.
Gschneidner Jr., K.A., Pecharsky, V.K., 1999. J. Phase Equilibria 20, 612.
Gschneidner Jr., K.A., Elliott, R.O., McDonald, R.R., 1962. J. Phys. Chem. Solids 23, 555.
Gschneidner Jr., K.A., Pecharsky, V.K., Cho, J., Martin, S.W., 1996. Scr. Mater. 34, 1717.
Gschneidner Jr., K.A., Pecharsky, V.K., Fort, D., 1997. Phys. Rev. Lett. 78, 4281.
Guido, M., Balducci, G., 1972. J. Chem. Phys. 57, 5611.
Guntherodt, H.J., Hauser, E., Künzi, H.U., Evans, R., Evers, J., Kaldis, E., 1976. J. Phys. F Met. Phys. 6, 1513.
Gurvich, L.V., Veits, I.V., Medvedev, V.A., Bergman, G.A., Yungman, V.S., Khachkuruzov, G.A., Yorish, V.S., Dorofeeva, O.V., Osina, E.L., Tolmach, P.I., Przheval'skii, I.N., Nazarenko, I.I., Aristova, N.M., Shenyavskaya, E.A., Gorokhov, L.N., Rogatskii, A.L., Efimov, M.E., Leonidov, V.Ya., Khait, Yu.G., Efimova, A.G., Tomberg, S.E., Gusarov, A.V., Khandamirova, N.E., Yurkov, G.N., Fokin, I.R., Kuratova, L.F., Gol'dshtein, A.D., 1982. Glushko, V.P., Gurvich, L.V., Bergman, G.A., Veits, I.V., Medvedev, V.A., Khachkuruzov, G.A., Yungman, V.S. (Eds.),

Termodinamicheskie Svoistva Individual'nykh Veshchestv (Thermodynamic Properties of Individual Substances), vol. 4. Nauka, Moscow.
Habermann, C.E., 1963. Ph.D. Thesis, Iowa State University of Science and Technology, Ames, Iowa.
Habermann, C.E., Daane, A.H., 1964. J. Chem. Phys. 41, 2818.
Han, W.H., Miyake, M., Nagai, T., Maeda, M., 2009. J. Alloys Compd. 481, 241.
Hayman, C., Comaskey, B., Eggert, J., Glaser, J., Ng, Ed, Paisner, J., Solarz, R., Worden, E., 1993. Laser Isotope Separation, vol. 1859. SPIE, Los Angeles, California, pp. 24–36.
Hegland, D.M., Legvold, S., Spedding, F.H., 1963. Phys. Rev. 131, 158.
Heltemes, E.C., Swenson, C.A., 1961. J. Chem. Phys. 35, 1264.
Herrick, C.C., 1964. J. Less Common Metals 7, 330.
Hill, R.W., 1991. Private Communication (August).
Hill, R.W., Gschneidner Jr., K.A., 1988. J. Phys. F Met. Phys. 18, 2545.
Hill, R.W., Cosier, J., Hukin, D.A., Wells, P., Lanchester, P.C., 1974. Phys. Lett. 49A, 101.
Hill, R.W., Cosier, J., Hukin, D.A., 1976. J. Phys. F Met. Phys. 6, 1731.
Hill, R.W., Cosier, J., Hukin, D.A., 1984. J. Phys. F Met. Phys. 14, 1267.
Hill, R.W., Collocott, S.J., Gschneidner Jr., K.A., Schmidt, F.A., 1987. J. Phys. F Met. Phys. 17, 1867.
Hoenig, C.L., Stout, N.D., Nordine, P.C., 1967. J. Am. Ceram. Soc. 50, 385.
Holley Jr., C.E., Huber Jr., E.J., Baker, F.B., 1968. Eyring, L. (Ed.), Progress in the Science and Technology of the Rare Earths, vol. 3. Pergamon Press, Oxford, pp. 343–433.
Holmström, B., Anderson, A.C., Krusius, M., 1969. Phys. Rev. 188, 888.
Hong-Ying, Zhao, Chang-Jian, Dai, Feng, Guan, 2009. J. Phys. B Atom. Mol. Opt. Phys. 42, Art. Nr. 065001 7pp.
Hounmann, J.G., Chapellier, M., Mackintosh, A.R., Bak, P., McMasters, O.D., Gschneidner Jr., K.A., 1975. Phys. Rev. Lett. 34, 587.
Hüfner, S., Wernick, J.H., 1968. Phys. Rev. 173, 448.
Hultgren, R., Desai, P.D., Hawkins, D.T., Gleiser, M., Kelley, K.K., Wagman, D.D., 1973. Selected Values of the Thermodynamic Properties of the Elements. American Society for Metals, Metals Park, OH.
Hurd, C.M., Alderson, J.E.A., 1973. Solid State Commun. 12, 375.
Ignatov, D.V., Lebedev, Yu.N., 1960. Prib. Tekh. Eksp. (6), 107.
Ignatov, D.V., Lebedev, Yu.N., 1961. Fiz. Khim. Osnovy Proizv. Stali, Akad. Nauk SSSR, Inst. Met. Tr 5-oi [Pyatoi], Konf., 1959, Moscow, pp. 305–310.
Ikeda, K., Gschneidner Jr., K.A., Takeshita, T., Jones, D.W., Farrant, S.P., 1985. Phys. Rev. B31, 5878.
Isaacs, L.L., 1973. Phys. Rev. B8, 3301.
Ivliev, A.D., Zinov'ev, V.E., 1981. Fiz. Tverd. Tela 23, 1190 (Sov. Phys. Solid State 23, 695–696).
Jackson, D.D., 1958. M.S. Thesis, University of Kansas.
Jackson, D.M., Trulson, O.C., Hudson, D.E., Spedding, F.H., 1961. Unpublished work quoted by Trulson et al. (1961).
Jaeger, F.M., Bottema, J.A., Rosenbohm, E., 1938. Rec. Trav. Chim. 57, 1137.
Jayasekharan, T., Razvi, M.A.N., Bhale, G.L., 1996. J. Opt. Soc. Am. B13, 641.
Jayasekharan, T., Razvi, M.A.N., Bhale, G.L., 2000a. J. Opt. Soc. Am. B17, 1607.
Jayasekharan, T., Razvi, M.A.N., Bhale, G.L., 2000b. J. Phys. B Atom. Mol. Opt. Phys. 33, 3123.
Jayasuriya, K.D., Campbell, S.J., Stewart, A.M., Gopal, E.S.R., 1983. J. Magn. Magn. Mater. 31–34, 1055.

Jayasuriya, K.D., Campbell, S.J., Stewart, A.M., Gopal, E.S.R., 1984. J. Phys. F Met. Phys. 14, 1725.
Jayasuriya, K.D., Campbell, S.J., Stewart, A.M., 1985a. J. Phys. F Met. Phys. 15, 225.
Jayasuriya, K.D., Campbell, S.J., Stewart, A.M., 1985b. Phys. Rev. B31, 6032.
Jayasuriya, K.D., Stewart, A.M., Campbell, S.J., 1986. Mater. Chem. Phys. 14, 525.
Jelinek, F.J., Gerstein, B.C., Griffel, M., Skochdopole, R.E., Spedding, F.H., 1966. Phys. Rev. 149, 489.
Jennings, L.D., 1960. Private Communication to Spedding et al. (1960b).
Jennings, L.D., Stanton, R.M., Spedding, F.H., 1957. J. Chem. Phys. 27, 909.
Jennings, L.D., Hill, E.D., Spedding, F.H., 1959. J. Chem. Phys. 31, 1240.
Jennings, L.D., Miller, R.E., Spedding, F.H., 1960. J. Chem. Phys. 33, 1849.
Jennings, L.D., Hill, E.D., Spedding, F.H., 1961. J. Chem. Phys. 34, 2082.
Jia, Liejuan, Jing, Chunyang, Zhou, Zhiyao, Lin, Fucheng, 1993. J. Opt. Soc. Am. B10, 1317.
Johansson, B., Rosengren, A., 1975. Phys. Rev. B11, 1367.
Johnson, D.L., 1966. Ph.D. Thesis, Iowa State University of Science and Technology, Ames, Iowa.
Johnson, D.A., 1974. J. Chem. Soc. Dalton Trans. 1671.
Johnson, D.L., Finnemore, D.K., 1967. Phys. Rev. 158, 376.
Johnson, R.G., Hudson, D.E., Caldwell, W.C., Spedding, F.H., Savage, W.R., 1956. J. Chem. Phys. 25, 917.
Kalvius, M., Keinle, P., Eicher, E., Weidemann, W., Schüler, C., 1963. Z. Phys. 172, 231.
Karelin, V.V., Nesmeyanov, An.N., Priselkov, Yu.A., 1962a. Dokl. Akad. Nauk SSSR 144, 352.
Karelin, V.V., Nesmeyanov, An.N., Priselkov, Yu.A., 1962b. Izv. Akad. Nauk SSSR, Otd. Met. i Topl. (Tekhn) (5), 117 (Russ. Metall. Fuels (5), 66).
Karelin, V.V., Nesmeyanov, An.N., Priselkov, Yu.A., Kun-Ying, Chou, 1962c. Vestn. Mosk. Univ. Ser. II Khim 17, 40.
Katerberg, J., Neimeyer, S., Penning, D., Zytfeld, J.B., 1975. J. Phys. F Met. Phys. 5, L74.
Kayser, F.X., 1970. Phys. Rev. Lett. 25, 662.
Khairulin, R.A., Stankus, S.V., 1989. Teplofiz. Vys. Temp. 27, 822.
Khim, J.-T., Yi, J., Rhee, Y., Lee, J., 2000. J. Kor. Phys. Soc. 37 (5), 701.
Kobayashi, S., Sano, N., Itoh, J., 1966. J. Phys. Soc. Jpn. 21, 1456.
Kobayashi, S., Sano, N., Itoh, J., 1967. J. Phys. Soc. Jpn. 22, 676.
Kolsky, H.G., Gilmer, R.M., Gilles, P.W., 1957. U.S. Atomic Energy Commission Rept. LA-2110.
Konings, R.J.M., Beneš, O., 2010. J. Phys. Chem. Ref. Data 39, Art. Nr. 043102 47pp.
Koskenmaki, D.C., Gschneidner Jr., K.A., 1978. Gschneidner Jr., K.A., Eyring, L. (Eds.), Handbook on the Physics and Chemistry of rare Earths, vol. 1. Metals, North Holland Publishing Co., Amsterdam, pp. 337–377.
Koskimaki, D.C., Gschneidner Jr., K.A., 1974. Phys. Rev. B10, 2055.
Koskimaki, D.C., Gschneidner Jr., K.A., 1975. Phys. Rev. B11, 4463.
Kovtun, G.P., Kruglykh, A.A., Pavlov, V.S., 1964. Ukr. Fiz. Zh. 9, 1089.
Kraftmakher, Ya.A., 1973. High Temp. High Pressures 5, 433.
Krikorian, O.H., 1963. J. Phys. Chem. 67, 1586.
Kröger, S., Tanriver, L., Kronfeldt, H.-D., Guthöhrlein, G., Behrens, H.-O., 1997a. Z. Phys. D41, 181.
Kröger, S., Wyart, J.-F., Luc, P., 1997b. Phys. Scr. 55, 579.

Kruglykh, A.A., Pavlov, V.S., 1965. Ukr. Fiz. Zh. 10, 1029.
Kruglykh, A.A., Pavlov, V.S., 1966. Izv. Akad. Nauk SSSR Metally 1, 178 (Russ. Metall. Metally (1), 103–113).
Kruglykh, A.A., Pavlov, V.S., Tikhinskii, G.F., 1964. Ukr. Fiz. Zh. 9, 214.
Kruglykh, A.A., Kovtun, G.P., Pavlov, V.S., 1965. Ukr. Fiz. Zh. 10, 432.
Krusius, M., Anderson, A.C., Holström, B., 1969. Phys. Rev. 177, 910.
Krusius, M., Pickett, G.R., Veuro, M.C., 1974. Solid State Commun. 14, 191.
Kulifeev, V.K., Stanolevich, G.P., Kozlov, V.G., 1971. Izv. Vyssh. Ucheb. Zaved. Tsvet. Met. 14 (1), 146.
Kuntz, L.K., Bautista, R.G., 1976. Met. Trans. B7, 107.
Kurichenko, A.A., Ivliev, A.D., Zinoviev, V.E., 1985. Solid State Commun. 56, 1065.
Kurichenko, A.A., Ivliev, A.D., Zinov'ev, V.E., 1986. Teplofiz. Vys. Temp. 24, 493 (High Temp. 24, 369–375).
Kurti, N., Safrata, R.S., 1958. Philos. Mag. 3, 780.
Lederman, F.L., Salamon, M.B., 1974. Solid State Commun. 15, 1373.
Legvold, S., Beaudry, B.J., Ostenson, J.E., Harmon, B.N., 1976. Solid State Commun. 21, 1061.
Legvold, F., Burgardt, P., Beaudry, B.J., Gschneidner Jr., K.A., 1977. Phys. Rev. B16, 2479.
Lindelof, P.E., Miller, I.E., Pickett, G.R., 1975. Phys. Rev. Lett. 35, 1297.
Lounasmaa, O.V., 1962a. Phys. Rev. 126, 1352.
Lounasmaa, O.V., 1962b. Phys. Rev. 128, 1136.
Lounasmaa, O.V., 1963. Phys. Rev. 129, 2460.
Lounasmaa, O.V., 1964a. Phys. Rev. A211–A218, 133.
Lounasmaa, O.V., 1964b. Phys. Rev. A219–A224, 133.
Lounasmaa, O.V., 1964c. Phys. Rev. A502–A509, 133.
Lounasmaa, O.V., 1964d. Phys. Rev. A1620–A1624, 134.
Lounasmaa, O.V., 1966. Phys. Rev. 143, 399.
Lounasmaa, O.V., Guenther, R.A., 1962a. Nachmann, J.F., Lundin, C.E. (Eds.), Proceedings of the Second Conference on Rare Earth Research, Glenwood Springs, Colorado, 24–27 September 1961. Gordon and Breach, New York, pp. 197–202.
Lounasmaa, O.V., Guenther, R.A., 1962b. Phys. Rev. 126, 1357.
Lounasmaa, O.V., Kalvius, G.M., 1967. Phys. Lett. 26A, 21.
Lounasmaa, O.V., Roach, P.R., 1962. Phys. Rev. 128, 622.
Lounasmaa, O.V., Sundström, L.J., 1966. Phys. Rev. 150, 399.
Lounasmaa, O.V., Sundström, L.J., 1967. Phys. Rev. 158, 591.
Lounasmaa, O.V., Veuro, M.C., 1972. Phys. Lett. 40A, 371.
Lundin, C.E., Yamamoto, A.S., 1967. U.S. Atomic Energy Commission Rept. DRI-2437.
Lyapunov, K.M., Bafinskii, A.V., Stankus, S.V., 2001. Zh. Fiz. Khim. 75, 831 (Russ. J. Phys. Chem. 75, 739–741).
Lyman, P., Scurlock, R.G., Wray, E.M., 1965. Daunt, J.G., Edwards, D.O., Milford, F.J., Yaqub, M. (Eds.), Proceedings of the IXth International Conference on Low Temperature Physics, Colombo, 1964. Plenum Press, New York p. 905.
Mackenzie, J.S., McCausland, M.A.H., Wagg, A.R., 1974. J. Phys. F Met. Phys. 4, 315.
Maeda, H., Mizuga, Y., Matsumoto, Y., Susuki, A., Takana, M., 1989. J. Phys. B Atom. Mol. Phys. L511–L516, 22.
Maezawa, K., Saito, Y., Wakabayashi, S., 1985. Jpn. J. Appl. Phys. 24, 28.
Mar, R.W., Bedford, R.G., 1980. J. Less Common Metals 71, 317.

Mardykin, I.P., Kashin, V.I., 1973. Izv. Akad. Nauk SSSR Metally 4, 77 (Russ. Metall. Metally (4), 59–61).
Mardykin, I.P., Vertman, A.A., 1972. Izv. Akad. Nauk SSSR Metally 1, 95 (Russ. Metall. Metally (1), 68–72).
Mardykin, I.P., Kashin, V.I., Vertman, A.A., 1972. Izv. Akad. Nauk SSSR Metally 6, 96 (Russ. Metall. Metally 6, 72–75).
Mardykin, I.P., Kashin, V.I., Sbitnev, P.P., 1973. Izv. Akad. Nauk SSSR Metally 6, 77 (Russ. Metall. Metally (6), 44–47).
Martin, W.C., Zalabas, R., Hagen, L., 1978. Atomic Energy Levels—The Rare-Earth Elements, Nat. Bur. Stand. Nat. Stand. Ref. Data Ser., NSRDS-NBS 60, U.S. Government Printing Office, Washington, DC.
McCausland, M.A.H., 1976. Private Communication quoted by Hill et al. 1976.
McCormack, J.M., Platt, P.R., Saxer, R.K., 1971. J. Chem. Eng. Data 16, 167.
McEwen, K.A., Cock, G.J., Roeland, L.W., Mackintosh, A.R., 1973. Phys. Rev. Lett. 30, 287.
McKeown, J.J., 1958. Ph.D. Thesis, Iowa State College, Iowa, USA.
Millhouse, A.H., McEwen, K.A., 1973. Phys. Rev. Lett. 30, 287.
Mito, M., Iriguchi, K., Taniguchi, Y., Kawase, M., Takagi, S., Deguchi, H., 2011. J. Phys. Soc. Jpn. 80, Art. Nr. 064707 5pp.
Miyabe, M., Wakaida, I., Arisawa, T., 1996. J. Phys. B Atom. Mol. Opt. Phys. 29, 4073.
Miyabe, M., Oba, M., Wakaida, I., 1998. J. Phys. B Atom. Mol. Opt. Phys. 31, 4559.
Mohr, P.J., Taylor, B.N., Newell, D.B., 2011. The 2010 CODATA Recommended Values of the Fundamental Physical Constants (Web Version 6.0). http://physics.nist.gov/constants. National Institute of Standards and Technology, Gaithersburg, MD 20899, USA
Montgomery, H., Pells, G.P., 1961. Proc. Phys. Soc. Lond. 78, 622.
Moore, C.E., 1971. Atomic Energy Levels, Nat. Bur. Stand. Nat. Stand. Ref. Data Ser., NSRDS-NBS 35, vol. II, U.S. Government Printing Office, Washington, DC.
Morin, F.J., Maita, J.P., 1963. Phys. Rev. 129, 1115.
Morss, L.R., 1976. Chem. Rev. 76, 827.
Nachman, J.F., Lundin, C.E., Yamamoto, A.S., 1962. Nachman, J.F., Lundin, C.E. (Eds.), Proceedings of the Second International Conference on Rare Earth Research, Glenwood Springs, Colorado, 24–27 September 1961. Gordon and Breach, New York, London, pp. 163–173.
Nachman, J.F., Lundin, C.E., Yamamoto, A.S., 1963. Aeronautical Research Laboratories, Office of Aerospace Research, U.S. Air Force Report ARL-63-15.
Nakhate, S.G., Razvi, M.A.N., Bale, G.L., Ahmad, S.A., 1996. J. Phys. B Atom. Mol. Opt. Phys. 29, 1439.
Nakhate, S.G., Razvi, M.A.N., Ahmad, S.A., 2000a. J. Phys. B Atom. Mol. Opt. Phys. 33, 191.
Nakhate, S.G., Razvi, M.A.N., Connerade, J.P., Ahmad, S.A., 2000b. J. Phys. B Atom. Mol. Opt. Phys. 33, 5191.
Nave, G., 2005. Private Communication (2000) to Sansonetti, J.E., Martin, W.C., J. Phys. Chem. Ref. Data 34, 1559–2259.
Nave, G., Griesmann, U., 2000. Phys. Scr. 62, 463.
Nesmeyanov, A.N., Priselkov, Yu.A., Karelin, V.V., 1962. Proceedings of a Symposium on Thermodynamics of Nuclear Materials, IAEA, Vienna, 21–25 May 1962. IAEA, Vienna.
Nighat, Y., Raith, M., Hussain, M., Windholz, L., 2010. J. Phys. B Atm. Mol. Opt. Phys. 43, Art. Nr. 125001 10pp.
Nikitin, S.A., Tishin, A.M., Savenchenkova, S.F., Spichkin, Yu.I., Chistykov, O.D., Red'ko, S.V., Nesterov, Yu.A., 1991. J. Magn. Magn. Mater. 96, 26.

Novikov, I.I., Mardykin, I.P., 1973. Teplofiz. Vys. Temp. 11, 527 (High Temp. 11, 472–476).
Novikov, I.I., Mardykin, I.P., 1974. Atom. Energ. 37, 348.
Novikov, I.I., Mardykin, I.P., 1975. Teplofiz. Vys. Temp. 13, 318 (High Temp. 13, 293–297).
Novikov, I.I., Mardykin, I.P., 1976. Izv. Akad. Nauk SSSR Metally 1, 27 (Russ. Metall. Metally (1), 27–30).
Novikov, I.I., Filippov, L.P., Kostyukov, V.I., 1977. Atom. Energ. 43, 300.
Novikov, I.I., Kostyukin, V.I., Filippov, L.P., 1978. Izv. Akad. Nauk SSSR Metally 4, 89 (Russ. Metall. Metally (4), 65–69).
Ohtsuka, T., Sato, J., 1966. Ann. Acad. Sci. Fenn. Ser. A6 (210), 92.
Palmer, B.A., 1977. Ph.D. Thesis, Purdue University, West Lafayette, Indiana.
Palmer, S.B., 1978, Private Communication (1977) to Sundström, L.J. in Gschneidner Jr., K.A., Eyring, L. (Eds.), Handbook on the Physics and Chemistry of the Rare Earths, Vol. 1: Metals. North Holland Publishing Co., Amsterdam, pp. 379–410.
Palmer, S.B., Lee, E.W., 1972. Proc. R. Soc. Lond. A 327, 519.
Pan, P.H., Finnemore, D.K., Bevolo, A.J., Shanks, H.R., Beaudry, B.J., Schmidt, F.A., Danielson, G.C., 1980. Phys. Rev. B 21, 2809.
Panousis, N.T., Gschneidner Jr., K.A., 1970. Solid State Commun. 8, 1779.
Parkinson, D.H., Roberts, L.M., 1957. Proc. Phys. Soc. B70, 471.
Parkinson, D.H., Simon, F.E., Spedding, F.H., 1951. Proc. R. Soc. Lond. A 207, 137.
Parks, R.D., 1962. Nachmann, J.F., Lundin, C.E. (Eds.), Proceedings of the Second Conference on Rare Earth Research, Glenwood Springs, Colorado, 24–27 September 1961. Gordon and Breach, New York, pp. 225–232.
Pecharsky, V.K., 2006. Private Communication (April) Pecharsky, V.K., Gschneidner Jr., K.A., Fort, D., 1993. Phys. Rev. B47, 5063–5071.
Pecharsky, V.K., Gschneidner Jr., K.A., Fort, D., 1993. Phys. Rev. 5063–5071, B47.
Pecharsky, V.K., Gschneidner Jr., K.A., Fort, D., 1996. Scr. Mater. 35, 843.
Peterson, D.T., Colburn, R.P., 1966. J. Phys. Chem. 70, 468.
Peterson, D.T., Fattore, V.G., 1961. J. Phys. Chem. 65, 2062.
Phillips, N.E., Ho, J.C., Smith, T.F., 1968. Phys. Lett. A27, 49.
Pleschiutschnig, J., Blaschko, O., Reichardt, W., 1991. Phys. Rev. B44, 6794.
Polovov, V.M., 1973. Zh. Eksp. Teor. Fiz. 65, 1557 (Sov. Phys. JETP 38, 775–778).
Polovov, V.M., Maĭstrenko, L.G., 1975. Zh. Eksp. Teor. Fiz. 68, 1418 (Sov. Phys. JETP 41, 707–709).
Polyachenko, O.G., Novikov, G.I., 1963a. Zh. Obshch. Khim. 33, 2796.
Polyachenko, O.G., Novikov, G.I., 1963b. Zh. Neorgan. Khim. 8, 2631 (Russ. J. Inorg. Chem. 8, 1378–1381).
Postma, H., Marshak, H., Sailor, V.I., Shore, F.J., Reynolds, C.A., 1962. Phys. Rev. 126, 979.
Pozdeyev, A.N., Ivliyev, A.D., Kurichenko, A.A., Rivman, Ye.Z., Moreva, N.I., 1990. Fiz. Metal. Metalloved. 9, 85 (Phys. Met. Metall. 70(3), 83–88).
Ralchenko, Yu, Kraminda, A.E., Reader, J., the NIST ASD Team, 2012. NIST Atomic Spectra Database (ver. 4.1.0). http://physics.nist.gov/asd3, National Institute for Standards and Technology, Gaithersberg, MD, USA
Rao, R.R., Narayana Murty, J.V.S.S., 1978. J. Low Temp. Phys. 33, 413.
Roberts, L.M., 1957. Proc. Phys. Soc. Lond. 70B, 434.
Rosen, M., 1967. Phys. Rev. Lett. 19, 695.
Rosen, M., 1968a. Phys. Rev. 166, 561.
Rosen, M., 1968b. Phys. Rev. 174, 504.
Rosen, M., 1971. J. Phys. Chem. Solids 32, 2351.

Rosen, M., Klimker, H., 1970. Phys. Rev. 1, 3748.
Rosen, M., Kalir, D., Klimker, H., 1974. J. Phys. Chem. Solids 35, 1333.
Ruczkowski, J., Stachowska, E., Elantkowski, M., Guthöhrlein, G.H., Dembczyński, J., 2003. Phys. Scr. 68, 133.
Sailor, V.L., Schermer, R.I., Shore, F.J., Reynolds, C.A., Marshak, H., Postma, H., 1962. Phys. Rev. 127, 1124.
Sano, N., Itoh, J., 1972. J. Phys. Soc. Jpn. 32, 95.
Sano, N., Kobayashi, S., Itoh, I., 1970. Prog. Theor. Phys. (Suppl. 46), 84.
Sano, N., Teraoka, M., Shimizu, K., Itoh, J., 1972. J. Phys. Soc. Jpn. 32, 571.
Satoh, J., Ohtsuka, T., 1966. Phys. Lett. 20, 565.
Satoh, J., Ohtsuka, T., 1967. J. Phys. Soc. Jpn. 23, 9.
Savage, W.E., Hudson, D.E., Spedding, F.H., 1959. J. Chem. Phys. 30, 221.
Savitskii, Ye.M., Terekhova, V.F., Naumkin, O.P., 1960. Tsvet. Met. 1, 43 (Sov. J. Non-Ferrous Metals (1), 63–70).
Schmitzer, C., Hilscher, G., Vajda, P., Daou, J.N., 1987. J. Phys. F Met. Phys. 17, 865.
Scott, T.E., 1978. Gschneidner Jr., K.A., Eyring, L. (Eds.), Handbook of the Physics and Chemistry of Rare Earths, vol. 1. Metals, North Holland Publishing Co., Amsterdam, pp. 591–705.
Shamim, K., Siddiqui, I., Windolz, L., 2011. Eur. Phys. J. D64, 209.
Shen, Huasen, 1994. Ph.D. Thesis, Department of Materials Science and Engineering, University of Science and Technology, Beijing, Peoples Republic of China.
Shen, Huasen, Zhang, Weijing, Liu, Guoquan, Wang, Run, Du, Zhenmin, 1995. Rept. F-95–03, Research Group on Phase Equilibria in Materials, Department of Materials Science and Engineering, University of Science and Technology, Beijing, Peoples Republic of China
Shevchenko, V.G., Kononenko, V.L., Sukhman, A.L., 1978. Zh. Fiz. Khim. 52, 1867 (Russ. J. Phys. Chem. 52, 1084–1086).
Shoji, Y., Matsui, T., Nakamura, K., Inoue, T., 1997. J. Nucl. Mater. 247, 37.
Shoji, Y., Matsui, T., Nakamura, K., Inoue, T., 1998. J. Nucl. Mater. 254, 9.
Sinha, S.K., Brun, T.O., Muhlestein, L.P., Sakurai, J., 1970. Phys. Rev. B1, 2430.
Sirota, N.N., Kudel'ko, Zh.M., 1973. Dokl. Akad. Nauk SSSR 209, 1068 (Sov. Phys. Doklady 18, 243–244).
Sirota, N.N., Tomilo, Zh.M., 1982. Dokl. Akad. Nauk Belloruss. 26, 405.
Sirota, N.N., Tomilo, Zh.M., Kofman, N.A., 1983. Vopr. At. Nauki i Tekh.Obshchaya Yad. Fiz 2 (23), 66.
Skochdopole, R.E., Griffel, M., Spedding, F.H., 1955. J. Chem. Phys. 23, 2258.
Spedding, F.H., Daane, A.H., 1954. J. Metals 6, 504.
Spedding, F.H., Miller, C.F., 1951. U.S. Atomic Energy Commission, Iowa State College Rept. ISC-167, pp. 95–131.
Spedding, F.H., Barton, R.J., Daane, A.H., 1957. J. Am. Chem. Soc. 79, 5160.
Spedding, F.H., Hanak, J.J., Daane, A.H., 1958. Trans. Met. Soc. AIME 212, 379.
Spedding, F.H., Daane, A.H., Wakefield, G., Dennison, D.H., 1960a. Trans. Met. Soc. AIME 218, 608.
Spedding, F.H., McKeown, J.J., Daane, A.H., 1960b. J. Phys. Chem. 64, 289.
Spedding, F.H., Hanak, J.J., Daane, A.H., 1961. J. Less Common Metals 3, 110.
Spedding, F.H., Sanden, B., Beaudry, B.J., 1973. J. Less Common Metals 31, 1.
Stankus, S.V., Basin A.S., 1980. Fazovie Perekhodi v Chistkh Metallakh I Binarnikh Splavakh (Phase Transitions in Pure Metals and Alloys) Izd. Nauk (Siborskoe Otdelenie), Akad. Nauk SSSR, Novosibirsk Stankus, S.V., Khairlin, R.A., 1987, Teplofiz. Vys. Temp. 25, 274–278 (High Temp. 25, 195–199).

Stankus, S.V., Khairulin, R.A., 1987. Teplofiz. Vys. Temp. 25, 274 (High Temp., 25, 195–199).
Stankus, S.V., Khairulin, R.A., 1991. Russ. J. Eng. Thermophys. 1, 193.
Stankus, S.V., Tyagel'skii, P.V., 2000. Teplofiz. Vys. Temp. 38, 579 (High Temp. 38, 555–559).
Stankus, S.V., Tyagel'sky, P.V., Baginskii, A.V., Lyapov, L.M., 1995. High Temp. High Pressures 27/28, 485.
Stanton, R.M., Jennings, L.D., Spedding, F.H., 1960. J. Chem. Phys. 32, 530.
Stein, R.L., Butera, R.A., 1970. J. Solid State Chem. 2, 503.
Steinitz, M.O., Kahrizi, M., Tindall, D.A., Åström, H.U., Benediktsson, G., 1987. Phys. Rev. B35, 8747.
Stevens, W.N.R., Beaudry, B.J., Spedding, F.H., 1971. Private Communication quoted by Thome et al. (1978).
Stewart, A.M., Collocott, S.J., 1989. J. Phys. Condens. Matter 1, 677.
Stretz, L.A., 1973. Ph.D. Thesis, Iowa State University, Iowa.
Stretz, L.A., Bautista, R.G., 1974. Metall. Trans. 5, 921.
Stretz, L.A., Bautista, R.G., 1975a. J. Chem. Thermodyn. 7, 83.
Stretz, L.A., Bautista, R.G., 1975b. High Temp. Sci. 7, 197.
Stretz, L.A., Bautista, R.G., 1976. J. Chem. Eng. Data 21, 13.
Stull, D.R., Sinke, G.C., 1956. Thermodynamic Properties of the Elements, Advances in Chemistry Series No. 18. American Chemical Society, Washington.
Suganeyev, Yu.S., Taubin, M.L., Yakutovich, M.V., 1970. Izv. Akad. Nauk SSSR Metally 6, 215 (Russ. Metall. Metally (6), 139–141).
Swenson, C.A., 1996. Phys. Rev. B53, 3669.
Syed, T.I., Siddiqui, I., Shamim, K., Uddin, Z., Guthöhrlein, G.H., Windholz, L., 2011. Phys. Scr. 84, Art. Nr. 065303 12pp.
Szabadvary, F., 1988. Gschneidner Jr., K.A., Eyring, L. (Eds.), Handbook of the Physics and Chemistry of Rare Earths, vol. 11. North Holland Publishing Co. (Elsevier Science Publishers B.V), Amsterdam, pp. 33–80.
Taylor, W.A., Levy, M.B., Spedding, F.H., 1978. J. Phys. F Metal Phys. 8, 2293.
Teaney, D.T., Moruzzi, V.L., 1967. Bull. Am. Phys. Soc. 12, 134.
Ten Cate, J., Zwart, J., Van Zytfeld, J.B., 1980. J. Phys. F Met. Phys. 10, 669.
Thome, D.K., Gschneidner Jr., K.A., Mowry, G.S., Smith, J.F., 1978. Solid State Commun. 25, 297.
Thompson, P.W., Campbell, S.J., Chaplin, D.H., Edge, A.V.J., 1992. J. Magn. Magn. Mater. 104–107, 1503.
Tonnies, J.J., Gschneidner Jr., K.A., Spedding, F.H., 1971. J. Appl. Phys. 42, 3275.
Trulson, O.C., Hudson, D.E., Spedding, F.H., 1961. J. Chem. Phys. 35, 1018.
Tsang, T.W.E., Gschneidner Jr., K.A., Koskenmaki, D.C., Moorman, K.O., 1976a. Phys. Rev. B14, 4447.
Tsang, T.W.E., Gschneidner Jr., K.A., Schmidt, F.A., 1976b. Solid State Commun. 20, 737.
Tsang, T.W.E., Gschneidner Jr., K.A., Schmidt, F.A., Thome, D.K., 1985. Phys. Rev. B31, 235.
Van Kempen, H., Miedema, A.R., Huiskamp, W.J., 1964. Physica 30, 229.
Vedinikov, M.V., Burkov, A.T., Dvunitkin, V.G., Moreva, N.I., 1974. Phys. Lett. 48A, 293.
Vedinikov, M.V., Burkov, A.T., Dvunitkin, V.G., Moreva, N.I., 1977. J. Less Common Metals 52, 221.
Vergès, J., Wyart, J.-F., 1978. Phys. Scr. 17, 495.
Verhaegen, G., Smoes, S., Drowart, J., 1965. Wright Patterson Air Force Base, Ohio, Tech. Rept. WADD-TR-60-786, Part XXVIII.

Wakefield, G.F., Daane, A.H., Spedding, F.H., 1967. J. Chem. Phys. 47, 4994.
Ward, J.W., Hill, H.H., 1976. Müller, W., Blank, H. (Eds.), Heavy Element Properties. Proceedings of the Joint Session, Baden-Baden, 13 September 1975, 4th International Transplutonium Element Symposium, 5th International Conference on Plutonium and Other Actinides. North Holland Publishing Co., Amsterdam, pp. 65–79.
Watson, B., Ali, N., 1995. J. Phys. Condens. Matter 7, 4713.
Weir, R.D., Goldberg, R.N., 1996. J. Chem. Thermodyn. 28, 261.
Weller, W.W., Kelley, K.K., 1962. U.S. Bureau of Mines Rept. of Investigation 5984.
Wells, P., Lanchester, P.C., Jones, D.W., Jordan, R.G., 1974. J. Phys. F Met. Phys. 4, 1729.
Wells, P., Lanchester, P.C., Jones, D.W., Jordan, R.G., 1976. J. Phys. F Met. Phys. 6, 11.
Welty, J.R., Wicks, C.E., Boren, H.O., 1963. U.S. Bur. Mines Rept. Invest. 6155.
White, G.K., 1989. J. Phys. Condens. Matter 1, 677.
White, D., Walsh, P.N., Goldstein, H.W., Dever, D.F., 1961. J. Phys. Chem. 65, 1404.
Wieser, M.E., Coplen, T.B., 2011. Pure Appl. Chem. 83, 359.
Wilkinson, M.K., Koehler, W.C., Wollan, E.O., Cable, J.W., 1961. J. Appl. Phys. 32, S48.
Willis, F., Ali, N., 1992. J. Alloys Compd. 181, 287.
Wyart, J.-F., 1985. Phys. Scr. 32, 58.
Wyart, J.-F., Camus, P., 1979. Phys. Scr. 20, 43.
Wyart, J.-F., Camus, P., Vergès, J., 1977. Physica B + C 92, 377.
Xie, Jun, Dai, Chang-Jain, Li, Ming, 2011. J. Phys. B Atom. Mol. Opt. Phys. 44, Art. Nr. 015002 5pp.
Yamamoto, A.S., Lundin, C.E., Nachman, J.F., 1965. Eyring, L. (Ed.), Proceedings of the Fourth Conference on Rare Earth Research, Phoenix, Arizona, 22–25 April 1964. Gordon and Breach, New York and London, pp. 203–214.
Yao, Y.D., Ho, L.T., Young, C.Y., 1980. J. Less Common Metals 69, 355.
Ying, Xiao, Chang-Jian, Dai, Wen-Jie, Qin, 2009. Chin. Phys. B18, 4251.
Ying, Xiao, Chang-Jian, Dai, Wen-Jie, Qin, 2010. Chin. Phys. B19, Art. Nr. 063202 7pp.
Zaitsev, A.I., Mogutnov, B.M., 1988. High Temp. Sci. 28, 331.
Zaitsev, A.I., Priselkov, Yu.A., Nesmeyanov, An.N., 1982. Teplofiz. Vys. Temp. 20, 781.
Zaitsev, A.I., Priselkov, Yu.A., Khandamirova, N.E., 1989. Teplofiz. Vys. Temp. 27, 683 (High Temp. 27, 536–540).
Zh-Ming, Li, Feng-rong, Zhu, Zi-bin, Zhang, Li-hua, Zhai, Xiang-jun, Ren, Deng, Hu, Li-xing, Zhang, Fedoseev, V.N., 2002. Guangpuxue Yu Gangpu Fenxi (Spectrosc. Spectr. Anal.) 22, 709.
Zinov'ev, V.E., Gel'd, P.V., Sokolov, A.L., 1975. Fiz. Tverd. Tela 17, 413.
Zinov'ev, V.E., Gel'd, P.V., Sokolov, A.L., 1976. Fiz. Tverd. Tela 18, 1329.
Zochowski, S., McEwen, L.A., 1986. J. Magn. Magn. Mater. 54–57, 515.

Intentionally left as blank

Author Index

Note: Page numbers followed by "*f*" indicate figures, and "*t*" indicate tables.

C

D

E

F

G

H

I

J

K

L

M

N

O

P

Q

R

S

T

U

V

W

X

Y

Z

Subject Index

Note: Page numbers followed by "*f*" indicate figures, and "*t*" indicate tables.

E

M

N

O

P

Q

R

S

T

Intentionally left as blank